AD-A099 917 MICHIGAN UNIV ANN ARBOR COLL OF ENGINEERING F/G 5/2
PRELIMINARY REPORTS, MEMORANDA AND TECHNICAL NOTES OF THE MATER--ETC(U)
JUL 80 M J SINNOTT MDA903-80-C-0505
UNCLASSIFIED 018324 NL

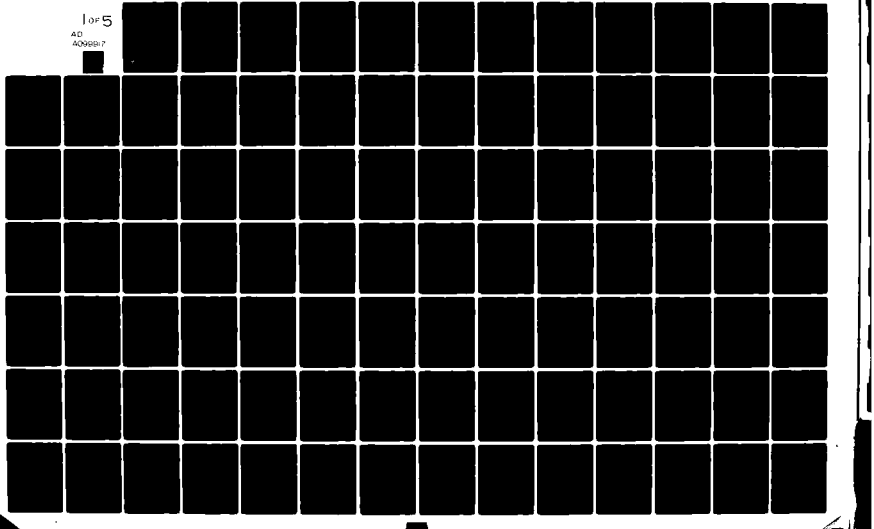

Preliminary Reports, Memoranda and Technical Notes of the Materials Research Council Summer Conference

La Jolla, California

July 1980

Sponsored by
Defense Advanced Research Projects Agency
ARPA Order No. 4000

Department of Materials and Metallurgical Engineering

Preliminary Reports, Memoranda and Technical Notes of the Materials Research Council Summer Conference

La Jolla, California

July 1980

Sponsored by
Defense Advanced Research Projects Agency
ARPA Order No. 4000

Department of Materials and Metallurgical Engineering

(14) ϕ16324

(12) 451

(1) C

(1)

PRELIMINARY REPORTS, MEMORANDA AND TECHNICAL NOTES

of the

MATERIALS RESEARCH COUNCIL SUMMER CONFERENCE

La Jolla, California .

(11) July 80

DARPA Order Number: 4000
Program Code Number: 0D10
Contractor: The Regents of The University of Michigan
Effective Date of Contract: 10 June 1980
Contract Expiration Date: 9 June 1981
Amount of Contract: $346,780
Contract Number: MDA903-80-C-0505
Principal Investigator: Associate Dean Maurice J. Sinnott
College of Engineering
The University of Michigan
Ann Arbor, Michigan 48109
(313) 763-0242

(10)

(15)

AD A100350

(14) ϕ16324

(12) 451

(1) C

(1)

PRELIMINARY REPORTS, MEMORANDA AND TECHNICAL NOTES

of the

MATERIALS RESEARCH COUNCIL SUMMER CONFERENCE

La Jolla, California .

(11) July 80

DARPA Order Number: 4000
Program Code Number: 0D10
Contractor: The Regents of The University of Michigan
Effective Date of Contract: 10 June 1980
Contract Expiration Date: 9 June 1981
Amount of Contract: $346,780
Contract Number: MDA903-80-C-0505
Principal Investigator: Associate Dean Maurice J. Sinnott
College of Engineering
The University of Michigan
Ann Arbor, Michigan 48109
(313) 763-0242

(10)

(15)

AD A100350

The views and conclusions contained in this document are those of the authors and should not be interpreted as necessarily representing the official policies, either expressed or implied, of the Defense Advanced Research Projects Agency or the U.S. Government.

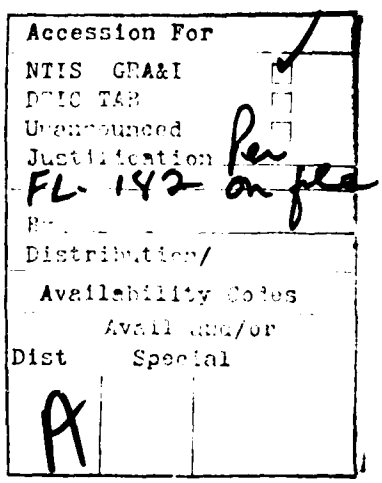

The views and conclusions contained in this document are those of the authors and should not be interpreted as necessarily representing the official policies, either expressed or implied, of the Defense Advanced Research Projects Agency or the U.S. Government.

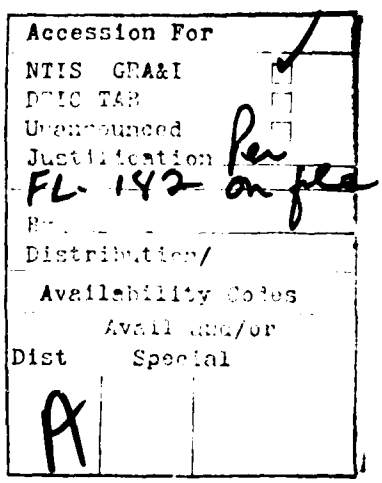

TABLE OF CONTENTS

TABLE OF CONTENTS

Steering Committee

Professor Henry Ehrenreich
Secretary of the Steering Committee
Pierce Hall
Harvard University
Cambridge, Massachusetts 02138

Professor Robert L. Coble
Materials Science Department
Massachusetts Institute of Technology
Cambridge, Massachusetts 02139

Dean Daniel C. Drucker
College of Engineering
University of Illinois
Urbana, Illinois 61801

Professor Anthony G. Evans
University of California
Lawrence Berkeley Laboratories
1 Cyclotron Road
Berkeley, California 94720

Professor Willis H. Flygare
School of Chemical Sciences
University of Illinois
Urbana, Illinois 61801

Professor Paul L. Richards
Department of Physics
University of California
Berkeley, California 94720

Professor Amnon Yariv
Electrical Engineering Department
California Institute of Technology
Pasadena, California 91125

Project Director

Associate Dean Maurice J. Sinnott
College of Engineering
The University of Michigan
Ann Arbor, Michigan 48109

Steering Committee

Professor Henry Ehrenreich
Secretary of the Steering Committee
Pierce Hall
Harvard University
Cambridge, Massachusetts 02138

Professor Robert L. Coble
Materials Science Department
Massachusetts Institute of Technology
Cambridge, Massachusetts 02139

Dean Daniel C. Drucker
College of Engineering
University of Illinois
Urbana, Illinois 61801

Professor Anthony G. Evans
University of California
Lawrence Berkeley Laboratories
1 Cyclotron Road
Berkeley, California 94720

Professor Willis H. Flygare
School of Chemical Sciences
University of Illinois
Urbana, Illinois 61801

Professor Paul L. Richards
Department of Physics
University of California
Berkeley, California 94720

Professor Amnon Yariv
Electrical Engineering Department
California Institute of Technology
Pasadena, California 91125

Project Director

Associate Dean Maurice J. Sinnott
College of Engineering
The University of Michigan
Ann Arbor, Michigan 48109

Members

Professor Nico Bloembergen
Division of Engineering & Applied Physics
Harvard University
Cambridge, Massachusetts 02138

Professor Bernard Budiansky
Division of Applied Sciences
Harvard University
Cambridge, Massachusetts 02138

Professor Brice Carnahan
Department of Chemical Engineering
The University of Michigan
Ann Arbor, Michigan 48109

Professor L. Eric Cross
Electrical Engineering
Pennsylvania State University
University Park, Pennsylvania 16802

Dr. John J. Gilman, Mgr. Corp. Res.
Standard Oil Company (Indiana)
Standard Oil Research Center
Naperville, Illinois 60540

Professor Robert Gomer
James Franck Institute
University of Chicago
Chicago, Illinois 60637

Professor Alan J. Heeger
Department of Physics/El
University of Pennsylvania
Philadelphia, Pennsylvania 19104

Professor John P. Hirth
Metallurgical Engineering Department
Ohio State University
Columbus, Ohio 43201

Professor Edward E. Hucke
Materials & Metallurgical Engineering Department
The University of Michigan
Ann Arbor, Michigan 48109

Professor John W. Hutchinson
Division of Applied Sciences
Harvard University
Cambridge, Massachusetts 02138

Professor Gordon S. Kino
Ginzton Laboratory
Stanford University
Stanford, California 94305

Professor Walter Kohn
Department of Physics
University of California
Santa Barbara, California 93106

Professor James A. Krumhansl
Department of Physics
Clark Hall
Cornell University
Ithaca, New York 14850

Dr. John L. Margrave, Vice President
Advanced Studies and Research
Rice University
Houston, Texas 77001

Professor Frank A. McClintock
Department of Mechanical Engineering
Massachusetts Institute of Technology
Cambridge, Massachusetts 02139

Professor Thomas C. McGill
California Institute of Technology
Pasadena, California 91125

Professor Elliott W. Montroll
Department of Physics
University of Maryland
College Park, Maryland 20740

Professor Howard Reiss
Department of Chemistry
University of California
Los Angeles, California 90024

Professor James R. Rice
Division of Engineering
Brown University
Providence, Rhode Island 02912

Dr. Robb M. Thomson
National Bureau of Standards
Center for Materials Science
Washington, D.C. 20234

Dr. Geoge H. Vineyard
Brookhaven National Laboratory
Upton, Long Island, New York 11973

Professor Gordon S. Kino
Ginzton Laboratory
Stanford University
Stanford, California 94305

Professor Walter Kohn
Department of Physics
University of California
Santa Barbara, California 93106

Professor James A. Krumhansl
Department of Physics
Clark Hall
Cornell University
Ithaca, New York 14850

Dr. John L. Margrave, Vice President
Advanced Studies and Research
Rice University
Houston, Texas 77001

Professor Frank A. McClintock
Department of Mechanical Engineering
Massachusetts Institute of Technology
Cambridge, Massachusetts 02139

Professor Thomas C. McGill
California Institute of Technology
Pasadena, California 91125

Professor Elliott W. Montroll
Department of Physics
University of Maryland
College Park, Maryland 20740

Professor Howard Reiss
Department of Chemistry
University of California
Los Angeles, California 90024

Professor James R. Rice
Division of Engineering
Brown University
Providence, Rhode Island 02912

Dr. Robb M. Thomson
National Bureau of Standards
Center for Materials Science
Washington, D.C. 20234

Dr. Geoge H. Vineyard
Brookhaven National Laboratory
Upton, Long Island, New York 11973

GUEST CONSULTANTS

Attwell M. Adair
AFWAL Materials Lab.
AFWAL/MLLM
Wright-Patterson AFB
Ohio 45433

Diran Apelian
Materials Engineering
Drexel University
Philadelphia, PA 19104

Ali S. Argon
Room 1-306
Massachusetts Inst. Tech.
Cambridge, MA 02139

Roy Athey
Pratt & Whitney Aircraft
P.O. Box 2691
West Palm Beach, FL 33402

Frederic A. Bick
Effects Technology, Inc.
5383 Hollister
Santa Barbara, CA 93111

Rubin Braunstein
Physics Department
University of California
Los Angeles, CA 90272

J. D. Buch
Aerospace Corporation
A6-1437
El Segundo, CA

Roland M. Cannon, Jr.
Ceramics Dept.
Massachusetts Inst. Tech.
Cambridge, MA 02139

John M. Carlyle
Naval Air Development Center
Code 60633
Warminster, PA 18974

Kenneth M. Case
Rockeffer University
Tower 1420
New York, NY 10021

Jeff T. Cheung
Rockwell International
1049 Camino Dos Rios
Thousand Oaks, CA 91360

John D. Clark
RD-2 Green Pond Road
Newfoundland, NJ 07435

Arthur R. Cox
Pratt & Whitney Aircraft
P.O. Box 2691
West Palm Beach, FL 33403

Thomas R. Dashiell
Department of Defense
The Pentagon, Room 3D129
Washington, D.C. 20301

Bruce E. Deal
Fairchild Camera & Instrument
Research & Development
Palo Alto, CA 94304

G. J. Dienes
Brookhaven National Lab.
Upton, NY 11973

Robert J. Duffy
General Electric Company
1000 Western Avenue
Lynn, MA 01901

Walter P. Eatherly
Oak Ridge National Lab.
Bldg. 4508
Oak Ridge, TN 37830

Philip Eckman
U.S. Government

Davis M. Egle
University of Oklahoma
865 Asp Street, Rm. 212
Norman, OK 73019

Donald Eitzen
National Bureau of Standards
Sound A147
Washington, D.C. 20234

GUEST CONSULTANTS

Attwell M. Adair
AFWAL Materials Lab.
AFWAL/MLLM
Wright-Patterson AFB
Ohio 45433

Diran Apelian
Materials Engineering
Drexel University
Philadelphia, PA 19104

Ali S. Argon
Room 1-306
Massachusetts Inst. Tech.
Cambridge, MA 02139

Roy Athey
Pratt & Whitney Aircraft
P.O. Box 2691
West Palm Beach, FL 33402

Frederic A. Bick
Effects Technology, Inc.
5383 Hollister
Santa Barbara, CA 93111

Rubin Braunstein
Physics Department
University of California
Los Angeles, CA 90272

J. D. Buch
Aerospace Corporation
A6-1437
El Segundo, CA

Roland M. Cannon, Jr.
Ceramics Dept.
Massachusetts Inst. Tech.
Cambridge, MA 02139

John M. Carlyle
Naval Air Development Center
Code 60633
Warminster, PA 18974

Kenneth M. Case
Rockeffer University
Tower 1420
New York, NY 10021

Jeff T. Cheung
Rockwell International
1049 Camino Dos Rios
Thousand Oaks, CA 91360

John D. Clark
RD-2 Green Pond Road
Newfoundland, NJ 07435

Arthur R. Cox
Pratt & Whitney Aircraft
P.O. Box 2691
West Palm Beach, FL 33403

Thomas R. Dashiell
Department of Defense
The Pentagon, Room 3D129
Washington, D.C. 20301

Bruce E. Deal
Fairchild Camera & Instrument
Research & Development
Palo Alto, CA 94304

G. J. Dienes
Brookhaven National Lab.
Upton, NY 11973

Robert J. Duffy
General Electric Company
1000 Western Avenue
Lynn, MA 01901

Walter P. Eatherly
Oak Ridge National Lab.
Bldg. 4508
Oak Ridge, TN 37830

Philip Eckman
U.S. Government

Davis M. Egle
University of Oklahoma
865 Asp Street, Rm. 212
Norman, OK 73019

Donald Eitzen
National Bureau of Standards
Sound A147
Washington, D.C. 20234

Katherine T. Faber
University of California
240 Hearst Mining Bldg.
Berkeley, CA 94720

Brennan A. Forcht
Vought Corporation
P.O. Box 5907
Dallas, TX 75222

Anthony H. Francis
University of Michigan
3028 Chemistry Bldg.
Ann Arbor, MI 48109

Ed Fuller
National Bureau of Standards
Room A113, Bldg. 223
Washington, DC 20234

J. J. Gebhardt
General Electric
Room U7025
Box 8555
Philadelphia, PA 19101

Lloyd J. Graham
Rockwell Science Center
1049 Camino Dos Rios
Thousand Oaks, CA 91360

Nicholas J. Grant
Materials Science & Engineering
Massachusetts Institute of Tech.
Room 8-305
Cambridge, MA 02139

A. Brunbaum
University of California
823 Evans
Berkeley, CA 94720

C. S. Harden
Chem. Systems Lab.
Bldg. E3330
Aberdeen Proving Ground, MD 21010

Edward W. Hart
Cornell University
Bard Hall
Ithaca, NY 14853

George Herrmann
Stanford University
Durand Building
Stanford, CA 94305

Robert A. Holzl
San Fernando Laboratories
10258 Norris Av.
Pacoima, CA 91011

Bill Hoover
University of California
Hertz Hall
Livermore, CA 94550

P. H. Hutton
Battelle Northwest
Box 999
Richland, WA 99352

Eugene A. Irene
IBM Thomas J. Watson Lab.
Box 218
Yorktown Heights, NY 10598

Loren A. Jacobson
US Air Force Systems Command
AFSC/DLF
Andrews AFB, DC 20334

Robert A. Johnson
University of Virginia
B225 Thornton Hall
Charlottesville, VA 22901

Ronald Kerans
Air Force Wright Aero Labs/ML
AFWAL/MLLM
Wright-Patterson AFB OH 45433

Marlin A. Kinna
Naval Sea Systems Command
SEA-62R4
Washington, DC 20360

Gerald E. Kovalenko
Naval Air Systems Command
Jefferson Davis Highway
Washington, DC

Kenneth A. Kreiss
Central Intelligence Agency
Office of Research & Development
Washington, DC 50036

Katherine T. Faber
University of California
240 Hearst Mining Bldg.
Berkeley, CA 94720

Brennan A. Forcht
Vought Corporation
P.O. Box 5907
Dallas, TX 75222

Anthony H. Francis
University of Michigan
3028 Chemistry Bldg.
Ann Arbor, MI 48109

Ed Fuller
National Bureau of Standards
Room A113, Bldg. 223
Washington, DC 20234

J. J. Gebhardt
General Electric
Room U7025
Box 8555
Philadelphia, PA 19101

Lloyd J. Graham
Rockwell Science Center
1049 Camino Dos Rios
Thousand Oaks, CA 91360

Nicholas J. Grant
Materials Science & Engineering
Massachusetts Institute of Tech.
Room 8-305
Cambridge, MA 02139

A. Brunbaum
University of California
823 Evans
Berkeley, CA 94720

C. S. Harden
Chem. Systems Lab.
Bldg. E3330
Aberdeen Proving Ground, MD 21010

Edward W. Hart
Cornell University
Bard Hall
Ithaca, NY 14853

George Herrmann
Stanford University
Durand Building
Stanford, CA 94305

Robert A. Holzl
San Fernando Laboratories
10258 Norris Av.
Pacoima, CA 91011

Bill Hoover
University of California
Hertz Hall
Livermore, CA 94550

P. H. Hutton
Battelle Northwest
Box 999
Richland, WA 99352

Eugene A. Irene
IBM Thomas J. Watson Lab.
Box 218
Yorktown Heights, NY 10598

Loren A. Jacobson
US Air Force Systems Command
AFSC/DLF
Andrews AFB, DC 20334

Robert A. Johnson
University of Virginia
B225 Thornton Hall
Charlottesville, VA 22901

Ronald Kerans
Air Force Wright Aero Labs/ML
AFWAL/MLLM
Wright-Patterson AFB OH 45433

Marlin A. Kinna
Naval Sea Systems Command
SEA-62R4
Washington, DC 20360

Gerald E. Kovalenko
Naval Air Systems Command
Jefferson Davis Highway
Washington, DC

Kenneth A. Kreiss
Central Intelligence Agency
Office of Research & Development
Washington, DC 50036

Hon Wai Lam
Texas Instruments
MS 944
Dallas, TX 75243

David Lee
USAF Institute of Tech.
AFIT/ENC, Bldg. 640
Wright-Patterson AFB, OH 45433

Richard E. Lewis
Lockheed Missiles & Space Co.
Dept. 52-31, Bldg. 204
3251 Hanover Street
Palo Alto, CA 94304

E. S. Machlin
Columbia University
1106 Mudd Bldg.
New York, NY 10027

William S. Magee, Jr.
Chemical Systems Laboratory
Room 111, E3330
Aberdeen Proving Ground, MD 21010

Alan J. Markworth
Battelle, Columbus Labs.
Physical Met. Section
Columbus, OH 43201

David Marshall
University of California
240 Hearst Mining Bldg.
Berkeley, CA 94720

J. O. McCaldin
California Institute Tech.
Mail Stop 116081
Pasadena, CA 91125

Raymond R. McGuire
Lawrence Livermore Lab.
L-324
Box 808
Livermore, CA 94550

C. J. McMahon, Jr.
University of Pennsylvania
205 LRSM K1
Philadelphia, PA 19104

Robert M. McMeeking
University of Illinois
317 Talbot Lab.
Urbana, IL 61820

John Miles
New England Research Center
Minuteman Drive
Sudbury, MA 01776

Joseph B. Moore
Pratt & Whitney Aircraft
P.O. Box 2691
West Palm Beach, FL 33458

Bill Moran
Lawrence Livermore Laboratory
L-200
Livermore, CA 94550

Walter F. Morrison
US Army BRL/ARRADCOM
Interior Ballistics Div.
Aberdeen Proving Ground MD 21005

Richard Osgood
MIT Lincoln Labs
C-166
Wood Street
Lexington, MA 02173

Yoh-Han Pao
Case Western Reserve University
Rm 509, Glannan Bldg.
Cleveland, OH

William J. Pardee
Rockwell International Science Center
1049 Camino Dos Rios
Thousand Oaks, CA 91360

Arthur Paskin
Queens College
Physics Dept.
Flushing, NY

R. C. Pastor
Hughes Research Labs
3011 Malibu Canyon Road
Malibu, CA 90265

Hon Wai Lam
Texas Instruments
MS 944
Dallas, TX 75243

David Lee
USAF Institute of Tech.
AFIT/ENC, Bldg. 640
Wright-Patterson AFB, OH 45433

Richard E. Lewis
Lockheed Missiles & Space Co.
Dept. 52-31, Bldg. 204
3251 Hanover Street
Palo Alto, CA 94304

E. S. Machlin
Columbia University
1106 Mudd Bldg.
New York, NY 10027

William S. Magee, Jr.
Chemical Systems Laboratory
Room 111, E3330
Aberdeen Proving Ground, MD 21010

Alan J. Markworth
Battelle, Columbus Labs.
Physical Met. Section
Columbus, OH 43201

David Marshall
University of California
240 Hearst Mining Bldg.
Berkeley, CA 94720

J. O. McCaldin
California Institute Tech.
Mail Stop 116081
Pasadena, CA 91125

Raymond R. McGuire
Lawrence Livermore Lab.
L-324
Box 808
Livermore, CA 94550

C. J. McMahon, Jr.
University of Pennsylvania
205 LRSM K1
Philadelphia, PA 19104

Robert M. McMeeking
University of Illinois
317 Talbot Lab.
Urbana, IL 61820

John Miles
New England Research Center
Minuteman Drive
Sudbury, MA 01776

Joseph B. Moore
Pratt & Whitney Aircraft
P.O. Box 2691
West Palm Beach, FL 33458

Bill Moran
Lawrence Livermore Laboratory
L-200
Livermore, CA 94550

Walter F. Morrison
US Army BRL/ARRADCOM
Interior Ballistics Div.
Aberdeen Proving Ground MD 21005

Richard Osgood
MIT Lincoln Labs
C-166
Wood Street
Lexington, MA 02173

Yoh-Han Pao
Case Western Reserve University
Rm 509, Glannan Bldg.
Cleveland, OH

William J. Pardee
Rockwell International Science Center
1049 Camino Dos Rios
Thousand Oaks, CA 91360

Arthur Paskin
Queens College
Physics Dept.
Flushing, NY

R. C. Pastor
Hughes Research Labs
3011 Malibu Canyon Road
Malibu, CA 90265

J. W. Patten
Battelle Northwest
200W-231Z
Richland, WA 99352

Paul W. Pellegrini
USAF/RADC
MS 64/ESE
Hanscom AFB, MA 01731

W. George Perkins
Sandia Labs
Div. 2516
Albuquerque, NM

James D. Plummer
Stanford University
Stanford Elec. Labs.
Stanford, CA 94040

Adrian A. Pollock
Dunegan/Endevw
San Juan Capistrano, CA 92675

T. M. Prociv
Battelle Memorial Institute
482/505 King Av.
Columbus, OH 43201

Amar Rana
University of California
Rm 240, Hearst Mining Bldg.
Berkeley, CA 94720

Russell Reed, Jr.
U.S. Naval Weapons Center
Code 388
China Lake, CA 93555

Richard A. Reynolds
Deputy Director, Mat. Sci. Ofc.
DARPA
1400 Wilson Blvd.
Arlington, VA 22209

John M. Richardson
Rockwell International
1049 Camino Dos Rios
Thousand Oaks, CA 91360

John Rodgers
AET
1812J Tribute Road
Sacramento, CA 95815

Carl Romney
Deputy Director, DARPA
1400 Wilson Blvd.
Arlington, VA 22209

Sven A. Roosild
Rome Air Development Center
Stop 64
Hanscom Field, VA 01731

Louis Rubin
Aerospace Corporation
P.O. Box 92957
Los Angeles, CA 90009

Wolfgang Sachse
Cornell University
417 Thurston Hall
Ithaca, NY 14853

T. E. Schmid
Pratt & Whitney Aircraft
P.O. Box 2691
West Palm Beach, FL 33402

Donald L. Schmidt
AFWAL/MLBE
Wright-Patterson AFB
Ohio 45433

J. C. Schutzler
PDA Engineering
1740 Garry Ave.
Santa Ana, CA

Curt Selph
USAF
Edwards AFB, CA 93523

David M. Shaford
Vought Corporation
Unit z-30400
Dallas, TX 75222

John A. Simmons
National Bureau of Standards
B263
Washington, DC 20234

Henry I. Smith
MIT Lincoln Lab.
E118E
P.O. Box 73
Lexington, MA 02173

Frans Spaepen
Harvard University
Pierce Hall
Cambridge, MA 02138

Glenn E. Spangler
Bendix EPID
1400 Taylor Ave.
Baltimore, MD 21204

John Spiesberger
University of California
IRPP A-025
La Jolla, CA 92037

Philip L. Stanton
Sandia Labs.
807/3028B
Albuquerque, NM 87175

Morris A. Steinberg
Lockheed Corporation
Bldg. 61, Dept. 03/10
P.O. Box 55
Burbank, CA 91520

Gerald Sterbutzel
Calspan Corporation
Advanced Technology Center
Buffalo, NY 14225

Norman M. Tallan
Materials Laboratory
Wright-Patterson AFB OH 45433

Clement Tatro
Lawrence Livermore National Lab.
L-342, P.O. Box 808
Livermore, CA 94550

William A. Tiller
Stanford University
Dept. of Materials Science
Stanford, CA 94305

John R. Tucker
The Aerospace Corporation
A6-1443
Los Angeles, CA 90009

E. C. van Reuth
Materials Science Office
DARPA
1400 Wilson Blvd.
Arlington, VA 22209

V. Vitek
University of Pennsylvania
219 LRSM/K1
Philadelphia, PA 19104

Herbert F. Volk
Union Carbide Corporation
Parma Tech. Center
P.O. Box 6116
Cleveland, OH 44101

H. Wadley
National Bureau of Standards
A125, Bldg. 223
Washington, DC 20234

Dick Watson
Brookhaven National Lab.
Physics Dept.
Upton, NY

J. Weertman
Materials Science Dept.
Northwestern Unviersity
Evanston, IL 60201

Edward J. Wesley
Naval Ocean Systems Center
San Diego, CA 92152

William L. Whittemore
General Atomic Co.
P.O. Box 81608
San Diego, CA 92138

H. H. Wieder
NOSC
Code 922
San Diego, CA

J. W. Patten
Battelle Northwest
200W-231Z
Richland, WA 99352

Paul W. Pellegrini
USAF/RADC
MS 64/ESE
Hanscom AFB, MA 01731

W. George Perkins
Sandia Labs
Div. 2516
Albuquerque, NM

James D. Plummer
Stanford University
Stanford Elec. Labs.
Stanford, CA 94040

Adrian A. Pollock
Dunegan/Endevw
San Juan Capistrano, CA 92675

T. M. Prociv
Battelle Memorial Institute
482/505 King Av.
Columbus, OH 43201

Amar Rana
University of California
Rm 240, Hearst Mining Bldg.
Berkeley, CA 94720

Russell Reed, Jr.
U.S. Naval Weapons Center
Code 388
China Lake, CA 93555

Richard A. Reynolds
Deputy Director, Mat. Sci. Ofc.
DARPA
1400 Wilson Blvd.
Arlington, VA 22209

John M. Richardson
Rockwell International
1049 Camino Dos Rios
Thousand Oaks, CA 91360

John Rodgers
AET
1812J Tribute Road
Sacramento, CA 95815

Carl Romney
Deputy Director, DARPA
1400 Wilson Blvd.
Arlington, VA 22209

Sven A. Roosild
Rome Air Development Center
Stop 64
Hanscom Field, VA 01731

Louis Rubin
Aerospace Corporation
P.O. Box 92957
Los Angeles, CA 90009

Wolfgang Sachse
Cornell University
417 Thurston Hall
Ithaca, NY 14853

T. E. Schmid
Pratt & Whitney Aircraft
P.O. Box 2691
West Palm Beach, FL 33402

Donald L. Schmidt
AFWAL/MLBE
Wright-Patterson AFB
Ohio 45433

J. C. Schutzler
PDA Engineering
1740 Garry Ave.
Santa Ana, CA

Curt Selph
USAF
Edwards AFB, CA 93523

David M. Shaford
Vought Corporation
Unit z-30400
Dallas, TX 75222

John A. Simmons
National Bureau of Standards
B263
Washington, DC 20234

William D. Wilson
Sandia National Labs
Theoretical Div.
Livermore, CA 94550

Harry V. Winsor
Program Manager
Materials Science Office
DARPA
1400 Wilson Boulevard
Arlington, VA 22209

Douglas P. Woodman
GTE Sylvania
P.O. Box 188
Mt. View, CA

Charles A. Young
Naval Ocean Systems Center
Code 523, Bldg. 46
San Diego, CA 92152

Henry I. Smith
MIT Lincoln Lab.
E118E
P.O. Box 73
Lexington, MA 02173

Frans Spaepen
Harvard University
Pierce Hall
Cambridge, MA 02138

Glenn E. Spangler
Bendix EPID
1400 Taylor Ave.
Baltimore, MD 21204

John Spiesberger
University of California
IRPP A-025
La Jolla, CA 92037

Philip L. Stanton
Sandia Labs.
807/3028B
Albuquerque, NM 87175

Morris A. Steinberg
Lockheed Corporation
Bldg. 61, Dept. 03/10
P.O. Box 55
Burbank, CA 91520

Gerald Sterbutzel
Calspan Corporation
Advanced Technology Center
Buffalo, NY 14225

Norman M. Tallan
Materials Laboratory
Wright-Patterson AFB OH 45433

Clement Tatro
Lawrence Livermore National Lab.
L-342, P.O. Box 808
Livermore, CA 94550

William A. Tiller
Stanford University
Dept. of Materials Science
Stanford, CA 94305

John R. Tucker
The Aerospace Corporation
A6-1443
Los Angeles, CA 90009

E. C. van Reuth
Materials Science Office
DARPA
1400 Wilson Blvd.
Arlington, VA 22209

V. Vitek
University of Pennsylvania
219 LRSM/K1
Philadelphia, PA 19104

Herbert F. Volk
Union Carbide Corporation
Parma Tech. Center
P.O. Box 6116
Cleveland, OH 44101

H. Wadley
National Bureau of Standards
A125, Bldg. 223
Washington, DC 20234

Dick Watson
Brookhaven National Lab.
Physics Dept.
Upton, NY

J. Weertman
Materials Science Dept.
Northwestern Unviersity
Evanston, IL 60201

Edward J. Wesley
Naval Ocean Systems Center
San Diego, CA 92152

William L. Whittemore
General Atomic Co.
P.O. Box 81608
San Diego, CA 92138

H. H. Wieder
NOSC
Code 922
San Diego, CA

ADVANCED CRUISE MISSILE ENGINES FROM COATED CARBON-CARBON COMPOSITES

E. E. Hucke

MEETING SUMMARY

A one day meeting of design and materials specialists was held to discuss the advantages and anticipated problem areas in the application of advanced carbon materials to an uncooled air breathing advanced cruise missile engine with hot component temperatures up to 3500°F (1927°C). A list of those attending is appended.

An introductory review of the main systems advantages, engine design concepts, stress levels, and material coatings required was given by Rubin of Aerospace Corporation. While many trade-offs are possible, the main advantages to be had are reduced specific fuel consumption, increased thrust, and decreased engine size. The carbon materials, when compared to ceramics, offer many inherent advantages with respect to: 1) specific strength at very high temperatures, 2) thermal stress, 2) toughness, and 4) fabricability. They have the obvious disadvantage of oxidation resistance and therefore require coating in combustion atmosphere containing excess oxygen.

William D. Wilson
Sandia National Labs
Theoretical Div.
Livermore, CA 94550

Harry V. Winsor
Program Manager
Materials Science Office
DARPA
1400 Wilson Boulevard
Arlington, VA 22209

Douglas P. Woodman
GTE Sylvania
P.O. Box 188
Mt. View, CA

Charles A. Young
Naval Ocean Systems Center
Code 523, Bldg. 46
San Diego, CA 92152

Forcht of Vought Corporation gave a preliminary review of a program now in progress to assess carbon-carbon technology for advanced cruise missile engines. This program involves engine design systems analysis as well as materials technology. Based upon experience with the space shuttle as well as parts in the augmentor sections of current metallic engines, there is substantial confidence in providing coatings on stressed C-C materials for period of 10-100 hours at temperatures up to 2500°F. These coatings are SiC based with additives of Al_2O_3 and in some cases boron, with silicate sealing systems to provide crack healing for low temperature oxidation resistance. Such coatings depend fundamentally on SiO_2 based oxidation layers and would be expected to fail by volatilization in carbon systems in the range of 2800-3000°F. Therefore a different approach is required to reach 3500°F. The stress level expected in the rotating parts is in the range of 35-50,000 psi maximum tension if current axial flow turbines are used. This strength level requires at least 2D, C-C composites with their inherent problems of anisotropy, susceptability to shear failure, and difficulty in making the very thin sections required in blading. Coefficient of expansion and anisotropic structure also pose difficult coating problems. Fully exploiting the C-C properties also points to smaller rotor diameters ($\approx$6 in), higher speeds ($\geq$60,000 RPM), and thinner sections. Current axial flow designs show trailing edges of about 10-20 mils with coatings at about 5 mils.

ADVANCED CRUISE MISSILE ENGINES FROM COATED CARBON-CARBON COMPOSITES

E. E. Hucke

MEETING SUMMARY

A one day meeting of design and materials specialists was held to discuss the advantages and anticipated problem areas in the application of advanced carbon materials to an uncooled air breathing advanced cruise missile engine with hot component temperatures up to 3500°F (1927°C). A list of those attending is appended.

An introductory review of the main systems advantages, engine design concepts, stress levels, and material coatings required was given by Rubin of Aerospace Corporation. While many trade-offs are possible, the main advantages to be had are reduced specific fuel consumption, increased thrust, and decreased engine size. The carbon materials, when compared to ceramics, offer many inherent advantages with respect to: 1) specific strength at very high temperatures, 2) thermal stress, 2) toughness, and 4) fabricability. They have the obvious disadvantage of oxidation resistance and therefore require coating in combustion atmosphere containing excess oxygen.

Schutzler of P.D.A. outlined many of the mechanical requirements in current designs. Hub tensile stresses were found to be critical and rather substantial shear stresses are also found in the hub due to rotational loading.

Schmid of Pratt-Whitney reviewed some advantages expected in C-C engines anticipated in 1985 and the more advanced systems expected by 1995. The payoffs in both systems were substantial. Extensive burner tests of SiC coated C-C parts at 2000°F and more limited experience on augmentor components at 2500°F have lead to optimism that C-C engines can be made for operating temperatures from 2500-2800°F. System studies together with data for components at 2500°F were discussed by Duffy of General Electric who appeared optimistic for applications at 2500°F.

A wide range of recent successful applications of coated carbon materials in oxidizing environments at 2000°F and higher was discussed. In general there was a great deal of optimism about providing limited life (≈50-100 hours) in parts up to perhaps 3000°F. There was however no specific data provided about applications tested at 3500°F. In many of the cases cited, the levels of stress, high and low frequency thermal cycling, dynamic loading, foreign body impact, and stress gradients were either absent or substantially less than expected in an advanced performance gas turbine. However, the successes of the past ten years in applying carbon in oxidizing high temperature applications are impressive.

Warren of Refractory Composites, Inc., discussed some C-C composites with complete internal CVD coatings of SiC. Some

attractive properties were obtained however at rather modest levels of carbon fiber loading.

Holzl of San Fernando Laboratories presented some data on very strong (>150,000 psi) CVD SiC materials. In addition, he proposed that HfO_2-TiO_2 would be useful in solving the coating problems for 3500°F. This system allows coefficient of expansion tailoring for interlayer consideration, but is probably not refractory enough with substantial TiO_2 contents.

Volk of U.C.C. Corporation reviewed some early experience with precious metal coatings (Ir) which might get some consideration at selected locations in the engine.

Patten of Battelle-Northwest discussed metal-metaloxide sputter coatings, some of which he felt could be extended to the temperature range of 3500°F. However, the proprietary nature of his work precluded his disclosing the coating system he envisioned.

The desired coating system must: 1) last 50 hours, 2) be free from holes and be no more than about 5 mils thick, 3) be "self-healing", 4) capable of chemical stability in combustion gases and carbon at 3500°F with excess oxygen, and 5) be able to withstand cyclic stresses, rotational stresses, and surface aerodynamic stresses. At this moment there is no known system that exhibits these qualities.

Schutzler of P.D.A. outlined many of the mechanical requirements in current designs. Hub tensile stresses were found to be critical and rather substantial shear stresses are also found in the hub due to rotational loading.

Schmid of Pratt-Whitney reviewed some advantages expected in C-C engines anticipated in 1985 and the more advanced systems expected by 1995. The payoffs in both systems were substantial. Extensive burner tests of SiC coated C-C parts at 2000°F and more limited experience on augmentor components at 2500°F have lead to optimism that C-C engines can be made for operating temperatures from 2500-2800°F. System studies together with data for components at 2500°F were discussed by Duffy of General Electric who appeared optimistic for applications at 2500°F.

A wide range of recent successful applications of coated carbon materials in oxidizing environments at 2000°F and higher was discussed. In general there was a great deal of optimism about providing limited life (≈50-100 hours) in parts up to perhaps 3000°F. There was however no specific data provided about applications tested at 3500°F. In many of the cases cited, the levels of stress, high and low frequency thermal cycling, dynamic loading, foreign body impact, and stress gradients were either absent or substantially less than expected in an advanced performance gas turbine. However, the successes of the past ten years in applying carbon in oxidizing high temperature applications are impressive.

Warren of Refractory Composites, Inc., discussed some C-C composites with complete internal CVD coatings of SiC. Some

"BLACK ENGINE" MEETING

J. D. Buch
Aerospace Corp.
A6-1437
El Segundo, CA
(213)648-7602

Robert J. Duffy
General Electric Co.
1000 Western Ave.
Bldg. 37428
Lynn, MA 09101

Walter P. Eatherly
Oak Ridge National Lab
Bldg. 4508
Oak Ridge, TN 37830
(615)574-5220

Brennan A. Forcht
Vought Corporation
P.O. Box 5907
Dallas, TX 75222
(214)266-4796

Joe Gebhardt
General Electric-RSD
Box 8555
Philadelphia, PA 19101
(215)962-1227

Robert A. Holzl
San Fernando Laboratories
10258 Norris Ave.
Pacoima, CA 91011
(213)899-7484

Ronald Kerans
Air Force Wright Aero Labs/ML
AFWAL/MLLM
Wright Patterson AFB, OH 45433
(513)255-4769

Marlin A. Kinna
Naval Sea Systems Comm.
Code 62R4
Washington, DC 20362

J. W. Patten
Battelle-Northwest
200W-2317
Richland, WA 99352
(509)373-2603

Dr. Louis Rubin
Aerospace Corporation
P.O. Box 92957
Los Angeles, CA 90009
(213)648-6028

T. E. Schmid
Pratt & Whitney Aircraft
P.O. Box 2691
West Palm Beach, FL 33402
(305)840-3232

Donald L. Schmidt
AFWAL/MLBE
Wright Patterson AFB
Ohio 45433
(513)255-2942

J. C. Schutzler
PDA Engineering
1740 Garry Ave.
Santa Ana, CA
(714)556-2880

David M. Shuford
Vought Corporation
Dallas, TX 75222
(214)266-7939

Norman M. Tallan
Materials Laboratory
Wright Patterson AFB
OH 45433
(513)255-3758

Herbert F. Volk
Union Carbide Corporation
Parma Technical Center
P.O. Box 6116
Cleveland, OH 44101
(206)676-2379

James W. Warren
24300 Aetna St.
Woodland Hills, CA 91364
(213)844-0149

COMMENTS ON CARBON ENGINE

A. G. Evans

Several items emerge as potential concerns with regard to the successful development of a carbon/carbon engine. The following are some related issues.

1. Shear Strength of Composites

Carbon composites are susceptible to damage ('kinking') in shear or compression. For example, kinking in typical c/c composites initiates at ∿3,000 psi in shear loading. The kinking damage consists of a shear band, in which the fibers are fractured at the band extremities. This region thus has little remnant tensile strength. A component with a contiguous series of damaged fiber bundles, created by shear, would thus be subject to failure if exposed to a subsequent tensile stress. This limiting characteristic of c/c composites must be fully appreciated in all structural designs.

2. Coatings

Microcracking. The microcracking of coatings due to thermal contraction mismatch is inevitable (unless a low viscosity coating is employed - see below). The microcracking is only a concern, however, if the microcracks do not resinter at temperatures below that at which appreciable oxygen penetration between the cracks leads to degradation of the underlying c/c material.

"BLACK ENGINE" MEETING

J. D. Buch
Aerospace Corp.
A6-1437
El Segundo, CA
(213)648-7602

Robert J. Duffy
General Electric Co.
1000 Western Ave.
Bldg. 37428
Lynn, MA 09101

Walter P. Eatherly
Oak Ridge National Lab
Bldg. 4508
Oak Ridge, TN 37830
(615)574-5220

Brennan A. Forcht
Vought Corporation
P.O. Box 5907
Dallas, TX 75222
(214)266-4796

Joe Gebhardt
General Electric-RSD
Box 8555
Philadelphia, PA 19101
(215)962-1227

Robert A. Holzl
San Fernando Laboratories
10258 Norris Ave.
Pacoima, CA 91011
(213)899-7484

Ronald Kerans
Air Force Wright Aero Labs/ML
AFWAL/MLLM
Wright Patterson AFB, OH 45433
(513)255-4769

Marlin A. Kinna
Naval Sea Systems Comm.
Code 62R4
Washington, DC 20362

J. W. Patten
Battelle-Northwest
200W-2317
Richland, WA 99352
(509)373-2603

Dr. Louis Rubin
Aerospace Corporation
P.O. Box 92957
Los Angeles, CA 90009
(213)648-6028

T. E. Schmid
Pratt & Whitney Aircraft
P.O. Box 2691
West Palm Beach, FL 33402
(305)840-3232

Donald L. Schmidt
AFWAL/MLBE
Wright Patterson AFB
Ohio 45433
(513)255-2942

J. C. Schutzler
PDA Engineering
1740 Garry Ave.
Santa Ana, CA
(714)556-2880

David M. Shuford
Vought Corporation
Dallas, TX 75222
(214)266-7939

Norman M. Tallan
Materials Laboratory
Wright Patterson AFB
OH 45433
(513)255-3758

Herbert F. Volk
Union Carbide Corporation
Parma Technical Center
P.O. Box 6116
Cleveland, OH 44101
(206)676-2379

James W. Warren
24300 Aetna St.
Woodland Hills, CA 91364
(213)844-0149

Specifically, a relatively low strength* coating which is subject to a high density of small microcracks can exhibit remarkable structural integrity (a characteristic used for thermal shock resistance, e.g., in advanced refractories). The small extension of the microcracks gives small crack openings and hence, limited oxygen penetration. Further, the opening displacements of small microcracks tend to be reversible and thus crack healing can easily proceed at surprisingly low temperature, i.e., temperatures at which surface diffusion becomes significant (about 400-600°C below the sintering temperature in Al_2O_3). Such controlled microcracking is facilitated by thin films, and crack healing can be assisted by additives (B in SiC?).

2. Viscosity

Low viscosity coatings have the advantage that mismatch with the c/c can be accomodated (this may be one role of B in SiC; an additive which is known to affect the grain boundary diffusivity). However, such low viscosity coatings can be readily lost in flowing gas streams at elevated temperatures and their utility for engine components is questionable.

---

*Low strength refers to a controlled density of weak points discretely created in the coating microstructure, e.g., by inclusions, precipitates, etc.

COMMENTS ON CARBON ENGINE

A. G. Evans

Several items emerge as potential concerns with regard to the successful development of a carbon/carbon engine. The following are some related issues.

1. Shear Strength of Composites

Carbon composites are susceptible to damage ('kinking') in shear or compression. For example, kinking in typical c/c composites initiates at ∿3,000 psi in shear loading. The kinking damage consists of a shear band, in which the fibers are fractured at the band extremities. This region thus has little remnant tensile strength. A component with a contiguous series of damaged fiber bundles, created by shear, would thus be subject to failure if exposed to a subsequent tensile stress. This limiting characteristic of c/c composites must be fully appreciated in all structural designs.

2. Coatings

Microcracking. The microcracking of coatings due to thermal contraction mismatch is inevitable (unless a low viscosity coating is employed - see below). The microcracking is only a concern, however, if the microcracks do not resinter at temperatures below that at which appreciable oxygen penetration between the cracks leads to degradation of the underlying c/c material.

COMMENTS - CARBON ENGINE DEVELOPMENT

J. J. Gilman

Considerable progress has been made in improving the behavior of fibrous carbon materials and structures made from them. However, this progress has been quite modest compared with the requirements of a high temperature engine that produces large specific thrust. This is not to say that the task cannot be accomplished. But it does indicate that great expense will be required which may mean that such a program will not be cost-effective.

Since I believe that the development of an effective engine that operates at (or near) 3500°F (1925°C) will be a very expensive project, I think that some cost estimates should be made in advance. There is no evidence that this has been done to date. Some important cost questions are:

a) What is the base cost of the fibrous-carbon material?

b) What is the cost of weaving (or equivalent) it into the necessary configuration?

c) What is the cost of the relatively slow process needed for coating the carbon?

d) What is the cost per engine of the development program that is comtemplated?

e) How does the cost of manufacturing the proposed carbon

Specifically, a relatively low strength* coating which is subject to a high density of small microcracks can exhibit remarkable structural integrity (a characteristic used for thermal shock resistance, e.g., in advanced refractories). The small extension of the microcracks gives small crack openings and hence, limited oxygen penetration. Further, the opening displacements of small microcracks tend to be reversible and thus crack healing can easily proceed at surprisingly low temperature, i.e., temperatures at which surface diffusion becomes significant (about 400-600°C below the sintering temperature in Al_2O_3). Such controlled microcracking is facilitated by thin films, and crack healing can be assisted by additives (B in SiC?).

2. Viscosity

Low viscosity coatings have the advantage that mismatch with the c/c can be accomodated (this may be one role of B in SiC; an additive which is known to affect the grain boundary diffusivity). However, such low viscosity coatings can be readily lost in flowing gas streams at elevated temperatures and their utility for engine components is questionable.

---

*Low strength refers to a controlled density of weak points discretely created in the coating microstructure, e.g., by inclusions, precipitates, etc.

engine compare with the cost of manufacturing conventional metal engines?

Now, I shall consider another point. It is related to the problem of estimating the potential performance of the materials from the basis of present knowledge. I think that this is a serious issue because present observations have been made under nearly steady conditions; whereas, the most stringent requirements are set by the fact that cyclic conditions prevail in engines. The most damaging cycles are not those associated with starting and stopping engines, but are those induced by the fact that the combustors are localized so the blades and vanes are not heated steadily but in pulses. The frequencies are relatively high. For example, if an engine has 12 combustors and a rotational speed of 50,000 rpm; then thermal cycling occurs with a frequency of 10^4 cps. This translates into 2×10^9 cycles for a 50 hour lifetime. For a reasonable thermal diffusivity of $10^{-3}cm^2/sec$, significant temperature changes can be expected during each cycle to a depth of about $3\times10^{-4}cm$ ($\sim10^{-4}$ in.).

Because of the importance of cyclic thermal and mechanical loading in engines, any development program should include early testing in a high frequency thermal-shock facility, such as a rotating holder and a localized combustor.

Finally, it seems prudent to me to advance the field of high temperature materials before attempting to construct an engine at a time when only marginal materials are available. Thus, work on oxide filaments might yield a material with adequate high

COMMENTS - CARBON ENGINE DEVELOPMENT

J. J. Gilman

Considerable progress has been made in improving the behavior of fibrous carbon materials and structures made from them. However, this progress has been quite modest compared with the requirements of a high temperature engine that produces large specific thrust. This is not to say that the task cannot be accomplished. But it does indicate that great expense will be required which may mean that such a program will not be cost-effective.

Since I believe that the development of an effective engine that operates at (or near) 3500°F (1925°C) will be a very expensive project, I think that some cost estimates should be made in advance. There is no evidence that this has been done to date. Some important cost questions are:

a) What is the base cost of the fibrous-carbon material?

b) What is the cost of weaving (or equivalent) it into the necessary configuration?

c) What is the cost of the relatively slow process needed for coating the carbon?

d) What is the cost per engine of the development program that is comtemplated?

e) How does the cost of manufacturing the proposed carbon

temperature strength. Or, instead of using SiC as a coating for carbon, it might be better to use SiC filaments for constructing the structure.

To support advances in the performances of high temperature materials, I urge that work on the material be done in conjunction with a specific hardware need. One should be selected that is demanding, but not excessively demanding, as is the case of a high performance turbine.

engine compare with the cost of manufacturing conventional metal engines?

Now, I shall consider another point. It is related to the problem of estimating the potential performance of the materials from the basis of present knowledge. I think that this is a serious issue because present observations have been made under nearly steady conditions; whereas, the most stringent requirements are set by the fact that cyclic conditions prevail in engines. The most damaging cycles are not those associated with starting and stopping engines, but are those induced by the fact that the combustors are localized so the blades and vanes are not heated steadily but in pulses. The frequencies are relatively high. For example, if an engine has 12 combustors and a rotational speed of 50,000 rpm; then thermal cycling occurs with a frequency of 10^4 cps. This translates into 2×10^9 cycles for a 50 hour lifetime. For a reasonable thermal diffusivity of $10^{-3}cm^2/sec$, significant temperature changes can be expected during each cycle to a depth of about $3\times10^{-4}cm$ ($\sim10^{-4}$ in.).

Because of the importance of cyclic thermal and mechanical loading in engines, any development program should include early testing in a high frequency thermal-shock facility, such as a rotating holder and a localized combustor.

Finally, it seems prudent to me to advance the field of high temperature materials before attempting to construct an engine at a time when only marginal materials are available. Thus, work on oxide filaments might yield a material with adequate high

OXIDATION AND GROWTH MECHANISMS RELEVANT TO SEMICONDUCTOR ELECTRONICS

H. Ehrenreich, J. P. Hirth, T. C. McGill

INTRODUCTION

The third of the annual MRC workshops devoted to aspects of VLSI was devoted to the subject of oxidation and growth mechanisms relevant to semiconductor electronics, graphoepitaxy, and HgCdTe infrared detectors. The meeting, organized by H. Ehrenreich (MRC and Harvard), T. C. McGill (MRC and CalTech), and R. A. Reynolds (DARPA), was held over a period of three days. Formal presentations were made in the moring of each day. The afternoons were devoted to informal workshop discussions and two short presentations on related subjects.

The first session dealt with the fundamental mechanisms of oxidation, and a review of some of the proposed mechanisms for oxidation of silicon with emphasis on the Deal-Plummer-Tiller model. This model has been developed largely at Stanford (and for that reason will be referred to as the "Stanford Model" below) and has received much thoughtful consideration. Further elaboration of the oxidation mechanisms was provided by E. A. Irene (IBM, Watson Labs) in a talk that provided additional experimental information and insight.

temperature strength. Or, instead of using SiC as a coating for carbon, it might be better to use SiC filaments for constructing the structure.

To support advances in the performances of high temperature materials, I urge that work on the material be done in conjunction with a specific hardware need. One should be selected that is demanding, but not excessively demanding, as is the case of a high performance turbine.

The second principal topic concerning the growth of crystal films on non-commensurate or amorphous substrates was developed in presentations by J. O. McCaldin (CalTech), H. I. Smith (Lincoln Labs, MIT), and H-W. Lam (TI). The importance of graphoepitaxy and generically related methods for achieving such crystal growth may well prove to be a crucial ingredient in the development of VLSI.

R. A. Reynolds (DARPA) gave the first of three talks dealing with HgCdTe infrared detectors by presenting a broad overview of the subject coupled with the admonition that we not succumb to the VLSI technology gap syndrome at the expense of other important technological needs. Further elaboration of the subject was provided by J. T. K. Cheung (Rockwell) who discussed novel molecular beam epitaxial approaches and J. L. Miles (New England Research Center).

These presentations, together with the afternoon discussions, provided a fruitful and stimulating exchange among experts in the field and MRC members. As a result of these discussions, critical perceptions were sharpened and a number of viewpoints as well as suggestions for experiments, summarized below, were put forward.

MECHANISMS FOR Si OXIDATION (H. Ehrenreich and J. R. Hirth)

Some of the essential material delineated in the first five presentations may be summarized by a brief characterization of two models for the oxidation of silicon, which we shall term

OXIDATION AND GROWTH MECHANISMS RELEVANT TO SEMICONDUCTOR ELECTRONICS

H. Ehrenreich, J. P. Hirth, T. C. McGill

INTRODUCTION

The third of the annual MRC workshops devoted to aspects of VLSI was devoted to the subject of oxidation and growth mechanisms relevant to semiconductor electronics, graphoepitaxy, and HgCdTe infrared detectors. The meeting, organized by H. Ehrenreich (MRC and Harvard), T. C. McGill (MRC and CalTech), and R. A. Reynolds (DARPA), was held over a period of three days. Formal presentations were made in the moring of each day. The afternoons were devoted to informal workshop discussions and two short presentations on related subjects.

The first session dealt with the fundamental mechanisms of oxidation, and a review of some of the proposed mechanisms for oxidation of silicon with emphasis on the Deal-Plummer-Tiller model. This model has been developed largely at Stanford (and for that reason will be referred to as the "Stanford Model" below) and has received much thoughtful consideration. Further elaboration of the oxidation mechanisms was provided by E. A. Irene (IBM, Watson Labs) in a talk that provided additional experimental information and insight.

the "Stanford Model" (Deal-Plummer-Tiller) and the "Ledge Model" (amplified below in a separate contribution by Hirth and Ehrenreich).

The Stanford Model

This is most easily described with the help of Fig. 1. Initial nucleation of the oxide on silicon is already assumed to have taken place and a layer of SiO_2 has formed. The model addresses the question of the mechanism permitting continued growth of the oxide. As indicated on Fig. 1, O_2 enters from the left and diffuses through the amorphous SiO_2 until it encounters a thin layer of β-cristobolite, perhaps some 20Å thick, located immediately next to the silicon. The existence of this material is experimentally somewhat circumstantial and based on some rather ambiguous transmission electromicroscopy results. At the cristobolite interface, labelled B in Fig. 1, the molecular oxygen interacts with vacancies to form atomic oxygen. These vacancies are created at interface A between the β-cristobolite and the crystalline filicon. As Fig. 2 illustrates in more detail, interface A contains a large number of edge dislocations which produce vacancies by dislocation climb. Silicon interstitials are formed concomitantly as illustrated in Fig. 3 by the arrow labelled "Int. Si". The figure also shows oxygens in the hexagonal ring combining with the interstitial silicon, and the formation of nascent β-cristobolite in the form of an interstitial complex. The remaining oxygen vacancy is indicated schematically. These reactions produce enormous strains that are of the order of the

The second principal topic concerning the growth of crystal films on non-commensurate or amorphous substrates was developed in presentations by J. O. McCaldin (CalTech), H. I. Smith (Lincoln Labs, MIT), and H-W. Lam (TI). The importance of graphoepitaxy and generically related methods for achieving such crystal growth may well prove to be a crucial ingredient in the development of VLSI.

R. A. Reynolds (DARPA) gave the first of three talks dealing with HgCdTe infrared detectors by presenting a broad overview of the subject coupled with the admonition that we not succumb to the VLSI technology gap syndrome at the expense of other important technological needs. Further elaboration of the subject was provided by J. T. K. Cheung (Rockwell) who discussed novel molecular beam epitaxial approaches and J. L. Miles (New England Research Center).

These presentations, together with the afternoon discussions, provided a fruitful and stimulating exchange among experts in the field and MRC members. As a result of these discussions, critical perceptions were sharpened and a number of viewpoints as well as suggestions for experiments, summarized below, were put forward.

MECHANISMS FOR Si OXIDATION (H. Ehrenreich and J. R. Hirth)

Some of the essential material delineated in the first five presentations may be summarized by a brief characterization of two models for the oxidation of silicon, which we shall term

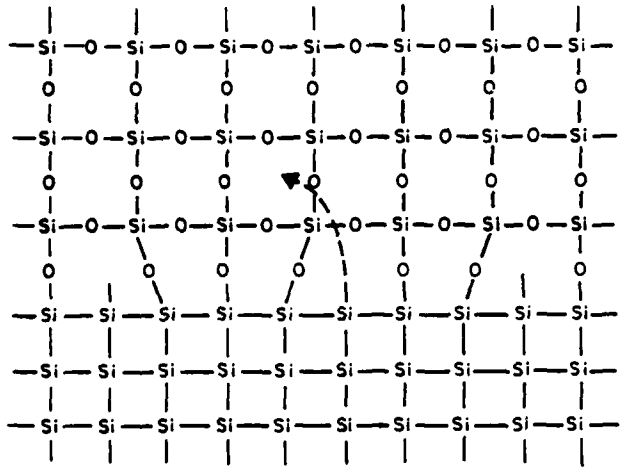

Figure 2. Interface dislocations at Plane A (Fig. 1) and interstitial Si formation.

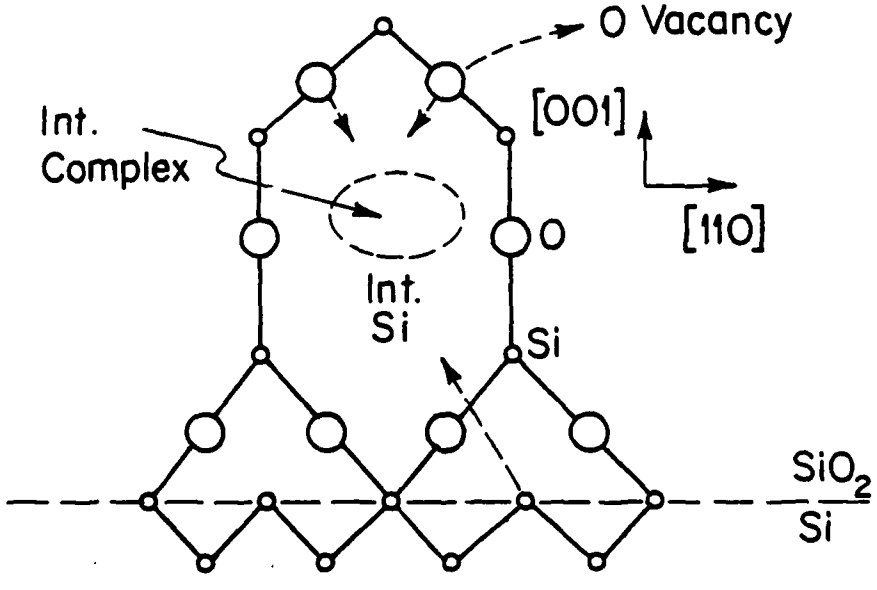

Figure 3. Towards the formation of β-Cristobolite.

the "Stanford Model" (Deal-Plummer-Tiller) and the "Ledge Model" (amplified below in a separate contribution by Hirth and Ehrenreich).

The Stanford Model

This is most easily described with the help of Fig. 1. Initial nucleation of the oxide on silicon is already assumed to have taken place and a layer of SiO_2 has formed. The model addresses the question of the mechanism permitting continued growth of the oxide. As indicated on Fig. 1, O_2 enters from the left and diffuses through the amorphous SiO_2 until it encounters a thin layer of β-cristobolite, perhaps some 20Å thick, located immediately next to the silicon. The existence of this material is experimentally somewhat circumstantial and based on some rather ambiguous transmission electromicroscopy results. At the cristobolite interface, labelled B in Fig. 1, the molecular oxygen interacts with vacancies to form atomic oxygen. These vacancies are created at interface A between the β-cristobolite and the crystalline filicon. As Fig. 2 illustrates in more detail, interface A contains a large number of edge dislocations which produce vacancies by dislocation climb. Silicon interstitials are formed concomitantly as illustrated in Fig. 3 by the arrow labelled "Int. Si". The figure also shows oxygens in the hexagonal ring combining with the interstitial silicon, and the formation of nascent β-cristobolite in the form of an interstitial complex. The remaining oxygen vacancy is indicated schematically. These reactions produce enormous strains that are of the order of the

reaction rate. Evans suggests that viscous flow of some kind may serve to remove the strain. The attractive feature of β-cristobolite formation is that, as shown in Fig. 3, alternate {100} plane atoms in the interface A match.

It should be emphasized that the various species alluded to here have ionic character. For simplicity the effects of ionicity in band formation have been neglected in the present characterization of the principal features of the Stanford Model. Finally, it should be noted (of Fig. 2) that the interface dislocations associated with plane A give rise to large numbers of dangling bonds and in turn interface states, ($\sim 10^{14}$-10^{15}cm^{-2}) which is much larger than the number observed (10^{13}cm^{-2}) in carefully prepared oxides utilizing dry oxygen.

The Ledge Model

This alternative model has several differing features. First it eliminates the need for β-cristobolite and in fact argues that the formation of this crystal interface next to the silicon is deleterious. cond, it eliminates the large strains which would undoubtedly lead to more broken bonds and hence interface states. Finally, the Ledge mechanism proposed here is very similar to the Burton-Cabrera-Frank mechanism for crystal growth in air. It indeed seems plausible (albeit not necessary) that the growth of material at the interface should be similar to that in the atmosphere. We wish to emphasize, however, that the features of the model to be delineated here are meant to be suggestive and have not received the same amount of careful analysis as the Stanford Model.

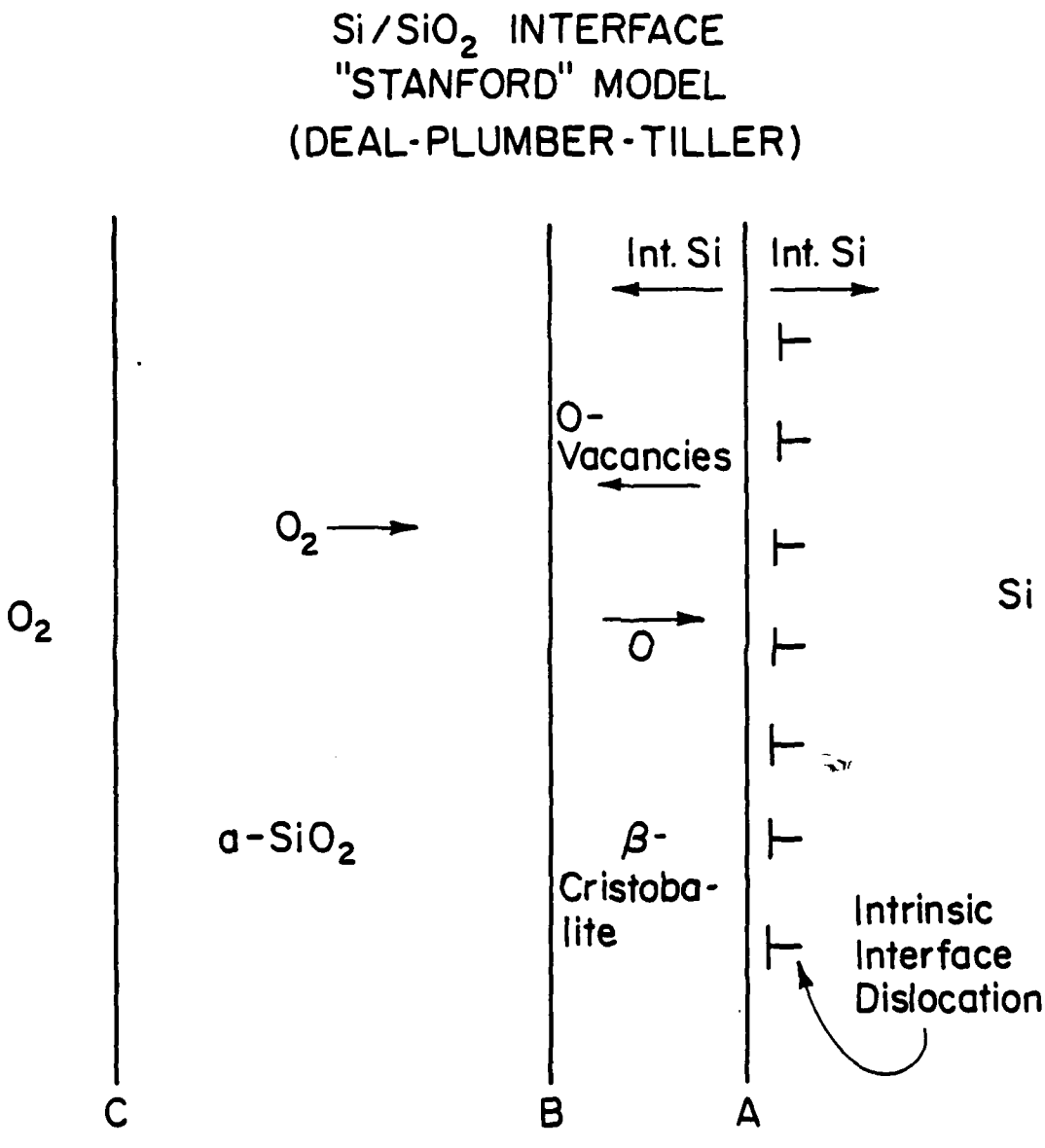
Si/SiO2 INTERFACE
"STANFORD" MODEL
(DEAL-PLUMBER-TILLER)
Int. Si
Int. Si
O-
Vacancies
O2
O2
O
Si
a-SiO2
β-
Cristoba-
lite
Intrinsic
Interface
Dislocation
C
B
A

FIGURE 1

The principal features of the Ledge Model are illustrated in simplified form in Fig. 4. A catalyzed dissociation of molecular oxygen to its monomer species is presumed to occur at interface C between the amorphous SiO_2 and oxygen. As indicated in an accompanying contribution by Margrave, the catalytic agent involved may well be hydrogen that could be present in sufficient abundance even in dry oxygen. The monomer species are of two types denoted by "fast" and "slow", respectively. The fast species diffuses rapidly to interface B which, as in the Stanford Model, may represent the onset of the β-cristobolite phase (although we shall argue later that the existence of this phase is in fact unlikely). In the vicinity of the plane B it combines with an oxygen vacancy generated at the plane A. The slow oxygen passes on to plane A. As in the Stanford Model, the rate is controlled by the slow diffusion occurring in the layer between planes B and A. The reason for separating the atomic oxygen species in this way is that it leads to a result in which the diffusion through the oxide layer is proportional to the molecular oxide pressure rather than its square root, which is consistent with experimental observation.

The ledges associated with interface A are of two types. The first is associated with SiO_2 molecules, whereas the second is associated with either Si atoms or SiO_2 molecules which are spatially contiguous. The ledges associated with the molecules occur twice as frequently. The transfer of oxygen and silicon in opposite directions along the ledges permits the growth of SiO_2 without the enormous strain fields necessitated by the Stanford

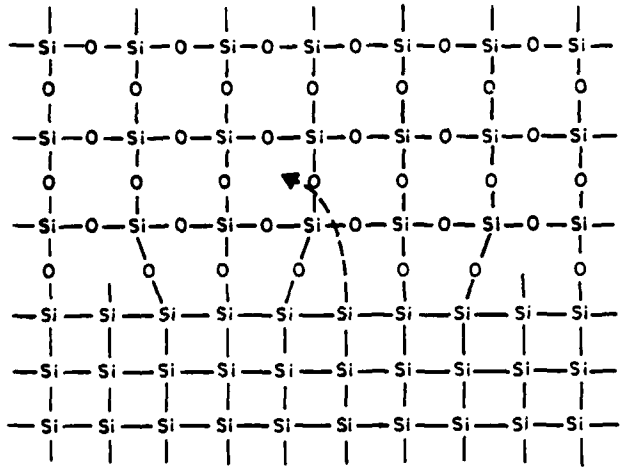

Figure 2. Interface dislocations at Plane A (Fig. 1) and interstitial Si formation.

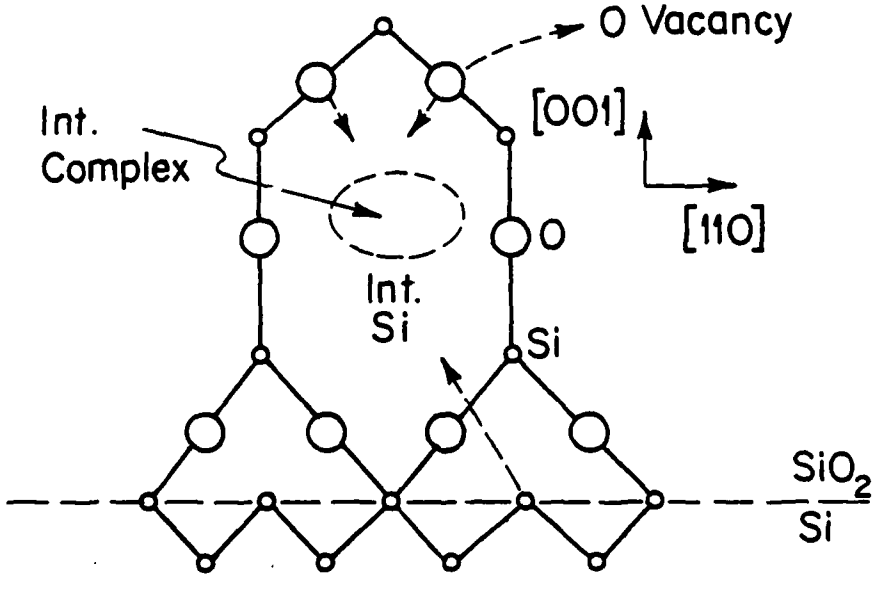

Figure 3. Towards the formation of β-Cristobolite.

reaction rate. Evans suggests that viscous flow of some kind may serve to remove the strain. The attractive feature of β-cristobolite formation is that, as shown in Fig. 3, alternate {100} plane atoms in the interface A match.

It should be emphasized that the various species alluded to here have ionic character. For simplicity the effects of ionicity in band formation have been neglected in the present characterization of the principal features of the Stanford Model. Finally, it should be noted (of Fig. 2) that the interface dislocations associated with plane A give rise to large numbers of dangling bonds and in turn interface states, ($\sim 10^{14}$-10^{15}cm^{-2}) which is much larger than the number observed (10^{13}cm^{-2}) in carefully prepared oxides utilizing dry oxygen.

The Ledge Model

This alternative model has several differing features. First it eliminates the need for β-cristobolite and in fact argues that the formation of this crystal interface next to the silicon is deleterious. cond, it eliminates the large strains which would undoubtedly lead to more broken bonds and hence interface states. Finally, the Ledge mechanism proposed here is very similar to the Burton-Cabrera-Frank mechanism for crystal growth in air. It indeed seems plausible (albeit not necessary) that the growth of material at the interface should be similar to that in the atmosphere. We wish to emphasize, however, that the features of the model to be delineated here are meant to be suggestive and have not received the same amount of careful analysis as the Stanford Model.

model. The physical picture may be visualized with the help of the diagram shown in Fig. 3 of the accompanying contribution by Hirth and Ehrenreich. Oxygen can diffuse to either kind of site whereas silicon either crosses the interface or diffuses parallel to it. Interstitials may occur but are not necessary. The spacing between ledge steps should be some reasonably large multiple ($\sim$100A) of the interatomic spacing because of the interaction of dislocation strain fields and that of interface diffusion fields.

Interface States and Their Origin

In the case of the Stanford Model interface states are likely to arise from the dangling bonds shown in Fig. 2 and possibly broken bonds arising from the necessity of accommodating large strains in the region shown in Fig. 3. In the case of the Ledge Model there will be two sources of interface states, the first from dislocation-associated dangling bonds at the ledges, and the second from interface states produced by unsatisfied silicon bonds arising from atoms at the silicon surface that are matched with atoms on the other side of the A interface. The density of these states is the same as that in the Stanford Model (about 10^{15} cm^{-2}). The ledge interface states have a far lower density of about 10^{13} cm^{-2}, which is close to the commonly accepted number of interface states in pure silicon oxidized in dry oxygen.

These results pose the problem of reconciling the observed density of interface states with that expected on the basis of either model which is about 100 times larger. Put differently, how are 99% of the interface states expected on the basis of the

The principal features of the Ledge Model are illustrated in simplified form in Fig. 4. A catalyzed dissociation of molecular oxygen to its monomer species is presumed to occur at interface C between the amorphous SiO_2 and oxygen. As indicated in an accompanying contribution by Margrave, the catalytic agent involved may well be hydrogen that could be present in sufficient abundance even in dry oxygen. The monomer species are of two types denoted by "fast" and "slow", respectively. The fast species diffuses rapidly to interface B which, as in the Stanford Model, may represent the onset of the β-cristobolite phase (although we shall argue later that the existence of this phase is in fact unlikely). In the vicinity of the plane B it combines with an oxygen vacancy generated at the plane A. The slow oxygen passes on to plane A. As in the Stanford Model, the rate is controlled by the slow diffusion occurring in the layer between planes B and A. The reason for separating the atomic oxygen species in this way is that it leads to a result in which the diffusion through the oxide layer is proportional to the molecular oxide pressure rather than its square root, which is consistent with experimental observation.

The ledges associated with interface A are of two types. The first is associated with SiO_2 molecules, whereas the second is associated with either Si atoms or SiO_2 molecules which are spatially contiguous. The ledges associated with the molecules occur twice as frequently. The transfer of oxygen and silicon in opposite directions along the ledges permits the growth of SiO_2 without the enormous strain fields necessitated by the Stanford

model to be passivated? We would like to suggest that bond angle distortions, as contrasted to energetically more unfavorable changes in length on both sides of the interface, can serve to remove many of the dangling bonds. It whould be noted that the existence of the crystalline phase such as β-cristobolite would be less favorable for the removal of these bonds. Indeed, energetic considerations suggest that the removal of dangling bonds through the formation of Si-Si or Si-O bonds is several electronvolts more favorable than the formation of a crystalline instead of an amorphous phase whose energy difference amounts to about 0.1 eV per atom.

It should be emphasized that interface state densities as low as 10^{10} cm^{-2} have been observed in the presence of small amounts of hydrogen, possibly originating from traces of water vapor. Most likely, hydrogen will passivate Si bonds much in the same way as in amorphous hydrogenated silicon which has been investigated extensively in connection with photovoltaic cells. The amounts of hydrogen required for this purpose are of the order of 10^{13} cm^{-3} provided that the hydrogen moves with the interface. This hypothesis is not unreasonable from an energetic point of view as we make clear below.

Kinetics

Reasonable fits to the kinetic data have been obtained using the Deal-Grove relation (J. Appl. Phys. 36, 3770 (1965)) as well as modifications due to E. Irene which involve a spatial and temporal origin (x_0,t_0) and an additional logarithmic term.

Si / SiO_2 INTERFACE
"LEDGE" MODEL (Simplified Veiw*)
(T= Ledges (Si or SiO_2) with extrinsic dislocation character)

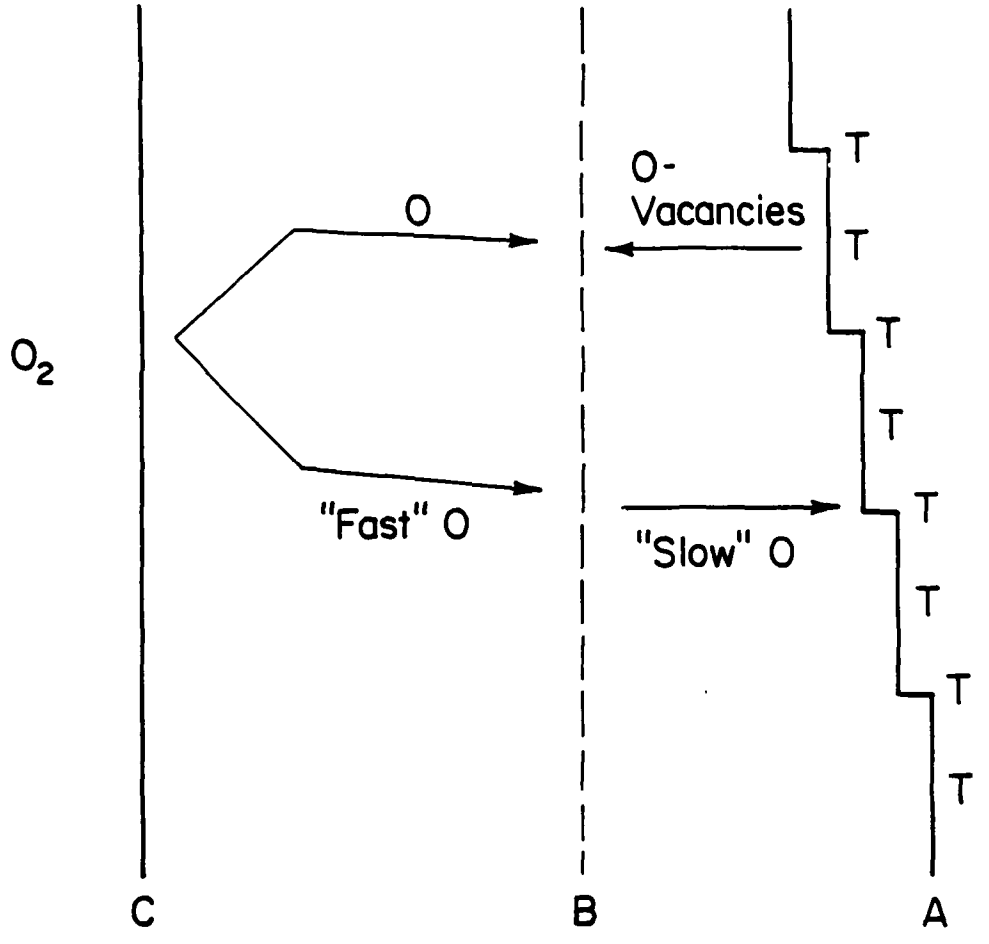

*The detailed picture is discussed by J.P. Hirth and H. Ehrenreich in a separate contribution.

FIGURE 4

The microscopic determination of the parameters involved in these models remains an outstanding problem. Their physical origin is also a matter of some dispute. Deal and the Stanford group maintain that the parameters are determined by interface characteristics, whereas Irene and collaborators have experimental evidence that pores may play a significant role in the determination of the kinetics.

The growth sequence may be characterized as follows:

1. $t < t_0$. The Mott-Cabrera mechanism involving field assisted tunneling probably plays an important role during this initial stage of oxide growth. The electric field in question arises from the presence of surface charges. According to Deal and Grove the values of x_0 corresponding to t_0 is about 230Å when oxidation takes place in the presence of dry oxygen. By contrast, x_0 is believed to be zero in the presence of moisture. This would imply that noisture somehow eliminates the surface charge and that the linear regime of the Deal-Grove mechanism relating oxide thickness and time sets in as soon as the silicon surface is exposed to oxygen.

2. $t > t_0$; linear regime. One way of obtaining a linear regime has been suggested by Irene and collaborators who have observed pores with diameter of about 10Å in the oxide. Such pores could transport oxygen efficiently by Knudsen-Poiseville flow. They exist only at small thicknesses when the films are prepared under dry conditions. Because of this, the mechanism leading to the parabolic regime in which the square of the thickness varies directly with time are not changed.

model. The physical picture may be visualized with the help of the diagram shown in Fig. 3 of the accompanying contribution by Hirth and Ehrenreich. Oxygen can diffuse to either kind of site whereas silicon either crosses the interface or diffuses parallel to it. Interstitials may occur but are not necessary. The spacing between ledge steps should be some reasonably large multiple ($\sim$100A) of the interatomic spacing because of the interaction of dislocation strain fields and that of interface diffusion fields.

Interface States and Their Origin

In the case of the Stanford Model interface states are likely to arise from the dangling bonds shown in Fig. 2 and possibly broken bonds arising from the necessity of accommodating large strains in the region shown in Fig. 3. In the case of the Ledge Model there will be two sources of interface states, the first from dislocation-associated dangling bonds at the ledges, and the second from interface states produced by unsatisfied silicon bonds arising from atoms at the silicon surface that are matched with atoms on the other side of the A interface. The density of these states is the same as that in the Stanford Model (about 10^{15} cm^{-2}). The ledge interface states have a far lower density of about 10^{13} cm^{-2}, which is close to the commonly accepted number of interface states in pure silicon oxidized in dry oxygen.

These results pose the problem of reconciling the observed density of interface states with that expected on the basis of either model which is about 100 times larger. Put differently, how are 99% of the interface states expected on the basis of the

We should note that the Mott-Cabrera mechanism involving field assisted tunneling at small thicknesses is not considered in any of these theories. Rather they emphasize the parabolic growth regime. This limitation is of some importance to the development of the VLSI technology. Whereas oxide thicknesses are of the order of 1000Å in the 5μm gate technology which is now well in hand, these thicknesses amount to only 60Å in the submicron regime when the gate dimensions are of the order of .25μm. None of the limiting cases of the Deal-Grove theory and its extensions (with the possible exception of the "wet" case) apply to this case, the important one for the future. Clearly further theoretical and experimental studies are required because of the relevance of these mechanisms to MOS technology.

Suggested Research Projects

1. Concerning interface states:

Additional insight concerning the interface state density and how it is affected by hydrogen could be obtained by further measurements using deep level transient spectroscopy, before and after annealing with hydrogen. (Some of these and other experiments mentioned here are discussed briefly in S. Pantelides, The Physics of SiO_2 and Its Interfaces (Pergamon, 1978).

2. Concerning the morphology of the surface during the initial stages of oxidation:

a. While Rutherford Back Scattering experiments have already been done, further investigations would be used to determine the interface profile of Si/SiO_2 more adequately.

model to be passivated? We would like to suggest that bond angle distortions, as contrasted to energetically more unfavorable changes in length on both sides of the interface, can serve to remove many of the dangling bonds. It whould be noted that the existence of the crystalline phase such as β-cristobolite would be less favorable for the removal of these bonds. Indeed, energetic considerations suggest that the removal of dangling bonds through the formation of Si-Si or Si-O bonds is several electronvolts more favorable than the formation of a crystalline instead of an amorphous phase whose energy difference amounts to about 0.1 eV per atom.

It should be emphasized that interface state densities as low as 10^{10} cm^{-2} have been observed in the presence of small amounts of hydrogen, possibly originating from traces of water vapor. Most likely, hydrogen will passivate Si bonds much in the same way as in amorphous hydrogenated silicon which has been investigated extensively in connection with photovoltaic cells. The amounts of hydrogen required for this purpose are of the order of 10^{13} cm^{-3} provided that the hydrogen moves with the interface. This hypothesis is not unreasonable from an energetic point of view as we make clear below.

Kinetics

Reasonable fits to the kinetic data have been obtained using the Deal-Grove relation (J. Appl. Phys. 36, 3770 (1965)) as well as modifications due to E. Irene which involve a spatial and temporal origin (x_0,t_0) and an additional logarithmic term.

b. Auger and LEED experiments can be used to define the thickness and the surface character of the oxide.

c. More high energy transmission electron microscopy investigations would be useful to characterize the postulated ledge structure.

d. The existence and characteristics of the ledge structure could be examined further after decoration with gold and subsequent electron microscopy.

e. Infrared spectroscopy would be useful to determine the presence of cristobolite which has associated characteristic peaks that arise as a consequence of the characteristic crystal structure.

f. Model building (with sticks and balls), which has been so successful in elucidating the structure of amorphous semiconductors might provide equally useful insight with respect to the models that have been described here and their geometrical feasibility. It is quite conceivable that models of the type considered so far may have to be modified appreciably.

3. Concerning kinetics:

It is necessary to explore thin film kinetics from both experimental and theoretical viewpoints. Because of the importance of oxides in submicron VLSI it is necessary to understand more fully the initial stages of oxidation including the effects of fields and low oxygen pressures. Examination of the hypothesis that the linear growth regime begins the same time as oxygen exposure in the presence of humid conditions also warrants further

The microscopic determination of the parameters involved in these models remains an outstanding problem. Their physical origin is also a matter of some dispute. Deal and the Stanford group maintain that the parameters are determined by interface characteristics, whereas Irene and collaborators have experimental evidence that pores may play a significant role in the determination of the kinetics.

The growth sequence may be characterized as follows:

1. $t < t_0$. The Mott-Cabrera mechanism involving field assisted tunneling probably plays an important role during this initial stage of oxide growth. The electric field in question arises from the presence of surface charges. According to Deal and Grove the values of x_0 corresponding to t_0 is about 230Å when oxidation takes place in the presence of dry oxygen. By contrast, x_0 is believed to be zero in the presence of moisture. This would imply that noisture somehow eliminates the surface charge and that the linear regime of the Deal-Grove mechanism relating oxide thickness and time sets in as soon as the silicon surface is exposed to oxygen.

2. $t > t_0$; linear regime. One way of obtaining a linear regime has been suggested by Irene and collaborators who have observed pores with diameter of about 10Å in the oxide. Such pores could transport oxygen efficiently by Knudsen-Poiseville flow. They exist only at small thicknesses when the films are prepared under dry conditions. Because of this, the mechanism leading to the parabolic regime in which the square of the thickness varies directly with time are not changed.

investigation. The nature of the Mott-Cabrera barrier would also be clarified by subjecting the silicon surface to photons or electric fields that would serve to reduce its effective height.

Because of the importance of the beginning stages of the oxidation process, the requirement of thin oxides in VLSI, and the development of highly sophisticated surface techniques during the course of the past few years, the formulation of a sound experimental program yielding reliable results should be entirely possible.

CONCLUDING COMMENTS

One of the principal reasons why silicon technology stands in the forefront of semiconductor electronics and why GaAs still remains to some degree a material of the future is connected with the remarkable properties of SiO_2 in passivating silicon and the fact that no correspondingly good material has yet been found for GaAs. The remarkable properties of SiO_2 appear to stem from the fact that it is the only stable oxide that can be made amorphous and that it is very sensitive to hydrogen as a means for passivating dangling bonds. Since the considerable lattice mismatch between Si and SiO_2 seems to be irrelevant in the formation of a passivating layer and having the desired electrical and mechanical characteristics, one might raise the question whether SiO_2 together with a low concentration of hydrogen might not similarly be used to passivate the surfaces of GaAs and other 3-5 compounds having useful device properties.

We should note that the Mott-Cabrera mechanism involving field assisted tunneling at small thicknesses is not considered in any of these theories. Rather they emphasize the parabolic growth regime. This limitation is of some importance to the development of the VLSI technology. Whereas oxide thicknesses are of the order of 1000Å in the 5μm gate technology which is now well in hand, these thicknesses amount to only 60Å in the submicron regime when the gate dimensions are of the order of .25μm. None of the limiting cases of the Deal-Grove theory and its extensions (with the possible exception of the "wet" case) apply to this case, the important one for the future. Clearly further theoretical and experimental studies are required because of the relevance of these mechanisms to MOS technology.

Suggested Research Projects

1. Concerning interface states:

   Additional insight concerning the interface state density

The purpose of this part of the meeting was to obtain an update of the work in this area and to explore some new viewpoints of how to improve and understand previously obtained results.

STATUS OF GRAPHOEPITAXY (Presentation by H. I. Smith: MIT Lincoln Laboratories):

b. Auger and LEED experiments can be used to define the thickness and the surface character of the oxide.

c. More high energy transmission electron microscopy investigations would be useful to characterize the postulated ledge structure.

d. The existence and characteristics of the ledge structure could be examined further after decoration with gold and subsequent electron microscopy.

e. Infrared spectroscopy would be useful to determine the presence of cristobolite which has associated characteristic peaks that arise as a consequence of the characteristic crystal structure.

f. Model building (with sticks and balls), which has been so successful in elucidating the structure of amorphous semiconductors might provide equally useful insight with respect to the models that have been described here and their geometrical feasibility. It is quite conceivable that models of the type considered so far may have to be modified appreciably.

3. Concerning kinetics:

It is necessary to explore thin film kinetics from both experimental and theoretical viewpoints. Because of the importance of oxides in submicron VLSI it is necessary to understand more fully the initial stages of oxidation including the effects of fields and low oxygen pressures. Examination of the hypothesis that the linear growth regime begins the same time as oxygen exposure in the presence of humid conditions also warrants further

Modeling of the graphoepitaxy process is being carried out by M. Geiss at Lincoln. Geiss suggests that the oxide cap is necessary to introduce high pressure and stresses during the anneal process (see paper by H. Reiss). Both Si and substrate become very plastic during the anneal process and the strain provides a driving force driving the film to a near single crystal orientation. Tiller proposed a model involving the absorptivity changes on freezing, producing rapid melting/freezing cycles and qualitatively following Smith's observation of "slush".

An alternative description of the growth process in which capillary growth of the Si occurs along the channels in the grating structure is presented in the paper by F. Spaepen.

The discussion during and after the session turned up a number of issues which need to be addressed. First the SiO_2 substrate softens and the grating degrades substantially during the annealing process. Smith speculated that if a harder grating material could be found, the results might be more spectacular. Since the grating is degraded during the anneal process, its precise role in producing the alignment is somewhat unclear. The physics and chemistry of the nucleation and anneal process are not understood.

LASER INDUCED REGROWTH OF POLYSILICON FILM (Hon-Wai Lam, Texas Instruments):

The basic idea in the work is to use concept of Gibbons and coworkers[2] to form islands of single crystal Si embedded in or on an insulating amorphous substrate. A scanning continuous

investigation. The nature of the Mott-Cabrera barrier would also be clarified by subjecting the silicon surface to photons or electric fields that would serve to reduce its effective height.

Because of the importance of the beginning stages of the oxidation process, the requirement of thin oxides in VLSI, and the development of highly sophisticated surface techniques during the course of the past few years, the formulation of a sound experimental program yielding reliable results should be entirely possible.

CONCLUDING COMMENTS

One of the principal reasons why silicon technology stands in the forefront of semiconductor electronics and why GaAs still remains to some degree a material of the future is connected with the remarkable properties of SiO_2 in passivating silicon and the fact that no correspondingly good material has yet been found for GaAs. The remarkable properties of SiO_2 appear to stem from the fact that it is the only stable oxide that can be made amorphous and that it is very sensitive to hydrogen as a means for passivating dangling bonds. Since the considerable lattice mismatch between Si and SiO_2 seems to be irrelevant in the formation of a passivating layer and having the desired electrical and mechanical characteristics, one might raise the question whether SiO_2 together with a low concentration of hydrogen might not similarly be used to passivate the surfaces of GaAs and other 3-5 compounds having useful device properties.

laser beam[5] is used to recrystallize a layer of polysilicon film into what is hoped to be single crystal with properties which are sufficiently good to allow the fabrication of devices. Two directions are being explored. The laser regrowth of isolated islands without a definite seed crystal (analogous to the Bridgman method of bulk crystal growth), and laser regrowth of islands over oxide in which the polysilicon layer is in contact with a seed crystal[6] (analogous to the zone melting technique).

Both methods produce crystalline material. However, a number of difficulties have been encountered. The material has large numbers of dislocations and grain boundaries, particularly near the edges and corners (where contact with the oxide produces high strain) and near the end of the zone melting process. For the case in which a seed with a definite orientation is not provided, the orientation of the crystalline islands is not the same from island to island. Lam noted that these difficulties indicate the need for a thorough understanding of the nucleation process in these systems. Further, the role of temperature profiles in determining the quality of the growth needs to be explored.

CONFINEMENT OF LIQUIDS AND THE GROWTH OF CRYSTALS ON AMORPHOUS SUBSTRATES (J. O. McCaldin):

This presentation gave an overview of some new ideas on the physics and material science of growth of single crystals on dissimilar substrates. McCaldin[7] indicated that the crystal growth could be viewed as being in analogy with bulk crystal

GROWTH OF SINGLE CRYSTAL SILICON ON AMORPHOUS SUBSTRATES

T. C. McGill

INTRODUCTION

One of the more promising ways of fabricating VLSI material is to use active layers of silicon that have been grown on insulating (frequently amorphous) substrates. The insulating layer would provide the isolation between devices, and produce lower inherent capacitances resulting in improved speed-power performance. Further, the development of such a technology would make it possible to fabricate three dimensional active device structures and hence open up a whole new set of possibilities for integrated circuit electronics.

In recent years the objective of producing single crystal Si on amorphous substrates[1] has been pursued intensively. Groups at Stanford under Professor Gibbons' direction have obtained single crystal islands of silicon by laser annealing silicon film deposited on flat amorphous substrates[2]. Smith and coworkers at MIT Lincoln Laboratories have obtained film of Si with high crystalline perfection by laying down layers of Si on fused silica substrates in which a grating pattern had been previously put down using lithographic techniques. Laser annealing was used to subsequently produce highly oriented crystalline films[3].

growth from a liquid phase where we are always growing single crystals in contact with dissimilar materials. In analogy with bulk crystal growth, the major problems are confinement of the liquid and control of the nucleation in such a way that a single seed dominates the growth.

For thin film growth, the stable confinement of the liquid in structures in or on the amorphous substrate depends on interface energies and on substrate geometry, particularly protruding features called "pinning points". The shape of the meniscus is determined by the filling of the structure plus the boundary conditions where the liquid encounters the walls. Suitable combinations of surface geometry and material enable a substrate to hold a thin liquid film captive.

Kruech and McCaldin[6] have performed experiments to demonstrate their conclusion on the confinement using Pb and Sn on SiO_2 substrates.

The control of nucleation has not been addressed directly yet. However, McCaldin indicated that techniques such as providing temperature gradients and spatial structures that have been used to control the nucleation in bulk crystal growth could be employed in the thin film case as well.

The major problems are to develop a better data base of interface energies between substrate materials and the appropriate liquids and the role that impurities might play in determining their values. Control of nucleation could turn out to be difficult since detailed experiments have yet to be performed using these concepts.

The purpose of this part of the meeting was to obtain an update of the work in this area and to explore some new viewpoints of how to improve and understand previously obtained results.

STATUS OF GRAPHOEPITAXY (Presentation by H. I. Smith: MIT Lincoln Laboratories):

Graphoepitaxy[3] is a term used to describe a technique in which a man-made structure is used to produce oriented crystals. As practiced now, a grating structure is put onto a glass substrate using high resolution lithographic techniques. One particular form of the grating is a square edged grating 0.1μm deep with a period of 3.8μm. A silicon layer is then put down on their grating pattern using evaporation or chemical vapor deposition (depending upon substrate temperature, this would result in an amorphous or polycrystalline layer[4]). Then the Si film is annealed in a controlled atmosphere by delivering heat by scanning a laser or a strip heater over the film surface.

At this meeting a number of previously unreported results were presented. First it was found that the anneal process, the well defined grating structure, had to be carried out in an oxygen atmosphere since the growth of an oxide layer on top of the silicon film seemed to play a major role obtaining highly oriented film after anneal. Second the best Si films were obtained by using a strip heater rather than a CW argon laser as had been employed in previous work. Thirdly, during the anneal process the well defined grating structure was degraded substantially.

CONCLUSIONS AND RECOMMENDATIONS

The methods reported for growing thin layers of crystalline semiconductors on dissimilar substrates show promise of being of great technical importance in the fabrication of a number of semiconductor devices. The program described here represents some of the strongest and most innovative in the country in this area. However, both Ti and MIT Lincoln Laboratories programs are aimed heavily at making device grade Si. While the technological potential of this kind of effort justifies its support, we find that all the groups identified a need to further understand the processes involved and to study the phenomenon in carefully controlled experiments. A broadly based research program is essential if this country is going to remain on the forefront in this field.

Modeling of the graphoepitaxy process is being carried out by M. Geiss at Lincoln. Geiss suggests that the oxide cap is necessary to introduce high pressure and stresses during the anneal process (see paper by H. Reiss). Both Si and substrate become very plastic during the anneal process and the strain provides a driving force driving the film to a near single crystal orientation. Tiller proposed a model involving the absorptivity changes on freezing, producing rapid melting/freezing cycles and qualitatively following Smith's observation of "slush".

An alternative description of the growth process in which capillary growth of the Si occurs along the channels in the grating structure is presented in the paper by F. Spaepen.

The discussion during and after the session turned up a number of issues which need to be addressed. First the SiO_2 substrate softens and the grating degrades substantially during the annealing process. Smith speculated that if a harder grating material could be found, the results might be more spectacular. Since the grating is degraded during the anneal process, its precise role in producing the alignment is somewhat unclear. The physics and chemistry of the nucleation and anneal process are not understood.

LASER INDUCED REGROWTH OF POLYSILICON FILM (Hon-Wai Lam, Texas Instruments):

The basic idea in the work is to use concept of Gibbons and coworkers[2] to form islands of single crystal Si embedded in or on an insulating amorphous substrate. A scanning continuous

PREPARATION AND PROPERTIES OF HgCdTe

T. C. McGill

HgCdTe Materials for Focal Plane Arrays

Detector arrays based on HgCdTe can operate with adequate values of the detectivity at temperatures which require smaller amounts of cooling than some of the other detector array systems (e.g., extrinsic Si detectors). Focal plane arrays would require the simultaneous fabrication of a large number of detectors and a compatible integrated circuit technology that would allow the fabrication of charge transfer devices. The DARPA program is aimed at producing such a device structure using HgCdTe.

Current detection and charge transfer devices are being fabricated in bulk grown HgCdTe. However, the degree of material control that is required for fabrication of large area devices totally in bulk grown crystals is not in hand. Liquid phase epitaxy is being explored as a method of growing large area single crystal layers with the requisite crystalline perfection and uniformity.

A preferable, if feasible, approach is to grow thin active layers of HgCdTe on various substrates including crystalline as well as amorphous material. This procedure would make possible the direct fabrication of active layers with the appropriate thickness ($\sim$10μm). These thin layers must also satisfy

laser beam[5] is used to recrystallize a layer of polysilicon film into what is hoped to be single crystal with properties which are sufficiently good to allow the fabrication of devices. Two directions are being explored. The laser regrowth of isolated

Two major difficulties have been encountered and solved. First, the pulsed laser produces splashing of finite size clusters of material from the source. However, by selection of a suitable position for the substrate relative to the source, one can minimize the number of clusters that hit the substrate. Second, the source does not necessarily evaporate congruently. However, by picking the scan rate and laser power approximately, it is possible to obtain congruent evaporation and deposition of the material. Layers 1-2μm with an electron concentration of $10^{16} cm^{-3}$ and electron mobilities of 700 cm^2/V sec have been prepared. The Uniformity of the response was tested on one sample and found to be rather good.

As yet this technique has not been fully investigated. The precise properties of the film and how close they can be made to the benchmark set by the best bulk material has yet to be determined. The questions of uniformity of the properties and surface morphology of the thin film layer have as yet not been tested adequately to see if they meet the specification for large area device fabrication.

Growth of Crystalline Thin-Films Compound on Foreigh Substrates

Presentation of J. L. Miles, New England Research Center)

A group of Polish investigators[2] have succeeded in growing HgCdTe films on CdTe layers vacuum-evaporated on mica, lithium niobate, sapphire, glass, quartz, and thermally oxidized silicon. The CdTe layer was laid down by the not wall technique. The

growth from a liquid phase where we are always growing single crystals in contact with dissimilar materials. In analogy with bulk crystal growth, the major problems are confinement of the liquid and control of the nucleation in such a way that a single seed dominates the growth.

For thin film growth, the stable confinement of the liquid in structures in or on the amorphous substrate depends on interface energies and on substrate geometry, particularly protruding features called "pinning points". The shape of the meniscus is determined by the filling of the structure plus the boundary conditions where the liquid encounters the walls. Suitable combinations of surface geometry and material enable a substrate to hold a thin liquid film captive.

Kruech and McCaldin[6] have performed experiments to demonstrate their conclusion on the confinement using Pb and Sn on SiO_2 substrates.

The control of nucleation has not been addressed directly yet. However, McCaldin indicated that techniques such as providing temperature gradients and spatial structures that have been used to control the nucleation in bulk crystal growth could be employed in the thin film case as well.

The major problems are to develop a better data base of interface energies between substrate materials and the appropriate liquids and the role that impurities might play in determining their values. Control of nucleation could turn out to be difficult since detailed experiments have yet to be performed using these concepts.

CONCLUSIONS AND RECOMMENDATIONS

The methods reported for growing thin layers of crystalline semiconductors on dissimilar substrates show promise of being of great technical importance in the fabrication of a number of semiconductor devices. The program described here represents some of the strongest and most innovative in the country in this area. However, both Ti and MIT Lincoln Laboratories programs are aimed heavily at making device grade Si. While the technological potential of this kind of effort justifies its support, we find

along with the more general questions about semiconductor nucleation and growth are areas where new knowledge could be of major technological importance.

References

1. H. Schwartz and H. A. Tourtellotte, J. Vac. Science and Technology 6, 373(19xx).

2. Z. Nowak, J. Piotrowski, T. Piotrowski, and J. Sadowski, Thin Solid Films 52, 405(1978).

PREPARATION AND PROPERTIES OF HgCdTe

T. C. McGill

HgCdTe Materials for Focal Plane Arrays

Detector arrays based on HgCdTe can operate with adequate values of the detectivity at temperatures which require smaller amounts of cooling than some of the other detector array systems (e.g., extrinsic Si detectors). Focal plane arrays would require the simultaneous fabrication of a large number of detectors and a compatible integrated circuit technology that would allow the fabrication of charge transfer devices. The DARPA program is aimed at producing such a device structure using HgCdTe.

Current detection and charge transfer devices are being fabricated in bulk grown HgCdTe. However, the degree of material control that is required for fabrication of large area devices totally in bulk grown crystals is not in hand. Liquid phase epitaxy is being explored as a method of growing large area single crystal layers with the requisite crystalline perfection and uniformity.

A preferable, if feasible, approach is to grow thin active layers of HgCdTe on various substrates including crystalline as well as amorphous material. This procedure would make possible the direct fabrication of active layers with the appropriate thickness ($\sim$10μm). These thin layers must also satisfy

THE LEDGE MODEL FOR OXIDATION OF SILICON

J. P. Hirth and H. Ehrenreich

INTRODUCTION

In the preceding Summary of the Meeting on Oxidation and Growth Mechanisms Relevant to Semiconductor Processing, a possible ledge model for oxidation was suggested which could also account for the linear dependence of the parabolic rate constant on the vapor pressure of oxygen molecules. Thomson[1] has noted that there is a controversy concerning the intrinsic point defects in silicon. Whether or not silicon interstitials are stable or not and can contribute to stacking fault formation at the Si-SiO_2 interface remains an open question. This issue is pertinent to stacking fault formation at internal oxides as well, as also discussed in the 1979 Report of the DARPA Materials Research Council.[2] The result of that work that suffices for the present discussion is that interstitials are not necessarily required for intrinsic fault formation; vacancies are an alternate defect for forming them.

Several aspects of the ledge model are discussed in more detail in this note for clarification. The basis for the specific ledge structure at the Si-SiO_2 interface is presented. The inter-ledge structure is considered. Then a derivation is given which

Two major difficulties have been encountered and solved. First, the pulsed laser produces splashing of finite size clusters of material from the source. However, by selection of a suitable position for the substrate relative to the source, one can minimize the number of clusters that hit the substrate. Second, the source does not necessarily evaporate congruently. However, by picking the scan rate and laser power approximately, it is possible to obtain congruent evaporation and deposition of the material. Layers 1-2μm with an electron concentration of $10^{16} cm^{-3}$ and electron mobilities of 700 cm^2/V sec have been prepared. The Uniformity of the response was tested on one sample and found to be rather good.

As yet this technique has not been fully investigated. The precise properties of the film and how close they can be made to the benchmark set by the best bulk material has yet to be determined. The questions of uniformity of the properties and surface morphology of the thin film layer have as yet not been tested adequately to see if they meet the specification for large area device fabrication.

Growth of Crystalline Thin-Films Compound on Foreigh Substrates

Presentation of J. L. Miles, New England Research Center)

A group of Polish investigators[2] have succeeded in growing HgCdTe films on CdTe layers vacuum-evaporated on mica, lithium niobate, sapphire, glass, quartz, and thermally oxidized silicon. The CdTe layer was laid down by the not wall technique. The

can produce the linear oxygen pressure dependence of the parabolic rate constant.

THE LEDGE STRUCTURE OF THE Si-SiO_2 INTERFACE

As discussed in the Summary, a ledge model in principle can produce oxidation of a planar interface without the development of large stresses. The detailed description of the manner in which this can occur is now discussed. It represents an alternative for one aspect of the model presented by Tiller,[3-5] giving a mechanistic way of eliminating Si at the interface, rather than producing Si interstitials and eliminating them within the oxide with attendant large stress fields in the oxide.

It is well known that most crystal growth and evaporation processes involving the vapor phase, and many involving the liquid phase, occur by the terrace-ledge-kink model introduced by Stranski[6] and developed kinetically for real crystals by Burton, et al.[7] Figure 1 shows a hypothetical process whereby silicon could oxidize to SiO_2 without the development of stresses. Silicon vaporizes at kink sites on ledges, which traverse the crystal as evaporation proceeds. Oxygen diffuses through SiO_2 and combines with condensing silicon at a kink site on the oxide causing ledge traverse and oxide growth. Since the molecules are accommodated at their equilibrium lattice spacing and at a free surface, evidently no stress or strain is [illegible]. Because the spacing of Si differs in the two cases, removal of one layer of Si will cause growth of several layers of SiO_2.

HgCdTe layers were produced by heating an ampoule certaining the CdTe layer on a substrate along with the proper amount of HgTe and Te. The temperature used was only 200-300°C. This procedure produced single crystal film on mica, lithium niobate, sapphire, and silicon with an oxide layer ≈300Å thick. Large grain polycrystalline films were produced on the other substrates. The procedure produced layers with surprisingly good optical and electrical properties, and spatial uniformity.

The group at New England Research Center working with SPIRE are attempting a somewhat analogous process. They are growing CdTe layers on the substrate using a hot wall technique. The CdTe is then recrystallized using an electron beam. Finally, Hg and Te are diffused isothermally as in the Polish process. A second approach that is being explored is to implant the CdTe layer with Hg and Te and then anneal the material using an electron beam. This program is just getting under way and few results have been obtained so far.

Concluding Comments

While several serious unresolved questions concerning HgCdTe remain, the technological potentialities of this material as an IR detector are sufficiently great that we cannot afford to neglect further intensive fundamental investigations of its growth and physical properties. Some of the novel methods for preparing HgCdTe discussed at the meeting appear to be sufficiently promising as to warrant further investigation. These techniques,

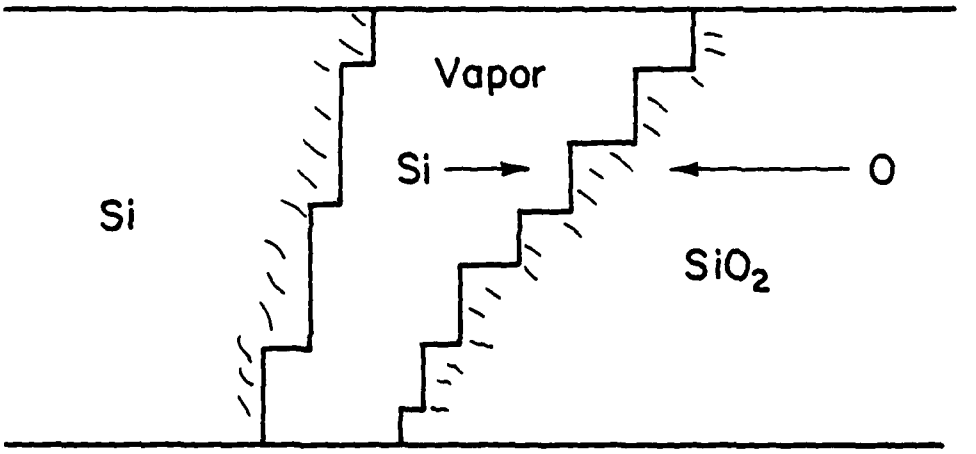

Figure 1. Hypothetical growth of SiO_2 by evaporation-condensation of Si by the terrace-ledge-kink model.

along with the more general questions about semiconductor nucleation and growth are areas where new knowledge could be of major technological importance.

References

1. H. Schwartz and H. A. Tourtellotte, J. Vac. Science and Technology 6, 373(19xx).

2. Z. Nowak, J. Piotrowski, T. Piotrowski, and J. Sadowski, Thin Solid Films 52, 405(1978).

Figure 2a shows this process in more detail. The volume per Si atom in the oxide is about a factor of 2.3 larger than that in the silicon crystal, corresponding to a factor of about 1.3 in the three linear dimensions. In the actual case there are free surfaces normal to the z-direction, so the 30% change in that direction can be accommodated without elastic or plastic strain within the bulk phases. If the remaining accommodation is to occur without bulk strain, removal of unit area (x,y) of silicon at the interface must be accompanied by creation of 1.7 unit areas of oxide at the interface. This can be accomplished if the ledge density of oxide ledges is a factor of 1.7 larger than those on the silicon. The situation is illustrated in Fig. 2a for a factor of 2 instead of 1.7 for ease in description. The transfer of atoms A and B are seen to give the proper area factor. Moreover, with the ledge density factor of 2, a stationary steady state is possible. Consider unit length in the y-direction. Atoms are removed at ledge I in Si at twice the rate they are deposited at ledge I in SiO_2. However, unit length of ledge I in SiO_2 sweeps twice the area (twice the length in the x-direction) as ledge I in Si so the ledges move with the same velocity in the x-direction.

In the actual case, the distribution of ledges with a factor 1.7 would correspond to 70% of the silicon terraces being matched by two ledges in SiO_2 and 30% with one ledge. The real situation also has no vapor phase but is in contact as shown in Fig. 2b. A perspective view of Fig. 2a is given in Fig. 3, where kink sites are also shown. The ledges now become extrinsic inter-

Oxidation and Growth Mechanisms
Relevant to Semiconductor Electronics

Guest Participants

Rubin Braunstein
Physics Department
3-152 Knudsen Hall
University of California
Los Angeles, CA 90024

Jeff T. Cheung
Rockwell International
1049 Camino Dos Rios
Thousand Oaks, CA 91360

Bruce E. Deal
Fairchild Camera and
Instrument
Research & Development
Palo Alto, CA 94304

Eugene A. Irene
IBM Thomas J. Watson
Laboratory
Box 218
Yorktown Heights, NY 10598

Hon Wai Lam
Texas Instruments
MS944
Dallas, TX 75243

J. O. McCaldin
California Inst. of Tech.
MS 116-81
Pasadena, CA 91125

John Miles
New England Research Center
Minuteman Drive
Sudbury, MA 01776

Richard Osgood
M.I.T. Lincoln Laboratory
C-166
Wood Street
Lexington, MA 02173

James D. Plummer
Stanford University
MCC 114, Stanford Elec. Labs.
Stanford, CA 94040

Henry I. Smith
M.I.T. Lincoln Laboratory
E118E
P.O. Box 73
Lexington, MA 02173

Frans Spaepen
Harvard University
Pierce Hall
29 Oxford Street
Cambridge, MA 02138

William A. Tiller
Stanford University
Department of Materials Science
Stanford, CA 94305

John R. Tucker
Aerospace Corporation
A6-1443
Los Angeles, CA 90009

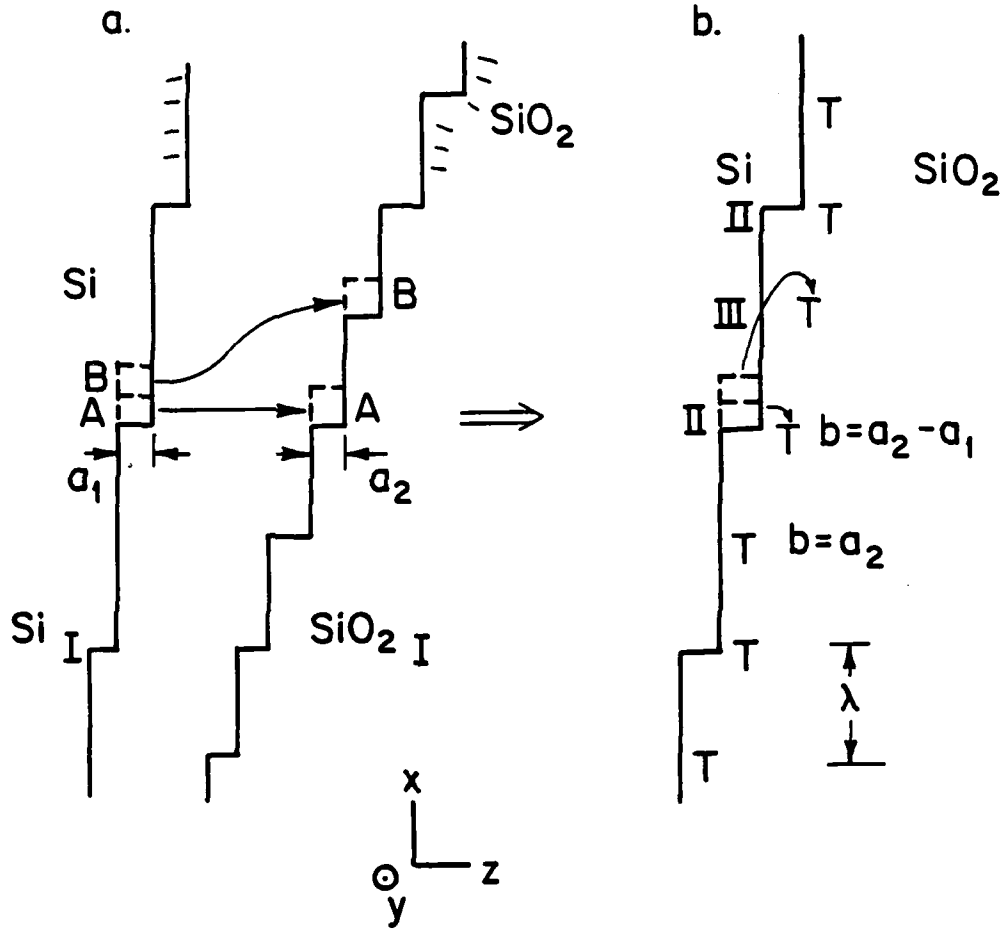

Figure 2a. Steady state growth by the mechanism of Figure 1 requires more ledges on the oxide when $a_2 > a_1$.

2b. The equivalent solid state case. The oxide ledges now become interface ledges with dislocation character. Where they match Si ledges the Burgers vector has magnitude $a_2 - a_1$, otherwise a_2.

THE LEDGE MODEL FOR OXIDATION OF SILICON

J. P. Hirth and H. Ehrenreich

INTRODUCTION

In the preceding Summary of the Meeting on Oxidation and Growth Mechanisms Relevant to Semiconductor Processing, a possible ledge model for oxidation was suggested which could also account for the linear dependence of the parabolic rate constant on the vapor pressure of oxygen molecules. Thomson[1] has noted that there is a controversy concerning the intrinsic point defects in silicon. Whether or not silicon interstitials are stable or not and can contribute to stacking fault formation at the Si-SiO_2 interface remains an open question. This issue is pertinent to stacking fault formation at internal oxides as well, as also discussed in the 1979 Report of the DARPA Materials Research Council.[2] The result of that work that suffices for the present discussion is that interstitials are not necessarily required for intrinsic fault formation; vacancies are an alternate defect for forming them.

Several aspects of the ledge model are discussed in more detail in this note for clarification. The basis for the specific ledge structure at the Si-SiO_2 interface is presented. The inter-ledge structure is considered. Then a derivation is given which

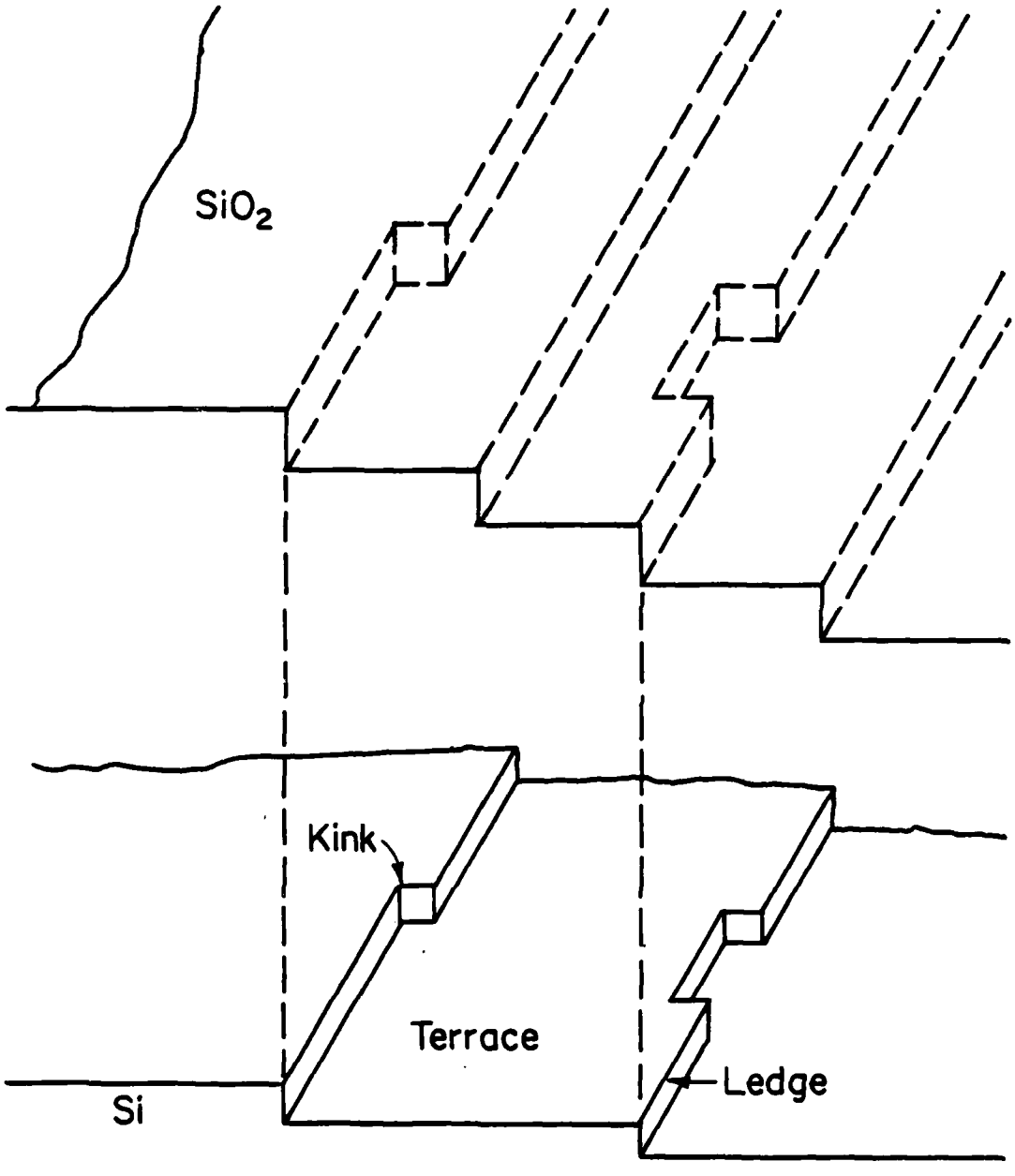

Figure 3. Perspective view of separated interface.

can produce the linear oxygen pressure dependence of the parabolic rate constant.

THE LEDGE STRUCTURE OF THE Si-SiO_2 INTERFACE

As discussed in the Summary, a ledge model in principle can produce oxidation of a planar interface without the development of large stresses. The detailed description of the manner in which this can occur is now discussed. It represents an alternative for one aspect of the model presented by Tiller,[3-5] giving a mechanistic way of eliminating Si at the interface, rather than producing Si interstitials and eliminating them within the oxide with attendant large stress fields in the oxide.

It is well known that most crystal growth and evaporation processes involving the vapor phase, and many involving the liquid phase, occur by the terrace-ledge-kink model introduced by Stranski[6] and developed kinetically for real crystals by Burton, et al.[7] Figure 1 shows a hypothetical process whereby silicon could oxidize to SiO_2 without the development of stresses. Silicon vaporizes at kink sites on ledges, which traverse the crystal as evaporation proceeds. Oxygen diffuses through SiO_2 and combines with condensing silicon at a kink site on the oxide causing ledge traverse and oxide growth. Since the molecules are accommodated at their equilibrium lattice spacing and at a free surface, evidently no stress or strain is [illegible]. Because the spacing of Si differs in the two cases, removal of one layer of Si will cause growth of several layers of SiO_2.

face dislocations as shown (dislocations with both Burgers vectors and short range strain fields extending over the dislocation spacing λ). Where the ledges in the two phases match (imagine just squeezing the surfaces of Fig. 2a together) the Burgers vector will be the difference in linear ledge height $a_2 - a_1 = 0.3a_1$. Where the ledges do not match the Burgers vectors will be a_2.

The model does not require that the SiO_2 be crystalline. Gilman[8], Argon[9], and others have demonstrated that dislocation-like entities exist in amorphous solids in a geometric sense. In the same way, dislocations with average Burgers vectors as above exist in the sense that ledge-like defects with an <u>average</u> ledge height a_2 are present at the interface.

Finally, we consider the local transport process. Oxygen is supplied at the ledges by bulk diffusion through the oxide. At ledges of type II, Si simply makes a single, rearrangement, diffusion jump at the interface. The transport of Si to ledges of type III occurs by interface diffusion from II to III or IV to III. This diffusion could occur by an interstitial flux from II to III or a vacancy flux from III to II. Hence, as for the stacking fault growth possibilities[2], interstitials are not necessarily required. Since the diffusion of the latter type is relatively slow, a uniform λ-spacing is probably unstable relative to a case $\lambda_{II-III} < \lambda_{III-IV}$. The stationary spacing would involve a maximization of growth calculation balancing the decreased diffusion distance, which would tend to directly increase the diffusion flux, with the elastic repulsion between dislocations which

would be reflected by a decreased chemical potential difference driving the diffusion. It is noteworthy at this point to mention that ledges on Si at the interface with terrace widths of $\sim 40\text{Å}$ have been observed in high resolution transmission electron microscopy.[19]

THE TERRACE STRUCTURE

As mentioned in the Summary, the Stanford oxidization model envisions that the SiO_2 has the ordered structure of α or β cristobalite at the interface as mentioned by Tiller.[3-5] Then a semi-coherent {100}// {100} plane matching would be possible with no long-range strain field in either phase but with intrinsic interface dislocations at the interface (distinguished from extrinsic dislocations by having Burgers vectors but no strain fields). As shown in Fig. 2 of the Summary, the intrinisc interface dislocations correspond to silicon planes ending in the interface and having dangling bonds there. Thus, the basis of the requirement for cristobalite is the elimination of coherency strains, but the creation of dislocation core energy in the dangling bonds. In that case the terraces between ledges II and III in Fig. 2b, for example, would have such a structure. As already mentioned, however, there is no topographical reason why the terrace structure could not be amorphous on the SiO_2 side.

We suggest, by analogy with bulk amorphous Si, that the SiO_2 would prefer on energetic grounds to be amorphous rather than crystalline in the vicinity of the interface. The energy

Figure 2a shows this process in more detail. The volume per Si atom in the oxide is about a factor of 2.3 larger than that in the silicon crystal, corresponding to a factor of about 1.3 in the three linear dimensions. In the actual case there are free surfaces normal to the z-direction, so the 30% change in that direction can be accommodated without elastic or plastic strain within the bulk phases. If the remaining accommodation is to occur without bulk strain, removal of unit area (x,y) of silicon at the interface must be accompanied by creation of 1.7 unit areas of oxide at the interface. This can be accomplished if the ledge density of oxide ledges is a factor of 1.7 larger than those on the silicon. The situation is illustrated in Fig. 2a for a factor of 2 instead of 1.7 for ease in description. The transfer of atoms A and B are seen to give the proper area factor. Moreover, with the ledge density factor of 2, a stationary steady state is possible. Consider unit length in the y-direction. Atoms are removed at ledge I in Si at twice the rate they are deposited at ledge I in SiO_2. However, unit length of ledge I in SiO_2 sweeps twice the area (twice the length in the x-direction) as ledge I in Si so the ledges move with the same velocity in the x-direction.

In the actual case, the distribution of ledges with a factor 1.7 would correspond to 70% of the silicon terraces being matched by two ledges in SiO_2 and 30% with one ledge. The real situation also has no vapor phase but is in contact as shown in Fig. 2b. A perspective view of Fig. 2a is given in Fig. 3, where kink sites are also shown. The ledges now become extrinsic inter-

penalty for bond bending in a-Si (in contrast to that for bond stretching) is small. Because of the oxygens intervening between neighboring silicons, the freedom for bond bending in a-SiO_2 would be expected to be greater than that ($\sim\pm10°$) in a-Si. Thus more bonds crossing the interface could be satisfied by utilizing the freedom for bond bending which is absent in cristobalite. As shown in Fig. 2 of the Summary for the semi-coherent interfaces, the number of dangling bonds (intrinsic interface dislocations) is $\sim10^{15}/cm^2$, the same order as the number of atoms on the interface plane. On the other hand the number of interface states, presumed to arise from dangling bonds is known to be $\sim10^{13}cm^{-2}$. The difference between these magnitudes is accounted for, according to the present model, by the ability of most of the unsatisfied bonds to adjust with respect to a-SiO_2.

The residual number of dangling bonds (leaving aside the increased distance between Si atoms in SiO_2) would be expected to be of the same order in a-SiO_2 and a-Si. This comes about because the Si-O bond energy ($\sim$90 kcal/mole) is evidently greater than the Si-Si bond energy ($\sim$50 kcal/mole)[10,11] so that the Si-O-Si bonds can always be presumed to be satisfied. EPR measurements show that there are roughly 10^{19} dangling bonds per cm^3 in a-Si. This would translate roughly to 10^{12}-$10^{13}cm^{-2}$ per plane, which is consistent with the observed number of interface states.

A remaining question concerns the much lower number of interface states ($\sim10^{10}cm^{-2}$) observed in actual SiO_2/Si interfaces. Deal[12] and Plummer[13] have suggested that the majority of the

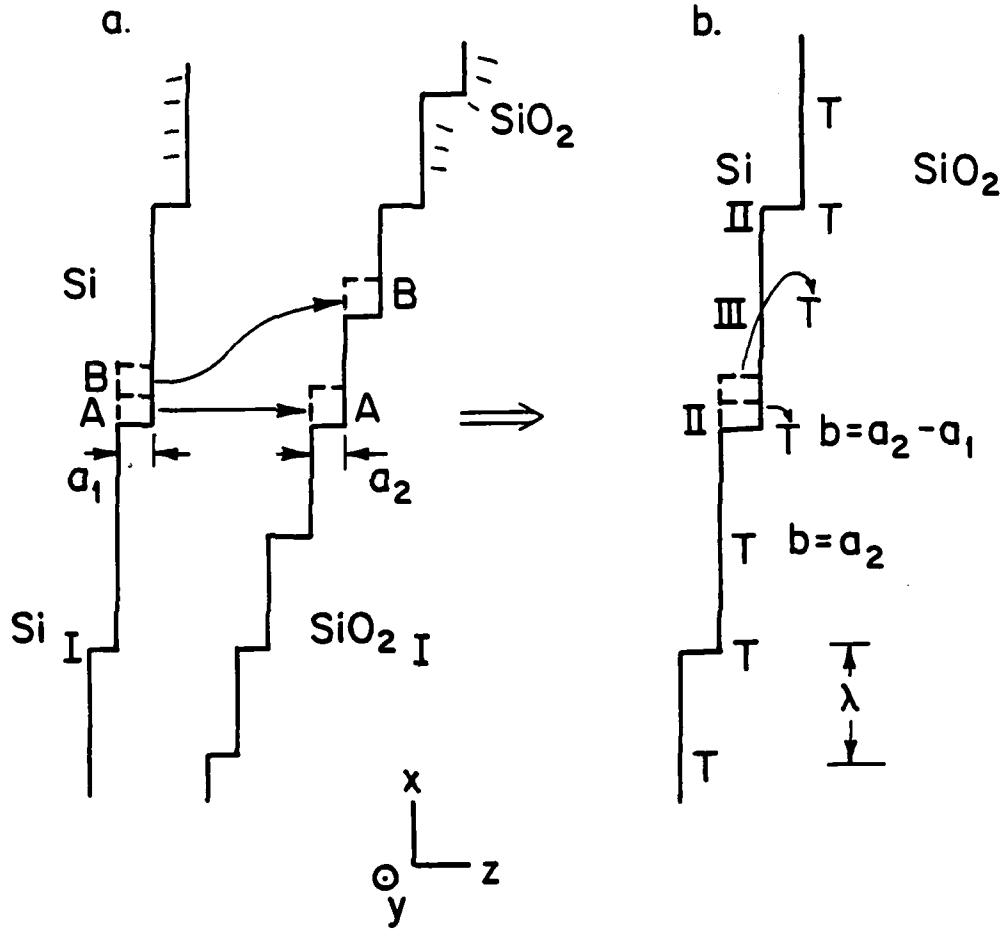

Figure 2a. Steady state growth by the mechanism of Figure 1 requires more ledges on the oxide when $a_2 > a_1$.

2b. The equivalent solid state case. The oxide ledges now become interface ledges with dislocation character. Where they match Si ledges the Burgers vector has magnitude $a_2 - a_1$, otherwise a_2.

remaining dangling bonds are satisfied by small amounts ($\sim 10^{13}$-$10^{14} cm^{-3}$) of residual H that are always present, possibly due to some small contamination associated with water vapor. This mechanism of satisfying dangling bonds, of course, is well known in amorphous hydrogenated Si and makes its doping possible.

The residual hydrogen would be expected to move with the Si/SiO_2 interface since the Si-H bond must be converted into an Si-O bond as the oxide forms. The latter is energetically preferable (90 kcal/mole) over the former (Si-H: 70 kcal/mole). Thus the same minute quantity of H would be made available to interact with each successive layer as the oxide interface moves. The residual bulk material would be hydrogen-free in agreement with observations.

A KINETIC OXIDATION RATE EQUATION

As noted in the Summary, the parabolic rate constant for oxidation depends linearly on oxygen pressure which is unusual in comparison to many other systems.[14] We present a simple suggestion which would give such behavior in the case that the oxide is fully amorphous. A somewhat more complex two-layer model which would apply if a thin cristobalite layer is present near the interface as suggested by Tiller[3-5], or which would apply if the defect structure of the oxide changes, is then outlined.

The instantaneous flux of oxygen through the oxide is

$$J = -D \frac{\partial c}{\partial x} = \text{constant} \qquad (1)$$

where D is the oxygen diffusivity and c is the oxygen concentration. The constancy is the quasi-steady state approximation of

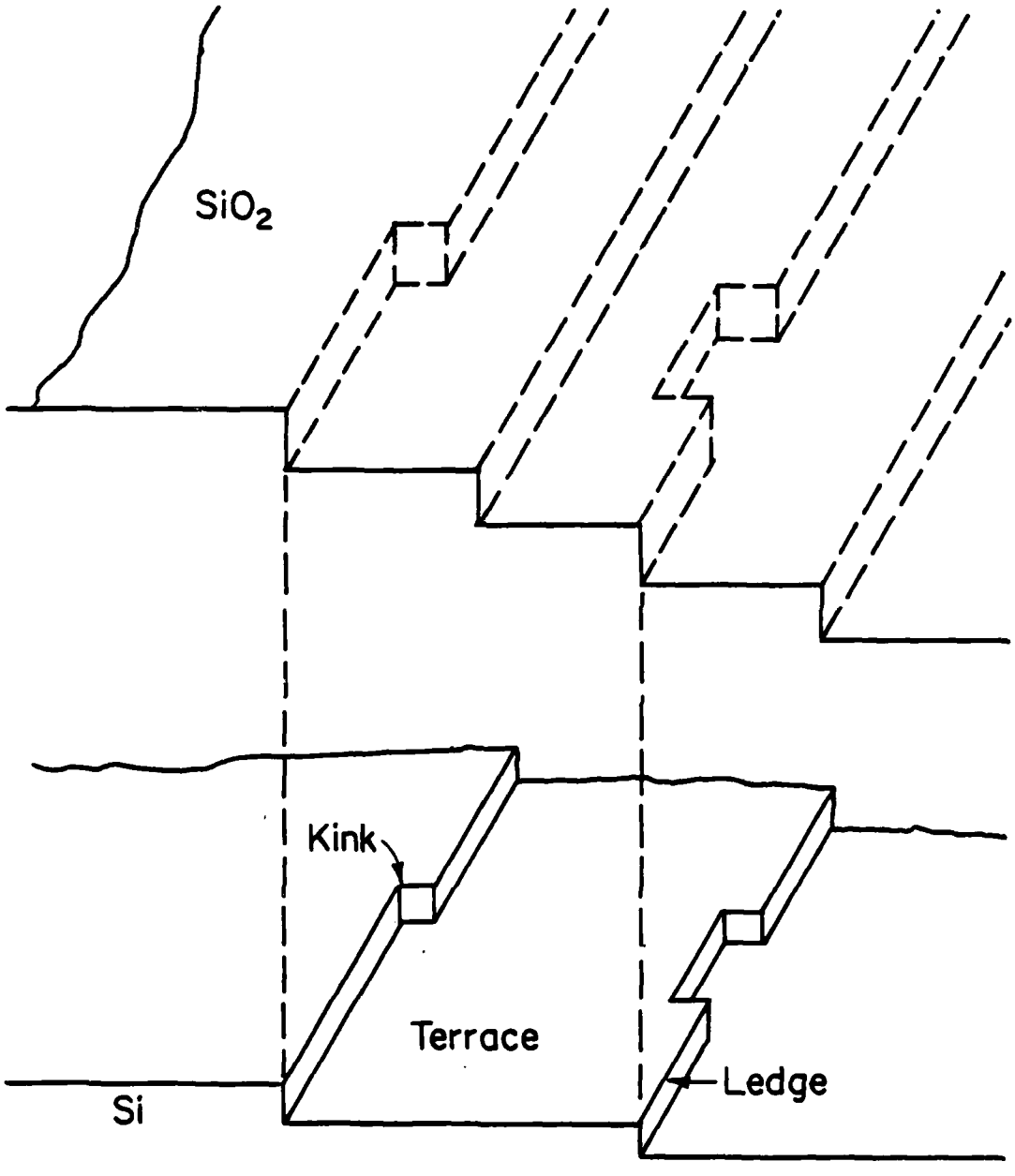

Figure 3. Perspective view of separated interface.

Wagner[15], equivalent to neglect of the moving boundary conditions in the problem, which is valid when $D/X >> v$. Here X is the oxide thickness and v is the velocity of the boundaries. The condition $D/X >> v$ is satisfied for the present case.

Suppose $D = D(c) = Mc$ where M is a constant, as in Fig. 4. Then transposing and integrating Eq. (1), we have

$$X = \int_{c_B}^{c_C} Ddc = \int_{c_B}^{c_C} Mcdc = \frac{M}{2}\left(c_C^2 - c_B^2\right) = \bar{D}(c_C - c_B) \simeq \frac{Mc_C^2}{2} \qquad (2)$$

Where $\bar{D}$ is the average diffusivity. The rate of change of thickness with time is

$$\frac{dX}{dt} = -\Omega D \frac{\partial c}{\partial x} = \frac{K}{X} \qquad (3)$$

where Ω is the molar volume of the oxide and K is Wagner's parabolic rate constant[15]. Since the result of Eq. (2) scales in the same manner with time, K is time independent and Q. (3) integrates to the form

$$X = 2Kt, \quad K = \Omega\bar{D}(c_C - c_B) \qquad (4)$$

Hence for this simple example $K \propto c_C^2$. As commonly assumed for parabolic oxidation[14,15], we suppose that oxygen molecules dissociate at the vapor-oxide interface with a local equilibrium condition of

$$O_2 \rightleftarrows 2O_C \qquad (5)$$

or

$$c_C \propto P_{O_2}^{\frac{1}{2}} \qquad (6)$$

face dislocations as shown (dislocations with both Burgers vectors and short range strain fields extending over the dislocation spacing λ). Where the ledges in the two phases match (imagine just squeezing the surfaces of Fig. 2a together) the Burgers vector will be the difference in linear ledge height $a_2 - a_1 = 0.3a_1$. Where the ledges do not match the Burgers vectors will be a_2.

The model does not require that the SiO_2 be crystalline. Gilman[8], Argon[9], and others have demonstrated that dislocation-like entities exist in amorphous solids in a geometric sense. In the same way, dislocations with average Burgers vectors as above exist in the sense that ledge-like defects with an <u>average</u> ledge height a_2 are present at the interface.

Finally, we consider the local transport process. Oxygen is supplied at the ledges by bulk diffusion through the oxide. At ledges of type II, Si simply makes a single, rearrangement, diffusion jump at the interface. The transport of Si to ledges of type III occurs by interface diffusion from II to III or IV to III. This diffusion could occur by an interstitial flux from II to III or a vacancy flux from III to II. Hence, as for the stacking fault growth possibilities[2], interstitials are not necessarily required. Since the diffusion of the latter type is relatively slow, a uniform λ-spacing is probably unstable relative to a case $\lambda_{II-III} < \lambda_{III-IV}$. The stationary spacing would involve a maximization of growth calculation balancing the decreased diffusion distance, which would tend to directly increase the diffusion flux, with the elastic repulsion between dislocations which

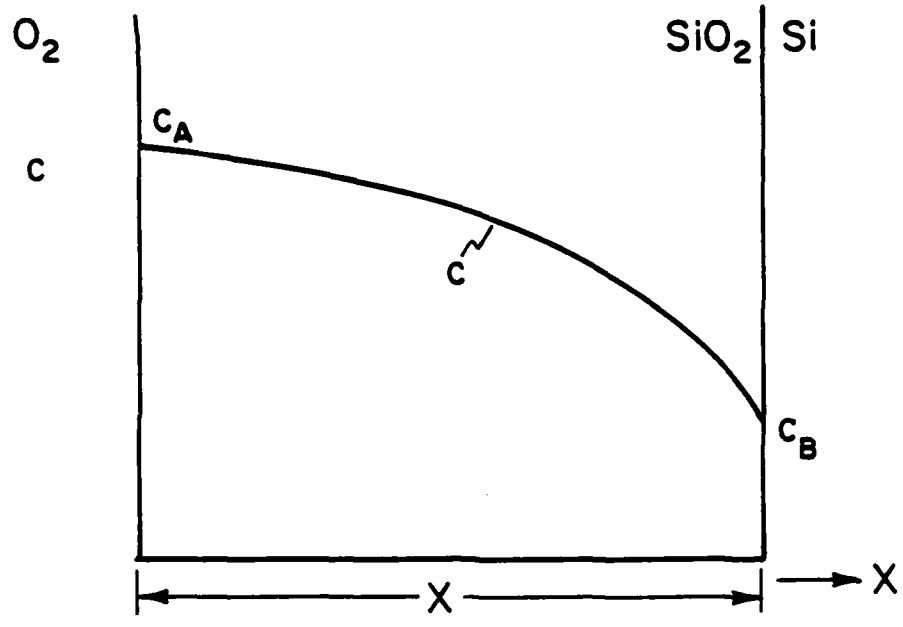

Figure 4. Steady state oxygen profile through the oxide when D = D(c).

would be reflected by a decreased chemical potential difference driving the diffusion. It is noteworthy at this point to mention that ledges on Si at the interface with terrace widths of $\sim 40\text{Å}$ have been observed in high resolution transmission electron microscopy.[19]

THE TERRACE STRUCTURE

As mentioned in the Summary, the Stanford oxidization model envisions that the SiO_2 has the ordered structure of α or β cristobalite at the interface as mentioned by Tiller.[3-5] Then a semi-coherent {100}// {100} plane matching would be possible with no long-range strain field in either phase but with intrinsic interface dislocations at the interface (distinguished from extrinsic dislocations by having Burgers vectors but no strain fields). As shown in Fig. 2 of the Summary, the intrinisc interface dislocations correspond to silicon planes ending in the interface and having dangling bonds there. Thus, the basis of the requirement for cristobalite is the elimination of coherency strains, but the creation of dislocation core energy in the dangling bonds. In that case the terraces between ledges II and III in Fig. 2b, for example, would have such a structure. As already mentioned, however, there is no topographical reason why the terrace structure could not be amorphous on the SiO_2 side.

We suggest, by analogy with bulk amorphous Si, that the SiO_2 would prefer on energetic grounds to be amorphous rather than crystalline in the vicinity of the interface. The energy

giving

$$K \propto P_{O_2} \tag{7}$$

where P_{O_2} is the oxygen pressure, as required. Thus, a finding that $K \propto P_{O_2}$ is not inconsistant with the ledge model and an amorphous oxide.

Other examples exist where $D = D(c)$, for example, carbon in iron[16], but where in the dilute regime $D \rightarrow$ constant as the excess defect causing diffusion becomes dilute. Thus, it is conceivable that $D \rightarrow$ constant as c_C decreases, i.e., at low P_{O_2}. In this regard, the observation cited by Plummer[13] that K becomes proportional to $P_{O_2}^{\frac{1}{2}}$ at low partial pressures of oxygen would also be explainable by the above derivation.

In a more complex situation one might have the situation in Fig. 5, where oxygen is imagined to diffuse rapidly in an oxygen-rich surface region and more slowly in the near interface region, which would be cristobalite in Tiller's model[3-5] or amorphous silica of different stoichiometry in the ledge model. The nature of the diffusing oxygen, whether interstitial or combining with a vacancy, and whether charged or not does not matter for present purposes, but will be considered in the next section. The problem is one which has been solved by Yurek et al.[17] While there are actually gradients through the oxide phases, Wagner[18] has shown that the kinetics can be accurately described by assuming that the interface reactions produce phases with the average defect concentration, here noted by α and β.

penalty for bond bending in a-Si (in contrast to that for bond stretching) is small. Because of the oxygens intervening between neighboring silicons, the freedom for bond bending in a-SiO_2 would be expected to be greater than that ($\sim\pm10°$) in a-Si. Thus more bonds crossing the interface could be satisfied by utilizing the freedom for bond bending which is absent in cristobalite. As shown in Fig. 2 of the Summary for the semi-coherent interfaces, the number of dangling bonds (intrinsic interface dislocations) is $\sim10^{15}/cm^2$, the same order as the number of atoms on the interface plane. On the other hand the number of interface states, presumed to arise from dangling bonds is known to be $\sim10^{13}cm^{-2}$. The difference between these magnitudes is accounted for, according to the present model, by the ability of most of the unsatisfied bonds to adjust with respect to a-SiO_2.

The residual number of dangling bonds (leaving aside the increased distance between Si atoms in SiO_2) would be expected to be of the same order in a-SiO_2 and a-Si. This comes about because the Si-O bond energy ($\sim$90 kcal/mole) is evidently greater than the Si-Si bond energy ($\sim$50 kcal/mole)[10,11] so that the Si-O-Si bonds can always be presumed to be satisfied. EPR measurements show that there are roughly 10^{19} dangling bonds per cm^3 in a-Si. This would translate roughly to 10^{12}-$10^{13}cm^{-2}$ per plane, which is consistent with the observed number of interface states.

A remaining question concerns the much lower number of interface states ($\sim10^{10}cm^{-2}$) observed in actual SiO_2/Si interfaces. Deal[12] and Plummer[13] have suggested that the majority of the

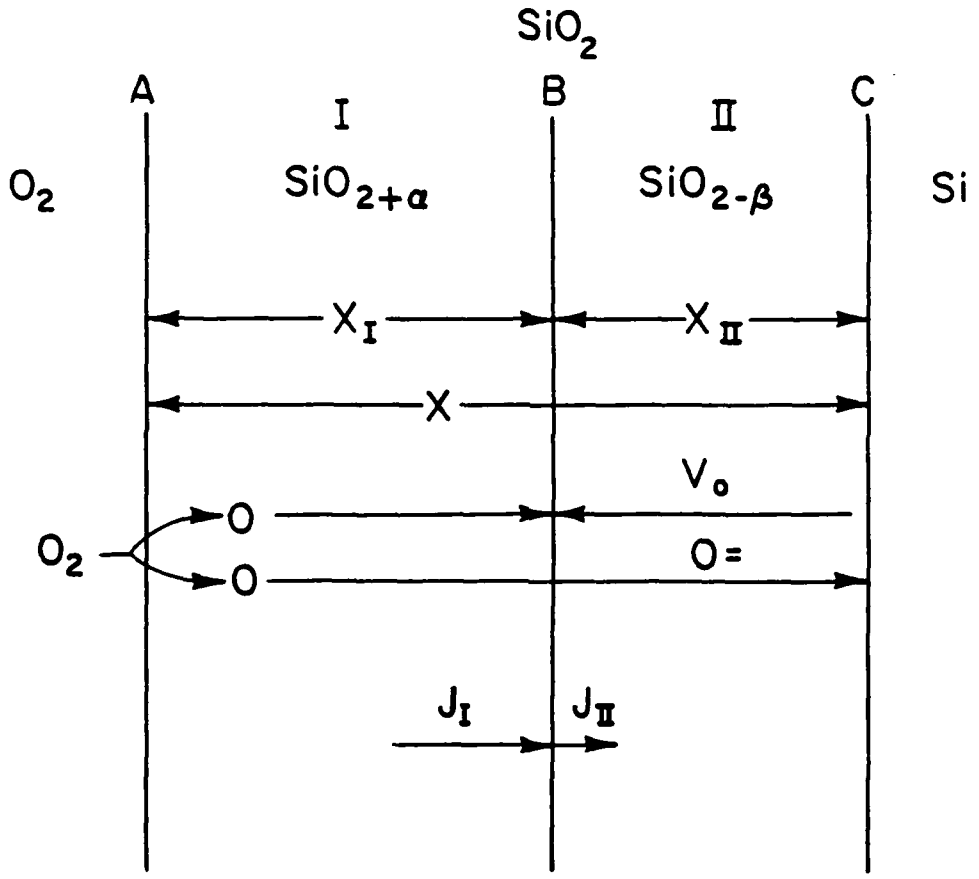

Figure 5. Various representations of the oxidation kinetics of silicon.

remaining dangling bonds are satisfied by small amounts ($\sim 10^{13}$-$10^{14} cm^{-3}$) of residual H that are always present, possibly due to some small contamination associated with water vapor. This mechanism of satisfying dangling bonds, of course, is well known in amorphous hydrogenated Si and makes its doping possible.

The residual hydrogen would be expected to move with the Si/SiO_2 interface since the Si-H bond must be converted into an Si-O bond as the oxide forms. The latter is energetically preferable (90 kcal/mole) over the former (Si-H: 70 kcal/mole). Thus the same minute quantity of H would be made available to interact with each successive layer as the oxide interface moves. The residual bulk material would be hydrogen-free in agreement with observations.

A KINETIC OXIDATION RATE EQUATION

As noted in the Summary, the parabolic rate constant for oxidation depends linearly on oxygen pressure which is unusual in comparison to many other systems.[14] We present a simple suggestion which would give such behavior in the case that the oxide is fully amorphous. A somewhat more complex two-layer model which would apply if a thin cristobalite layer is present near the interface as suggested by Tiller[3-5], or which would apply if the defect structure of the oxide changes, is then outlined.

The instantaneous flux of oxygen through the oxide is

$$J = -D \frac{\partial c}{\partial x} = \text{constant} \qquad (1)$$

where D is the oxygen diffusivity and c is the oxygen concentration. The constancy is the quasi-steady state approximation of

At C the relevant reaction is that of Eq. (5). At B the relation is

$$O + \frac{1}{\alpha+\beta} SiO_{2-\beta} \rightleftarrows \frac{1}{\alpha+\beta} SiO_{2+\alpha} \tag{8}$$

while at A it is

$$O + \frac{1}{2-\beta} Si \rightleftarrows SiO_{2-\beta} \tag{9}$$

The issue is that the flux entering at C according to Eq. (5) and (1) partitions as it reaches B, part causing region I to grow according to (8) (which also consumes region II) and part passing through region II to A where it causes region II to grow according to (9). The details of the analysis are presented by Yurek et al[17] and are beyond the scope of the present work. The key result from that work, in the limit that $D_{II} < D_I$, is that the parabolic rate constant is (their Eq. (30))

$$K = \frac{\left(1 + \frac{X_{II}}{X_I}\right)^2}{\left(1 + \frac{X_{II}\Omega_I}{X_I\Omega_{II}}\right)} \Omega_I D_I 2\alpha \tag{10}$$

where $c_C - c_B = 2\Omega_I\alpha$ in the present notation. Also,

$$\frac{X_{II}}{X_I} = \frac{D_{II}\beta(2-\beta)}{D_I\alpha(2+\alpha)} \tag{11}$$

Thus, in the limit $D_{II} << D_I$, $X_{II} << X_I$ and

$$K = 2\Omega_I D_I\alpha + 2\Omega_I\left(2 - \frac{\Omega_I}{\Omega_{II}}\right) D_{II}\beta\left(\frac{2-\beta}{2+\alpha}\right) \tag{12}$$

Wagner[15], equivalent to neglect of the moving boundary conditions in the problem, which is valid when $D/X >> v$. Here X is the oxide thickness and v is the velocity of the boundaries. The condition $D/X >> v$ is satisfied for the present case.

Suppose $D = D(c) = Mc$ where M is a constant, as in Fig. 4. Then transposing and integrating Eq. (1), we have

$$X = \int_{c_B}^{c_C} Ddc = \int_{c_B}^{c_C} Mcdc = \frac{M}{2}\left(c_C^2 - c_B^2\right) = \bar{D}(c_C - c_B) \simeq \frac{Mc_C^2}{2} \qquad (2)$$

Where $\bar{D}$ is the average diffusivity. The rate of change of thickness with time is

$$\frac{dX}{dt} = -\Omega D \frac{\partial c}{\partial x} = \frac{K}{X} \qquad (3)$$

where Ω is the molar volume of the oxide and K is Wagner's parabolic rate constant[15]. Since the result of Eq. (2) scales in the same manner with time, K is time independent and Q. (3) integrates to the form

$$X = 2Kt, \quad K = \Omega\bar{D}(c_C - c_B) \qquad (4)$$

Hence for this simple example $K \propto c_C^2$. As commonly assumed for parabolic oxidation[14,15], we suppose that oxygen molecules dissociate at the vapor-oxide interface with a local equilibrium condition of

$$O_2 \rightleftarrows 2O_C \qquad (5)$$

or

$$c_C \propto P_{O_2}^{\frac{1}{2}} \qquad (6)$$

Hence, in this case also, α will be proportional to $P_{O_2}^{\frac{1}{2}}$ and if $D_I \propto c \propto \alpha$, a linear dependence on P_{O_2} will obtain, the second term in (12) depending only very weakly on α.

CHARGE STATES AND FIELD EFFECTS

As reviewed by Tiller[3], various experiments on the influence of electrostatic fields on oxidation rates suggest that a charged species has some role in oxidation. Mills and Kroger[20] suggest that ionic conductivity in the range 0-700°C is accounted for by the diffusion of charged oxygen interstitials. There seems to be no support for the presence of this defect, however, in infrared and ultra-violet spectroscopy or in electron-spin-resonance studies[21]. Here, we suggest a model wherein charge effects are important only near the Si interface and in doing so provide a working definition for the B interface in Figs. 5 and 6.

Mott[22] and Harrison[23] suggest on the basis of theory and experiment that the effective charge q_L in defect-free SiO_2 is about 0.7e. Griscom[24], consistent with the dangling-bond defect structure for deep traps in SiO_2[21,22], suggests that the E' center found in both α-quartz and fused silica is an oxygen vacancy V with a trapped electron. As shown by Griscom, the vacancy can equivalently be thought of as a pair of dangling Si bonds which can dissociate, equivalent to the extension of the vacancy into two partial vacancies.

The other defect that concerns us is the interstitial which we assign a neutral charge because of the lack of spectroscopic data favoring its charge and because the uncharged inter-

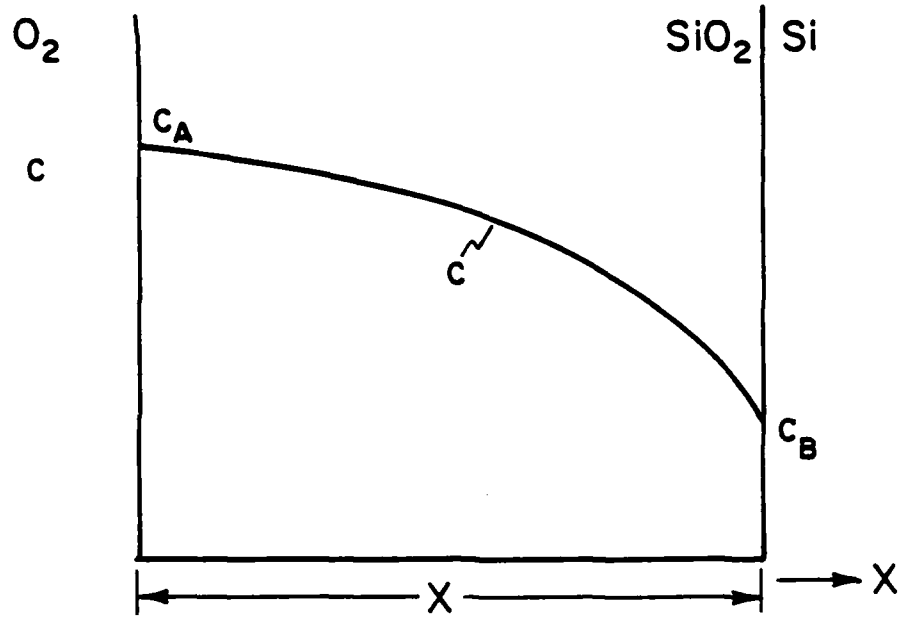

Figure 4. Steady state oxygen profile through the oxide when D = D(c).

stitial should have less strain energy contribution to the activation energy for diffusion. The model is then that of Fig. 6. Absolute charges relative to vacuum are assigned to lattice Si and O, designated Si_L and O_L, and to defects.

At the gas interface C, oxygen dissociates to form neutral oxygen interstitials. These diffuse to the B interface where they combine with oxygen vacancies. Oxygen vacancies are created at kinks at the interface A in the basic step of oxide growth. Near region A, which is highly deficient in oxygen relative to SiO_2, the bonding has a more covalent nature and the effective lattice charge is ~ 0. The charge increases with distance z from the interface as vacancies are annihilated, the stoichiometry approaches SiO_2, and the bonding assumes a more polar nature.

The reactions are then, at C:

$$\tfrac{1}{2}O_2 \rightarrow O_i^o \tag{13}$$

At B:

$$O_i^o + V^o + (-q_L) \rightarrow O_L^{-q_L} \tag{14}$$

$$Si_L^o \rightarrow Si_L^{q_L} + (-q_L) \tag{15}$$

The quantity $(-q_L)$ represents charge transfer from the Si valence charge to the oxygen interstitial entering the vacancy.

At A:

$$O_L^o + Si \rightarrow O_L^o + Si_L^o + V^o \tag{16}$$

Relative to field effects, the vacancy at A has a zero effective charge relative to both the majority Si atoms and the

giving

$$K \propto P_{O_2} \tag{7}$$

where P_{O_2} is the oxygen pressure, as required. Thus, a finding that $K \propto P_{O_2}$ is not inconsistant with the ledge model and an amorphous oxide.

Other examples exist where D = D(c), for example, carbon

large minority of lattice oxygen ions. However, at B, the vacancy has acquired a positive effective charge q_L relative to the lattice ions. Thus, a positive electrostatic charge in the gas phase relative to the silicon should provide a counter force to the oxygen chemical potential gradient, should tend to force vacancies toward the Si interface and should suppress oxidation, consistent with the observations by Jorgensen.[3,25,26]

ACKNOWLEDGEMENT

This research was supported by the Defense Advanced Research Projects Agency of the Department of Defense under Contract No. MDA903-80C-0505 with The University of Michigan.

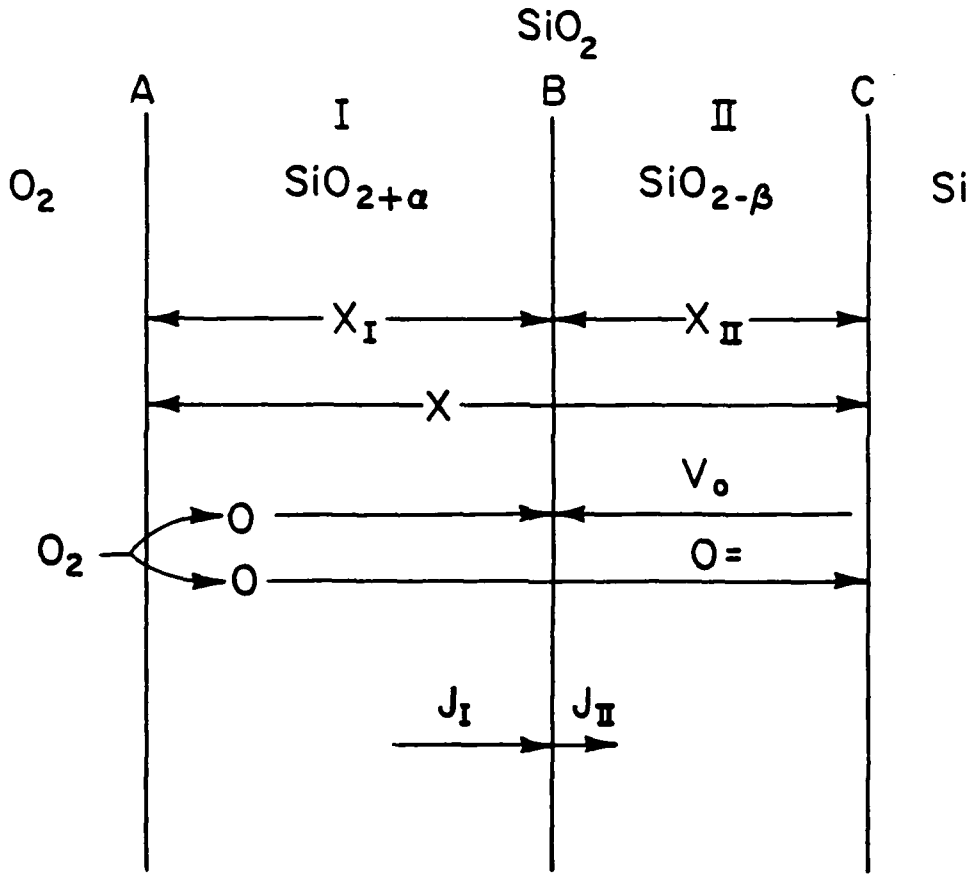

Figure 5. Various representations of the oxidation kinetics of silicon.

REFERENCES

1. R. Thomson, in ref. 2, p. 203.

2. Report of the DARPA Materials Research Council, University of Michigan, Ann Arbon, Mich., 1979

3. W. A. Tiller, J. Electrochem. Soc. 127, 619 (1980).

4. W. A. Tiller, ibid, p.625.

5. W. A. Tiller, ibid, in press.

6. I. N. Stranski, Z. Phys. Chem. 136, 259 (1928).

7. W. K. Burton, N. Cabrera and F. C. Frank, Phil. Trans. Roy. Soc. (London). 243A, 299 (1951).

8. J. J. Gilman, J. Appl. Phys. 46, 1625 (1975).

9. A. Argon, Proceedings of the Conference on Modeling of Physical Phenomena by Dislocations, Gainesville, Florida, Pergamon, New York, in press.

10. J. Margrave, private communications, July, 1980.

11. L. C. Pauling, The Nature of the Chemical Bond, Cornell Univ. Press, 1960.

12. B. E. Deal, reported at the 1980 Meeting of the DARPA Materials Research Council; see also Report TR DXG 569 ICL 7-77, Integrated Circuits Laboratory, Stanford University.

13. J. D. Plummer, ibid.

14. P. Kofstad, High-Temperature Oxidation of Metals, Wiley, New York, 1966.

15. C. Wagner, Z. Phys. Chem. B21, 25 (1933).

16. L. S. Darken and R. W. Gurry, Physical Chemistry of Metals, McGraw-Hill, New York, 1953, pp. 450-51.

17. G. J. Yurek, R. P. Rapp and J. P. Hirth, Oxidation of Metals, 8, 265 (1974).

18. C. Wagner, Acta Met. 17, 99 (1969).

19. O. L. Krivanek, D. C. Tsui, T. T. Sheng and A. Kamgar, in ref. 21, p.356.

20. T. G. Mills and F. A. Kröger, J. Electrochem. Soc. 120, 1582 (1973).

21. S. T. Pantelides, "The Physics of SiO_2", Pergamon, New York, (1978).

SOME COMMENTS ON
POSSIBLE MECHANISMS FOR GRAPHOEPITAXY

F. Spaepen

The most successful process so far for obtaining longer well oriented Si grains by graphoepitaxy involves the annealing in an oven of a Si film sandwiched between two vitreous SiO_2 layers, one the grating and the other a "cap".

Since the oven is heated to 1300°C and higher, the as deposited amorphous Si film crystalizes first to a randomly oriented polycrystalline one. The final process, therefore, is one of grain growth; i.e., some of the small grains, which have a preferred orientation, grow at the expense of the others. The speed of this process, however, is too large ($\sim$10 cm/sec) to be explainable by the standard mechanisms that involve motion of the grain boundaries by a diffusive process. Melting of some of the material would explain the growth velocity.

Capillarity probably plays an important role in selecting the grains that have a preferred orientation for growth. It is quite plausible that the interfacial tension between a Si grain and the vitreous SiO_2 would depend on the crystal orientation. If, for example, the [100] orientation has the lowest surface tension, the atoms in grains which have [100] faces in contact with both the substrate and a sidewall of the grating have a

stitial should have less strain energy contribution to the activation energy for diffusion. The model is then that of Fig. 6. Absolute charges relative to vacuum are assigned to lattice Si and O, designated Si_L and O_L, and to defects.

At the gas interface C, oxygen dissociates to form neutral oxygen interstitials. These diffuse to the B interface where they combine with oxygen vacancies. Oxygen vacancies are created at kinks at the interface A in the basic step of oxide growth. Near region A, which is highly deficient in oxygen relative to SiO_2, the bonding has a more covalent nature and the effective lattice charge is ~ 0. The charge increases with distance z from the interface as vacancies are annihilated, the stoichiometry approaches SiO_2, and the bonding assumes a more polar nature.

The reactions are then, at C:

$$\tfrac{1}{2}O_2 \rightarrow O_i^o \tag{13}$$

At B:

$$O_i^o + V^o + (-q_L) \rightarrow O_L^{-q_L} \tag{14}$$

$$Si_L^o \rightarrow Si_L^{q_L} + (-q_L) \tag{15}$$

The quantity $(-q_L)$ represents charge transfer from the Si valence charge to the oxygen interstitial entering the vacancy.

At A:

$$O_L^o + Si \rightarrow O_L^o + Si_L^o + V^o \tag{16}$$

Relative to field effects, the vacancy at A has a zero effective charge relative to both the majority Si atoms and the

lower chemical potential than those in grains of similar sizes, but of a different orientation. The preferred grains will then grow and form a well oriented film. This capillarity driven grain growth is a well known process in metals. The importance of the surface tension is illustrated by the fact that the preferred orientation sometimes changes with the annealing atmosphere.

It has been proposed that the SiO_2 "cap" on the Si is important because of the compression it introduces into the Si film, which in turn leads to a lowering of the melting point and contributes to the selection of the preferred orientation of the grains. The origin of the proposed compressive stress is the difference in thermal expansion between Si and SiO_2. We think that there are several reasons why the stress probably does not play such an important role.

The main reason is that vitreous SiO_2 becomes too soft at these high temperatures to sustain high stresses. This is clear from the direct observations that the grating in the substrate deforms and that the top surface becomes uneven during processing. It can also be seen from the following brief analysis. The viscosity of a SiO_2 is 3×10^9 $Nsecm^{-2}$ at the melting point of Si (1680°K). An estimate of the possible stress in the Si due to differential thermal expansion gives an upper limit of 5×10^8 Nm^{-2}. This could lead to a lowering of the melting point by $\Delta T = 50K$. However, at this temperature, the viscosity is still only 1.4×10^{10} $Nsecm^{-2}$. At these high stresses, this would mean that the strain rate of the SiO_2 is on the order of $10^{-2}sec^{-1}$, which would lead to a very quick relaxation of the stress.

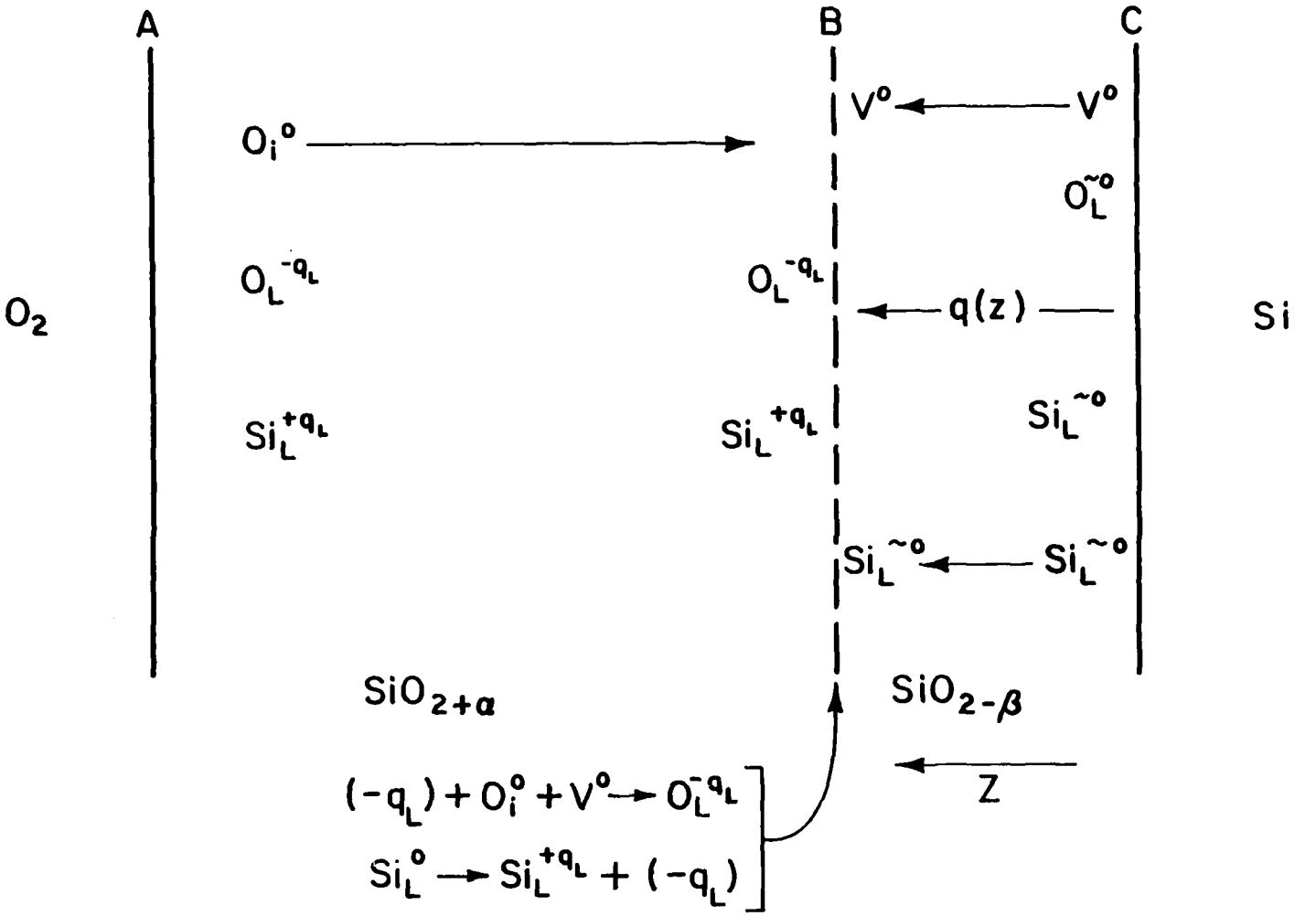

Figure 6. Charge states and reactions

Furthermore, even during the heating up at lower temperatures, the stresses probably do not get very high. The same process which leads to compression in the Si also induces tension in the SiO_2. Although silica can be quite strong in compression, it fails easily in tension, and this would relieve the stresses. We have also seen at the meeting (presentation by E. A. Irene) that the oxide on a polycrystalline Si film already has cracks in it above the Si boundaries.

Since it seems clear that the SiO_2 cap improves the quality of the final produce, its function must be sought elsewhere. The simplest explanation would be that it reinforces the capillarity effect. It could also prevent preferential growth of wrongly oriented crystals that could occur if the top surface remained free or it it would collect heterogeneous inclusions.

What is most needed is a careful investigation of the transformation process itself, to determine how much melting occurs, and at what temperature. It is possible that a small stress effect could halp regulate the transformation; the effect is then certainly a transient one, and should be analyzed carefully as a dynamic process with appropriate viscosity relaxation in t'e $_2$.

large minority of lattice oxygen ions. However, at B, the vacancy has acquired a positive effective charge q_L relative to the lattice ions. Thus, a positive electrostatic charge in the gas phase relative to the silicon should provide a counter force to the oxygen chemical potential gradient, should tend to force vacancies toward the Si interface and should suppress oxidation, consistent with the observations by Jorgensen.[3,25,26]

ACKNOWLEDGEMENT

This research was supported by the Defense Advanced Research Projects Agency of the Department of Defense under Contract No. MDA903-80C-0505 with The University of Michigan.

GRAPHO-EPITAXY AND THE POSSIBLE EFFECTS OF STRESS

H. Reiss

The remarkable orientational influence of a "grating" of grooves, leading to grapho-epitaxy still needs definitive explanation. Tentative (and credible) explanations have already been advanced by Spaepen and Turnbull who suggest that crystals, aligned in the grooves, so that low surface free energies are achieved by their habit, are stable enough to grow or take part in recrystallization processes at the expense of less favorably aligned crystals. The prediction of orientation and habit in such cases involves a modified "Gibbs-Wulff construction" which accounts for the directionally defined interfacial energy between groove substrate and crystal.

Another possible, but not so probable, explanation would involve the effects of a uniform gradient of stress, possibly produced by the combination of grating and "cap" used, for example, in the grapho-epitaxy of silicon.

To account for gradients of stress it is necessary to develop another "modified" Gibbs-Wulff construction. The conventional construction is based on the minimization of total surface free energy, accounting for the differing free energies of different crystal faces, at constant volume. This construction assumes that the bulk contribution to the free energy will remain

REFERENCES

1. R. Thomson, in ref. 2, p. 203.

2. Report of the DARPA Materials Research Council, University of Michigan, Ann Arbon, Mich., 1979

3. W. A. Tiller, J. Electrochem. Soc. 127, 619 (1980).

4. W. A. Tiller, ibid, p.625.

5. W. A. Tiller, ibid, in press.

6. I. N. Stranski, Z. Phys. Chem. 136, 259 (1928).

7. W. K. Burton, N. Cabrera and F. C. Frank, Phil. Trans. Roy. Soc. (London). 243A, 299 (1951).

8. J. J. Gilman, J. Appl. Phys. 46, 1625 (1975).

9. A. Argon, Proceedings of the Conference on Modeling of Physical Phenomena by Dislocations, Gainesville, Florida, Pergamon, New York, in press.

10. J. Margrave, private communications, July, 1980.

11. L. C. Pauling, The Nature of the Chemical Bond, Cornell Univ. Press, 1960.

12. B. E. Deal, reported at the 1980 Meeting of the DARPA Materials Research Council; see also Report TR DXG 569 ICL 7-77, Integrated Circuits Laboratory, Stanford University.

13. J. D. Plummer, ibid.

14. P. Kofstad, High-Temperature Oxidation of Metals, Wiley, New York, 1966.

15. C. Wagner, Z. Phys. Chem. B21, 25 (1933).

16. L. S. Darken and R. W. Gurry, Physical Chemistry of Metals, McGraw-Hill, New York, 1953, pp. 450-51.

17. G. J. Yurek, R. P. Rapp and J. P. Hirth, Oxidation of Metals, 8, 265 (1974).

constant as long as the volume remains constant, a point of view which is valid when there is no gradient of stress.

When a gradient is present this cannot be the case since the free energy always has a contribution from the strain-energy density function. For uniform stress this contribution depends only on volume and not on shape. In the presence of a gradient it depends upon shape. Apparently a "modified" construction taking into account the gradient of stress has not been developed. Even the construction for the simple, usual case of a uniform stress field is not easy to establish and, in fact, was not proved, for two dimensions, until 1951 and, for three dimensions, not until 1955.

Progress has now been made by the author in the statement and proof of the construction in the presence of a gradient of stress, but the proof is not yet complete. Prospects for its early completion are, however, good, especially for the two dimensional case.

18. C. Wagner, Acta Met. 17, 99 (1969).

19. O. L. Krivanek, D. C. Tsui, T. T. Sheng and A. Kamgar, in ref. 21, p.356.

20. T. G. Mills and F. A. Kröger, J. Electrochem. Soc. 120, 1582 (1973).

21. S. T. Pantelides, "The Physics of SiO_2", Pergamon, New York, (1978).

22. N. F. Mott, in ref. 21, p.1.

23. W. A. Harrison, in ref. 21, p.105.

24. D. L. Griscom, in ref. 21, p.232.

25. P. J. Jorgensen, J. Chem. Phys. 37, 874 (1962).

26. P. J. Jorgensen and F. J. Norton, General Electric Res. Lab. Rept. 65-RL-4003X, July, 1963.

REPORT ON ACOUSTIC EMISSION WORKSHOP

B. Budiansky, A. G. Evans, J. Hutchinson, G. S. Kino,
F. A. McClintock and J. R. Rice

INTRODUCTION

A one day MRC workshop on Acoustic Emission was organized by G. S. Kino, M. Buckley and A. G. Evans. Its aim was to determine the present status of the field and its practical applications, the status of basic research and the needs for further basic research.

The initial studies on acoustic emission stem from the work of Kaiser which indicated relationships between the occurrence of acoustic emission, certain material properties and the quantitative state of stress in the material. The acoustic emission is typically detected with a piezoelectric transducer operating over part of the frequency range from 100kHz to 2MHz, placed in contact with the material being tested.

Kaiser concluded from his measurements that structures often emit noise when subject to stress, such that the rate of emission tends to increase with the applied stress until the point of failure. Also it was noted that the emission in unloaded structures did not recommence until the applied load exceeded the original value. After further investigation, it was realized that such simple behavior is by no means always obeyed.

SOME COMMENTS ON
POSSIBLE MECHANISMS FOR GRAPHOEPITAXY

F. Spaepen

The most successful process so far for obtaining longer well oriented Si grains by graphoepitaxy involves the annealing in an oven of a Si film sandwiched between two vitreous SiO_2 layers, one the grating and the other a "cap".

Since the oven is heated to 1300°C and higher, the as deposited amorphous Si film crystalizes first to a randomly oriented polycrystalline one. The final process, therefore, is one of grain growth; i.e., some of the small grains, which have a preferred orientation, grow at the expense of the others. The speed of this process, however, is too large ($\sim$10 cm/sec) to be explainable by the standard mechanisms that involve motion of the grain boundaries by a diffusive process. Melting of some of the material would explain the growth velocity.

Capillarity probably plays an important role in selecting the grains that have a preferred orientation for growth. It is quite plausible that the interfacial tension between a Si grain and the vitreous SiO_2 would depend on the crystal orientation. If, for example, the [100] orientation has the lowest surface tension, the atoms in grains which have [100] faces in contact with both the substrate and a sidewall of the grating have a

The major problem of the field is to determine useful correlations between the acoustic emission rate, the damage rate, and properties of the material and structure being examined, and the ultimate structural failure. There are many possible sources of acoustic emission. Some examples are, fracture of brittle particles, martensitic phase transformations, twinning, grain fracture, decohesion of grain boundaries, movement of dislocations (especially during breakaway from impediments), and the extension of pre-existing cracks. In composites the fracture of individual fibers, fiber-matrix distortion and matrix crazing give rise to yet other sources of emission.

Acoustic emission has the desirable property that its presence can be associated with the failure mechanisms, through the microstructure of the material. In particular, it has the potential for accessing failure-related information in materials which involve brittle cracking events as failure precursors, because large amplitude emissions are associated with such events. It can often be effective in detecting growing flaws and determining their location by triangulation. The increment in total crack area can, in controlled systems, be deduced from appropriate measures of the acoustic emission. However, no direct information about the size of flaws is available in the emission data; other NDE techniques are required for this purpose.

A major problem in acoustic emission testing is to distinguish between the many possible sources of emission. Only then is it possible to consistently isolate failure information from

lower chemical potential than those in grains of similar sizes, but of a different orientation. The preferred grains will then grow and form a well oriented film. This capillarity driven grain growth is a well known process in metals. The importance of the surface tension is illustrated by the fact that the preferred orientation sometimes changes with the annealing atmosphere.

It has been proposed that the SiO_2 "cap" on the Si is important because of the compression it introduces into the Si film, which in turn leads to a lowering of the melting point and contributes to the selection of the preferred orientation of the grains. The origin of the proposed compressive stress is the difference in thermal expansion between Si and SiO_2. We think that there are several reasons why the stress probably does not play such an important role.

The main reason is that vitreous SiO_2 becomes too soft at these high temperatures to sustain high stresses. This is clear from the direct observations that the grating in the substrate deforms and that the top surface becomes uneven during processing. It can also be seen from the following brief analysis. The viscosity of a SiO_2 is 3×10^9 $Nsecm^{-2}$ at the melting point of Si (1680°K). An estimate of the possible stress in the Si due to differential thermal expansion gives an upper limit of 5×10^8 Nm^{-2}. This could lead to a lowering of the melting point by $\Delta T = 50K$. However, at this temperature, the viscosity is still only 1.4×10^{10} $Nsecm^{-2}$. At these high stresses, this would mean that the strain rate of the SiO_2 is on the order of $10^{-2}sec^{-1}$, which would lead to a very quick relaxation of the stress.

other sources of noise, such as the movement of a rivet within a bolt hole.

SUMMARY OF THE WORKSHOP PROCEEDINGS

At the meeting itself, J. Rodgers (Acoustic Emission Technology) and C. Tatro (Lawrence, Livermore) reviewed the present status and practical applications of acoustic emission measurements. They indicated major applications in composites (where NDE methods are not very effective), the testing of aircraft structures and of the pressure vessels and pipelines used in the petrochemical and nuclear industries. At the other extreme in size, an important application is the assessment of integrity and bonding in integrated circuits. Acoustic emission often provides indications of problems in materials like welds which are difficult to evaluate by other techniques. A beginning has been made on the application of signal processing techniques and adaptive learning to the interpretation of acoustic emission data. However, situations in which acoustic emission could be employed as an unequivocal indicator of failure were not clearly identified. It would appear to be used primarily as an early indication of problems, which are then checked by other NDE techniques.

Information of more direct relevance to ultimate failure (derived from in-flight emission data obtained on aircraft) was presented by Carlyle and Hutton (NADC and Battelle). Of particular significance is an in-flight study presently being conducted by Battelle in cooperation with the Australian Air Force on operating Maccetti aircraft trainers. Using a small portable

Furthermore, even during the heating up at lower temperatures, the stresses probably do not get very high. The same process which leads to compression in the Si also induces tension in the SiO_2. Although silica can be quite strong in compression, it fails easily in tension, and this would relieve the stresses. We have also seen at the meeting (presentation by E. A. Irene) that the oxide on a polycrystalline Si film already has cracks in it above the Si boundaries.

Since it seems clear that the SiO_2 cap improves the quality of the final produce, its function must be sought elsewhere. The simplest explanation would be that it reinforces the capillarity effect. It could also prevent preferential growth of wrongly oriented crystals that could occur if the top surface remained free or it it would collect heterogeneous inclusions.

What is most needed is a careful investigation of the transformation process itself, to determine how much melting occurs, and at what temperature. It is possible that a small stress effect could halp regulate the transformation; the effect is then certainly a transient one, and should be analyzed carefully as a dynamic process with appropriate viscosity relaxation in t'e $_2$.

instrument (operating in a narrow band aroung 400kHz) has been obtained from a region in the vicinity of a rivet hole in which fatigue cracks were extending during flight. The total emission amplitude was demonstrated to be proportional to the change in the total crack area (the crack length is measured magnetically and the depth ultrasonically every 400 hours; crack lengths of the order of 1-4mm were observed). An interesting additional observation was that AE was weak in high level flying, and did not increase substantially during aerobatic flying. But low level flying, which causes considerable buffeting, gave rise to radically increased acoustic emission levels. Adaptive learning routines to measure the autocorrelation of the acoustic emission at specific delays, and for particular parts of the frequency spectrum were also discussed. It is hoped, for example, that algorithms which recognize acoustic emission from fatigue cracks will emerge. The programs thus developed will then be transferred to the microprocessor systems employed in the portable aircraft testing unit.

Simmons (NBS) and Sachse (Cornell) discussed closely related techniques for examining the fundamental processes of acoustic emission. The emphasis of both groups is to examine the acoustic emission over relatively short times (of the order of a few microseconds), instead of averaging bursts over several milliseconds. By taking measurements in this time frame, it is possible to detect signals which have been subject to (at most) a few internal reflections. Deconvolutions of the received

signals can then be achieved, either theoretically or by using a calibrated source. Good success in deconvolving simple sources was shown by Sachse. Simmons showed that reproducible emission could be obtained by using a indentation system to achieve the fracture events. Both groups demonstrated that directly transmitted longitudinal and shear waves are observed at a transducer placed at a location opposite the source (with multiple echo plate modes appearing later). Earlier work indicated that the most important component received at a transducer placed on the same side of the plate as the source was the Rayleigh wave.

Simmons developed a theoretical formulation to describe acoustic emission that resulted from a stress drop at the source. The procedure regards an acoustic emission origin as a multipole source and employs a Green's tensor with a fairly complicated multipole expansion. He concludes that measurements from at least six locations would be needed to deconvolve the Green's function tensor. On the basis of this theory small sources would emit frequency independent noise in the frequency range normally of interest.

H. Wadley described a fundamental program on acoustic emission being conducted at Harwell. He discussed simple models of acoustic emission based on a penny shaped crack or a dislocation loop expanding at constant velocity. In two sets of mechanical experiments he used, respectively, a narrow band piezoelectric sensor and a broad band capacitive sensor (placed 2μm from the surface) to obtain acoustic emission information.

He demonstrated: (1) the integrated acoustic emission power in a narrow band obtained from a deformation test is linearly proportional to the imposed strain rate; (2) the acoustic emission power exhibited the typically observed maximum in the vicinity of the yield strain; (3) the integrated emission energy from a pure polycrystalline Al increased with increased grain size; (4) an Al alloy with 1.3% wt Mg exhibited an emission maximum at an intermediate grain size ($\sim$100μm), as well as small emission peaks presumed to be associated with solute unpinning events. The results could be tentatively correlated with simple models based on the expansion of small dislocation loops.

Finally, he noted that in certain low strength steels, ductile crack extension does not generate detectable acoustic emission (as also noted in certain pressure vessel studies). This observation presumably pertains to materials in which hole initiation at inclusions occurs at small stress/strain levels. Materials for which hole formation occurs by inclusion cracking at more significant local stress levels would undoubtedly be more amenable to AE techniques. Such knowledge could bias the choice of materials to be selected for applications where AE has a demonstrable, unique potential for predicting failure imminence.

L. Graham described experiments which confined the failure zone to a narrow spatial region in the test specimen and examined the acoustic emission characteristics derived from different failure processes. He noted that four characteristic frequency spectra could be associated with the various failure

REPORT ON ACOUSTIC EMISSION WORKSHOP

B. Budiansky, A. G. Evans, J. Hutchinson, G. S. Kino,
F. A. McClintock and J. R. Rice

INTRODUCTION

A one day MRC workshop on Acoustic Emission was organized

The central issue is to associate acoustic emission with the onset of structural failure by invoking basic relations between the increase in crack volume at the failure source (the quantity that dictates the emission amplitude) to some measure of the acoustic emission, from the significant* signals. The principal problems limiting the application of acoustic emission are contained in a restricted ability to address the following issues: (i) the isolation of significant signals by using a pattern recognition process; (ii) the influence of the structure on the magnitude of significant signals; and (iii) relating the

other sources of noise, such as the movement of a rivet within a bolt hole.

SUMMARY OF THE WORKSHOP PROCEEDINGS

At the meeting itself, J. Rodgers (Acoustic Emission Technology) and C. Tatro (Lawrence, Livermore) reviewed the present status and practical applications of acoustic emission measurements. They indicated major applications in composites (where NDE methods are not very effective), the testing of aircraft structures and of the pressure vessels and pipelines used in the petrochemical and nuclear industries. At the other extreme in size, an important application is the assessment of integrity and bonding in integrated circuits. Acoustic emission often provides indications of problems in materials like welds which are difficult to evaluate by other techniques. A beginning has been made on the application of signal processing techniques and adaptive learning to the interpretation of acoustic emission data. However, situations in which acoustic emission could be employed as an unequivocal indicator of failure were not clearly identified. It would appear to be used primarily as an early indication of problems, which are then checked by other NDE techniques.

Information of more direct relevance to ultimate failure (derived from in-flight emission data obtained on aircraft) was presented by Carlyle and Hutton (NADC and Battelle). Of particular significance is an in-flight study presently being conducted by Battelle in cooperation with the Australian Air Force on operating Maccetti aircraft trainers. Using a small portable

other NDE measurements (e.g., acoustic backscattering) to provide more information about the localization of damage. Note, however, that deterministic predictions of failure can never be achieved. Conversely, for a single, discrete crack (that ultimately produces failure) the potential exists for relating the AE to final failure, provided that the two other issues noted above, can be effectively addressed.

The fundamental event in fracture is crack growth by steps of the order of a few microns or less, corresponding to frequencies of the order of $f = c/\lambda = (5000\ m/s)/(5\times10^{-6}\ m) = 1000$ MHz. These very high frequencies are scattered by the grain, phase and inclusion structures. For these and practical considerations the transducers are limited to a few MHz. Therefore, a problem is how the low frequency effects of an incremental burst, perhaps strengthened through resonance with the adjacent crack, can reach the detector and be reported. The occurrence of such individual bursts is often widely enough separated so that they can be detected individually. For instance, for a burst frequency of 0.1 MHz, with crack growth by 1μm/burst and bursts around the edge of a 1mm crack, the crack growth rate would be

$$\frac{\Delta A}{A} = \frac{(1\mu m)^2}{(1000\ \mu m)^2}\ (10^5/s) = 0.10/s$$

For slower crack growth rates of practical interest, the individual events would be even more widely separated, so the detection of individual bursts is of interest.

instrument (operating in a narrow band aroung 400kHz) has been obtained from a region in the vicinity of a rivet hole in which fatigue cracks were extending during flight. The total emission amplitude was demonstrated to be proportional to the change in the total crack area (the crack length is measured magnetically and the depth ultrasonically every 400 hours; crack lengths of the order of 1-4mm were observed). An interesting additional observation was that AE was weak in high level flying, and did not increase substantially during aerobatic flying. But low level flying, which causes considerable buffeting, gave rise to radically increased acoustic emission levels. Adaptive learning routines to measure the autocorrelation of the acoustic emission at specific delays, and for particular parts of the frequency spectrum were also discussed. It is hoped, for example, that algorithms which recognize acoustic emission from fatigue cracks will emerge. The programs thus developed will then be transferred to the microprocessor systems employed in the portable aircraft testing unit.

Simmons (NBS) and Sachse (Cornell) discussed closely related techniques for examining the fundamental processes of acoustic emission. The emphasis of both groups is to examine the acoustic emission over relatively short times (of the order of a few microseconds), instead of averaging bursts over several milliseconds. By taking measurements in this time frame, it is possible to detect signals which have been subject to (at most) a few internal reflections. Deconvolutions of the received

At the present time acoustic emission results are highly irreproducible, with a few isolated examples of carefully tailored reproducibility (e.g., Simmons' work). This is probably not fundamental, but is in large part due to incomplete understanding of the microstructural problems, the response of the transducers on different structures and poor standardization.

We recommend that:

(1) Research should be concentrated on a clearly defined problem which can be worked through in detail. An example would be a well characterized system with a single crack (e.g., a fatigue crack) present.

(2) Experiments should be initiated which permit a variety of other NDE methods to be employed at the same time as acoustic emission tests. As examples, acoustic backscattering from discrete cracks or localized accumulations of damage, attenuation measurements and measurements of acoustic velocity changes (associated with stress concentrations and microstructure modifications) should be undertaken. The measurements could be correlated with the acoustic emission data to ascertain a more detailed knowledge of the emission source.

(3) It is essential that the influence of structure on the results be determined. It is important here to retain a connection with the practical applications. For example, if most of the energy is usually contained in Rayleigh waves, should transducers be designed for Rayleigh wave detection? Is it possible to deconvolve the structural response? Alternatively, is it more

signals can then be achieved, either theoretically or by using a calibrated source. Good success in deconvolving simple sources was shown by Sachse. Simmons showed that reproducible emission could be obtained by using a indentation system to achieve the fracture events. Both groups demonstrated that directly transmitted longitudinal and shear waves are observed at a transducer placed at a location opposite the source (with multiple echo plate modes appearing later). Earlier work indicated that the most important component received at a transducer placed on the same side of the plate as the source was the Rayleigh wave.

Simmons developed a theoretical formulation to describe acoustic emission that resulted from a stress drop at the source. The procedure regards an acoustic emission origin as a multipole source and employs a Green's tensor with a fairly complicated multipole expansion. He concludes that measurements from at least six locations would be needed to deconvolve the Green's function tensor. On the basis of this theory small sources would emit frequency independent noise in the frequency range normally of interest.

H. Wadley described a fundamental program on acoustic emission being conducted at Harwell. He discussed simple models of acoustic emission based on a penny shaped crack or a dislocation loop expanding at constant velocity. In two sets of mechanical experiments he used, respectively, a narrow band piezoelectric sensor and a broad band capacitive sensor (placed 2μm from the surface) to obtain acoustic emission information.

expedient to take long time averages to emphasize the final structural response? How important is it to place the receiving transducers as closely as possible to the emission source? How is emission affected by the location and angular position of cracks? What is the best method for locating emission sources in complicated structures?

(4) Further studies are needed on a range of important materials to determine relationships between the microstructural events that generate the principal emission, the emission characteristics and fracture rleated properties (e.g., $J,\Delta a$). For example, does inclusion cracking provide emission that can be related to J in certain important alloy systems? Are the significant emission characteristics contained in the frequency spectra, the amplitude distribution, the event rate, etc.?

(5) A careful study of transducers is required. Not enough attention has been paid to the directional and modal sensitivity of the various types of transducer. This tends to indicate the need for development of very small sized transducer. The development of reliable, well-standarized and characterized transducers is also needed. It would be useful to determine if transducers which respond only to the incident energy, such as acoustoelectric transducers, would improve the reliability of measurements. New types of transudcers such as fiber optic sensors, thin film zinc oxide integrated circuit transducers, and polyvinylidene fluoride transducers should be studies for their possible applications to this field.

He demonstrated: (1) the integrated acoustic emission power in a narrow band obtained from a deformation test is linearly proportional to the imposed strain rate; (2) the acoustic emission power exhibited the typically observed maximum in the vicinity of the yield strain; (3) the integrated emission energy from a pure polycrystalline Al increased with increased grain size; (4) an Al alloy with 1.3% wt Mg exhibited an emission maximum at an intermediate grain size ($\sim$100μm), as well as small emission peaks presumed to be associated with solute unpinning events. The results could be tentatively correlated with simple models based on the expansion of small dislocation loops.

Finally, he noted that in certain low strength steels, ductile crack extension does not generate detectable acoustic emission (as also noted in certain pressure vessel studies). This observation presumably pertains to materials in which hole initiation at inclusions occurs at small stress/strain levels. Materials for which hole formation occurs by inclusion cracking at more significant local stress levels would undoubtedly be more amenable to AE techniques. Such knowledge could bias the choice of materials to be selected for applications where AE has a demonstrable, unique potential for predicting failure imminence.

L. Graham described experiments which confined the failure zone to a narrow spatial region in the test specimen and examined the acoustic emission characteristics derived from different failure processes. He noted that four characteristic frequency spectra could be associated with the various failure

It is apparent that the acoustic emission field is still relatively immature. Much research remains to be done, and correlation of basic research with practical applications in the field is essential to successful exploitation of this technique for the consistent prediction of failure imminence in complex structures.

RECOMMENDATIONS FOR FUTURE MRC PARTICIPATION

It is apparent that the physics of the basic sources of acoustic emission is not well understood. It is desirable to arrive at a fundamental formulation which could predict the expected frequency spectra, angular distribution of emission, and excitation of surface and bulk waves by the different types of sources. Some of these concepts have been developed in part in the seismology field.

These basic aspects of the emission can be coupled with the statistical character of microcracking events (occurring during crack extension, etc.) to predict such measurable parameters as the amplitude distribution, pertinent to the various damage processes that lead to ultimate failure. Some indication of characteristic changes in the acoustic emission signals prior to ultimate failure may emerge, which would be suitable for exploitation in failure prediction procedures.

We therefore suggest that a workshop should be held early next year to examine what has been done in the field of seismology, and discuss the fundamental mechanisms of acoustic emission. We

processes. He also suggested that amplitude distributions would be separated into (up to four) different underlying extreme value forms: again, presumably, related to different damage mechanisms occurring in the material. This very careful characterization may have fundamental significance (requiring further exploitation) with regard to the isolation of signals from the damage events of primary interest. Further attempts at relating characteristic spectra or amplitude distributions to damage events are encouraged by these observations.

A final paper by D. Egle discussed the problem of the distortion of the acoustic emission signal by acoustic resonances in a small sample. He showed that the time response of a system at long times after the emission event would be dominated by the characteristics of the structure, and that most of the final energy would be associated with shear waves.

CONCLUSIONS

It is apparent that there is a considerable dichotomy between the work being carried out in the field and fundamental methods being examined in the research laboratory. As an example, for triangulation to find emission measured from structures in the field, the signal arrival times are essentially correlated with Rayleigh wave velocities on the structure surface; while the fundamental laboratory measurements are taken as close to the emission sources possible, and deconvolution is attempted in relatively simple cases.

believe that at the MRC there is an almost ideal mix of expertise in fracture mechanics, statistical processes, and acoustic wave propagation effects, to carry out fundamental studies to establish the nature of the basic sources of acoustic emission

The central issue is to associate acoustic emission with the onset of structural failure by invoking basic relations between the increase in crack volume at the failure source (the quantity that dictates the emission amplitude) to some measure of the acoustic emission, from the significant* signals. The principal problems limiting the application of acoustic emission are contained in a restricted ability to address the following issues: (i) the isolation of significant signals by using a pattern recognition process; (ii) the influence of the structure on the magnitude of significant signals; and (iii) relating the crack volume change inferred from the AE measurement to the imminence of failure.

The final issue is of particular concern for materials that fail by a statistical accumulation of damage and coalescence prior to ultimate failure (microcracking in cermaics/rocks, fiber/matrix fractures in composites, fatigue damage in initiation controlled fatigue). For these materials, the characterization of early damage provided by AE can only be probabilistically related to the final failure. Probabilistic relations based on the micro-mechanics/statistics of failure for specific materials and failure modes may be useful for establishing the most expedient relation between AE and the failure probability. Improved probabilistic predictions may be possible if the AE information is coupled with

---

*Significant signals refers to the signals that emanate from the failure process, excluding signals from extraneous (failure insensitive) sources.

other NDE measurements (e.g., acoustic backscattering) to provide more information about the localization of damage. Note, however, that deterministic predictions of failure can never be achieved. Conversely, for a single, discrete crack (that ultimately produces failure) the potential exists for relating the AE to final failure, provided that the two other issues noted above, can be effectively addressed.

The fundamental event in fracture is crack growth by steps of the order of a few microns or less, corresponding to frequencies of the order of $f = c/\lambda = (5000\ m/s)/(5\times10^{-6}\ m) = 1000$ MHz. These very high frequencies are scattered by the grain, phase and inclusion structures. For these and practical considerations the transducers are limited to a few MHz. Therefore, a problem is how the low frequency effects of an incremental burst, perhaps strengthened through resonance with the adjacent crack, can reach the detector and be reported. The occurrence of such individual bursts is often widely enough separated so that they can be detected individually. For instance, for a burst frequency of 0.1 MHz, with crack growth by 1μm/burst and bursts around the edge of a 1mm crack, the crack growth rate would be

$$\frac{\Delta A}{A} = \frac{(1\mu m)^2}{(1000\ \mu m)^2}\ (10^5/s) = 0.10/s$$

For slower crack growth rates of practical interest, the individual events would be even more widely separated, so the detection of individual bursts is of interest.

ACOUSTIC EMISSION WORKSHOP

Guest Participants

Frederic Bick
Effects Technology, Inc.
5383 Hollister
Santa Barbara, CA 93111

John M. Carlyle
Naval Air Dev. Center
Code 60633
Warminster, PA 18974

Davis M. Egle
University of Oklahoma
865 Asp St., Room 212
Norman, Oklahoma 73019

Lloyd J. Graham
Rockwell Science Center
Thousand Oaks, CA 91360

P. H. Hutton
Battelle Northwest
Box 999
Richland, Washington 99352

William Joseph Pardee
Rockwell Int'l. Science Center
1049 Camino Dos Rios
Thousand Oaks, CA 91360

Adrian A. Pollock
Dunegan/Endevco
San Juan Capistrano, CA 92675

John Rodgers
AET
1812 J. Tribute Road
Sacramento, CA 95815

John A. Simmons
NBS
B263
Washington, D.C. 20234

Clement Tatro
Lawrence Livermore Nat'l Lab.
L-342, P.O. Box 808
Livermore, CA 94550

H. Wadley
NBS
A125, Bldg. 223
Washington, D.C. 20234

Donald Eitzen
NBS
Sound A147
Washington, D.C. 20234

Wolfgang Sachse
Cornell University
417 Thurston Hall
Ithaca, NY 14853

A POLYMER MATERIAL - COMPOSITE NEUTRON DETECTOR

Kenneth A. Kress

INTRODUCTION AND SUMMARY

A neutron detector based on a composite of polymer semiconductor and neutron active materials is described. The detector

expedient to take long time averages to emphasize the final structural response? How important is it to place the receiving transducers as closely as possible to the emission source? How is emission affected by the location and angular position of cracks? What is the best method for locating emission sources in complicated structures?

(4) Further studies are needed on a range of important materials to determine relationships between the microstructural events that generate the principal emission, the emission characteristics and fracture rleated properties (e.g., $J,\Delta a$). For example, does inclusion cracking provide emission that can be related to J in certain important alloy systems? Are the significant emission characteristics contained in the frequency spectra, the amplitude distribution, the event rate, etc.?

(5) A careful study of transducers is required. Not enough attention has been paid to the directional and modal sensitivity of the various types of transducer. This tends to indicate the need for development of very small sized transducer. The development of reliable, well-standarized and characterized transducers is also needed. It would be useful to determine if transducers which respond only to the incident energy, such as acoustoelectric transducers, would improve the reliability of measurements. New types of transudcers such as fiber optic sensors, thin film zinc oxide integrated circuit transducers, and polyvinylidene fluoride transducers should be studies for their possible applications to this field.

AD-A099 917 MICHIGAN UNIV ANN ARBOR COLL OF ENGINEERING F/G 5/2
PRELIMINARY REPORTS, MEMORANDA AND TECHNICAL NOTES OF THE MATER--ETC(U)
JUL 80 M J SINNOTT MDA903-80-C-0505
UNCLASSIFIED 018324 NL

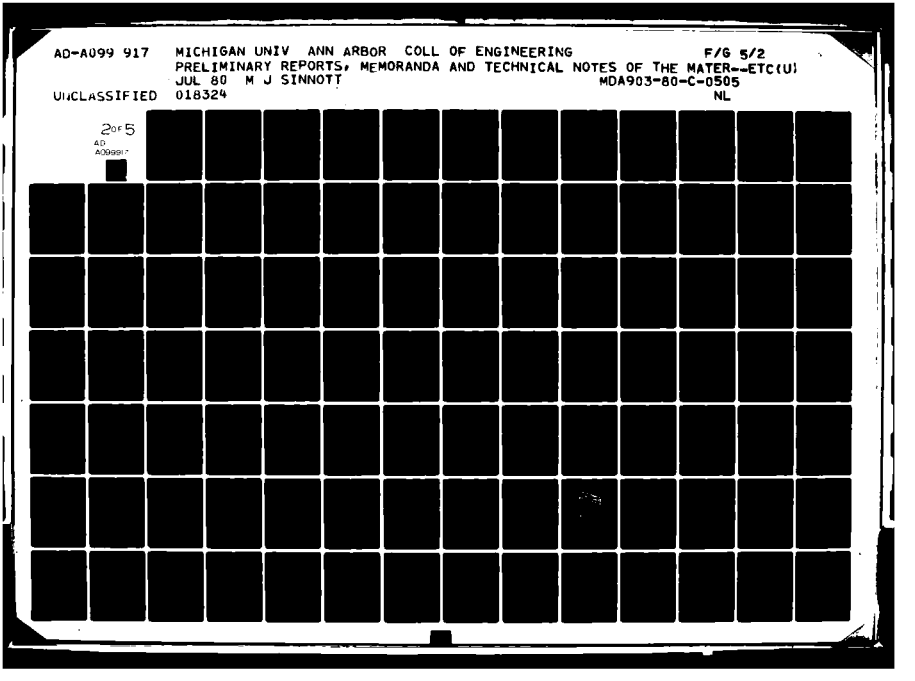

It is apparent that the acoustic emission field is still relatively immature. Much research remains to be done, and correlation of basic research with practical applications in the field is essential to successful exploitation of this technique for the consistent prediction of failure imminence in complex structures.

RECOMMENDATIONS FOR FUTURE MRC PARTICIPATION

It is apparent that the physics of the basic sources of acoustic emission is not well understood. It is desirable to arrive at a fundamental formulation which could predict the expected frequency spectra, angular distribution of emission, and excitation of surface and bulk waves by the different types of sources. Some of these concepts have been developed in part in the seismology field.

These basic aspects of the emission can be coupled with the statistical character of microcracking events (occurring during crack extension, etc.) to predict such measurable parameters as the amplitude distribution, pertinent to the various damage processes that lead to ultimate failure. Some indication of characteristic changes in the acoustic emission signals prior to ultimate failure may emerge, which would be suitable for exploitation in failure prediction procedures.

We therefore suggest that a workshop should be held early next year to examine what has been done in the field of seismology, and discuss the fundamental mechanisms of acoustic emission. We

junction and consequently producing a depletion layer on both sides of the neutron active layer. An ohmic contact is placed on the outer surfaces of the semiconductor polymer to form an electrical contact and provide shielding. Other variations of this basic design are possible, for example, the inner layer neutron active material could also be a different semiconductor material or doping change of the appropriate character to form a rectifying junction. To discuss a specific example and because of its particular promise, we consider the design and performance of a $(CH)_x$-^6Li composite detector.

QUALITATIVE DESCRIPTION

Consider the qualitative effects of a neutron on the detector shown in Fig. 1. There are several types of neutron interactions. The most important is that neutrons are absorbed within the ^6Li with a cross-section that varies with neutron energy as shown in Fig. 2. The absorption releases energy according to

$$n + {}^6Li \rightarrow {}^3H\ (2.73\ MeV) + {}^4He\ (2.05\ MeV) \qquad (1)$$

The triton (^3H) and/or alpha (^4He) reaction particles will escape the ^6Li layer and deposit energy into the semiconducting polymer layer. The deposited energy produces electron-hole pairs in the semiconductor which, because of the Schottky junction built-in or an externally supplied voltage, produces a current pulse. This pulse can be detected with a standard voltage or charge sensitive circuit.

believe that at the MRC there is an almost ideal mix of expertise in fracture mechanics, statistical processes, and acoustic wave propagation effects, to carry out fundamental studies to establish the nature of the basic sources of acoustic emission.

Because of the hydrogen in the semiconductor, there is a small sensitivity of the detector to high energy neutrons. As seen in Fig. 2, hydrogen has a relatively large collision cross-section for high energy neutrons. There is no energy released during these collisons, but kinetic energy is imparted to the hydrogen. This "knock-out" proton also produces free carriers, or signals, in the semiconductor. Even though hydrogen has a relatively high fast neutron cross-section, it is low compared with that of thermal neutrons in ^{6}Li (cf. Fig. 2), and produces correspondingly less sensitivity per incident neutron. Neutron interactions with materials other than hydrogen and ^{6}Li have very small collision and reaction cross-sections, and therefore produce no significant signal.

The design of a detector requires consideration of several device parameters which cannot all be simultaneously optimized. Some of these parameters are:

1. The neutron active layer should be thick enough to absorb the incident thermal neutrons, but thin enough to allow the reaction particles to escape with reasonable excess energy.

2. The semiconductor must be thick enough to absorb the escape energy of the reaction particles.

3. The semiconductor must be thin enough and have high enough quality that a fully depleted layer can be produced causing the free carriers to migrate with little loss.

ACOUSTIC EMISSION WORKSHOP

Guest Participants

Frederic Bick
Effects Technology, Inc.
5383 Hollister
Santa Barbara, CA 93111

John M. Carlyle
Naval Air Dev. Center
Code 60633
Warminster, PA 18974

Davis M. Egle
University of Oklahoma
865 Asp St., Room 212
Norman, Oklahoma 73019

Lloyd J. Graham
Rockwell Science Center
Thousand Oaks, CA 91360

P. H. Hutton
Battelle Northwest
Box 999
Richland, Washington 99352

William Joseph Pardee
Rockwell Int'l. Science Center
1049 Camino Dos Rios
Thousand Oaks, CA 91360

Adrian A. Pollock
Dunegan/Endevco
San Juan Capistrano, CA 92675

John Rodgers
AET
1812 J. Tribute Road
Sacramento, CA 95815

John A. Simmons
NBS
B263
Washington, D.C. 20234

Clement Tatro
Lawrence Livermore Nat'l Lab.
L-342, P.O. Box 808
Livermore, CA 94550

H. Wadley
NBS
A125, Bldg. 223
Washington, D.C. 20234

Donald Eitzen
NBS
Sound A147
Washington, D.C. 20234

Wolfgang Sachse
Cornell University
417 Thurston Hall
Ithaca, NY 14853

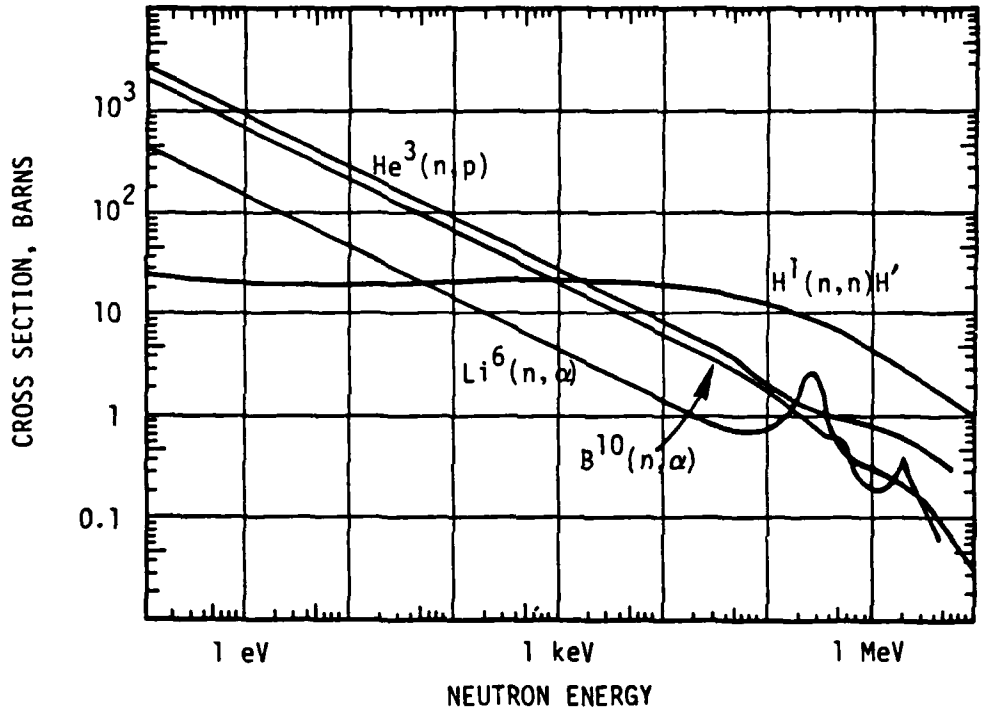
CROSS SECTION, BARNS
10^3
10^2
10
1
0.1
$He^3(n,p)$
$H^1(n,n)H'$
$Li^6(n,\alpha)$
$B^{10}(n,\alpha)$
1 eV
1 keV
1 MeV
NEUTRON ENERGY

FIGURE 2

A POLYMER MATERIAL - COMPOSITE NEUTRON DETECTOR

Kenneth A. Kress

INTRODUCTION AND SUMMARY

A neutron detector based on a composite of polymer semiconductor and neutron active materials is described. The detector operates at ambient temperature, is sensitive to thermal neutrons and has a smaller sensitivity to fast neutrons. When used as a stacked, series system, fast neutron sensitivity increases and an energy discriminative system results. The characteristics of the detector are high sensitivity per unit volume, light weight, potential for large area and modest costs. A qualitative description of the concept and quantitative estimates of the performance of a particular design are given.

THE DETECTOR CONCEPT

With the discovery of semiconducting polymers with a wide variety of desirable properties,[1,2,3] new neutron detector concepts are possible. The general concept is to fabricate a composite layered detector as schematically shown in Fig. 1. This detector has three distinct layers, and forms a standard diode detector. The inner layer is a neutron active metal. Surrounding both surfaces of the neutron active metal is a layer of polymer semiconductor chosen to produce a Schottky barrier rectifying

DETECTOR DESIGN AND PERFORMANCE

To develop an "optimized" detector design, a detailed Monte Carlo calculation of the neutron and reaction particle transport effects is required. Such a calculation has been done for two cases intuitively expected to be close to "optimal." The elements of the calculation are outlined, and the results for the two special cases presented.

Thermal neutrons incident on the neutron active layer are absorbed with a probability determined by the absorption cross-section and layer thickness in the direction of their velocity. These absorbed neutrons isotropically release particles which have some probability of escaping the neutron active layer with a fraction of their initial energy determined by the interaction of the reaction particles with the neutron active layer. The reaction particles then deposit energy into the surrounding semiconductor. The deposited energy is determined by the semiconductor-reaction particle interaction, direction of the reaction particles travel, semiconductor thickness and initial reaction particle energy.

If a Monte Carlo calculation of the above factors is performed for an isotropic incident neutron flux and given material thicknesses, all these aprocesses can be combined into an effective absorption probability, P, and average induced charge, ΔQ. These factors are discussed somewhat more quantitatively below.

It is intuitively apparent for a detector of the design shown in Fig. 1, the semiconductor layer should be thick enough to absorb most of the energy of the escaping reaction particles. A

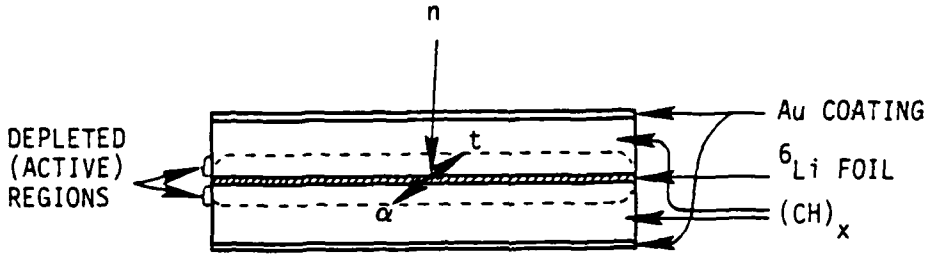

FIGURE 1

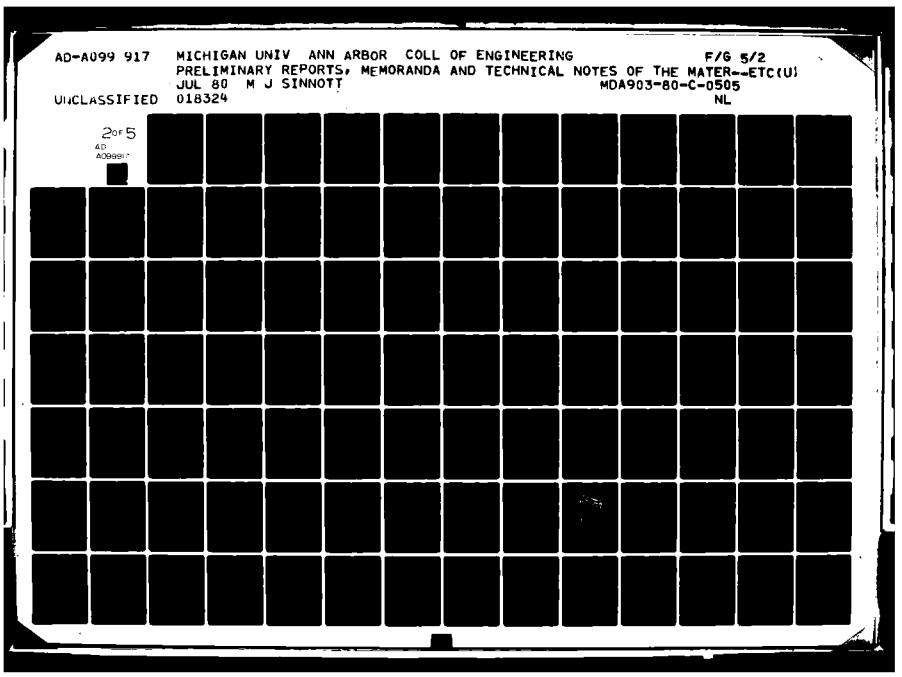
AD-A099 917 MICHIGAN UNIV ANN ARBOR COLL OF ENGINEERING F/G 5/2
PRELIMINARY REPORTS, MEMORANDA AND TECHNICAL NOTES OF THE MATER--ETC(U)
JUL 80 M J SINNOTT MDA903-80-C-0505
UNCLASSIFIED 018324 NL
2 OF 5
AD
A099917

junction and consequently producing a depletion layer on both sides of the neutron active layer. An ohmic contact is placed on the outer surfaces of the semiconductor polymer to form an electrical contact and provide shielding. Other variations of this basic design are possible, for example, the inner layer neutron active material could also be a different semiconductor material or doping change of the appropriate character to form a rectifying junction. To discuss a specific example and because of its particular promise, we consider the design and performance of a $(CH)_x$-^6Li composite detector.

QUALITATIVE DESCRIPTION

Consider the qualitative effects of a neutron on the detector shown in Fig. 1. There are several types of neutron interactions. The most important is that neutrons are absorbed within the ^6Li with a cross-section that varies with neutron energy as shown in Fig. 2. The absorption releases energy according to

$$n + {}^6Li \rightarrow {}^3H\ (2.73\ MeV) + {}^4He\ (2.05\ MeV) \qquad (1)$$

The triton (^3H) and/or alpha (^4He) reaction particles will escape the ^6Li layer and deposit energy into the semiconducting polymer layer. The deposited energy produces electron-hole pairs in the semiconductor which, because of the Schottky junction built-in or an externally supplied voltage, produces a current pulse. This pulse can be detected with a standard voltage or charge sensitive circuit.

Because of the hydrogen in the semiconductor, there is a small sensitivity of the detector to high energy neutrons. As seen in Fig. 2, hydrogen has a relatively large collision cross-section for high energy neutrons. There is no energy released during these collisons, but kinetic energy is imparted to the hydrogen. This "knock-out" proton also produces free carriers, or signals, in the semiconductor. Even though hydrogen has a relatively high fast neutron cross-section, it is low compared with that of thermal neutrons in ^{6}Li (cf. Fig. 2), and produces correspondingly less sensitivity per incident neutron. Neutron interactions with materials other than hydrogen and ^{6}Li have very small collision and reaction cross-sections, and therefore produce no significant signal.

The design of a detector requires consideration of several device parameters which cannot all be simultaneously optimized. Some of these parameters are:

1. The neutron active layer should be thick enough to absorb the incident thermal neutrons, but thin enough to allow the reaction particles to escape with reasonable excess energy.

2. The semiconductor must be thick enough to absorb the escape energy of the reaction particles.

3. The semiconductor must be thin enough and have high enough quality that a fully depleted layer can be produced causing the free carriers to migrate with little loss.

the neutron absorption. A detailed calculation shows the escape fraction of tritons and alphas from a 50μ layer of 96% ^{6}Li is about 0.8 and 0.2, respectively.[7] This same calculation shows that on an average, about 1.8 MeV is deposited in the wrap-around 140μ thick $(CH)_x$ layer producing the average signal charge shown in Table I. This signal exceeds the fundamental shot-noise limitation of a 100 cm^2 detector by more than an order of magnitude, indicating a useful signal level.

If a detector is optimized to sense the alpha reaction particle, the neutron active layer must be thin to allow reasonable alpha escape probability. Correspondingly, the semiconductor layer can be thin because of the range of the alpha in $(CH)_x$ is only about 27μ. Reducing the lithium layer to 14μ and the thickness of the $(CH)_x$ layer to the range of the unattenuated alpha in $(CH)_x$, Type II detector performance parameters are shown on the right side of Table I.

Somewhat surprisingly, there is little signal difference between the Type I and II design. This result occurs because as the Li thickness is decreased for the Type II design allowing more alphas to escape, less $(CH)_x$ is needed to absorb the same amount of reaction particle energy. Thus within the range of parameters for the Type I and II design, the average signal is approximately constant.

The semiconductor properties needed to create a completely depleted semiconductor layer and collect the unduced free charge are given for both designs in Table II. The penalty for the

DETECTOR DESIGN AND PERFORMANCE

To develop an "optimized" detector design, a detailed Monte Carlo calculation of the neutron and reaction particle transport effects is required. Such a calculation has been done for two cases intuitively expected to be close to "optimal." The elements of the calculation are outlined, and the results for the two special cases presented.

Thermal neutrons incident on the neutron active layer are absorbed with a probability determined by the absorption cross-section and layer thickness in the direction of their velocity. These absorbed neutrons isotropically release particles which have some probability of escaping the neutron active layer with a fraction of their initial energy determined by the interaction of the reaction particles with the neutron active layer. The reaction particles then deposit energy into the surrounding semiconductor. The deposited energy is determined by the semiconductor-reaction particle interaction, direction of the reaction particles travel, semiconductor thickness and initial reaction particle energy.

If a Monte Carlo calculation of the above factors is performed for an isotropic incident neutron flux and given material thicknesses, all these aprocesses can be combined into an effective absorption probability, P, and average induced charge, ΔQ. These factors are discussed somewhat more quantitatively below.

It is intuitively apparent for a detector of the design shown in Fig. 1, the semiconductor layer should be thick enough to absorb most of the energy of the escaping reaction particles. A

Type II design is reduced neutron absorption per detector and a small decrease in signal and an increase in noise.

The discrimination of background gamma rays signal from these detectors should not be a problem. The Compton electrons from a few MeV gamma are typically 200-600 KeV. Using an average electron stopping power of 2 MeV $g^{-1}cm^2$, the energy deposited in 140μ of $(CH)_x$ is about 10 KeV, much smaller than the deposited energy from a neutron event.

MULTIPLE DETECTORS AND FAST NEUTRON SENSITIVITY

As seen from the estimated absorption values, P, in Table I, a single detector does not absorb all incident thermal neutrons. For many applications multiple or stacked detectors would increase overall sensitivity. Assuming a thin ohmic contact and ignoring an environmental package thickness, the individual detectors are quite thin; for the Type I design, a little more than 0.3mm and for Type II less than 0.1mm. Therefore, a stack of three Type I detectors, which absorbs about 85% of a thermal neutron flux, is about one millimeter thick.

If fast neutron detection is desirable, even thicker stacks can be made which, because of the integral hydrogen, will both moderate fast neutrons, producing subsequent thermal neutron absorption in the ^6Li, and detect the knock out proton interaction produced from each moderating collision. This latter effect should be quite useful for not only counting fast neutrons, but also determining their energy. If the detector stack is several

reasonable thickness is the range, L, of the unattenuated range is certainly greater than that of the average.

With the thickness of the semiconducting layer determined, other materials parameters are now constrained. For example, to insure efficient charge collection, the semiconductor layer should be fully depleted. The necessary degree of compensation in the semiconductor, N_a-N_b, and/or externally applied bias V is obtained from the standard Schottky junction depletion width expression,

$$L = \sqrt{\frac{\varepsilon_o K(\phi_\beta + V)}{\varepsilon(N_a - N_b)}} \qquad (2)$$

where K is the semiconductor dielectric constant, ε_o, the permitivity constant (mks units), ϕ_β, the built-in voltage, and e the elementary electron charge and thermal effects are neglected.[5] Similarly, the life time for the induced carriers is given by the minimum time required for an electron or hole to drift through the entire depletion layer under the influence of the internal voltage. If, for a first approximation, we assume a uniform internal electric field, this condition reduces to

$$\tau\mu \simeq \frac{L^2}{\phi_\beta + V} \qquad (3)$$

where T is the carrier lifetime, and μ is the mobility of the hole or electron assumed to be equal. From Eq. 3 it is seen that if L^2 increases, the product of the lifetime and mobility must increase.

Assuming a device can be fabricated with the required parameters, the "average" response of the detector after neutron

centimeters thick, a fast neutron should lose most of its energy in the detector and produce several essentially coincidental pulses. The coincidence of several pulses will uniquely indicate a fast neutron interaction and analysis of the total current produced and/or the distribution of individual current pulse amplitudes should allow an estimate of the fast neutron energy. Analysis of these pulses will also provide some information on the direction of the incident neutron.

GENERAL DISCUSSION

Although the $(CH)_x$-^6Li composite described above is not the only, or perhaps even the best combination of materials, it has several attractive properties which recommend it.[8] Based on already known processes, high quality $(CH)_x$ films can be formed by catalytic polymerization of acetylene gas, onto metallic surfaces. Also, metal films are known to form good junctions with $(CH)_x$. A film of $(CH)_x$ has been determined to be intrinsically P-type and can be easily compensated to very low net charge levels by exposure to NH_3 gas. These properties mean that the described detector can probably be produced by simple evaporation and gas exposure techniques. The first reported measurements of the $\tau\mu$ produce for trans $(CH)_x$ are about $10^{-10}cm^2/v$, which is not adequate.[9] However, band structure calculations indicate $(CH)_x$ is an indirect band gap material, implying long carrier lifetime. Typical values for other well developed indirect band-gap semiconductors are $10^{-5}cm^2/v$ for Cds and unity for Si, hence, it is reasonable to expect improvements

absorption can be estimated. The energy deposited in the semiconductor quickly decays into electron-hole pairs with approximately one band gap energy. As confirmed by past semiconductor detector experience, it requires about 3 band gaps of energy to crease an electron-hole pair.[6] Thus the total electron or hole charge generated in the depleted semiconductor is;

$$\Delta Q \simeq \frac{eE}{3\ E_b} \tag{4}$$

where E is the energy deposited, E_b the band gap energy and e the elementary electron charge. Because of the assumed good carrier life-time and mobility, the electron-hole pairs will accelerate to opposite sides of the detector without loss, producing a current pulse. Clearly the maximum expected charge in that current pulse is given by Eq. 4. An estimate of the voltage signal available from the detector can be obtained from elementary circuit analysis.

For a $(CH)_x$-^6Li composite detector, there are two reaction particles which have quite different transport properties. The ranges of the reaction triton and alpha in metallic lithium are about 135μ and 28μ, respectively. The unattenuated range of the reaction triton and alpha in $(CH)_x$ is almost the same, about 140μ and 27μ, respectively. Detectors can be optimized to detect either or perhaps both reaction particles. We consider two cases. A Type I design, optimized to detect the reaction triton, and Type II optimized to detect the reaction alpha.

The lithium thickness for a Type I detector should be less than the range of the triton but as thick as possible to maximize

in this parameter for $(CH)_x$.[9] Studies further indicate that anisotropy in the electrical conductivity exists with greatly increased conductivity (and mobility) in the direction of the fibrils. If the detector can be fabricated with the fibrils oriented perpendicular to the metal layers, the enhanced mobility would be in the desired orientation. Since the material has the above mentioned desirable detector properties and already has an initial technology fabrication base, it should be given priority consideration in any near term detector development program.

Considerable research is underway to create new doping options and organic polymers. Given the possibility of the proper materials, other detector designs became possible. Provided larger electronegativity metals can be used, ^{235}U and or ^{239}Pu can be used for the neutron active layer. These materials have a large thermal neutron cross-section similar to ^{6}Li (580 barns for ^{235}U compared with 940 barns for ^{6}Li). More importantly, the energy release of ^{235}U neutron capture is over 200 MeV, about two orders of magnitude greater than ^{6}Li. These fission fragments have a small range and therefore the semiconducting layer can be thin, reducing the need for a large depletion width and long carrier lifetime. Thus, such a detector could produce more signal and be easier to fabricate than the $(CH)_x$-^{6}Li composite. Other possibilities include diode detectors formed with regions highly doped with neutron active ^{6}Li or ^{10}B, diodes made with heterojunctions of ^{6}Li or ^{10}B, or diodes made with heterojunctions of ^{6}Li or ^{10}B semiconducting compound materials.

the neutron absorption. A detailed calculation shows the escape fraction of tritons and alphas from a 50μ layer of 96% ^{6}Li is about 0.8 and 0.2, respectively.[7] This same calculation shows that on an average, about 1.8 MeV is deposited in the wrap-around 140μ thick $(CH)_x$ layer producing the average signal charge shown in Table I. This signal exceeds the fundamental shot-noise limitation of a 100 cm^2 detector by more than an order of magnitude, indicating a useful signal level.

If a detector is optimized to sense the alpha reaction particle, the neutron active layer must be thin to allow reasonable alpha escape probability. Correspondingly, the semiconductor layer can be thin because of the range of the alpha in $(CH)_x$ is only about 27μ. Reducing the lithium layer to 14μ and the thickness of the $(CH)_x$ layer to the range of the unattenuated alpha in $(CH)_x$, Type II detector performance parameters are shown on the right side of Table I.

Somewhat surprisingly, there is little signal difference between the Type I and II design. This result occurs because as the Li thickness is decreased for the Type II design allowing more alphas to escape, less $(CH)_x$ is needed to absorb the same amount of reaction particle energy. Thus within the range of parameters for the Type I and II design, the average signal is approximately constant.

The semiconductor properties needed to create a completely depleted semiconductor layer and collect the unduced free charge are given for both designs in Table II. The penalty for the

From the above discussion it is obvious that the concept of a polymer-semiconductor, neutron-active material composite detector has numerous possible design alternatives which could be used to develop an important new type of all-solid neutron detector. The optimal combination of materials is yet to be determined, but ^{6}Li and $(CH)_x$ offer an attractive, near term detector development option.

Type II design is reduced neutron absorption per detector and a small decrease in signal and an increase in noise.

The discrimination of background gamma rays signal from these detectors should not be a problem. The Compton electrons from a few MeV gamma are typically 200-600 KeV. Using an average electron stopping power of 2 MeV $g^{-1}cm^2$, the energy deposited in 140μ of $(CH)_x$ is about 10 KeV, much smaller than the deposited energy from a neutron event.

MULTIPLE DETECTORS AND FAST NEUTRON SENSITIVITY

As seen from the estimated absorption values, P, in Table I, a single detector does not absorb all incident thermal neutrons. For many applications multiple or stacked detectors would increase overall sensitivity. Assuming a thin ohmic contact and ignoring an environmental package thickness, the individual detectors are quite thin; for the Type I design, a little more than 0.3mm and for Type II less than 0.1mm. Therefore, a stack of three Type I detectors, which absorbs about 85% of a thermal neutron flux, is about one millimeter thick.

If fast neutron detection is desirable, even thicker stacks can be made which, because of the integral hydrogen, will both moderate fast neutrons, producing subsequent thermal neutron absorption in the ^6Li, and detect the knock out proton interaction produced from each moderating collision. This latter effect should be quite useful for not only counting fast neutrons, but also determining their energy. If the detector stack is several

TABLE I. The physical parameters and predicted performance characteristics of Type I and II $(CH)_x$-^6Li composite detectors. A band gap of 1.48 eV and dielectric constant of 2 has been assumed for $(CH)_x$. P is the average probability of absorption for an isotropic incident thermal neutron flux per unit area of 96% enriched ^6Li detector. The noise estimate is for a 100 cm^2 detector.

	Type I Design	Type II Design
Li -6 Thickness	50 Microns	14 Microns
$(CH)_x$ Thickness	140 Microns	27 Microns
P (Probability of neutron absorption)	0.37	0.16
ΔQ	4.1×10^5 electrons	3.5×10^5 electrons
Thermal Noise	1.2×10^4 electrons	2.8×10^4 electrons

centimeters thick, a fast neutron should lose most of its energy in the detector and produce several essentially coincidental pulses. The coincidence of several pulses will uniquely indicate a fast neutron interaction and analysis of the total current produced and/or the distribution of individual current pulse amplitudes should allow an estimate of the fast neutron energy. Analysis of these pulses will also provide some information on the direction of the incident neutron.

GENERAL DISCUSSION

Although the $(CH)_x$-^6Li composite described above is not the only, or perhaps even the best combination of materials, it has several attractive properties which recommend it.[8] Based on already known processes, high quality $(CH)_x$ films can be formed by catalytic polymerization of acetylene gas, onto metallic surfaces. Also, metal films are known to form good junctions with $(CH)_x$. A film of $(CH)_x$ has been determined to be intrinsically P-type and can be easily compensated to very low net charge levels by exposure to NH_3 gas. These properties mean that the described detector can probably be produced by simple evaporation and gas exposure techniques. The first reported measurements of the $\tau\mu$ produce for trans $(CH)_x$ are about $10^{-10}cm^2/v$, which is not adequate.[9] However, band structure calculations indicate $(CH)_x$ is an indirect band gap material, implying long carrier lifetime. Typical values for other well developed indirect band-gap semiconductors are $10^{-5}cm^2/v$ for Cds and unity for Si, hence, it is reasonable to expect improvements

TABLE II. Comparison of the electronic parameters of the semiconducting polymer for Type I and II $(CH)_x$-^6Li composite detectors. The internal Schottky barrier induced voltage is assumed to be 0.5 volts.

	Type I Design		Type II Design	
N_d-Na (cm^{-3})	10^{12}	10^{10}	10^{12}	10^{10}
V (volts)	2.0	1.6	7.3	0
$\tau\mu$ (cm^2/v)	9.3×10^{-7}	9.3×10^{-5}	9.3×10^{-7}	1.5×10^{-5}

in this parameter for $(CH)_x$.[9] Studies further indicate that anisotropy in the electrical conductivity exists with greatly increased conductivity (and mobility) in the direction of the fibrils. If the detector can be fabricated with the fibrils oriented perpendicular to the metal layers, the enhanced mobility would be in the desired orientation. Since the material has the above mentioned desirable detector properties and already has an initial technology fabrication base, it should be given priority consideration in any near term detector development program.

Considerable research is underway to create new doping options and organic polymers. Given the possibility of the proper materials, other detector designs became possible. Provided larger electronegativity metals can be used, ^{235}U and or ^{239}Pu can be used for the neutron active layer. These materials have a large thermal neutron cross-section similar to ^{6}Li (580 barns for ^{235}U compared with 940 barns for ^{6}Li). More importantly, the energy release of ^{235}U neutron capture is over 200 MeV, about two orders of magnitude greater than ^{6}Li. These fission fragments have a small range and therefore the semiconducting layer can be thin, reducing the need for a large depletion width and long carrier lifetime. Thus, such a detector could produce more signal and be easier to fabricate than the $(CH)_x$-^{6}Li composite. Other possibilities include diode detectors formed with regions highly doped with neutron active ^{6}Li or ^{10}B, diodes made with heterojunctions of ^{6}Li or ^{10}B, or diodes made with heterojunctions of ^{6}Li or ^{10}B semiconducting compound materials.

References

1. MacDiarmid, Alan G., and Alan J. Heeger, "Organic Metals and Semiconductors: The Chemistry of Polyacetylene, $(CH)_x$, and its Derivatives," presented at the Advanced Study Institute of the Physics and Chemistry of Low-Dimensional Solids, Tomar, Portugal, August 26-September 7, 1979.

2. "New Conducting Polymers Join Polyacetylene," Phys. Today 32(9), 19-21(1979).

3. Ozali, M., D. L. Peebles, B. R. Weinberger, C. K. Chiang, A. J. Heeger, and A. G. MacDiarmid, "Junction Formation with Pure Doped Polyacetylene," Appl. Phys. Lett. 35, 83-85(1979).

4. Price, William J., Nuclear Radiation Detection, McGraw-Hill, New York, 1964, pp. 430.

5. Sze, S. M., "Physics of Semiconductor Devices," Wiley-Interscience (1969), p. 371.

6. Price, W. J., Nuclear Radiation Detection, McGraw-Hill, New York, 1964, pp. 215-216.

7. W. E. Selph, private communication 15 May 1980. The average charge per absorbed neutron was calculated with a Monte Carlo simulated code developed and described in IRT 8169-004, "An Investigation of Parallel Plate Neutron Detector Concepts," by W. E. Selph and S. J. Friesenhahn, June 27, 1978.

8. Fischer, C. R., Jr., M. O. Zaki, M. Tanaka, D. Peebles, L. Lauchlan, A. J. Heeger, and A. G. MacDiarmid, "Electric Structure of Polyacetylene: Optical and Infrared Studies of Undoped Semiconducting $(CH)_x$ and Heavily Doped Metallic $(CH)_x$", Phys. Rev. B20, 1589-1602(1979).

9. Tani, T., P. M. Grant, W. D. Gill, G. B. Street and T. C. Clarke, "Phototransport Effects in Polyacetylene, $(CH)_x$," Sol. St. Comm. 33, pp. 490-503(1980).

From the above discussion it is obvious that the concept of a polymer-semiconductor, neutron-active material composite detector has numerous possible design alternatives which could be used to develop an important new type of all-solid neutron detector. The optimal combination of materials is yet to be determined, but ^{6}Li and $(CH)_x$ offer an attractive, near term detector development option.

PROPOSAL FOR A SOLID STATE NEUTRON DETECTOR

T. C. McGill

ABSTRACT

A neutron detector based on a Schottky barrier or a p-n junction between B_4C or Li_5B_4 and a silicon is proposed. The detector shows promise of being portable, lower powered, and reliable.

TABLE I. The physical parameters and predicted performance characteristics of Type I and II $(CH)_x$-^6Li composite detectors. A band gap of 1.48 eV and dielectric constant of 2 has been assumed for $(CH)_x$. P is the average probability of absorption for an isotropic incident thermal neutron flux per unit area of 96% enriched ^6Li detector. The noise estimate is for a 100 cm^2 detector.

	Type I Design	Type II Design
Li -6 Thickness	50 Microns	14 Microns
$(CH)_x$ Thickness	140 Microns	27 Microns
P (Probability of neutron absorption)	0.37	0.16
ΔQ	4.1×10^5 electrons	3.5×10^5 electrons
Thermal Noise	1.2×10^4 electrons	2.8×10^4 electrons

PROPOSAL FOR A SOLID STATE NEUTRON DETECTOR

T. C. McGill

INTRODUCTION

A solid state neutron detector that is portable, requires small amounts of power, and is reliable, could be used in a number of different applications. Recently, Kress[1] has proposed a solid

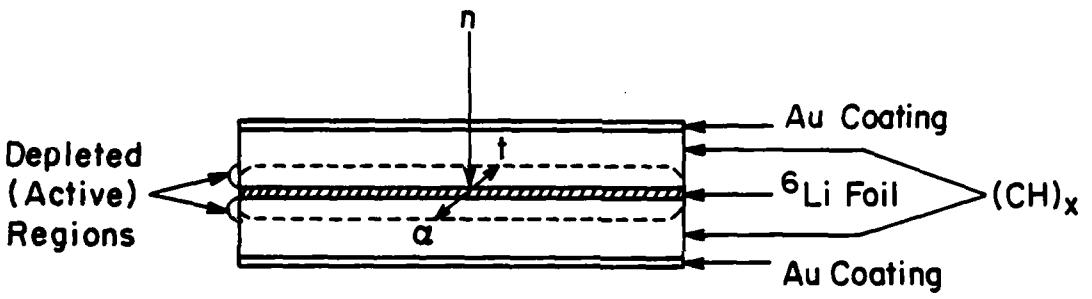

Figure 1. The Schottky barrier detector proposed by Kress (Ref. 1).

produce in quantity with reproducible electrical and optical properties. The lithium is likely to diffuse into and attack polyacetylene even at the room temperature leading to instability in the device performance. Protection of a device involving two

SCHEMATIC STRUCTURE FOR

SCHOTTKY BARRIER NEUTRON DETECTOR

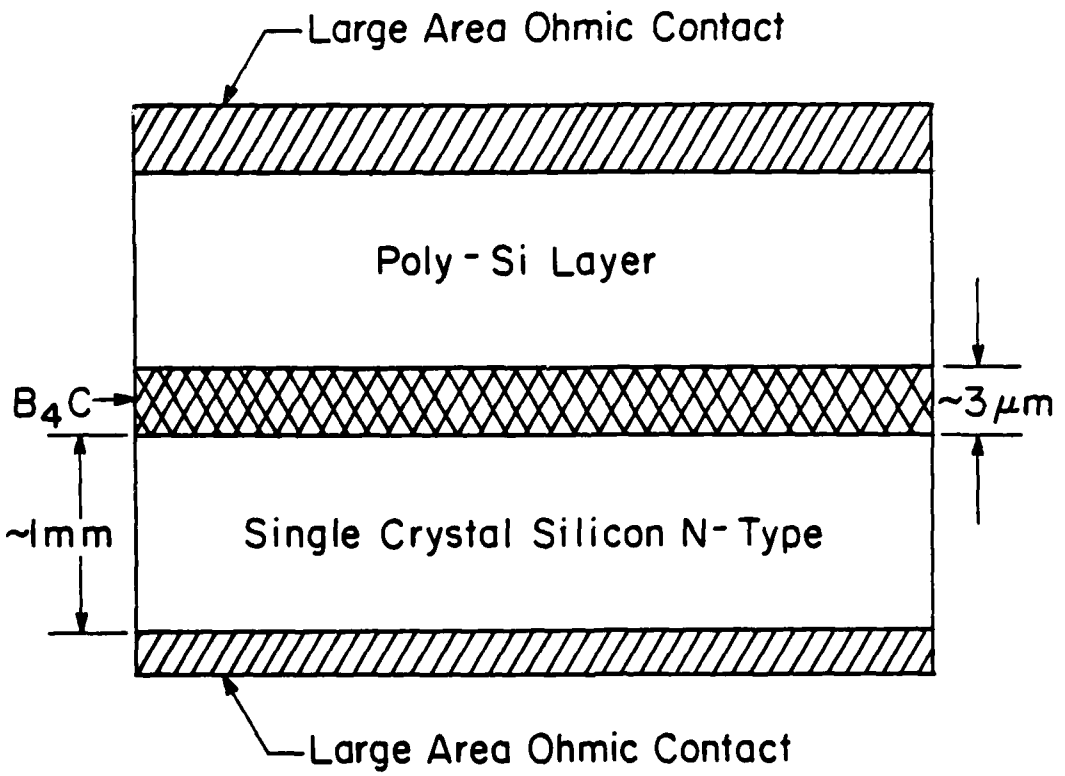

Figure 2. A schematic structure for a Schottky barrier detector based on Si. The B_4C could be replaced by Li_5B_4 in which case the layer should be increased to perhaps 7μm.

SCHEMATIC STRUCTURE FOR P-N JUNCTION NEUTRON DETECTOR

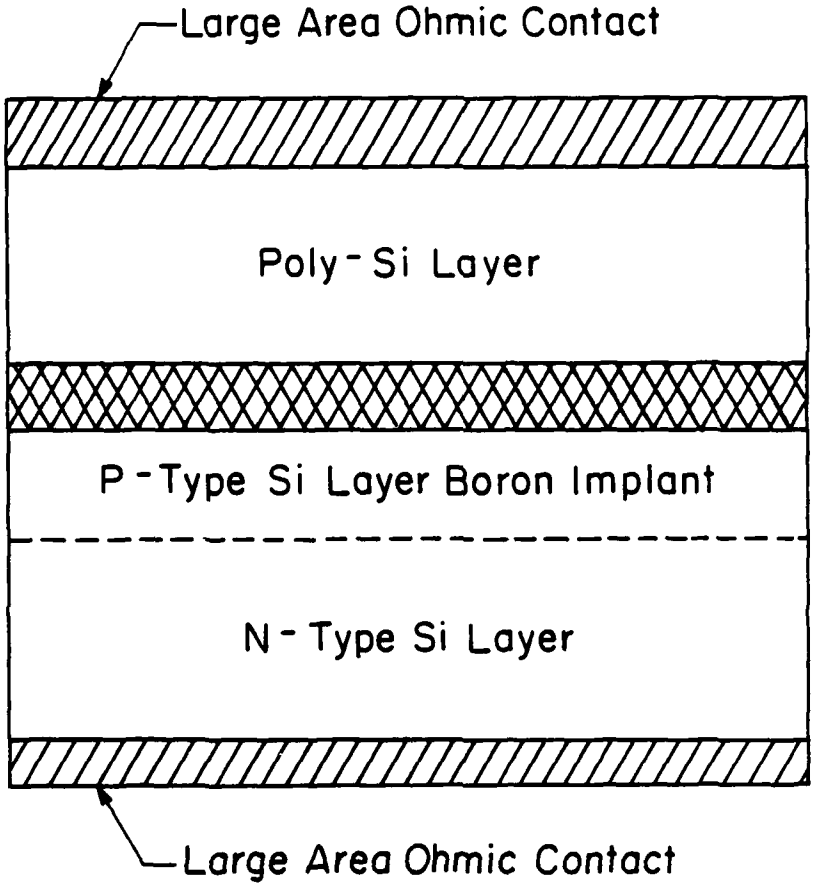

Figure 3. A schematic structure for a p-n junction detector based on Si. The B_4C could be replaced by Li_5B_4 in which case the layer should be increased to perhaps 7μm.

produce in quantity with reproducible electrical and optical properties. The lithium is likely to diffuse into and attack polyacetylene even at the room temperature leading to instability in the device performance. Protection of a device involving two such reactive substances is likely to be very difficult.

In this report, we propose a similar detector concept that takes advantage of the highly developed semiconductor technology based on Si. The device shows promise of being portable, low powered, relatively easily manufactured, and reliable in use.

Proposal for a Si Based Neutron Detector

The proposed detector consists of simply replacing the polyacetylene layer with a layer of n-type Si and replacing the unstable Li with a layer of either B_4C[2] or Li_5B_4[3]. The detector would behave in exactly the same manner as the previously described detector. A schematic of the detector is shown in Fig. 2. A variant of this detector could be produced by unimplanting a boron layer to produce a p-n junction (see Fig. 3).

Why Si?

Silicon is ideally suited for this kind of detector application. For the Schottky barrier detector, the doping can be controlled so that the depletion region is as wide as desired. We would recommend that the doping be about $10^{14}cm^{-3}$ which gives an unbiased depletion layer of about 3μm wide.[4] The doping should be n-type since this is likely to result in the largest built in field for Si Schottky barrier. The depletion layer width of 3μm is comparable to the range of MeV alpha particles in Si and means

that most of the charge will be generated in a region of high electric field resulting in efficient separation of the generated electron-hole pairs.

For the p-n junction case a fairly heavy implant of B with doping in the range of $10^{16}10^{17}cm^{-3}$ (or perhaps higher) could be produced by ion implantation into the n-type wafer. The implant energy should be chosen to produce a shallow junction. In this case the electron-hole pairs would be separated by the p-n junction. This variation would be required if the Schottky barrier turns out to be too leaky.

Silicon may also detect high energy neutrons. The cross section for elastic scattering of MeV neutrons is a few barns for ^{28}Si which is comparable to that for hydrogen. The energy transfer from the neutron to the Si in a single event is likely to be quite a bit smaller than for the lighter elements such as hydrogen. However, unlike polyacetylene, neutron scattering events >0.1 mm deep in the Si will produce some response in the detector. This difference is because the minority carrier diffusion length in Si ($\sim$1mm) is likely to be quite long compared to that in polyacetylene. Hence, a much greater thickness of material can be used to intercept the high energy neutrons and produce a detectable signal.

Why B_4C or Li_5B_4?

Both B_4C and Li_5B_4 are metals and can be loaded with ^{10}B and ^{6}Li heavily to produce strong thermal neutron absorbers (see attached Table I) that will produce detectable charged particles.

SCHEMATIC STRUCTURE FOR

SCHOTTKY BARRIER NEUTRON DETECTOR

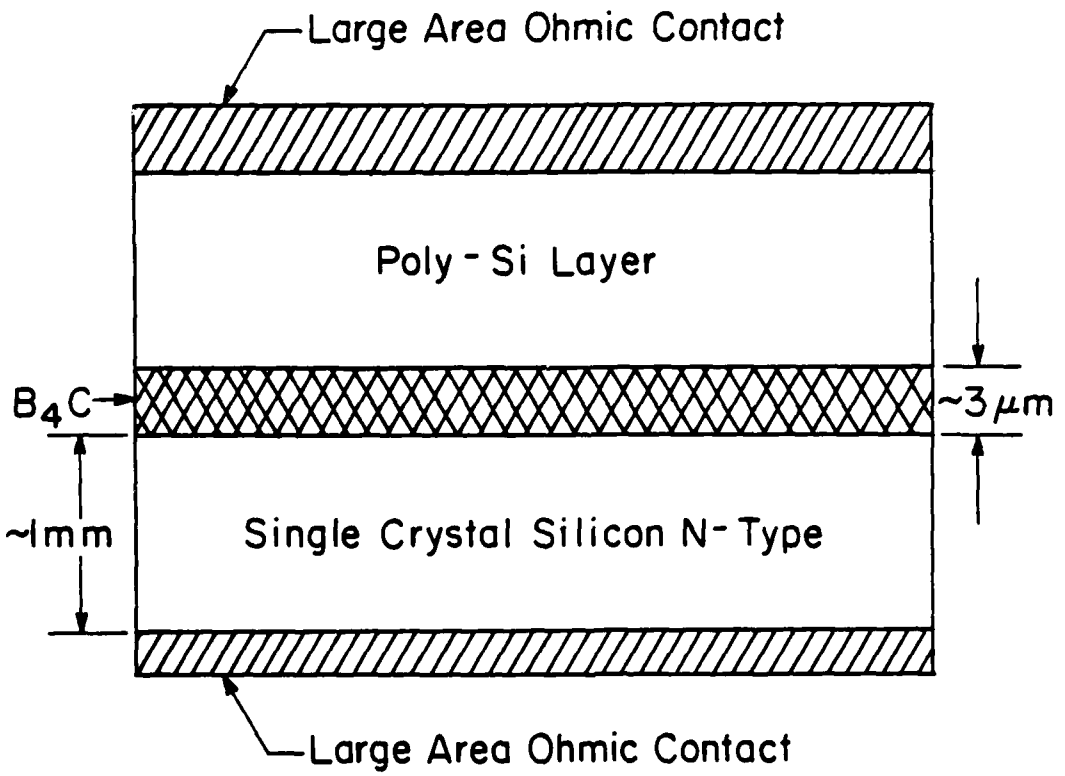

Figure 2. A schematic structure for a Schottky barrier detector based on Si. The B_4C could be replaced by Li_5B_4 in which case the layer should be increased to perhaps 7μm.

TABLE 1. RELEVANT PARAMETERS FOR SOME MATERIALS USEFUL AS THERMAL NEUTRON DETECTOR

MATERIAL	$N_{Li}c(m^{-3})$	$N_B(cm^{-3})$	$l_{abs}^{10B}(\mu m)$	$l_{abs}^{6Li}(\mu m)$	R^{α} *(μm) 1.47 MeV	R *(μm) 2.05 MeV	R^{T} *(μm) 2.75 MeV
Li (metal)	4.63×10^{22}	0	-	229.0	-	20μm	135μm
B (semiconductor)	0	1.30×10^{23}	20.0	-	3.0	-	-
B_4C	0	1.10×10^{23}	23.7	-	2.8	-	-
Li_5B_4	3.94×10^{22}	3.15×10^{22}	82.7	269.0	6.3	23μm	78μm

*Ranges are estimated using the estimates from C. A. Young (NOSC) for ^{6}Li and ^{10}B. The ranges R are R are assumed to vary as $R = \frac{A}{NM_a^{\frac{1}{2}}}$ where A is a constant for a given energy, N is the number of atoms per unit volume and $Ma^{\frac{1}{2}}$ is the mass of the element. For composite materials R was assumed to add reciprocally.

SCHEMATIC STRUCTURE FOR P-N JUNCTION NEUTRON DETECTOR

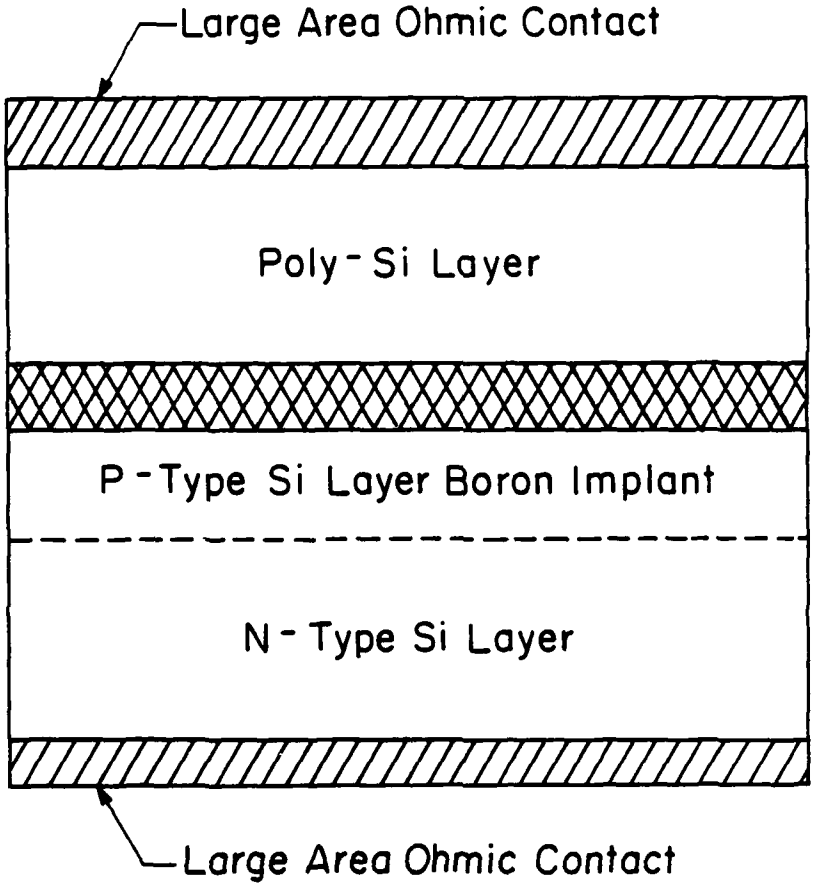

Figure 3. A schematic structure for a p-n junction detector based on Si. The B_4C could be replaced by Li_5B_4 in which case the layer should be increased to perhaps 7μm.

To obtain maximum performance one wants to have the largest number of triton or alphas deposit their energy in the silicon for a given flux of incident thermal neutrons. To meet these criteria, we want to use elements with small atomic numbers since small atomic numbers imply longer range. Both Li_5B_4 and B_4C satisfy this criteria. Other substances such as boron silicide would not do as well since the Si would increase the energy loss rate for alpha and triton particles. B_4C is a well-known material and probably could be sputtered onto the Si surface. Li_5B_4[3] might also be useful but the method for putting it down on the Si surface is rather unclear at this time.

Both these substances may be rather stable even in contrast with the silicon surface. My own guess is that B_4C will be more stable since it does not contain Li. Hence, I prefer B_4C over Li_5B_4.

These metals are both likely to produce Schottky barriers with a height of about 0.7 to 0.8 eV to the conduction band. Both are likely to be good enough conductors to provide an adequate pathway for the charge out of the detector.

If difficulty is encountered in making a good Schottky barrier, then I would propose that the p-n junction device be fabricated.

Economics

The Si technology is a well developed technology. Detector arrays could probably be produced at between \$2000-\$5000/m^2. The

precise price would depend on quantity, military specifications, cost of the Li^6 and B^{10} isotopes, etc.

Fabrication

I would propose that one start with lightly doped n-type 3" diameter wafers. A large area ohmic contact could be placed on

be fabricated to see if it gives substantially better response characteristics. The first detector would not require a poly-silicon overlayer and this could be added later if desired. Theoretically, this detector scheme could be modeled quite simply for the neutron spectra one expects to encounter so that estimates of device performance can be made, and the parameters in the device structure optimized.

ACKNOWLEDGEMENT

M. Sinnott and E. Hucke suggested the B_4C and Li_5B_4 systems as potential candidates for the B and/or Li bearing metal. The author has profited from a number of discussions with H. Ehrenreich about the concepts involved in such a detector. This research was supported by the Defense Advanced Research Projects Agency of the Department of Defense under Contract No. MDA903-80C-0505 with The University of Michigan.

TABLE 1. RELEVANT PARAMETERS FOR SOME MATERIALS USEFUL AS THERMAL NEUTRON DETECTOR

MATERIAL	$N_{Li}c(m^{-3})$	$N_B(cm^{-3})$	$l_{abs}^{10B}(\mu m)$	$l_{abs}^{6Li}(\mu m)$	R^{α} *(μm) 1.47 MeV	R *(μm) 2.05 MeV	R^{T} *(μm) 2.75 MeV
Li (metal)	4.63×10^{22}	0	-	229.0	-	20μm	135μm
B (semiconductor)	0	1.30×10^{23}	20.0	-	3.0	-	-
B_4C	0	1.10×10^{23}	23.7	-	2.8	-	-
Li_5B_4	3.94×10^{22}	3.15×10^{22}	82.7	269.0	6.3	23μm	78μm

*Ranges are estimated using the estimates from C. A. Young (NOSC) for ^{6}Li and ^{10}B. The ranges R are R are assumed to vary as $R = \frac{A}{NM_a^{\frac{1}{2}}}$ where A is a constant for a given energy, N is the number of atoms per unit volume and $Ma^{\frac{1}{2}}$ is the mass of the element. For composite materials R was assumed to add reciprocally.

References

1. K. A. Kress, "A Polymer Material-Composite Neutron Detector."

2. M. Sinnott, private communication.

3. F. E. Wang, Met. Trans. 10A, 10, 343 (1979). This is a rather unusual material which sets upon a solid at 500-550°C.

4. Wafers with doping as low as $10^{14}cm^{-3}$ may be expensive. However, layers with dopings of 10^{15}-$10^{16}cm^{-3}$ are readily available. In this case, a bias of about 10 volts would result in a depletion width of 1-4μm thick. This thickness of the depletion layer should be adequate for application here.

To obtain maximum performance one wants to have the largest number of triton or alphas deposit their energy in the silicon for a given flux of incident thermal neutrons. To meet these criteria, we want to use elements with small atomic numbers since small atomic numbers imply longer range. Both Li_5B_4 and B_4C satisfy this criteria. Other substances such as boron silicide would not do as well since the Si would increase the energy loss rate for alpha and triton particles. B_4C is a well-known material and probably could be sputtered onto the Si surface. Li_5B_4[3] might also be useful but the method for putting it down on the Si surface is rather unclear at this time.

Both these substances may be rather stable even in contrast with the silicon surface. My own guess is that B_4C will be more stable since it does not contain Li. Hence, I prefer B_4C over Li_5B_4.

These metals are both likely to produce Schottky barriers with a height of about 0.7 to 0.8 eV to the conduction band. Both are likely to be good enough conductors to provide an adequate pathway for the charge out of the detector.

If difficulty is encountered in making a good Schottky barrier, then I would propose that the p-n junction device be fabricated.

Economics

The Si technology is a well developed technology. Detector arrays could probably be produced at between \$2000-\$5000/m^2. The

LOW-FLUX THERMAL NEUTRON DETECTORS BASED ON SOLID BORON

J. J. Gilman

Sensitive detectors of thermal neutrons are needed to discover and monitor the presence of strategic nuclear materials. This must be done from a considerable distance in most cases, so sensitivity to fluxes at the natural background level is desired. Background neutrons have a flux on about 0.007 neutrons/cm^2-sec. A low flux indeed!

Present detectors are principally large Geiger counters (15 cm. dia. and 180 cm. long). These contain $^{10}BF_3$ gas at a pressure of about one atmosphere or a ^{10}B density of about 10^{19} molecules/cm^3. Such large tubular counters are bulky and heavy. Therefore more compact detectors are desired, and the best way to achieve them is by means of solid-state detectors.

Solid boron and lithium are the most likely substances for solid-state detectors because they have large capture cross-sections for thermal neutrons. The reaction for boron is:

$$^{10}B(n,\alpha)\,^{7}Li \qquad K(\alpha) = 2.3 \text{ Mev}$$

while for Li:

$$^{6}Li(n,\alpha)T \qquad K(\alpha) = 2.0 \text{ Mev}$$

$$K(T) = 2.7 \text{ Mev}$$

precise price would depend on quantity, military specifications, cost of the Li^6 and B^{10} isotopes, etc.

Fabrication

I would propose that one start with lightly doped n-type 3" diameter wafers. A large area ohmic contact could be placed on the bulk of the structure using techniques developed in the solar cell industry. (For the p-n junction structure the wafer would be implanted with boron). A layer of B_4C would then be sputtered on. The layer should be about 3μm thick. Then a layer of large grain, n-type polysilicon would be grown on top of the B_4C using CVD. This layer is not essential but would make it possible to detect neutrons which result in α particles that are directed out of the layers. Finally a large area ohmic contact would be made to the polysilicon layer. Some attention should be paid to keeping α sources in packaging materials from contributing to the background.

Spatial Resolution

Arrays make up a set of individual detection offers the opportunity for obtaining spatial as well as temporal information about the incident neutron fluence. This information may be valuable in identifying some sources.

Recommendation

I recommend that some compnay be asked to produce such a detector structure, particularly using B_4C and that the performance of this detector be evaluated to determine its limitations. The program could begin by putting down B_4C on a Si layer to see if it makes an adequate Schottky barrier. The p-n junction device should

Boron has an atomic density of 2.8×10^{23} atoms/cm^3, while lithium has a density of 1.1×10^{23} atoms/cm^3. Thus both are about 10^4 times as dense as a typical gas (STP conditions). Therefore, a solid slab of ^{10}B about 10μ thick would be equivalent in neutron capturing capacity to the large Geiger tubes presently used.

Workers in the U.S. Navy have been developing schemes for using solid lithium in detectors, but boron has several virtues in comparison with lithium so it will be emphasized here. Its virtues include: being a semiconductor rather than a metal, being passivated by an oxide skin against many reactive environments, being mechanically rugged instead of soft, and having a larger thermal neutron capture cross-section than lithium. Its figure-of-merit is not as high as that of lithium if the range of the decay products is important. If the range is not important, its figure-of-merit is much better (by an order-of-magnitude). These comparisons are made in Table I.

For a device in which a nuetron capture event is converted into an electron-hole avalanche or other detectable electrical changes, the decay product ranges should not be important. Then M_2 is the appropriate figure of merit and boron is clearly superior to lithium as a potential detector.

Several years ago boron was investigated as a semiconductor. It was shown to have an energy gap of 1.4 eV; to have a strong negative temperature coefficient of resistivity, to possess both p- and n- type conduction, and to have a strong photo-

be fabricated to see if it gives substantially better response characteristics. The first detector would not require a poly-silicon overlayer and this could be added later if desired. Theoretically, this detector scheme could be modeled quite simply for the neutron spectra one expects to encounter so that estimates of device performance can be made, and the parameters in the device structure optimized.

ACKNOWLEDGEMENT

M. Sinnott and E. Hucke suggested the B_4C and Li_5B_4 systems as potential candidates for the B and/or Li bearing metal. The author has profited from a number of discussions with H. Ehrenreich about the concepts involved in such a detector. This research was supported by the Defense Advanced Research Projects Agency of the Department of Defense under Contract No. MDA903-80C-0505 with The University of Michigan.

TABLE I. Comparison of the Neutron Detection Parameters of Boron and Lithium

Material	Capture Cross-Section (Barns)	Single Bond Radius (A)	Atoms/ Volume (cm^{-8})	Decay Particle Range (Microns)	M_1 $\times 10^{-8}$	M_2 $\times 10^{-11}$
^{10}B	3837	0.81	$1.89 \times 10^{+24}$	5(α)	3.6	7.3
^{6}Li	945	1.23	0.54 M"	27(α),135(T)	6.9	0.51

M_1 = figure-of-merit = (cross-section)×(range)×(atoms/volume)

M_2 = figure-of-merit = (cross-section)×(atoms/volume)

References

1. K. A. Kress, "A Polymer Material-Composite Neutron Detector."

2. M. Sinnott, private communication.

3. F. E. Wang, Met. Trans. 10A, 10, 343 (1979). This is a rather unusual material which sets upon a solid at 500-550°C.

4. Wafers with doping as low as $10^{14}cm^{-3}$ may be expensive. However, layers with dopings of 10^{15}-$10^{16}cm^{-3}$ are readily available. In this case, a bias of about 10 volts would result in a depletion width of 1-4μm thick. This thickness of the depletion layer should be adequate for application here.

conduction peak excited by photons in the energy range of 0.5-1.5 microns.[1] In short, it has the characteristics needed to make solid-state electronic devices.

A simple neutron detector based on boron was made about sixteen years ago.[2] It consisted of a resistance bridge with one leg containing ^{10}B and the other ^{11}B. Neutron absorption heated the former more than the latter and this was measured as a resistance change. This detector was effective in a nuclear reactor at a flux level of $2\times10^{11}m/cm^2$-sec. This sensitivity is inadequate for present purposes, but could be improved considerably by using a different device design.

It should be possible, for example, to make some kind of avalanche breakdown device from boron that would have considerably higher sensitivity than the device described above. An avalanche device might consist of a thin piece of ^{10}B placed between two electrodes and subjected to an electric field near the breakdown level such that a neutron capture event would create enough electron/hole pairs to cause breakdown. This would send a pulse through the external circuit and temporarily reduce the electric field so as to stop breakdown. The device would then reset in preparation for another event. The configuration of this device could be designed to produce locally enhanced fields; and to inhibit surface breakdown (Figure 1).

Since one of the better ways of making solid boron is to deposit it onto a hot wire via CVD, it might be desirable to make a detector with the cylindrical configuration of a Geiger counter

LOW-FLUX THERMAL NEUTRON DETECTORS BASED ON SOLID BORON

J. J. Gilman

Sensitive detectors of thermal neutrons are needed to discover and monitor the presence of strategic nuclear materials. This must be done from a considerable distance in most cases, so sensitivity to fluxes at the natural background level is desired. Background neutrons have a flux on about 0.007 neutrons/cm^2-sec. A low flux indeed!

Present detectors are principally large Geiger counters (15 cm. dia. and 180 cm. long). These contain $^{10}BF_3$ gas at a pressure of about one atmosphere or a ^{10}B density of about 10^{19} molecules/cm^3. Such large tubular counters are bulky and heavy. Therefore more compact detectors are desired, and the best way to achieve them is by means of solid-state detectors.

Solid boron and lithium are the most likely substances for solid-state detectors because they have large capture cross-sections for thermal neutrons. The reaction for boron is:

$$^{10}B(n,\alpha)\,^{7}Li \qquad K(\alpha) = 2.3 \text{ Mev}$$

while for Li:

$$^{6}Li(n,\alpha)T \qquad K(\alpha) = 2.0 \text{ Mev}$$

$$K(T) = 2.7 \text{ Mev}$$

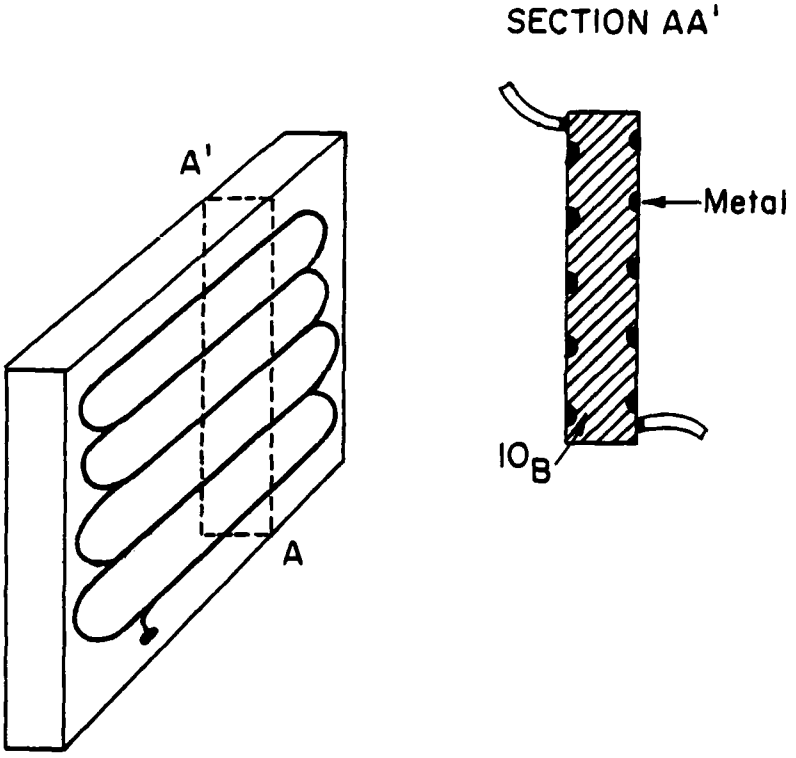

FIGURE 1

Boron has an atomic density of 2.8×10^{23} atoms/cm^3, while lithium has a density of 1.1×10^{23} atoms/cm^3. Thus both are about 10^4 times as dense as a typical gas (STP conditions). Therefore, a solid slab of ^{10}B about 10μ thick would be equivalent in neutron capturing capacity to the large Geiger tubes presently used.

Workers in the U.S. Navy have been developing schemes for using solid lithium in detectors, but boron has several virtues in comparison with lithium so it will be emphasized here. Its virtues include: being a semiconductor rather than a metal, being passivated by an oxide skin against many reactive environments, being mechanically rugged instead of soft, and having a larger thermal neutron capture cross-section than lithium. Its figure-of-merit is not as high as that of lithium if the range of the decay products is important. If the range is not important, its figure-of-merit is much better (by an order-of-magnitude). These comparisons are made in Table I.

For a device in which a nuetron capture event is converted into an electron-hole avalanche or other detectable electrical changes, the decay product ranges should not be important. Then M_2 is the appropriate figure of merit and boron is clearly superior to lithium as a potential detector.

Several years ago boron was investigated as a semiconductor. It was shown to have an energy gap of 1.4 eV; to have a strong negative temperature coefficient of resistivity, to possess both p- and n- type conduction, and to have a strong photo-

as suggested in Figure 2. This would require a minimum amount of processing of the boron.

Since the Hall mobility that has been observed in boron is about $10^{-1}cm^2/V\text{-}sec.$, the average drift velocity would be about $10^4cm/sec.$ with applied fields in the breakdown regime; that is, $10^5V/cm$. Then, if the device were 10 microns thick, the transit time would be about 10^{-7} sec. which yields a time-resolution that is at least as good as that of a Geiger counter.

A secondary advantage of this type of counter is that only modest applied voltages are needed. If the device is 10 microns thick only 100 volts need to be applied to produce a field of $10^5V/cm$. If it is desired to make the device 10 times as thick, or it is desired to operate at 10 times higher electric field, the necessary applied voltage is only one kilo-volt.

The performance of a solid-state detector of this type would probably decrease with age as a result of radiation damage. But this would take considerable time in the presence of the low fluxes which are to be detected.

Acknowledgement

This research was supported by the Defense Advanced Research Projects Agency of the Department of Defense under Contract No. MDA903-80C-0505 with The University of Michigan

TABLE I. Comparison of the Neutron Detection Parameters of Boron and Lithium

Material	Capture Cross-Section (Barns)	Single Bond Radius (A)	Atoms/ Volume (cm^{-8})	Decay Particle Range (Microns)	M_1 $\times 10^{-8}$	M_2 $\times 10^{-11}$
^{10}B	3837	0.81	$1.89 \times 10^{+24}$	5(α)	3.6	7.3
^{6}Li	945	1.23	0.54 M"	27(α),135(T)	6.9	0.51

M_1 = figure-of-merit = (cross-section)×(range)×(atoms/volume)

M_2 = figure-of-merit = (cross-section)×(atoms/volume)

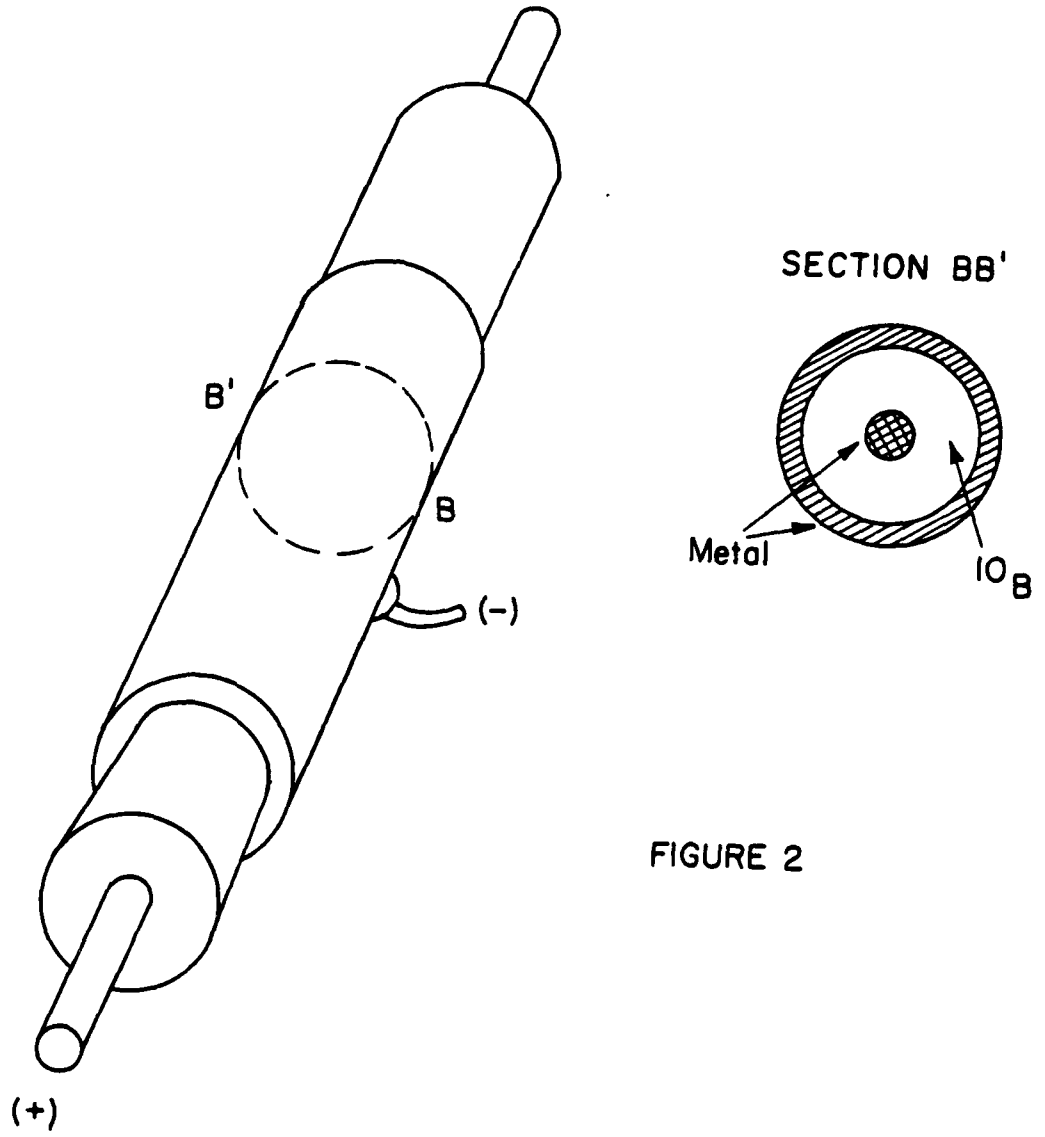

FIGURE 2

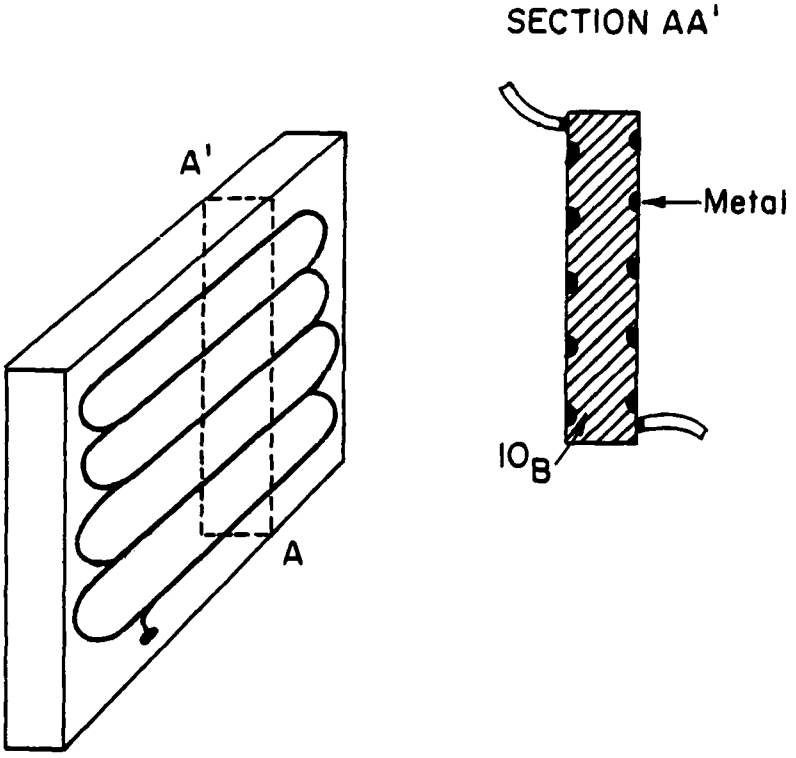

FIGURE 1

References

1. Boron-Volume 2, Ed by G. K. Gaule, Plenum Press, New York (1965) p. 143.

2. Ibid., p. 317.

3. Ibid., p. 301.

as suggested in Figure 2. This would require a minimum amount of processing of the boron.

Since the Hall mobility that has been observed in boron is about $10^{-1}cm^2/V\text{-}sec.$, the average drift velocity would be about $10^4cm/sec.$ with applied fields in the breakdown regime; that is, $10^5V/cm$. Then, if the device were 10 microns thick, the transit time would be about 10^{-7} sec. which yields a time-resolution that is at least as good as that of a Geiger counter.

A secondary advantage of this type of counter is that only modest applied voltages are needed. If the device is 10 microns thick only 100 volts need to be applied to produce a field of $10^5V/cm$. If it is desired to make the device 10 times as thick, or it is desired to operate at 10 times higher electric field, the necessary applied voltage is only one kilo-volt.

The performance of a solid-state detector of this type would probably decrease with age as a result of radiation damage. But this would take considerable time in the presence of the low fluxes which are to be detected.

Acknowledgement

This research was supported by the Defense Advanced Research Projects Agency of the Department of Defense under Contract No. MDA903-80C-0505 with The University of Michigan

ADIABATIC FLOWS IN FLUIDS AND SOLIDS

W. G. Hoover and A. J. C. Ladd

INTRODUCTION

Nonequilibrium microscopic simulations of bulk matter usually proceed by solving the Newtonian or Hamiltonian atomistic equations of motion. Although these equations are exact, the solution process is time consuming. In some cases time can be saved, without the sacrifice of physical fidelity, by modifying the exact reversible equations, to improve the efficiency of the simulation. One of the earliest such modifications was developed to describe Brownian motion. In that case rapid collisions, which a single massive Brownian particle undergoes with much-less-massive water molecules, could be replaced by superposing a statistical drag force, proportional to the Brownian velocity, and a random, velocity-independent, fluctuating force. The relative strengths of the drag and fluctuating forces must be adjusted to give the correct long-time limit for the Brownian particle's kinetic energy.

Alternatively, drag forces based on the second moment of the velocity distribution could be used. Such forces may prove useful in treating liquid-metal flows, in which electronic thermal damping affects the heat conductivity much more than it does the shear viscosity.

Here we address neither of these simple nonequilibrium modifications of equilibrium molecular dynamics, but rather one which has just recently been developed and analyzed. The new technique, by now fairly well understood, makes it possible to describe, via nonequilibrium molecular dynamics, adiabatic flows in fluids and solids.

FLOW DESCRIPTIONS

We consider flows described by the macroscopic strain-rate tensor, $\overleftrightarrow{\nabla}\vec{u}$, where $\vec{u}$ is the macroscopic stream velocity. We imagine that the motion varies slowly, so that the strain rate is a well-defined function of space and time. Two examples of the strain-rate tensor, corresponding to (i) homogeneous compression and (ii) shearing, are as follows:

$$\begin{pmatrix} -\dot{\epsilon} & 0 & 0 \\ 0 & -\dot{\epsilon} & 0 \\ 0 & 0 & -\dot{\epsilon} \end{pmatrix} \qquad \text{and} \qquad \begin{pmatrix} 0 & \dot{\epsilon} & 0 \\ 0 & 0 & 0 \\ 0 & 0 & 0 \end{pmatrix}$$

(i) (ii)

The flows we consider are irreversible, but adiabatic, with irreversible effects producing entropy increases in the absence of heat transfer.

Macroscopic Description

A comoving macroscopic space coordinate $\vec{q}$, embedded in a flowing continuum, has a velocity given by the dot product of that coordinate with the macroscopic strain-rate tensor:

$$\dot{\vec{q}} = \vec{q} \cdot \overleftrightarrow{\nabla} \vec{u} \quad . \tag{1}$$

In this description the material is treated as a continuum, without local velocity fluctuations. Such a crude macroscopic description is inadequate on a microscopic scale, where momenta (corresponding to kinetic heat) must also be introduced.

Microscopic Description

In addition to the macroscopic hydrodynamic convective motion just described, microscopic particles have additional velocity components, described by the momenta {p}:

$$\dot{\vec{q}} = (\vec{p}/m) + \vec{q} \cdot \overleftrightarrow{\nabla} \vec{u} \quad . \tag{2}$$

Likewise, the energy includes, in addition to the convective mass-motion part, an internal energy, $E = \Phi(\{q\}) + \sum(p^2/2m)$. In an adiabatic process thermodynamics gives the change of internal energy with time in terms of the pressure tensor:

$$\dot{E} = -\overleftrightarrow{\nabla} \overleftrightarrow{P} : \overleftrightarrow{\nabla} \vec{u} \quad . \tag{3}$$

This thermodynamic relation (3) is also exact microscopically, provided that the momenta change with time in a way analogous to (2):

$$\dot{\vec{p}} = \vec{F} - \overleftrightarrow{\nabla} \vec{u} \cdot \vec{p} \quad . \tag{4}$$

Then the equations of motion, (2) and (4), provide a complete microscopic description of macroscopic adiabatic flow.

ADIABATIC FLOWS IN FLUIDS AND SOLIDS

W. G. Hoover and A. J. C. Ladd

INTRODUCTION

Nonequilibrium microscopic simulations of bulk matter usually proceed by solving the Newtonian or Hamiltonian atomistic equations of motion. Although these equations are exact, the

Shear Viscosity

In a dense fluid undergoing adiabatic shear, with $\dot{\varepsilon} = du_x/dy$, the Hamiltonian equations of motion relate the momentum to a moving coordinate frame and also incorporate a velocity-dependent force:

$$\begin{aligned} &\dot{x} = (p_x/m + \dot{\varepsilon}y \; ; \; \dot{y} = (p_y/m) \quad ; \; \dot{z} = (p_z.m) \quad ; \\ &\dot{p}_x = F_x \quad ; \; \dot{p}_y = F_y - \dot{\varepsilon}p_x \; ; \; \dot{p}_z = F_z \quad . \end{aligned} \tag{6}$$

When these equations of motion (6) are solved numerically, the resulting shear stress, $-P_{xy}$, can be related to the shear viscosity coefficient: $\eta = -P_{xy}/\dot{\varepsilon}$. Calculations carried out in this way[3] agree well both with experimental data for simple fluids and with previous less-efficient computer simulations.[5]

Bulk Viscosity

In order to determine the fluid bulk viscosity coefficient, which describes the pressure-volume hysteresis present in cyclic compression and expensions, the strain rate must depend upon the time. For a sinusoidal volume variation, the net work done per cycle is simply related to the bulk viscosity:

$$\text{Work per Cycle} = \eta_v(\delta V/V)^2 \omega \pi V \quad , \tag{7}$$

where ω is the frequency (in radians per second) and $(\delta V/V)$ is the (maximum) volume strain. The results from these nonequilibrium calculations have shown that (i) the Enskog theory of dense fluids grossly overestimates the bulk viscosity in the region near the melting line[1], and (ii) the dense-fluid shear and bulk viscosities are both sufficiently frequency-dependent that careful laboratory experiments on rare gases should detect this effect.[3]

Here we address neither of these simple nonequilibrium modifications of equilibrium molecular dynamics, but rather one which has just recently been developed and analyzed. The new technique, by now fairly well understood, makes it possible to describe, via nonequilibrium molecular dynamics, adiabatic flows in fluids and solids.

FLOW DESCRIPTIONS

We consider flows described by the macroscopic strain-rate tensor, $\overleftrightarrow{\nabla}\vec{u}$, where $\vec{u}$ is the macroscopic stream velocity. We imagine that the motion varies slowly, so that the strain rate is a well-defined function of space and time. Two examples of the strain-rate tensor, corresponding to (i) homogeneous compression and (ii) shearing, are as follows:

$$\begin{pmatrix} -\dot{\epsilon} & 0 & 0 \\ 0 & -\dot{\epsilon} & 0 \\ 0 & 0 & -\dot{\epsilon} \end{pmatrix} \qquad \text{and} \qquad \begin{pmatrix} 0 & \dot{\epsilon} & 0 \\ 0 & 0 & 0 \\ 0 & 0 & 0 \end{pmatrix}$$

(i) (ii)

The flows we consider are irreversible, but adiabatic, with irreversible effects producing entropy increases in the absence of heat transfer.

Macroscopic Description

A comoving macroscopic space coordinate $\vec{q}$, embedded in a flowing continuum, has a velocity given by the dot product of that coordinate with the macroscopic strain-rate tensor:

Shockwaves

The transport coefficients obtained from nonequilibrium molecular dynamics have recently been used to solve the Navier-Stokes continuum equations for the structure of dense-fluid shockwaves.[6,7] The shockwaves investigated carried a liquid from about normal density to twice that density, corresponding, for liquid argon, to a maximum pressure of nearly half a megabar. The Navier-Stokes solutions were compared with shockwave profiles obtained by direct atomistic simulations. The comparison indicates that the continuum picture predicts shockwave thicknesses which are nearly correct for weak shocks, and which are slightly too thin for very strong shocks. These dense-fluid results qualitatively resemble those found for gases by analyzing the Boltzmann equation and the Navier-Stokes equations at low density.

Plastic Deformation of Solids

The same nonequilibrium technique just described for fluids is now being applied to solids. We have already studied the properties of individual dislocations[8] and are now in the process of simulating the motion of many interacting dislocations, by incorporating large-amplitude shears in microscopic simulations.

We are also pursuing a macroscopic approach to this same problem. We begin with the analytic stress field due to a vertical column of edge dislocations (with horizontal Burgers' vectors). By superposing such stress fields we obtain the stress field associated with an infinite hexagonal net of these defects. This network function can then be used to obtain the stress field

produced by a periodic array of dislocations, with several hundred dislocations per unit cell. By combining the total stress field at each dislocation with the equation of motion found in Ref. 8 we can follow the time history of solid-phase plastic flows. Provision is made for the incorporation of Burgers'-vector-conserving "chemical reactions" which create and annihilate dislocations.

ACKNOWLEDGEMENT

The work just described has involved the efforts of many individuals. Much of this effort is described in the references. Generous support for this work has been furnished by the University of California, the Australian-American Educational Foundation, the United States Army Research Office, and the Lawrence Livermore National Laboratory.

$$\dot{\vec{q}} = \vec{q} \cdot \overleftrightarrow{\nabla} \vec{u} \quad . \tag{1}$$

In this description the material is treated as a continuum, without local velocity fluctuations. Such a crude macroscopic description is inadequate on a microscopic scale, where momenta (corresponding to kinetic heat) must also be introduced.

Microscopic Description

In addition to the macroscopic hydrodynamic convective motion just described, microscopic particles have additional velocity components, described by the momenta {p}:

$$\dot{\vec{q}} = (\vec{p}/m) + \vec{q} \cdot \overleftrightarrow{\nabla} \vec{u} \quad . \tag{2}$$

Likewise, the energy includes, in addition to the convective mass-motion part, an internal energy, $E = \Phi(\{q\}) + \sum(p^2/2m)$. In an adiabatic process thermodynamics gives the change of internal energy with time in terms of the pressure tensor:

$$\dot{E} = -\overleftrightarrow{\nabla} \overleftrightarrow{P} : \overleftrightarrow{\nabla} \vec{u} \quad . \tag{3}$$

This thermodynamic relation (3) is also exact microscopically, provided that the momenta change with time in a way analogous to (2):

$$\dot{\vec{p}} = \vec{F} - \overleftrightarrow{\nabla} \vec{u} \cdot \vec{p} \quad . \tag{4}$$

Then the equations of motion, (2) and (4), provide a complete microscopic description of macroscopic adiabatic flow.

Hamiltonian Description

It is particularly interesting and significant that both the nonequilibrium equations of motion, (2) and (4), characteristic of adiabatic flows, can be derived from a microscopic Hamiltonian function.[1] This nonequilibrium Hamiltonian contains, in addition to the internal energy, a perturbation composed of the product of Doll's Tensor and the strain-rate tensor[2]:

$$H \equiv E(\{q\},\{p\}) + \sum \overleftrightarrow{qp} : \overleftrightarrow{\nabla u} \quad . \tag{5}$$

The equations of motion then follow by differentiation: $\dot{q} = \partial H/\partial p$; $\dot{p} = -\partial H/\partial q$.

The novel Hamiltonian formulation (5) provides equilibrium fluctuation expressions for nonequilibrium quantities. Not only the known "Green-Kubo" expressions for the viscosity coefficients[3] but also new expressions for nonequilibrium distribution functions[4] have been derived from (5).

An analog of (5) for heat flow has not yet been developed.

APPLICATIONS

Our purpose in analyzing adiabatic flow is to improve our understanding of the connection between microscopic mechanisms, on the level of atoms and crystal defects, such as dislocations, and macroscopic deformations. Our work so far has explored fluid shear[3,5] and bulk[1,3] viscosities, shockwaves,[6,7] and plastic deformation of solids, both from the atomistic and dislocation points of view.

Shear Viscosity

In a dense fluid undergoing adiabatic shear, with $\dot{\varepsilon} = du_x/dy$, the Hamiltonian equations of motion relate the momentum to a moving coordinate frame and also incorporate a velocity-dependent force:

$$\begin{aligned} &\dot{x} = (p_x/m + \dot{\varepsilon}y \; ; \; \dot{y} = (p_y/m) \quad ; \; \dot{z} = (p_z.m) \quad ; \\ &\dot{p}_x = F_x \quad ; \; \dot{p}_y = F_y - \dot{\varepsilon}p_x \; ; \; \dot{p}_z = F_z \quad . \end{aligned} \tag{6}$$

When these equations of motion (6) are solved numerically, the resulting shear stress, $-P_{xy}$, can be related to the shear viscosity coefficient: $\eta = -P_{xy}/\dot{\varepsilon}$. Calculations carried out in this way[3] agree well both with experimental data for simple fluids and with previous less-efficient computer simulations.[5]

Bulk Viscosity

In order to determine the fluid bulk viscosity coefficient, which describes the pressure-volume hysteresis present in cyclic compression and expensions, the strain rate must depend upon the time. For a sinusoidal volume variation, the net work done per cycle is simply related to the bulk viscosity:

$$\text{Work per Cycle} = \eta_v(\delta V/V)^2 \omega \pi V \quad , \tag{7}$$

where ω is the frequency (in radians per second) and $(\delta V/V)$ is the (maximum) volume strain. The results from these nonequilibrium calculations have shown that (i) the Enskog theory of dense fluids grossly overestimates the bulk viscosity in the region near the melting line[1], and (ii) the dense-fluid shear and bulk viscosities are both sufficiently frequency-dependent that careful laboratory experiments on rare gases should detect this effect.[3]

Shockwaves

The transport coefficients obtained from nonequilibrium molecular dynamics have recently been used to solve the Navier-Stokes continuum equations for the structure of dense-fluid shockwaves.[6,7] The shockwaves investigated carried a liquid from about normal density to twice that density, corresponding, for liquid argon, to a maximum pressure of nearly half a megabar. The Navier-Stokes solutions were compared with shockwave profiles obtained by direct atomistic simulations. The comparison indicates that the continuum picture predicts shockwave thicknesses which are nearly correct for weak shocks, and which are slightly too thin for very strong shocks. These dense-fluid results qualitatively resemble those found for gases by analyzing the Boltzmann equation and the Navier-Stokes equations at low density.

Plastic Deformation of Solids

The same nonequilibrium technique just described for fluids is now being applied to solids. We have already studied the properties of individual dislocations[8] and are now in the process of simulating the motion of many interacting dislocations, by incorporating large-amplitude shears in microscopic simulations.

We are also pursuing a macroscopic approach to this same

produced by a periodic array of dislocations, with several hundred dislocations per unit cell. By combining the total stress field at each dislocation with the equation of motion found in Ref. 8 we can follow the time history of solid-phase plastic flows. Pro-

A holistic view is not yet possible, even though the experimental side is now able to contribute a large body of detailed information. This will continue to be a very active and fruitful field for future research.

4) High temperature creep induced fracture in both metals and ceramics is getting a great deal of recent attention, and the general outlines of the phenomena are being clarified. Nucleation in metals appears to be relatively easy, and has been considered to proceed primarily at particles on sliding boundaries. In ceramics void nucleation normally occurs at boundary nodes, and diaplay characteristic shapes subject to theoretical description. The parameters governing growth involve such details as diffusivity and energy of surfaces and interfaces; quantities that are difficult to access at the requisite local level. Uncertainties in the magnitude of these parameters is likely to remain for some time. Experimental results indicate an appreciable range of cavitation susceptibilities at grain boundaries in both metals and ceramics. The inhomogeneous cavity distributions that result exert a profound influence upon the evolution of failure, to an extent that depends on the details of the cavitation process. In the case of ceramics the details of how a cluster of neighboring boundaries interact through the continuum stress fields between them was a notable example of interdisciplinary collaboration by members of the council.

5) Plastic flow localization frequently sets a limit to the achievable ductility of structural metals. This happens by large

REFERENCES

1. W. G. Hoover, A. J. C. Ladd, R. B. Hickman, and B. L. Holian, Phys. Rev. 21A, 1756(1980).

2. C. H. Fawcett, Hobbies 63, 41(1958).

3. W. G. Hoover, D. J. Evans, R. B. Hickman, A. J. C. Ladd, W. T. Ashurst, and B. Moran, "Lennard-Jones Triple-Point Bulk and Shear Viscosities, Green-Kubo Theory, Hamiltonian Mechanics, and Nonequilibrium Molecular Dynamics", Phys. Rev. (in press, 1980).

4. D. J. Evans, W. G. Hoover, and A. J. C. Ladd, Phys. Rev. Letts. 45, 124(1980).

5. W. G. Hoover and W. T. Ashurst, "Nonequilibrium Molecular Dynamics," in Theoretical Chemistry, Advances and Perspectives 1, 1 (Academic Press, New York, 1975).

6. W. G. Hoover, Phys. Rev. Letts. 42, 1531(1979).

7. G. L. Holian, W. G. Hoover, B. Moran, and G. K. Straub, "Shockwave Structure via Nonequilibrium Molecular Dynamics and Navier-Stokes Continuum Mechanics," Phys. Rev. (submitted, 1980).

8. W. G. Hoover, N. E. Hoover, and W. C. Moss, J. Appl. Phys. 50, 829(1979).

scale shear band instabilities (e.g., in plane-strain tension) as well as on the microscale where localized shearing-off between rupture cavities, nucleated at inclusions, causes them to join well before void coalescence conditions as predicted for stable plastic flow are met. The problem is particularly evident at macro-scale crack tips in ductile metals, where localized shearing (promoted in some instances by prestrain, but inherent to the as-heat-treated structure in others) can result in a J_{IC} or δ_{IC} significantly below that expected on the basis of conventional hole growth concepts.

Very significant progress has been made on the continuum plasticity of localization instabilities. This work relates conditions for localization to various "non-classical" features of the plastic flow relations, such as vertex formation on yield surfaces from the underlying polycrystalline slip process and progressive weakening of material through internal cavity nucleation and growth. The study of small initial imperfections in the continuum plasticity context has also been a focus of recent attention. Shearing in localized zones may, depending on details of the constitutive relation and imperfection type, remain stable for some amount of overall deformation beyond the bifurcation strain or may (as for a non-linear elastic material) become unstable even before the bifurcation strain in the presence of suitable imperfections.

Other work reported related to an apparent shear localization in the indentation failure of glass, and to a macro-scale

FRACTURE WORKSHOP

H. Ehrenreich, R. Thomson, J. Hirth
J. Rice, A. Evans, J. Hutchinson

On July 16-18, a workshop exploring essentially the entire spectrum of fundamental mechanisms controlling fracture in materials was held. In addition to the members of the Council, about 20 outside visitors also participated. The workshop was organized to give a maximum opportunity for open discussion of idead and major challenges and to encourage interaction among people from a variety of disciplinary backgrounds.

The highlights are as follows:

1) Numerous groups in this country and abroad are now undertaking chemical cluster-type of calculations looking toward a full scale attack on the atomic configuration at a crack tip. At this meeting, there was little hope expressed that these attempts would lead to a successful outcome for transition metals. The reason is that the number of atoms involved in the crack configuration is too large to allow a full calculation of the relaxed configuration. On the other hand, if a less ambitious goal is adopted then current condensed matter theory can be useful. That is, given that atomic simulations will continue to be attempted then guidance in the types of force have to be used, and perhaps some sense of their limitations can be hoped for from general theory.

localization in the internal buckling of fiber composites under compressive load.

A key problem in localization as part of microscale ductile fracture processes is that of whether the phenomenon is due to some inherent instability of the 3-D multi-dislocation motion process, reflected in macro-plastic constitutive relations, or whether it is due to the progressive weakening by fracture-in-progress through cavity nucleation. It is also important to examine the triggering role of large, local inhomogeneities like voids or microcracks on the localization process.

6) Hole growth and coalescence is one of the dominant ductile fracture mechanisms and recent work has attempted to quantify the process by which a growing void interacts with a crack tip. Voids are nucleated by inclusion debonding or cracking, and thus the spacing between inclusions and their size are important factors in determining fracture toughness. Efforts to predict the onset of crack advance as related to the spacing and size of inclusions on the basis of void growth calculations have achieved some degree of success, although there are a number of factors which make quantitative predictions difficult. Knowledge of debonding or cracking stress conditions for inclusions, which is limited, is essential to the process. Plastic flow about voids can be terminated by localization instabilities leading to decreased ductility, as discussed above.

Ductile metals are capable of considerable quasi-state stable crack growth in that crack advance, once initiated,

continues only under increasing applied load or displacement. A theory for predicting crack advance under the high constraint conditions associated with contained yielding in plane strain appears promising and has reproduced experimental data on a steel with moderate ductility under conditions of small and intermediate scale yielding.

Plastic does not seem to be important in the fracture of ceramics, but an interesting plasticity-like mechanism which does enhance fracture toughness of a ceramic is the volumetric expansion associated with the stress-induced phase transformation of a second phase of embedded particles such as zirconia. In a way which is not clearly understood, the zone of transformed particles in the vicinity of a crack tip lowers the stresses acting in this region.

7) In summary, areas discussed of particular interest to the future are 1) identification of useful force laws for modeling purposes, 2) competition between brittle and ductile response, 3) environmentally affected fracture, 4) toughening or embrittling of grain boundaries by trace elements, 5) statistical effects in nucleation of fracture, and 6) stress-strain-internal parameter relations for non-radial loading.

8) Some important problems and opportunities left for future discussion and work are fatigue nucleation, finite element procedures to fully plastic crack growth across an element of $\sim$1 mm in size and asymmetric cracks in locally plastic parts of structures.

A holistic view is not yet possible, even though the experimental side is now able to contribute a large body of detailed information. This will continue to be a very active and fruitful field for future research.

4) High temperature creep induced fracture in both metals and ceramics is getting a great deal of recent attention, and the general outlines of the phenomena are being clarified. Nucleation in metals appears to be relatively easy, and has been considered to proceed primarily at particles on sliding boundaries. In ceramics void nucleation normally occurs at boundary nodes, and diaplay characteristic shapes subject to theoretical description. The parameters governing growth involve such details as diffusivity and energy of surfaces and interfaces; quantities that are difficult to access at the requisite local level. Uncertainties in the magnitude of these parameters is likely to remain for some time. Experimental results indicate an appreciable range of cavitation susceptibilities at grain boundaries in both metals and ceramics. The inhomogeneous cavity distributions that result exert a profound influence upon the evolution of failure, to an extent that depends on the details of the cavitation process. In the case of ceramics the details of how a cluster of neighboring boundaries interact through the continuum stress fields between them was a notable example of interdisciplinary collaboration by members of the council.

5) Plastic flow localization frequently sets a limit to the achievable ductility of structural metals. This happens by large

potentials was questioned since they are not directly applicable to any of these. Despite the shortcomings of electronic structure calculations, which were discussed (the use of approximate exchange-correlation potentials, finite basis sets, to mention but a few), simple physical properties dependent only on the knowledge of the energy levels have been calculated with remarkable accuracy. The same is not as valid for wave function dependent properties since similar band calculations do not always yield identical wave functions. Many-body effects are also treated in a highly approximate fashion through the use of effective potentials.

Despite the fact that chemically relevant information is energetically too small to be determined absolutely by these techniques, calculations *can nevertheless* produce useful information if they are performed in the same manner to a given accuracy for corresponding systems that are being compared. The heats of formation of hydrides were cited as one example.

At a Battelle symposium (June 1971) the issue of employing cluster calculations to estimate pair potentials was raised. Since a cluster calculation involves few atoms and therefore has a distinct molecular form, the relevance of a pair potential derived from such a calculation to a solid can be no better than that of the cluster calculation. Watson mentioned several examples from transition metal electronic structures which indicated that physical discrepancies exist between band calculations on the one hand and molecular calculations on the other. Hückel calculations, whose attractiveness rests on their simplicity, are not really adequate

localization in the internal buckling of fiber composites under compressive load.

A key problem in localization as part of microscale ductile fracture processes is that of whether the phenomenon is due to some inherent instability of the 3-D multi-dislocation motion process, reflected in macro-plastic constitutive relations, or whether it is due to the progressive weakening by fracture-in-progress through cavity nucleation. It is also important to examine the triggering role of large, local inhomogeneities like voids or microcracks on the localization process.

6) Hole growth and coalescence is one of the dominant ductile fracture mechanisms and recent work has attempted to quantify the process by which a growing void interacts with a crack tip. Voids are nucleated by inclusion debonding or cracking, and thus the spacing between inclusions and their size are important factors in determining fracture toughness. Efforts to predict the onset of crack advance as related to the spacing and size of inclusions on the basis of void growth calculations have achieved some degree of success, although there are a number of factors which make quantitative predictions difficult. Knowledge of debonding or cracking stress conditions for inclusions, which is limited, is essential to the process. Plastic flow about voids can be terminated by localization instabilities leading to decreased ductility, as discussed above.

Ductile metals are capable of considerable quasi-state stable crack growth in that crack advance, once initiated,

when applied to clusters of transition metal atoms since convergence is difficult to achieve even for clusters having 80 atoms or more.

W. Wilson, R. Johnson, E. Machlin, and A. Paskin discussed some of these ideas from a somewhat different viewpoint based on their own extensive experience with cluster calculations, pair potentials, and computations of defects in solids. One important question that surfaced frequently concerns the existence of a best pair potential or more precisely, how one is going to characterize the quality of such a potential.

The viewpoint that empirical pair potentials yield useful information quite independently of whether they are linked rigorously to band theory or not was developed by Johnson. Wilson discussed finite element, semiempirical lattice calculations in connection with finite defects. His calculations perhaps are closest to being able to deal at least approximately with crack formation in a solid. Rice raised the issue of whether such calculations are better or even different in content from that yielded by macroscopic elastic calculations.

Paskin discussed his computer simulation for equations of state using Lennard-Jones pair potentials. The agreement with experiment obtained from his results is better than that found from band calculations.

Machlin discussed pair potentials in alloys. He made two principal points. The first concerned the need for a volume dependent term and directional bond bending terms. The second

continues only under increasing applied load or displacement. A theory for predicting crack advance under the high constraint conditions associated with contained yielding in plane strain appears promising and has reproduced experimental data on a steel with moderate ductility under conditions of small and intermediate scale yielding.

Plastic does not seem to be important in the fracture of ceramics, but an interesting plasticity-like mechanism which does enhance fracture toughness of a ceramic is the volumetric expansion associated with the stress-induced phase transformation of a second phase of embedded particles such as zirconia. In a way which is not clearly understood, the zone of transformed particles in the vicinity of a crack tip lowers the stresses acting in this region.

7) In summary, areas discussed of particular interest to the future are 1) identification of useful force laws for modeling purposes, 2) competition between brittle and ductile response, 3) environmentally affected fracture, 4) toughening or embrittling of grain boundaries by trace elements, 5) statistical effects in nucleation of fracture, and 6) stress-strain-internal parameter relations for non-radial loading.

8) Some important problems and opportunities left for future discussion and work are fatigue nucleation, finite element procedures to fully plastic crack growth across an element of $\sim$1 mm in size and asymmetric cracks in locally plastic parts of structures.

dealt with the question of how to describe local density changes adequately. Whether volume changes can be parameterized adequately by distance changes was a matter of some dispute.

Ehrenreich argued on the basis of the ab initio pair potential developed in collaboration with his group that it might be more fruitful to think of families of pair potentials, each member being appropriate to a particular scale of spatial variation of the defect existing in the solid. For example, the pair potential appropriate for a phonon whose wavelength is much larger than the interatomic distance must surely be different from that appropriate for calculating a stacking fault whose distance variation is of the order of an interatomic spacing. These ideas are useful in the present context only insofar as they might lead to the formulation of some theoretical underpinnings which would shed light on the reason for the enormous success that empirical pair potentials have enjoyed.

FORCE LAWS

H. Ehrenreich

The central theme of this section was electronic structure calculations for various types of many-atomic systems, what they have accomplished, and the present state of the art. After several hours of stimulating and sometimes heated discussion, the central points that emerged were: (1) In their present state, no form of ab initio quantum mechanical calculations, however approximate, is able to cope adequately with the fracture problem; and (2) pair potentials are frequently extremely successful in describing all sorts of complicated phenomena in solids including equations of state. This, despite the fact that there is yet no underlying theoretical structure for deriving such potentials in general from first principles, and that they in general fail to yield results that are consistent with the Cauchy relations.

The session began with an overview by R. E. Watson (Brookhaven) who described the present accomplishments of calculations concerning the electronic structure and various physical properties of solids. The techniques used include band theory, cluster calculations, and interatomic potentials. Band calculations have been successful in providing estimates of the cohesive energy, theoretical strength, surface properties, and a variety of electronic properties of solids. The relevance of cluster calculations to either bulk, molecular behavior, or pair

HIGH TEMPERATURE FAILURE

A. G. Evans

This session consisted of two overviews and two short contributions concerned primarily with high temperature cavitation and failure induced by diffusive mechanisms, and two short contributions discussing hole and crack growth in the presence of time dependent plasticity.

The first overview, presented by A. S. Argon, emphasized the nucleation stage of failure in metallic systems. The essential conclusion (derived both from experimental studies conducted on stainless steel and from concomitant analysis) was that cavities nucleated primarily from particles located at grain boundaries due to local stress concentrations induced by grain boundary sliding transients. The requirement for local stress concentrations (up to $\sim 20\sigma_\infty$) invoked in this study was inferred from critical nucleation size estimates, based on surface energy values typical of metallic systems. A source of suitable stress concentration was sought by evaluating the stresses that can develop from sliding transients, partially accommodated by power law creep or interface diffusion. The analyses suggested that suitable stress concentrations ($5\text{-}16\sigma_\infty$) could develop at particles on sliding boundaries under conditions wherein power law creep accommodation was prevalent (i.e., for relatively large particles, >0.1 μm for the high stress levels used). The principal implication of the analysis was that the nucleation process should be expected to dominate

potentials was questioned since they are not directly applicable to any of these. Despite the shortcomings of electronic structure calculations, which were discussed (the use of approximate exchange-correlation potentials, finite basis sets, to mention but a few), simple physical properties dependent only on the knowledge of the energy levels have been calculated with remarkable accuracy. The same is not as valid for wave function dependent properties since similar band calculations do not always yield identical wave functions. Many-body effects are also treated in a highly approximate fashion through the use of effective potentials.

Despite the fact that chemically relevant information is energetically too small to be determined absolutely by these techniques, calculations *can nevertheless* produce useful information if they are performed in the same manner to a given accuracy for corresponding systems that are being compared. The heats of formation of hydrides were cited as one example.

At a Battelle symposium (June 1971) the issue of employing cluster calculations to estimate pair potentials was raised. Since a cluster calculation involves few atoms and therefore has a distinct molecular form, the relevance of a pair potential derived from such a calculation to a solid can be no better than that of the cluster calculation. Watson mentioned several examples from transition metal electronic structures which indicated that physical discrepancies exist between band calculations on the one hand and molecular calculations on the other. Hückel calculations, whose attractiveness rests on their simplicity, are not really adequate

on sliding boundaries containing particles of large size. The nucleation events occur during sliding transients (viz. during load application, or when boundary migration, etc., permits incremental sliding under steady-state conditions). Such significant implications about nucleation are clearly amenable to detailed experimental scrutiny. Additionally, it was noted that the initial stages of coalescence occur preferentially near triple junctions, probably when grain boundary sliding transients induce stress concentrations in the vicinity of the triple point. The coalesced cavities resembly 'wedge' cracks.

The second overview, by A. G. Evans, considered the growth and coalescence stages of failure, pertinent primarily to ceramic systems. The principal emphasis was the important influence of material and cavitation inhomogeneity upon the cavity evolution sequence and hence, on the failure time. The observed inhomogeneity was principally attributed to local variations in the grain boundary diffusivity (due to grain orientations, augmented by impurity distributions). The presence of some boundaries with diffusivities at the large extreme of the distribution was shown to accelerate the initial formation and growth of crack-like cavities and account for the observation of such cavities at the early stages of failure. However, the creation of local zones of cavitation was also shown to generate constraints on the cavitation zone that both suppress the growth of the initially formed cavities and enhance the extension of cavities around the zone periphery. A spreading of the cavitation zone was thus anticipated, in

when applied to clusters of transition metal atoms since convergence is difficult to achieve even for clusters having 80 atoms or more.

W. Wilson, R. Johnson, E. Machlin, and A. Paskin discussed some of these ideas from a somewhat different viewpoint based on their own extensive experience with cluster calculations, pair potentials, and computations of defects in solids. One important question that surfaced frequently concerns the existence of a best pair potential or more precisely, how one is going to characterize the quality of such a potential.

The viewpoint that empirical pair potentials yield useful information quite independently of whether they are linked rigorously to band theory or not was developed by Johnson. Wilson discussed finite element, semiempirical lattice calculations in connection with finite defects. His calculations perhaps are closest to being able to deal at least approximately with crack formation in a solid. Rice raised the issue of whether such calculations are better or even different in content from that yielded by macroscopic elastic calculations.

Paskin discussed his computer simulation for equations of state using Lennard-Jones pair potentials. The agreement with experiment obtained from his results is better than that found from band calculations.

Machlin discussed pair potentials in alloys. He made two principal points. The first concerned the need for a volume dependent term and directional bond bending terms. The second

conformance with experimental observations on ceramics. Failure evolution estimates based upon zone spreading and eventual coalescence were provided that exhibit the essential characteristics observed during creep experiments. Further quantification of the failure process based upon inhomogeneity effects and related constraints was proposed.

The first short presentation, by J. R. Rice, demonstrated the crucial importance of inhomogeneous cavitation upon the failure time in materials subject to the growth of equilibrium (Hull-Rimmer) cavities. The coalescence time was computed for an isolated grain facet subject to cavitation. The constraint derived from the non-cavitating surroundings was demonstrated to dominate the failure evolution, when the stress was low and for small values of both the cavity spacing within the facet and of the grain facet length. In this limit, the time-to-failure was illustrated to depend inversely upon the steady state creep rate of the surrounding structure, in accord with the expectations of a Monkman-Grant relation. This result resolves the dilemma of poor failure predictability generally attributed to the Hull-Rimmer process in the presence of uniformly cavitating boundaries. The growth of the cavities becomes less constrained by the creep rate of the surrounding material either when the cavitation occurs more homogeneously throughout the polycrystal or when the grain size becomes large. It remains to examine the homogeneity of nucleation as a function of microstructure and strain history, as a basis for distinguishing Monkman-Grant behavior from cavity growth controlled failure.

dealt with the question of how to describe local density changes adequately. Whether volume changes can be parameterized adequately by distance changes was a matter of some dispute.

Ehrenreich argued on the basis of the ab initio pair potential developed in collaboration with his group that it might be more fruitful to think of families of pair potentials, each member being appropriate to a particular scale of spatial variation of the defect existing in the solid. For example, the pair potential appropriate for a phonon whose wavelength is much larger than the interatomic distance must surely be different from that appropriate for calculating a stacking fault whose distance variation is of the order of an interatomic spacing. These ideas are useful in the present context only insofar as they might lead to the formulation of some theoretical underpinnings which would shed light on the reason for the enormous success that empirical pair potentials have enjoyed.

The second short presentation, by R. M. Cannon, described some issues associated with cavity nucleation at grain junctions in ceramics. It was emphasized that the important issues concerned with nucleation are similar to those encountered in metals; the dihedral angle, the local stress magnitude and the time at stress. The dihedral angle has a special significance at triple junctions and four grain junctions, were geometric conditions upon cavity curvature require dihedral angles >60° and 70°, respectively, to prohibit spontaneous cavity nucleation. Dihedral angles in ceramics appear to approch this critical range. However, the stress concentrations near these junctions induced by sliding are highly transient, because of a rapid alleviation associated with boundary diffusion. The incidence of cavitation was thus concluded to be sensitive to the details of the diffusive stress relaxation and the site availability associated with triple junctions, as well as the magnitude of the dihedral angle. Careful experimental studies and theoretical estimates pertinent to junction nucleation are evidently needed to establish a full comprehension of cavity nucleation in ceramics.

The third short presentation, by B. Budiansky, was concerned with the hole growth that accompanies time dependent plastic flow. It was demonstrated that holes in linear materials invariably elongate in the direction of the maximum principal tensile stress. However, for non-linear materials hole elongation in the plane normal to the maximum tension was predicted for a range of stress ratios. The characteristic geometric changes predicted by the

HIGH TEMPERATURE FAILURE

A. G. Evans

This session consisted of two overviews and two short contributions concerned primarily with high temperature cavitation and failure induced by diffusive mechanisms, and two short contributions discussing hole and crack growth in the presence of time dependent plasticity.

The first overview, presented by A. S. Argon, emphasized the nucleation stage of failure in metallic systems. The essential conclusion (derived both from experimental studies conducted on stainless steel and from concomitant analysis) was that cavities nucleated primarily from particles located at grain boundaries due to local stress concentrations induced by grain boundary sliding transients. The requirement for local stress concentrations (up to $\sim 20\sigma_\infty$) invoked in this study was inferred from critical nucleation size estimates, based on surface energy values typical of metallic systems. A source of suitable stress concentration was sought by evaluating the stresses that can develop from sliding transients, partially accommodated by power law creep or interface diffusion. The analyses suggested that suitable stress concentrations ($5\text{-}16\sigma_\infty$) could develop at particles on sliding boundaries under conditions wherein power law creep accommodation was prevalent (i.e., for relatively large particles, >0.1 μm for the high stress levels used). The principal implication of the analysis was that the nucleation process should be expected to dominate

analysis should provide perspectives for anticipating the behavior of holes growing ahead of a ductile crack.

The final short presentation, by E. Hart, considered the behavior of the crack tip singularity in a material subject to time dependent plasticity. The local (non-zero) K at the crack tip was related to the applied K by selecting appropriate constitutive laws for the plastic deformation. The local K was then incorporated into a crack growth law (based on a thermally activated kink mechanism) to predict relations between the crack growth rate and the applied stress intensity factor. The predictions indicated two branches in the crack growth curve at different velocity ranges. The predictions should be subject to experimental comparison. A basis for further analysis based on determinations of local K levels would then emerge.

One of the principal implications of the session was the emergence of cavitation inhomogeneity, and the concomitant constraints from the non-cavitating region, as a central issue with regard to creep rupture. Inhomogeneity was anticipated to result in failure behavior ranging from complete dominance by the creep-rate of the surrounding structure to creep-rate independence. Many situations will lie between these limits. Experimental studies which both delineate those microstructural aspects that dictate the failure evolution, and develop unique correlations between cavity observations and the predictions derived from constrained cavity growth models, are clearly demanded.

on sliding boundaries containing particles of large size. The nucleation events occur during sliding transients (viz. during load application, or when boundary migration, etc., permits incremental sliding under steady-state conditions). Such significant implications about nucleation are clearly amenable to detailed experimental scrutiny. Additionally, it was noted that the initial stages of coalescence occur preferentially near triple junctions, probably when grain boundary sliding transients induce stress concentrations in the vicinity of the triple point. The coalesced cavities resembly 'wedge' cracks.

The second overview, by A. G. Evans, considered the growth and coalescence stages of failure, pertinent primarily to ceramic systems. The principal emphasis was the important influence of material and cavitation inhomogeneity upon the cavity evolution sequence and hence, on the failure time. The observed inhomogeneity was principally attributed to local variations in the grain boundary diffusivity (due to grain orientations, augmented by impurity distributions). The presence of some boundaries with diffusivities at the large extreme of the distribution was shown to accelerate the initial formation and growth of crack-like cavities and account for the observation of such cavities at the early stages of failure. However, the creation of local zones of cavitation was also shown to generate constraints on the cavitation zone that both suppress the growth of the initially formed cavities and enhance the extension of cavities around the zone periphery. A spreading of the cavitation zone was thus anticipated, in

The deliberations on cavity nucleation indicate an uncertainty concerning the relative roles of the dihedral angle (at inclusion/matrix interfaces, grain junctions, etc.) and of local sliding induced stress concentrations (as alleviated by diffusion or power law creep) in specific materials systems. One or both of these effects must be important since cavitation occurs at applied stresses well below those required for homogeneous nucleation. The calculations of the local stress levels are now sufficiently developed that it is appropriate to devote some attention to the precise measurement of dihedral angles, in order to permit a range of important nucleation problems to be addressed at the quantitative level. Early cavity detection schemes (such as neutron scattering) are also of particular significance, especially when used in conjunction with loading rate experiments which determine the extent to which nucleation occurs during loading induced transients (rather than requiring nucleation during sliding transients in steady-state creep). Since the morphology of cavity arrays has a substantial influence upon the cavity growth constraints and hence, upon the failure time, careful studies of nucleation could be an essential constituent in the ultimate comprehension of failure.

conformance with experimental observations on ceramics. Failure evolution estimates based upon zone spreading and eventual coalescence were provided that exhibit the essential characteristics observed during creep experiments. Further quantification of the failure process based upon inhomogeneity effects and related constraints was proposed.

The first short presentation, by J. R. Rice, demonstrated the crucial importance of inhomogeneous cavitation upon the failure time in materials subject to the growth of equilibrium (Hull-Rimmer) cavities. The coalescence time was computed for an isolated grain facet subject to cavitation. The constraint derived from the non-cavitating surroundings was demonstrated to dominate the failure evolution, when the stress was low and for small values of both the cavity spacing within the facet and of the grain facet length. In this limit, the time-to-failure was illustrated to depend inversely upon the steady state creep rate of the surrounding structure, in accord with the expectations of a Monkman-Grant relation. This result resolves the dilemma of poor failure predictability generally attributed to the Hull-Rimmer process in the presence of uniformly cavitating boundaries. The growth of the cavities becomes less constrained by the creep rate of the surrounding material either when the cavitation occurs more homogeneously throughout the polycrystal or when the grain size becomes large. It remains to examine the homogeneity of nucleation as a function of microstructure and strain history, as a basis for distinguishing Monkman-Grant behavior from cavity growth controlled failure.

CHEMICAL EFFECTS IN FRACTURE

J. P. Hirth

E. Fuller presented an overview of chemical effects in brittle materials. He provided a general classification in terms of the usual three-stage plot of log of crack velocity for stable crack growth versus applied stress intensity factor. For a variety of glasses and ceramics, he showed that region I was predominantly reaction rate limited at the crack tip, being independent of the fugacity of the damaging species at the crack root. Stage II was predominantly diffusion limited. Stage III was close to the limiting velocity in air (at $\sim K_{IC}$) but was found to weakly depend on environment in some cases.

He then discussed crack propagation by breaking of bonds at kinks in a crack tip. The model of a set of springs normal to two stiff rods with the springs breaking at a critical extension (Fuller and Thomson) modeled the cracking. It was shown to give a stress-dependent activation barrier for crack propagation which would be lowered by the presence of another chemical species (bond weakener) at the cracked surface.

A critical experiment for surface effects would be to more closely examine transient behavior on load increase and decrease after varying waiting times as suggested by Evans. This would relate both to the v-K behavior discussed above and to the stress-dissolution model for that case proposed by Charles and Hillig.

The second short presentation, by R. M. Cannon, described some issues associated with cavity nucleation at grain junctions in ceramics. It was emphasized that the important issues concerned with nucleation are similar to those encountered in metals; the dihedral angle, the local stress magnitude and the time at stress. The dihedral angle has a special significance at triple junctions and four grain junctions, were geometric conditions upon cavity curvature require dihedral angles >60° and 70°, respectively, to prohibit spontaneous cavity nucleation. Dihedral angles in ceramics appear to approch this critical range. However, the stress concentrations near these junctions induced by sliding are highly transient, because of a rapid alleviation associated with boundary diffusion. The incidence of cavitation was thus concluded to be sensitive to the details of the diffusive stress relaxation and the site availability associated with triple junctions, as well as the magnitude of the dihedral angle. Careful experimental studies and theoretical estimates pertinent to junction nucleation are evidently needed to establish a full comprehension of cavity nucleation in ceramics.

The third short presentation, by B. Budiansky, was concerned with the hole growth that accompanies time dependent plastic flow. It was demonstrated that holes in linear materials invariably elongate in the direction of the maximum principal tensile stress. However, for non-linear materials hole elongation in the plane normal to the maximum tension was predicted for a range of stress ratios. The characteristic geometric changes predicted by the

McMahon gave an overview of intergranular fracture, mainly in steels. He showed that the local stress intensity for propagation of a microcrack at a grain boundary tended to decrease approximately hyperbolically with increase in grain boundary coverage of group V-VI elements. The impurities, detected by Auger analysis, increased in severity of embrittlement in the order P, Sn, Sb for the most studied cases. He cited other analogous cases of S in Ni and O in Mo. Also mentioned was the role of third elements in enhancing embrittlement, Ni and Mn attracting P, Si repelling it from the matrix in steel for example. On the otherhand, Ti co-segregates with Sb and reduces embrittlement and carbon tends to replace O, for example, with carbon strengthening the grain boundary.

He presented a model of his (with Vitek) in which the major role of impurities was to reduce the critical stress concentration for crack advance without reducing that for dislocation emission to the same extent, if at all. Thus, the plastic work accompanying fracture would be less as would J or the Orowan effective surface energy. He called for fundamental guidance from the physicists and chemists in understanding the solute effects, but the short-term outlook for progress in this area was gloomy.

Machlin discussed pair potential calculation for solutes. These were deemed to be the proper use of pair potentials by Watson because they used the same potentials to compare two systems rather than attempting absolute calculations for one system. An interesting finding was that a soft solute tends to segragate in a hard matrix while the inverse case does not give segregation.

analysis should provide perspectives for anticipating the behavior of holes growing ahead of a ductile crack.

The final short presentation, by E. Hart, considered the behavior of the crack tip singularity in a material subject to time dependent plasticity. The local (non-zero) K at the crack tip was related to the applied K by selecting appropriate constitutive laws for the plastic deformation. The local K was then incorporated into a crack growth law (based on a thermally activated kink mechanism) to predict relations between the crack growth rate and the applied stress intensity factor. The predictions indicated two branches in the crack growth curve at different velocity ranges. The predictions should be subject to experimental comparison. A basis for further analysis based on determinations of local K levels would then emerge.

One of the principal implications of the session was the emergence of cavitation inhomogeneity, and the concomitant constraints from the non-cavitating region, as a central issue with regard to creep rupture. Inhomogeneity was anticipated to result in failure behavior ranging from complete dominance by the creep-rate of the surrounding structure to creep-rate independence. Many situations will lie between these limits. Experimental studies which both delineate those microstructural aspects that dictate the failure evolution, and develop unique correlations between cavity observations and the predictions derived from constrained cavity growth models, are clearly demanded.

McClintock presented a theory for creep cracking at elevated temperature in superalloys where oxidation in the grain boundary accompanies or precedes cracking. He treated the coupled diffusion problem for a moving crack and was able to rationalize observations for a nickel-base superalloy.

The other major point in the discussion referred to grain boundaries where Vitek made a case for pair potential type atomic calculations in classifying types of phenomena. He presented results showing that some high angle grain boundaries had dislocation character in the sense of local strain fields while others did not, an effect that would influence solute segregation. Other important issues were the need for double kink information energies for a complete kink theory of cracking; the question of whether dislocation emission or absorption near crack tips preceded, accompanied or followed the cracking process.

The deliberations on cavity nucleation indicate an uncertainty concerning the relative roles of the dihedral angle (at inclusion/matrix interfaces, grain junctions, etc.) and of local sliding induced stress concentrations (as alleviated by diffusion or power law creep) in specific materials systems. One or both of these effects must be important since cavitation occurs at applied stresses well below those required for homogeneous nucleation. The calculations of the local stress levels are now sufficiently developed that it is appropriate to devote some attention to the precise measurement of dihedral angles, in order to permit a range of important nucleation problems to be addressed at the quantitative level. Early cavity detection schemes (such as neutron scattering) are also of particular significance, especially when used in conjunction with loading rate experiments which determine the extent to which nucleation occurs during loading induced transients (rather than requiring nucleation during sliding transients in steady-state creep). Since the morphology of cavity arrays has a substantial influence upon the cavity growth constraints and hence, upon the failure time, careful studies of nucleation could be an essential constituent in the ultimate comprehension of failure.

LATTICE SIMULATIONS OF CRACKS

R. M. Thomson

G. J. Dienes reviewed the past work on lattice simulations of cracks and presented the latest computer simulation - his own, with Paskin and Gohar - much of it still unpublished. The lattice work is of two generic types - those performed on computers with finite numbers of atoms, and those built on analytical formalisms containing an infinite number of atoms. In the former, two dimensional arrays can be studied with realistic force laws and lattice structures in both static and dynamic situations. In the latter, finite sample size effects are not present, and it is not necessary to graft discrete to continuum regions.

In the most recent calculations of Dienes and Paskin, about 5000 atoms in a two dimensional hexagonal array were studied with the Lennard-Jones interatomic potential. The potential is artificially cut off at 1.6 lattice spacings. In this calculation, the system is on the borderline of the Rice-Thomson ductile/brittle criterion, and depending on how the initial conditions are set, the authors can generate dislocations, or clean brittle fracture. Hence the criterion seems to be verified in this case. They also looked for evidence of lattice trapping, but were unable to find it. Presumably the force law is sufficiently soft to make lattice trapping fall to a value below their sensitivity - i.e., lower than a few percent of the applied stress. This result should be confirmable at least in an approximate way from the Greens function/

CHEMICAL EFFECTS IN FRACTURE

J. P. Hirth

E. Fuller presented an overview of chemical effects in brittle materials. He provided a general classification in terms of the usual three-stage plot of log of crack velocity for stable crack growth versus applied stress intensity factor. For a variety of glasses and ceramics, he showed that region I was predominantly reaction rate limited at the crack tip, being independent of the fugacity of the damaging species at the crack root. Stage II was predominantly diffusion limited. Stage III was close to the limiting velocity in air (at $\sim K_{IC}$) but was found to weakly depend on environment in some cases.

He then discussed crack propagation by breaking of bonds at kinks in a crack tip. The model of a set of springs normal to two stiff rods with the springs breaking at a critical extension (Fuller and Thomson) modeled the cracking. It was shown to give a stress-dependent activation barrier for crack propagation which would be lowered by the presence of another chemical species (bond weakener) at the cracked surface.

A critical experiment for surface effects would be to more closely examine transient behavior on load increase and decrease after varying waiting times as suggested by Evans. This would relate both to the v-K behavior discussed above and to the stress-dissolution model for that case proposed by Charles and Hillig.

lattice statics approach. It was also found that the energy deposited in the overall elastic field may be quite different from the Griffith result under dynamic conditions.

The general conclusions here are that lattice trapping effects are strongly dependent on the shape of the interatomic potential, and perhaps also on the crystal structure. Also, in cases where the lattice is close to the ductile/brittle criterion, dislocations may be formed spontaneously from the crack tip or not, depending upon detailed conditions such as whether the crack is static or dynamic, and perhaps on other location conditions which may apply in real crack situations.

In other contributions, V. Vitek presented a model in which dislocations are continuously formed from the crack tip as it moves. The rate of formation as a function of the surface energy is presented, and rationalized with observed intergranular fracture. The open question here, and emphasized by Vitek, is whether the dislocation production follows a Rice-Thomson type of criterion, or whether continuous production can occur as he proposes.

Weertman also presented a new look at dislocation production at crack tips. In his work, the production of dislocation pairs in the crack tip strain field was investigated, which seemed to correlate in a rough way with the previous Rice-Thomson results.

Markworth reported work on the search for the saddle point in a lattice trapping situation. He found the previously reported algorithm for finding the saddle point fails in cases where the energy surface in configuration space is complex.

McMahon gave an overview of intergranular fracture, mainly in steels. He showed that the local stress intensity for propagation of a microcrack at a grain boundary tended to decrease approximately hyperbolically with increase in grain boundary coverage of group V-VI elements. The impurities, detected by Auger analysis, increased in severity of embrittlement in the order P, Sn, Sb for the most studied cases. He cited other analogous cases of S in Ni and O in Mo. Also mentioned was the role of third elements in enhancing embrittlement, Ni and Mn attracting P, Si repelling it from the matrix in steel for example. On the otherhand, Ti co-segregates with Sb and reduces embrittlement and carbon tends to replace O, for example, with carbon strengthening the grain boundary.

He presented a model of his (with Vitek) in which the major role of impurities was to reduce the critical stress concentration for crack advance without reducing that for dislocation emission to the same extent, if at all. Thus, the plastic work accompanying fracture would be less as would J or the Orowan effective surface energy. He called for fundamental guidance from the physicists and chemists in understanding the solute effects, but the short-term outlook for progress in this area was gloomy.

Machlin discussed pair potential calculation for solutes. These were deemed to be the proper use of pair potentials by Watson because they used the same potentials to compare two systems rather than attempting absolute calculations for one system. An interesting finding was that a soft solute tends to segragate in a hard matrix while the inverse case does not give segregation.

The session closed with a return to discussion of force laws. Among the physicists, there was a continuing skepticism regarding the ability of any current techniques to address the crack problem in metals from anything like first principles. On the other hand, results from cluster calculations and band theory, etc., might be useful as a guide in picking and delineating the range of validity of empirically chosen laws. For example, cluster calculations might help answer how important long range potentials might be. Thus in the spirit that lattice simulations can lead to qualitative guides regarding the types of physical phenomena which might be displayed by cracks, by combining a variety of results from current theory, some guidance in the choice of potentials may be possible. So one example of a place to look for such guidance, the chemical schemes of Miedema should be consulted.

FRACTURE WORKSHOP

July 16-18, 1980

PROGRAM

July 16 A.M.	Force Laws	Chairman: H. Ehrenreich

Introductory Comments: R. Thomson

Overview: R. Watson, BNL

Short Contributions: W. Wilson, R. Johnson, E. Machlin

Discussion: H. Ehrenreich

July 16 P.M.	Lattice Crack Simulations	Chairman: R. Thomson

Overview, Computer Simulations: G. J. Dienes

Short Contributions: V. Vitek, A. Markworth, J. Weertman

Discussion: R. Thomson

July 17 A.M.	Chemical Effects In Fracture	Chairman: J. Hirth

Overview, Chemical Effects in Brittle Materials: E. Fuller

Overview, Grain Boundary Fracture: C. McMahon

Short Contributions: E. Machlin, J. Hirth, F. McClintock

Discussion

July 17 P.M.	Plastic Flow Localization	Chairman: J. Rice

Overview, Plastic Flow Localization: J. Hutchinson

Short Contributions: J. Hirth, D. Marshall, B. Budiansky

Discussion: J. Rice

Discussion of Future Conference Plans

July 18 A.M.	High Temperature Fracture	Chairman: A. Evans

Overview, Cavity Nucleation: A. Argon

Overview, High Temperature Fracture: A. Evans

Short Contributions: V. Vitek, J. Rice, B. Budiansky

Discussion: A. Evans

July 18 P.M.	Crack Tip Ductile Processes	Chairman: J. Hutchinson

Overview, Plastic Fracture Initiation: R. McMeeking

Short Contributions: J. Rice, J. Hutchinson, A. Evans and F. McClintock

Discussion: J. Hutchinson

LATTICE SIMULATIONS OF CRACKS

R. M. Thomson

G. J. Dienes reviewed the past work on lattice simulations of cracks and presented the latest computer simulation - his own, with Paskin and Gohar - much of it still unpublished. The lattice work is of two generic types - those performed on computers with finite numbers of atoms, and those built on analytical formalisms containing an infinite number of atoms. In the former, two dimensional arrays can be studied with realistic force laws and lattice structures in both static and dynamic situations. In the latter, finite sample size effects are not present, and it is not necessary to graft discrete to continuum regions.

In the most recent calculations of Dienes and Paskin, about 5000 atoms in a two dimensional hexagonal array were studied with the Lennard-Jones interatomic potential. The potential is artificially cut off at 1.6 lattice spacings. In this calculation, the system is on the borderline of the Rice-Thomson ductile/brittle criterion, and depending on how the initial conditions are set, the authors can generate dislocations, or clean brittle fracture. Hence the criterion seems to be verified in this case. They also looked for evidence of lattice trapping, but were unable to find it. Presumably the force law is sufficiently soft to make lattice trapping fall to a value below their sensitivity - i.e., lower than a few percent of the applied stress. This result should be confirmable at least in an approximate way from the Greens function/

FRACTURE WORKSHOP

Guest Participants

Ali S. Argon
M.I.T.
Room 1-306
Cambridge, MA 02139

G. J. Dienes
Brookhaven National Lab.
Room 510B
Upton, NY 11973

Katherine T. Faber
University of California
240 Hearst Mining Bldg.
Berkeley, CA 94720

Ed Fuller
National Bureau of Standards
Room A113, Bldg. 223
Washington, DC 20234

Edward W. Hart
Bard Hall
Cornell University
Ithaca, NY 14853

George Herrmann
Durand Building
Stanford University
Stanford, CA 94305

Robert A. Johnson
University of Virginia
B225 Thornton Hall
Charlottesville, CA 22901

E. S. Machlin
Columbia University
1106 Mudd Bldg.
New York, NY 10027

Alan J. Markworth
Battelle, Columbus Labs.
Physical Metallurgy Section
Columbus, OH 43201

David Marshall
University of California
240 Hearst Mining Bldg.
Berkeley, CA 94720

C. J. McMahon, Jr.
University of Pennsylvania
205 LRSM K1
Philadelphia, PA 19104

Robert M. McMeeking
University of Illinois
317 Talbot Lab.
Urbana, IL 61820

Bill Moran
Lawrence Livermore Laboratory
L-200
Livermore, CA 94550

Arthur Paskin
Physics Department
Queens College
Flushing, NY

Amar Rana
University of California
240 Hearst Mining Bldg.
Berkeley, CA 94720

V. Vitek
University of Pennsylvania
219 LRSM 1K1
Philadelphia, PA 19104

H. Wadley
National Bureau of Standards
A125, Bldg. 223
Washington, DC 20234

Dick Watson
Brookhaven National Laboratory
Physics Department
Upton, NY 11973

J. Weertman
Materials Science Dept.
Northwestern University
Evanston, IL 60201

William D. Wilson
Theoretical Division
Sandia National Laboratories
Livermore, CA 94550

lattice statics approach. It was also found that the energy deposited in the overall elastic field may be quite different from the Griffith result under dynamic conditions.

The general conclusions here are that lattice trapping effects are strongly dependent on the shape of the interatomic potential, and perhaps also on the crystal structure. Also, in cases where the lattice is close to the ductile/brittle criterion, dislocations may be formed spontaneously from the crack tip or not, depending upon detailed conditions such as whether the crack is static or dynamic, and perhaps on other location conditions which may apply in real crack situations.

In other contributions, V. Vitek presented a model in which dislocations are continuously formed from the crack tip as it moves. The rate of formation as a function of the surface energy is presented, and rationalized with observed intergranular fracture. The open question here, and emphasized by Vitek, is whether the dislocation production follows a Rice-Thomson type of criterion, or whether continuous production can occur as he proposes.

Weertman also presented a new look at dislocation production at crack tips. In his work, the production of dislocation pairs in the crack tip strain field was investigated, which seemed to correlate in a rough way with the previous Rice-Thomson results.

Markworth reported work on the search for the saddle point in a lattice trapping situation. He found the previously reported algorithm for finding the saddle point fails in cases where the energy surface in configuration space is complex.

PLASTIC SHIELDING OF SHARP CRACK TIPS

J. Hutchinson, F. McClintock, R. Thomson

ABSTRACT

A completely brittle crack is an often discussed abstraction with little practical importance. On the other hand, it is possible that an atomically sharp crack might exist in some materials, but surrounded by a shielding cloud of dislocations. The cloud of dislocations can be modeled by a continuum distribution, or equivalently by a continuum plasticity solution. A number of such solutions exist for specific constitutive relations. These solutions should not be used down to regions of the order of atomic dimensions, however, because the dislocations must be discretized on a scale approximating the maximum density possible in a material. Then a sharp crack will generate an elastic field, not a plastic one, in its immediate vicinity. Several recent papers have addressed this problem of matching an elastic enclave to a continuum solution with contradictory results.

We have shown that two simple special cases exist. In the first, we match both total strain and stress on the boundary between the inner elastic enclave and the surrounding continuum solution. In the second, we match only the stress. We find this can be done in Mode III.

The session closed with a return to discussion of force laws. Among the physicists, there was a continuing skepticism regarding the ability of any current techniques to address the crack problem in metals from anything like first principles. On the other hand, results from cluster calculations and band theory, etc., might be useful as a guide in picking and delineating the range of validity of empirically chosen laws. For example, cluster calculations might help answer how important long range potentials might be. Thus in the spirit that lattice simulations can lead to qualitative guides regarding the types of physical phenomena which might be displayed by cracks, by combining a variety of results from current theory, some guidance in the choice of potentials may be possible. So one example of a place to look for such guidance, the chemical schemes of Miedema should be consulted.

For perfect plasticity, we take a solution in the elastic enclave of the form

$$W = \frac{K_{el}}{G}\sqrt{\frac{2r}{\pi}}\sin\frac{\theta}{2} + \frac{A}{G}r^{3/2}\sin\frac{\theta}{2} \qquad (1)$$

where the term in A is introduced to provide matching of both stress and strain on the enclave boundary. For Mode III perfect plasticity, we find that

$$K^2 \simeq \tau_o\sqrt{r_o}\,\frac{2\sqrt{2\pi}}{3}\,K_{el} \qquad (2)$$

where K is the externally measured K-field, r_o is the radius of the internal enclave, τ_o is the yield stress of the material, and K_{el} is the K for the internal elastic enclave.

When we match only the stress on the boundary of the elastic enclave, the solution is indeterminate. The reason is that everywhere inside the plastic continuum, the stress is simply constant. Hence, no stress signal is transmitted to the elastic enclave about the size of the external stress. (Since a strain signal is transmitted, one is allowed to find the solution (2). Alternatively, there is no way of defining how many dislocations have flowed through the elastic enclave, reducing its stress.

For a work-hardening plastic region, we find that the stress boundary conditions can be satisfied. Take

$$\tau = \tau_o\left(\frac{\gamma}{\gamma_o}\right)^n \qquad (3)$$

In that case, the internal and external K-fields are related by

FRACTURE WORKSHOP

July 16-18, 1980

PROGRAM

July 16 A.M.	Force Laws	Chairman: H. Ehrenreich

Introductory Comments: R. Thomson

Overview: R. Watson, BNL

Short Contributions: W. Wilson, R. Johnson, E. Machlin

Discussion: H. Ehrenreich

July 16 P.M.	Lattice Crack Simulations	Chairman: R. Thomson

Overview, Computer Simulations: G. J. Dienes

Short Contributions: V. Vitek, A. Markworth, J. Weertman

Discussion: R. Thomson

July 17 A.M.	Chemical Effects In Fracture	Chairman: J. Hirth

Overview, Chemical Effects in Brittle Materials: E. Fuller

Overview, Grain Boundary Fracture: C. McMahon

Short Contributions: E. Machlin, J. Hirth, F. McClintock

Discussion

July 17 P.M.	Plastic Flow Localization	Chairman: J. Rice

Overview, Plastic Flow Localization: J. Hutchinson

Short Contributions: J. Hirth, D. Marshall, B. Budiansky

Discussion: J. Rice

Discussion of Future Conference Plans

July 18 A.M.	High Temperature Fracture	Chairman: A. Evans

Overview, Cavity Nucleation: A. Argon

Overview, High Temperature Fracture: A. Evans

Short Contributions: V. Vitek, J. Rice, B. Budiansky

Discussion: A. Evans

July 18 P.M.	Crack Tip Ductile Processes	Chairman: J. Hutchinson

Overview, Plastic Fracture Initiation: R. McMeeking

Short Contributions: J. Rice, J. Hutchinson, A. Evans and F. McClintock

Discussion: J. Hutchinson

$$K^2 = 2\pi\tau_o\left(2\pi r_o\right)^{\frac{2+n}{2n}}\left(\frac{K_{el}}{\tau_o}\right)^{\frac{1+n}{n}} \qquad (4)$$

In neither of these solutions is it true that an equilibrium crack satisfies the relation

$$K \alpha (\Gamma)^{\frac{1}{2}} \qquad (5)$$

where Γ is the intrinsic for surface energy, as in the Griffith relation for brittle cracks. Eq. (5) was predicted by Weertman[1]. Equation (4) is the same as Thomson's estimate[2].

Our two solutions correspond to two rather different physical situations, which points to the fact that the $K(K_{el})$ relation should depend upon the detailed behavior of dislocations in the vicinity of the crack. In case I, the elastic enclave is constrained to have the same amount of total strain as in the plastic region. This means that as the crack is made and stressed, that no dislocations cross through the elastic enclave. Also, the cleavage surface is exactly that of an elastic (but discrete) sharp crack. On the other hand there is no reason, physically, to require for the crack tip region, after a cut has been made, and as the stress is increased, that no dislocations cross the elastic enclave. In fact, to the contrary, we expect that this region will sustain a plastic strain. The important point is that so far as stresses are concerned, the material is (discrete) elastic, and the stress concentration at the crack tip must generate a stress characteristic of that elastic enclave. The

FRACTURE WORKSHOP

Guest Participants

Ali S. Argon
M.I.T.
Room 1-306
Cambridge, MA 02139

G. J. Dienes
Brookhaven National Lab.
Room 510B
Upton, NY 11973

Katherine T. Faber
University of California
240 Hearst Mining Bldg.
Berkeley, CA 94720

Ed Fuller
National Bureau of Standards
Room A113, Bldg. 223
Washington, DC 20234

Edward W. Hart
Bard Hall
Cornell University
Ithaca, NY 14853

George Herrmann
Durand Building
Stanford University
Stanford, CA 94305

Robert A. Johnson
University of Virginia
B225 Thornton Hall
Charlottesville, CA 22901

E. S. Machlin
Columbia University
1106 Mudd Bldg.
New York, NY 10027

Alan J. Markworth
Battelle, Columbus Labs.
Physical Metallurgy Section
Columbus, OH 43201

David Marshall
University of California
240 Hearst Mining Bldg.
Berkeley, CA 94720

C. J. McMahon, Jr.
University of Pennsylvania
205 LRSM K1
Philadelphia, PA 19104

Robert M. McMeeking
University of Illinois
317 Talbot Lab.
Urbana, IL 61820

Bill Moran
Lawrence Livermore Laboratory
L-200
Livermore, CA 94550

Arthur Paskin
Physics Department
Queens College
Flushing, NY

Amar Rana
University of California
240 Hearst Mining Bldg.
Berkeley, CA 94720

V. Vitek
University of Pennsylvania
219 LRSM 1K1
Philadelphia, PA 19104

H. Wadley
National Bureau of Standards
A125, Bldg. 223
Washington, DC 20234

Dick Watson
Brookhaven National Laboratory
Physics Department
Upton, NY 11973

J. Weertman
Materials Science Dept.
Northwestern University
Evanston, IL 60201

William D. Wilson
Theoretical Division
Sandia National Laboratories
Livermore, CA 94550

plastic strain will however modify the shape of the cleavage surface, and for sufficient plastic flaw, this shape modification (blunting) will be important.

In conclusion, the solution for the stresses in the vicinity of the crack tip is not unique, and cannot be known without further knowledge of the actual dislocation motion and structure in the vicinity of the crack tip.

ACKNOWLEDGEMENT

This research was supported by the Defense Advanced Research Projects Agency of the Department of Defense under Contract MDA903-80C-0505 with The University of Michigan.

References

1. J. Weertman, Fracture Stress Obtained from the Elastic Crack Tip Enclave Model, J. Mat. Sci. In press.

2. R. Thomson, J. Mat. Sci. 13, 128(1978).

PLASTIC SHIELDING OF SHARP CRACK TIPS

J. Hutchinson, F. McClintock, R. Thomson

ABSTRACT

A completely brittle crack is an often discussed abstraction with little practical importance. On the other hand, it is possible that an atomically sharp crack might exist in some materials, but surrounded by a shielding cloud of dislocations. The cloud of dislocations can be modeled by a continuum distribution, or equivalently by a continuum plasticity solution. A number of such solutions exist for specific constitutive relations. These solutions should not be used down to regions of the order of atomic dimensions, however, because the dislocations must be discretized on a scale approximating the maximum density possible in a material. Then a sharp crack will generate an elastic field, not a plastic one, in its immediate vicinity. Several recent papers have addressed this problem of matching an elastic enclave to a continuum solution with contradictory results.

We have shown that two simple special cases exist. In the first, we match both total strain and stress on the boundary between the inner elastic enclave and the surrounding continuum solution. In the second, we match only the stress. We find this can be done in Mode III.

For perfect plasticity, we take a solution in the elastic enclave of the form

$$W = \frac{K_{el}}{G}\sqrt{\frac{2r}{\pi}}\sin\frac{\theta}{2} + \frac{A}{G}r^{3/2}\sin\frac{\theta}{2} \qquad (1)$$

where the term in A is introduced to provide matching of both stress and strain on the enclave boundary. For Mode III perfect plasticity, we find that

$$K^2 \simeq \tau_o\sqrt{r_o}\,\frac{2\sqrt{2\pi}}{3}\,K_{el} \qquad (2)$$

where K is the externally measured K-field, r_o is the radius of the internal enclave, τ_o is the yield stress of the material, and K_{el} is the K for the internal elastic enclave.

When we match only the stress on the boundary of the elastic enclave, the solution is indeterminate. The reason is that everywhere inside the plastic continuum, the stress is simply constant. Hence, no stress signal is transmitted to the elastic enclave about the size of the external stress. (Since a strain signal is transmitted, one is allowed to find the solution (2). Alternatively, there is no way of defining how many dislocations have flowed through the elastic enclave, reducing its stress.

For a work-hardening plastic region, we find that the stress boundary conditions can be satisfied. Take

$$\tau = \tau_o\left(\frac{\gamma}{\gamma_o}\right)^n \qquad (3)$$

In that case, the internal and external K-fields are related by

Although this list is not exhaustive, it will illustrate the wide variety of potential applications for detection of chemical agents.

Any or all of the following requirements for detection and identification may be important depending upon the specific application anticipated:

(1) Speed of analysis

(2) Sensitivity of analysis

(3) Specificity of analysis

(4) Cost of instrumentation

(5) Size of instrumentation

(6) Opportunity for remote detection

(7) Quantitative nature of the analysis

The above diversity of applications and requirements notwithstanding, there would appear to be excellent prospects in existing technology to meet the requirements of detection and identification. When evaluating various alarm systems, it is important to link the application requirements to the technique employed. For example, the logistics disadvantage attached to operation of the M8 alarm discussed below, may not pertain to rear areas or certain non-military applications. In some situations, the wet chemical alarm may be the most practical solution to the problem of detecting or monitoring chemical agents.

plastic strain will however modify the shape of the cleavage surface, and for sufficient plastic flaw, this shape modification (blunting) will be important.

In conclusion, the solution for the stresses in the vicinity of the crack tip is not unique, and cannot be known without further knowledge of the actual dislocation motion and structure in the vicinity of the crack tip.

ACKNOWLEDGEMENT

This research was supported by the Defense Advanced Research Projects Agency of the Department of Defense under Contract MDA903-80C-0505 with The University of Michigan.

References

1. J. Weertman, Fracture Stress Obtained from the Elastic Crack Tip Enclave Model, J. Mat. Sci. In press.

2. R. Thomson, J. Mat. Sci. 13, 128(1978).

POINT MONITORING DEVICES

Sensitive and reliable point-monitoring alarms are essential against the threat of chemical attack with G and V agents because: (1) contamination at casualty levels is undetectable by the unaided human senses and (2) continuous exposure at levels $<1\mu g/m^3$ will result in casualties.

Personal Hand Held Alarm

The currently employed detector consists of chemically treated indicator paper (ABC-M8) and paper strips (M9) which may be attached to CW protective clothing. This scheme dates from WWl and so do the attendant difficulties. The paper is sensitive to nerve agents and mustard, but will also yield a positive indication with a variety of common battlefield chemicals such as certain rifle greases and organic solvents. The paper is sensitive to liquid or thickened agent upon contact, but will not detect gases and vapors.

The most promising device, which would meet the requirements for a small, low-cost, personal alarm device, is the piezoelectric detector currently under contract investigation by Prof. Guilbault at the University of New Orleans. The detection scheme consists of observing the change in frequency or phase of oscillation of a small piezoelectric element upon adsorption of a chemical agent. It is probable that a completely self-contained device based on this principal could be packaged as a wrist-watch size personal alarm. The principal of operation

DETECTION AND IDENTIFICATION OF CW AGENTS

A. H. Francis, H. Reiss,
J. L. Margrave and E. E. Hucke

INTRODUCTION

The primary objectives of the session were: (1) to assess the present status of detection and identification of chemical warfare agents and, (2) to examine the possibilities of detection and identification of chemical agents within the context of the present technology base.

Biological agents were not specifically included in the topics discussed; neither was the detection of chemical agents in water supplies considered in detail.

Specific applications which may be anticipated for modern detectors include:

(1) Mapping of contaminated terrain

(2) Monitoring decontamination operations

(3) Monitoring air filtration systems on vehicles and personnel enclosures

(4) Detection of individual contamination

(5) Detection of equipment contamination

(6) Warning of chemical attack

(7) Monitoring chemical munition manufacture, shipment, storage and demilitarization.

is the same as that of piezoelectric microbalances and thin film vacuum deposition monitors. The device would probably be used to detect gases and vapors rather than liquid or thickened agent.

The principal technical difficulty in developing the piezoelectric detector is likely to be in obtaining the necessary selectivity. It is necessary to devise some scheme by which only the agent (V,H,G) is adsorbed on the piezoelectric element. Two approaches to this problem seem plausible: (1) Devise a method of separating agents from common contaminents using semi-permeable membranes or molecular sieve material. In this regard, we note that a semi-permeable (silicon rubber) membrane has been employed successfully by Bendix/EPID to largely eliminate contaminents from the M8 product improvement device discussed below. (2) Coat the piezoelectric element with a material which will selectively chemi- or physi-sorb agents. Several possibilities exist for a coating with the desired properties. H agents are highly reactive toward a variety of materials and G agents may be effectively bound by compounds which mimic AChE. Indeed, an immobilized enzyme surface coating might be employed for G agents.

Considerable improvement in the sensitivity/specificity of piezoelectric devices might be obtained if microporous piezoelectric materials such as those developed by Prof. E. Cross, Pennsylvania State Univ., were employed in place of the conventional quartz piezoelectric element. Improved sensitivity would result from the greatly increased surface area, while the microporous structure might be utilized to provide agent selectivity.

Although this list is not exhaustive, it will illustrate the wide variety of potential applications for detection of chemical agents.

Any or all of the following requirements for detection and identification may be important depending upon the specific application anticipated:

(1) Speed of analysis

(2) Sensitivity of analysis

(3) Specificity of analysis

(4) Cost of instrumentation

(5) Size of instrumentation

(6) Opportunity for remote detection

(7) Quantitative nature of the analysis

The above diversity of applications and requirements notwithstanding, there would appear to be excellent prospects in existing technology to meet the requirements of detection and identification. When evaluating various alarm systems, it is important to link the application requirements to the technique employed. For example, the logistics disadvantage attached to operation of the M8 alarm discussed below, may not pertain to rear areas or certain non-military applications. In some situations, the wet chemical alarm may be the most practical solution to the problem of detecting or monitoring chemical agents.

Complementing the ABC-M8 paper detectors is the automatic liquid agent detector (ALAD) alarm. The detector element consists of a metal loaded polymer and the detection scheme relies upon variations in the electrical conductivity/resistivity of the polymeric material sensor when exposed to certain of the CW agents. The polymer is sensitive to a variety of G agents as well as mustard, but also is affected by common battlefield contaminents such as vehicle fuels. In this regard, then, its limitations are similar to the ABC-M8 paper. Its principal advantage lies in the semi-quantitative indication obtained instrumentally, eliminating the need for subjective evaluation of color change.

Two additional methods were discussed which might ultimately provide a small low-cost, easily portable, personal detection device. Neither technique, however, is currently under active investigation.

The first of these techniques would rely upon a characteristic feature in the IR absorption spectrum of the agent detected. In the case of G-agents, this is likely to be the P=O stretching vibration at $\sim 1000\ cm^{-1}$ or the O-P-O bend at $\sim 500\ cm^{-1}$. Miniaturization would be achieved through the use of a LED-photodiode pair with the LED tuned to the characteristic frequency. Both (HgCdTe) and (PbSnTe) would offer possibilities for constructing such an LED. It is doubtful if sufficient sensitivity could be achieved over the path length afforded by an easily portable (wearable) device in a direct absorption mode. Typically, to obtain a 1% variation in transmitted intensity using a 10 cm pathlength, a

POINT MONITORING DEVICES

Sensitive and reliable point-monitoring alarms are essential against the threat of chemical attack with G and V agents because: (1) contamination at casualty levels is undetectable by the unaided human senses and (2) continuous exposure at levels $<1\mu g/m^3$ will result in casualties.

Personal Hand Held Alarm

The currently employed detector consists of chemically treated indicator paper (ABC-M8) and paper strips (M9) which may be attached to CW protective clothing. This scheme dates from WWl and so do the attendant difficulties. The paper is sensitive to nerve agents and mustard, but will also yield a positive indication with a variety of common battlefield chemicals such as certain rifle greases and organic solvents. The paper is sensitive to liquid or thickened agent upon contact, but will not detect gases and vapors.

The most promising device, which would meet the requirements for a small, low-cost, personal alarm device, is the piezoelectric detector currently under contract investigation by Prof. Guilbault at the University of New Orleans. The detection scheme consists of observing the change in frequency or phase of oscillation of a small piezoelectric element upon adsorption of a chemical agent. It is probable that a completely self-contained device based on this principal could be packaged as a wrist-watch size personal alarm. The principal of operation

concentration of ∿300 mg/m^3 would be required. However, any of several multiple reflection techniques could be employed to improve sensitivity. For example, agent could be selectively adsorbed on the surface of an infra-red transmitting substrate to which the LED-photodiode pair are bonded. As illustrated in Fig. 1. Either the substrate or a laminated IR filter material could be used to obtain the desired bandpass characteristics. Operated in either the total or multiple internal reflectance mode, such a device should be approximately X10^4 more sensitive than direct absorption and therefore able to detect as little as ∿30 μg/m^3 vapor concentration of agent. Internal reflectance spectroscopy has, in fact, already been used extensively for the spectroscopic investigation of gases and vapors. It is employed in a variety of dew-point meters and, tuned to the OH stretching frequency, IRS has been used to monitor the presence of water in ultrapure gases. IRS has also been employed in air polution studies and for detection of microgram quantities of phosphorus pesticides similar in chemical composition to G-agents.

The device would be operated in a sampling mode to avoid excessive battery drain by the LED. We note that both LED/Photodiode and piezoelectric detectors could be combined easily with microprocessor technology to improve both sensitivity and selectivity. For example, spectroscopic information (vibrational frequencies or vibrational envelope characteristics) contained in a ROM could be used to accurately "fingerprint" a variety of chemical agents. A typical silicon multireflection element is shown in Fig. 2.

is the same as that of piezoelectric microbalances and thin film vacuum deposition monitors. The device would probably be used to detect gases and vapors rather than liquid or thickened agent.

The principal technical difficulty in developing the piezoelectric detector is likely to be in obtaining the necessary selectivity. It is necessary to devise some scheme by which only the agent (V,H,G) is adsorbed on the piezoelectric element. Two approaches to this problem seem plausible: (1) Devise a method of separating agents from common contaminents using semi-permeable membranes or molecular sieve material. In this regard, we note that a semi-permeable (silicon rubber) membrane has been employed successfully by Bendix/EPID to largely eliminate contaminents from the M8 product improvement device discussed below. (2) Coat the piezoelectric element with a material which will selectively chemi- or physi-sorb agents. Several possibilities exist for a coating with the desired properties. H agents are highly reactive toward a variety of materials and G agents may be effectively bound by compounds which mimic AChE. Indeed, an immobilized enzyme surface coating might be employed for G agents.

Considerable improvement in the sensitivity/specificity of piezoelectric devices might be obtained if microporous piezoelectric materials such as those developed by Prof. E. Cross, Pennsylvania State Univ., were employed in place of the conventional quartz piezoelectric element. Improved sensitivity would result from the greatly increased surface area, while the microporous structure might be utilized to provide agent selectivity.

Complementing the ABC-M8 paper detectors is the automatic liquid agent detector (ALAD) alarm. The detector element consists of a metal loaded polymer and the detection scheme relies upon variations in the electrical conductivity/resistivity of the polymeric material sensor when exposed to certain of the CW agents. The polymer is sensitive to a variety of G agents as well as mustard, but also is affected by common battlefield contaminents such as vehicle fuels. In this regard, then, its limitations are similar to the ABC-M8 paper. Its principal advantage lies in the semi-quantitative indication obtained instrumentally, eliminating the need for subjective evaluation of color change.

Two additional methods were discussed which might ultimately provide a small low-cost, easily portable, personal detection device. Neither technique, however, is currently under active investigation.

The first of these techniques would rely upon a characteristic feature in the IR absorption spectrum of the agent detected. In the case of G-agents, this is likely to be the P=O stretching vibration at $\sim 1000\ cm^{-1}$ or the O-P-O bend at $\sim 500\ cm^{-1}$. Miniaturization would be achieved through the use of a LED-photodiode pair with the LED tuned to the characteristic frequency. Both (HgCdTe) and (PbSnTe) would offer possibilities for constructing such an LED. It is doubtful if sufficient sensitivity could be achieved over the path length afforded by an easily portable (wearable) device in a direct absorption mode. Typically, to obtain a 1% variation in transmitted intensity using a 10 cm pathlength, a

concentration of ∿300 mg/m^3 would be required. However, any of several multiple reflection techniques could be employed to improve sensitivity. For example, agent could be selectively adsorbed on the surface of an infra-red transmitting substrate to which the LED-photodiode pair are bonded. As illustrated in Fig. 1. Either the substrate or a laminated IR filter material could be used to obtain the desired bandpass characteristics. Operated in either the total or multiple internal reflectance mode, such a device should be approximately X10^4 more sensitive than direct absorption and therefore able to detect as little as ∿30 μg/m^3 vapor concentration of agent. Internal reflectance spectroscopy has, in fact, already been used extensively for the spectroscopic investigation of gases and vapors. It is employed in a variety of dew-point meters and, tuned to the OH stretching frequency, IRS has been used to monitor the presence of water in ultrapure gases. IRS has also been employed in air polution studies and for detection of microgram quantities of phosphorus pesticides similar in chemical composition to G-agents.

The device would be operated in a sampling mode to avoid excessive battery drain by the LED. We note that both LED/Photodiode and piezoelectric detectors could be combined easily with microprocessor technology to improve both sensitivity and selectivity. For example, spectroscopic information (vibrational frequencies or vibrational envelope characteristics) contained in a ROM could be used to accurately "fingerprint" a variety of chemical agents. A typical silicon multireflection element is shown in Fig. 2.

respond to high concentrations of rocket propellant, signaling or screening smoke, and engine exhaust. The principal disadvantage associated with operation of the M8 alarm is the need for replacement of reagent solutions every 12 hours in continuous use and the

While the initial development costs for such a device are likely to be great, when produced in quantity, such devices should compete in cost/unit with detector paper.

The principal technical difficulty in developing a device based on these techniques is again likely to be attaining selective surface absorption of the CW agents in the presence of other chemical interferences.

Differential detection techniques may be employed to advantage in all of the above devices. Thus, the relative phase angle or the beat frequency between two piezoelectric elements with different absorptive coatings or masked with different semi-permeable filters, could be used to increase both sensitivity and/or selectivity. In a similar fashion the differential signal developed between two ATR substrates, one of which is exposed only to vapors, could distinguish gel and liquid contamination from a vapor threat.

A technique which is intrinsically both highly sensitive and specific might be designed about a chemi- or bio-luminescence process. Certain bioluminescent or chemi-luminescent reactions, either inhibited by or involving the G-agents, might serve as ultra-sensitive indicators.

Portable Point Monitoring Systems

The current M8 "wet" chemical point monitoring alarm with 6 hour battery weighs approximately 14 lbs. and utilizes a CN^-, ion-specific, electrochemical reaction to detect G, C and V agents in concentrations of 1 bm/m^3 or less. The M8 system will also

The technique of ion mobility mass spectrometry, developed by Professor Francis W. Karesek at the University of Waterloo, offers the possibility of improved selectivity with only a moderate increase in instrumental complexity. The technique is currently under active development at Bendix/EPID. Either negative or positive ions, produced by a small radioactive source (Americium 95), are electrostatically gated into a drift chamber maintained at 1 atmosphere pressure and are ultimately distinguished by their different drift velocities. Selective chemical ionization processes may be used to provide additional selectivity. A counterflow of helium gas in the drift chamber has also improved device performance. Proton transfer has been shown to be the principal mechanism of positive ion formation in the ion mobility spectrometer, and most current research utilizes the positive ion current. However, chemical interferences seem to be substantially lower in the negative ion mode. Ammonia is a significant cause of chemical interference, but may be excluded by use of a silicon rubber semi-permeable membrane which also serves to remove particulates.

The variety of potential chemical interferences is the principal technical difficulty in developing point monitoring alarms based on ion mobility spectrometry. One technique under consideration involves chemical alteration of the agent prior to analysis. For example, oxidation of mustard to the sulfoxide by premixing with electronically generated ozone, produces a more easily distinguished species.

respond to high concentrations of rocket propellant, signaling or screening smoke, and engine exhaust. The principal disadvantage associated with operation of the M8 alarm is the need for replacement of reagent solutions every 12 hours in continuous use and the attendant logistics problem. A similar "wet" chemical system introduced by the British employs the electrochemical half-potential of a covalently immobilized cholinesterase electrode. The device also requires periodic replenishment of a (thiocholine) reagent.

The logistics problems associated with "wet" chemical alarms have provided the impetus for development of "dry" point monitoring systems. Although many opportunities exist for sensitive and agent specific "dry" devices, current research seems tightly focussed upon mass spectrometry. In particular, alarms utilizing ion "chromatrography" or ion-mobility mass spectrometry, appear to offer considerable promise of providing sufficient sensitivity and selectivity.

The Honeywell ionization detector is a small device containing a radioactive ionization source. Sampled gas is partially ionized by the radioactive element and then passed through a highly convoluted pathway between two electrodes with a potential difference of approximately 100 VDC. The current through, or the voltage drop across, the cell is strongly dependent upon the composition of the sampled gases. The device suffers from lack of specificity toward chemical agents.

Several additional possibilities exist for development of sensitive point monitoring alarms, however, none appear to be under investigation currently. Flame photometry has been demonstrated to be a technique of extraordinary sensitivity for the detection of phosphorus and sulfur compounds and therefore could provide the basis for a point monitoring system sensitive to <1 ppb of G and H agents.

The principal upon which the detector is based is the photometric detection of flame emission from phosphorus emission at 5260 Å and sulfur emission at 3940 Å. The detector is sensitive to 0.25 nanograms of phosphorus compound and the response is linear over two orders of magnitude. The selectivity is such that 250 ppb triethylphosphate is easily detectable at a 250 ppm mixture of organic compounds containing oxygen, nitrogen and halogens. A typical design of a flame photometric detector is shown in Fig. 3.

Vapor phase chemi-luminescence has provided the most sensitive method of air contaminent analysis devised to date. Commercially available systems will produce rapid (1 second), selective, quantitative analyses for oxides of sulfur and nitrogen in the ppb concentration range. Most chemi-luminescence detectors utilize a vapor phase reaction between electronically generated ozone and the air contaminent in a continuous flow system. It is likely that a chemi-luminescense reaction involving organophosphorus compounds and O_3 could be devised. We note that several of the oxy-anions of phosphorous are isoelectronic with

The technique of ion mobility mass spectrometry, developed by Professor Francis W. Karesek at the University of Waterloo, offers the possibility of improved selectivity with only a moderate increase in instrumental complexity. The technique is currently under active development at Bendix/EPID. Either negative or positive ions, produced by a small radioactive source (Americium 95), are electrostatically gated into a drift chamber maintained at 1 atmosphere pressure and are ultimately distinguished by their different drift velocities. Selective chemical ionization processes may be used to provide additional selectivity. A counterflow of helium gas in the drift chamber has also improved device performance. Proton transfer has been shown to be the principal mechanism of positive ion formation in the ion mobility spectrometer, and most current research utilizes the positive ion current. However, chemical interferences seem to be substantially lower in the negative ion mode. Ammonia is a significant cause of chemical interference, but may be excluded by use of a silicon rubber semi-permeable membrane which also serves to remove particulates.

The variety of potential chemical interferences is the principal technical difficulty in developing point monitoring alarms based on ion mobility spectrometry. One technique under consideration involves chemical alteration of the agent prior to analysis. For example, oxidation of mustard to the sulfoxide by premixing with electronically generated ozone, produces a more easily distinguished species.

Several additional possibilities exist for development of sensitive point monitoring alarms, however, none appear to be under investigation currently. Flame photometry has been demonstrated to be a technique of extraordinary sensitivity for the detection of phosphorus and sulfur compounds and therefore could provide the basis for a point monitoring system sensitive to <1 ppb of G and H agents.

The principal upon which the detector is based is the photometric detection of flame emission from phosphorus emission at 5260 Å and sulfur emission at 3940 Å. The detector is sensitive to 0.25 nanograms of phosphorus compound and the response is linear over two orders of magnitude. The selectivity is such that 250 ppb triethylphosphate is easily detectable at a 250 ppm mixture of organic compounds containing oxygen, nitrogen and halogens. A typical design of a flame photometric detector is shown in Fig. 3.

Vapor phase chemi-luminescence has provided the most sensitive method of air contaminent analysis devised to date. Commercially available systems will produce rapid (1 second), selective, quantitative analyses for oxides of sulfur and nitrogen in the ppb concentration range. Most chemi-luminescence detectors utilize a vapor phase reaction between electronically generated ozone and the air contaminent in a continuous flow system. It is likely that a chemi-luminescense reaction involving organophosphorus compounds and O_3 could be devised. We note that several of the oxy-anions of phosphorous are isoelectronic with

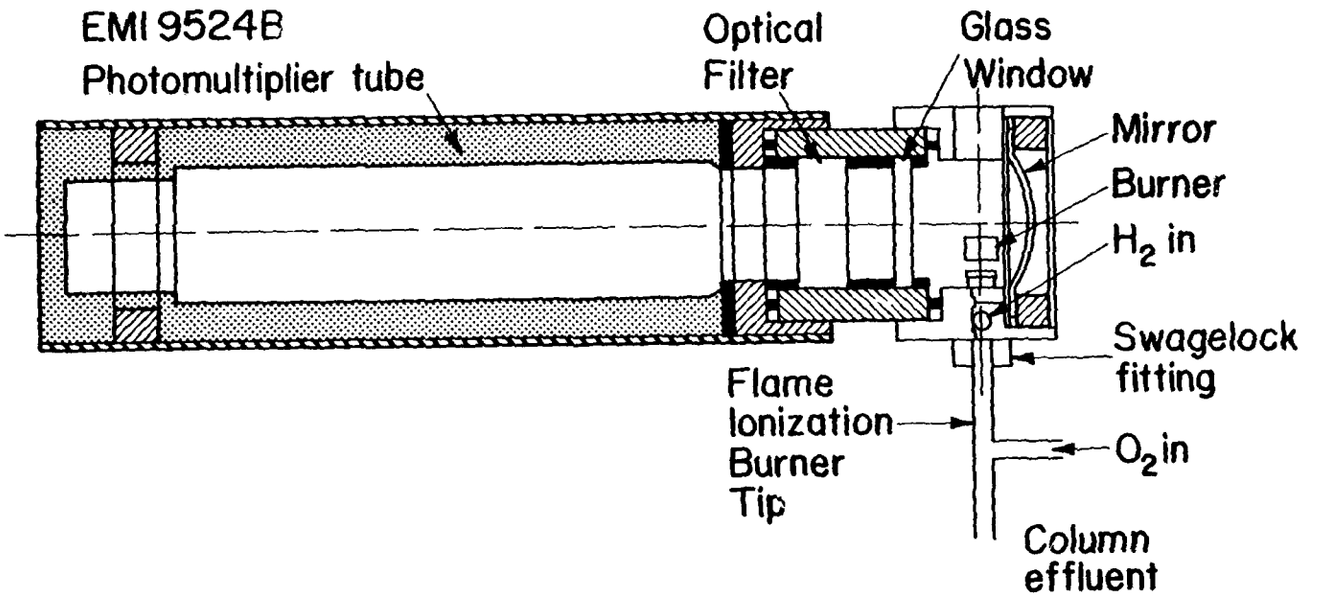

FIG. 3. FLAME PHOTOMETRIC DETECTOR

highly luminescent oxides or oxy-anions of nitrogen and sulfur (i.e., NO_2^-, SO_2, O_3, PO_2^-).

Nucleation represents a sensitive means of detection, and this has been known for a long time. Single ions can be detected through drop nucleation in polar supersaturated vapors. To date, however, there is no evidence that single neutral molecules can be detected, although this is not out of the realm of things possible. Since single ions can be detected by other means (e.g., ionization guages) nucleation would not necessarily represent an advantageous technique where ions are concerned. It is definitely an advantageous technique where neutrals are concerned - although even here laser-induced fluorescense exhibits the capability of single molecule detection.

In order to introduce selectivity into the nucleation method it must be combined with spectroscopy and photochemistry, in such a way that excitation in a given wavelength region produces a photochemical product which nucleates drops in a supersaturated vapor. The photochemical product may exercise its effect in either of several ways. For example, (1) it may simply be involatile, (2) it may possess a large dipole moment and form clusters in a polar supersaturated vapor, or (3) it may be a free radical and induce polymerization which may lead to very involatile products.

In a certain sense, all three porcesses have been observed. An example of (1) is the photochemical production of involatile sulfur in supersaturated alcohol, beginning with a photolyzable

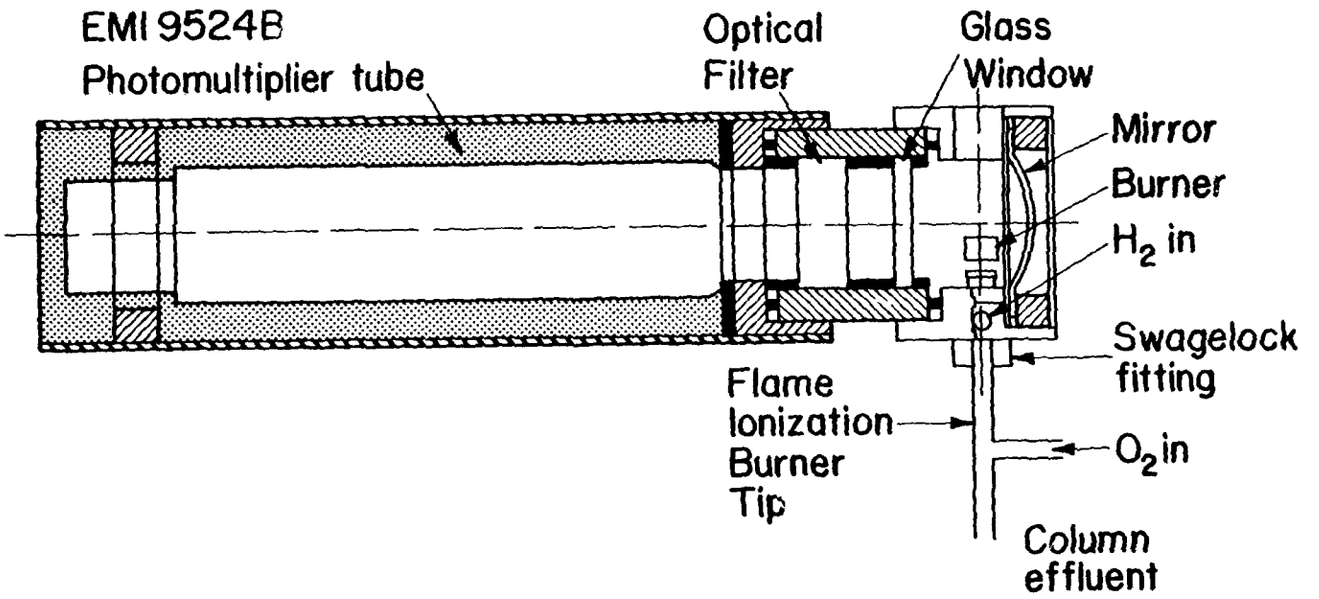

FIG. 3. FLAME PHOTOMETRIC DETECTOR

sulfur bearing compound such as diethyl sulfine. An example of (2) is the photochemical production of H_2SO_4 from SO_2 in supersaturated water vapor. An example of (3) is the formation of long chain paraffins in supersaturated nonane, through the photochemical production of free radicals from NO_2 or alkyl iodides.

So far the record for detection of neutrals seems to be 10^7 molecules per cm^3. This occurred for H_2SO_4 in water vapor at relative humidities of about 280% at 25°C. 10^7 molecules per cm^3 represents about <u>one part in 10^{12}</u> at atmospheric pressure. Undoubtedly research in other systems (or even in the same system) could substantially improve this detection capability.

For example, it might be possible to choose as a supersaturated vapor a vinyl monomer. Free radicals produce additional polymerization in vinylmonomers in such a manner that a <u>single</u> free radical could produce a polymer molecule which could in turn act as a center for the condensation of the supersaturated monomer. However, this experiment is frought with difficulties (not all insurmountable) such as the polymerization of monomer in the absence of radiation, the formation of gunks, and the effects of chain transfer in shortening polymer length.

Photoinduced nucleation experiments are generally carried out in diffusion cloud chamber, a device for maintaining a steady state of supersaturation in a vapor. Light of specified wavelength illuminates the vapor and a trace impurity may be photolyzed to produce a nucleating product. The nucleated drops fall through a laser beam (He-Ne) and are counted electronically. The rate

highly luminescent oxides or oxy-anions of nitrogen and sulfur (i.e., NO_2^-, SO_2, O_3, PO_2^-).

Nucleation represents a sensitive means of detection, and this has been known for a long time. Single ions can be detected through drop nucleation in polar supersaturated vapors. To date, however, there is no evidence that single neutral molecules can be detected, although this is not out of the realm of things possible. Since single ions can be detected by other means (e.g., ionization guages) nucleation would not necessarily represent an advantageous technique where ions are concerned. It is definitely an advantageous technique where neutrals are concerned - although even here laser-induced fluorescense exhibits the capability of single molecule detection.

In order to introduce selectivity into the nucleation method it must be combined with spectroscopy and photochemistry, in such a way that excitation in a given wavelength region produces a photochemical product which nucleates drops in a supersaturated vapor. The photochemical product may exercise its effect in either of several ways. For example, (1) it may simply be involatile, (2) it may possess a large dipole moment and form clusters in a polar supersaturated vapor, or (3) it may be a free radical and induce polymerization which may lead to very involatile products.

In a certain sense, all three porcesses have been observed. An example of (1) is the photochemical production of involatile sulfur in supersaturated alcohol, beginning with a photolyzable

of nucleation is thus studied as a function of wavelength. Each impurity has its own action spectrum which in many cases has been shown to be the product of its extinction coefficient and the quantum yield for its photolysis.

The response time will usually be of the order of seconds when the concentration of the impurity is as low as one part in 10^{12}. It can be shorter at higher concentrations.

The main drawback to general analysis, however, remains the fact that past experiments have been conducted only in closed chambers. It is, in principle, possible to develop a flow diffusion chamber with appropriate filters but very little research has been completed in this respect. In fact there are only a handful of people throughout the world working in the field of photo-induced nucleation. This suggests that even a small increment of research in the field could lead to appreciable relative advances. Such research might be both cost and strategy effective.

The apparatus involved is inexpensive and could be made light weight and compact. However, the diffusion cloud chamber is a device which supports a non-uniform medium and, for stability, does require careful procedures. If one is only interested in qualitative effects it might be possible to use a reciprocating expansion cloud chamber, but this is uncertain.

Nucleation will probably find to use in remote detection - unless a few molecules of the contaminant diffuse to where measurements are being conducted.

sulfur bearing compound such as diethyl sulfine. An example of (2) is the photochemical production of H_2SO_4 from SO_2 in supersaturated water vapor. An example of (3) is the formation of long chain paraffins in supersaturated nonane, through the photochemical production of free radicals from NO_2 or alkyl iodides.

So far the record for detection of neutrals seems to be 10^7 molecules per cm^3. This occurred for H_2SO_4 in water vapor at relative humidities of about 280% at 25°C. 10^7 molecules per cm^3 represents about <u>one part in 10^{12}</u> at atmospheric pressure. Undoubtedly research in other systems (or even in the same system) could substantially improve this detection capability.

For example, it might be possible to choose as a supersaturated vapor a vinyl monomer. Free radicals produce additional polymerization in vinylmonomers in such a manner that a <u>single</u> free radical could produce a polymer molecule which could in turn act as a center for the condensation of the supersaturated monomer. However, this experiment is frought with difficulties (not all insurmountable) such as the polymerization of monomer in the absence of radiation, the formation of gunks, and the effects of chain transfer in shortening polymer length.

Photoinduced nucleation experiments are generally carried out in diffusion cloud chamber, a device for maintaining a steady state of supersaturation in a vapor. Light of specified wavelength illuminates the vapor and a trace impurity may be photolyzed to produce a nucleating product. The nucleated drops fall through a laser beam (He-Ne) and are counted electronically. The rate

Finally, the thermionic emission detector is both sensitive and specific to halogens and phosphorus. Small, easily portable and currently commercially available, this device may serve well as the detector element in a point monitor alarm for G and H agents.

AREA MONITORING SYSTEMS

The principle use of area monitoring systems is to provide advance warning of chemical attack and to identify the nature of the chemical threat. To some degree, deficiencies in protective apparatus and decontamination capability can be offset by advanced warning alarms.

The E49 long path infrared (LOPAIR) alarm is a device utilizing an electro-optical IR transceiver and retro-reflector which may be located up to 365 meters apart. The alarm can detect as little as 0.1 mg/cm^3 of G agent as well as mustard, with reduced sensitivity. The E49 alarm has been used chiefly to monitor stockpiles of CW agent and is not currently in production. The alarm sensitivity is severely affected by rain and smoke or other gases and vapors which absorb or scatter 10μ radiation.

An area monitoring system currently under development by Sylvania/GTE, Electro-Optics Division, is designed to detect 100 mg/m^3 concentrations at shorter range. The system is designed about a CO_2 laser with an output power of approximately 750 mJ per pulse in the 10μ spectral region. The pulse repetition rate is 110 Hz and the output beam is scanned in direction and azemuth

of nucleation is thus studied as a function of wavelength. Each impurity has its own action spectrum which in many cases has been shown to be the product of its extinction coefficient and the quantum yield for its photolysis.

The response time will usually be of the order of seconds when the concentration of the impurity is as low as one part in 10^{12}. It can be shorter at higher concentrations.

The main drawback to general analysis, however, remains the fact that past experiments have been conducted only in closed chambers. It is, in principle, possible to develop a flow diffusion chamber with appropriate filters but very little research has been completed in this respect. In fact there are only a handful of people throughout the world working in the field of photo-induced nucleation. This suggests that even a small increment of research in the field could lead to appreciable relative advances. Such research might be both cost and strategy effective.

The apparatus involved is inexpensive and could be made light weight and compact. However, the diffusion cloud chamber is a device which supports a non-uniform medium and, for stability, does require careful procedures. If one is only interested in qualitative effects it might be possible to use a reciprocating expansion cloud chamber, but this is uncertain.

Nucleation will probably find to use in remote detection - unless a few molecules of the contaminant diffuse to where measurements are being conducted.

by a servo-controlled reflector. Detection and identification and the range of an airborne CW agent is achieved using differential absorption of the laser backscatter (LIDAR). In this mode of operation the time decay of backscattered IR radiation is monitored by a cooled HgCdTe photodevice which is gated on after the laser burst. The decay is exponential in time (distance) with singularities due to reflection or absorption by liquid agent droplets in the laser path. Both the absorptive and reflective component of the backscatter singularity are wavelength dependent.

Research by Sylvania/GTE has indicated that by appropriate choice of four CO_2 laser frequencies a sufficiently characteristic "signature" of the absorbing droplets can be obtained to distinguish the various chemical agents from one another and from possible interferences, such as water droplets. The LIDAR signature is unaffected by droplet size (aerosol, vapor, droplets). Several additional techniques are employed in the Sylvania/GTE design to considerably improve the agent "signature". Laser heterodyning could substantially improve the sensitivity of a LIDAR system, however, this would require the availability of several laser frequencies simultaneously. The proposed system would include a computer and software package. Although laboratory tests of the DIAL system have not yet been conducted, there is reason to anticipate considerable success from this approach to an area monitoring alarm. Previous area defense alarms have employed infrared radiometers which measured total spectral irradiance.

Finally, the thermionic emission detector is both sensitive and specific to halogens and phosphorus. Small, easily portable and currently commercially available, this device may serve well as the detector element in a point monitor alarm for G and H agents.

AREA MONITORING SYSTEMS

The principle use of area monitoring systems is to provide advance warning of chemical attack and to identify the nature of the chemical threat. To some degree, deficiencies in protective apparatus and decontamination capability can be offset by advanced warning alarms.

The E49 long path infrared (LOPAIR) alarm is a device utilizing an electro-optical IR transceiver and retro-reflector which may be located up to 365 meters apart. The alarm can detect as little as 0.1 mg/cm^3 of G agent as well as mustard, with reduced sensitivity. The E49 alarm has been used chiefly to monitor stockpiles of CW agent and is not currently in production. The alarm sensitivity is severely affected by rain and smoke or other gases and vapors which absorb or scatter 10μ radiation.

An area monitoring system currently under development by Sylvania/GTE, Electro-Optics Division, is designed to detect 100 mg/m^3 concentrations at shorter range. The system is designed about a CO_2 laser with an output power of approximately 750 mJ per pulse in the 10μ spectral region. The pulse repetition rate is 110 Hz and the output beam is scanned in direction and azemuth

ACKNOWLEDGEMENT

This research was supported by the Defense Advanced Research Projects Agency of the Department of Defense under Contract No. MDA903-80C-0505 with The University of Michigan.

by a servo-controlled reflector. Detection and identification and the range of an airborne CW agent is achieved using differential absorption of the laser backscatter (LIDAR). In this mode of operation the time decay of backscattered IR radiation is monitored by a cooled HgCdTe photodevice which is gated on after the laser burst. The decay is exponential in time (distance) with singularities due to reflection or absorption by liquid agent droplets in the laser path. Both the absorptive and reflective component of the backscatter singularity are wavelength dependent.

Research by Sylvania/GTE has indicated that by appropriate choice of four CO_2 laser frequencies a sufficiently characteristic "signature" of the absorbing droplets can be obtained to distinguish the various chemical agents from one another and from possible interferences, such as water droplets. The LIDAR signature is unaffected by droplet size (aerosol, vapor, droplets). Several additional techniques are employed in the Sylvania/GTE design to considerably improve the agent "signature". Laser heterodyning could substantially improve the sensitivity of a LIDAR system, however, this would require the availability of several laser frequencies simultaneously. The proposed system would include a computer and software package. Although laboratory tests of the DIAL system have not yet been conducted, there is reason to anticipate considerable success from this approach to an area monitoring alarm. Previous area defense alarms have employed infrared radiometers which measured total spectral irradiance.

ADDENDUM:

Some applications for detectors present a special problem due to the possibility of entrapment of CW agents. The decontamination of equipment will present situations in which agent may remain undetectable due to absorption by porous surfaces, cracks, crevases, etc., and present a future or long term exposure hazard to users of the equipment. There would currently seem to be no satisfactory method for detection with certainty of trapped agent and prudent equipment design to avoid this situation is advisable. A detector for trapped agent would require the highest level of both sensitivity and selectivity. Selectivity would be required in order to avoid false signals due to interference from the large number of chemicals likely to be present in the areas where agent is entrapped (e.g., volatile components of plastics, greases, oils).

The possibility that a hand held probe similar to laser and plasma spark microprobes currently employed in industry may provide sufficient sensitivity and selectivity to detect absorbed agent in certain porous materials.

There is little possibility of detecting agent trapped in bearing races, gasket retainers, etc., where it represents a long term exposure hazard, and proper design to avoid this eventuality is therefore imperative; physical decontamination of such structures requiring a prohibitively large expendature of labor.

ACKNOWLEDGEMENT

This research was supported by the Defense Advanced Research Projects Agency of the Department of Defense under Contract No. MDA903-80C-0505 with The University of Michigan.

REFERENCES

Flame Photometric Detector, S. S. Brody, J. E. Chaney, J. Gas Chromatography 4, 42(1966).

Nucleation and the Detection and Amplification of Chemical Physical Phenomena, Howard Reiss. To be published: Adv. in Appl. Phys.

Cloud Chamber Study of the Gas Phase Photo-oxidation of Sulfur Dioxide, Dean C. Marvin, Howard Reiss, J. Chem. Phys. 59, 1897 (1978)

The Ultraviolet Absorption Spectra of Prylphosphonic and Diarylphosphonic Acids, H. H. Jaffé, L. D. Freedman, J. Am. Chem. Soc. 48, 1069(1952).

Measurements of H_2O_2 and HNO_3 in Rural Air, Thomas J. Kelly, Donald H. Stedman, G. L. Koe, Annal. Chem. 6, 375(1979)

Internal Reflection Spectroscopy, N. J. Harrick, Interscience, New York, 1967.

Identification of Trace Amounts of Organophosphorus Pesticides by Frustrated Multiple Internal Reflectance Spectroscopy, Appl. Spectry. 19, 10(1965).

ADDENDUM:

Some applications for detectors present a special problem due to the possibility of entrapment of CW agents. The decontamination of equipment will present situations in which agent may remain undetectable due to absorption by porous surfaces, cracks, crevases, etc., and present a future or long term exposure hazard to users of the equipment. There would currently seem to be no satisfactory method for detection with certainty of trapped agent and prudent equipment design to avoid this situation is advisable. A detector for trapped agent would require the highest level of both sensitivity and selectivity. Selectivity would be required in order to avoid false signals due to interference from the large number of chemicals likely to be present in the areas where agent is entrapped (e.g., volatile components of plastics, greases, oils).

The possibility that a hand held probe similar to laser and plasma spark microprobes currently employed in industry may provide sufficient sensitivity and selectivity to detect absorbed agent in certain porous materials.

There is little possibility of detecting agent trapped in bearing races, gasket retainers, etc., where it represents a long term exposure hazard, and proper design to avoid this eventuality is therefore imperative; physical decontamination of such structures requiring a prohibitively large expendature of labor.

TABLE I: References

1. See discussion under Portable Point Monitoring Alarms.
2. Column retention time a possible technical problem. Superior sensitivity and selectivity possible through use of etched miniature columns and thermionic detectors.
3. Remote detection possible in the backscatter mode. Lowered sensitivity relative to point sampling techniques. See discussion.
4. Unlikely to achieve sufficient sensitivity due to nature of physical process.
5. Coherent Anti-Stokes Raman Scattering. Unlikely to prove sufficiently sensitive due to high-order nature of process. Offers possibility of remote detection.
6. Inelastic Electron Tunnelling Spectroscopy. Offers the possibility of obtaining vibrational spectra without recourse to radiation sources or detectors. Active element consists of a tunnel diode with semi-permeable electrode. Considerable development required.
7. Some work currently in progress. May provide remote sensing.
8. Technique would employ two lasers; one to heat contaminated surface, the second to sense the local heating by changes in reflection from the surface.
9. Unlikely to be sufficiently sensitive due to absence of strongly allowed electronic transitions in visible or near UV.
10. See discussion under chemi-luminescence.

REFERENCES

Flame Photometric Detector, S. S. Brody, J. E. Chaney, J. Gas Chromatography 4, 42(1966).

Nucleation and the Detection and Amplification of Chemical Physical Phenomena, Howard Reiss. To be published: Adv. in Appl. Phys.

Cloud Chamber Study of the Gas Phase Photo-oxidation of Sulfur Dioxide, Dean C. Marvin, Howard Reiss, J. Chem. Phys. 59, 1897 (1978)

The Ultraviolet Absorption Spectra of Prylphosphonic and Diarylphosphonic Acids, H. H. Jaffé, L. D. Freedman, J. Am. Chem. Soc. 48, 1069(1952).

Measurements of H_2O_2 and HNO_3 in Rural Air, Thomas J. Kelly, Donald H. Stedman, G. L. Koe, Annal. Chem. 6, 375(1979)

Internal Reflection Spectroscopy, N. J. Harrick, Interscience, New York, 1967.

Identification of Trace Amounts of Organophosphorus Pesticides by Frustrated Multiple Internal Reflectance Spectroscopy, Appl. Spectry. 19, 10(1965).

11. Work currently in progress.

12. See discussion under nucleation.

13. See discussion under ion mobility mass spectrometry.

14. See discussion under piezoelectric detector.

TABLE I: References

1. See discussion under Portable Point Monitoring Alarms.
2. Column retention time a possible technical problem. Superior sensitivity and selectivity possible through use of etched miniature columns and thermionic detectors.
3. Remote detection possible in the backscatter mode. Lowered sensitivity relative to point sampling techniques. See discussion.
4. Unlikely to achieve sufficient sensitivity due to nature of physical process.
5. Coherent Anti-Stokes Raman Scattering. Unlikely to prove sufficiently sensitive due to high-order nature of process. Offers possibility of remote detection.
6. Inelastic Electron Tunnelling Spectroscopy. Offers the possibility of obtaining vibrational spectra without recourse to radiation sources or detectors. Active element consists of a tunnel diode with semi-permeable electrode. Considerable development required.
7. Some work currently in progress. May provide remote sensing.
8. Technique would employ two lasers; one to heat contaminated surface, the second to sense the local heating by changes in reflection from the surface.
9. Unlikely to be sufficiently sensitive due to absence of strongly allowed electronic transitions in visible or near UV.
10. See discussion under chemi-luminescence.

TABLE 1 presents a summary of the techniques considered for the detection and identification of Chemical Warfare agents. The notation uses X to indicate probable advantage and (X) to indicate possible advantage.

DETECTION METHOD	SPEED	SPECIFICITY	SENSITIVITY	QUANTITATIVE	COST/COMPLEX	REMOTE	NOTES
WET CHEMICAL	(X)	(X)	(X)		(X)		
DRY CHEMICAL	(X)	(X)	(X)		X		
FLAME IONIZATION	X	(X)	X	(X)	X		1
VPC	(X)	X	X	X			2
VIBRATIONAL SPECTROSCOPIES:							
IR	X	X	(X)	X	(X)	X	3
Raman	X	X	(X)				4
CARS	X	X				X	5
IETS	(X)	X					6
Opto-Acoustic	X	X	X	X		X	7
Thermal Lense	X	X				X	8
ELECTRONIC SPECTROSCOPIES:							
Absorption	X	X	(X)	X		X	9
Fluorescence	X	X	X	X			9
Luminescence	X	X	X	X			9
Chemical-Luminescence	X	(X)	X	X	(X)		10
Multi-Photo Ionization	X	X	X	X			11
Opto-Acoustic	X	X		X			
LIGHT SCATTERING:							
Nucleation	(X)	(X)	X				12
Refraction/Reflection	X					X	8
MASS SPECTROMETRIC	X	X	X	X			
ELECTROCHEMICAL	(X)	(X)	(X)	(X)	(X)		
DIELECTRIC RELAXATION	X	(X)	(X)		(X)		14

11. Work currently in progress.

12. See discussion under nucleation.

13. See discussion under ion mobility mass spectrometry.

14. See discussion under piezoelectric detector.

DETECTION AND IDENTIFICATION OF CW AGENTS

July 21, 1980

AGENDA

Morning Session: Review and Background Material

Overview of CW programs with emphasis on problems related to detection and identification of CW agents. Discussion of tactical situations and adversary capabilities as related to identification and detection of specific chemical and biological agents.

Thomas Dashiell, Office of the Under Secretary of Defense for Research and Engineering

Review of problems in physical protection and decontamination related to the identification and detection of chemical agents.

William McGee, Chief, Technical Group, Physical Protection Division, Chemical Systems Laboratory

Review of problems in life sciences related to the need for rapid identification and detection.

Ted Prociv, Projects Manager, Hazardous Materials Program Office, Battelle Columbus Laboratories

Review of current methods for detection and identification of CW agents. Evaluation of effectiveness of methods. Discussion of current problems in future requirements for detection and identification.

Steve Harden, Chief, Applied Chemistry Section, Chemical Branch Research Division, Chemical Systems Laboratory

Afternoon Session: Defense Industry Programs and Summary

Sylvania/GTE Area Defense System Presentation. Discussion and evaluation.

Ted Prociv
Doug Woodman, Senior Scientist, Electro-Optics Division Sylvania/GTE

Bendix Point Sampling Dry Systems. Discussion and evaluation.

Dr. Glen Spangler, Sr. Staff Scientist, Bendix Environmental and Process Inst. Div.

Summary by Participants.

TABLE 1 presents a summary of the techniques considered for the detection and identification of Chemical Warfare agents. The notation uses X to indicate probable advantage and (X) to indicate possible advantage.

DETECTION METHOD	SPEED	SPECIFICITY	SENSITIVITY	QUANTITATIVE	COST/COMPLEX	REMOTE	NOTES
WET CHEMICAL	(X)	(X)	(X)		(X)		
DRY CHEMICAL	(X)	(X)	(X)		X		
FLAME IONIZATION	X	(X)	X	(X)	X		1
VPC	(X)	X	X	X			2
VIBRATIONAL SPECTROSCOPIES:							
IR	X	X	(X)	X	(X)	X	3
Raman	X	X	(X)				4
CARS	X	X				X	5
IETS	(X)	X					6
Opto-Acoustic	X	X	X	X		X	7
Thermal Lense	X	X				X	8
ELECTRONIC SPECTROSCOPIES:							
Absorption	X	X	(X)	X		X	9
Fluorescence	X	X	X	X			9
Luminescence	X	X	X	X			9
Chemical-Luminescence	X	(X)	X	X	(X)		10
Multi-Photo Ionization	X	X	X	X			11
Opto-Acoustic	X	X		X			
LIGHT SCATTERING:							
Nucleation	(X)	(X)	X				12
Refraction/Reflection	X					X	8
MASS SPECTROMETRIC	X	X	X	X			
ELECTROCHEMICAL	(X)	(X)	(X)	(X)	(X)		
DIELECTRIC RELAXATION	X	(X)	(X)		(X)		14

CW Agents

Guest Participants

Thomas R. Dashiell
Dept. of Defense
The Pentagon, Room JD129
Washington, D.C. 20301
(202) 697-8714

C. S. Harden
Chem. Systems Lab.
Aberdeen Proving Ground
MD 21010
(301) 671-3614

Dr. William S. Magee, Jr.
Chemical Systems Laboratory
Aberdeen Proving Ground
MD 21010
(301) 671-3234

T. M. Prociv
Battelle Memorial Institute
Columbus, OH 43201
(614) 424-4248

Dr. Glenn Spangler
Bendix EPID
Baltimore, Maryland 21204
(301) 321-5261

Douglas Woodman
GTE Syvania
Mt. View, CA
(415) 966-3207

DETECTION AND IDENTIFICATION OF CW AGENTS

July 21, 1980

AGENDA

Morning Session: Review and Background Material

Overview of CW programs with emphasis on problems related to detection and identification of CW agents. Discussion of tactical situations and adversary capabilities as related to identification and detection of specific chemical and biological agents.

Thomas Dashiell, Office of the Under Secretary of Defense for Research and Engineering

Review of problems in physical protection and decontamination related to the identification and detection of chemical agents.

William McGee, Chief, Technical Group, Physical Protection Division, Chemical Systems Laboratory

Review of problems in life sciences related to the need for rapid identification and detection.

Ted Prociv, Projects Manager, Hazardous Materials Program Office, Battelle Columbus Laboratories

Review of current methods for detection and identification of CW agents. Evaluation of effectiveness of methods. Discussion of current problems in future requirements for detection and identification.

Steve Harden, Chief, Applied Chemistry Section, Chemical Branch Research Division, Chemical Systems Laboratory

Afternoon Session: Defense Industry Programs and Summary

Sylvania/GTE Area Defense System Presentation. Discussion and evaluation.

Ted Prociv
Doug Woodman, Senior Scientist, Electro-Optics Division Sylvania/GTE

Bendix Point Sampling Dry Systems. Discussion and evaluation.

Dr. Glen Spangler, Sr. Staff Scientist, Bendix Environmental and Process Inst. Div.

Summary by Participants.

AD-A099 917 MICHIGAN UNIV ANN ARBOR COLL OF ENGINEERING F/G 5/2
PRELIMINARY REPORTS, MEMORANDA AND TECHNICAL NOTES OF THE MATER--ETC(U)
JUL 80 M J SINNOTT MDA903-80-C-0505
UNCLASSIFIED 018324 NL

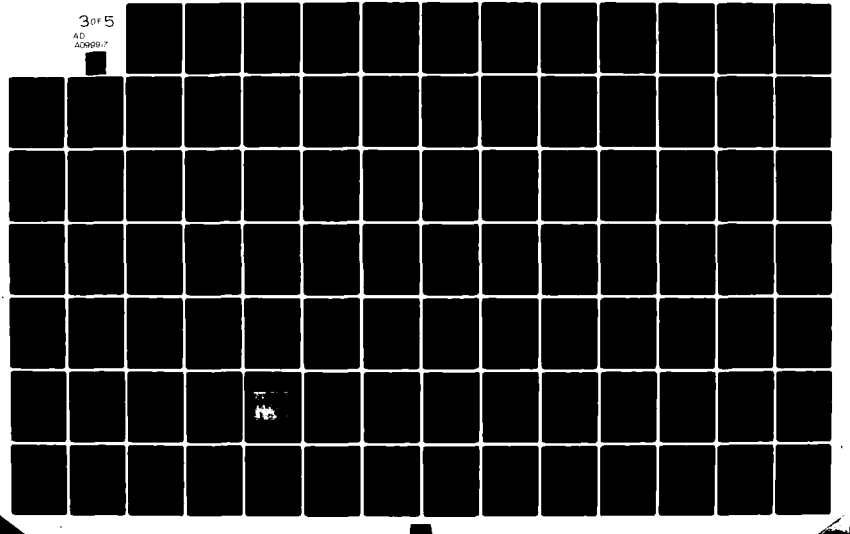

CW Agents

Guest Participants

Thomas R. Dashiell
Dept. of Defense
The Pentagon, Room JD129
Washington, D.C. 20301
(202) 697-8714

C. S. Harden
Chem. Systems Lab.
Aberdeen Proving Ground
MD 21010
(301) 671-3614

Dr. William S. Magee, Jr.
Chemical Systems Laboratory
Aberdeen Proving Ground
MD 21010
(301) 671-3234

T. M. Prociv
Battelle Memorial Institute
Columbus, OH 43201
(614) 424-4248

Dr. Glenn Spangler
Bendix EPID
Baltimore, Maryland 21204
(301) 321-5261

Douglas Woodman
GTE Syvania
Mt. View, CA
(415) 966-3207

DETECTION AND EVALUATION OF SMALL FLAWS IN OPTICAL FIBERS

G. S. Kino and R. M. Thomson

ABSTRACT

After discussion with H. Winsor we evaluated the problem of measuring the presence of small flaws 20-100Å in size near the surface of an optical fiber. We conclude that optical and acoustic methods are not sensitive enough to be useful for this purpose; this is particularly true for high speed testing. We conclude that any flaws found would be irreparable. So destructive testing is the only answer. We suggest techniques using small roller for the test, which tend to allow only small regions of the fiber to be affected at a time. This is of importance in evaluating the nature of the flaw, so as to allow improvements in manufacturing techniques.

AD-A099 917 MICHIGAN UNIV ANN ARBOR COLL OF ENGINEERING F/G 5/2
PRELIMINARY REPORTS, MEMORANDA AND TECHNICAL NOTES OF THE MATER--ETC(U)
JUL 80 M J SINNOTT MDA903-80-C-0505
UNCLASSIFIED 018324 NL

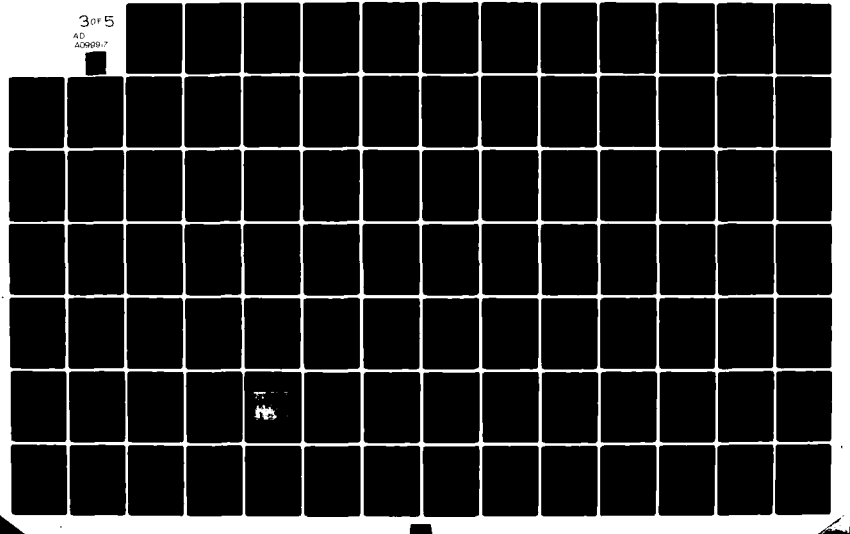

DETECTION AND EVALUATION OF SMALL FLAWS IN OPTICAL FIBERS

G. S. Kino and R. M. Thomson

INTRODUCTION

After discussion with H. Winsor we considered the problem of detecting small flaws in optical fibers. The yield strength of such glass fibers, which are typically of the order of 100 μm diameter is, in the main, dictated by the presence of small near-surface flaws in the form of half penny shaped cracks in the size range 20Å-100Å diameter. The problem is to detect these cracks.

The problem arises. If the cracks can be detected can they be repaired? One would normally expect such small cracks, if perfectly clean, to be self-healing to essentially the full strength of the fiber. Hence it would not be necessary to repair them after releasing tension on the fiber. Similarly it would not be necessary to detect the cracks for they would not do any damage.

We therefore conclude that such cracks or defects are only of importance if there is some growth or imperfection present which can provide a permanent source of localized stress. In this case, they cannot be healed. So when they are detected they must be cut out and the fiber repaired.

It is not adequate to just detect these cracks either. It is necessary to detect them relatively quickly at essentially

DETECTION AND EVALUATION OF SMALL FLAWS IN OPTICAL FIBERS

G. S. Kino and R. M. Thomson

ABSTRACT

After discussion with H. Winsor we evaluated the problem of measuring the presence of small flaws 20-100Å in size near the surface of an optical fiber. We conclude that optical and acoustic methods are not sensitive enough to be useful for this purpose; this is particularly true for high speed testing. We conclude that any flaws found would be irreparable. So destructive testing is the only answer. We suggest techniques using small roller for the test, which tend to allow only small regions of the fiber to be affected at a time. This is of importance in evaluating the nature of the flaw, so as to allow improvements in manufacturing techniques.

the speed at which fiber is produced, i.e., is wound onto reels, otherwise there is far too much information to process. One result would be that the time required for fiber inspection would severely limit the rate of production.

FLUORESCENCE

We considered optical and acoustic techniques for detection of cracks. One approach which we considered is the use of fluorescence of a laser excited fiber from the neighborhood of the crack tip. This fluorescence line could be expected to shift when large stresses below the breaking stress are affected. However, only a few hundred atoms, at most, would be expected to contribute to the fluorescence line of interest. So an extremely sensitive detector of small size (probably involving the use of a microscope) would be required. This, in turn, implies very slow speeds of fiber movement to look at the flaw regions. It also implies, for adequate detection sensitivity, that narrow band lock-in-amplifier detection systems would be required. This, again, implies extremely slow speed detection of flaws.

ACOUSTIC TECHNIQUES

The next measuring system that we considered involved the use of acoustic waves, which could be expected to respond to the mismatch in acoustic impedance at the crack. This effect is proportionately far larger than the change in impedance for EM waves. In is apparent that in order to arrive at a high speed search capability for surface cracks, and as good a sensitivity

DETECTION AND EVALUATION OF SMALL FLAWS IN OPTICAL FIBERS

G. S. Kino and R. M. Thomson

INTRODUCTION

After discussion with H. Winsor we considered the problem of detecting small flaws in optical fibers. The yield strength of such glass fibers, which are typically of the order of 100 μm diameter is, in the main, dictated by the presence of small near-surface flaws in the form of half penny shaped cracks in the size range 20Å-100Å diameter. The problem is to detect these cracks.

The problem arises. If the cracks can be detected can they be repaired? One would normally expect such small cracks, if perfectly clean, to be self-healing to essentially the full strength of the fiber. Hence it would not be necessary to repair them after releasing tension on the fiber. Similarly it would not be necessary to detect the cracks for they would not do any damage.

We therefore conclude that such cracks or defects are only of importance if there is some growth or imperfection present which can provide a permanent source of localized stress. In this case, they cannot be healed. So when they are detected they must be cut out and the fiber repaired.

It is not adequate to just detect these cracks either. It is necessary to detect them relatively quickly at essentially

the speed at which fiber is produced, i.e., is wound onto reels, otherwise there is far too much information to process. One result would be that the time required for fiber inspection would severely limit the rate of production.

FLUORESCENCE

as possible, it is wise to employ relatively high frequency Rayleigh waves propagating in the axial direction along the fiber. The advantage of using a wave propagating in this direction, it that it can automatically interrogate a region whose length is controlled only by its attenuation. By using a relatively high frequency Rayleigh wave, only the region near the surface, which is of main interest, is interrogated. This is important as the sensitivity tends to depend on the ratio of the effective cross sectional area of the flaw to the area of the interrogating beam.

We can estimate the reflection coefficient of a crack from the formula

$$\Gamma \simeq \frac{16\pi^2}{3} \frac{a^3}{\lambda^2 \omega} K \qquad (1)$$

where K is a numerical coefficient of value <0.5, λ the acoustic wavelength, W the width of the beam, a the crack radius.[1]

Assuming a frequency of 1 GHz (if suitable transducers could be realized) λ = 3 μm. For a 100 μm diameter fiber, w ≃ 3 μm. Taking a = 25Å, K = 1, we find that $\Gamma \simeq 10^{-9}$. It follows that, as the reflected power is proportional to Γ^2, there is absolutely no hope of detecting such flaws with acoustic waves.

Calculations for acoustic emission due to a flaw expanding would give equally pessimistic estimates because of the very poor radiation efficiency of the flaw at any reasonable acoustic frequency.

In effect, we propose a proof test for the glass fiber. There is an extensive literature on the subject[2], because of a subtlety in inferring the maximum size flaw in the material after the proof test has been performed. The problem arises because glass is subject to subcritical crack growth. That is, at stresses below that where the crack expands catastrophically, it extends by creep. Therefore, if a crack is somewhat smaller than the Griffith value at the maximum stress (region A of Fig. 1), it will grow during the period of maximum stress, and as the stress is released (region B of Fig. 1), significant crack growth can occur. If the release is slow enough, and the crack growth law is appropriate, then during the release portion of the proof test, the flaw can actually grow to a size significantly larger than the critical size which the proof test was designed to find. Obviously, the initial statistical distribution of flaw sizes, the shape of the proof test stress pulse, the crack growth law, and the atmosphere in which the test is accomplished must all be considered in interpreting the results of a proof test. The designers of the test procedures must therefore consider this effect as an important aspect of the problem.

We suggest that the proper method to break the fiber is to wind it around a feeding roller A, shown in Fig. 2, of the order of 10 cm diameter. This roller applies a small tension. The plastic-metal coated fiber then passes around roller 1 of radius b. If the required strain of the fiber surface is ε, and the fiber radius is a, the strain will be

MECHANICAL TESTING

We therefore conclude that the only reasonable test for the presence of flaws is a proof test. As we have already indicated, it is unlikely that the flaw can be repaired, and it must be cut out of the fiber anyway, this is not a disadvantage. It is quick, simple and effective.

The main problem is that if a significant length of a fiber is stretched to break it, the fiber "whips" because of the large elastic stored energy in the length of fiber and damage occurs over a relatively long length of fiber, shards of glass may land on the rest of the fiber and damage and contaminate it further. Furtherfore, it is very difficult to analyze the cause of flaw formation.

CONCLUSION

We therefore suggest that the emphasis should be better mechanical design of the testing system. The following steps should be taken:

(1) The fiber should tend to be broken by bending rather than in axial tension. This causes the crack to grow more uniformly;

(2) The region over which stress is applied should be very short so as to decrease the whipping effect;

(3) The fiber must be immersed in water free inert liquid (a hydrocarbon) to prevent stress corrosion. Alternatively, and perhaps more simply, the fiber should be coated with metal then plastic in the normal way before testing.

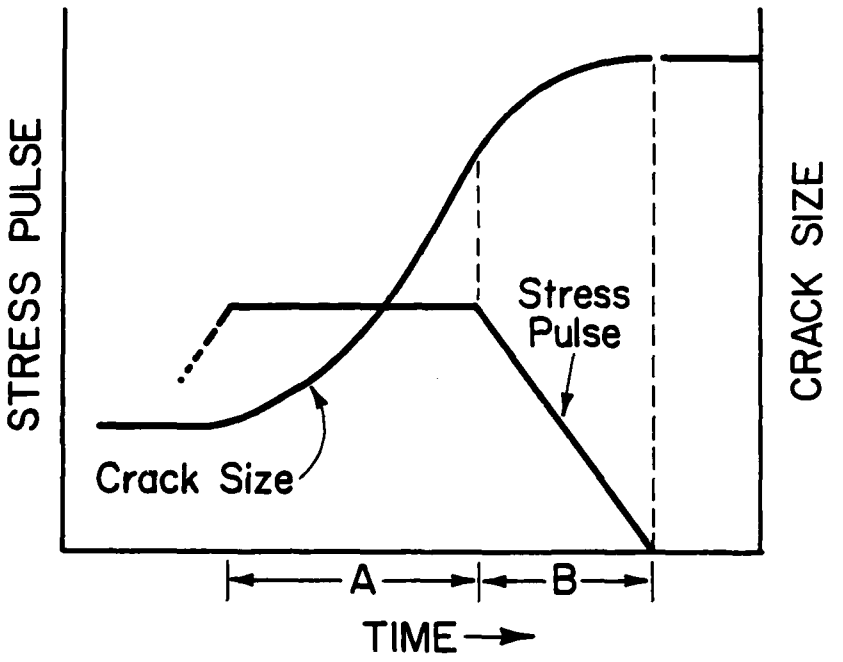

Figure 1. Stress pulse and crack size time history designing a proof test. During region A a small crack can grow to near critical size. During the release portion, growth will continue, perhaps to a size larger than the critical size.

In effect, we propose a proof test for the glass fiber. There is an extensive literature on the subject[2], because of a subtlety in inferring the maximum size flaw in the material after the proof test has been performed. The problem arises because glass is subject to subcritical crack growth. That is, at stresses below that where the crack expands catastrophically, it extends by creep. Therefore, if a crack is somewhat smaller than the Griffith value at the maximum stress (region A of Fig. 1), it will grow during the period of maximum stress, and as the stress is released (region B of Fig. 1), significant crack growth can occur. If the release is slow enough, and the crack growth law is appropriate, then during the release portion of the proof test, the flaw can actually grow to a size significantly larger than the critical size which the proof test was designed to find. Obviously, the initial statistical distribution of flaw sizes, the shape of the proof test stress pulse, the crack growth law, and the atmosphere in which the test is accomplished must all be considered in interpreting the results of a proof test. The designers of the test procedures must therefore consider this effect as an important aspect of the problem.

We suggest that the proper method to break the fiber is to wind it around a feeding roller A, shown in Fig. 2, of the order of 10 cm diameter. This roller applies a small tension. The plastic-metal coated fiber then passes around roller 1 of radius b. If the required strain of the fiber surface is ε, and the fiber radius is a, the strain will be

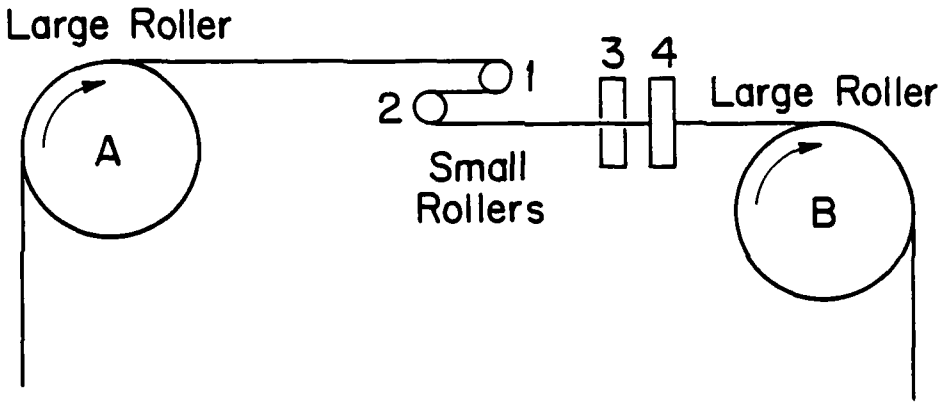

Figure 2. A schematic of the fiber testing system.

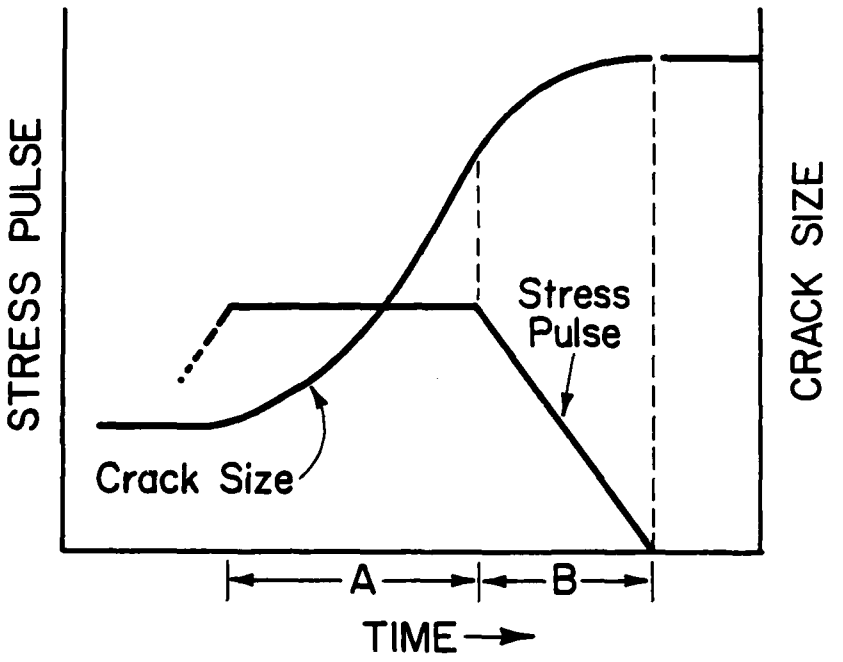

Figure 1. Stress pulse and crack size time history designing a proof test. During region A a small crack can grow to near critical size. During the release portion, growth will continue, perhaps to a size larger than the critical size.

$$\varepsilon = \frac{2a}{b} \tag{2}$$

for 5% elongation and a = 60 μm, b = 2.4 μm. For V = 2 meters/minute feed rate, the small roller speed is

$$f = \frac{V}{2\pi b} = \frac{2}{2\pi \times 2.4 \times 10^{3}} = 133 \text{ rpm} \tag{3}$$

The fiber then passes around roller 2 to stretch the opposite surface. A series of rollers 3, 4, 5, 6 placed with their axes at 90°, 45°, etc., to the original rollers can be used to ensure elongation of all parts of the fiber surface. Only the 90° rollers are shown in Fig. 2.

By this means the fiber is stretched for only 6 milliseconds at a time. It is wise, however, to look into the rate of crack growth to determine what strain should be used and the optimum speed for passing the fiber through the testing system.

At all events a system of this type should make it possible to test for cracks, allowing only a small region to be under tension at any given time. By this means, only a small region of the fiber will be affected, and it should be relatively easy to analyze the cracks that were present.

ACKNOWLEDGEMENT

This research was supported by the Defense Advanced Research Projects Agency of the Department of Defense under Contract No. MDA903-0C-0505 with The University of Michigan.

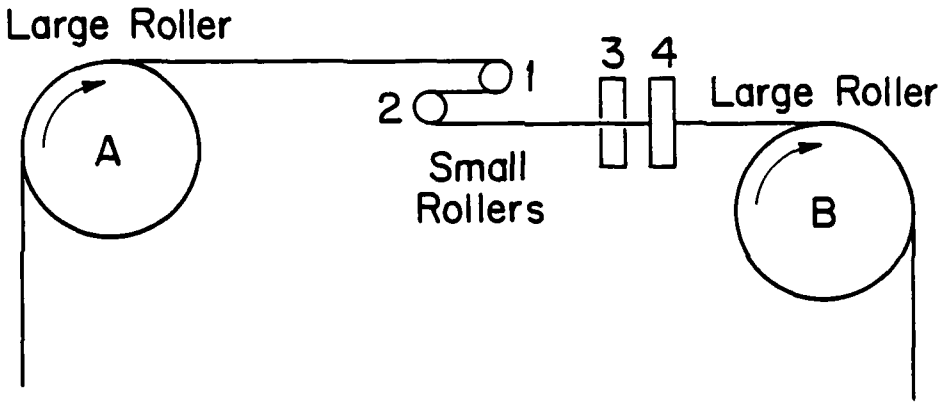

Figure 2. A schematic of the fiber testing system.

References

1. B. T. Khuri Yakub, A. G. Evans, and G. S. Kino, Acoustic Surface Wave Measurements of Surface Cracks in Ceramics, J. Amer. Ceram. Soc., accepted for publication.

2. J. Ritter, P. Oates, E. Fuller, and S. Wiederhorn, Proof Testing of Ceramics, I & II, J. Mat. Sci., to be published. Currently available in preprint form from S. Wiederhorn, Center for Materials Research, National Bureau of Standards, Washington, D.C. 20234.

$$\varepsilon = \frac{2a}{b} \tag{2}$$

for 5% elongation and a = 60 μm, b = 2.4 μm. For V = 2 meters/minute feed rate, the small roller speed is

$$f = \frac{V}{2\pi b} = \frac{2}{2\pi \times 2.4 \times 10^{3}} = 133 \text{ rpm} \tag{3}$$

The fiber then passes around roller 2 to stretch the opposite surface. A series of rollers 3, 4, 5, 6 placed with their axes at 90°, 45°, etc., to the original rollers can be used to ensure elongation of all parts of the fiber surface. Only the 90° rollers are shown in Fig. 2.

By this means the fiber is stretched for only 6 milliseconds at a time. It is wise, however, to look into the rate of crack growth to determine what strain should be used and the optimum speed for passing the fiber through the testing system.

At all events a system of this type should make it possible to test for cracks, allowing only a small region to be under tension at any given time. By this means, only a small region of the fiber will be affected, and it should be relatively easy to analyze the cracks that were present.

ACKNOWLEDGEMENT

This research was supported by the Defense Advanced Research Projects Agency of the Department of Defense under Contract No. MDA903-0C-0505 with The University of Michigan.

FRACTURE TOUGHNESS AND TENSILE STRENGTH OF ZERO CTE AND OTHER CERAMIC PARTICLE - DUCTILE MATRIX COMPOSITES

D. C. Drucker

EXTENDED SUMMARY

The proposal has been made to fabricate a structural material of zero or low coefficient of thermal expansion by embedding an appropriate and necessarily large volume fraction of ceramic particles in a very ductile matrix. On the assumption of perfect bonding or of zero bond strength, thermal expansion coefficients and elastic moduli can be calculated from the values for each constituent without consideration of the size scale. Except as f is altered, the results are independent of whether the diameter d of the particles, their spacing D, and the interparticle distances are in the submicron, micron, or millimeter range.

Inelastic mechanical properties, such as yield strength and fracture toughness, also can be predicted from the geometry and the mechanical properties of the constituents. However, absolute size or scale does matter. The strength of the particles and their effective interface bond to the matrix increase with decrease of d and the accompanying decrease in defect size. The yield and flow strength σ_o of the very ductile matrix also are likely to show a similar significant size dependence when interparticle distances are of the order of a micron or less and relatively few

References

1. B. T. Khuri Yakub, A. G. Evans, and G. S. Kino, Acoustic Surface Wave Measurements of Surface Cracks in Ceramics, J. Amer. Ceram. Soc., accepted for publication.

2. J. Ritter, P. Oates, E. Fuller, and S. Wiederhorn, Proof Testing of Ceramics, I & II, J. Mat. Sci., to be published. Currently available in preprint form from S. Wiederhorn, Center for Materials Research, National Bureau of Standards, Washington, D.C. 20234.

mobile dislocations are available. Normally this size effect can be ignored for a reasonably regular array of roughly equi-axed particles in a very ductile matrix when interparticle distances exceed 5 μm (e.g., d is at least 100 μm and f does not exceed 0.95). Particles of millimeter diameter give more than ample interparticle distances for the bulk flow properties of a very ductile matrix to apply on the microscale without correction.

As a first approximation the assumption is made that the composite in the working range of stress has its particles weakly bonded to the matrix but under appreciable compression as a result of the large relative contraction of the metal matrix on cooling down from the fabrication temperature. The elastic and the thermal response of the composite therefore differs little if any from that for perfectly bonded particles. However, when yielding occurs as at high overload stresses or in the vicinity of a sharp notch or crack, the matrix will separate from the particle. The effective average yield or flow strength $\bar{\sigma}_o$ at appreciable plastic strain for the relevant picture of close to uniaxial strain with moderate to large f, then is not very different from that of a metal matrix with holes instead of particles. For $f > 0.30$, $\bar{\sigma}_o \simeq \sigma_o(1-f)$ seems a reasonable approximation to this average tensile flow strength and therefore to the tensile failure strength.

The separation distance δ for ductile rupture, or the crack opening displacement in this model of a succession of individual ductile ligaments separating by necking down between unbonded particles as the crack advances, will be of the order of

FRACTURE TOUGHNESS AND TENSILE STRENGTH OF ZERO CTE AND OTHER CERAMIC PARTICLE - DUCTILE MATRIX COMPOSITES

D. C. Drucker

EXTENDED SUMMARY

The proposal has been made to fabricate a structural material of zero or low coefficient of thermal expansion by embedding an appropriate and necessarily large volume fraction of ceramic particles in a very ductile matrix. On the assumption of perfect bonding or of zero bond strength, thermal expansion coefficients and elastic moduli can be calculated from the values for each constituent without consideration of the size scale. Except as f is altered, the results are independent of whether the diameter d of the particles, their spacing D, and the interparticle distances are in the submicron, micron, or millimeter range.

Inelastic mechanical properties, such as yield strength and fracture toughness, also can be predicted from the geometry and the mechanical properties of the constituents. However, absolute size or scale does matter. The strength of the particles and their effective interface bond to the matrix increase with decrease of d and the accompanying decrease in defect size. The yield and flow strength σ_o of the very ductile matrix also are likely to show a similar significant size dependence when interparticle distances are of the order of a micron or less and relatively few

the interparticle distances or ligament thickness. These average (1-f)D for a random array and will be closely $\frac{1-f}{3}$ D for an array of cubical particles at high volume fractions. A choice of $\frac{1-f}{2}$ D should be well within a factor of 2.

The average work of separation per unit area for a fully ductile matrix that does not adhere to the particles in this uniaxial strain picture ahead of a running crack then is of magnitude $\bar{\sigma}_o \delta$, and is chosen as $\frac{D^2}{2} \bar{\sigma}_o \delta \simeq \frac{1}{4} \sigma_o (1-f)^2 D^3$ for an area D^2 of crack advance. The average work per unit area within a factor of 2 or so is

$$G_c \simeq \frac{1}{4} \sigma_o (1-f)^2 D \tag{1}$$

The critical stress intensity K_c is given by

$$K_c^2 = G_c E \simeq \frac{1}{4} \sigma_o (1-f)^2 DE \tag{2}$$

where E is the Young's modulus of the composite in the moderately stressed elastic region well away from the crack tip. The "rule" of mixtures given an upper bound

$$E \leq (1-f) E_M + f E_p \tag{3}$$

where E_M and E_p are the Young's moduli for matrix and particle respectively.

The critical crack length c for instability of crack extension under an applied tensile stress σ_c far from the crack is given by

mobile dislocations are available. Normally this size effect can be ignored for a reasonably regular array of roughly equi-axed particles in a very ductile matrix when interparticle distances exceed 5 μm (e.g., d is at least 100 μm and f does not exceed 0.95). Particles of millimeter diameter give more than ample interparticle distances for the bulk flow properties of a very ductile matrix to apply on the microscale without correction.

As a first approximation the assumption is made that the composite in the working range of stress has its particles weakly bonded to the matrix but under appreciable compression as a result of the large relative contraction of the metal matrix on cooling down from the fabrication temperature. The elastic and the thermal response of the composite therefore differs little if any from that for perfectly bonded particles. However, when yielding occurs as at high overload stresses or in the vicinity of a sharp notch or crack, the matrix will separate from the particle. The effective average yield or flow strength $\bar{\sigma}_o$ at appreciable plastic strain for the relevant picture of close to uniaxial strain with moderate to large f, then is not very different from that of a metal matrix with holes instead of particles. For $f > 0.30$, $\bar{\sigma}_o \simeq \sigma_o(1-f)$ seems a reasonable approximation to this average tensile flow strength and therefore to the tensile failure strength.

The separation distance δ for ductile rupture, or the crack opening displacement in this model of a succession of individual ductile ligaments separating by necking down between unbonded particles as the crack advances, will be of the order of

$$c = (K_c/\sigma_c)^2/2\pi$$

$$K_c \simeq \tfrac{1}{2}\sigma_o(1-f)(DE/\sigma_o)^{\frac{1}{2}} = \tfrac{1}{2}\bar{\sigma}_o(DE/\sigma_o)^{\frac{1}{2}} \qquad (4)$$

$$c \simeq \frac{D}{8\pi}\left(\frac{\bar{\sigma}_o}{\sigma_c}\right)^2\frac{E}{\sigma_o} \quad ; \quad \bar{\sigma}_o = \sigma_o(1-f)$$

For $\sigma_c < \bar{\sigma}_o$ and E/σ_o in the common range of 100 to 1000, c is many times D. This large ductility on the microscale and rather low average yield and failure strengths in tension for high volume fractions f carries over to considerable ductility on the macroscale for d (and D) in the millimeter range. However, it does not for d in the micron range and f large as in commercial cemented carbides (with or without any scale effect on σ_o). The macroscopic behavior predicted *is very brittle despite the absence of* bond between particle and matrix at the crack tip.

With the rather arbitrary choices of D = 2 μm, σ_o = 600 MN/m^2, E = 300,000 MN/m^2, and f = 0.90 <u>for an unbonded composite</u>.

$$\delta \simeq \tfrac{1}{2}(1-f)D = 0.1\ \mu m$$

$$\bar{\sigma}_o \simeq \sigma_o(1-f) = 60\ MN/m^2$$

$$G_c \simeq \tfrac{1}{2}\bar{\sigma}_o\delta = 3\ J/m^2 \text{ or } 3\ Nm/m^2 \qquad (5)$$

$$K_c = \sqrt{G_c E} = 0.95(MN/m^2)m^{\frac{1}{2}}$$

$$c \simeq \frac{D}{8\pi}\left(\frac{\bar{\sigma}_o}{\sigma_c}\right)^2\frac{E}{\sigma_o} = 40(\bar{\sigma}_o/\sigma_c)^2\ \mu m$$

At the rather low applied stress of σ_c = 30 MN/m^2 (less than

5000 psi) that is about half the effective tensile strength of the unbonded composite $\bar{\sigma}_o$, the critical crack length is very small; c = 160 μm. At $\sigma_c = \bar{\sigma}_o$ which is still a low stress, but all that the unbonded composite can take, c is down to 40 μm.

Tensile strengths of 2000 MN/m^2 are reached in test bars and beams of commercial cemented carbides with their strong bonding of particles to matrix. Yet G_c and K_c would be closely the same for the strong composite and for the weak unbonded composite as calculated, $\bar{\sigma}_o$ = 60 MN/m^2, if forward of a sufficiently long and sharp crack the stresses in the bonded composite cause debonding and drastic local stress reduction to $\bar{\sigma}_o$ on average in the close-in plastic zone. If high bond strength is maintained immediately ahead of the crack so that the average stress level there is of order 2000 MN/m^2, K_c will be an order of magnitude higher than for the unbonded composite. Of course, starting a running crack from the root of a blunt notch (root radius >>D) takes far greater σ_c for the bonded than the unbonded composite.

Measurement of fracture toughness parameters with any accuracy and meaning is possible only with cracks of at least 5 particle spacings in length and root radius no greater than particle radius. At the minimum crack length of 10 μm for 2 μm particles, $\sigma_c < 2\bar{\sigma}_o$ = 120 MN/m^2 which is far below the tensile strength of 2000 MN/m^2. A more comfortable crack length of 1 mm calls for σ_c = 12 MN/m^2. At σ_c equal to the tensile strength of the bonded composite, the calculated value of critical length becomes less than 0.04 μm. So small a fraction of the particle

diameter can serve only as the crudest of indications of a governing defect dimension.

At a given f, $\bar{\sigma}_o$ is unchanged but the larger the particle spacing D_o the larger d, the larger the interparticle distances $\frac{1}{2}(1-f)D$, and the greater G_c and K_c become for the unbonded composite or the bonded composite that becomes unbonded as the crack advances. In a bonded composite, the larger d the smaller the tensile stress that will cause the particle itself to fracture. A running crack is observed to go around the WC particles in a micron size WC-Co bonded composite but to go through the particles when they are 10 μm in size. In this size range, if bond is maintained ahead of a running crack, G_c and K_c may decrease with increase in d at a given f.

Millimeter size particles will be weaker still and very likely to fracture and debond in front of a crack. However, such a debonded or fractured composite has ample macroscopic ductility. Most of the microscopic physical brittleness and problems of interpretation so troublesome on the micron scale disappear on the millimeter scale. Just a modest bond strength and particle tensile strength contribute importantly to the yield strength of the composite at large f. G_c and K_c then are likely to be the same as for an unbonded composite of the same d and f.

With D = 2 mm instead of 2 μm, the following calculations demonstrate the change to macroscopic ductility rather than brittleness at moderate applied stress despite the large ceramic volume fraction f = 0.90.

5000 psi) that is about half the effective tensile strength of the unbonded composite $\bar{\sigma}_o$, the critical crack length is very small; c = 160 μm. At $\sigma_c = \bar{\sigma}_o$ which is still a low stress, but all that the unbonded composite can take, c is down to 40 μm.

Tensile strengths of 2000 MN/m^2 are reached in test bars and beams of commercial cemented carbides with their strong bonding of particles to matrix. Yet G_c and K_c would be closely the same for the strong composite and for the weak unbonded composite as calculated, $\bar{\sigma}_o$ = 60 MN/m^2, if forward of a sufficiently long and sharp crack the stresses in the bonded composite cause debonding and drastic local stress reduction to $\bar{\sigma}_o$ on average in the close-in plastic zone. If high bond strength is maintained immediately ahead of the crack so that the average stress level there is of order 2000 MN/m^2, K_c will be an order of magnitude higher than for the unbonded composite. Of course, starting a running crack from the root of a blunt notch (root radius >>D) takes far greater σ_c for the bonded than the unbonded composite.

Measurement of fracture toughness parameters with any accuracy and meaning is possible only with cracks of at least 5 particle spacings in length and root radius no greater than particle radius. At the minimum crack length of 10 μm for 2 μm particles, $\sigma_c < 2\bar{\sigma}_o$ = 120 MN/m^2 which is far below the tensile strength of 2000 MN/m^2. A more comfortable crack length of 1 mm calls for σ_c = 12 MN/m^2. At σ_c equal to the tensile strength of the bonded composite, the calculated value of critical length becomes less than 0.04 μm. So small a fraction of the particle

$$
\begin{aligned}
\delta &\simeq 0.1 \text{ mm is 1000X larger} \\
\bar{\sigma}_o &\simeq 60 \text{ MN/m}^2 \text{ as before} \\
G_c &\simeq 3000 \text{ J/m}^2 \text{ is 1000X larger} \\
K_c &\simeq 30(\text{MN/m}^2)\text{m}^{\frac{1}{2}} \text{ is 32X larger} \\
c &\simeq 40(\bar{\sigma}_o/\sigma_c)^2 \text{ mm is 1000X larger}
\end{aligned} \tag{6}
$$

A bond and fracture strength sufficient to permit the composite to carry $\sigma_o = 2\bar{\sigma}_o = \sigma_o/5 = 120$ MN/m^2 safely gives the sizeable critical crack length c = 10 mm or 5 particle spacings.

At a volume fraction f = 0.50, instead of 0.90, with D = 2 mm, the fracture would clearly appear ductile to the unaided eye.

$$
\begin{aligned}
\delta &\simeq 0.5 \text{ mm} \\
\bar{\sigma}_o &\simeq 300 \text{ MN/m}^2 \\
G_c &\simeq 75{,}000 \text{ J/m}^2 \\
K_c &\simeq 150(\text{MN/m}^2)\text{m}^{\frac{1}{2}} \\
c &\simeq 40(\bar{\sigma}_o/\sigma_c)^2
\end{aligned} \tag{7}
$$

At what is a high stress for a bulk ceramic and requires considerable bond strength, $\sigma_c = 2\bar{\sigma}_o = \sigma_o = 600$ MN/m^2, c = 10 mm. At the reasonably moderate but still substantial applied tensile stress of $\bar{\sigma}_c = \bar{\sigma}_o/2 = 150$ MN/m^2, no bond strength is needed and c = 160 mm.

The principal features of the mechanical behavior of a ceramic particle - very ductile metal matrix composite as a function of f, d or D, σ_o, E, and bond strength appear to be illustrated reasonably well by the examples given. However, σ_o and E, as well as f and D, have been chosen quite arbitrarily. Application of

the formulas and concepts to a particular composite does require use of the appropriate values for all the variables, and a check on the applicability of the basic concept of crack advance by earlier bond failure and the necking of fully ductile ligaments in a field of uniaxial strain ahead of the crack.

ACKNOWLEDGEMENT

Helpful discussions with Professors A. G. Evans and J. R. Rice are gratefully acknowledged. This research was conducted under the support of the of the Defense Advanced Research Projects Agency of the Department of Defense under Contract No. MDA903-80C-0505 with The University of Michigan.

diameter can serve only as the crudest of indications of a governing defect dimension.

At a given f, $\bar{\sigma}_o$ is unchanged but the larger the particle spacing D_o the larger d, the larger the interparticle distances $\frac{1}{2}(1-f)D$, and the greater G_c and K_c become for the unbonded composite or the bonded composite that becomes unbonded as the crack advances. In a bonded composite, the larger d the smaller the tensile stress that will cause the particle itself to fracture. A running crack is observed to go around the WC particles in a micron size WC-Co bonded composite but to go through the particles when they are 10 μm in size. In this size range, if bond is maintained ahead of a running crack, G_c and K_c may decrease with increase in d at a given f.

Millimeter size particles will be weaker still and very likely to fracture and debond in front of a crack. However, such a debonded or fractured composite has ample macroscopic ductility. Most of the microscopic physical brittleness and problems of interpretation so troublesome on the micron scale disappear on the millimeter scale. Just a modest bond strength and particle tensile strength contribute importantly to the yield strength of the composite at large f. G_c and K_c then are likely to be the same as for an unbonded composite of the same d and f.

With D = 2 mm instead of 2 μm, the following calculations demonstrate the change to macroscopic ductility rather than brittleness at moderate applied stress despite the large ceramic volume fraction f = 0.90.

IMPROVED GUN PROPELLANTS

J. L. Margrave

On July 14-15, members of the Materials Research Council met with ten invited visitors to discuss current viewpoints and state-of-the-art regarding gun propellants. Major Harry Winsor made the initial presentation and enumerated several goals, including higher density propellants with self-regulating deflagration rates which were "completely safe". Such goals clearly require the further development of our understanding of propellant science.

Among the problem areas identified by Major Winsor were

1. Deflagration - Detonation Transitions
2. Shock Sensitivity
3. Unreliable/Spontaneous Ignition
4. Pressure Affects Burning Rates
5. Smoke Production
6. Gun Barrel Wear and Erosion
7. Aging of Propellants
8. Toxicity of Propellants and Combustion Products

As background for discussion, there were several presentations as indicated on the schedule. Four of these will be reviewed here.

$$
\begin{aligned}
\delta &\simeq 0.1 \text{ mm is 1000X larger} \\
\bar{\sigma}_o &\simeq 60 \text{ MN/m}^2 \text{ as before} \\
G_c &\simeq 3000 \text{ J/m}^2 \text{ is 1000X larger} \\
K_c &\simeq 30(\text{MN/m}^2)\text{m}^{\frac{1}{2}} \text{ is 32X larger} \\
c &\simeq 40(\bar{\sigma}_o/\sigma_c)^2 \text{ mm is 1000X larger}
\end{aligned} \tag{6}
$$

A bond and fracture strength sufficient to permit the composite to carry $\sigma_o = 2\bar{\sigma}_o = \sigma_o/5 = 120$ MN/m^2 safely gives the sizeable critical crack length c = 10 mm or 5 particle spacings.

At a volume fraction f = 0.50, instead of 0.90, with D = 2 mm, the fracture would clearly appear ductile to the unaided eye.

$$
\begin{aligned}
\delta &\simeq 0.5 \text{ mm} \\
\bar{\sigma}_o &\simeq 300 \text{ MN/m}^2 \\
G_c &\simeq 75{,}000 \text{ J/m}^2 \\
K_c &\simeq 150(\text{MN/m}^2)\text{m}^{\frac{1}{2}} \\
c &\simeq 40(\bar{\sigma}_o/\sigma_c)^2
\end{aligned} \tag{7}
$$

At what is a high stress for a bulk ceramic and requires considerable bond strength, $\sigma_c = 2\bar{\sigma}_o = \sigma_o = 600$ MN/m^2, c = 10 mm. At the reasonably moderate but still substantial applied tensile stress of $\bar{\sigma}_c = \bar{\sigma}_o/2 = 150$ MN/m^2, no bond strength is needed and c = 160 mm.

The principal features of the mechanical behavior of a ceramic particle - very ductile metal matrix composite as a function of f, d or D, σ_o, E, and bond strength appear to be illustrated reasonably well by the examples given. However, σ_o and E, as well as f and D, have been chosen quite arbitrarily. Application of

Dr. Ray McGuire of the Lawrence Livermore Laboratory discussed various studies of the kinetics of thermal decomposition for nitrocellulose, TNT, MXM, TATB, etc. He emphasized two points: (a) Thermal decompositions of energetic materials take place in a sequence of endothermic and exothermic steps, as shown for HMX (Fig. 1). (b) When quantitative energy measurements are made in a constant volume, high pressure cell, there is a much greater evolution of heat then if a low pressure flow system is used (Fig. 2). Such differences in confinement (pressure) can lead to slow, low energy burning in one case and rapid, explosions on the other.

A full understanding of heat capacities, thermal conductivities and diffusivities and the chemistry of decomposition has been used at LLL to develop predictive codes to estimate when or if an explosion should occur.

Dr. Gerald Sterbutzel of the CalSpan Labs presented an extensive review of the current art and science concerning wear and erosion in gun barrels. The CalSpan program utilizes sophisticated electronic, photographic and mechanical experimental techniques, supplemented by mathematical modeling to achieve better designs for guns and ammunition. Chemical erosion by combustion gases, mechanical wear and heating by the exiting projectile, burn rates, and other factors are taken into account of modeling calculations and verified by experiments. Their studies emphasized the continuing need for new materials and a well-coordinated testing/evaluation program. (Fig. 3).

the formulas and concepts to a particular composite does require use of the appropriate values for all the variables, and a check on the applicability of the basic concept of crack advance by earlier bond failure and the necking of fully ductile ligaments in a field of uniaxial strain ahead of the crack.

ACKNOWLEDGEMENT

Helpful discussions with Professors A. G. Evans and J. R. Rice are gratefully acknowledged. This research was conducted under the support of the of the Defense Advanced Research Projects Agency of the Department of Defense under Contract No. MDA903-80C-0505 with The University of Michigan.

Dr. Walter Morrison of the Ballistics Research Laboratory, Aberdeen Proving Grounds, discussed the BRL Liquid Propellants Program, including LP guns and the use of ballistic piston systems to smooth and extend the pressure pulse as it drives a projectile, and thus, to achieve maximum muzzle velocity and range. He reviewed the extensive in-house and contractual efforts of BRL in LP technology.

Dr. Russell Reed of the Naval Weapons Center, China Lake, presented a description of an inhibited propellant system using a silane resin coating to give better control of burning rates/maximum muzzle velocity of projectile. The amine silane polymer resin attaches to a nitrocellulose propellant surface as shown in Fig. 4 and appreciably affects the burning rate as shown in Figs. 5 and 6. The potential payoffs of inhibited gun propellants are summarized in Fig. 7. Dr. Reed also discussed several new azido - and tetrazone binders, oxidizers and deflagrating additives which were low-temperature, gas-producing compounds. These are under investigation at China Lake.

Dr. Margrave described new hydridometal alkyls or alkoxy derivatives which could be useful additives to propellant systems.

Future areas of research in connection with gun propellants were discussed, including:

(a) Molecular Dynamics & Modeling of Burning and Detonation

(b) Laser-spectroscopic diagnostics of propellant burning as f(T) and F(t).

(c) Phase Diagrams of Propellant Systems

IMPROVED GUN PROPELLANTS

J. L. Margrave

On July 14-15, members of the Materials Research Council met with ten invited visitors to discuss current viewpoints and state-of-the-art regarding gun propellants. Major Harry Winsor made the initial presentation and enumerated several goals, including higher density propellants with self-regulating deflagration rates which were "completely safe". Such goals clearly require the further development of our understanding of propellant science.

Among the problem areas identified by Major Winsor were

1. Deflagration - Detonation Transitions
2. Shock Sensitivity
3. Unreliable/Spontaneous Ignition
4. Pressure Affects Burning Rates
5. Smoke Production
6. Gun Barrel Wear and Erosion
7. Aging of Propellants
8. Toxicity of Propellants and Combustion Products

As background for discussion, there were several presentations as indicated on the schedule. Four of these will be reviewed here.

(d) Critical Point Phenomena

(e) Encapsulation of Propellants

(f) Applications of Colloid Science to Propellant Systems

(g) Synthesis of New Propellants

There appear to be many excellent research areas/ideas which could lead to significant improvements in propellant performance.

Dr. Ray McGuire of the Lawrence Livermore Laboratory discussed various studies of the kinetics of thermal decomposition for nitrocellulose, TNT, MXM, TATB, etc. He emphasized two points: (a) Thermal decompositions of energetic materials take place in a

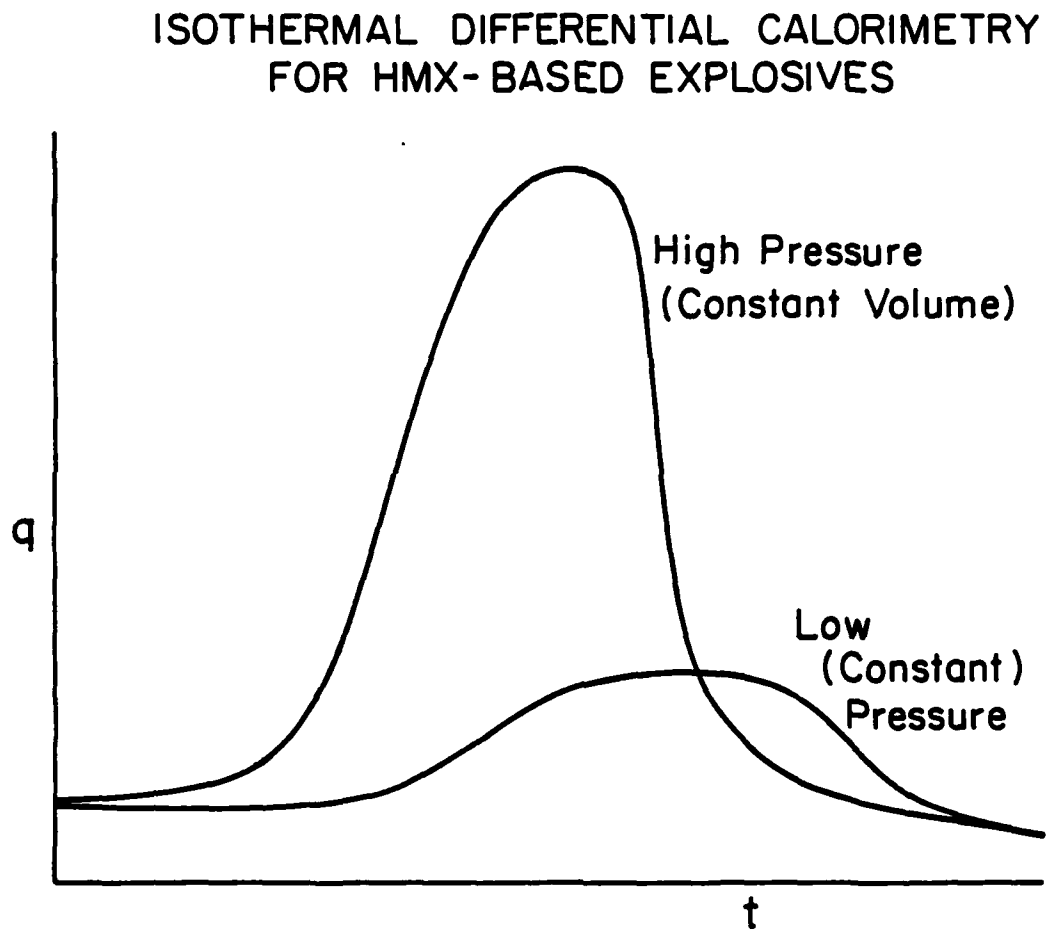

Figure 2. Rate constants in high pressure capsules are ≈10X rate constants at low pressure. Heats of reaction in high pressure capsules are 3 to 5X heats of reaction at low pressure.

Dr. Walter Morrison of the Ballistics Research Laboratory, Aberdeen Proving Grounds, discussed the BRL Liquid Propellants Program, including LP guns and the use of ballistic piston systems to smooth and extend the pressure pulse as it drives a projectile, and thus, to achieve maximum muzzle velocity and range. He reviewed the extensive in-house and contractual efforts of BRL in LP technology.

Dr. Russell Reed of the Naval Weapons Center, China Lake, presented a description of an inhibited propellant system using a silane resin coating to give better control of burning rates/maximum muzzle velocity of projectile. The amine silane polymer resin attaches to a nitrocellulose propellant surface as shown in Fig. 4 and appreciably affects the burning rate as shown in Figs. 5 and 6. The potential payoffs of inhibited gun propellants are summarized in Fig. 7. Dr. Reed also discussed several new azido - and tetrazone binders, oxidizers and deflagrating additives which were low-temperature, gas-producing compounds. These are under investigation at China Lake.

Dr. Margrave described new hydridometal alkyls or alkoxy derivatives which could be useful additives to propellant systems.

Future areas of research in connection with gun propellants were discussed, including:

(a) Molecular Dynamics & Modeling of Burning and Detonation

(b) Laser-spectroscopic diagnostics of propellant burning as f(T) and F(t).

(c) Phase Diagrams of Propellant Systems

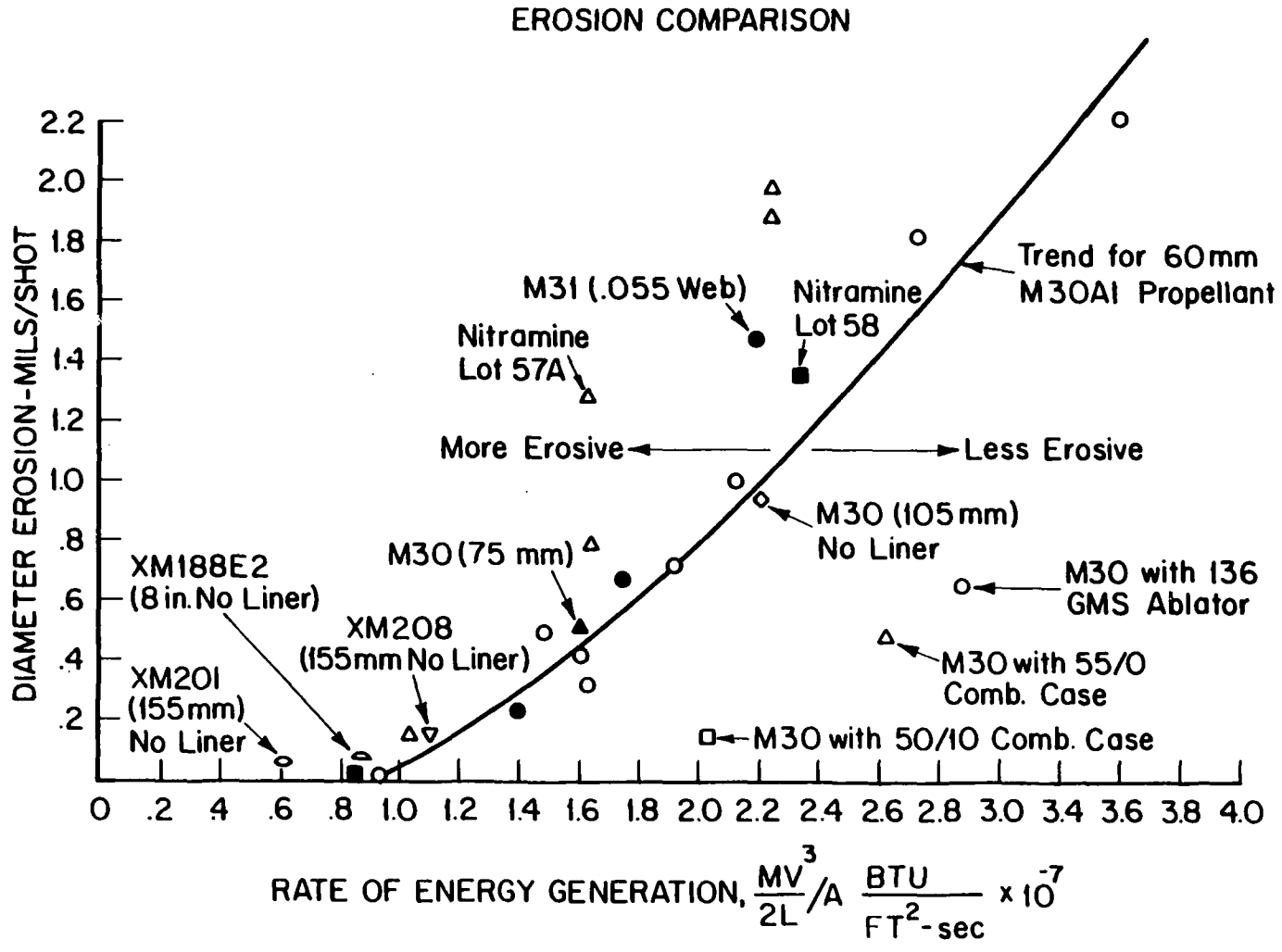
EROSION COMPARISON
DIAMETER EROSION-MILS/SHOT
2.2
2.0
1.8
1.6
1.4
1.2
1.0
.8
.6
.4
.2
M31 (.055 Web)
Nitramine Lot 58
Trend for 60mm M30A1 Propellant
Nitramine Lot 57A
More Erosive
Less Erosive
M30 (105mm) No Liner
M30 (75 mm)
XM188E2 (8 in. No Liner)
M30 with 136 GMS Ablator
XM208 (155mm No Liner)
M30 with 55/0 Comb. Case
XM201 (155mm) No Liner
M30 with 50/10 Comb. Case
0 .2 .4 .6 .8 1.0 1.2 1.4 1.6 1.8 2.0 2.2 2.4 2.6 2.8 3.0 3.4 3.6 3.8 4.0
RATE OF ENERGY GENERATION, $\frac{MV^3}{2L}/A$ $\frac{BTU}{FT^2\text{-sec}}$ $\times 10^{-7}$

Figure 3.

(d) Critical Point Phenomena

(e) Encapsulation of Propellants

(f) Applications of Colloid Science to Propellant Systems

(g) Synthesis of New Propellants

There appear to be many excellent research areas/ideas which could lead to significant improvements in propellant performance.

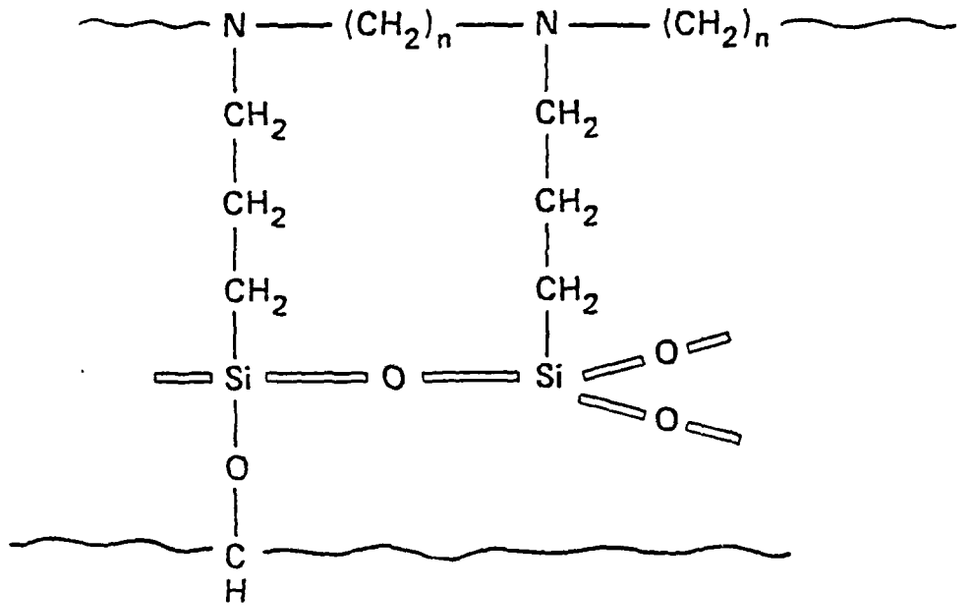

NITROCELLULOSE PROPELLANT

Figure 4. Probable Structure of Coating

THE DECOMPOSITION OF HMX

DEPOLYMERIZATION

$$C_4H_3N_2O_2 \longrightarrow CH_2 = N\text{-}NO_2 \text{ OR } \dot{C}H_2\text{-}N = N\langle^{\dot{O}}_{O}$$

E_A = 52.7 KCAL/MOLE Q = 100 CAL/GM (ENDO)

DECOMPOSITION

$$CH_2 = N\text{-}NO_2 \longrightarrow CH_2O + N_2O$$

E_A = 44 KCAL/MOLE Q = -300 CAL/GM (EXO)

GAS PHASE RXN

$$CH_2O + N_2O \longrightarrow H_2O + N_2 + CO + CO_2 + H_2 + \cdots$$

E_A = 34 KCAL/MOLE Q = -1200 CAL/CM (EXO)

Figure 1

CLOSED BOMB NOSOL 318 SINGLE PERF.
1.61% INHIBITOR Y5987

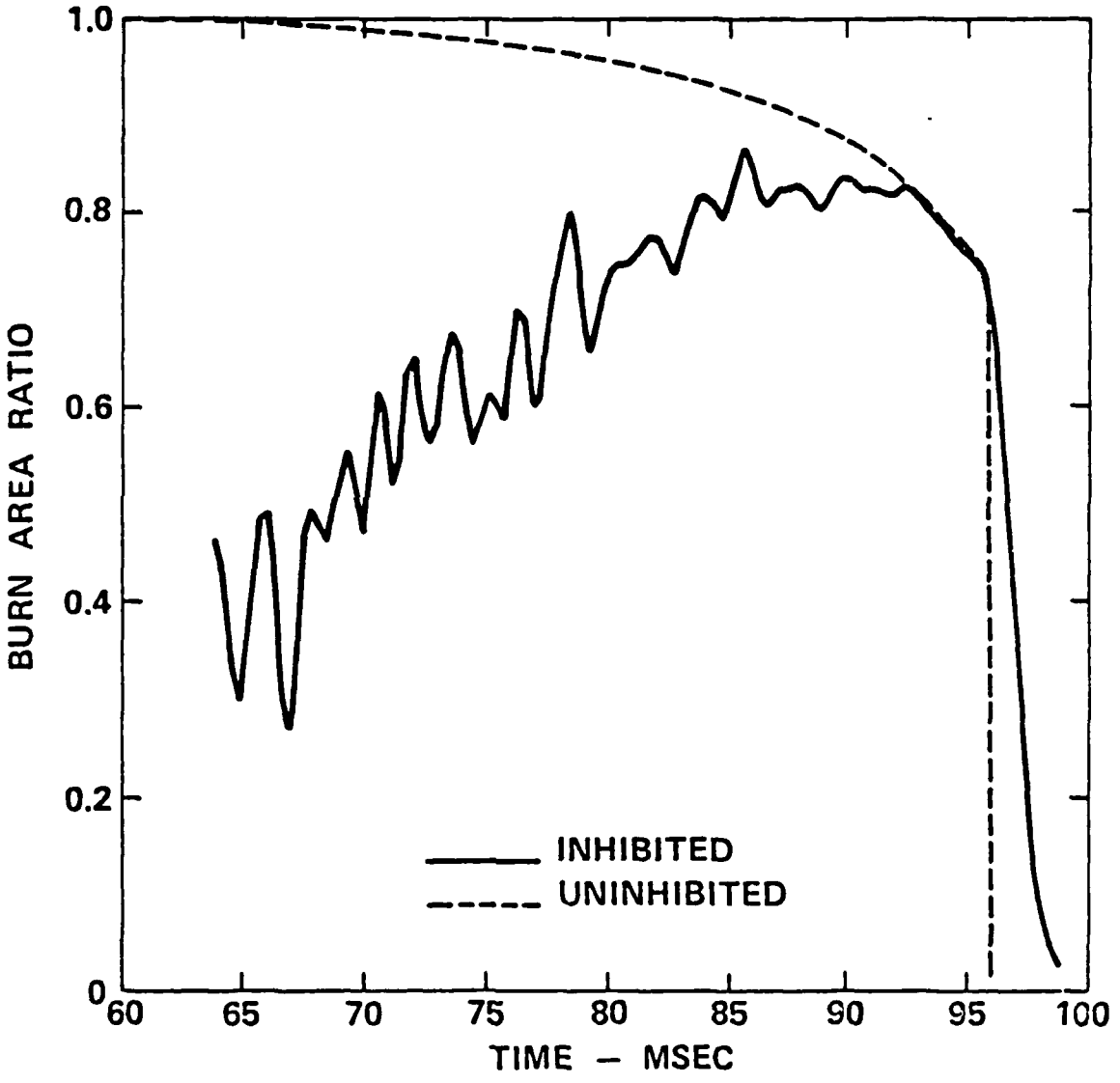

Figure 5

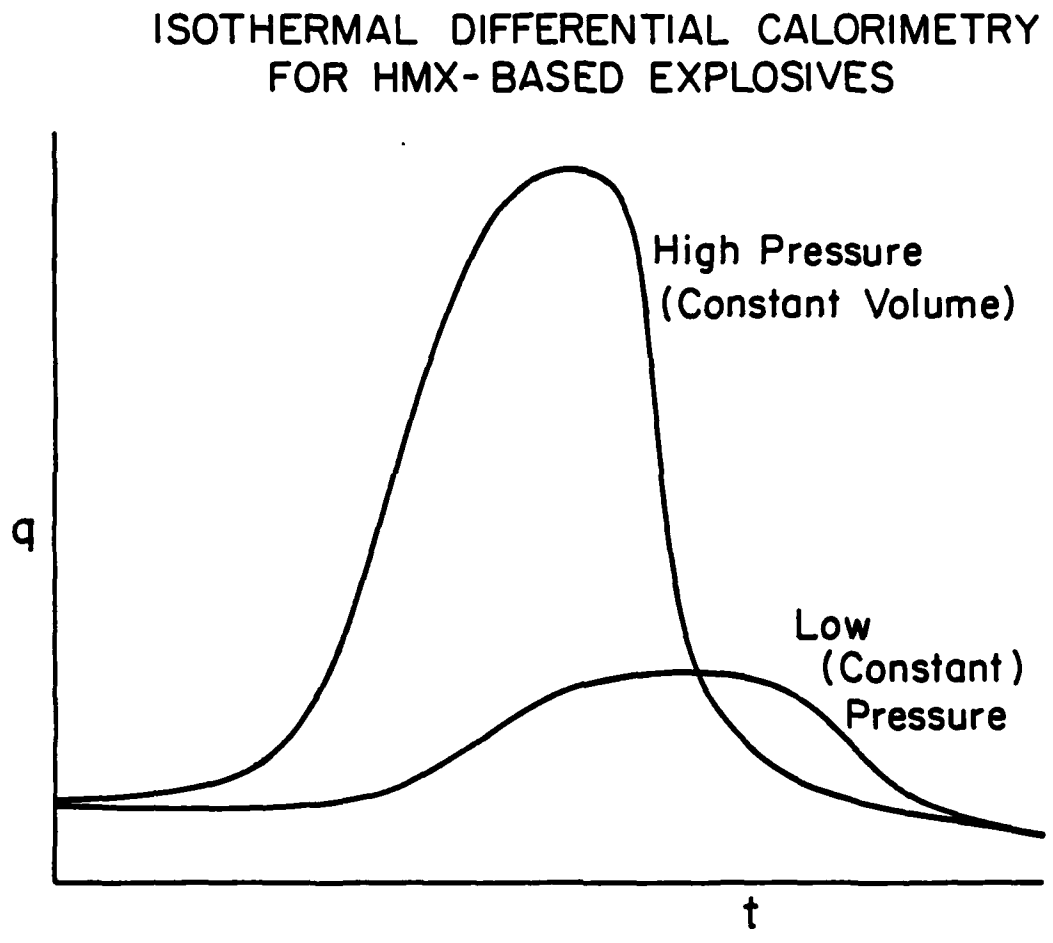

Figure 2. Rate constants in high pressure capsules are ≈10X rate constants at low pressure. Heats of reaction in high pressure capsules are 3 to 5X heats of reaction at low pressure.

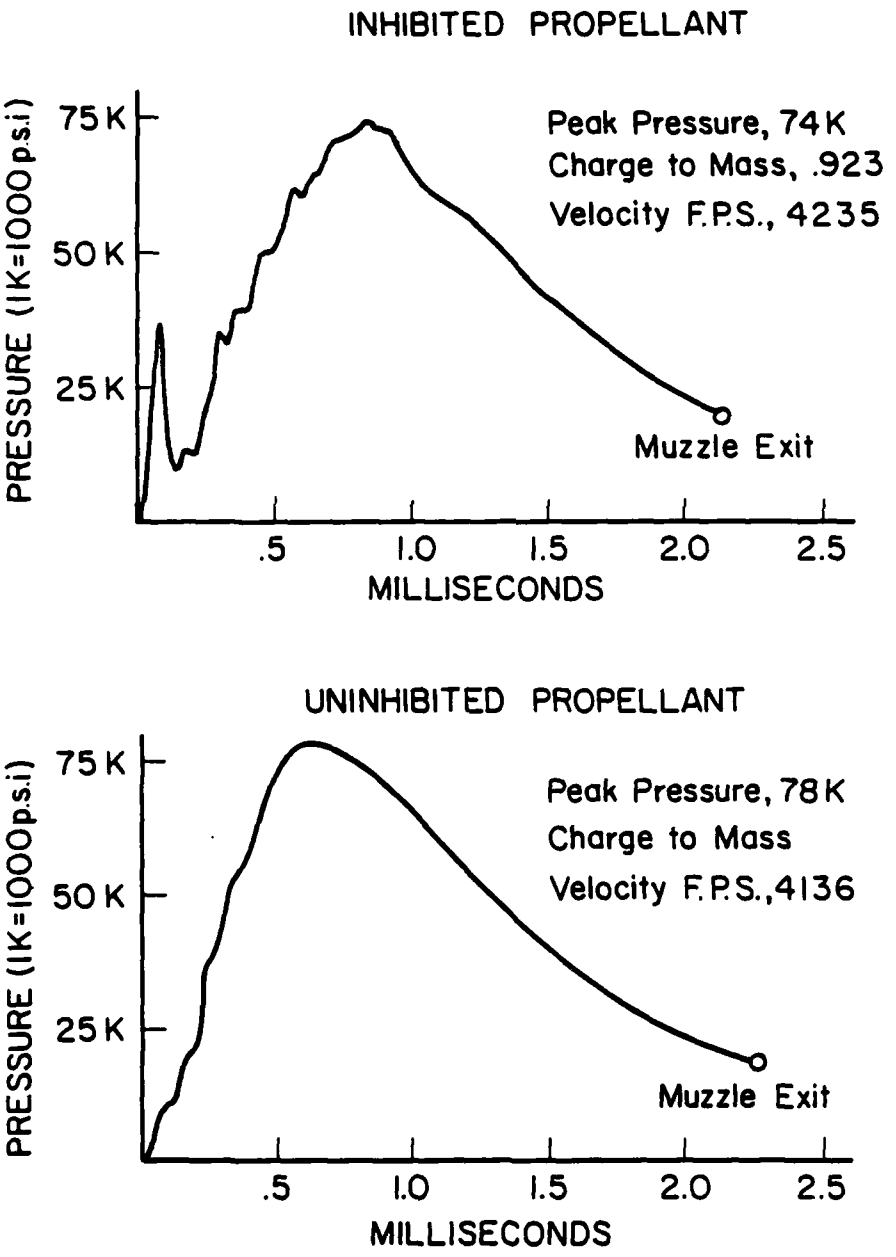
INHIBITED PROPELLANT
PRESSURE (1K=1000p.s.i)
75K
50K
25K
Peak Pressure, 74K
Charge to Mass, .923
Velocity F.P.S., 4235
Muzzle Exit
.5
1.0
1.5
2.0
2.5
MILLISECONDS
UNINHIBITED PROPELLANT
PRESSURE (1K=1000p.s.i)
75K
50K
25K
Peak Pressure, 78K
Charge to Mass
Velocity F.P.S.,4136
Muzzle Exit
.5
1.0
1.5
2.0
2.5
MILLISECONDS

Figure 6.

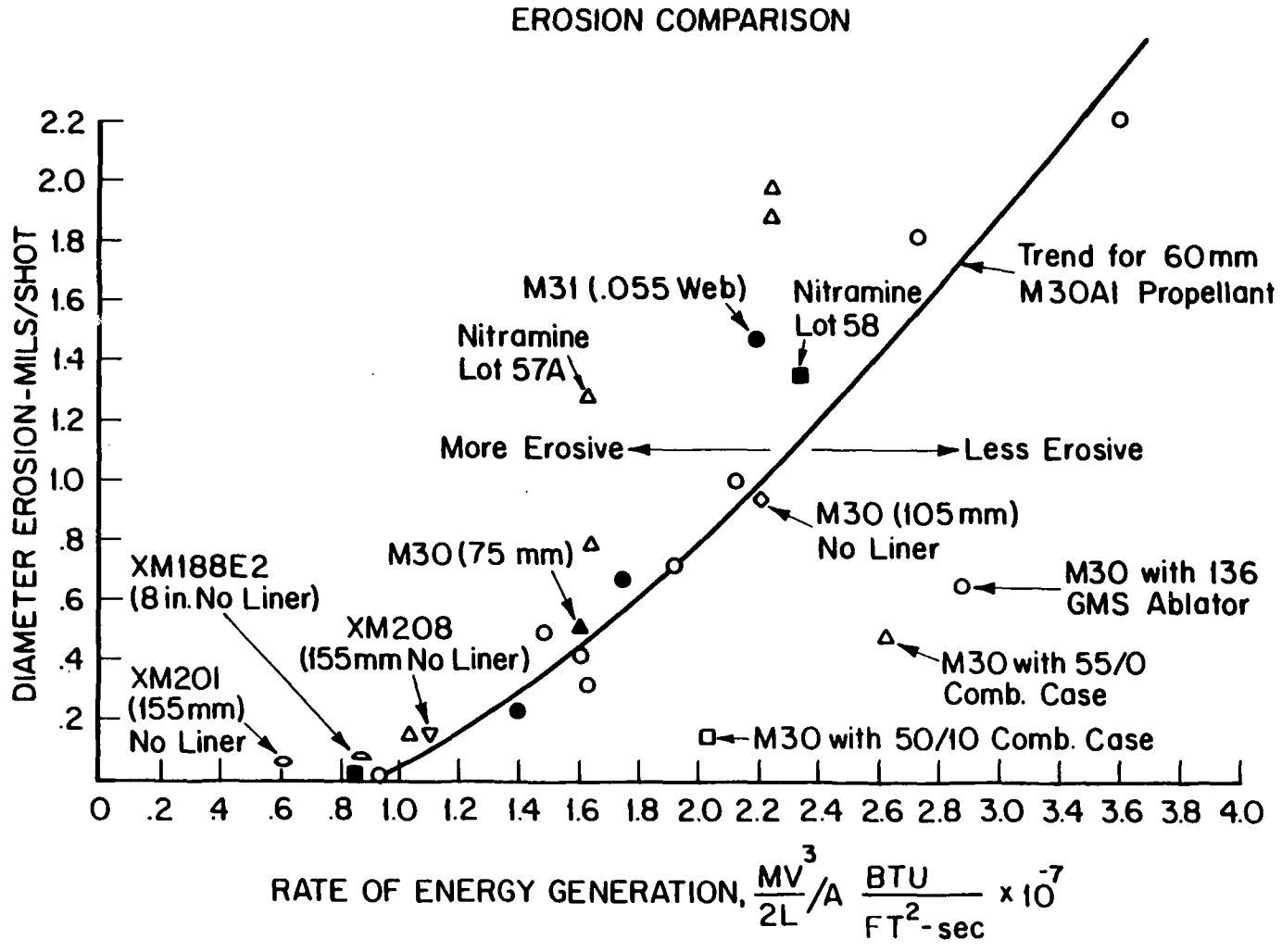
EROSION COMPARISON
DIAMETER EROSION-MILS/SHOT
2.2
2.0
1.8
1.6
1.4
1.2
1.0
.8
.6
.4
.2
M31 (.055 Web)
Nitramine Lot 58
Trend for 60mm M30A1 Propellant
Nitramine Lot 57A
More Erosive
Less Erosive
M30 (105mm) No Liner
M30 (75 mm)
XM188E2 (8 in. No Liner)
M30 with 136 GMS Ablator
XM208 (155mm No Liner)
M30 with 55/0 Comb. Case
XM201 (155mm) No Liner
M30 with 50/10 Comb. Case
0 .2 .4 .6 .8 1.0 1.2 1.4 1.6 1.8 2.0 2.2 2.4 2.6 2.8 3.0 3.4 3.6 3.8 4.0
RATE OF ENERGY GENERATION, $\frac{MV^3}{2L}/A$ $\frac{BTU}{FT^2\text{-sec}}$ $\times 10^{-7}$

Figure 3.

POTENTIAL PAYOFF OF INHIBITED GUN PROPELLANTS

- HIGHER VELOCITY PROJECTILES WITHOUT EXCESSIVE CHAMBER PRESSURES (MORE EFFECTIVE GUNS)
- MORE EFFICIENT USE OF PROPELLANT (LESS PROPELLANT NEEDED)
- LOWER PEAK PRESSURES (LIGHTER GUNS)
- LOWER PROJECTILE ACCELERATIONS (REDUCED INCIDENCE OF PREMATURES)
- LESS BORE EROSION (GREATER ACCURACY IN COMBAT)(REDUCED COST)
- MORE REPRODUCIBLE BALLISTICS (CONVENTIONAL PROPELLANT HAS TO BE REQUALIFIED UPON AGING BECAUSE DETERRANT FLAKES-OFF)
- LOWER VULNERABILITY IN COMBAT (REDUCED FLAME SPREADING IF IGNITED BY SMALL FRAGMENTS)

Figure 7

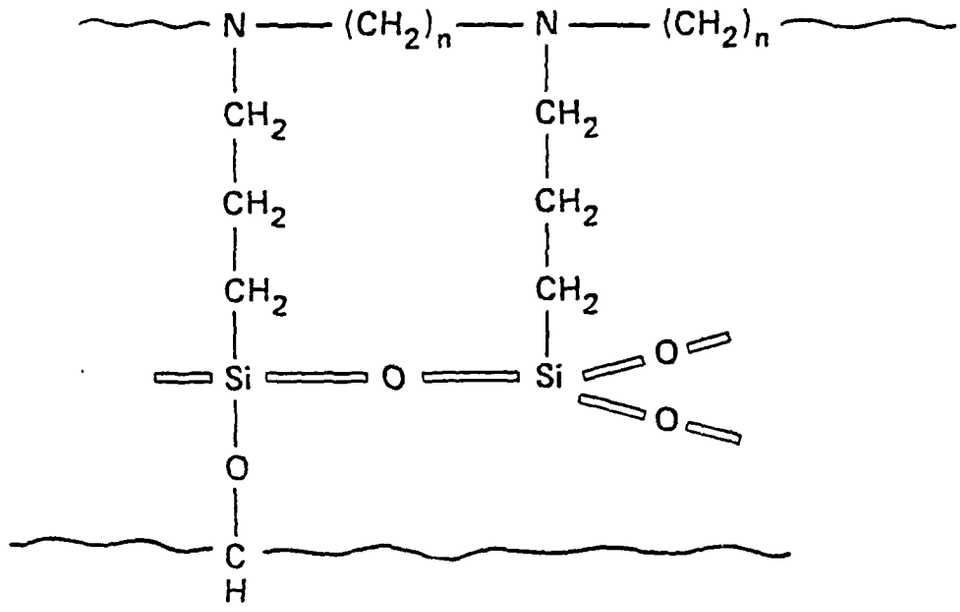

NITROCELLULOSE PROPELLANT

Figure 4. Probable Structure of Coating

IMPROVED GUN PROPELLANTS

Meeting Agenda

July 14-15, 1980

Monday, July 14

Harry Winsor, DARPA
"The Problem and Some Suggested Research Areas"

Ray McGuire, Lawrence Livermore Labs., California
"Chemistry of Decomposition of Energetic Materials"

John D. Clark, Liquid Rocket Propulsion Lab.,
New Jersey (Ret.)
"Past, Present & Future of Propellants"

Rick Morrison, Ballistics Research Lab., Maryland
"Liquid Propellant Program Survey"

Gerald Sterbutzel, CalSpan Labs., Buffalo, New York
"Heating and Erosion in Gun Barrels"

William G. Hoover, Dept. of Chemistry, UC-Davis
"Microsimulation of Adiabatic Flow"

Russell Reed, Naval Weapons Center, China Lake, California
"Gun Propellant Inhibition"

Discussion

Tuesday, July 15

Discussion

CLOSED BOMB NOSOL 318 SINGLE PERF.
1.61% INHIBITOR Y5987

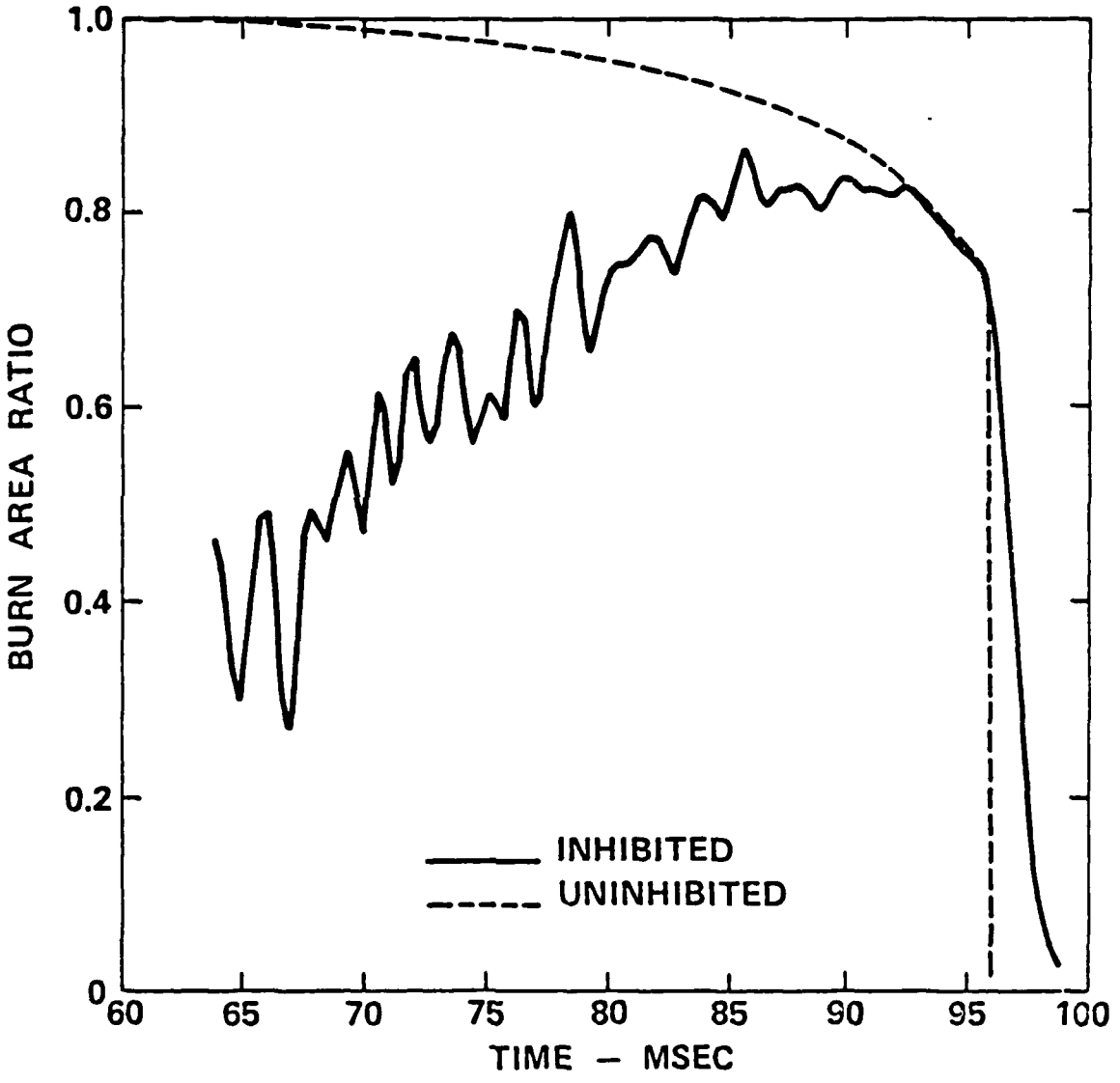

Figure 5

IMPROVED GUN PROPELLANTS

Guest Participants

John D. Clark
RD-2 Green Pond Road
Newfoundland, N.J. 07435

William G. Hoover
University of California
Hertz Hall
Berkeley, CA 94720

Gerald E. Kovalenko
Naval Air Systems Command
Jefferson Davis Highway
Washington, D.C.

Raymond McGuire
Lawrence Livermore Laboratory
L-324, Box 808
Livermore, CA 94550

Walter Morrison
U.S. Army BRL/ARRADCOM
Interior Ballistics Division
Aberdeen Proving Ground
Maryland 21005

W. George Perkins
Sandia Labs.
Division 2516
Albuquerque, NM

Russell Reed, Jr.
U.S. Naval Weapons Center
Code 388
China Lake, CA 93555

Curt Selph
U.S.A.F.
Edwards AFB, CA 93523

Philip L. Stanton
Sandia Labs.
807/3028B
Albuquerque, NM 87175

Gerald Sterbutzel
CalSpan Corporation
Advanced Technology Center
Buffalo, NY 14225

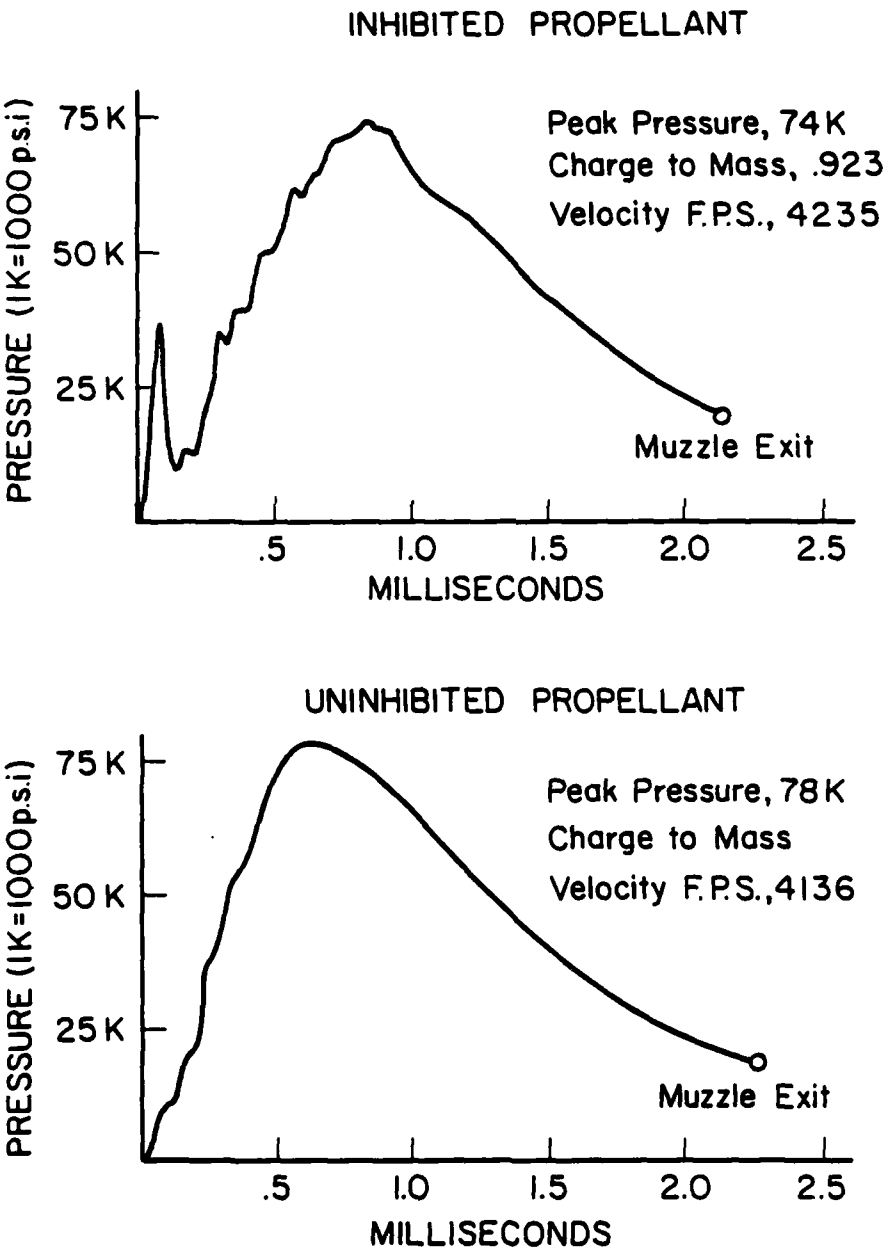
INHIBITED PROPELLANT
PRESSURE (1K=1000p.s.i)
75K
50K
25K
Peak Pressure, 74K
Charge to Mass, .923
Velocity F.P.S., 4235
Muzzle Exit
.5
1.0
1.5
2.0
2.5
MILLISECONDS
UNINHIBITED PROPELLANT
PRESSURE (1K=1000p.s.i)
75K
50K
25K
Peak Pressure, 78K
Charge to Mass
Velocity F.P.S.,4136
Muzzle Exit
.5
1.0
1.5
2.0
2.5
MILLISECONDS

Figure 6.

CONSTRAINTS ON THE DIFFUSIVE CAVITATION OF ISOLATED GRAIN BOUNDARY FACETS IN CREEPING POLYCRYSTALS

J. R. Rice

ABSTRACT

Following concepts introduced by B. F. Dyson (Metal Science, 1976, 349-353), the diffusive cavitation of grain facets is considered in circumstances for which the cavitated facets are well separated from one another. In this case the requirement of geometric compatibility between the opening grain facets and the creep-deforming polycrystalline surroundings reduces the stress transmitted to the cavitated facets, and hence increases the rupture lifetime. An evaluation of the rupture time, t_r, based on diffusional cavity growth to coalescence shows that t_r is given by the sum of two terms, one proportional to $1/D\sigma_\infty$ (where D is the grain boundary diffusion parameter and σ_∞ the stress which would act on a non-cavitated facet) and another proportional to $1/\dot{E}_\infty$ (here $\dot{E}_\infty$ is the creep rate of a similarly loaded polycrystal with uncavitated boundaries). The latter term is found to be much larger than the first at sufficiently low stress and temperature, as long as the cavitated facets are indeed well separated. This circumstance leads to results in which the cavity growth process and strain to rupture are consistent with the diffusional mechanism, but in which the rupture time t_r follows a Monkman-Grant correlation with t_r proportional to $1/\dot{E}_\infty$.

POTENTIAL PAYOFF OF INHIBITED GUN PROPELLANTS

- HIGHER VELOCITY PROJECTILES WITHOUT EXCESSIVE CHAMBER PRESSURES (MORE EFFECTIVE GUNS)
- MORE EFFICIENT USE OF PROPELLANT (LESS PROPELLANT NEEDED)
- LOWER PEAK PRESSURES (LIGHTER GUNS)
- LOWER PROJECTILE ACCELERATIONS (REDUCED INCIDENCE OF PREMATURES)
- LESS BORE EROSION (GREATER ACCURACY IN COMBAT)(REDUCED COST)
- MORE REPRODUCIBLE BALLISTICS (CONVENTIONAL PROPELLANT HAS TO BE REQUALIFIED UPON AGING BECAUSE DETERRANT FLAKES-OFF)
- LOWER VULNERABILITY IN COMBAT (REDUCED FLAME SPREADING IF IGNITED BY SMALL FRAGMENTS)

Figure 7

rate at which creep deformations of the surrounding material can accommodate such openings. The cavitated facets must then generally shed load to the surroundings until the stress σ that they carry is reduced sufficiently relative to σ_∞ that the opening rate $\dot{\delta}$ is compatible with the deformation rate of the surroundings. The result of the reduction in σ is a reduction of the rate of the diffusive cavity growth process and, in the limit of very low overall creep rates, the rate of cavity growth is determined entirely by the overall creep rate and not by the kinetics of the diffusive cavitation process.

This limiting situation, in which the cavity growth rate is proportional to the overall creep rate of essentially uncavitated material (and denoted as $\dot{E}_\infty$ here) is compatible with a Monkman-Grant[6] correlation (i.e., $\dot{E}_\infty t_r$ approximately constant, where t_r is the rupture time). Curiously, the theoretical basis for such a correlation has been sought recently[7,8,4] by concentrating on an opposite limiting case, in which the overall dislocation creep rate is large enough to interact significantly with the mecnanism of diffusive matter transport. A fairly definitive analysis[4] of this coupled process suggests, however, that predicted times for cavity growth to coalescence (based again on the tacit assumption that $\sigma = \sigma_\infty$) lead to a Monkman-Grant product that increases with stress and temperature over the practical range of each in creep applications.

This paper is an attempt to quantify Dyson's concepts in a simple but approximate manner, so that the rate of cavity growth and rupture time can be predicted.

IMPROVED GUN PROPELLANTS

Meeting Agenda

July 14-15, 1980

Monday, July 14

Harry Winsor, DARPA
"The Problem and Some Suggested Research Areas"

Ray McGuire, Lawrence Livermore Labs., California
"Chemistry of Decomposition of Energetic Materials"

John D. Clark, Liquid Rocket Propulsion Lab.,
New Jersey (Ret.)
"Past, Present & Future of Propellants"

Rick Morrison, Ballistics Research Lab., Maryland
"Liquid Propellant Program Survey"

Gerald Sterbutzel, CalSpan Labs., Buffalo, New York
"Heating and Erosion in Gun Barrels"

William G. Hoover, Dept. of Chemistry, UC-Davis
"Microsimulation of Adiabatic Flow"

Russell Reed, Naval Weapons Center, China Lake, California
"Gun Propellant Inhibition"

Discussion

Tuesday, July 15

Discussion

Analysis of Constrained Cavity Growth

Figure 1a shows the configuration which has been analyzed for void growth. Details of the calculation are done by considering the geometry of Fig. 1b, where a spherical caps void of radius a is centered in a right-circular cylinder bi-crystal of radius b; b is chosen so that $a^2/b^2 = f$ = area fraction of grain boundary which is cavitated. The applied stress is σ, as shown, and the problem is analyzed subject to a boundary condition that J_B, the grain boundary diffusive flux, vanishes at the outer radius of the grain boundary in Fig. 1b.

When σ is sufficiently small, it is appropriate to assume that the void retains a quasi-equilibrium spherical caps shape[3] and that deformability of the adjoining crystals can be neglected[4] (in the sense that the separation velocity $\dot{\delta}$ can be regarded as being the same at all points along the grain interface). In this case the expression for the rate of cavity growth can be taken from Ref. 4, which incorporates some corrections of previously published results. The result for the rate of increase of volume V of an individual void is

$$\dot{V} = 4\pi D[\sigma-(1-f)\sigma_0]/[\ell n(1/f)-(3-f)(1-f)/2] \qquad (1)$$

Here

$$D = D_B\delta_B\Omega kT$$

is the grain boundary diffusion parameter ($D_B\delta_B$ = boundary diffusivity, Ω = atomic volume, kT = energy measure of temperature, and

IMPROVED GUN PROPELLANTS

Guest Participants

John D. Clark
RD-2 Green Pond Road
Newfoundland, N.J. 07435

William G. Hoover
University of California
Hertz Hall
Berkeley, CA 94720

Gerald E. Kovalenko
Naval Air Systems Command
Jefferson Davis Highway
Washington, D.C.

Raymond McGuire
Lawrence Livermore Laboratory
L-324, Box 808
Livermore, CA 94550

Walter Morrison
U.S. Army BRL/ARRADCOM
Interior Ballistics Division
Aberdeen Proving Ground
Maryland 21005

W. George Perkins
Sandia Labs.
Division 2516
Albuquerque, NM

Russell Reed, Jr.
U.S. Naval Weapons Center
Code 388
China Lake, CA 93555

Curt Selph
U.S.A.F.
Edwards AFB, CA 93523

Philip L. Stanton
Sandia Labs.
807/3028B
Albuquerque, NM 87175

Gerald Sterbutzel
CalSpan Corporation
Advanced Technology Center
Buffalo, NY 14225

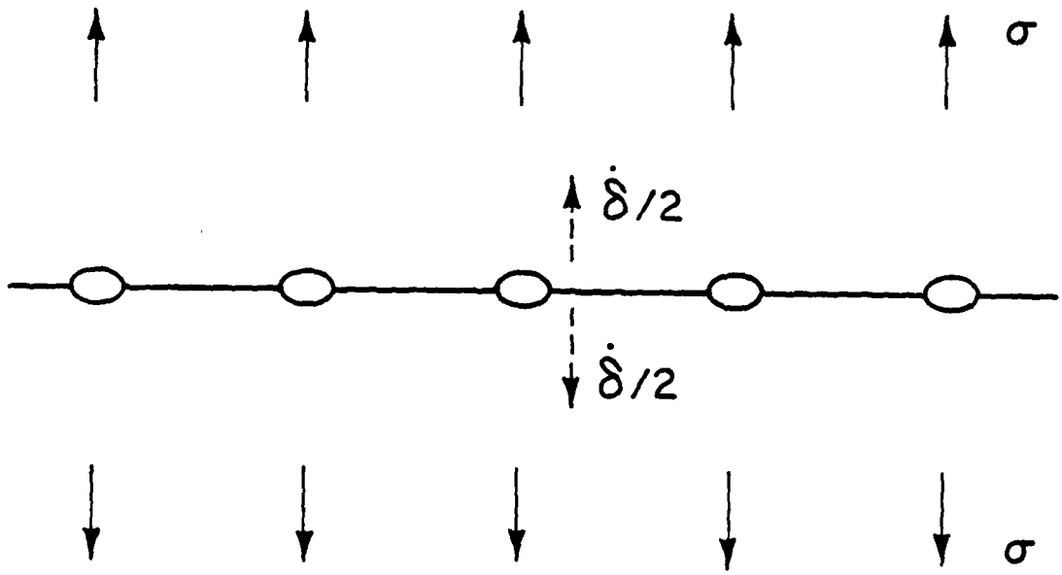

Figure 1a. A cavitated grain boundary, subjected to stress σ and separating at rate $\dot{\delta}$ due to diffusional flow of matter from the cavity surfaces into the grain boundary.

CONSTRAINTS ON THE DIFFUSIVE CAVITATION OF ISOLATED GRAIN BOUNDARY FACETS IN CREEPING POLYCRYSTALS

J. R. Rice

ABSTRACT

Following concepts introduced by B. F. Dyson (Metal Science, 1976, 349-353), the diffusive cavitation of grain facets is considered in circumstances for which the cavitated facets are well separated from one another. In this case the requirement of geometric compatibility between the opening grain facets and the creep-deforming polycrystalline surroundings reduces the stress transmitted to the cavitated facets, and hence increases the rupture lifetime. An evaluation of the rupture time, t_r, based on diffusional cavity growth to coalescence shows that t_r is given by the sum of two terms, one proportional to $1/D\sigma_\infty$ (where D is the grain boundary diffusion parameter and σ_∞ the stress which would act on a non-cavitated facet) and another proportional to $1/\dot{E}_\infty$ (here $\dot{E}_\infty$ is the creep rate of a similarly loaded polycrystal with uncavitated boundaries). The latter term is found to be much larger than the first at sufficiently low stress and temperature, as long as the cavitated facets are indeed well separated. This circumstance leads to results in which the cavity growth process and strain to rupture are consistent with the diffusional mechanism, but in which the rupture time t_r follows a Monkman-Grant correlation with t_r proportional to $1/\dot{E}_\infty$.

$a^2/b^2 = f$

$\cos\cdot\psi = \gamma_B/2\gamma_S$

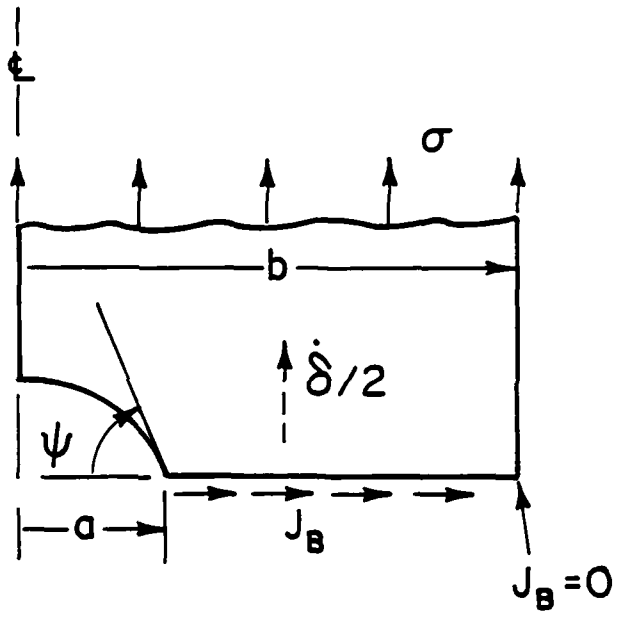

Figure 1b. Axi-symmetric geometry employed for analysis of cavity growth; f is the area fraction of cavitated boundary.

rate at which creep deformations of the surrounding material can accommodate such openings. The cavitated facets must then generally shed load to the surroundings until the stress σ that they carry is reduced sufficiently relative to σ_∞ that the opening rate $\dot{\delta}$ is compatible with the deformation rate of the surroundings. The result of the reduction in σ is a reduction of the rate of the diffusive cavity growth process and, in the limit of very low overall creep rates, the rate of cavity growth is determined entirely by the overall creep rate and not by the kinetics of the diffusive cavitation process.

This limiting situation, in which the cavity growth rate is proportional to the overall creep rate of essentially uncavitated material (and denoted as $\dot{E}_\infty$ here) is compatible with a Monkman-Grant[6] correlation (i.e., $\dot{E}_\infty t_r$ approximately constant, where t_r is the rupture time). Curiously, the theoretical basis for such a correlation has been sought recently[7,8,4] by concentrating on an opposite limiting case, in which the overall dislocation creep rate is large enough to interact significantly with the mecnanism of diffusive matter transport. A fairly definitive analysis[4] of this coupled process suggests, however, that predicted times for cavity growth to coalescence (based again on the tacit assumption that $\sigma = \sigma_\infty$) lead to a Monkman-Grant product that increases with stress and temperature over the practical range of each in creep applications.

This paper is an attempt to quantify Dyson's concepts in a simple but approximate manner, so that the rate of cavity growth and rupture time can be predicted.

$$\sigma_0 = 2\gamma_s \ (\sin \psi)/a$$

is the "sintering" stress (γ_s = surface free energy, ψ = cavity tip angle, Fig. 1b). Two related parameters of interest are calculated from Eq. (1). First, by writing the cavity volume as

$$V = (4\pi/3)a^3h \qquad (2)$$

where[3] $h = h(\psi)$ depends on the cavity tip angle (and $h = 0.6$ for $\psi = 70°$, as is typical), one has

$$\dot{a} = \dot{V}/4\pi a^2 h = (D/a^2h)[\sigma-(1-f)\sigma_0]/[\ell n(1/f)-(3-f)(1-f)/2] \qquad (3)$$

for the rate of cavity growth. Also, for mass conservation it is evident from the geometry of Fig. 1b that

$$\dot{V} = \pi b^2 \dot{\delta} \quad ,$$

so that the rate of opening of the cavitated boundary is

$$\dot{\delta} = \dot{V}/\pi b^2 = (4D/b^2)[\sigma-(1-f)\sigma_0]/[\ell n(1/f)-(3-f)(1-f)/2] \qquad (4)$$

Now, as noted in the discussion based on Dyson's[5] paper, for a relatively isolated, cavitated grain facet (Fig. 1c), the stress σ and opening rate $\dot{\delta}$ in Eq. (4) must be consistent with the constraints set the surroundings of that facet. The deformation of the surroundings should be modelled in a way dependent, for example, on the proximity of other cavitated facets, on the ease of sliding of grain boundaries, and on the deformation mode (dislocation and/or diffusional creep) of the grains. In the

Analysis of Constrained Cavity Growth

Figure 1a shows the configuration which has been analyzed for void growth. Details of the calculation are done by considering the geometry of Fig. 1b, where a spherical caps void of radius a is centered in a right-circular cylinder bi-crystal of radius b; b is chosen so that $a^2/b^2 = f$ = area fraction of grain boundary which is cavitated. The applied stress is σ, as shown, and the problem is analyzed subject to a boundary condition that J_B, the grain boundary diffusive flux, vanishes at the outer radius of the grain boundary in Fig. 1b.

When σ is sufficiently small, it is appropriate to assume that the void retains a quasi-equilibrium spherical caps shape[3] and that deformability of the adjoining crystals can be neglected[4] (in the sense that the separation velocity $\dot{\delta}$ can be regarded as being the same at all points along the grain interface). In this case the expression for the rate of cavity growth can be taken from Ref. 4, which incorporates some corrections of previously published results. The result for the rate of increase of volume V of an individual void is

$$\dot{V} = 4\pi D[\sigma-(1-f)\sigma_0]/[\ell n(1/f)-(3-f)(1-f)/2] \qquad (1)$$

Here

$$D = D_B\delta_B\Omega kT$$

is the grain boundary diffusion parameter ($D_B\delta_B$ = boundary diffusivity, Ω = atomic volume, kT = energy measure of temperature, and

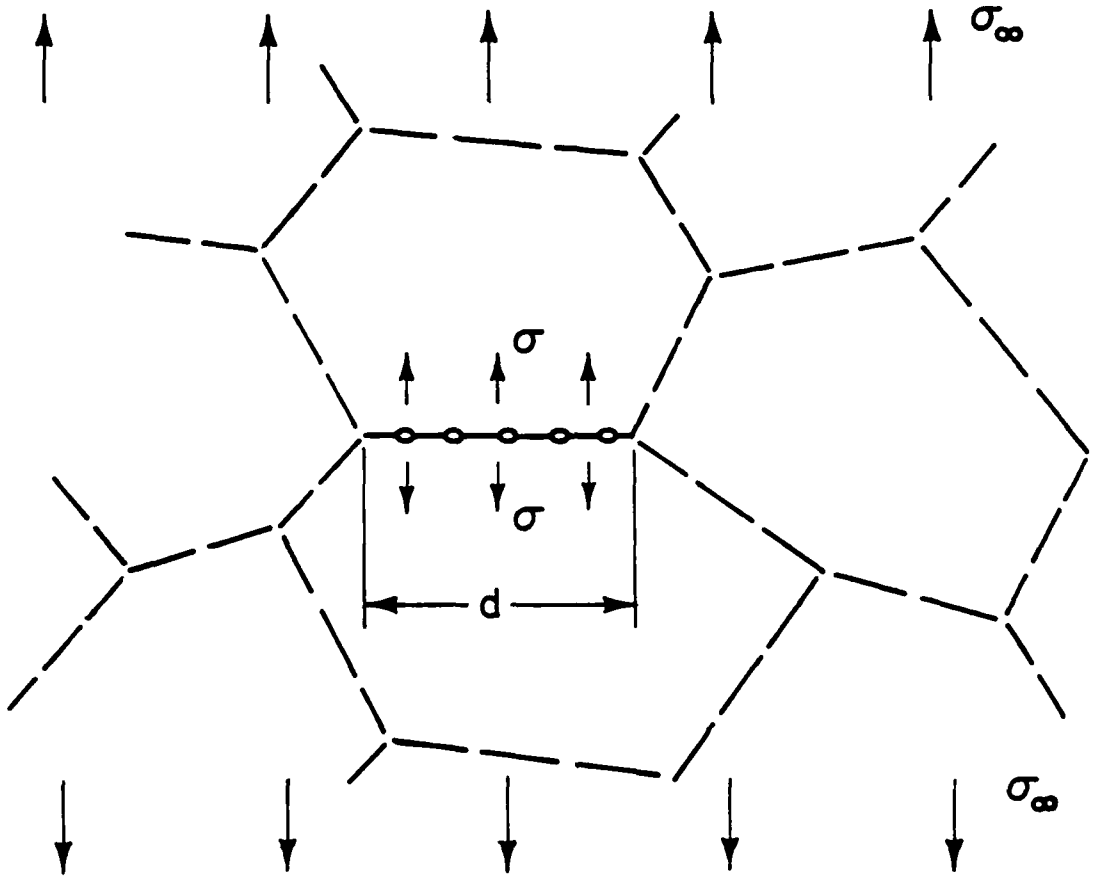

Figure 1c. An isolated, cavitated grain boundary facet in a polycrystal; the stress σ will generally be reduced from the stress σ_∞ which would act across the facet in the absence of cavitation.

interest of developing a simple approximation, we shall consider σ and $\dot{\delta}$ to represent average quantities for the facet and neglect the fact that both of these will be nonuniform.

If the grain facet of diameter d (Fig. 1c) is modelled as

close in the case of a linear viscous material in uniaxial tension; the spherical hole opens at a rate which is just $\pi/4$ times that for the disc-shaped void[4].) Taking the ratio of the volumetric growth rate from Budiansky et al.[9] for a void in a nonlinear viscous material with n=5 to that for a void in a linear material, and noting the form of Eq. (5), one estimates that

$$\alpha/\alpha_{linear} \simeq 1.42 \quad \text{for } n = 5 \ .$$

Thus, since $\alpha_{linear} = 2/\pi = 0.64$, the estimate is $\alpha = 0.90$ for $n = 5$. Corresponding results are $\alpha = 0.84$ for $n = 3$ and $\alpha = 0.98$ for $n = 10$. Hence, if power-law dislocation creep takes place among the adjoining grains, with negligible grain boundary sliding, a value of $\alpha = 0.9$ can be considered representative in Eq. (5).

Slightly different forms of the result in Eq. (5) result for other mechanisms. For example, if all grain boundaries slide freely, it is appropriate to interpret σ_∞ in Eq. (5) not as the remotely applied stress but rather as the stress which would result on a coherent, non-cavitating grain facet oriented perpendicular to the tensile stress. This is estimated in the Appendix as $\sigma_\infty \simeq 1.5 \times$ (the remotely applied stress); the result applies regardless of whether the grains deform by linear or nonlinear creep or, indeed, whether the grain interiors remain rigid and all macroscopic deformation occurs by diffusional volume and/or grain boundary transport. The presence of freely sliding grain boundaries does, however, increase α over the estimates given previously. The amount of increase is unknown but it is argued

in the Appendix that perhaps a doubling of the previous α values (equivalent to doubling the effective size of the cavitated facet diameter, d, would provide a reasonable estimate, so long as the cavitated boundaries are indeed very well isolated from one another.

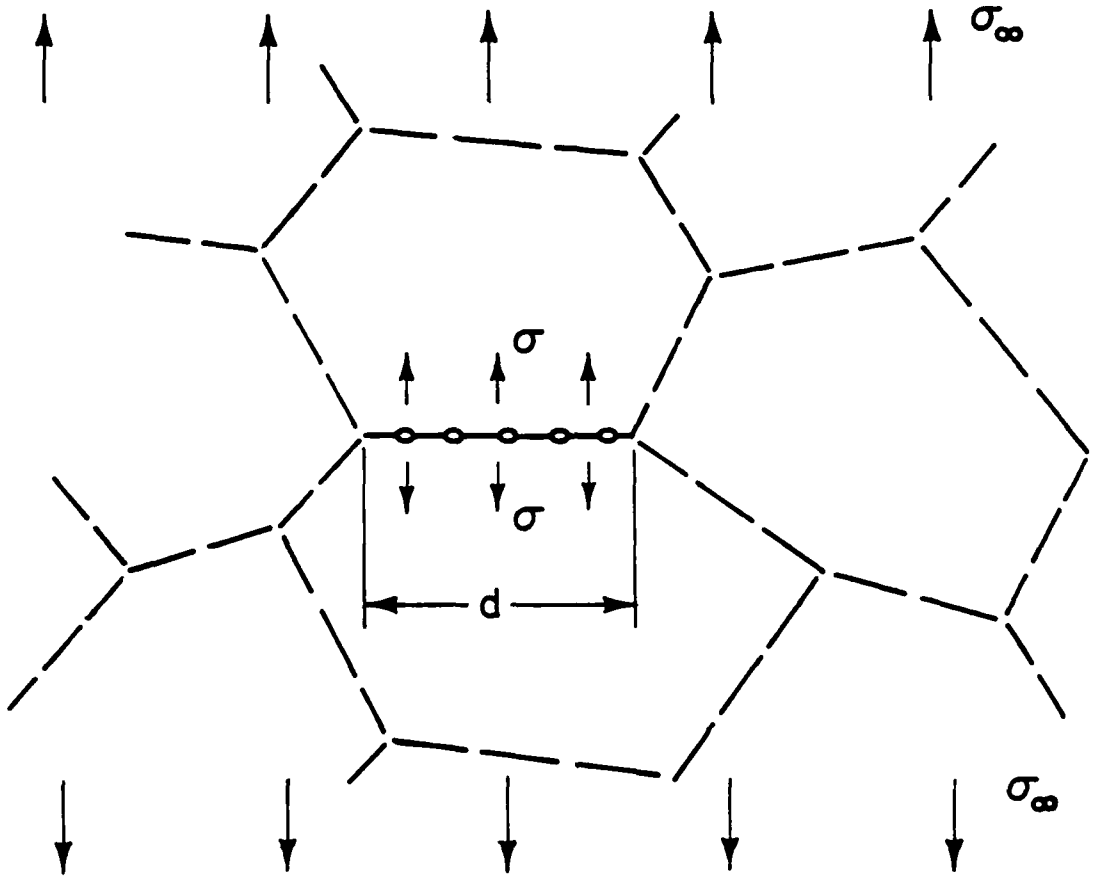

Figure 1c. An isolated, cavitated grain boundary facet in a polycrystal; the stress σ will generally be reduced from the stress σ_∞ which would act across the facet in the absence of cavitation.

Here

$$L = (D\sigma_\infty/\dot{E}_\infty)^{1/3} \tag{7}$$

is a stress level and temperature dependent parameter with length dimensions introduced by Rice[10]. Extensive tabulations of its values for pure metals undergoing power-law creep (with activation energy equal to that for self diffusion) have been given by Needleman and Rice[4]. The parameter has the form[4,10]

$$L = L_0 \exp(\kappa T_m/T)(\mu/10^3\sigma_\infty)^{(n-1)/3}$$

where μ is the elastic shear modulus and L_0 and κ are tabulated constants. The results are such that at $T=0.5T_m$ and $\sigma_\infty = 10^{-3}\mu$, $L \simeq 2$ to 6 μm for fcc metals (but lower for Al and higher for Ag) and 0.25 to 0.35 μm for bcc metals. The sizes for L increase by about a factor of 20 when σ_∞ is reduced by a factor of 10 to 10^{-4} μ; L also increases with decreasing temperature, in a manner consistent with $\kappa \simeq 2.4$ to 3.9 for fcc and 1.7 to 2.2 for bcc.

The significance of the parameter L as introduced in Refs. 4 and 10 is that when L (but as based on the <u>local</u> stress σ and associated strain rate in the adjoining grains) is comparable to or smaller than the void half spacing length b, interactions between creep deformability of the grains and diffusion occur which invalidate Eqs. (1,3,4). When L is sufficiently large, such interactions do not occur. But it is seen from Eq. (6) that the constraint effects discussed here become important when L is large (more precisely, when $4L^3/\alpha b^2 d$ is comparable to or larger than

$\ell n(1/f)$ and σ may then be very much reduced from σ_∞, at least if the cavitated facets are well isolated.

The result for $\sigma-(1-f)\sigma_0$ from Eq. (6) may be used in Eq. (3) for $\dot{a}$ to obtain

$$\dot{a} = (D/a^2h)[\sigma_\infty-(1-f)\sigma_0]/[(4L^3/\alpha b^2 d)+\ell n(1/f)-(3-f)(1-f)/2] \quad (8)$$

This expresses the cavity growth rate under constrained conditions.

To compute t_r as defined, we represent $\dot{a}$ of Eq. (8) symbolically as $\dot{a} = 1/f(a)$ so that the rupture time is given as

$$t_r = \int_{a_i}^{b} F(a)da \tag{9}$$

where a_i is the initial cavity radius. Now, by inspection it is clear that F(a) can be split into the sum of two terms

$$F(a) = F_1(a) + F_2(a) \tag{10}$$

where

$$F_1(a) = (ha^2/D\sigma_\infty)[\ell n(1/f)-(3-f)(1-g)/2]/[1-(1-f)2\gamma_s \sin\psi/\sigma_\infty a]$$

$$F_2(a) = (ha^2/D\sigma_\infty)(4L^3/\alpha b^2 d)/[1-(1-f)2\gamma_s \sin\psi/\sigma_\infty a] \tag{11}$$

$$= (4ha^2/\alpha \dot{E}_\infty b^2 d)/[1-(1-f)2\gamma_s \sin\psi/\sigma_\infty a]$$

and where it is recalled that $f = a^2/b^2$. The first of these, $F_1(a)$, is the form taken by F(a) in the unconstrained case, when $\sigma = \sigma_\infty$ throughout the growth process. Accordingly,

$$t_r = (t_r)_1 + (t_r)_2 \tag{12}$$

where

$$(t_r)_1 = \int_{a_i}^{b} F_1(a)da \tag{13}$$

is the rupture time as predicted on the basis of the Hull-Rimmer growth mechanism for the unconstrained case of an infinite g.b. (Fig. 1a) with $\sigma = \sigma_\infty$, and where

close in the case of a linear viscous material in uniaxial tension; the spherical hole opens at a rate which is just $\pi/4$ times that for the disc-shaped void[4].) Taking the ratio of the volumetric growth rate from Budiansky et al.[9] for a void in a nonlinear viscous material with n=5 to that for a void in a linear material, and noting the form of Eq. (5), one estimates that

$$\alpha/\alpha_{linear} \simeq 1.42 \quad \text{for } n = 5 \ .$$

Thus, since $\alpha_{linear} = 2/\pi = 0.64$, the estimate is $\alpha = 0.90$ for $n = 5$. Corresponding results are $\alpha = 0.84$ for $n = 3$ and $\alpha = 0.98$ for $n = 10$. Hence, if power-law dislocation creep takes place among the adjoining grains, with negligible grain boundary sliding, a value of $\alpha = 0.9$ can be considered representative in Eq. (5).

Slightly different forms of the result in Eq. (5) result for other mechanisms. For example, if all grain boundaries slide freely, it is appropriate to interpret σ_∞ in Eq. (5) not as the remotely applied stress but rather as the stress which would result on a coherent, non-cavitating grain facet oriented perpendicular to the tensile stress. This is estimated in the Appendix as $\sigma_\infty \simeq 1.5 \times$ (the remotely applied stress); the result applies regardless of whether the grains deform by linear or nonlinear creep or, indeed, whether the grain interiors remain rigid and all macroscopic deformation occurs by diffusional volume and/or grain boundary transport. The presence of freely sliding grain boundaries does, however, increase α over the estimates given previously. The amount of increase is unknown but it is argued

$$(t_r)_2 = \int_{a_i}^{b} F_2(a)\,da \tag{14}$$

includes the effect of constraints on the growth mechanism. Note that these times scale with the parameters of the problem as

$$(t_r)_1 = (hb^3/D\sigma_\infty)\times(\text{a function of } a_i/b \text{ and } 2\gamma_s\sin\psi/\sigma_\infty a_i)$$

$$(t_r)_2 = (hb/\alpha\dot{E}_\infty d)\times(\text{another function of } a_i/b \text{ and } 2\gamma_s\sin\psi/\sigma_\infty a_i) \tag{15}$$

It is remarkable that $(t_r)_1$ contains only terms that refer to grain boundary diffusion and $(t_r)_2$ to the deformations of he constraining surroundings.

The last parameter, $2\gamma_s\sin\psi/\sigma_\infty a_i$, is the ratio of the sintering stress level at the start of growth to the remotely applied stress. This is often quite small compared to unity and when it is the integrals involved in Eqs. (13,14) are elementary, resulting in

$$(t_r)_1 = \frac{16hb^3}{315D\sigma_\infty}\left[1 - \frac{105}{16} f_i^{3/2} \ln(1/f_i) - \frac{1}{8} f_i^{3/2}\left(63 f_i^{1/2} - \frac{175}{4} - \frac{45}{4} f_i\right)\right]$$

$$(t_r)_2 = \frac{4hb}{3\alpha\dot{E}_\infty d}\left(1 - f_i^{3/2}\right) \tag{16}$$

where

$$f_i = a_i^2/b^2 \quad .$$

It is instructive to consider the ratio of these two contributions to t_r. First consider the case when a_i/b is sufficiently small (say, 1/10 or less) that f_i can be replaced

by zero in Eqs. (16). In that case

$$(t_r)_2/(t_r)_3 = 105D\sigma_\infty/4\alpha\dot{E}_\infty b^2 d = (105/4\alpha)(L^3/b^2 d) \qquad (17)$$

Where L is the temperature and stress level dependent parameter of Eq. (7). Obviously, if the stress and temperature are suffi-

Conclusions

The problem of diffusive void growth on isolated grain boundary facets has been analyzed. It is shown that the "rupture time", as defined in the previous section, can be split as in Eq. (12) into the sum of two contributions, $(t_r)_1$ and $(t_r)_2$. As indicated by Eqs. (15,16), $(t_r)_1$ is proportional to $b^3/D\sigma_\infty$ where 2b is the cavity spacing, D is the grain boundary diffusion parameter (defined following Eq. (1)), and where σ_∞ is either the applied stress or a factor of approximately 1.5 times it, depending on whether the grain boundaries are nonslipping or freely sliding; $(t_r)_2$ is proportional to $b/\alpha\dot{E}_\infty d$ where d is the grain facet size, $\dot{E}_\infty$ the creep rate of a similarly loaded but noncavitated polycrystal, and α is a parameter which has been estimated to vary from approximately 0.9 to 1.8 (depending again on whether the g.b.'s are nonslipping or freely sliding) for well isolated, noninteresting, cavitated facets, but which can be very much larger for interacting facets.

The ratio of $(t_r)_2$ to $(t_r)_1$ is approximately $(105/4\alpha)$ (L^3/b^2d), at least for small initial radii of the cavities and applied stress levels which are well above the sintering limit. Here L is the length parameter of Eq. (7) and Refs. 4,10; it decreases with increasing temperature and stress in the power-law creep regime. This ratio of $(t_r)_2$ to $(t_r)_1$ can be very much larger than unity at sufficiently low stress and temperature. In such circumstances the Monkman-Grant product $\dot{E}_\infty t_r$ is predicted to have a constant value, equal approximately to $0.8b/\alpha d$, which is

Here

$$L = (D\sigma_\infty/\dot{E}_\infty)^{1/3} \tag{7}$$

is a stress level and temperature dependent parameter with length dimensions introduced by Rice[10]. Extensive tabulations of its values for pure metals undergoing power-law creep (with activation energy equal to that for self diffusion) have been given by Needleman and Rice[4]. The parameter has the form[4,10]

$$L = L_0 \exp(\kappa T_m/T)(\mu/10^3\sigma_\infty)^{(n-1)/3}$$

where μ is the elastic shear modulus and L_0 and κ are tabulated constants. The results are such that at $T=0.5T_m$ and $\sigma_\infty = 10^{-3}\mu$, $L \simeq 2$ to 6 μm for fcc metals (but lower for Al and higher for Ag) and 0.25 to 0.35 μm for bcc metals. The sizes for L increase by about a factor of 20 when σ_∞ is reduced by a factor of 10 to 10^{-4} μ; L also increases with decreasing temperature, in a manner consistent with $\kappa \simeq 2.4$ to 3.9 for fcc and 1.7 to 2.2 for bcc.

The significance of the parameter L as introduced in Refs. 4 and 10 is that when L (but as based on the <u>local</u> stress σ and associated strain rate in the adjoining grains) is comparable to or smaller than the void half spacing length b, interactions between creep deformability of the grains and diffusion occur which invalidate Eqs. (1,3,4). When L is sufficiently large, such interactions do not occur. But it is seen from Eq. (6) that the constraint effects discussed here become important when L is large (more precisely, when $4L^3/\alpha b^2 d$ is comparable to or larger than

of the order 0.4 to 0.9 b/d for well isolated, noninteracting cavitated facets.

The paper shows, following concepts introduced by Dyson[5], that the void growth mechanism may be diffusional, and that rupture strains may have small values usually associated with diffusional growth, while the time to rupture is controlled by the overall dislocation creep rate.

It remains for future work to deal with cases for which the cavitated grain facets are sufficiently close to interact with one another[5], or for which the stress levels transmitted to the cavitated facets are large enough to invalidate the Hull-Rimmer diffusional growth model with a quasi-equilibrium, spherical-caps cavity shape[3] and with effectively rigid separation of the adjoining grains[4].

ACKNOWLEDGEMENT

This research was initiated under support of the NSF Materials Research Laboratory at Brown University and completed under support of the Defense Advanced Research Projects Agency of the Department of Defense under Contract No. MDA903-80C-0505 with The University of Michigan. The author is grateful to B. F. Dyson, A. G. Evans, D. MacLean and J. W. Hutchinson for helpful discussions.

$\ell n(1/f)$ and σ may then be very much reduced from σ_∞, at least if the cavitated facets are well isolated.

The result for $\sigma-(1-f)\sigma_0$ from Eq. (6) may be used in Eq. (3) for $\dot{a}$ to obtain

$$\dot{a} = (D/a^2h)[\sigma_\infty-(1-f)\sigma_0]/[(4L^3/\alpha b^2 d)+\ell n(1/f)-(3-f)(1-f)/2] \quad (8)$$

This expresses the cavity growth rate under constrained conditions. Comparing to Eq. (3), it is seen that σ_∞ replaces σ and the numerator has been augmented by $4L^3/\alpha b^2 d$.

Expression for the Rupture Time

Using the previous result for $\dot{a}$, the "rupture time" t_r is calculated here. This time is defined as that for cavities to grow from some initial radius a_i to coalescence (a=b) on the cavitated facet. It should agree with the actual lifetime if the time to cavity nucleation is insignificant and if final failure follows shortly after complete cavitation of the isolated grain boundary facets. Otherwise, t_r might be considered a lower bound, although it is well to remember that the rupture process may be rather more complicated than this simple description suggests. For example, the shedding of load from the cavitated facets, which becomes more severe as f increases towards unity (see Eq. (6)), implies an increase of stress in adjoining material. This stress concentration may locally accelerate the grain boundary sliding rates and cause cavities to nucleate and grow on nearby facets which are favorably oriented relative to the tensile direction.

References

1. D. Hull and D. E. Rimmer, Phil. Mag., 4, 673 (1959).

2. R. Raj and M. F. Ashby, Acta Met., 23, 653 (1975).

3. T-j. Chuang, K. I. Kagawa, J. R. Rice and L. Sills, Acta Met., 27, 265 (1979).

4. A. Needleman and J. R. Rice, Acta Met., in press (1980).

5. B. F. Dyson, Metal Sci., 349 (1976).

6. F. C. Monkman and N. J. Grant, Proc. ASTM, 56, 593 (1956).

7. W. Beere and M. V. Speight, Metal Sci., 12, 172 (1978).

8. G. H. Edward and M. F. Ashby, Acta Met., 27, 1505 (1979).

9. B. Budiansky, J. W. Hutchinson, and S. Slutsky, in Mechanics of Solids, The Rodney Hill 60th Anniversary Volume (edited by H. G. Hopkins and M. J. Sewell), Pergamon Press, Oxford, publication expected, 1981.

10. J. R. Rice, in Time-Dependent Fracture of Materials at Elevated Temperature (edited by S. M. Wolf), U. S. Dept. of Energy Report CONF790236 UC-25, p.130 (1979).

11. A. E. Green and W. Zerna, Theoretical Elasticity, Oxford (Clarendon) Press, Oxford (1954).

To compute t_r as defined, we represent $\dot{a}$ of Eq. (8) symbolically as $\dot{a} = 1/f(a)$ so that the rupture time is given as

$$t_r = \int_{a_i}^{b} F(a)da \tag{9}$$

where a_i is the initial cavity radius. Now, by inspection it is clear that F(a) can be split into the sum of two terms

$$F(a) = F_1(a) + F_2(a) \tag{10}$$

where

$$F_1(a) = (ha^2/D\sigma_\infty)[\ell n(1/f)-(3-f)(1-g)/2]/[1-(1-f)2\gamma_s \sin\psi/\sigma_\infty a]$$

$$F_2(a) = (ha^2/D\sigma_\infty)(4L^3/\alpha b^2 d)/[1-(1-f)2\gamma_s \sin\psi/\sigma_\infty a] \tag{11}$$

$$= (4ha^2/\alpha \dot{E}_\infty b^2 d)/[1-(1-f)2\gamma_s \sin\psi/\sigma_\infty a]$$

and where it is recalled that $f = a^2/b^2$. The first of these, $F_1(a)$, is the form taken by F(a) in the unconstrained case, when $\sigma = \sigma_\infty$ throughout the growth process. Accordingly,

$$t_r = (t_r)_1 + (t_r)_2 \tag{12}$$

where

$$(t_r)_1 = \int_{a_i}^{b} F_1(a)da \tag{13}$$

is the rupture time as predicted on the basis of the Hull-Rimmer growth mechanism for the unconstrained case of an infinite g.b. (Fig. 1a) with $\sigma = \sigma_\infty$, and where

APPENDIX

Consider a disc-shaped crack of diameter d in a homogeneous linear elastic solid subjected to uniform tension σ_∞ far from the crack. The opening displacement ΔU between the upper and lower crack surfaces is available from many sources (e.g., Green and Zerna[11]) and is

$$\Delta U = [4\sigma_\infty(1-\nu)/\pi G]\ \sqrt{(d/2)^2-r^2}$$

where r is the distance from the crack center, ν the Poisson ratio and G the shear modulus. By integrating ΔU over the area of the crack and writing the results as $\pi(d/2)^2\delta$, so that δ is the average opening, one obtains

$$\delta = 4(1-\nu)\sigma_\infty d/3\pi G \quad .$$

If the crack surfaces are not stress free, but instead transmit a tension σ then, by an elementary superposition

$$\delta = 4(1-\nu)(\sigma_\infty-\sigma)d/3\pi G \quad .$$

Now, since the remote strain E_∞ due to the remote uniaxial tension is $\sigma_\infty/2(1+\nu)G$, the result may be rewritten as

$$\delta = [8(1-\nu^2)/3\pi][(\sigma_\infty-\sigma)/\sigma_\infty]E_\infty d \quad .$$

By the analogy between linear elastic and linear viscous materials, the same result holds for a crack in a homogeneous linear viscous material if δ and E_∞ are replaced by their rates and, since the linear viscous material is usually regarded as

$$(t_r)_2 = \int_{a_i}^{b} F_2(a)\,da \tag{14}$$

includes the effect of constraints on the growth mechanism. Note that these times scale with the parameters of the problem as

$$(t_r)_1 = (hb^3/D\sigma_\infty)\times(\text{a function of } a_i/b \text{ and } 2\gamma_s\sin\psi/\sigma_\infty a_i)$$

$$(t_r)_2 = (hb/\alpha\dot{E}_\infty d)\times(\text{another function of } a_i/b \text{ and } 2\gamma_s\sin\psi/\sigma_\infty a_i) \tag{15}$$

It is remarkable that $(t_r)_1$ contains only terms that refer to grain boundary diffusion and $(t_r)_2$ to the deformations of he constraining surroundings.

The last parameter, $2\gamma_s\sin\psi/\sigma_\infty a_i$, is the ratio of the sintering stress level at the start of growth to the remotely applied stress. This is often quite small compared to unity and when it is the integrals involved in Eqs. (13,14) are elementary, resulting in

$$(t_r)_1 = \frac{16hb^3}{315D\sigma_\infty}\left[1 - \frac{105}{16} f_i^{3/2} \ln(1/f_i) - \frac{1}{8} f_i^{3/2}\left(63 f_i^{1/2} - \frac{175}{4} - \frac{45}{4} f_i\right)\right]$$

$$(t_r)_2 = \frac{4hb}{3\alpha\dot{E}_\infty d}\left(1 - f_i^{3/2}\right) \tag{16}$$

where

$$f_i = a_i^2/b^2 \quad .$$

It is instructive to consider the ratio of these two contributions to t_r. First consider the case when a_i/b is sufficiently small (say, 1/10 or less) that f_i can be replaced

incompressible, ν is replaced by 1/2. Hence, one writes

$$\dot{\delta} = \alpha[(\sigma_\infty - \sigma)/\sigma_\infty]\dot{E}_\infty d \quad ,$$

as in Eq. (5) of the body of the paper where $\alpha = 2/\pi$.

As mentioned in the paper, the same equation but with different α can be used approximately in other cases. When the material is inhomogeneous in the sense of having freely sliding grain boundaries, it is evident that σ_∞ should be interpreted as the value of σ when the opening rate $\dot{\delta}$ of the grain facet is zero. To obtain an approximate estimate of the relation of σ_∞ to the applied stress (say, σ_{appl}) in that case, suppose that the grain boundary array of Fig. 1c is changed into a regular two-dimensional array of hexagons and that there is no cavitation. In this case $\sigma = \sigma_\infty$ is to be interpreted as the average stress acting over the horizontal facet of width d in the figure. If one lets σ' denote the average stress in the same direction acting over the widest dimension of the hexagon, then overall equilibrium requires that

$$2\sigma' + \sigma_\infty = 3\sigma_{appl}$$

From symmetry considerations this widest horizontal line, as well as the vertical bisector of a hexagon, are acted upon by zero shear stress. Hence if one isolated a quarter of a hexagon, bounded by such horizontal and vertical lines, as a free body and sums forces parallel to the inclined grain boundary (which can transmit no shear stress) one obtains

by zero in Eqs. (16). In that case

$$(t_r)_2/(t_r)_3 = 105D\sigma_\infty/4\alpha\dot{E}_\infty b^2 d = (105/4\alpha)(L^3/b^2 d) \qquad (17)$$

Where L is the temperature and stress level dependent parameter of Eq. (7). Obviously, if the stress and temperature are sufficiently low that L^3 is of the order of $b^2 d$ or larger, and if the cavitated facets are sufficiently isolated that α is of the order of unity, then $(t_r)_2$ is many times larger than $(t_r)_1$. The ratio $(t_r)_2/(t_r)_1$ also increases with increasing a_i/b; for values of a_i/b equal to 1/5, 1/3, and 1/2 the ratio is, respectively, 1.15, 1.67 and 8.92 times the result for very small a_i/b in Eq. (17).

The Monkman-Grant product $\dot{E}_\infty t_r$ can be written as

$$\begin{aligned}\dot{E}_\infty t_r &= (4h/3\alpha)(b/d)(1-f_i^{3/2})[1+(t_r)_1/(t_r)_2] \\ &= (4h/3\alpha)(b/d)(1-f_i^{3/2})\{1+(4\alpha b^2 d/105L^3)[G(f_i)/(1-f_i^{3/2})]\}\end{aligned} \qquad (18)$$

where the function $F(f_i)$ represents the bracketed expression in the first of Eqs. (16). Hence, in the circumstances just discussed when $(t_r)_1/(t_r)_2$ is small compared to unity,

$$\dot{E}_\infty t_r \simeq (4h/3\alpha)(b/d)(1-f_i^{3/2}) \qquad (19)$$

Typically, $h \simeq 0.6$. Also, if the cavitated facets are indeed well isolated from one another, then it has been estimated that $\alpha = 0.9$ for power-law dislocation creep without grain boundary sliding and that α might increase to 1.8 for freely sliding boundaries. Hence in this case the factor in Eqs. (18,19) has the range

$$4h/3\alpha \simeq 0.44 \text{ to } 0.89$$

$$2\sigma' = \sigma_\infty$$

Hence, by simultaneous solution, for uncavitated grain facets and freely slipping grain boundaries this regular hexagon model gives

$$\sigma = \sigma_\infty = (3/2)\sigma_{appl} \quad , \quad \sigma' = (3/4)\sigma_{appl}$$

Hence σ_∞ in Eq. (5) is to be interpreted as approximately 1.5 σ_{appl} for freely slipping grains.

No analysis is available for estimation of the factor α in Eq. (5) for the freely slipping case. However, a simple approach suggested by the geometry of the regular hexagon model is to choose an effective facet width equal to d plus the projected width of the inclined facets, which gives a total effective width of 2d, and to use the values of α as estimated for homogeneous materials. This is equivalent to using Eq. (5) with values of α which are twice as large as those estimated for homogeneous materials.

Conclusions

The problem of diffusive void growth on isolated grain boundary facets has been analyzed. It is shown that the "rupture time", as defined in the previous section, can be split as in Eq. (12) into the sum of two contributions, $(t_r)_1$ and $(t_r)_2$. As indicated by Eqs. (15,16), $(t_r)_1$ is proportional to $b^3/D\sigma_\infty$ where 2b is the cavity spacing, D is the grain boundary diffusion parameter (defined following Eq. (1)), and where σ_∞ is either the applied stress or a factor of approximately 1.5 times it, depending on whether the grain boundaries are nonslipping or freely sliding; $(t_r)_2$ is proportional to $b/\alpha\dot{E}_\infty d$ where d is the grain facet size, $\dot{E}_\infty$ the creep rate of a similarly loaded but noncavitated polycrystal, and α is a parameter which has been estimated to vary from approximately 0.9 to 1.8 (depending again on whether the g.b.'s are nonslipping or freely sliding) for well isolated, noninteresting, cavitated facets, but which can be very much larger for interacting facets.

The ratio of $(t_r)_2$ to $(t_r)_1$ is approximately $(105/4\alpha)$ (L^3/b^2d), at least for small initial radii of the cavities and applied stress levels which are well above the sintering limit. Here L is the length parameter of Eq. (7) and Refs. 4,10; it decreases with increasing temperature and stress in the power-law creep regime. This ratio of $(t_r)_2$ to $(t_r)_1$ can be very much larger than unity at sufficiently low stress and temperature. In such circumstances the Monkman-Grant product $\dot{E}_\infty t_r$ is predicted to have a constant value, equal approximately to $0.8b/\alpha d$, which is

CAVITY NUCLEATION DURING HIGH TEMPERATURE CREEP

R. M. Cannon and A. G. Evans

ABSTRACT

Classical nucleation theory predicts that significant rates of cavity nucleation are only expected if $\sigma/E \sim 10^{-2}$, for most materials. Thus to understand the significant cavity formation which is observed in both metals and ceramics at applied stresses as low as $\sigma/E \sim 10^{-4}$ it is necessary to invoke either large stress concentrations or geometrical factors which reduce nucleation barriers.

Significant stress concentrations can develop at triple points or particles, due to grain boundary sliding or at slip band-grain boundary intersections. However, at high temperatures these are quickly relaxed by diffusion. In steady state diffusional creep the maximum stresses are only about twice the applied stress, an amount which is insufficient to explain cavity nucleation at low stresses. Although the peak transient stresses may be nominally high enough to account for nucleation, there are several problems with invoking high transient stresses, particularly for single phase materials: 1) The high stresses may decay faster than the time necessary to develop a significant population of nuclei or before they can grow to a sufficient size to remain stable as the

of the order 0.4 to 0.9 b/d for well isolated, noninteracting cavitated facets.

The paper shows, following concepts introduced by Dyson[5], that the void growth mechanism may be diffusional, and that rupture strains may have small values usually associated with diffusional growth, while the time to rupture is controlled by the overall dislocation creep rate.

It remains for future work to deal with cases for which the cavitated grain facets are sufficiently close to interact with one another[5], or for which the stress levels transmitted to the cavitated facets are large enough to invalidate the Hull-Rimmer diffusional growth model with a quasi-equilibrium, spherical-caps cavity shape[3] and with effectively rigid separation of the adjoining grains[4].

ACKNOWLEDGEMENT

This research was initiated under support of the NSF Materials Research Laboratory at Brown University and completed under support of the Defense Advanced Research Projects Agency of the Department of Defense under Contract No. MDA903-80C-0505 with The University of Michigan. The author is grateful to B. F. Dyson, A. G. Evans, D. MacLean and J. W. Hutchinson for helpful discussions.

stress concentrations decay; 2) The stresses decay most rapidly at the places where nucleation is geometrically favored, e.g., at triple points and four grain junctions; 3) If the load is applied slowly, high stress concentrations may never develop.

Purely geometric factors lower the nucleation barrier at interfaces and interface junctions. For single phase materials there will be a significant reduction in the nucleation barrier and the stresses necessary to cause nucleation if the dihedral angle at cavity-grain boundary junctions is less than 120°. (If the dihedral angle is below 70°, pores would spontaneously nucleate at four grain junctions even at zero stress). This may, in part, account for the greater ease of cavity formation which is observed in ceramics than in pure metals. For a number of oxides or carbides dihedral angles have been purported to be in the range of 80-120°. In a uniform stress field (e.g., hydrostatic), geometrical effects favor nucleation at four grain junctions. Only under conditions of high stress and low growth rates (lower temperature) is significant nucleation on grain faces favored.

References

1. D. Hull and D. E. Rimmer, Phil. Mag., 4, 673 (1959).

2. R. Raj and M. F. Ashby, Acta Met., 23, 653 (1975).

3. T-j. Chuang, K. I. Kagawa, J. R. Rice and L. Sills, Acta Met., 27, 265 (1979).

4. A. Needleman and J. R. Rice, Acta Met., in press (1980).

5. B. F. Dyson, Metal Sci., 349 (1976).

6. F. C. Monkman and N. J. Grant, Proc. ASTM, 56, 593 (1956).

7. W. Beere and M. V. Speight, Metal Sci., 12, 172 (1978).

8. G. H. Edward and M. F. Ashby, Acta Met., 27, 1505 (1979).

9. B. Budiansky, J. W. Hutchinson, and S. Slutsky, in Mechanics of Solids, The Rodney Hill 60th Anniversary Volume (edited by H. G. Hopkins and M. J. Sewell), Pergamon Press, Oxford, publication expected, 1981.

10. J. R. Rice, in Time-Dependent Fracture of Materials at Elevated Temperature (edited by S. M. Wolf), U. S. Dept. of Energy Report CONF790236 UC-25, p.130 (1979).

11. A. E. Green and W. Zerna, Theoretical Elasticity, Oxford (Clarendon) Press, Oxford (1954).

INTERACTIONS OF PURE METALS WITH WATER

J. W. Kauffman, R. H. Hauge and J. L. Margrave

Abstract

Atoms, diatoms and other small clusters of various metals have been co-deposited with water in an excess of argon at 12-20K. Initially adducts of the $M{:}\ddot{O}H_2$ structure with C_{2v} symmetry are formed. UV-photolysis leads to oxidation insertion and formation of HMOH, HMOMH, HM_2OH, MOH, $M(OH)_2$, MO, M_2O and other related species. Vibrational spectra are presented for new studies of Si, Ge, Sn and Pb reactions with water.

INTERACTIONS OF PURE METALS WITH WATER

J. W. Kauffman, R. H. Hauge and J. L. Margrave

Corrosion of pure metals in the presence of concentrations of water vapor has been the subject of many studies, from the oxidation of nickel[1] to the corrosion of aluminum in microelectronic devices[2] to the corrosion of tellurium films on polymethyl methacrylate in information storage systems[3] to the oxidation of silicon[4]. In many cases the ultimate product after reaction with water is less valuable or even useless, although the controlled oxidation of silicon is commercially important. It is clear that a fundamental understanding of metal reactions with water could lead to the development of better systems for protection of surfaces and/or to the development of better chemical methods for the controlled oxidation of metal surfaces as currently practiced in the semiconductor industry.

Extensive studies of metal atoms or diatoms interacting with water, or a mole for mole basis, in an excess of argon at 10-20K have been conducted.[5] Thus, Li, Na, K, Cs, Mg, Ca, Sr, Ba, Al, Ga, In, Tl, Si, Ge, Sn, Pb, Sc, Ti, V, Cr, Mn, Fe, Co, Ni, Cu and Zn have been co-deposited with water at various ratios. There are many possible reactions [illegible] for Group IV elements in Table I. The decision among the alternatives can be made

TABLE I. Estimated Heats of Reaction (kcal/mole) of Metal-Water Reactions

	H
$Si + H_2O \rightarrow HSiOH$	-67
$\rightarrow SiO + H_2$	-77
$\rightarrow H_2SiO$	-85
$Ge + H_2O \rightarrow HGeOH$	-49
$\rightarrow GeO + H_2$	-43
$\rightarrow H_2GeO$	-77
$Sn + H_2O \rightarrow HSnOH$	-32
$\rightarrow SnO + H_2$	-8.2
$\rightarrow H_2SnO$	-26
$Pb + H_2O \not\rightarrow HPbOH$	3.7
$\not\rightarrow PbO + H_2$	27
$\not\rightarrow H_2PbO$	48

partially on the basis of thermodynamics and bond energies but low temperature processes are slow and can be helped by a stimulating exposure to ultraviolet radiation. Such stimulation has lead to the formation of many new compounds -- HMOH, HM_2OH,

CAVITY NUCLEATION DURING HIGH TEMPERATURE CREEP

R. M. Cannon and A. G. Evans

ABSTRACT

Classical nucleation theory predicts that significant rates of cavity nucleation are only expected if $\sigma/E \sim 10^{-2}$, for most materials. Thus to understand the significant cavity formation which is observed in both metals and ceramics at applied stresses as low as $\sigma/E \sim 10^{-4}$ it is necessary to invoke either large stress concentrations or geometrical factors which reduce nucleation barriers.

Significant stress concentrations can develop at triple points or particles, due to grain boundary sliding or at slip band-grain boundary intersections. However, at high temperatures these are quickly relaxed by diffusion. In steady state diffusional creep the maximum stresses are only about twice the applied stress, an amount which is insufficient to explain cavity nucleation at low stresses. Although the peak transient stresses may be nominally high enough to account for nucleation, there are several problems with invoking high transient stresses, particularly for single phase materials: 1) The high stresses may decay faster than the time necessary to develop a significant population of nuclei or before they can grow to a sufficient size to remain stable as the

TABLE II. Measured Frequency Changes (cm^{-1}) for the $H_2O(v_2)$ Bending Mode in Metal-Water Adducts

	M_1		M_1		M_1	M_2		M_1	M_2
Li	17.5	Mg	15.7	Al	*		Si	19.5	-
Na	7.4	Ca	30.8	Ga	26.6	14.4	Ge	15.4	31.6
K	6.6	Sr	27.7	In	16.5	10.6	Sn	15.8	20.8
Rb	-	Ba	34.0	Tl	9.6	-	Pb	8.0	16.0
Cs	2.7								

*reacted

stress concentrations decay; 2) The stresses decay most rapidly at the places where nucleation is geometrically favored, e.g., at triple points and four grain junctions; 3) If the load is applied slowly, high stress concentrations may never develop.

Purely geometric factors lower the nucleation barrier at interfaces and interface junctions. For single phase materials there will be a significant reduction in the nucleation barrier and the stresses necessary to cause nucleation if the dihedral angle at cavity-grain boundary junctions is less than 120°. (If the dihedral angle is below 70°, pores would spontaneously nucleate at four grain junctions even at zero stress). This may, in part, account for the greater ease of cavity formation which is observed in ceramics than in pure metals. For a number of oxides or carbides dihedral angles have been purported to be in the range of 80-120°. In a uniform stress field (e.g., hydrostatic), geometrical effects favor nucleation at four grain junctions. Only under conditions of high stress and low growth rates (lower temperature) is significant nucleation on grain faces favored.

TABLE III. Reaction Products From Group IVa Metals and Water

(Argon Matrix)

	HSiOH		HGeOH		HSnOH
[a](HSi) 1971	1885.2	[a](HGe) (1835)	1741.3	[a](HSn) (1580)	1605.8
	1849.1				1597.9
	936.9				782.1
[a](SiF) 847	850.5	[a](GeF) 659	660.6	[a](SnF) 578	569.1
	722.6				480.6
	595.8				476.1

SiO	GeO
1222.2	975.3
	972.9
	970.6

(a) gaseous diatomic values

INTERACTIONS OF PURE METALS WITH WATER

J. W. Kauffman, R. H. Hauge and J. L. Margrave

Abstract

Atoms, diatoms and other small clusters of various metals have been co-deposited with water in an excess of argon at 12-20K. Initially adducts of the $M{:}\ddot{O}H_2$ structure with C_{2v} symmetry are formed. UV-photolysis leads to oxidation insertion and formation of HMOH, HMOMH, HM_2OH, MOH, $M(OH)_2$, MO, M_2O and other related species. Vibrational spectra are presented for new studies of Si, Ge, Sn and Pb reactions with water.

for the HMOH and MO species which form on UV-photolysis. Comparisons of diatomic M-H and M-F stretches are also cited.

DISCUSSION

Extension of the ideas presented here to the interactions of metal surfaces with water lead one to the following mechanistic pictures of corrosion:

(1) Water Only

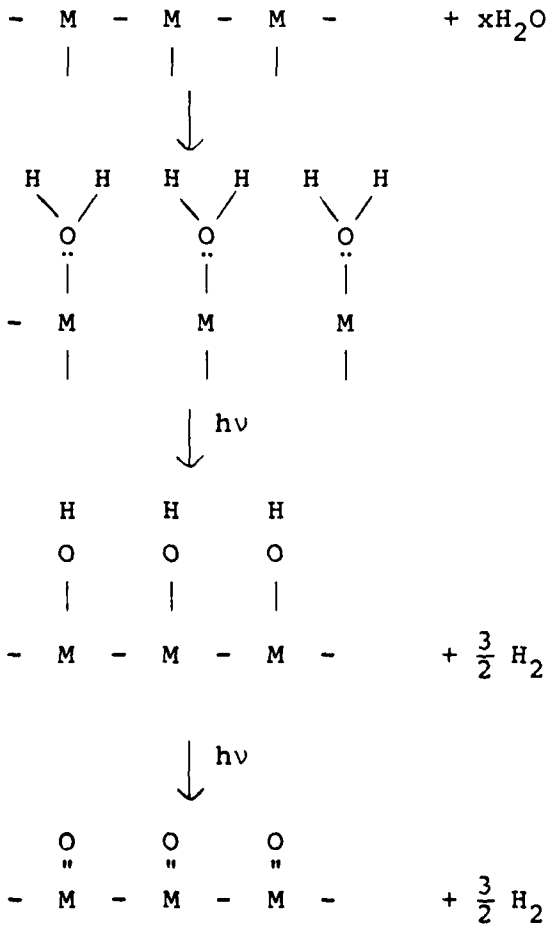

(2) Water + O_2

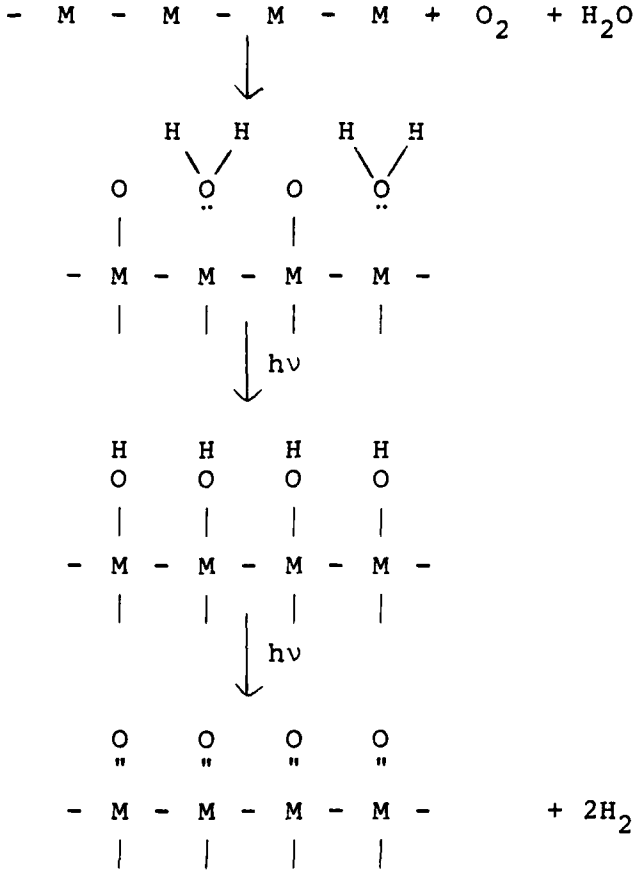

Similar surface adsorption on metals or matrix reactions at low temperatures with isolated atoms are observed for alcohols[6,7], ethers[6,7], ammonia[5], and various substituted amines[5]. Such chemicals are common constituents of corrosion inhibiting chemical systems for protection of metals.

TABLE I. Estimated Heats of Reaction (kcal/mole) of Metal-Water Reactions

	H
$Si + H_2O \rightarrow HSiOH$	-67
$\rightarrow SiO + H_2$	-77
$\rightarrow H_2SiO$	-85
$Ge + H_2O \rightarrow HGeOH$	-49
$\rightarrow GeO + H_2$	-43
$\rightarrow H_2GeO$	-77
$Sn + H_2O \rightarrow HSnOH$	-32
$\rightarrow SnO + H_2$	-8.2
$\rightarrow H_2SnO$	-26
$Pb + H_2O \not\rightarrow HPbOH$	3.7
$\not\rightarrow PbO + H_2$	27
$\not\rightarrow H_2PbO$	48

REFERENCES

1. S. H. Kulpa and R. P. Frankenthal, J. Electrochemical Society 124, (1977), 1588.

2. G. F. Cerofolini and C. Rovere, Thin Solid Films 47, (1977), 83.

3. A. Milch and P. Tasaico, J. Electrochemical Society 127, (1980), 884.

4. J. W. Kauffman, R. H. Hauge and J. L. Margrave, Abstracts, ACS Meeting, Houston, Texas, March 1980.

5. (a) J. W. Kauffman, PhD Thesis, Rice University, Houston, Texas, 1980.

   (b) P. F. Meier, R. H. Hauge and J. L. Margrave, Ber. Bunsenges. Phys. Chem. 82, (1978), 102

   (c) P. F. Meier, R. H. Hauge and J. L. Margrave, J. Am. Chem. Soc. 100, (1978), 2108.

   (d) R. H. Hauge, J. W. Kauffman, and J. L. Margrave, J. Am. Chem. Soc. 102, (1980), in press.

6. M. Konarski, W. E. Billups, R. H. Hauge and J. L. Margrave, J. Am. Chem. Soc. 102, (1980), in press.

7. M. M. Konarski, Ph.D. Thesis, Rice University, Houston, Texas, 1980.

partially on the basis of thermodynamics and bond energies but low temperature processes are slow and can be helped by a stimulating exposure to ultraviolet radiation. Such stimulation has lead to the formation of many new compounds -- HMOH, HM_2OH, HMOMH, $M(OH)_x$, etc. Structures, symmetries, bond angles, etc., can be derived from spectroscopic data on isotopically substituted species.

In this note, interest in concentrated on the Group IV metals -- Si, Ge, Sn and Pb. Atoms and diatoms have been co-deposited with water in an excess of argon on a polished copper surface at 12-20K. Initially, adducts with water are formed of the $M:\ddot{O}H_2$ structure with C_{2v} symmetry. UV-photolysis leads to further reactions for Si, Ge, and Sn. Products like HSiOH, HGeOH, HSnOH, SiO, GeO and SnO have been identified. Other species like $H_2Si{=}O$, $Si(OH)_2$, HSi_2OH, $Si(OH)_x$, etc. appear to be formed in small amounts.

These species are characterized by infrared absorption spectra as summarized in Table II and III. Thus, Table II shows that appreciable electron density is moved out of the non-bonding $2a_1$ orbital of water into the σ-bond between the metal atom and oxygen, as evidenced by the shifts in ν_2, the bending frequency of H_2O. Shifts for metal atom-water interactions of Groups I, II, III and IV are compared, and several examples of metal dimers interacting to yield $M_2:\ddot{O}H_2$ are listed.

In Table III are listed the characteristic frequencies

GASEOUS MOLECULES WITH VERY HIGH MOLECULAR WEIGHTS

J. P. Bell, R. H. Hauge, J. L. Margrave
J. G. Edwards, and R. McFarland

Polyperfluorovinyl ethers which are commercially available from various industrial sources[1] are well known to boil, vaporize, condense. and liquify without decomposition and in a completely reversible manner at temperatures in the 180-250°C range, depending on the pressure. Speculation as to the nature of the vapor species involved in this liquid-gas equilibrium process has been considerable, but we can now report several pieces of evidence which demonstrate that the major gaseous species in equilibrium with typical polyperfluorovinyl ethers have very high molecular weights, in the range 2000-8000! These gas-phase molecular weights are consistent with the known degree of polymerization in the liquid from a variety of other studies and to the best of our knowledge are the highest molecular weight neutral gaseous molecules yet observed.

Evidence for the unusually high molecular weight of the equilibrium vapor is based on the following kinds of studies:

(a) Direct boiling point measurements which have been correlated with transpiration weight loss measurements, providing two equations in two unknowns - total equilibrium pressure and average molecular weight of the vapor[2],

TABLE II. Measured Frequency Changes (cm^{-1}) for the $H_2O(v_2)$ Bending Mode in Metal-Water Adducts

	M_1		M_1		M_1	M_2		M_1	M_2
Li	17.5	Mg	15.7	Al	*		Si	19.5	-
Na	7.4	Ca	30.8	Ga	26.6	14.4	Ge	15.4	31.6
K	6.6	Sr	27.7	In	16.5	10.6	Sn	15.8	20.8
Rb	-	Ba	34.0	Tl	9.6	-	Pb	8.0	16.0
Cs	2.7								

*reacted

(b) Torque-Knudsen studies[3] showing that the equilibrium vapors effusing from double-orificed cells suspended from a micro-balance have average molecular weights in the range 6000-8000,

(c) Mass spectrometric examination[4] of the vapors formed by room temperature irradiation of a DuPont Krytox Oil shows heavy ions over the entire mass range from monomer (M=166) to 50-mer (M-8300) and probably still higher. From such studies, molecular weights in the range 2000-8000 have been calculated for different polymer samples made available to us by the DuPont Company.

Information about very heavy gaseous molecules is of importance in chemistry for several reasons:

(1) One is interested in the structures of gaseous molecules with masses in the range 2000-8000 because they are so complicated in comparison to molecules of masses 100-150. Are such heavy molecular entities long chains or have these flexible chains curled and twisted to form relatively compact, clump-like configurations?

(2) Such structural questions are directly connected to questions regarding physical properties. Can a liquid phase made of species with average molecular weights in the range 2000-8000 be involved in rapid thermodynamic equilibrium with gas phase species of the same high molecular weights? Can long chains escape from a tangled random array in the liquid or solid to give the same undamaged chain as the vapor species? When one condenses the vapors do they reenter in the condensed phase, more or less

TABLE III. Reaction Products From Group IVa Metals and Water

(Argon Matrix)

	HSiOH		HGeOH		HSnOH
[a](HSi) 1971	1885.2	[a](HGe) (1835)	1741.3	[a](HSn) (1580)	1605.8
	1849.1				1597.9
	936.9				782.1
[a](SiF) 847	850.5	[a](GeF) 659	660.6	[a](SnF) 578	569.1
	722.6				480.6
	595.8				476.1

SiO	GeO
1222.2	975.3
	972.9
	970.6

(a) gaseous diatomic values

for the HMOH and MO species which form on UV-photolysis. Comparisons of diatomic M-H and M-F stretches are also cited.

DISCUSSION

Extension of the ideas presented here to the interactions of metal surfaces with water lead one to the following mechanistic pictures of corrosion:

(1) Water Only

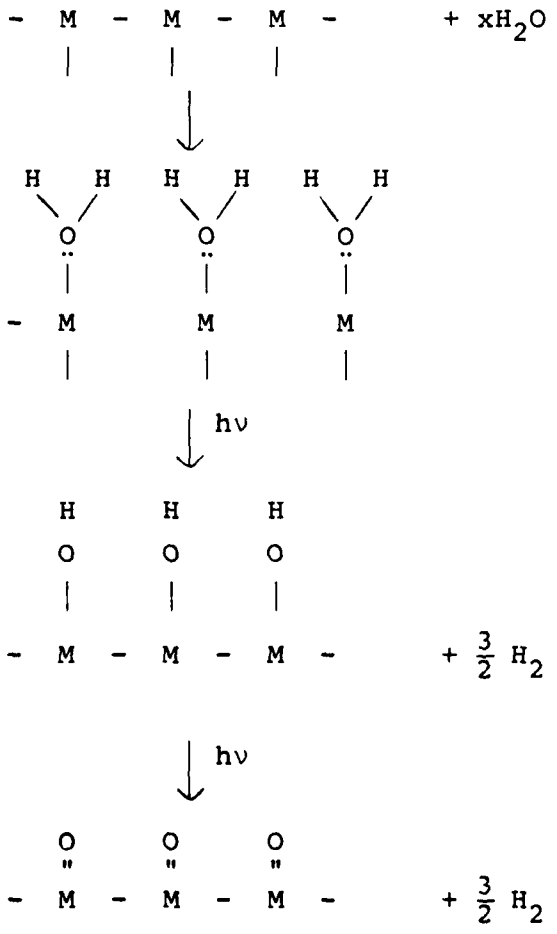

intertwined clump of molecular weight 2000-8000 would appear to an external observer as a symmetrical and electronically satisfied species. Would matrices made from such high molecular weight

REFERENCES

1. S. H. Kulpa and R. P. Frankenthal, J. Electrochemical Society 124, (1977), 1588.

2. G. F. Cerofolini and C. Rovere, Thin Solid Films 47, (1977), 83.

3. A. Milch and P. Tasaico, J. Electrochemical Society 127, (1980), 884.

4. J. W. Kauffman, R. H. Hauge and J. L. Margrave, Abstracts, ACS Meeting, Houston, Texas, March 1980.

5. (a) J. W. Kauffman, PhD Thesis, Rice University, Houston, Texas, 1980.

   (b) P. F. Meier, R. H. Hauge and J. L. Margrave, Ber. Bunsenges. Phys. Chem. 82, (1978), 102

   (c) P. F. Meier, R. H. Hauge and J. L. Margrave, J. Am. Chem. Soc. 100, (1978), 2108.

   (d) R. H. Hauge, J. W. Kauffman, and J. L. Margrave, J. Am. Chem. Soc. 102, (1980), in press.

6. M. Konarski, W. E. Billups, R. H. Hauge and J. L. Margrave, J. Am. Chem. Soc. 102, (1980), in press.

7. M. M. Konarski, Ph.D. Thesis, Rice University, Houston, Texas, 1980.

ACKNOWLEDGEMENT

This work has been supported by funds from the United States Army Research Office, Durham, by the National Science Foundation, and by the Robert A. Welch Foundation. Mass spectrometric studies at Texas A&M University are sponsored by the Robert A. Welch Foundation. Preparation of this report was sponsored by the Advanced Research Projects Agency of the Department of Defense under Contract No. MDA903-80C-0505 with The University of Michigan.

GASEOUS MOLECULES WITH VERY HIGH MOLECULAR WEIGHTS

J. P. Bell, R. H. Hauge, J. L. Margrave
J. G. Edwards, and R. McFarland

Polyperfluorovinyl ethers which are commercially available from various industrial sources[1] are well known to boil, vaporize, condense. and liquify without decomposition and in a completely reversible manner at temperatures in the 180-250°C range, depending on the pressure. Speculation as to the nature of the vapor species involved in this liquid-gas equilibrium process has been considerable, but we can now report several pieces of evidence which demonstrate that the major gaseous species in equilibrium with typical polyperfluorovinyl ethers have very high molecular weights, in the range 2000-8000! These gas-phase molecular weights are consistent with the known degree of polymerization in the liquid from a variety of other studies and to the best of our knowledge are the highest molecular weight neutral gaseous molecules yet observed.

Evidence for the unusually high molecular weight of the equilibrium vapor is based on the following kinds of studies:

(a) Direct boiling point measurements which have been correlated with transpiration weight loss measurements, providing two equations in two unknowns - total equilibrium pressure and average molecular weight of the vapor[2],

REFERENCES

1. (a) Montecatini-Edison, Milan, Italy, Markets "Fomblin" Fluorocarbon Oils and Greases.

   (b) E.I. Du Pont De Nemours, Wilmington, Delaware, Markets "Krytox" Fluorocarbon Oils and Greases.

2. J. P. Bell, R. H. Hauge and J. L. Margrave, unpublished work, 1977-79; manuscript in preparation.

3. J. P. Bell, J. G. Edwards, R. H. Hauge and J. L. Margrave, unpublished work, 1979-80; manuscript in preparation.

4. J. P. Bell, R. H. Hauge, R. McFarland and J. L. Margrave, unpublished work, 1979-80; manuscript in preparation.

5. For information regarding "Krytox" Oils and Greases contact Dr. Stuart Wright, Jackson Laboratory, E.I. Dupont Company, Wilmington, Delaware.

(b) Torque-Knudsen studies[3] showing that the equilibrium vapors effusing from double-orificed cells suspended from a micro-balance have average molecular weights in the range 6000-8000,

(c) Mass spectrometric examination[4] of the vapors formed by room temperature irradiation of a DuPont Krytox Oil shows heavy ions over the entire mass range from monomer (M=166) to 50-mer (M-8300) and probably still higher. From such studies, molecular weights in the range 2000-8000 have been calculated for different polymer samples made available to us by the DuPont Company.

Information about very heavy gaseous molecules is of importance in chemistry for several reasons:

(1) One is interested in the structures of gaseous molecules with masses in the range 2000-8000 because they are so complicated in comparison to molecules of masses 100-150. Are such heavy molecular entities long chains or have these flexible chains curled and twisted to form relatively compact, clump-like configurations?

(2) Such structural questions are directly connected to questions regarding physical properties. Can a liquid phase made of species with average molecular weights in the range 2000-8000 be involved in rapid thermodynamic equilibrium with gas phase species of the same high molecular weights? Can long chains escape from a tangled random array in the liquid or solid to give the same undamaged chain as the vapor species? When one condenses the vapors do they reenter in the condensed phase, more or less

ACOUSTIC SCATTERING FROM SURFACE CRACKS IN CERAMICS: IMPLICATIONS FOR FAILURE PREDICTION

A. G. Evans, G. S. Kino and B. Budiansky

ABSTRACT

The scattering of surface acoustic waves by surface cracks in ceramics depends sensitively upon the state of residual stress acting over the crack surfaces. A comprehension of the scattering problem can be developed by examining the crack opening derived from acoustic measurements, as a function of applied stress level. The measured crack opening has been used to deduce both the residual stress and the residual crack surface separations, using fracture mechanics techniques. The predictions have been correlated with observed crack morphologies to provide a consistent description of the opening process. The implications of the analysis for predicting failure from surface cracks are described.

CREEP FRACTURE IN CERAMICS

A. G. Evans

ABSTRACT

Creep rupture in ceramics occurs by the nucleation, growth and coalescence of cavities in localized, inhomogeneous arrays. The cavities grow by diffusive mechanisms; a process which has previously been analyzed for uniform cavity distributions. However, experimental results indicate that the inhomogeneity exerts substantial perturbations upon the failure sequence and hence, on the failure time. The principal inhomogeneity influence resides in the development of constraints that limit the cavity growth rate. The failure sequence in the presence of inhomogeneity effects is addressed in this paper. A model is developed that accounts for the experimentally observed damage accumulation features and predicts the influence of inhomogeneity upon the failure time. Specifically, the development of linear arrays of cavities prior to coalescence is predicted, as well as the spreading rate of the cavitation zone that eventually generates the critical crack.

intertwined clump of molecular weight 2000-8000 would appear to an external observer as a symmetrical and electronically satisfied species. Would matrices made from such high molecular weight molecules be the least perturbing of all matrices, even less perturbing than neon, CF_4, or elemental fluorine?

(7) Are the heats of vaporization of such high molecular weight liquids fundamental measures of induced dipole interactions for chemical systems? The large number of atoms involved and the relatively large volume per molecular unit would tend to assure spherical symmetry. There are no individual chemical bonds between molecules so that the main binding forces between such molecules are solely from Van der Waal's effects.

In summary, we report here the observation of an extreme form of matter in which the range of molecular weights for gases is extended far beyond the normal expectations of traditional chemistry. Fundamental properties like vaporization, boiling, and sublimation are measurable and molecular weights can be established by a variety of direct and indirect techniques. There should be unique applications for such heavy molecules. Their transitional velocities at a given temperature are unusually low as compared with other molecules. Collisions are energetically soft and the possibilities for chemical applications are unexplored. We plan to continue this work and to make further reports on the properties of these unusual chemical species.

CREEP FRACTURE IN CERAMICS

A. G. Evans

INTRODUCTION

High temperature failure in ceramics often occurs by the gradual growth and coalescence of cavities by diffusion, until a macrocrack is formed that propagates to failure. The process is inhomogeneous, involving perferential cavitation in certain regions of the polycrystalline array (Fig. 1). The intent of this paper is to examine the role of cavitation inhomogeneity upon the cavity evolution process and hence, upon the time to failure.

The principal source of inhomogeneity is assumed to derive from local variations in the grain boundary diffusivity (attributed to grain orientation effects augmented by impurity distributions); although similar trends could result from a grain size distribution or from variations in the surface diffusivity. The inhomogeneity is needed to obtain preferred sites for initial cavity formation, but may be of secondary importance for the zone spreading and coalescence aspects of failure.

Although inhomogeneity effects are the principal concern of this paper, some important results from homogeneous cavitation models[1,2] will be invoked, as appropriate. Of particular interest are the transition between the equilibrium and crack-like modes of cavity growth[2] (Fig. 2) and the rate of matter deposition between uniform arrays of equilibrium and crack-like cavities.

ACKNOWLEDGEMENT

This work has been supported by funds from the United States Army Research Office, Durham, by the National Science Foundation, and by the Robert A. Welch Foundation. Mass spectrometric studies at Texas A&M University are sponsored by the Robert A. Welch Foundation. Preparation of this report was sponsored by the Advanced Research Projects Agency of the Department of Defense under Contract No. MDA903-80C-0505 with The University of Michigan.

CREEP FRACTURE IN CERAMICS

A. G. Evans

ABSTRACT

Creep rupture in ceramics occurs by the nucleation, growth and coalescence of cavities in localized, inhomogeneous arrays. The cavities grow by diffusive mechanisms; a process which has pre-

The present analysis pertains to situations in which the failure strains are greater than a few times the elastic strain. Small strain failure processes based on statistical accumulations of cavities have been examined in previous studies[3].

INITIAL CAVITATION

Initial cavitation is considered here to dominate on boundaries with diffusivities that deviate from the average diffusivity. The nucleation susceptibility on these boundaries is not expected to appreciably differ from the general nucleation propensity, but the initial growth can occur at very different rates. Consider the matter deposition on a pair of contiguous boundary facets (Fig. 3) when this region has a diffusivity, D_b', that differs from that of the surrounding boundaries, D_b. The surrounding material will creep at a rate that dictates the displacement of the neighboring grain centers, δ, in accord with the relation[4],

$$\dot{\delta} \simeq \frac{14\pi\Omega D_b \delta_b \sigma_\infty}{kTg^2} \qquad (1)$$

where Ω is the atomic volume, σ_∞ is the applied stress and g is the grain size. However, the displacement rate around the boundaries with the disparate diffusivities will tend to deviate from that of surrounding structure, leading to the generation of constraints. The local stress then differs from the applied stress by an amount $\Delta\sigma$, which can be approximately related to the average deviation in displacement rate $\Delta\dot{\delta}$ by[5];

CREEP FRACTURE IN CERAMICS

A. G. Evans

INTRODUCTION

High temperature failure in ceramics often occurs by the gradual growth and coalescence of cavities by diffusion, until a macrocrack is formed that propagates to failure. The process is inhomogeneous, involving perferential cavitation in certain regions of the polycrystalline array (Fig. 1). The intent of this paper is to examine the role of cavitation inhomogeneity upon the cavity evolution process and hence, upon the time to failure.

The principal source of inhomogeneity is assumed to derive from local variations in the grain boundary diffusivity (attributed to grain orientation effects augmented by impurity distributions); although similar trends could result from a grain size distribution or from variations in the surface diffusivity. The inhomogeneity is needed to obtain preferred sites for initial cavity formation, but may be of secondary importance for the zone spreading and coalescence aspects of failure.

Although inhomogeneity effects are the principal concern of this paper, some important results from homogeneous cavitation models[1,2] will be invoked, as appropriate. Of particular interest are the transition between the equilibrium and crack-like modes of cavity growth[2] (Fig. 2) and the rate of matter deposition between uniform arrays of equilibrium and crack-like cavities.

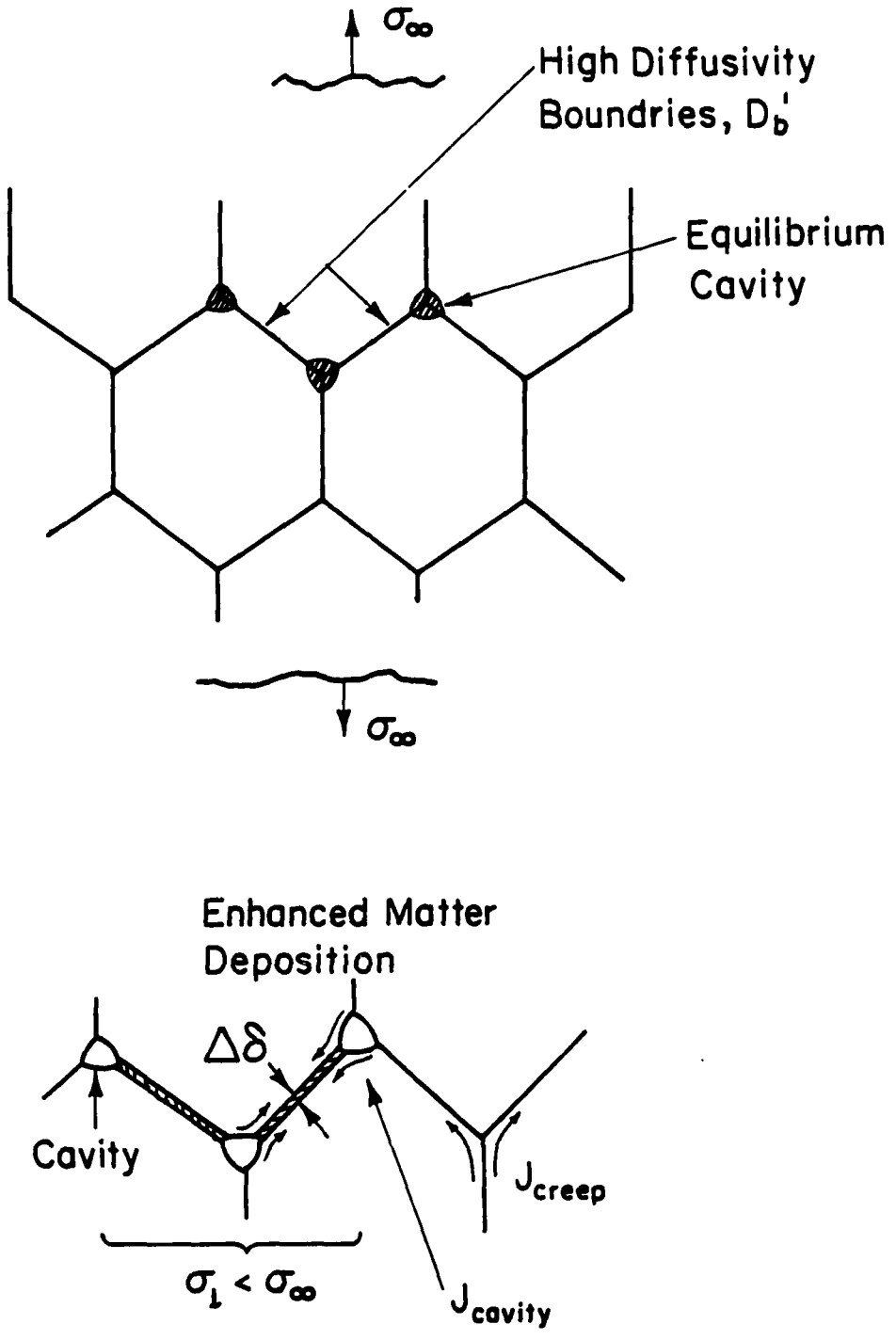

Figure 3. A schematic illustrating two contiguous boundaries with larger than average diffusivities, exhibiting preferred cavitation.

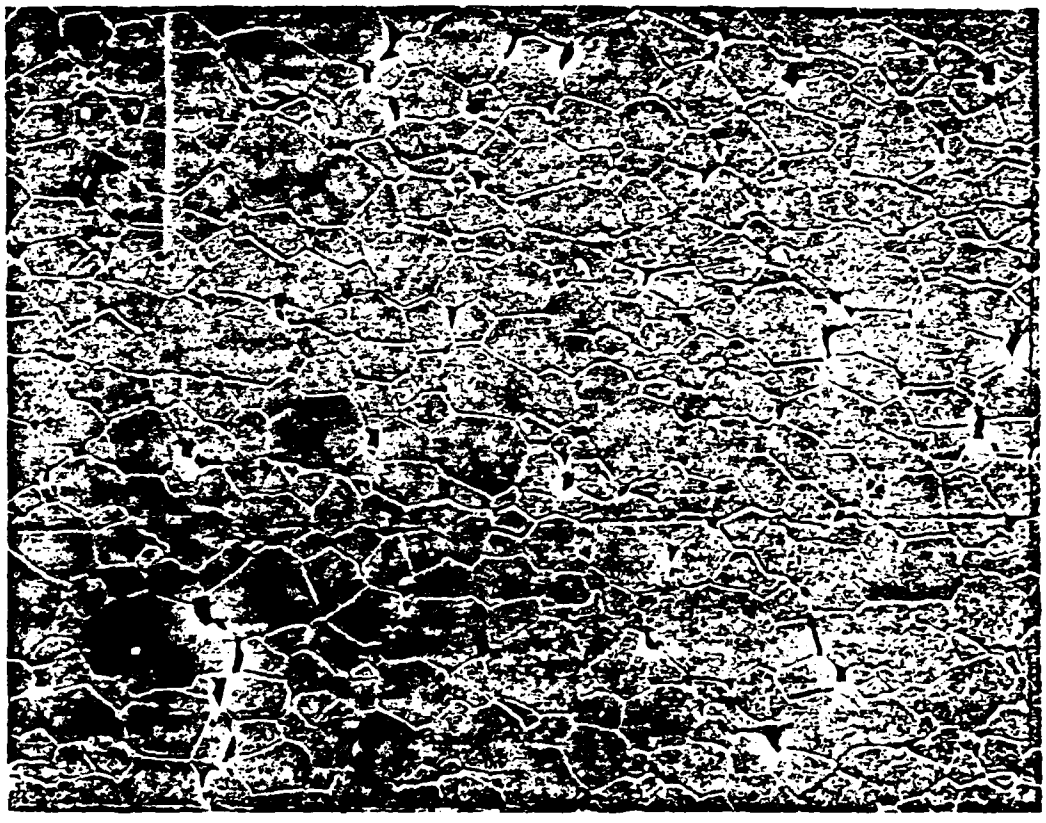

Figure 1. A scanning electron micrograph of cavitation inhomogeneity in Al_2O_3 (courtesy W. Blumenthal).

$$\Delta\sigma \simeq \frac{\pi \Delta\dot{\delta}\sigma_\infty}{2\dot{\varepsilon}_\infty d} \tag{2}$$

where d is the length of the zone of differing displacement rate (g in this instance) and $\dot{\varepsilon}_\infty$ is the creep rate of the surrounding structure. Substitution of the creep rate derived from Eq. (1) then gives;

$$\Delta\sigma = \frac{\Delta\dot{\delta} kTg^3}{28\Omega D_b \delta_b d} \tag{3}$$

The deviation in displacement-rate can be estimated from the difference in creep rate in the two regions (by recognizing the stress differential) as,

$$\Delta\dot{\delta} = \frac{14\pi}{kTg^2}\,\Omega\delta_b[D_b'(\sigma_\infty - \Delta\sigma) - D_b\sigma_\infty] \tag{4}$$

Eliminating $\Delta\dot{\delta}$ from Eqs. (3) and (4) then gives,

$$\frac{\Delta\sigma}{\sigma_\infty} = \frac{[D_b/D_b' - 1]}{[1 + (2/\pi)(d/g)(D_b/D_b')]} \tag{5}$$

and the local stress σ_ℓ becomes;

$$-\frac{\sigma_\ell}{\sigma_\infty} = \left[1 - \frac{\Delta\sigma}{\sigma_\infty}\right] = \frac{(D_b/D_b')[1 + (2/\pi)(d/g)]}{[1 + (2/\pi)(d/g)(D_b/D_b')]} \tag{6}$$

The stress can thus be substantially diminished at a boundary with a larger than average diffusivity, but can only be slightly enhanced on boundaries with small diffusivities. However, the time taken to generate cavities of significant size is still somewhat smaller on the boundaries with the higher diffusivities, because

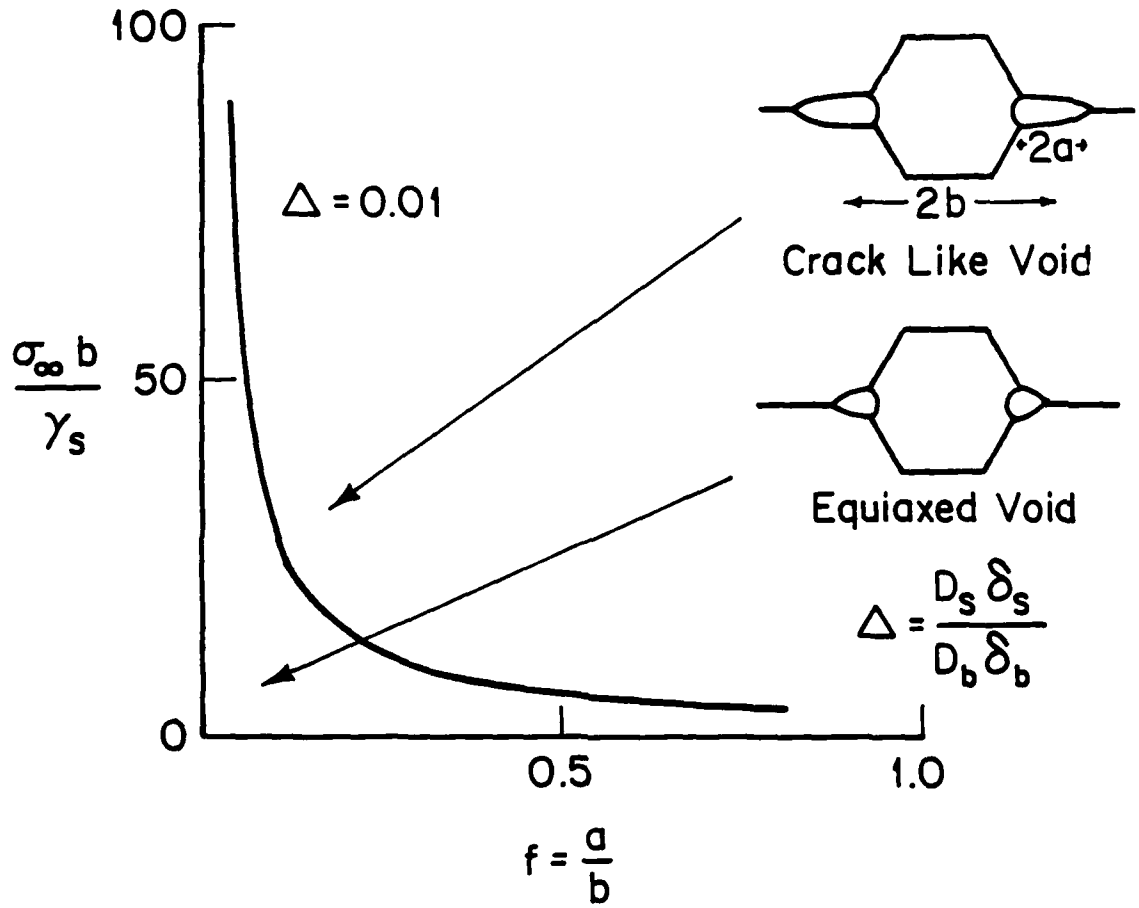

Figure 2a. A schematic indicating the transition between equilibrium and crack-like cavity growth.

the growth rate of equilibrium shaped cavities is itself dependent upon the boundary diffusivity[2];

$$\dot{a} = \left[\frac{\Omega D_b \delta_b}{kTa^2 h}\right] \frac{[\sigma_\ell - (1-f^2)\sigma_o]}{[\ell n(1/f^2) - (3-f^2)(1-f^2)/2]} \qquad (7)$$

where h depends upon the dihedral angle Ψ, σ_o is the sintering stress ($= 2\gamma_s \sin\Psi/a$, where γ_s is the surface energy) and f is the ratio of the cavity radius a to the cavity spacing b. For the small values of f pertinent to initial growth, substituting σ_ℓ from Eq. (6) gives a ratio R of the cavity growth rate on the high diffusivity boundaries to that on the general boundaries:

$$R = \frac{[1 + (2/\pi)(d/g)]\sigma_\infty - (D_b'/D_b)\sigma_o}{\sigma_\infty - \sigma_o} \qquad (8)$$

The growth rate near the sintering limit is suppressed on the high diffusivity boundaries, but becomes enhanced as the cavities extend ($\sigma_\infty >> \sigma_o$). The growth immediately after nucleation occurs very rapidly and most of the extension time entailed in the development of a cavity of observable size occurs when $\sigma_\infty >> \sigma_o$. The ratio of the effective time taken to develop observable cavities, t_o'/t_o, is thus;

$$t_o'/t_o = [1 + (2/\pi)(d/g)]^{-1} \qquad (9)$$

which for $d \sim g$ gives $t_o' \sim 0.6\ t_o$. By contrast, the propagation time on boundaries with low diffusivities ($D_b \gtrsim 10 D_b'$) is usually slightly larger than the general value;

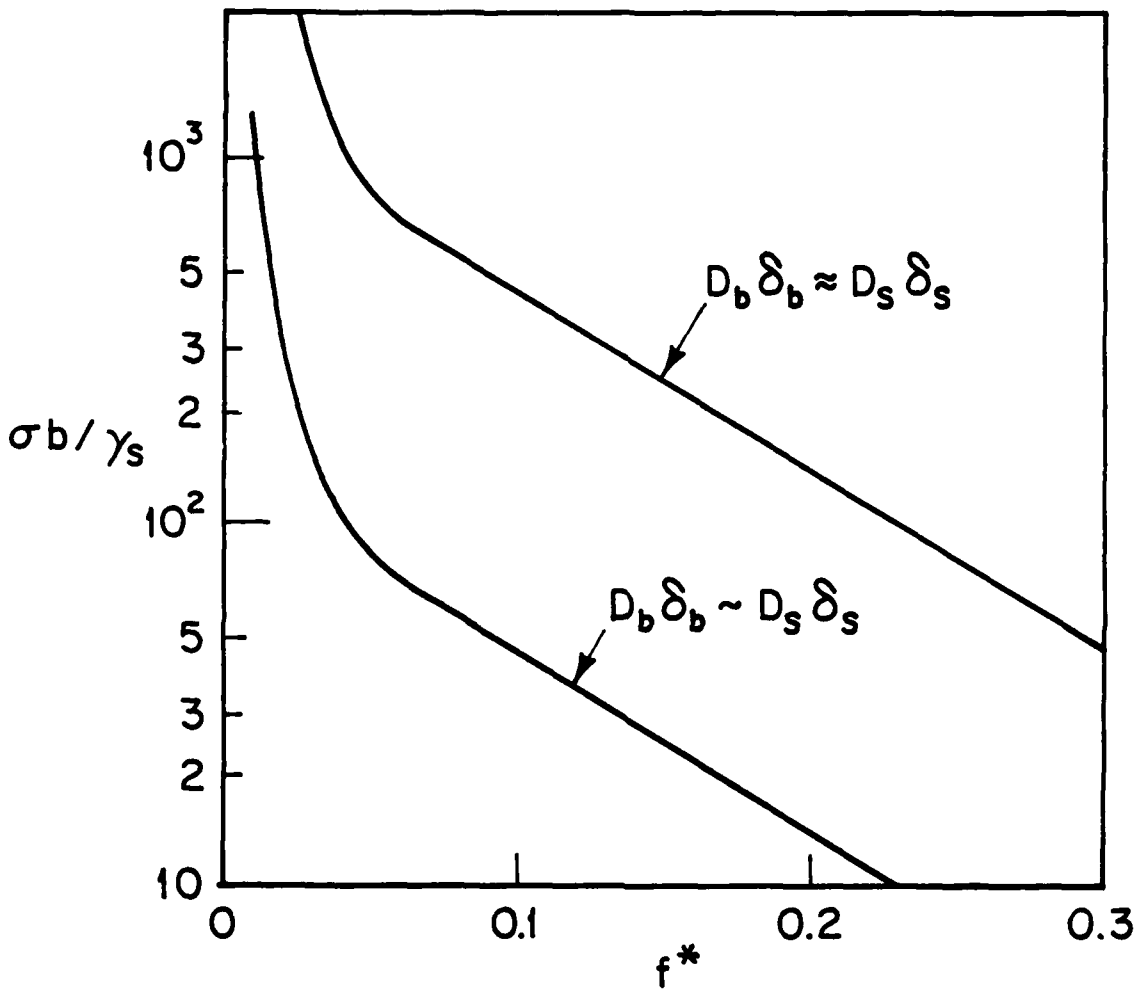

Figure 2b. Transitions for two ratios of $D_s\delta_s/D_b\delta_b$.

$$t'_o/t_o = (D_b/D'_b)(2/\pi)(d/g)[1 + (2/\pi)(d/g)]^{-1} \qquad (10)$$

which for $d \sim g$ gives $t'_o \sim 0.4\ D_b/D'_b$. However, it is emphasized that the local diffusivity has a relatively minor influence on the equilibrium cavity development time.

More significantly, the transition from equilibrium to crack-like cavity morphologies occurs at smaller values of cavity size f* on the boundaries with the larger boundary diffusivities (assuming that D_s is substantially unaltered), as expressed by the relation[6]

$$\left(\frac{\sigma_\ell b}{2\gamma_s}\right) f^* + 15.6\ (\ell n f^*)\left(\frac{D_b\delta_s}{D_b\delta_b}\right) = -11.7\left(\frac{D_s\delta_s}{D_b\delta_b}\right) \qquad (11)$$

A plot of f* (Fig. 2b) indicates that for typical $(\sigma_\ell b/\gamma_s)$ of $<10^2$, transitions in the observed range ($f^* \sim 0.1$) can occur on boundaries with D_b/D_s about 5-10 times larger than an average value of ~ 1. This transition to crack-like morphology represents the commencement of the actual failure process. The time consumed at this juncture ($f^* << 1$) is;

$$t = \left(\frac{hg^3kT}{D_b\delta_b\Omega\sigma_\infty}\right)\int_{f_o}^{f^*} f^3\ \frac{\{\ell n(1/f^2) - 3/2 + (2/7\pi)(g/d)\}df}{[f - 2\gamma_s\ \sin\Psi/\sigma_\infty g]} \qquad (12)$$

CAVITY GROWTH

Once crack-like cavities develop on two contiguous high diffusivity boundary facets, cavity growth will proceed at a relatively rapid rate. This leads to a significently enhanced

The present analysis pertains to situations in which the failure strains are greater than a few times the elastic strain. Small strain failure processes based on statistical accumulations of cavities have been examined in previous studies[3].

INITIAL CAVITATION

Initial cavitation is considered here to dominate on boundaries with diffusivities that deviate from the average diffusivity. The nucleation susceptibility on these boundaries is not expected to appreciably differ from the general nucleation propensity, but the initial growth can occur at very different rates. Consider the matter deposition on a pair of contiguous boundary facets (Fig. 3) when this region has a diffusivity, D_b', that differs from that of the surrounding boundaries, D_b. The surrounding material will creep at a rate that dictates the displacement of the neighboring grain centers, δ, in accord with the relation[4],

$$\dot{\delta} \simeq \frac{14\pi\Omega D_b \delta_b \sigma_\infty}{kTg^2} \qquad (1)$$

where Ω is the atomic volume, σ_∞ is the applied stress and g is the grain size. However, the displacement rate around the boundaries with the disparate diffusivities will tend to deviate from that of surrounding structure, leading to the generation of constraints. The local stress then differs from the applied stress by an amount $\Delta\sigma$, which can be approximately related to the average deviation in displacement rate $\Delta\dot{\delta}$ by[5];

matter deposition rate on the cavitating boundaries, and the resultant development of constraints. The time variation of the cavity velocity can be deduced by examining the magnitude of the constraints as a function of the enhanced matter deposition rate.

The additional matter deposition occurring on the cavitating boundaries is given by;

$$\Delta\dot{\delta} = \left(\frac{6\Omega D_b' \delta_b}{kTb^2}\right) \frac{[\sigma_\ell - \sigma_{tip}(1-f)]}{4 + 2f^3 - 6f}$$

where σ_{tip} is the stress at the cavity tip given by[2];

$$\sigma_{tip} = (2 - \gamma_b/\gamma_s)^{\frac{1}{2}} \left(\frac{kT\gamma_s^2}{\Omega D_s \delta_s}\right)^{1/3} \dot{a}^{1/3} \tag{14}$$

Conservation of matter requires that the change in cacity volume $\dot{V}$ be related to the thickening rate by;

$$\dot{V} = b\Delta\dot{\delta} \tag{15}$$

where

$$\dot{V} \simeq w\dot{a} + a\dot{w} \tag{16}$$

and w is the cavity thickness given by[2];

$$w = 1.4 \left(\frac{D_s \delta_s \gamma_s \Omega}{kT}\right)^{1/3} \dot{a}^{-1/3} \tag{17}$$

For conditions which pertain in the present problem it will be demonstrated that the acceleration term $\dot{w}$ is negligible, allowing the thickening differential to be expressed as;

$$\Delta\dot{\delta} = 1.4\ \dot{a}^{2/3} \left(\frac{D_s \delta_s \gamma_s \Omega}{kTb^3}\right)^{1/3} \tag{18}$$

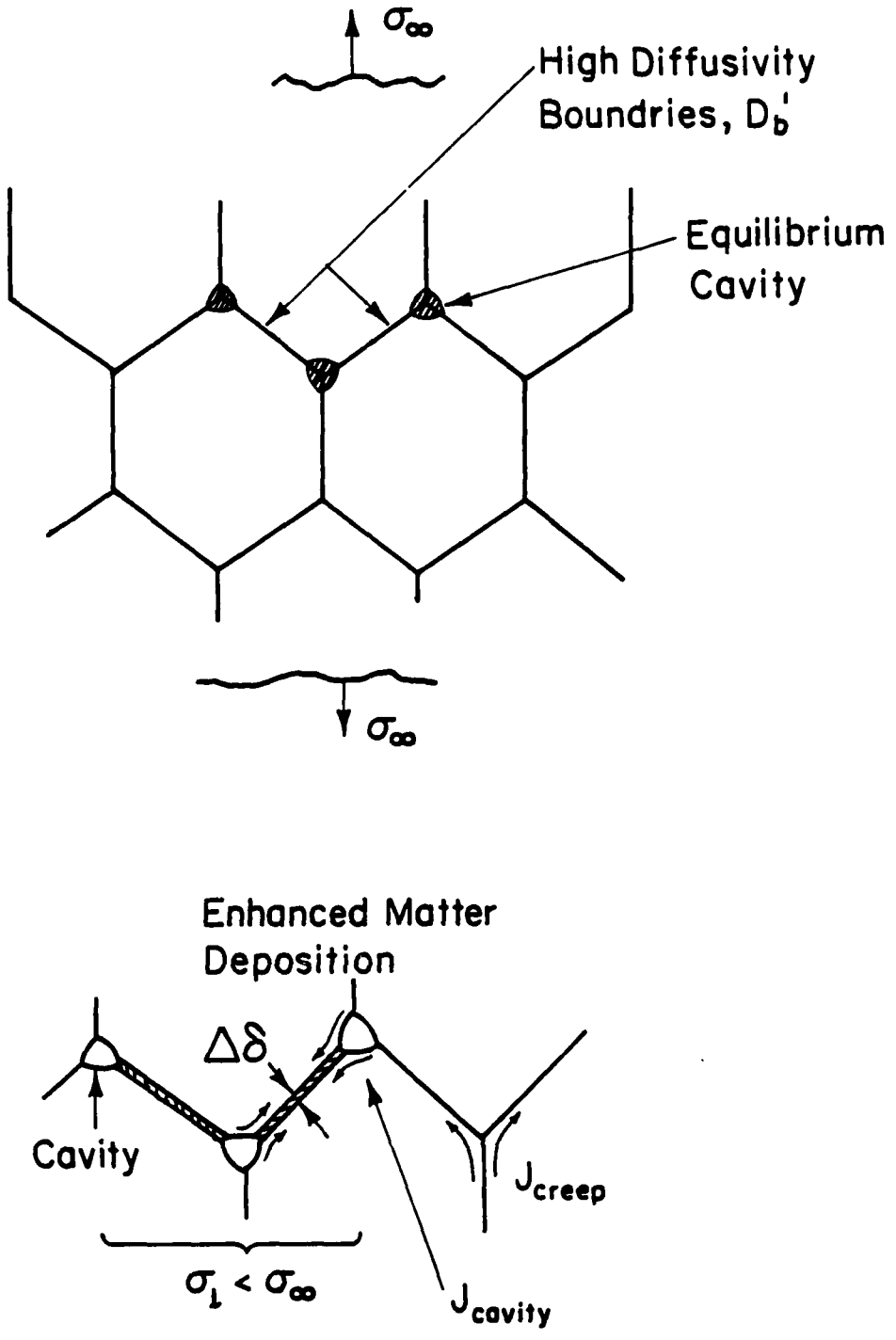

Figure 3. A schematic illustrating two contiguous boundaries with larger than average diffusivities, exhibiting preferred cavitation.

Now, deducing the constraint from Eq. (2) and the creep rate of the surrounding structure from Eq. (1), the cavity velocity becomes;

$$v^{2/3} + v^{1/3} \frac{84\ (1-f)(2-\gamma_b/\gamma_s)^{\frac{1}{2}} - 42\sqrt{2}\ (\sigma_\infty b/\gamma_s)}{[14\ F(f)(D_b/D_b') + 3(g/b)^2(g/d)](D_s\delta_s/D_b\delta_b)} = 0 \qquad (19)$$

where $v = akTb^3/D_s\delta_s\gamma_s\Omega$ and $F(f) = 4 + 2f^3 - 6f$. For all reasonable values of the stress, $\sigma_\infty b/\gamma_s > 10$, the most important solution of Eq. (19) is;

$$v^{2/3} = \frac{42\sqrt{2}\ (\sigma_\infty b/\gamma_s)}{(D_s\delta_s/D_b\delta_b)[14\ F(f)(D_b/D_b') + 3(g/b)^2(g/d)]} \qquad (20)$$

Inspection of Eq. (20) indicates that the velocity only differs from that of the uniform array ($d \to \infty$) when

$$F(f) \gtrsim \frac{g^3(D_b'/D_b)}{b^2 d} \qquad (21)$$

Also, it is noted that the velocity should approach an asymptotic value (Fig. 4) when the cavity separations become small (as $f \to$), given by;

$$v_{ss} = 88(\sigma_\infty b/\gamma_s)^{3/2}(D_b\delta_b/D_s\delta_s)^{3/2}(b/g)^3(d/g)^{3/2} \qquad (22)$$

The asymptotic velocity[†] is independent of the diffusivity on the cavitating boundary, and can thus be comparable to the initial velocity of the crack-like cavity when D_b' is appreciably larger than D_b (Fig. 4).

[†]The appearance of a steady state is the essential justification for the neglect of acceleration terms.

$$\Delta\sigma \simeq \frac{\pi \Delta\dot{\delta}\sigma_\infty}{2\dot{\varepsilon}_\infty d} \tag{2}$$

where d is the length of the zone of differing displacement rate (g in this instance) and $\dot{\varepsilon}_\infty$ is the creep rate of the surrounding structure. Substitution of the creep rate derived from Eq. (1) then gives;

$$\Delta\sigma = \frac{\Delta\dot{\delta} kTg^3}{28\Omega D_b \delta_b d} \tag{3}$$

The deviation in displacement-rate can be estimated from the difference in creep rate in the two regions (by recognizing the stress differential) as,

$$\Delta\dot{\delta} = \frac{14\pi}{kTg^2}\,\Omega\delta_b[D_b'(\sigma_\infty - \Delta\sigma) - D_b\sigma_\infty] \tag{4}$$

Eliminating $\Delta\dot{\delta}$ from Eqs. (3) and (4) then gives,

$$\frac{\Delta\sigma}{\sigma_\infty} = \frac{[D_b/D_b' - 1]}{[1 + (2/\pi)(d/g)(D_b/D_b')]} \tag{5}$$

and the local stress σ_ℓ becomes;

$$-\frac{\sigma_\ell}{\sigma_\infty} = \left[1 - \frac{\Delta\sigma}{\sigma_\infty}\right] = \frac{(D_b/D_b')[1 + (2/\pi)(d/g)]}{[1 + (2/\pi)(d/g)(D_b/D_b')]} \tag{6}$$

The stress can thus be substantially diminished at a boundary with a larger than average diffusivity, but can only be slightly enhanced on boundaries with small diffusivities. However, the time taken to generate cavities of significant size is still somewhat smaller on the boundaries with the higher diffusivities, because

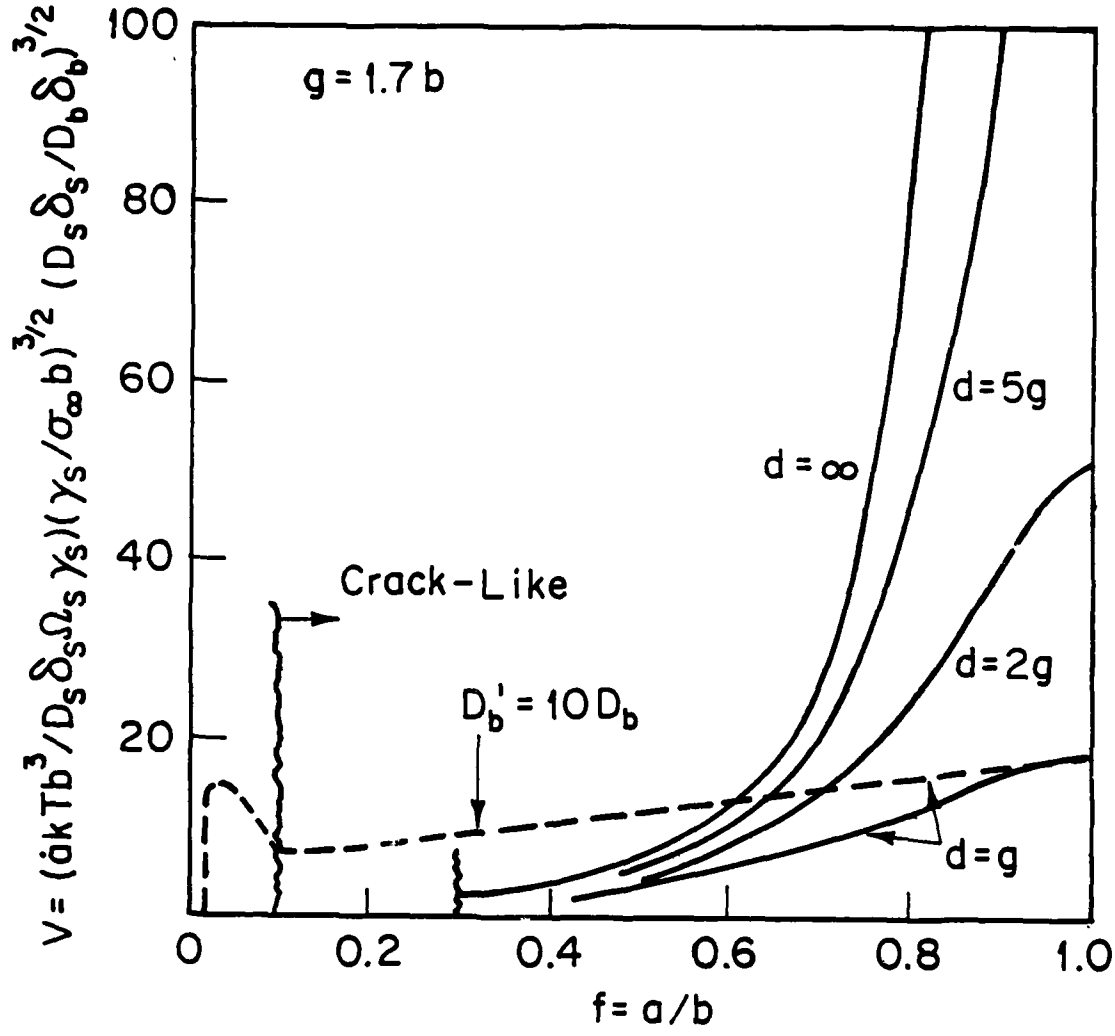

Figure 4. The dependence of cavity velocity on cavity length for several cavitation zone lengths.

the growth rate of equilibrium shaped cavities is itself dependent upon the boundary diffusivity[2];

$$\dot{a} = \left[\frac{\Omega D_b \delta_b}{kTa^2 h}\right] \frac{[\sigma_\ell - (1-f^2)\sigma_o]}{[\ell n(1/f^2) - (3-f^2)(1-f^2)/2]} \qquad (7)$$

where h depends upon the dihedral angle Ψ, σ_o is the sintering stress ($= 2\gamma_s \sin\Psi/a$, where γ_s is the surface energy) and f is the ratio of the cavity radius a to the cavity spacing b. For the small values of f pertinent to initial growth, substituting σ_ℓ from Eq. (6) gives a ratio R of the cavity growth rate on the high diffusivity boundaries to that on the general boundaries:

$$R = \frac{[1 + (2/\pi)(d/g)]\sigma_\infty - (D_b'/D_b)\sigma_o}{\sigma_\infty - \sigma_o} \qquad (8)$$

The growth rate near the sintering limit is suppressed on the high diffusivity boundaries, but becomes enhanced as the cavities extend ($\sigma_\infty >> \sigma_o$). The growth immediately after nucleation occurs very rapidly and most of the extension time entailed in the development of a cavity of observable size occurs when $\sigma_\infty >> \sigma_o$. The ratio of the effective time taken to develop observable cavities, t_o'/t_o, is thus;

$$t_o'/t_o = [1 + (2/\pi)(d/g)]^{-1} \qquad (9)$$

which for $d \sim g$ gives $t_o' \sim 0.6\ t_o$. By contrast, the propagation time on boundaries with low diffusivities ($D_b \gtrsim 10 D_b'$) is usually slightly larger than the general value;

When the velocity deviates from that of the uniform array, the stress on the cavitating region diminishes. The resultant stress σ_ℓ obtained by inserting v from Eq. (20) into Eqs. (3) and (18) is

$$\frac{\sigma_\ell}{\sigma_\infty} = \frac{14\ F(f)\,(b^2d/g^3)}{[3 + 14\ F(f)\,(b^2d/g^3)]} \qquad (23)$$

This stress is plotted in Fig. 5. It is noted that the stress diminishes quite rapidly for $f > 0.7$. There will then be a corresponding increase in the tension outside the cavitation zone (Fig. 6). This enhanced peripheral tension is likely to accelerate the growth of the pheripheral cavities, causing the cavitation zone to spread, as experimentally observed (Fig. 1). The zone spreading is an integral constituent of the failure sequence. Its essential features will be discussed in the following section.

ZONE SPREADING

The incidence of zone spreading is contingent upon the development of enhanced tensions and thus, accelerated cavity growth, around the periphery of the cavitation zone. A detailed solution of this problem involves complex considerations. A useful estimate of zone spreading tendencies can be obtained by determining the velocity of approach of cavities in the peripheral zone subject to the average stress active over the zone.

The enhanced tension in the peripheral zone is related to the stress drop $\Delta\sigma$ in the cavitating zone by;

$$\hat{\sigma} = \frac{\Delta\sigma x}{\sqrt{x^2-d^2}} \qquad (23)$$

$$t'_o/t_o = (D_b/D'_b)(2/\pi)(d/g)[1 + (2/\pi)(d/g)]^{-1} \qquad (10)$$

which for $d \sim g$ gives $t'_o \sim 0.4\ D_b/D'_b$. However, it is emphasized that the local diffusivity has a relatively minor influence on the equilibrium cavity development time.

More significantly, the transition from equilibrium to crack-like cavity morphologies occurs at smaller values of cavity size f* on the boundaries with the larger boundary diffusivities (assuming that D_s is substantially unaltered), as expressed by the relation[6]

$$\left(\frac{\sigma_\ell b}{2\gamma_s}\right) f^* + 15.6\ (\ell n f^*)\left(\frac{D_b\delta_s}{D_b\delta_b}\right) = -11.7\left(\frac{D_s\delta_s}{D_b\delta_b}\right) \qquad (11)$$

A plot of f* (Fig. 2b) indicates that for typical $(\sigma_\ell b/\gamma_s)$ of $<10^2$, transitions in the observed range ($f^* \sim 0.1$) can occur on boundaries with D_b/D_s about 5-10 times larger than an average value of ~ 1. This transition to crack-like morphology represents the commencement of the actual failure process. The time consumed at this juncture ($f^* << 1$) is;

$$t = \left(\frac{hg^3kT}{D_b\delta_b\Omega\sigma_\infty}\right)\int_{f_o}^{f^*} f^3\ \frac{\{\ell n(1/f^2) - 3/2 + (2/7\pi)(g/d)\}df}{[f - 2\gamma_s\ \sin\Psi/\sigma_\infty g]} \qquad (12)$$

CAVITY GROWTH

Once crack-like cavities develop on two contiguous high diffusivity boundary facets, cavity growth will proceed at a relatively rapid rate. This leads to a significently enhanced

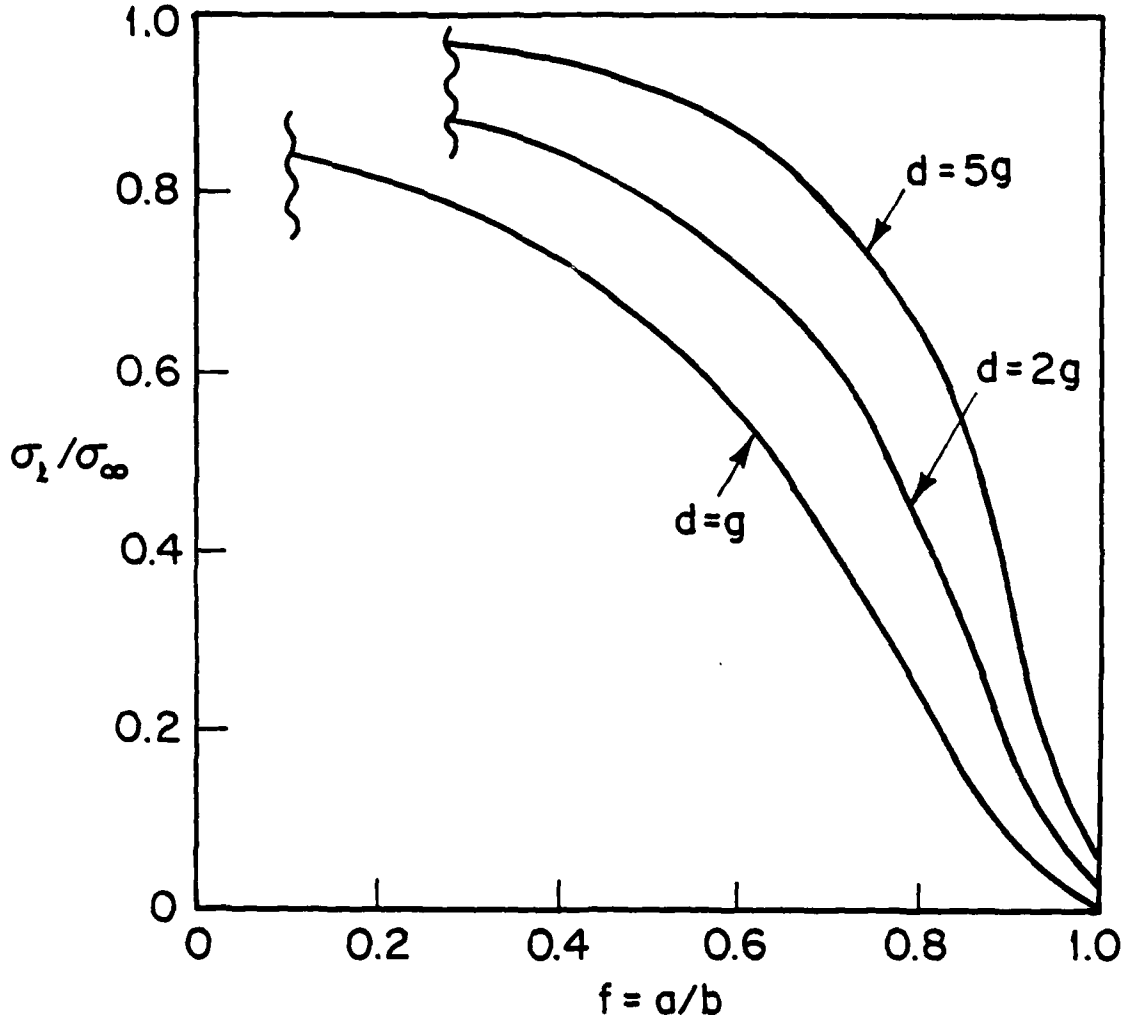

Figure 5. The change in local stress over the cavity region as a function of cavity length.

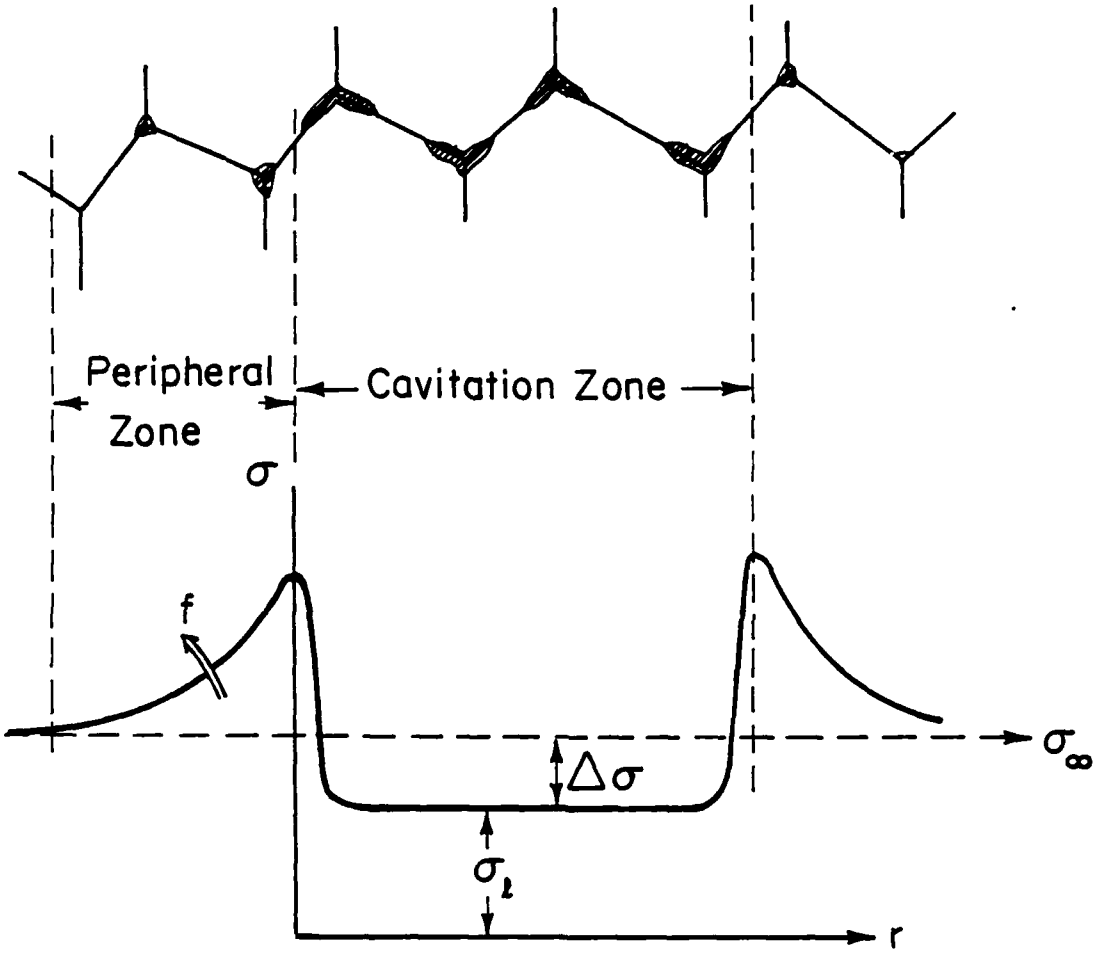

Figure 6. A schematic indicating the changes in the stress field around a cavitation zone as a function of the relative cavity size, f.

Now, deducing the constraint from Eq. (2) and the creep rate of the surrounding structure from Eq. (1), the cavity velocity becomes;

$$v^{2/3} + v^{1/3} \frac{84\ (1-f)(2-\gamma_b/\gamma_s)^{\frac{1}{2}} - 42\sqrt{2}\ (\sigma_\infty b/\gamma_s)}{[14\ F(f)(D_b/D_b') + 3(g/b)^2(g/d)](D_s\delta_s/D_b\delta_b)} = 0 \qquad (19)$$

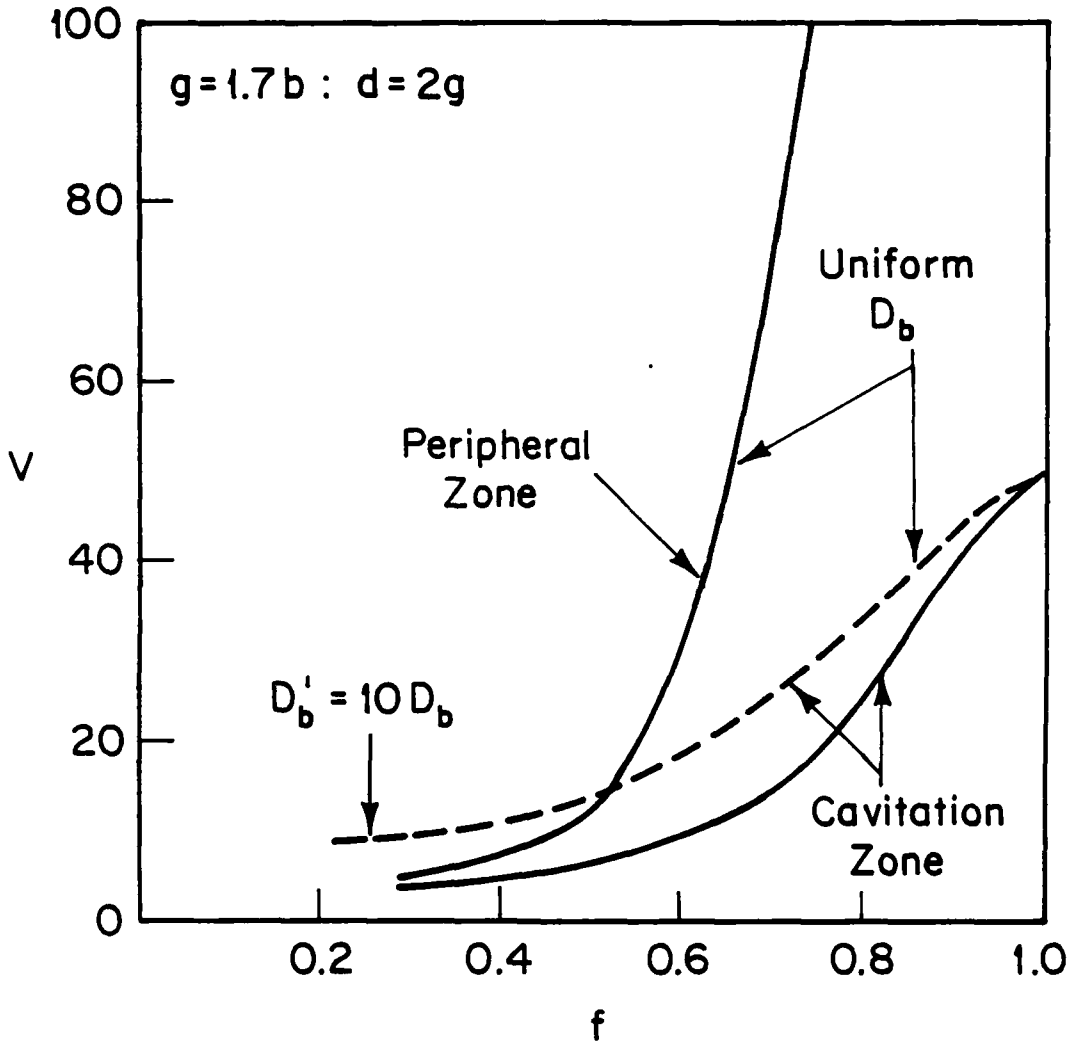

Figure 7. The relative velocities of cavities inside and outside the cavitation zone.

peripheral boundaries, i.e., zone spreading can not be induced. This accounts for the observation (Fig. 1) of isolated full-facet sized cavities that then widen without extending. These regions are relatively innocuous with regard to final failure. Secondly, behavior with slightly larger diffusivities than the general level (by $\sim$2) can induce zone spreading, and are thus capable of developing the cracks that generate failure. Finally, it is noted that if a series of contiguous boundaries with very high diffusivities occur in a material, then complete cavitation would develop very readily in this region, because the constraint is minimal. The probability of occurrence and the failure time would then be given by probabilistic considerations of the type presented in a previous paper[3]. The incidence of these possible modes of cavitation need to be examined experimentally, to determine the materials and conditions that dictate their relative importance.

ACKNOWLEDGEMENT

This research was supported by the Defense Advanced Research Projects Agency of the Department of Defense under Contract No. MDA903-80C-0505 with The University of Michigan.

REFERENCES

1. D. Hull and D. E. Rimmer, Phil. Mag. 4, 673 (1959).

2. T. J. Chuang, K. I. Kagawa, J. R. Rice and L. B. Sills, Acta Met. 27, 265 (1979).

3. A. G. Evans and A. Rana, Acta Met. 28, 115 (1980).

4. R. Raj and M. F. Ashby, Acta Met. 23, 653 (1975).

5. J. R. Rice, to be published.

6. A. Needleman and J. R. Rice, Acta Met., in press.

When the velocity deviates from that of the uniform array, the stress on the cavitating region diminishes. The resultant stress σ_ℓ obtained by inserting v from Eq. (20) into Eqs. (3) and (18) is

$$\frac{\sigma_\ell}{\sigma_\infty} = \frac{14\ F(f)\,(b^2d/g^3)}{[3 + 14\ F(f)\,(b^2d/g^3)]} \qquad (23)$$

This stress is plotted in Fig. 5. It is noted that the stress diminishes quite rapidly for $f > 0.7$. There will then be a corresponding increase in the tension outside the cavitation zone (Fig. 6). This enhanced peripheral tension is likely to accelerate the growth of the pheripheral cavities, causing the cavitation zone to spread, as experimentally observed (Fig. 1). The zone spreading is an integral constituent of the failure sequence. Its essential features will be discussed in the following section.

ZONE SPREADING

The incidence of zone spreading is contingent upon the development of enhanced tensions and thus, accelerated cavity growth, around the periphery of the cavitation zone. A detailed solution of this problem involves complex considerations. A useful estimate of zone spreading tendencies can be obtained by determining the velocity of approach of cavities in the peripheral zone subject to the average stress active over the zone.

The enhanced tension in the peripheral zone is related to the stress drop $\Delta\sigma$ in the cavitating zone by;

$$\hat{\sigma} = \frac{\Delta\sigma x}{\sqrt{x^2-d^2}} \qquad (23)$$

CREEP CAVITATION OF GRAIN INTERFACES

J. R. Rice

ABSTRACT

The paper presents an analysis of diffusional cavity growth on grain interfaces. Derivation of the growth rate is reviewed for the simplest case when cavities retain a quasi-equilibrium, spherical caps shape and when the adjoining grains separate in an effectively rigid manner. Modifications of the results are then discussed based on the possibility of non-equilibrium cavity shapes, dislocation creep of the adjoining grains, and constraints which arise when cavitated grain facets are relatively isolated in a polycrystalline aggregate.

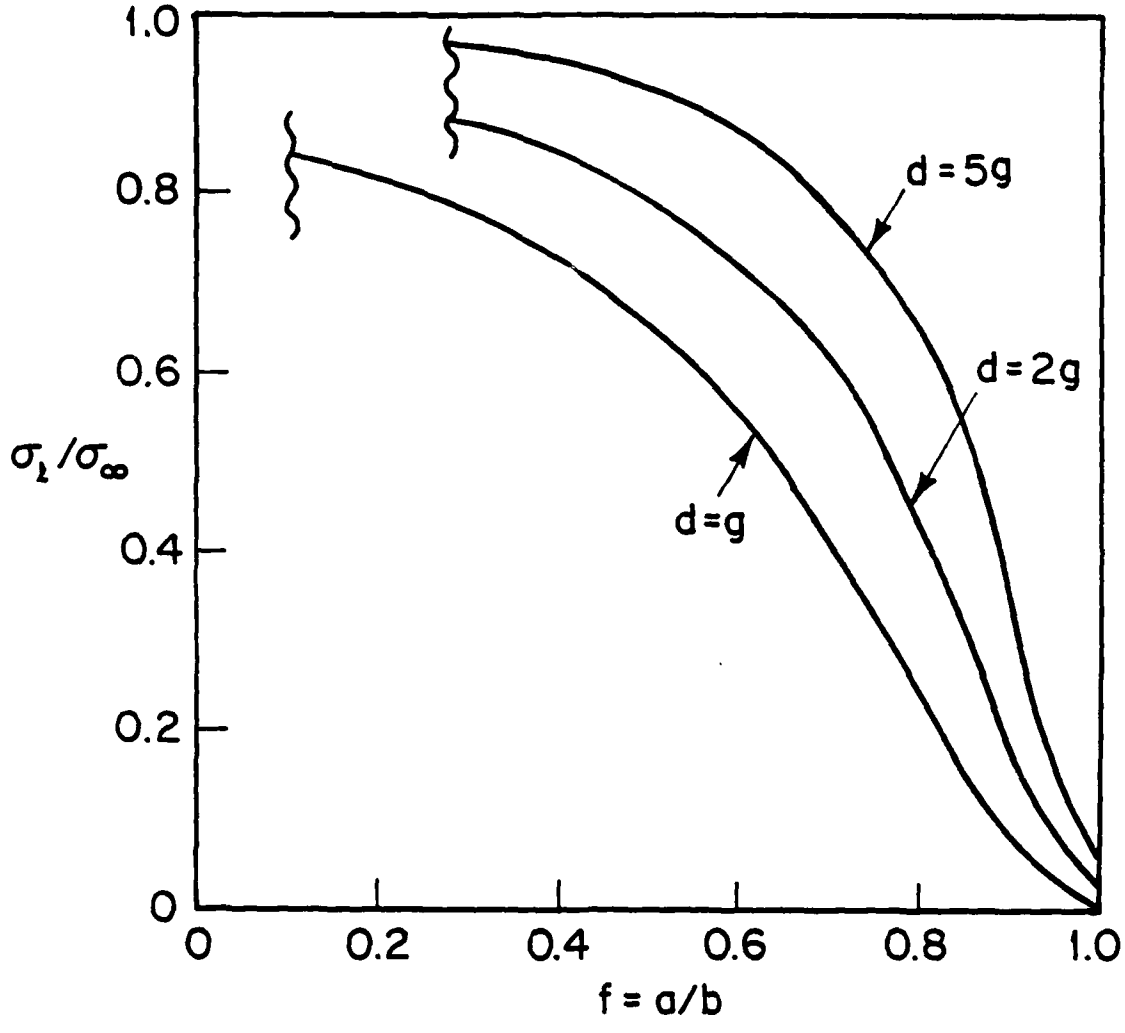

Figure 5. The change in local stress over the cavity region as a function of cavity length.

CREEP CAVITATION OF GRAIN INTERFACES

J. R. Rice

INTRODUCTION

At elevated temperatures, of the order 0.5 T_m and higher, polycrystalline materials generally fracture by the initiation and growth of cavities along grain boundaries. Various analyses suggest that owing to the usual size range of these cavities (say, 0.1 to 1 μm), the dominant growth mechanism is by surface and grain boundary diffusion. (See, e.g., the comparison of characteristic times for different matter transport mechanisms by Chuang et. al. (1979)).

This mechanism of cavitation was suggested by Balluffi and Seigle (1957) and modelled quantitatively by Hull and Rimmer (1959). The latter analysis has been corrected and improved in various ways in subsequent work (e.g., Raj and Ashby, 1975). Such studies have been reviewed recently by Chuang et. al. (1979), who also consider extensions of the Hull-Rimmer model to non-equilibrium cavity shapes, and by Needleman and Rice (1980) who consider the coupling of dislocation creep to the diffusive growth process.

The present paper summarizes results on the diffusive growth process and its various modifications due to non-equilibrium cavity shapes, dislocation creep, and interactions between cavitating grain facets and their surroundings.

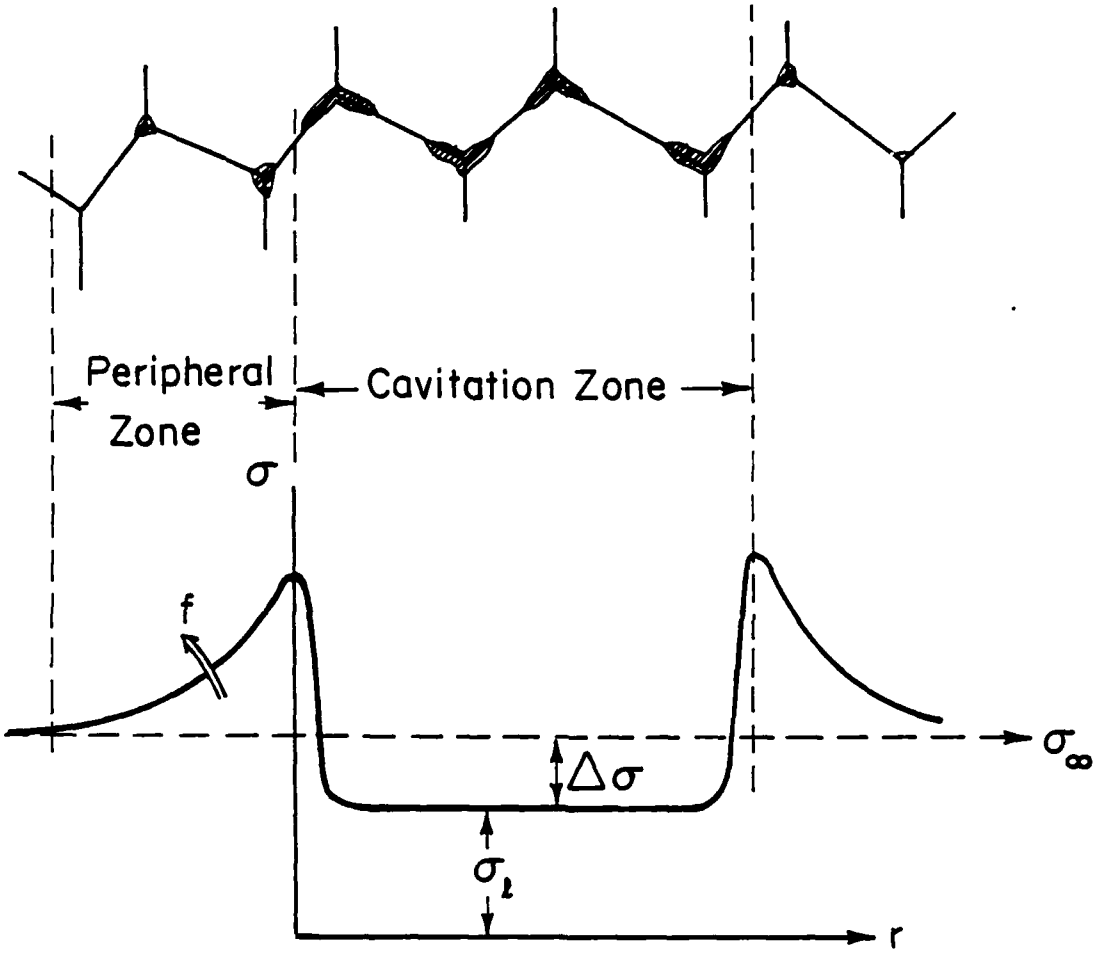

Figure 6. A schematic indicating the changes in the stress field around a cavitation zone as a function of the relative cavity size, f.

ANALYSIS OF DIFFUSIVE CAVITATION

As remarked, the dominant transport mechanisms are usually surface and grain boundary diffusion. Here the basic equations governing the cavitation process are presented based on the assumption that essentially all matter transport is by these mechanisms.

Figure 1a shows a cavitated grain boundary subjected to stress σ. The problem is conventionally simplified by considering (Fig. 1b) the axi-symmetric problem of a circular cylindrical bi-crystal subject to the same stress σ. The cavity radius is a and the outer radius b is chosen to that $a^2/b^2 = f$, the area fraction of the grain boundary which is cavitated. To simulate interactions between neighboring cavities, the grain boundary flux J_B is set equal to zero at radius $r = b$.

The basic equations describing the diffusion process are those of matter conservation and of the (linearized) kinetic relation between the diffusive flux J and gradient of chemical potential μ along the flow path. Thus

$$\Omega \underline{\nabla} \cdot \underline{J}_S = V_n,$$

$$\Omega \underline{J}_S = (D_S \delta_S / kT) \underline{\nabla} \mu \quad \text{where } \mu = -\gamma_S \Omega (K_1 + K_2), \tag{1}$$

on the cavity surfaces, and

$$\Omega \nabla \cdot \underline{J}_B + \dot{\delta} = 0,$$

$$\Omega \underline{J}_B = -(D_B \delta_B / kT) \underline{\nabla} \mu \quad \text{where } \mu = -\Omega \sigma_{zz} \tag{2}$$

on the grain boundary. Here the fluxes $\underline{J}_S$, $\underline{J}_B$ (of magnitudes

where x is the distance from the center of the cavitation zone. The average stress enhancement up to the next set of triple junctions is thus;

$$\langle\hat{\sigma}\rangle = \Delta\sigma\sqrt{1+2d/b} \tag{24}$$

and the total stress is

$$\frac{\sigma}{\sigma_\infty} = 1 + (\Delta\sigma/\sigma_\infty)\sqrt{1+2d/b} \tag{25}$$

Combining Eqs. (20), (23) and (25), the cavity velocity in the peripheral region becomes,

$$v_p^{2/3} = \frac{3\sqrt{2}(\sigma_\infty b/\gamma_s)\{1 + 3\sqrt{1+2d/b}/[3 + 14\ F(f)b^2d/g^3]\}}{(D_s\delta_s/D_b\delta_b)F(f)} \tag{26}$$

This velocity is compared in Fig. 7 with the cavity velocity inside the cavitating zone. It is noted that the cavity velocity in the peripheral zone exceeds the internal velocity unless the diffusivity in the cavitation zone is larger. The extent of cavitation in the two zones will thus become comparable as cavitation proceeds. A choice pertinent to zone spreading might thus be made on the basis of equal cavitation extension in the internal and peripheral zones. At that juncture the zone can be considered to extend from d to d+b, and the process continued.

The detailed computation of the failure time is not conducted here. However, certain important characteristics are noted. Firstly, when the boundary diffusivity is very much larger (>10) then the average diffusivity, complete cavitation of the boundary occurs before appreciable cavity growth enhancement can be achieved on the

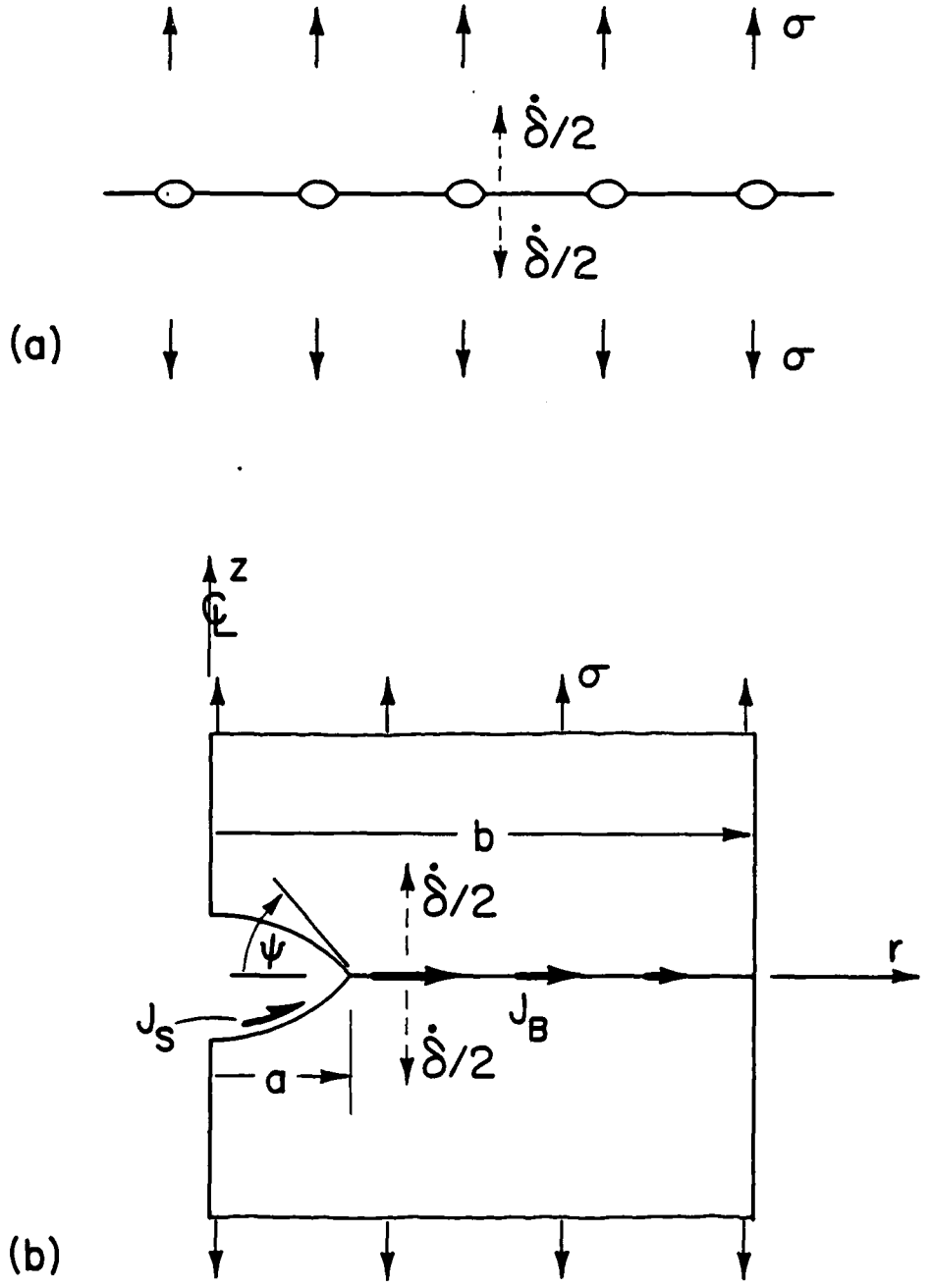

Figure 1. (a) Cavitated grain boundary.
(b) Axi-symmetric bi-crystal configuration used for analysis.

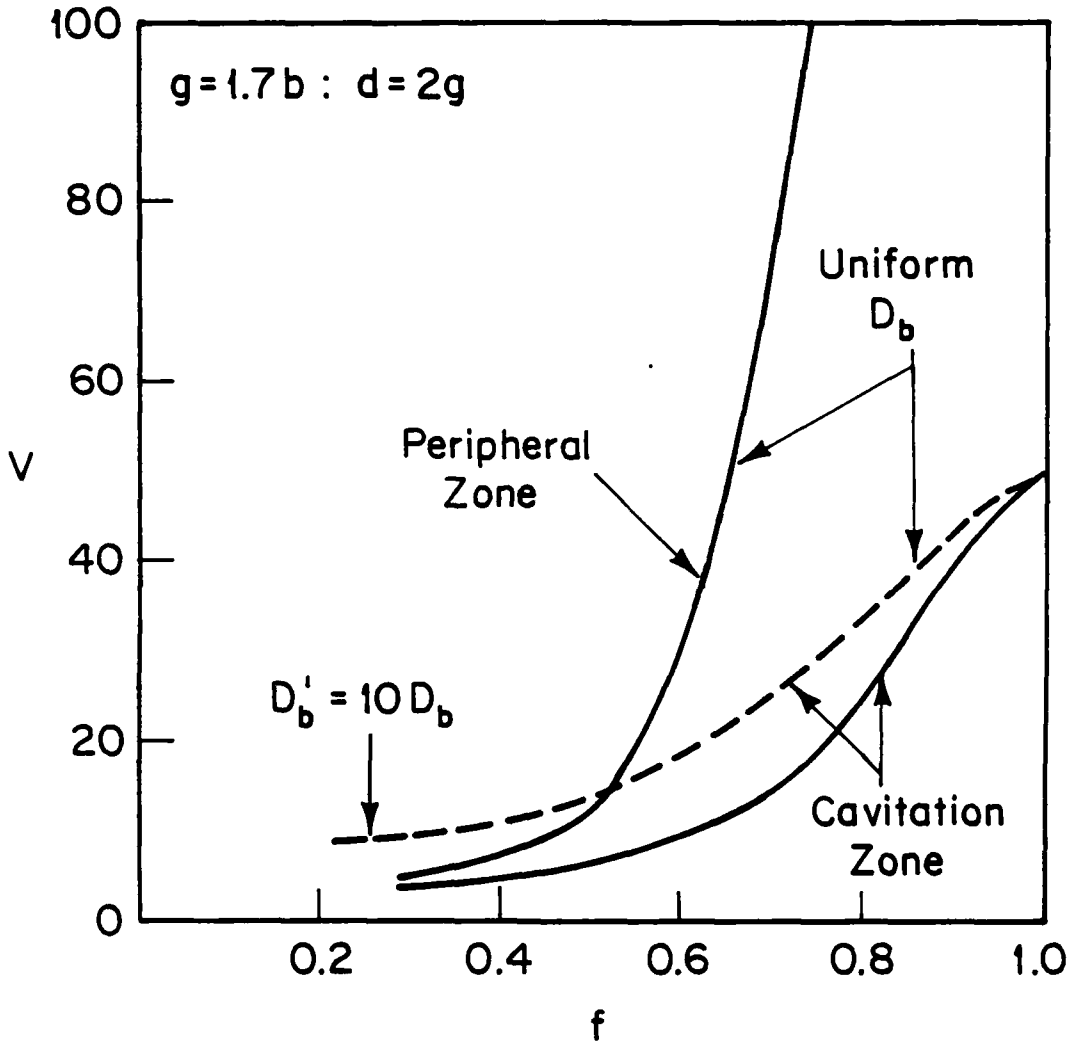

Figure 7. The relative velocities of cavities inside and outside the cavitation zone.

J_S, J_B) are measured in units of atoms crossing unit length per unit time, Ω is atomic volume, $\underline{\nabla}$ is a surface gradient operator, V_n is the normal recession velocity of the void surface relative to adjoining material, $\dot{\delta}$ is the opening rate across the grain boundary (due to matter addition), $D_S\delta_S$ and $D_B\delta_B$ are diffusion coefficients, kT is the energy measure of temperature, γ_S is the surface energy, K_1 and K_2 are the principal curvatures of the cavity surface, and σ_{zz} is the local normal stress acting along the grain boundary.

In addition, the angle Ψ (Fig. 1b) at the cavity tip is assumed to be given by the equilibrium expression,

$$\cos \Psi = \gamma_B/2\gamma_S \quad ,$$

where γ_B is the boundary energy, and the potential μ and matter flow are continuous at the cavity tip, so that

$$\gamma_S(K_1 + K_2)_{tip} = (\sigma_{zz})_{tip}, \; (2J_S)_{tip} = (J_B)_{tip} \quad . \qquad (3)$$

Completion of the set of governing equations requires a specification of the manner by which the adjoining grains in Fig. 1b deform. Without specifying details of possible constitutive relations, such considerations couple the distribution of stress σ_{zz} on the grain boundary to the distribution of opening displacement $\dot{\delta}$ (precisely, to the distribution of gradients in $\dot{\delta}$). Of course, by overall equilibrium the stress distribution σ_{zz} is constrained to balance the stress σ acting far from the boundary in Fig. 1b.

peripheral boundaries, i.e., zone spreading can not be induced. This accounts for the observation (Fig. 1) of isolated full-facet sized cavities that then widen without extending. These regions are relatively innocuous with regard to final failure. Secondly, behavior with slightly larger diffusivities than the general level (by $\sim$2) can induce zone spreading, and are thus capable of developing the cracks that generate failure. Finally, it is noted that if a series of contiguous boundaries with very high diffusivities occur in a material, then complete cavitation would develop very readily in this region, because the constraint is minimal. The probability of occurrence and the failure time would then be given by probabilistic considerations of the type presented in a previous paper[3]. The incidence of these possible modes of cavitation need to be examined experimentally, to determine the materials and conditions that dictate their relative importance.

ACKNOWLEDGEMENT

This research was supported by the Defense Advanced Research Projects Agency of the Department of Defense under Contract No. MDA903-80C-0505 with The University of Michigan.

SOLUTION OF QUASI-EQUILIBRIUM CAVITY SHAPE AND RIGID GRAIN SEPARATION

The problem of cavity growth is straightforward to solve in the case for which the following simplifications are made:

(i) Surface diffusion is assumed to be sufficiently rapid compared to boundary diffusion that the cavities retain a quasi-equilibrium, spherical caps shape during growth, and

(ii) Grain deformations are assumed to be small enough that the two crystals of Fig. 1b can be taken to move apart rigidly from one another at an opening rate $\dot{\delta}$ that is independent of position along the grain boundary.

When condition (ii) is met, the stress distribution on the grain boundary may be found by integrating Eq. (2), subject to $J_B = 0$ at $r = b$, which results in

$$\sigma_{zz} = \sigma_o + (\dot{\delta}/2D)\{b^2 \ell n(r/a) - (r^2-a^2)/2\} \tag{4}$$

where

$$D = D_B \delta_B \Omega/kT \tag{5}$$

and where $\sigma_o \equiv (\sigma_{zz})_{tip}$, i.e., the value of σ_{zz} at the cavity tip, $r = a$. From this result it follows by overall equilibrium that the applied stress σ is related to σ_o and $\dot{\delta}$ by

$$\sigma = (1-f)\sigma_o + (b^2\dot{\delta}/4D)\{\ell n(1/f) - (3-f)(1-f)/2\}, \tag{6}$$

and that the volumetric rate at which matter flows into the grain boundary at the void tip is

$$(2\pi a)(\Omega J_B)_{tip} = \pi b^2 (1-f)\dot{\delta} \tag{7}$$

REFERENCES

1. D. Hull and D. E. Rimmer, Phil. Mag. 4, 673 (1959).

2. T. J. Chuang, K. I. Kagawa, J. R. Rice and L. B. Sills, Acta Met. 27, 265 (1979).

3. A. G. Evans and A. Rana, Acta Met. 28, 115 (1980).

4. R. Raj and M. F. Ashby, Acta Met. 23, 653 (1975).

5. J. R. Rice, to be published.

6. A. Needleman and J. R. Rice, Acta Met., in press.

AD-A099 917 MICHIGAN UNIV ANN ARBOR COLL OF ENGINEERING F/G 5/2
PRELIMINARY REPORTS, MEMORANDA AND TECHNICAL NOTES OF THE MATER--ETC(U)
JUL 80 M J SINNOTT MDA903-80-C-0505
UNCLASSIFIED 018324 NL

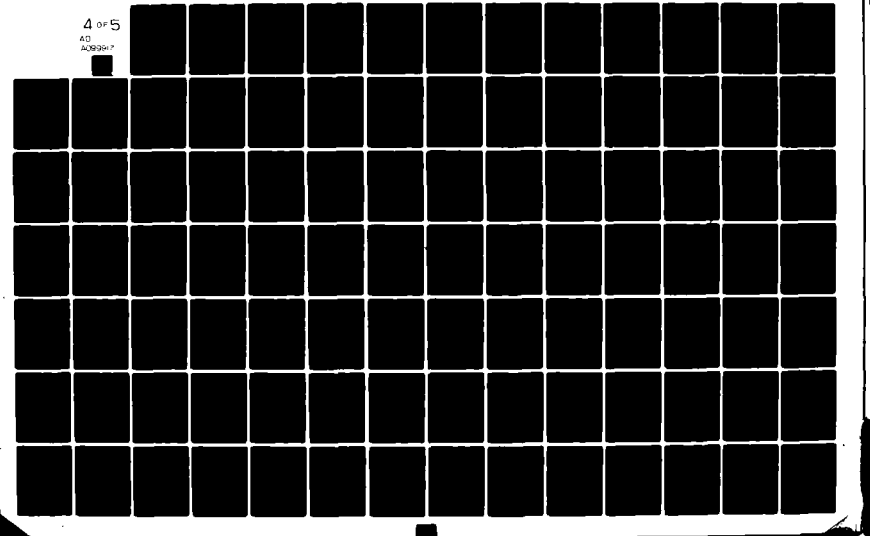

CREEP CAVITATION OF GRAIN INTERFACES

J. R. Rice

ABSTRACT

The paper presents an analysis of diffusional cavity growth on grain interfaces. Derivation of the growth rate is reviewed for the simplest case when cavities retain a quasi-equilibrium, spherical caps shape and when the adjoining grains separate in an effectively rigid manner. Modifications of the results are then discussed based on the possibility of non-equilibrium cavity shapes, dislocation creep of the adjoining grains, and constraints which arise when cavitated grain facets are relatively isolated in a polycrystalline aggregate.

When simplification (i) applies, the curvatures of the void are given by $K_1 = K_2 = (\sin \Psi)/a$, so that the first of Eq. (3) implies

$$\sigma_o = (2\gamma_S/a)\sin \Psi \quad . \tag{8}$$

Also, the volume of the void may be written as

$$V = (4\pi/3)a^3 h \tag{9}$$

where (e.g., Chuang et al., 1979)

$$h = h(\Psi) = \{1/1+\cos\Psi)-(\cos\Psi)/2\}/\sin\Psi \quad ;$$

$h = 1$ when $\Psi = 90°$ and $h \simeq 0.6$ when $\Psi = 70°$, as is typical. Now, it follows by overall mass conservation for the configuration of Fig. 1b that

$$\int_S (V_{mat})_n \, dS + 2\pi a(\Omega J_B)_{tip} = \dot{V} = 4\pi h a^2 \dot{a} \tag{10}$$

where S denotes the surface of the void and $(V_{mat})_n$ is the normal velocity of material points immediately adjacent to the void surface.

If the grains separate rigidly at rate $\dot{\delta}$, the integral in Eq. (10) is easily shown to equal $\pi a^2 \dot{\delta}$ so that, using Eq. (7), one obtains

$$\pi a^2 \dot{\delta} + 2\pi a(\Omega J_B)_{tip} = \pi b^2 \dot{\delta} = \dot{V} = 4\pi h a^2 \dot{a} \tag{11}$$

Hence $\dot{\delta} = 4hf\dot{a}$, and using this in Eq. (6) one obtains

$$\dot{a} = (D/ha^2)\{\sigma-2(1-f)(\gamma_S/a)\sin\Psi\}/\{\ell n(1/f)-(3-f)(1-f)/2\} \tag{12}$$

This last equation expresses the cavity growth rate when simplifications (i), pertaining to the quasi-equilibrium cavity

CREEP CAVITATION OF GRAIN INTERFACES

J. R. Rice

INTRODUCTION

At elevated temperatures, of the order 0.5 T_m and higher, polycrystalline materials generally fracture by the initiation and growth of cavities along grain boundaries. Various analyses suggest that owing to the usual size range of these cavities (say, 0.1 to 1 μm), the dominant growth mechanism is by surface and grain boundary diffusion. (See, e.g., the comparison of characteristic times for different matter transport mechanisms by Chuang et. al. (1979)).

This mechanism of cavitation was suggested by Balluffi and Seigle (1957) and modelled quantitatively by Hull and Rimmer (1959). The latter analysis has been corrected and improved in various ways in subsequent work (e.g., Raj and Ashby, 1975). Such studies have been reviewed recently by Chuang et. al. (1979), who also consider extensions of the Hull-Rimmer model to non-equilibrium cavity shapes, and by Needleman and Rice (1980) who consider the coupling of dislocation creep to the diffusive growth process.

The present paper summarizes results on the diffusive growth process and its various modifications due to non-equilibrium cavity shapes, dislocation creep, and interactions between cavitating grain facets and their surroundings.

shape, and (ii), pertaining to rigid grains, apply. Note, however, that Eqs. (8) to (10) apply whenever the quasi-equilibrium shape can be assumed, whether or not the grains deform, whereas Eqs. (4) to (7) apply whenever the grains can be assumed to separate rigidly, whether or not the cavity has the quasi-equilibrium shape.

Equation (12) was given by Needleman and Rice (1980), who observe that it corrects an undue factor of (1-f) in previous presentations of the result (e.g., Raj and Ashby, 1975, Chuang et al., 1979); the factor arose from neglect of the surface integral in Eq. (10). They observe also that the derivation tacitly assumes that the surface tension (in the sense of surface stress, and as distinct from surface energy) is zero. The inclusion of surface tension T_s adds a term $(-2fT_s/a)\sin\Psi$ to the bracketed term in Eq. (12) that contains σ. This is generally a small effect.

If the growth rate law is written symbolically as $\dot{a} = 1/F(a)$, then the time to rupture, t_r, associated with cavity growth from some initial size, a_i, to coalescence, $a = b$, is given by

$$t_r = \int_{a_i}^{b} F(a)\,da \qquad (13)$$

This is straightforward to compute when the applied stress σ is constant throughout the growth process and is much larger than the "sintering stress" $(2\gamma_s/a_i)\sin\Psi$ at the onset of growth. In that case the expression for $\dot{a}$ of Eq. (12) leads to

$$t_r = \frac{16}{315}\frac{hb}{D\sigma}\left\{1 - \frac{105}{16} f_i^{3/2} \ln(1/f_i) - \frac{1}{8} f_i^{3/2} \left(63 f_i^{1/2} - \frac{175}{4}\frac{45}{4} f_i\right)\right\} \qquad (14)$$

ANALYSIS OF DIFFUSIVE CAVITATION

As remarked, the dominant transport mechanisms are usually surface and grain boundary diffusion. Here the basic equations governing the cavitation process are presented based on the assumption that essentially all matter transport is by these mechanisms.

Figure 1a shows a cavitated grain boundary subjected to stress σ. The problem is conventionally simplified by considering (Fig. 1b) the axi-symmetric problem of a circular cylindrical bi-crystal subject to the same stress σ. The cavity radius is a and the outer radius b is chosen to that $a^2/b^2 = f$, the area fraction of the grain boundary which is cavitated. To simulate interactions between neighboring cavities, the grain boundary flux J_B is set equal to zero at radius $r = b$.

The basic equations describing the diffusion process are those of matter conservation and of the (linearized) kinetic relation between the diffusive flux J and gradient of chemical potential μ along the flow path. Thus

$$\Omega \underline{\nabla} \cdot \underline{J}_S = V_n,$$

$$\Omega \underline{J}_S = (D_S \delta_S / kT) \underline{\nabla} \mu \quad \text{where } \mu = -\gamma_S \Omega (K_1 + K_2), \tag{1}$$

on the cavity surfaces, and

$$\Omega \nabla \cdot \underline{J}_B + \dot{\delta} = 0,$$

$$\Omega \underline{J}_B = -(D_B \delta_B / kT) \underline{\nabla} \mu \quad \text{where } \mu = -\Omega \sigma_{zz} \tag{2}$$

on the grain boundary. Here the fluxes $\underline{J}_S$, $\underline{J}_B$ (of magnitudes

where $f_i = a_i^2/b^2$. This rupture time is inversely proportional to stress and to the grain boundary diffusion coefficient $D_B\delta_B$. This estimate of the rupture time neglects details of cavity nucleation (see Raj and Ashby, 1975), but the result does not depend strongly on the initial value of a_i. Indeed, the bracketed term involving f_i can be replaced by unity for f_i less than 1/10 or so.

The validity of simplifications (i) and (ii) is now examined.

NON-EQUILIBRIUM CAVITY SHAPE

For this section simplification (ii) is retained, but not (i). That is, the possibility is considered that surface diffusion may not be fast enough to allow retention of the quasi-equilibrium, spherical caps shape.

The problem in this form was addressed by Chuang et al. (1979), who point out that according to an appropriate solution of Eq. (1), the relaxation time for a doubly periodic surface disturbance with half-wavelength equated to cavity diameter, 2a, is approximately $a^4/24B$, where

$$B = D_S\delta_S\Omega\gamma_S/kT \tag{15}$$

A characteristic time associated with exposure of new cavity surface to the surface diffusion process is $a/\dot{a}$, and this identifies the dimensionless parameter

$$a^3\dot{a}/24B \tag{16}$$

with the following interpretation: When the parameter is small

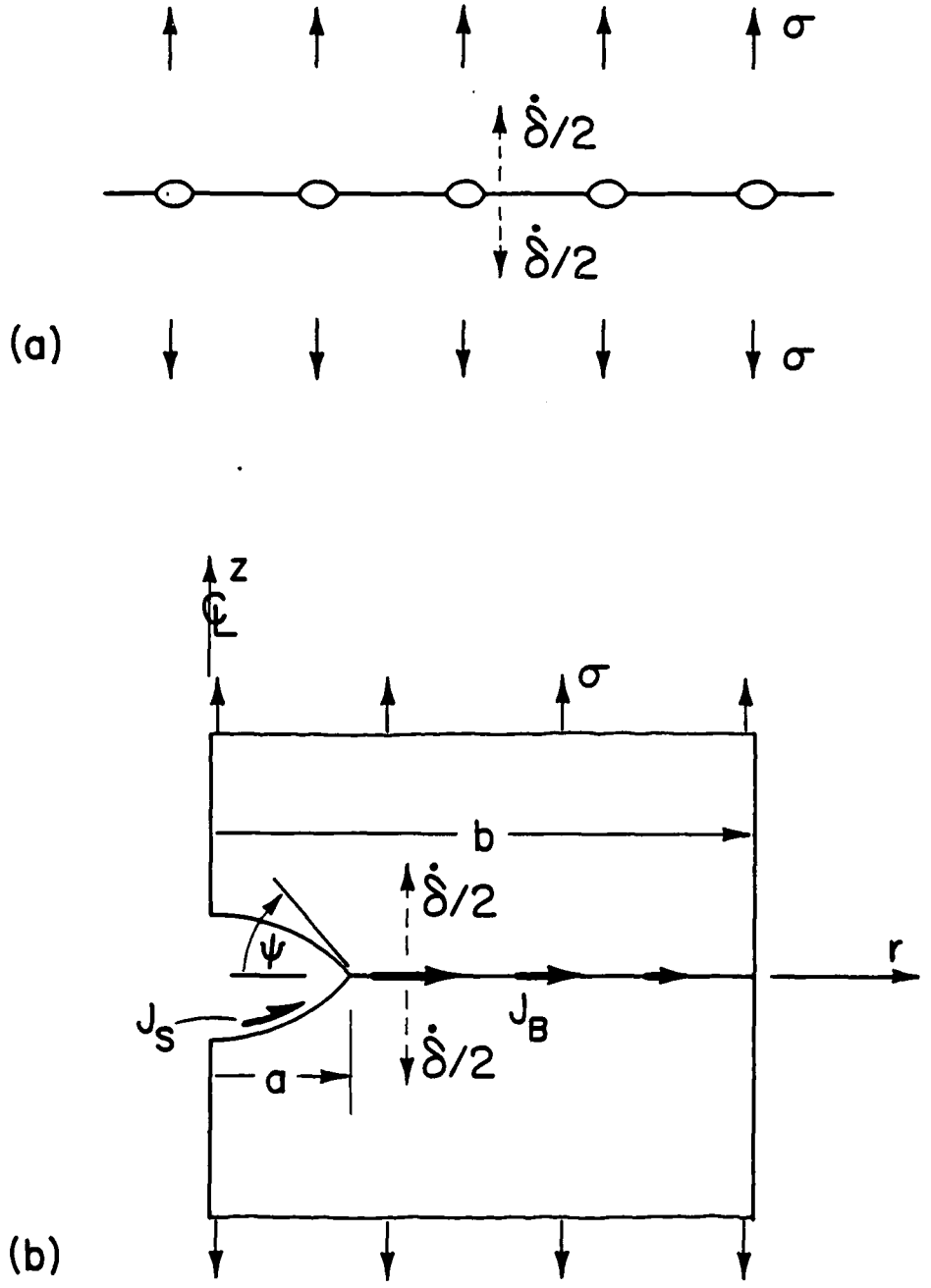

Figure 1. (a) Cavitated grain boundary.
(b) Axi-symmetric bi-crystal configuration used for analysis.

compared to unity the quasi-equilibrium analysis of the last section applies, whereas when it is much greater than unity the cavity can be assumed to grow in a narrow "crack-like" mode as discussed by Chuang and Rice (1973) and Chuang et al. (1979).

This crack-like mode of cavity growth emerges in the analysis of Chuang et al. (1979) as a limiting singular perturbation form of the solutions to Eq. (1) as the parameter $(B/a^3\dot{a}) \to 0$ and all lengths near the cavity tip are scaled by the length parameter $(B/a)^{1/3}$. In this case one obtains the asymptotic results

$$\begin{aligned} (K_1 + K_2)_{tip} &\to 2 \sin(\Psi/2)(\dot{a}/B)^{1/3} \\ (\Omega J_S)_{tip} &\to 2 \sin(\Psi/2)(B\dot{a}^2)^{1/3} \end{aligned} \tag{17}$$

These expressions may be used in Eq. (3) to calculate $(\sigma_{zz})_{tip}$ [$\equiv\sigma_o$ of Eqs. (4) and (6)] and $(\Omega J_B)_{tip}$. The latter is then used in Eq. (7) to calculate $\dot{\delta}$. The result is that the term σ_o and $\dot{\delta}$ in Eq. (6) are known in terms of the cavity growth rate and, when the expression is inverted, one obtains (Chuang et al., 1979)

$$\dot{a} = \frac{27}{64} \frac{B}{b^3\Delta} \frac{\{(1 + Q\Sigma\Delta)^{1/2} - 1\}^3}{(1-f)^3 \, Q^3} \tag{18}$$

Here

$$\begin{aligned} Q &= \{3f^{1/3}/2(1-f)^3\}\{\ell n(1/f) - (3-f)(1-f)/2\} \quad , \\ \Sigma &= 4\sigma b/3\gamma_S \sin(\Psi/2) \quad , \end{aligned} \tag{19}$$

and

$$\Delta = D_S\delta_S/D_B\delta_B \tag{20}$$

J_S, J_B) are measured in units of atoms crossing unit length per unit time, Ω is atomic volume, $\underline{\nabla}$ is a surface gradient operator, V_n is the normal recession velocity of the void surface relative to adjoining material, $\dot{\delta}$ is the opening rate across the grain boundary (due to matter addition), $D_S\delta_S$ and $D_B\delta_B$ are diffusion coefficients, kT is the energy measure of temperature, γ_S is the surface energy, K_1 and K_2 are the principal curvatures of the cavity surface, and σ_{zz} is the local normal stress acting along the grain boundary.

In addition, the angle Ψ (Fig. 1b) at the cavity tip is assumed to be given by the equilibrium expression,

$$\cos \Psi = \gamma_B/2\gamma_S \quad ,$$

where γ_B is the boundary energy, and the potential μ and matter flow are continuous at the cavity tip, so that

$$\gamma_S(K_1 + K_2)_{tip} = (\sigma_{zz})_{tip}, \; (2J_S)_{tip} = (J_B)_{tip} \quad . \qquad (3)$$

Completion of the set of governing equations requires a specification of the manner by which the adjoining grains in Fig. 1b deform. Without specifying details of possible constitutive relations, such considerations couple the distribution of stress σ_{zz} on the grain boundary to the distribution of opening displacement $\dot{\delta}$ (precisely, to the distribution of gradients in $\dot{\delta}$). Of course, by overall equilibrium the stress distribution σ_{zz} is constrained to balance the stress σ acting far from the boundary in Fig. 1b.

The function Q is not strongly variable; it lies between approximately 0.5 and 0.65 for $0.01<f<1$, although $Q \to 0$ as $f \to 0$.

By comparisons of predictions of Eqs. (12) and (18) against a family of self-similar solutions for cavity growth, Chuang et al. (1979) conclude that Eq. (12) is valid for $a^3\dot{a}/B$ less than approximately 10, whereas Eq. (18) is valid for $a^3\dot{a}/B$ greater than approximately 30. A tolerable approximation, valid over the entire range of $\dot{a}$, was found to be that of taking $\dot{a}$ as the maximum of the expressions of Eqs. (12) and (18).

Chuang et al. (1979) present various inequalities for

AD-A099 917 MICHIGAN UNIV ANN ARBOR COLL OF ENGINEERING F/G 5/2
PRELIMINARY REPORTS, MEMORANDA AND TECHNICAL NOTES OF THE MATER--ETC(U)
JUL 80 M J SINNOTT MDA903-80-C-0505
UNCLASSIFIED 018324 NL

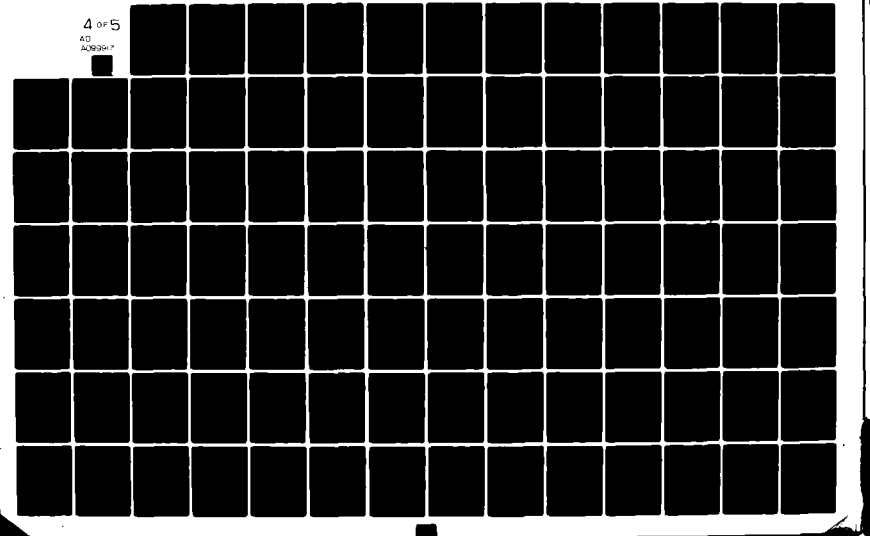

when σ is less than σ^* growth occurs in the quasi-equilibrium mode, and when σ is greater than σ^* growth occurs in the crack-like mode.

Estimated values of Δ in tabulations by Chuang et al. (1979) cover a considerable range, from approximately 0.1 to 100 and sometimes higher, depending on material and temperature. Since $2\gamma_s/a$ is essentially the sintering stress limit, and is usually much lower than applied stress levels, it is evident that growth will frequently be in the crack-like mode when Δ is of the order unity. On the other hand, the more typical cases of large Δ will generally correspond to growth in the quasi-equilibrium mode.

DEFORMABILITY OF THE ADJOINING GRAINS

Now simplification (i) is retained, i.e., it is assumed that Δ is large enough to retain the quasi-equilibrium cavity shape, but simplification (ii) is relaxed in that deformability of the adjoining grains in Fig. 1 is considered. Various estimates of the effect of elastic deformability of the grains suggest that at least for cases of sustained loading and for cavities that are not spaced at great distances from one another, elastic effects can be disregarded. (Different conclusions may apply for cyclic loading and transient effects.)

Plastic dislocation creep of the adjoining grains provides a more significant mechanisms, however, at least at sufficiently high stress levels. The mechanism was analyzed in a preliminary manner by Beere and Speight (1978) and later by Edward and Ashby (1979) and Rice (1979). A definitive analysis based on the

When simplification (i) applies, the curvatures of the void are given by $K_1 = K_2 = (\sin \Psi)/a$, so that the first of Eq. (3) implies

$$\sigma_o = (2\gamma_S/a)\sin \Psi \quad . \tag{8}$$

Also, the volume of the void may be written as

$$V = (4\pi/3)a^3 h \tag{9}$$

where (e.g., Chuang et al., 1979)

$$h = h(\Psi) = \{1/1+\cos\Psi)-(\cos\Psi)/2\}/\sin\Psi \quad ;$$

$h = 1$ when $\Psi = 90°$ and $h \simeq 0.6$ when $\Psi = 70°$, as is typical. Now, it follows by overall mass conservation for the configuration of Fig. 1b that

$$\int_S (V_{mat})_n \, dS + 2\pi a(\Omega J_B)_{tip} = \dot{V} = 4\pi h a^2 \dot{a} \tag{10}$$

where S denotes the surface of the void and $(V_{mat})_n$ is the normal velocity of material points immediately adjacent to the void surface.

If the grains separate rigidly at rate $\dot{\delta}$, the integral in Eq. (10) is easily shown to equal $\pi a^2 \dot{\delta}$ so that, using Eq. (7), one obtains

$$\pi a^2 \dot{\delta} + 2\pi a(\Omega J_B)_{tip} = \pi b^2 \dot{\delta} = \dot{V} = 4\pi h a^2 \dot{a} \tag{11}$$

Hence $\dot{\delta} = 4hf\dot{a}$, and using this in Eq. (6) one obtains

$$\dot{a} = (D/ha^2)\{\sigma-2(1-f)(\gamma_S/a)\sin\Psi\}/\{\ell n(1/f)-(3-f)(1-f)/2\} \tag{12}$$

This last equation expresses the cavity growth rate when simplifications (i), pertaining to the quasi-equilibrium cavity

formulation by Rice has been given recently by Needleman and Rice (1980), and is summarized briefly here.

The chief effect of dislocation creep is to shorten the diffusive path length. For example, because non-rigid grains can open non-uniformly across their boundary, it is not necessary that matter be transported over a distance comparable to the inter-void spacing. Instead it is found that matter can be accommodated by non-uniform openings which take place over a distance of order L ahead of the void (at least when a + L is less than b), where L is a stress and temperature dependent parameter defined by

$$L = (D\sigma/\dot{\varepsilon}_{cr})^{1/3} \tag{21}$$

Here $\dot{\varepsilon}_{cr}$ is the creep rate of the adjoining grains due to stress σ.

The analysis assumes that the grains undergo non-linear power-law creep with deformation rates $D_{\alpha\beta}$ given by

$$D_{\alpha\beta} = \frac{3}{2} \Lambda^{-n} \{3\sigma'_{\gamma\delta}\sigma'_{\gamma\delta}/2\}^{(n-1)/2} \sigma'_{\gamma\delta} \tag{22}$$

where $\sigma'_{\gamma\delta}$ is the deviatoric stress and Λ and n are constants. The outer radius, r = b, in Fig. 1b is subjected to zero shear tractions and to a radial velocity $v_r = -\dot{\varepsilon}_{cr} b/2$, where $\dot{\varepsilon}_{cr} = (\sigma/\Lambda)^n$. The following functional F is defined for all axisymmetric velocity fields v_α, with associated deformation rates $D_{\alpha\beta}$ and grain boundary fluxes $j(=\Omega J_B/2)$ where

$$D_{\alpha\beta} = \text{symmetric part of } \partial v_\alpha/\partial x_\beta$$

and

$$\underline{\nabla} \cdot \underline{j} + v_z = 0 \text{ on the grain boundary} \quad ,$$

shape, and (ii), pertaining to rigid grains, apply. Note, however, that Eqs. (8) to (10) apply whenever the quasi-equilibrium shape can be assumed, whether or not the grains deform, whereas Eqs. (4) to (7) apply whenever the grains can be assumed to separate rigidly, whether or not the cavity has the quasi-equilibrium shape.

Equation (12) was given by Needleman and Rice (1980), who observe that it corrects an undue factor of (1-f) in previous presentations of the result (e.g., Raj and Ashby, 1975, Chuang et al., 1979); the factor arose from neglect of the surface integral in Eq. (10). They observe also that the derivation tacitly assumes that the surface tension (in the sense of surface stress, and as distinct from surface energy) is zero. The inclusion of surface tension T_s adds a term $(-2fT_s/a)\sin\Psi$ to the bracketed term in Eq. (12) that contains σ. This is generally a small effect.

If the growth rate law is written symbolically as $\dot{a} = 1/F(a)$, then the time to rupture, t_r, associated with cavity growth from some initial size, a_i, to coalescence, $a = b$, is given by

$$t_r = \int_{a_i}^{b} F(a)\,da \qquad (13)$$

This is straightforward to compute when the applied stress σ is constant throughout the growth process and is much larger than the "sintering stress" $(2\gamma_s/a_i)\sin\Psi$ at the onset of growth. In that case the expression for $\dot{a}$ of Eq. (12) leads to

$$t_r = \frac{16}{315}\frac{hb}{D\sigma}\left\{1 - \frac{105}{16} f_i^{3/2} \ln(1/f_i) - \frac{1}{8} f_i^{3/2} \left(63 f_i^{1/2} - \frac{175}{4}\frac{45}{4} f_i\right)\right\} \qquad (14)$$

with the understanding that j vanishes at the outer radius and than v_α meets the velocity boundary conditions on r = b:

$$F = \int_{\text{Vol.}} \left\{ \frac{n}{1+n} \Lambda \left(\frac{2}{3} D_{\alpha\beta} D_{\alpha\beta} \right)^{(1+n)/n} \right\} d(\text{Vol.}) + \int_a^b (j^2/D) 2\pi r dr - \int_0^b \sigma (v_z)_{\text{top}} \, 2\pi r dr + 2\pi a \sigma_o J_o \tag{23}$$

Here "Vol." denotes the volume of the upper crystal in Fig. 1b, $(v_z)_{top}$ is the vertical velocity of the upper loaded surface in Fig. 1b, σ_o is the stress at the void tip as given by Eq. (8), and j_o is the value of j at r = a. The functional F is minimized by the true velocity field, and this principle was used by Needleman and Rice (1980) to construct a finite-element procedure for determining the velocity field. By solving the deformation rate problem in this way and hence evaluating the left side of Eq. (10) to determine the cavity growth rate, they found that results could be put in either of the (equivalent) forms

$$\dot{a} = (D\sigma/a^2) \times (\text{a function of } a/L, \text{ f and } \sigma_o/\sigma)$$

or

$$\dot{a} = a\dot{\varepsilon}_{cr} \times (\text{another function of } a/L, \text{ f and } \sigma_o/\sigma).$$

The former form enables comparisons with the result given in Eq. (12) for rigid grain behavior. The case of greatest interest is that for which σ is much greater than the sintering limit σ_o. Results of Needleman and Rice (1980) for this case are summarized in Table 1, where the ratio of the predicted value of $\dot{a}$ for creeping

where $f_i = a_i^2/b^2$. This rupture time is inversely proportional to stress and to the grain boundary diffusion coefficient $D_B\delta_B$. This estimate of the rupture time neglects details of cavity nucleation (see Raj and Ashby, 1975), but the result does not depend strongly on the initial value of a_i. Indeed, the bracketed term involving f_i can be replaced by unity for f_i less than 1/10 or so.

The validity of simplifications (i) and (ii) is now examined.

NON-EQUILIBRIUM CAVITY SHAPE

For this section simplification (ii) is retained, but not (i). That is, the possibility is considered that surface diffusion may not be fast enough to allow retention of the quasi-equilibrium, spherical caps shape.

The problem in this form was addressed by Chuang et al. (1979), who point out that according to an appropriate solution of Eq. (1), the relaxation time for a doubly periodic surface disturbance with half-wavelength equated to cavity diameter, 2a, is approximately $a^4/24B$, where

$$B = D_S\delta_S\Omega\gamma_S/kT \tag{15}$$

A characteristic time associated with exposure of new cavity surface to the surface diffusion process is $a/\dot{a}$, and this identifies the dimensionless parameter

$$a^3\dot{a}/24B \tag{16}$$

with the following interpretation: When the parameter is small

TABLE 1: Ratio of cavity growth rate $\dot{a}$ between creeping grains to that for rigid grain response (Eq. (12); parameter L defined by Eq. (21); from Needleman and Rice (1980) for stress σ much larger than the sintering threshold.

a/L \ a/b	1/10	1/5	1/3	2/3
0.10	1.04	1.01	1.00	1.00
0.32	1.72	1.18	1.04	1.00
1.0	6.8	3.95	2.14	1.09
3.2	66	38	19	3.46
10.0	1330	746	385	6.0

grains to that calculated on the basis of Eq. (12) for rigid grains is shown.

Evidently, large differences from the rigid-grains analysis, Eq. (12), result when a + L is significantly less than b. In fact, based on an observation of Dr. I. W. Chen of M.I.T. (privately communicated by Prof. A. S. Argon), a reasonable approximation to the results of Needleman and Rice (1980), which predicts the cavity growth rate to within an error or about 30% for all a/L less than 10 or so, is to predict $\dot{a}$ from Eq. (12) but to use for f the maximum of $(a/b)^2$ and $\{a/(a+L)\}^2$.

Needleman and Rice (1980) tabulate values of L for various pure metals. They observe, following Rice (1979), that when power-law creep occurs with an activation energy equal to that for bulk (lattice) diffusion, L can be expressed in the form

$$L = L_o \exp(\kappa T_m/T)(10^{-3}\mu/\sigma)^{(n-1)/3} \qquad (24)$$

where L_o and κ are constants and is the shear modulus. For fcc metals at $T = 0.5\ T_m$ and $\sigma = 10^{-3}\mu$, L ranges from 2 to 8 μm (although lower for Al and higher for Ag); for bcc metals under the same conditions L ranges from 0.25 to 0.35 μm. A lower stress of $\sigma = 10^{-4}\ \mu$ at the same temperature increase these numbers by about a factor of 20. Hence, at $0.5\ T_m$ the assistance of diffusive rupture by plastic creep flow can be significant at $\sigma = 10^{-3}\ \mu$, especially for bcc metals, but will generally be insignificant, certainly for fcc metals, at $\sigma = 10^{-4}\ \mu$. The parameter κ ranges from 2.4 to 3.9 for fcc metals and from 1.7 to 2.2 for bcc metals.

Hence, increases in temperature from, say, 0.5 T_m to 0.8 T_m decrease L by a factor between approximately 0.05 and 0.28, depending on the material, for fixed σ/μ.

DISCUSSION

The paper has presented an analysis of diffusional cavity growth based on the standard assumptions of quasi-equilibrium cavity shapes and effectively rigid grain separations, and has indicated the range of validity of each of these assumptions. Results of fuller analyses, based on non-equilibrium, crack-like cavity shapes and on dislocation creep of the adjoining grains have been summarized.

In applications of these results it is important to properly choose the stress σ in relation to the applied stress and to the geometry of the cavitating grain boundary facets in a polycrystalline aggregate. Dyson (1976) has emphasized the constraints on diffusive cavity growth that can occur if the cavitated grain facets are well separated from one another. In such cases, the requirement that the opening rate $\dot{\delta}$ across such cavitated facets be compatible with the deformation rate of the surroundings serves to reduce σ from the value (say, σ_∞) which would act across a similar grain facet in an uncavitated polycrystal. A recent analysis of such constraint effects has been presented by Rice (1980), who considers an isolated, cavitated facet of diameter d and observes that approximately the opening rate is given by

$$\dot{\delta} = \alpha\{(\sigma_\infty - \sigma)/\sigma_\infty\}\dot{E}_\infty d \qquad (25)$$

where $\dot{E}_\infty$ is the strain rate of a similarly loaded but uncavitated

when σ is less than σ^* growth occurs in the quasi-equilibrium mode, and when σ is greater than σ^* growth occurs in the crack-like mode.

Estimated values of Δ in tabulations by Chuang et al. (1979) cover a considerable range, from approximately 0.1 to 100 and sometimes higher, depending on material and temperature. Since $2\gamma_s/a$ is essentially the sintering stress limit, and is usually much lower than applied stress levels, it is evident that growth will frequently be in the crack-like mode when Δ is of the order unity. On the other hand, the more typical cases of large Δ will generally correspond to growth in the quasi-equilibrium mode.

DEFORMABILITY OF THE ADJOINING GRAINS

Now simplification (i) is retained, i.e., it is assumed that Δ is large enough to retain the quasi-equilibrium cavity shape, but simplification (ii) is relaxed in that deformability of the adjoining grains in Fig. 1 is considered. Various estimates of the effect of elastic deformability of the grains suggest that at least for cases of sustained loading and for cavities that are not spaced at great distances from one another, elastic effects can be disregarded. (Different conclusions may apply for cyclic loading and transient effects.)

Plastic dislocation creep of the adjoining grains provides a more significant mechanisms, however, at least at sufficiently high stress levels. The mechanism was analyzed in a preliminary manner by Beere and Speight (1978) and later by Edward and Ashby (1979) and Rice (1979). A definitive analysis based on the

polycrystal. Here the coefficient α is estimated as equal approximately to 1 for power-law creep with non-sliding grain boundaries and to 2 for freely sliding boundaries, at least if the cavitated facets are far-separated and effectively non-interacting; α would be extremely large in the opposite limit when all boundaries approximately perpendicular to the tensile direction are cavitated, especially with freely sliding boundaries. Assuming that σ is within the range for which Eq. (12) is valid and calculating a related expression for $\dot{\delta}$ from Eq. (11), Rice (1980) shows that the constraint effects, namely, that the expressions for $\dot{\delta}$ based on Eqs. (11), (12) and (25) should agree, reduces σ from σ_∞ and leads to a growth rate

$$\dot{a} = (D/ha^2)\{\sigma_\infty - 2(1-f)(\gamma_S/a)\sin\Psi\}/\{(4L_\infty^3/\alpha b^2 d) + \ell n(1/f) - (3-f)(1-f)/2\} \tag{26}$$

where

$$L_\infty = (D\sigma_\infty/\dot{E}_\infty)^{1/3} \tag{27}$$

(Rice (1980) used the notation L, but L_∞ is used here to avoid confusion with the "local" L of Eq. (12).)

The associated rupture time, calculated as in Eq. (13), is found to be given by

$$t_r = (t_r)_1 + (t_r)_2 \tag{28}$$

where $(t_r)_1$ is given by Eq. (14) with σ replaced by σ_∞ in that expression and where

$$(t_r)_2 = (4hb/3\alpha\dot{E}_\infty d)(1-f_i^{3/2}) \tag{29}$$

formulation by Rice has been given recently by Needleman and Rice (1980), and is summarized briefly here.

The chief effect of dislocation creep is to shorten the diffusive path length. For example, because non-rigid grains can open non-uniformly across their boundary, it is not necessary that matter be transported over a distance comparable to the inter-void spacing. Instead it is found that matter can be accommodated by non-uniform openings which take place over a distance of order L ahead of the void (at least when a + L is less than b), where L is a stress and temperature dependent parameter defined by

$$L = (D\sigma/\dot{\varepsilon}_{cr})^{1/3} \tag{21}$$

Here $\dot{\varepsilon}_{cr}$ is the creep rate of the adjoining grains due to stress σ.

The analysis assumes that the grains undergo non-linear power-law creep with deformation rates $D_{\alpha\beta}$ given by

$$D_{\alpha\beta} = \frac{3}{2} \Lambda^{-n} \{3\sigma'_{\gamma\delta}\sigma'_{\gamma\delta}/2\}^{(n-1)/2} \sigma'_{\gamma\delta} \tag{22}$$

where $\sigma'_{\gamma\delta}$ is the deviatoric stress and Λ and n are constants. The outer radius, r = b, in Fig. 1b is subjected to zero shear tractions and to a radial velocity $v_r = -\dot{\varepsilon}_{cr} b/2$, where $\dot{\varepsilon}_{cr} = (\sigma/\Lambda)^n$. The following functional F is defined for all axisymmetric velocity fields v_α, with associated deformation rates $D_{\alpha\beta}$ and grain boundary fluxes $j(=\Omega J_B/2)$ where

$$D_{\alpha\beta} = \text{symmetric part of } \partial v_\alpha/\partial x_\beta$$

and

$$\underline{\nabla} \cdot \underline{j} + v_z = 0 \text{ on the grain boundary} \quad ,$$

For small f_i the ratio of $(t_r)_2$ to $(t_r)_1$ is $(105/4\alpha)(L_\infty^3/b^2d)$. Conditions might often be encountered when this ratio is large (e.g., low σ_∞ and well separated facets), and in such cases the analysis suggests a Monkman-Grant (1956) type of correlation of t_r with $\dot{E}_\infty$.

ACKNOWLEDGEMENT

This research was supported by the Defense Advanced Research Projects Agency of the Department of Defense under Contract No. *MDA903-80C-0505 with The University of Michigan.*

REFERENCES

Balluffi, R. W. and Seigle, L. L., "Growth of voids in metals during diffusion and creep," Acta Met. 5, 449-454 (1957).

Beere, W. and Speight, M.V., "Creep cavitation by vacancy diffusion in a plastically deforming solid," Metal Sci. 12, 172-176 (1978).

Chuang, T-j. and Rice, J. R., "The shape of intergranular cracks growing by surface diffusion," Acta Met. 21, 1625-1628 (1973).

Chuang, T-j., Kagawa, K. I., Rice, J. R. and Sills, L., "Non-equilibrium models for diffusive cavitation of grain interfaces," Acta Met. 27, 265-284 (1979).

Dyson, B. F., "Constraints on diffusional cavity growth rates," Metal Sci., 349-353 (1976).

Edward, G. H. and Ashby, M. F., "Intergranular fracture during power-law creep," Acta Met. 27, 1505-1518 (1979).

Hull, D. and Rimmer, D. E., "The growth of grain boundary voids under stress," Phil. Mag. 4, 673-687 (1959).

Monkman, F. W. and Grant, N. J., "An empirical relation between rupture life and minimum creep rate," Proc. ASTM 56, 593-605 (1956).

Needleman, A. and Rice, J. R., "Plastic creep flow effects in diffusive cavitation of grain boundaries," Acta Met. - in press.

Raj, R. and Ashby, M. F., "Intergranular fracture at elevated temperature," Acta Met. 23, 653-666 (1975).

Rice, J. R., "Plastic creep flow processes in fracture at elevated temperature," in Time-Dependent Fracture of Materials at Elevated Temperature (edited by S. M. Wolf), U.S. Department of Energy Report CONF790236 UC-25, pp. 130-145 (1979).

Rice, J. R., "Constraints on the cavitation of isolated grain boundary facets in creeping polycrystals," submitted for publication.

with the understanding that j vanishes at the outer radius and than v_α meets the velocity boundary conditions on r = b:

$$F = \int_{\text{Vol.}} \left\{ \frac{n}{1+n} \Lambda \left(\frac{2}{3} D_{\alpha\beta} D_{\alpha\beta} \right)^{(1+n)/n} \right\} d(\text{Vol.}) + \int_a^b (j^2/D) 2\pi r dr - \int_0^b \sigma (v_z)_{\text{top}} \, 2\pi r dr + 2\pi a \sigma_o J_o \tag{23}$$

Here "Vol." denotes the volume of the upper crystal in Fig. 1b, $(v_z)_{top}$ is the vertical velocity of the upper loaded surface in Fig. 1b, σ_o is the stress at the void tip as given by Eq. (8), and j_o is the value of j at r = a. The functional F is minimized by the true velocity field, and this principle was used by Needleman and Rice (1980) to construct a finite-element procedure for determining the velocity field. By solving the deformation rate problem in this way and hence evaluating the left side of Eq. (10) to determine the cavity growth rate, they found that results could be put in either of the (equivalent) forms

$$\dot{a} = (D\sigma/a^2) \times (\text{a function of } a/L, \text{ f and } \sigma_o/\sigma)$$

or

$$\dot{a} = a\dot{\varepsilon}_{cr} \times (\text{another function of } a/L, \text{ f and } \sigma_o/\sigma).$$

The former form enables comparisons with the result given in Eq. (12) for rigid grain behavior. The case of greatest interest is that for which σ is much greater than the sintering limit σ_o. Results of Needleman and Rice (1980) for this case are summarized in Table 1, where the ratio of the predicted value of $\dot{a}$ for creeping

ONE DIMENSIONAL MELT SUBJECTED TO RAPID QUENCH

Howard Reiss

ABSTRACT

A melt is represented by a one dimensional lattice containing atoms and vacant sites. Only atoms on adjacent sites are able to interact. The jumping frequencies and coupling parameters are made reasonably time dependent through the dependence of temperature on time. Then the time dependence of the pair correlation function, as the melt is quenched, is computed by a kinetic method which leads to the correct equilibrium description of the correlation function.

The development of correlation is influenced by both the "squeezing out" of free volume from clusters as they form as the melt is cooled and in the reduction of overall free volume (decrease in the fraction of vacancies). We are only able to treat the first effect directly. However by comparing systems with different constant vacancy contents we can form some idea of the second effect. As expected, correlation develops more easily, on cooling, when there is more free volume. The effect of jumping frequency activation energy is also examined.

These results should be of conceptual use in rapid solidification processes.

TABLE 1: Ratio of cavity growth rate $\dot{a}$ between creeping grains to that for rigid grain response (Eq. (12); parameter L defined by Eq. (21); from Needleman and Rice (1980) for stress σ much larger than the sintering threshold.

a/L \ a/b	1/10	1/5	1/3	2/3
0.10	1.04	1.01	1.00	1.00
0.32	1.72	1.18	1.04	1.00
1.0	6.8	3.95	2.14	1.09
3.2	66	38	19	3.46
10.0	1330	746	385	6.0

ONE DIMENSIONAL MELT SUBJECTED TO RAPID QUENCH

Howard Reiss

INTRODUCTION

The author has recently published[1] a study of a one dimensional Ising model subjected to a rapid quench. Exact analytical solutions were obtained for the case in which temperature varied with time in any manner, and it was possible to study the spin structures which evolved in order to see if they contained features which were independent of the manner of quench. Such features were indeed found.

The solvable model was Glauber's model of the one dimensional ferromagnetic, whereas systems which are normally subjected to rapid quench are liquids. Such liquids may form glasses and it is the development of structure in these systems which is of primary interest. As a diagnostic for these systems the ferromagnet is lacking in several respects. A particularly serious omission is the feature of "densification" in which "free volume" is squeezed out of the liquid as it is cooled. This reduction in free volume affects the rate of structure development while itself depending on structure. It would therefore be nice to have a model, alternative to the ferromagnet, which incorporates at least some of this feature. Such a model is available in a system of atoms and vacancies on a one dimensional lattice, the atoms interacting only with nearest neighbors. To a first approximation this may be taken as a model for a one dimensional liquid. As the temperature is lowered the

grains to that calculated on the basis of Eq. (12) for rigid grains is shown.

Evidently, large differences from the rigid-grains analysis, Eq. (12), result when a + L is significantly less than b. In fact, based on an observation of Dr. I. W. Chen of M.I.T. (privately communicated by Prof. A. S. Argon), a reasonable approximation to the results of Needleman and Rice (1980), which predicts the cavity growth rate to within an error or about 30% for all a/L less than 10 or so, is to predict $\dot{a}$ from Eq. (12) but to use for f the maximum of $(a/b)^2$ and $\{a/(a+L)\}^2$.

Needleman and Rice (1980) tabulate values of L for various pure metals. They observe, following Rice (1979), that when power-law creep occurs with an activation energy equal to that for bulk (lattice) diffusion, L can be expressed in the form

$$L = L_o \exp(\kappa T_m/T)(10^{-3}\mu/\sigma)^{(n-1)/3} \qquad (24)$$

where L_o and κ are constants and is the shear modulus. For fcc metals at $T = 0.5\ T_m$ and $\sigma = 10^{-3}\mu$, L ranges from 2 to 8 μm (although lower for Al and higher for Ag); for bcc metals under the same conditions L ranges from 0.25 to 0.35 μm. A lower stress of $\sigma = 10^{-4}\ \mu$ at the same temperature increase these numbers by about a factor of 20. Hence, at $0.5\ T_m$ the assistance of diffusive rupture by plastic creep flow can be significant at $\sigma = 10^{-3}\ \mu$, especially for bcc metals, but will generally be insignificant, certainly for fcc metals, at $\sigma = 10^{-4}\ \mu$. The parameter κ ranges from 2.4 to 3.9 for fcc metals and from 1.7 to 2.2 for bcc metals.

atoms will tend to form local regions of densification (clusters) in which movement will be hampered by the shortage of vacancies. Thus is one follows the development of the pair correlation function as the temperature is lowered this development will have incorporated the effects of this shortage.

On the other hand a true "squeezing out" of free volume would correspond to a reduction in the total number of vacancies on the lattice as the temperature is lowered. A model containing this feature is much more difficult to contrive, and in this paper we make no attempt in this direction. One possibility however is to deal with a lattice subject to constant pressure rather than constant volume. Another approach (which we exercise later) is to simply compare the behaviors of systems with different constant vacancy contents.

Even with the constant volume model we are not yet able to produce an exact analytical solution as in the case of the ferromagnet, but the approach will speak for itself as being reasonable, and does yield the exact equilibrium solution. We discuss the model and derive the differential equation governing its time behavior in the next two sections.

The Model

Consider a one dimensional lattice consisting of N sites, N_1 of which are occupied by atoms which interact, as nearest neighbors only, with an interaction energy, ε. This quantity is defined as a binding energy, i.e. ε is positive when the atoms attract one another. We define, $N_o = N-N_1$, as the number of vacant lattice sites. Then the number of "bonds" between atoms will be

Hence, increases in temperature from, say, 0.5 T_m to 0.8 T_m decrease L by a factor between approximately 0.05 and 0.28, depending on the material, for fixed σ/μ.

DISCUSSION

The paper has presented an analysis of diffusional cavity growth based on the standard assumptions of quasi-equilibrium cavity shapes and effectively rigid grain separations, and has indicated the range of validity of each of these assumptions. Results of fuller analyses, based on non-equilibrium, crack-like cavity shapes and on dislocation creep of the adjoining grains have been summarized.

In applications of these results it is important to properly choose the stress σ in relation to the applied stress and to the geometry of the cavitating grain boundary facets in a polycrystalline aggregate. Dyson (1976) has emphasized the constraints on diffusive cavity growth that can occur if the cavitated grain facets are well separated from one another. In such cases, the requirement that the opening rate $\dot{\delta}$ across such cavitated facets be compatible with the deformation rate of the surroundings serves to reduce σ from the value (say, σ_∞) which would act across a similar grain facet in an uncavitated polycrystal. A recent analysis of such constraint effects has been presented by Rice (1980), who considers an isolated, cavitated facet of diameter d and observes that approximately the opening rate is given by

$$\dot{\delta} = \alpha\{(\sigma_\infty - \sigma)/\sigma_\infty\}\dot{E}_\infty d \qquad (25)$$

where $\dot{E}_\infty$ is the strain rate of a similarly loaded but uncavitated

$$N_{11} = N_1 - N_{10} \tag{1}$$

where N_{10} is half the number of atom-vacancy nearest neighbors pairs. Similarly the number of vacancy-vacancy pairs, or bonds, is

$$N_{00} = N_0 - N_{10} \tag{2}$$

The total energy of a given configuration is

$$E = N_{11}\varepsilon \tag{3}$$

At equilibrium at a temperature, T, it is well known[3] that the equilibrium values of N_{11}, N_{00}, and N_{10} are related "exactly" by the "quasichemical equilibrium" expression,

$$\frac{N_{11}N_{00}}{N_{10}^2} = e^{\varepsilon/kt} = \lambda^{-1} \tag{4}$$

where the last equation defines λ and where k is the Boltzmann constant. Substituting from Eqs. (1) and (2) yields a relation which determines N_{10}. Thus

$$\frac{(N_1 - N_{10})(N_0 - N_{10})}{N_{10}^2} = \lambda \tag{5}$$

polycrystal. Here the coefficient α is estimated as equal approximately to 1 for power-law creep with non-sliding grain boundaries and to 2 for freely sliding boundaries, at least if the cavitated facets are far-separated and effectively non-interacting; α would be extremely large in the opposite limit when all boundaries approximately perpendicular to the tensile direction are cavitated, especially with freely sliding boundaries. Assuming that σ is within the range for which Eq. (12) is valid and calculating a related expression for $\dot{\delta}$ from Eq. (11), Rice (1980) shows that the constraint effects, namely, that the expressions for $\dot{\delta}$ based on Eqs. (11), (12) and (25) should agree, reduces σ from σ_∞ and leads to a growth rate

$$\dot{a} = (D/ha^2)\{\sigma_\infty - 2(1-f)(\gamma_S/a)\sin\Psi\}/\{(4L_\infty^3/\alpha b^2 d) + \ell n(1/f) - (3-f)(1-f)/2\} \tag{26}$$

where

$$L_\infty = (D\sigma_\infty/\dot{E}_\infty)^{1/3} \tag{27}$$

(Rice (1980) used the notation L, but L_∞ is used here to avoid confusion with the "local" L of Eq. (12).)

The associated rupture time, calculated as in Eq. (13), is found to be given by

$$t_r = (t_r)_1 + (t_r)_2 \tag{28}$$

where $(t_r)_1$ is given by Eq. (14) with σ replaced by σ_∞ in that expression and where

$$(t_r)_2 = (4hb/3\alpha\dot{E}_\infty d)(1-f_i^{3/2}) \tag{29}$$

Some additional notation is now in order.

For the probability that a given bond is of the type 10, 01, 00 or 11 we use the symbols

$$P_{10} = \frac{N_{10}}{N} \tag{6}$$

$$P_{01} = \frac{N_{01}}{N} \tag{7}$$

$$P_{00} = \frac{N_{00}}{N} \tag{8}$$

$$P_{11} = \frac{N_{11}}{N} \tag{9}$$

The 01 bonds are introduced for later conceptual reasons and are distinguished from 10 bonds by direction only. Clearly

$$N_{01} = N_{10} \tag{10}$$

by reason of symmetry.

For the conditional probability that a site next to one occupied by an atom is also occupied by an atom we use the symbol g_{11} and note that

$$g_{11} = \frac{N_{11}}{N_{11} + N_{10}} = \frac{P_{11}}{P_{11} + P_{10}} \tag{11}$$

Similarly the conditional probability that the site is occupied by a vacancy is

$$g_{10} = \frac{P_{10}}{P_{11} + P_{10}} \tag{12}$$

The meanings and specifications of g_{00} and g_{01} follow, and should be clear

$$g_{00} = \frac{P_{00}}{P_{00} + P_{01}} \tag{13}$$

$$g_{01} = \frac{P_{01}}{P_{00} + P_{01}} \tag{14}$$

It was for ease of understanding of Eqs. (13) and (14) that the quantity N_{01} was introduced. We define

$$x = \frac{N_1}{N} \tag{15}$$

Then

$$xg_{11} = \frac{N_1}{N}\left(\frac{N_{11}}{N_{11} + N_{10}}\right) \tag{16}$$

$$= \frac{N_1}{N} \frac{N_{11}}{(N_1 - N_{10}) + N_{10}} = \frac{N_{11}}{N} = P_{11}$$

where we have used Eqs. (1) and (11). In the same way we can show that

$$xg_{10} = P_{10} \tag{17}$$

$$(1-x)g_{00} = P_{00} \tag{18}$$

$$(1-x)g_{01} = P_{01} \tag{19}$$

It is also clear that

$$g_{11} + g_{10} = 1 \tag{20}$$

$$g_{00} + g_{01} = 1 \tag{21}$$

Finally, symmetry requires

$$P_{10} = P_{01} \tag{22}$$

so that from Eqs. (17) and (19) we have

$$xg_{10} = (1-x)g_{01} \tag{23}$$

At equilibrium, it is known, for this one dimensional system, that the superposition approximation holds exactly. Thus, given that a particular site is occupied by an atom, the probability

ONE DIMENSIONAL MELT SUBJECTED TO RAPID QUENCH

Howard Reiss

ABSTRACT

A melt is represented by a one dimensional lattice containing atoms and vacant sites. Only atoms on adjacent sites are able to interact. The jumping frequencies and coupling parameters are made reasonably time dependent through the dependence of temperature on time. Then the time dependence of the pair correlation function, as the melt is quenched, is computed by a kinetic method which leads to the correct equilibrium description of the correlation function.

The development of correlation is influenced by both the "squeezing out" of free volume from clusters as they form as the melt is cooled and in the reduction of overall free volume (decrease in the fraction of vacancies). We are only able to treat the first effect directly. However by comparing systems with different constant vacancy contents we can form some idea of the second effect. As expected, correlation develops more easily, on cooling, when there is more free volume. The effect of jumping frequency activation energy is also examined.

These results should be of conceptual use in rapid solidification processes.

that its nearest neighbor and next nearest neighbor are also occupied by atoms, i.e. the triplet probability, g_{111}, is given by

$$g_{111} = g_{11}g_{11} \tag{24}$$

Similarly

$$g_{110} = g_{11}g_{10} \tag{25}$$

$$g_{101} = g_{10}g_{01} \tag{26}$$

etc. The same rule applies to higher order probabilities, e.g. to quartet and quintet situations. We shall have occasion to use this rule later, but there is as yet no proof that it applies to nonequilibrium situations.

Time Dependence of the Model

In order to derive a differential equation which provides an adequate description of the time behavior of the model we assume that the superposition approximation holds for nonequilibrium situations. This approximation (as it probably is - since superposition ignores the history of the system) at least (as we shall see) leads to the correct equilibrium configuration of the system.

The jumping frequency for an atom whose two nearest neighbors are vacancies will be denoted by ν and expressed in an

Arrhenius-like form,

$$\nu = \nu_o e^{-\psi/kT} \tag{27}$$

where ν_o is a constant frequency and ψ is the activation energy for jumping. If one of the atom's nearest neighbors is another atom then the activation energy for jumping must be augmented by the binding energy ε so that the new jumping frequency will be

$$\nu_1 = \nu_o e^{-(\psi+\varepsilon)/kT} = \nu e^{-\varepsilon/kT} \tag{28}$$

$$= \nu\lambda$$

where λ is obviously defined by

$$\lambda = e^{-\varepsilon/kT} \tag{29}$$

Now consider changes which occur in the underlined pair of sites in the following diagram

$$X1\underline{00} \quad \rightleftarrows \quad X0\underline{10} \tag{30}$$

$$\underline{11}0X \quad \rightleftarrows \quad \underline{10}1X \tag{31}$$

In this diagram a zero represents a vacancy and a one, an atom. The X indicates a one or a zero. Both processes

ONE DIMENSIONAL MELT SUBJECTED TO RAPID QUENCH

Howard Reiss

INTRODUCTION

The author has recently published[1] a study of a one dimensional Ising model subjected to a rapid quench. Exact analytical solutions were obtained for the case in which temperature varied with time in any manner, and it was possible to study the spin structures which evolved in order to see if they contained features which were independent of the manner of quench. Such features were indeed found.

The solvable model was Glauber's model of the one dimensional ferromagnetic, whereas systems which are normally subjected to rapid quench are liquids. Such liquids may form glasses and it is the development of structure in these systems which is of primary interest. As a diagnostic for these systems the ferromagnet is lacking in several respects. A particularly serious omission is the feature of "densification" in which "free volume" is squeezed out of the liquid as it is cooled. This reduction in free volume affects the rate of structure development while itself depending on structure. It would therefore be nice to have a model, alternative to the ferromagnet, which incorporates at least some of this feature. Such a model is available in a system of atoms and vacancies on a one dimensional lattice, the atoms interacting only with nearest neighbors. To a first approximation this may be taken as a model for a one dimensional liquid. As the temperature is lowered the

are indicated to be reversible. The forward process in Eq. (30) transforms a 00 pair into a 10 pair while the reverse process destroys a 10 pair. In Eq. (31) the forward process creates a 10 pair from a 11 pair and the reverse destroys it. We calculate the rate of change, with time, of P_{10}. Suppose X on the left side of Eq. (30) is a vacancy. Then using the superposition approximation the probability of the configuration on the left will be

$$P_{00} g_{01} g_{10} \tag{32}$$

The forward rate in Eq. (30) creates 10 pairs and contributes a term

$$\nu P_{00} g_{01} g_{10} \tag{33}$$

to dP_{10}/dt where t is time. ν and not ν_1 is the appropriate frequency since X is a vacancy. If X is an atom a similar line of reasoning leads to the contribution

$$\nu_1 P_{10} g_{01} g_{11} \tag{34}$$

For the reverse process in Eq. (30) we get only the term

$$-\nu P_{10} g_{10} \tag{35}$$

since there is a zero to the right of the one and the character

atoms will tend to form local regions of densification (clusters) in which movement will be hampered by the shortage of vacancies. Thus is one follows the development of the pair correlation function as the temperature is lowered this development will have incorporated the effects of this shortage.

On the other hand a true "squeezing out" of free volume would correspond to a reduction in the total number of vacancies on the lattice as the temperature is lowered. A model containing this feature is much more difficult to contrive, and in this paper we make no attempt in this direction. One possibility however is to deal with a lattice subject to constant pressure rather than constant volume. Another approach (which we exercise later) is to simply compare the behaviors of systems with different constant vacancy contents.

Even with the constant volume model we are not yet able to produce an exact analytical solution as in the case of the ferromagnet, but the approach will speak for itself as being reasonable, and does yield the exact equilibrium solution. We discuss the model and derive the differential equation governing its time behavior in the next two sections.

The Model

Consider a one dimensional lattice consisting of N sites, N_1 of which are occupied by atoms which interact, as nearest neighbors only, with an interaction energy, ε. This quantity is defined as a binding energy, i.e. ε is positive when the atoms attract one another. We define, $N_o = N-N_1$, as the number of vacant lattice sites. Then the number of "bonds" between atoms will be

of the X is not at issue. We could use the two terms

$$-\nu P_{10} g_{10} g_{00} - \nu P_{10} g_{10} g_{01} \tag{36}$$

but these simply add (by Eq. (21)) to yield Eq. (35). Thus the contribution of Eq. (30) to dP_{10}/dt is the sum of Eqs. (33), (34) and (35), namely

$$\nu P_{00} g_{01} g_{10} + \nu_1 P_{10} g_{01} g_{11} - \nu P_{10} g_{10} \tag{37}$$

and proceeding in a similar manner for Eq. (31) we obtain

$$\begin{aligned} \frac{dP_{10}}{dt} = {} & \nu P_{00} g_{01} g_{10} + \nu_1 P_{10} g_{01} g_{11} - \nu P_{10} g_{10} \\ & + \nu_1 P_{11} g_{10} - \nu_1 P_{10} g_{01} g_{11} - \nu P_{10} g_{01} g_{10} \end{aligned} \tag{38}$$

Using Eqs. (16) through (23) and Eqs. (28) and (29) we can convert Eq. (38) into

$$\frac{dg_{10}}{d\tau} = 2\lambda g_{10}(1-g_{10})(1-\theta g_{10}) - 2\theta g_{10}^3 \tag{39}$$

where

$$\tau = \int_0^t \nu \, dt' \tag{40}$$

$$N_{11} = N_1 - N_{10} \tag{1}$$

where N_{10} is half the number of atom-vacancy nearest neighbors pairs. Similarly the number of vacancy-vacancy pairs, or bonds, is

$$N_{00} = N_0 - N_{10} \tag{2}$$

The total energy of a given configuration is

$$E = N_{11}\varepsilon \tag{3}$$

At equilibrium at a temperature, T, it is well known[3] that the equilibrium values of N_{11}, N_{00}, and N_{10} are related "exactly" by the "quasichemical equilibrium" expression,

$$\frac{N_{11}N_{00}}{N_{10}^2} = e^{\varepsilon/kt} = \lambda^{-1} \tag{4}$$

where the last equation defines λ and where k is the Boltzmann constant. Substituting from Eqs. (1) and (2) yields a relation which determines N_{10}. Thus

$$\frac{(N_1 - N_{10})(N_0 - N_{10})}{N_{10}^2} = \lambda \tag{5}$$

and

$$\theta = \frac{x}{1-x} \tag{41}$$

As in Ref. 1 both ν and λ are presumed time dependent through the dependence of temperature T on time. If an isothermal process is involved then ν will be constant and

$$\tau = \nu t \tag{42}$$

which is the average number of steps an atom may take in time t.

If rapid cooling is involved τ will still represent the average number of steps but, as in the case of Ref. 1, τ will have a maximum value, τ_{max}, and only a finite number of steps will be allowed each atom. Thus the quenched system may get "stuck".

We may consider the equilibrium state achieved when the process is isothermal. At equilibrium the derivative on the left of Eq. (39) vanishes and the resulting equation is

$$\frac{(1-g_{10})(1-\theta g_{10})}{\theta g_{10}^2} = \lambda^{-1} \tag{43}$$

Using Eq. (41) together with Eqs. (16) through (23) easily converts this equation to Eq. (5) so that despite the approximation inherent in the kinetic equations the system tends towards the physically correct equilibrium state.

Some additional notation is now in order.

For the probability that a given bond is of the type 10, 01, 00 or 11 we use the symbols

$$P_{10} = \frac{N_{10}}{N} \tag{6}$$

$$P_{01} = \frac{N_{01}}{N} \tag{7}$$

$$P_{00} = \frac{N_{00}}{N} \tag{8}$$

$$P_{11} = \frac{N_{11}}{N} \tag{9}$$

The 01 bonds are introduced for later conceptual reasons and are distinguished from 10 bonds by direction only. Clearly

$$N_{01} = N_{10} \tag{10}$$

by reason of symmetry.

For the conditional probability that a site next to one occupied by an atom is also occupied by an atom we use the symbol g_{11} and note that

$$g_{11} = \frac{N_{11}}{N_{11} + N_{10}} = \frac{P_{11}}{P_{11} + P_{10}} \tag{11}$$

Structure

The most convenient function for indexing the degree of structure is the pair correlation function $g^{(n)}$, i.e. the probability that the n-1 nearest neighbor site is occupied by an atom when it is known that the given site is so occupied. If we continue to assume the validity of the superposition approximation then

$$g^{(n)} = \Sigma g_{1i} g_{ij} g_{jk} - - - g_{s1} \tag{44}$$

where i, j, k, s, etc. may be 1 or 0 and the sum goes over all combinations of these numbers. Since there will be n-1 g factors in the sum there are 2^{n-2} terms in the sum.

The sum, and therefore $g^{(n)}$ can best be evaluated using the transfer matrix technique[4]. We first generalize the typical term in the sum of Eq. (44) so that the last factor may have an index ending in 0 as well as 1 and also consider terms having numbers of factors other than n, say m factors. Then we denote the sum of all terms containing m factors and ending with a factor whose last index is 1 by $g_1^{(m)}$ while the similar term ending with 0 index is denoted by $g_0^{(m)}$. Clearly then,

$$\begin{aligned} g_1^{(m)} &= g_1^{(m-1)} g_{11} + g_0^{(m-1)} g_{01} \\ g_0^{(m)} &= g_1^{(m-1)} g_{10} + g_0^{(m-1)} g_{00} \end{aligned} \tag{45}$$

Similarly the conditional probability that the site is occupied by a vacancy is

$$g_{10} = \frac{P_{10}}{P_{11} + P_{10}} \tag{12}$$

The meanings and specifications of g_{00} and g_{01} follow, and should be clear

$$g_{00} = \frac{P_{00}}{P_{00} + P_{01}} \tag{13}$$

$$g_{01} = \frac{P_{01}}{P_{00} + P_{01}} \tag{14}$$

It was for ease of understanding of Eqs. (13) and (14) that the quantity N_{01} was introduced. We define

$$x = \frac{N_1}{N} \tag{15}$$

Then

$$xg_{11} = \frac{N_1}{N}\left(\frac{N_{11}}{N_{11} + N_{10}}\right) \tag{16}$$

$$= \frac{N_1}{N} \frac{N_{11}}{(N_1 - N_{10}) + N_{10}} = \frac{N_{11}}{N} = P_{11}$$

If $g_1^{(m)}$ and $g_0^{(m)}$ are considered to be the components of a vector $\vec{g}_m$,

$$\vec{g}_m = \begin{pmatrix} g_1^{(m)} \\ g_0^{(m)} \end{pmatrix} , \tag{46}$$

then Eq. (45) may be represented in matrix form as

$$\vec{g}_m = \underset{\sim}{M} \cdot \vec{g}_{m-1} \tag{47}$$

where the matrix $\underset{\sim}{M}$ has the form

$$\underset{\sim}{M} = \begin{pmatrix} g_{11} & g_{01} \\ g_{10} & g_{00} \end{pmatrix} \tag{48}$$

We simplify notation by writing

$$\begin{aligned} g_{11} &= g \quad , \quad & g_{01} &= h \\ g_{10} &= 1-g \quad , \quad & g_{00} &= 1-h \end{aligned} \tag{49}$$

where we have used Eqs. (1) and (11). In the same way we can show that

$$xg_{10} = P_{10} \tag{17}$$

$$(1-x)g_{00} = P_{00} \tag{18}$$

$$(1-x)g_{01} = P_{01} \tag{19}$$

It is also clear that

$$g_{11} + g_{10} = 1 \tag{20}$$

$$g_{00} + g_{01} = 1 \tag{21}$$

Finally, symmetry requires

$$P_{10} = P_{01} \tag{22}$$

so that from Eqs. (17) and (19) we have

$$xg_{10} = (1-x)g_{01} \tag{23}$$

At equilibrium, it is known, for this one dimensional system, that the superposition approximation holds exactly. Thus, given that a particular site is occupied by an atom, the probability

where account has been taken of Eqs. (20) and (21). Thus

$$\underset{\sim}{M} = \begin{pmatrix} g & h \\ 1-g & 1-h \end{pmatrix} \tag{50}$$

Now we know that

$$\vec{g}_2 = \begin{pmatrix} g \\ 1-g \end{pmatrix} \tag{51}$$

Thus,

$$\vec{g}_n = \underset{\sim}{M}^{m-2} \cdot \vec{g}_2 \tag{52}$$

and then the pair correlation function, Eq. (44), is simply

$$g^{(n)} = g_1^{(n)} = \vec{\delta} \cdot \underset{\sim}{M}^{n-2} \cdot g_2 \tag{53}$$

where $\vec{\delta}$ is the vector,

$$\vec{\delta} = \begin{pmatrix} 1 \\ 0 \end{pmatrix} \tag{54}$$

that its nearest neighbor and next nearest neighbor are also occupied by atoms, i.e. the triplet probability, g_{111}, is given by

$$g_{111} = g_{11}g_{11} \tag{24}$$

Similarly

$$g_{110} = g_{11}g_{10} \tag{25}$$

$$g_{101} = g_{10}g_{01} \tag{26}$$

etc. The same rule applies to higher order probabilities, e.g. to quartet and quintet situations. We shall have occasion to use this rule later, but there is as yet no proof that it applies to nonequilibrium situations.

Time Dependence of the Model

In order to derive a differential equation which provides an adequate description of the time behavior of the model we assume that the superposition approximation holds for nonequilibrium situations. This approximation (as it probably is - since superposition ignores the history of the system) at least (as we shall see) leads to the correct equilibrium configuration of the system.

The jumping frequency for an atom whose two nearest neighbors are vacancies will be denoted by ν and expressed in an

Let $\underset{\sim}{\Lambda}$ be the matrix which diagonalizes $\underset{\sim}{M}$. Thus

$$\underset{\sim}{D} = \underset{\sim}{\Lambda}^{-1} \cdot \underset{\sim}{M} \cdot \underset{\sim}{\Lambda} \tag{55}$$

is a diagonal matrix whose diagonal elements are the eigenvalues of $\underset{\sim}{M}$. Then the matrix produce $\underset{\sim}{M}^{n-2}$ may be written as

$$\begin{aligned} \underset{\sim}{M}^{n-2} &= \underset{\sim}{\Lambda}(\underset{\sim}{\Lambda}^{-1}\underset{\sim}{M}\underset{\sim}{\Lambda}\underset{\sim}{\Lambda}^{-1}\underset{\sim}{M}\underset{\sim}{\Lambda}\text{----}\underset{\sim}{\Lambda}^{-1}\underset{\sim}{M}\underset{\sim}{\Lambda})\underset{\sim}{\Lambda}^{-1} \\ &= \underset{\sim}{\Lambda}\underset{\sim}{D}^{n-2}\underset{\sim}{\Lambda}^{-1} \end{aligned} \tag{56}$$

It is easy to show, by standard means[5], that

$$\underset{\sim}{\Lambda} = \begin{pmatrix} 1 & h \\ -1 & 1-g \end{pmatrix} \tag{57}$$

and

$$\underset{\sim}{\Lambda}^{-1} = \frac{1}{1-g+h} \begin{pmatrix} 1-g & -h \\ 1 & 1 \end{pmatrix} \tag{58}$$

and then

$$\underset{\sim}{D} = \begin{pmatrix} g-h & 0 \\ 0 & 1 \end{pmatrix} \tag{59}$$

$$\underset{\sim}{D}^{n-2} = \begin{pmatrix} (g-h)^{n-2} & 0 \\ 0 & 1 \end{pmatrix}$$

Arrhenius-like form,

$$\nu = \nu_o e^{-\psi/kT} \tag{27}$$

where ν_o is a constant frequency and ψ is the activation energy for jumping. If one of the atom's nearest neighbors is another atom then the activation energy for jumping must be augmented by the binding energy ε so that the new jumping frequency will be

$$\nu_1 = \nu_o e^{-(\psi+\varepsilon)/kT} = \nu e^{-\varepsilon/kT} \tag{28}$$

$$= \nu\lambda$$

where λ is obviously defined by

$$\lambda = e^{-\varepsilon/kT} \tag{29}$$

Now consider changes which occur in the underlined pair of sites in the following diagram

$$X1\underline{00} \quad \rightleftarrows \quad X0\underline{10} \tag{30}$$

$$\underline{11}0X \quad \rightleftarrows \quad \underline{10}1X \tag{31}$$

In this diagram a zero represents a vacancy and a one, an atom. The X indicates a one or a zero. Both processes

Evaluating $\underset{\sim}{M}^{n-2}$, according to Eq. (56), and making use of Eq. (53) we obtain

$$g^{(n)} = \frac{(g-h)^{n-1}(1-g)+h}{1-g+h} \tag{60}$$

Using Eqs. (49), Eqs. (16) - (23), and Eq. (41), Eq. (60) may be written in terms of g_{10} alone. Thus

$$g^{(n)} = \frac{[1-(1+\theta)g_{10}]^{n-1} + \theta}{1+\theta} \tag{61}$$

Thus we may use the solution of Eq. (39) to evaluate $g^{(n)}(t)$.

Incorporation of the Cooling Rate

A convenient and realistic dependence of temperature on time during quench[1] is the following

$$\frac{1}{kt} = a+bt \tag{62}$$

where a and b are constants and k is the Boltzmann constant. The quantity b is a measure of the cooling rate. Eq. (62) may be placed in the alternative (but less convenient) form

$$T = \frac{1}{k(a+bt)} \tag{63}$$

are indicated to be reversible. The forward process in Eq. (30) transforms a 00 pair into a 10 pair while the reverse process destroys a 10 pair. In Eq. (31) the forward process creates a 10 pair from a 11 pair and the reverse destroys it. We calculate the rate of change, with time, of P_{10}. Suppose X on the left side of Eq. (30) is a vacancy. Then using the superposition approximation the probability of the configuration on the left will be

$$P_{00} g_{01} g_{10} \tag{32}$$

The forward rate in Eq. (30) creates 10 pairs and contributes a term

$$\nu P_{00} g_{01} g_{10} \tag{33}$$

to dP_{10}/dt where t is time. ν and not ν_1 is the appropriate frequency since X is a vacancy. If X is an atom a similar line of reasoning leads to the contribution

$$\nu_1 P_{10} g_{01} g_{11} \tag{34}$$

For the reverse process in Eq. (30) we get only the term

$$-\nu P_{10} g_{10} \tag{35}$$

since there is a zero to the right of the one and the character

From this equation we see that as $t \to \infty$ τ approaches a maximum value τ_{max},

$$\tau_{max} = \frac{\nu_o e^{-a\psi}}{b\psi} \tag{68}$$

As indicated at the end of section III, τ_{max} represents the average number of steps allowed to an atom during the cooling process. Clearly, if τ_{max} is small the system will get "stuck". From Eq. (68), large values of b and ψ, i.e. of cooling rate and activation energy for jumping, lead to small τ_{max}.

The dependence of λ on time will be

$$\lambda = e^{-a\varepsilon} e^{-b\varepsilon t} \tag{69}$$

Solving for t in Eq. (67) and inserting the result in Eq. (69) gives

$$\begin{aligned} \lambda &= e^{-a\varepsilon} \left\{ 1 - \left[\frac{b\psi e^{a\psi}}{\nu_o} \right] \tau \right\}^{\varepsilon/\psi} \\ &= e^{-a\varepsilon} \left[1 - \frac{\tau}{\tau_{max}} \right]^{\varepsilon/\psi} \end{aligned} \tag{70}$$

so that λ may be expressed as a function of τ for the purpose of use in Eq. (39).

of the X is not at issue. We could use the two terms

$$-\nu P_{10} g_{10} g_{00} - \nu P_{10} g_{10} g_{01} \tag{36}$$

but these simply add (by Eq. (21)) to yield Eq. (35). Thus the contribution of Eq. (30) to dP_{10}/dt is the sum of Eqs. (33), (34) and (35), namely

$$\nu P_{00} g_{01} g_{10} + \nu_1 P_{10} g_{01} g_{11} - \nu P_{10} g_{10} \tag{37}$$

and proceeding in a similar manner for Eq. (31) we obtain

$$\begin{aligned} \frac{dP_{10}}{dt} = {} & \nu P_{00} g_{01} g_{10} + \nu_1 P_{10} g_{01} g_{11} - \nu P_{10} g_{10} \\ & + \nu_1 P_{11} g_{10} - \nu_1 P_{10} g_{01} g_{11} - \nu P_{10} g_{01} g_{10} \end{aligned} \tag{38}$$

Using Eqs. (16) through (23) and Eqs. (28) and (29) we can convert Eq. (38) into

$$\frac{dg_{10}}{d\tau} = 2\lambda g_{10}(1-g_{10})(1-\theta g_{10}) - 2\theta g_{10}^3 \tag{39}$$

where

$$\tau = \int_0^t \nu \, dt' \tag{40}$$

To express a and b in more physical terms we denote the initial (high) temperature by T_0 and room temperature (say 300°K) by T_R while denoting the time required to reach room temperature by t_R. Then it follows immediately that

$$a = \frac{1}{kT_o} \tag{64}$$

and

$$b = \frac{1}{kt_R} \left(\frac{1}{T_R} - \frac{1}{T_o} \right) \tag{65}$$

Thus if t_R is small (cooling rate, high) b is large. Sometimes it will be convenient to replace k by the gas constant (calories per mole per degree) in which case the size and units of a and b will change accordingly.

In terms of Eq. (62) the time dependence of ν is

$$\nu = \nu_o e^{-a\psi} e^{-b\psi t} \tag{66}$$

and from Eq. (40)

$$\tau = \frac{\nu_o e^{-a\psi}}{b\psi} \left(1 - e^{-b\psi t} \right) \tag{67}$$

and

$$\theta = \frac{x}{1-x} \tag{41}$$

As in Ref. 1 both ν and λ are presumed time dependent through the dependence of temperature T on time. If an isothermal process is involved then ν will be constant and

$$\tau = \nu t \tag{42}$$

which is the average number of steps an atom may take in time t.

If rapid cooling is involved τ will still represent the average number of steps but, as in the case of Ref. 1, τ will have a maximum value, τ_{max}, and only a finite number of steps will be allowed each atom. Thus the quenched system may get "stuck".

We may consider the equilibrium state achieved when the process is isothermal. At equilibrium the derivative on the left of Eq. (39) vanishes and the resulting equation is

$$\frac{(1-g_{10})(1-\theta g_{10})}{\theta g_{10}^2} = \lambda^{-1} \tag{43}$$

Using Eq. (41) together with Eqs. (16) through (23) easily converts this equation to Eq. (5) so that despite the approximation inherent in the kinetic equations the system tends towards the physically correct equilibrium state.

Calculations and Discussion

We have examined a system for which

$$\varepsilon = 23380 \text{ cal mole}^{-1} \tag{71}$$

Note the units (cal mole^{-1}) so that k in Eq. (62) must be replaced by the gas constant. Eq. (71) represents a binding energy of about 1 ev. For ψ we have chosen values between 200,000 and 300,000 cal mole^{-1}, but we only discuss the limiting cases, i.e.

$$\psi = \begin{matrix} 200,000 \\ 300,000 \end{matrix} \quad \text{cal mole}^{-1}, \tag{72}$$

since the other results interpolate nicely. For ν_o we pick

$$\nu_o = 10^{13} \text{ sec}^{-1} \tag{73}$$

All quenches begin at a temperature, T_o, of 12000°K. This leads to a value of a given by

$$a = 4.188 \times 10^{-5} \text{ mole cal}^{-1} \tag{74}$$

We have also examined the system for two value of Θ, namely,

$$\Theta = 1,3 \tag{75}$$

corresponding to

$$X = 0.5,\ 0.75 \tag{76}$$

The solution of Eq. (39), incorporating the function λ of Eq. (70), was performed numerically for a starting condition in which g_{10} corresponded to the equilibrium distribution at T_o,

Structure

The most convenient function for indexing the degree of structure is the pair correlation function $g^{(n)}$, i.e. the probability that the n-1 nearest neighbor site is occupied by an atom when it is known that the given site is so occupied. If we continue to assume the validity of the superposition approximation then

$$g^{(n)} = \Sigma g_{1i} g_{ij} g_{jk} - - - g_{s1} \tag{44}$$

where i, j, k, s, etc. may be 1 or 0 and the sum goes over all combinations of these numbers. Since there will be n-1 g factors in the sum there are 2^{n-2} terms in the sum.

The sum, and therefore $g^{(n)}$ can best be evaluated using the transfer matrix technique[4]. We first generalize the typical term in the sum of Eq. (44) so that the last factor may have an index ending in 0 as well as 1 and also consider terms having numbers of factors other than n, say m factors. Then we denote the sum of all terms containing m factors and ending with a factor whose last index is 1 by $g_1^{(m)}$ while the similar term ending with 0 index is denoted by $g_0^{(m)}$. Clearly then,

$$\begin{aligned} g_1^{(m)} &= g_1^{(m-1)} g_{11} + g_0^{(m-1)} g_{01} \\ g_0^{(m)} &= g_1^{(m-1)} g_{10} + g_0^{(m-1)} g_{00} \end{aligned} \tag{45}$$

i.e. at 12000°K. This value of g_{10} was obtained from Eq. (43) with $\lambda=\lambda(o)$. The solution to Eq. (43) is

$$g_{10} = \frac{-\lambda(1+\theta)}{2\theta(1-\lambda)} + \left\{\frac{\lambda^2(1+\theta)^2}{4\theta^2(1-\lambda)^2} + \frac{\lambda}{(1-\lambda)\theta}\right\}^{\frac{1}{2}} \tag{77}$$

Since $\lambda=0$ when T=0, i.e. at absolute zero (achieved at τ_{max})

$$g_{10}(T=0) = 0, \tag{78}$$

i.e., in the thermodynamic limit, no atoms are adjacent to vacancies and all atoms are adjacent to other atoms. Thus with an infinitely slow quench ($t_R=\infty$) we expect to achieve a structure with $g_{10}= 0$. Eq. (61) then requires

$$g^{(n)} = 1, \text{ all } n \tag{79}$$

This represents the limiting degree of correlation in the quench, and can only be achieved with infinitely slow cooling. We will denote the equilibrium values of $g^{(n)}$ at $T=T_o$ and T=0 by $g_0^{(n)}$ and $g_\infty^{(n)}$ respectively.

Our primary interest will be the actual nonequilibrium values of $g^{(n)}$ produced at $\tau=\tau_{max}$, i.e. the quenched-in structures. These are obtained by substituting the solution of Eq. (39) at $\tau=\tau_{max}$ into Eq. (61).

If $g_1^{(m)}$ and $g_0^{(m)}$ are considered to be the components of a vector $\vec{g}_m$,

$$\vec{g}_m = \begin{pmatrix} g_1^{(m)} \\ g_0^{(m)} \end{pmatrix} , \tag{46}$$

then Eq. (45) may be represented in matrix form as

$$\vec{g}_m = \underset{\sim}{M} \cdot \vec{g}_{m-1} \tag{47}$$

where the matrix $\underset{\sim}{M}$ has the form

$$\underset{\sim}{M} = \begin{pmatrix} g_{11} & g_{01} \\ g_{10} & g_{00} \end{pmatrix} \tag{48}$$

We simplify notation by writing

$$\begin{aligned} g_{11} &= g \quad , \quad & g_{01} &= h \\ g_{10} &= 1-g \quad , \quad & g_{00} &= 1-h \end{aligned} \tag{49}$$

Figure 1 shows some results for $g^{(n)}(\tau_{max})$ out to n=10, i.e. out to the ninth nearest neighbor. The curves in this Figure correspond to a system for which x=0.75 and for which ψ = 200,000 cal mole^{-1}. The starting distribution $g_o^{(m)}$ is shown as the lowest curve in the Figure. It may be seen that correlation virtually disappears (for the starting state at 12000°K) at site 5, i.e. the fourth nearest neighbor. The curves lying above $g_o^{(n)}$ correspond to $g^{(n)}(\tau_{max})$ for increasingly slow quenches. As expected more correlation develops (the curves are higher) as the quench is slowed. The times, t_R, to reach room temperature (300°K) from 12000°K are indicated at the left end of each curve. The horizontal line at 1.0 on the ordinate is $g_\infty^{(n)}$.

The values of τ_{max} are shown on each curve. Thus for t_R=10 sec. an atom is allowed to take 7.05×10^7 steps in the quench period. It is not surprising that considerable correlation develops. For $t_R=10^{-2}$ sec the system cools 12000°K in 10^{-2} sec for an average rate of 1.2×10^6 deg K sec^{-1}. Still some correlation develops.

Although the effect of squeezing out "free volume" is not fully handled by our model since x and therefore the number of vacancies, 1-x, is constant throughout the quench, we can get some idea of the effect by comparing the curves of Fig. 1 with those for another system where the only difference is a reduced value of x and hence an increased number of vacancies. For this purpose we choose x=0.5. Results for this system are shown in Fig. 2.

where account has been taken of Eqs. (20) and (21). Thus

$$\underset{\sim}{M} = \begin{pmatrix} g & h \\ 1-g & 1-h \end{pmatrix} \tag{50}$$

Now we know that

$$\vec{g}_2 = \begin{pmatrix} g \\ 1-g \end{pmatrix} \tag{51}$$

Thus,

$$\vec{g}_n = \underset{\sim}{M}^{m-2} \cdot \vec{g}_2 \tag{52}$$

and then the pair correlation function, Eq. (44), is simply

$$g^{(n)} = g_1^{(n)} = \vec{\delta} \cdot \underset{\sim}{M}^{n-2} \cdot g_2 \tag{53}$$

where $\vec{\delta}$ is the vector,

$$\vec{\delta} = \begin{pmatrix} 1 \\ 0 \end{pmatrix} \tag{54}$$

$T_0 = 12000\ °K$

$\theta = 3,\ x = 0.75$

$\phi = 200000\ \text{cal mole}^{-1}$

$\epsilon = 23880\ \text{cal mole}^{-1}$

$\nu = 10^{13}\ \text{sec}^{-1}$

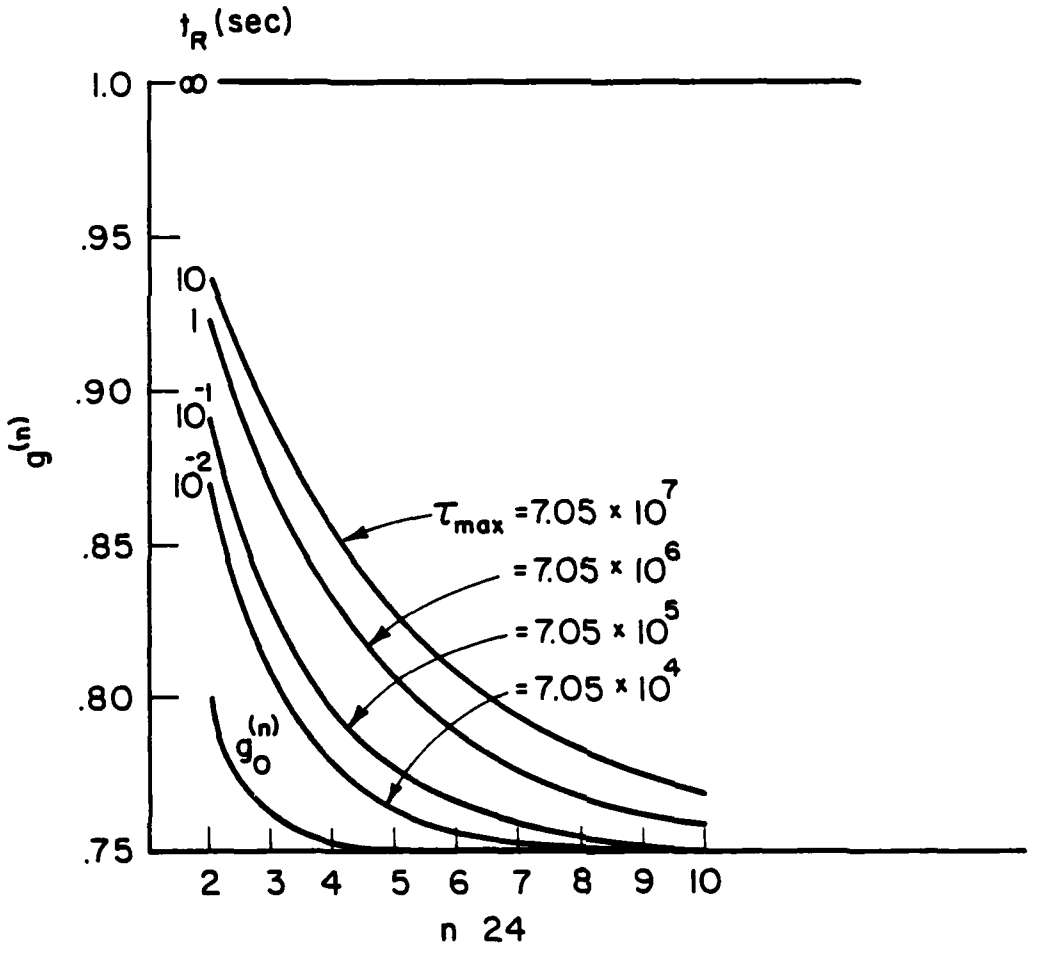

Figure 1

Let $\underset{\sim}{\Lambda}$ be the matrix which diagonalizes $\underset{\sim}{M}$. Thus

$$\underset{\sim}{D} = \underset{\sim}{\Lambda}^{-1} \cdot \underset{\sim}{M} \cdot \underset{\sim}{\Lambda} \tag{55}$$

is a diagonal matrix whose diagonal elements are the eigenvalues of $\underset{\sim}{M}$. Then the matrix produce $\underset{\sim}{M}^{n-2}$ may be written as

$$\begin{aligned} \underset{\sim}{M}^{n-2} &= \underset{\sim}{\Lambda}(\underset{\sim}{\Lambda}^{-1}\underset{\sim}{M}\underset{\sim}{\Lambda}\underset{\sim}{\Lambda}^{-1}\underset{\sim}{M}\underset{\sim}{\Lambda}\text{----}\underset{\sim}{\Lambda}^{-1}\underset{\sim}{M}\underset{\sim}{\Lambda})\underset{\sim}{\Lambda}^{-1} \\ &= \underset{\sim}{\Lambda}\underset{\sim}{D}^{n-2}\underset{\sim}{\Lambda}^{-1} \end{aligned} \tag{56}$$

It is easy to show, by standard means[5], that

$$\underset{\sim}{\Lambda} = \begin{pmatrix} 1 & h \\ -1 & 1-g \end{pmatrix} \tag{57}$$

and

$$\underset{\sim}{\Lambda}^{-1} = \frac{1}{1-g+h} \begin{pmatrix} 1-g & -h \\ 1 & 1 \end{pmatrix} \tag{58}$$

and then

$$\underset{\sim}{D} = \begin{pmatrix} g-h & 0 \\ 0 & 1 \end{pmatrix} \tag{59}$$

$$\underset{\sim}{D}^{n-2} = \begin{pmatrix} (g-h)^{n-2} & 0 \\ 0 & 1 \end{pmatrix}$$

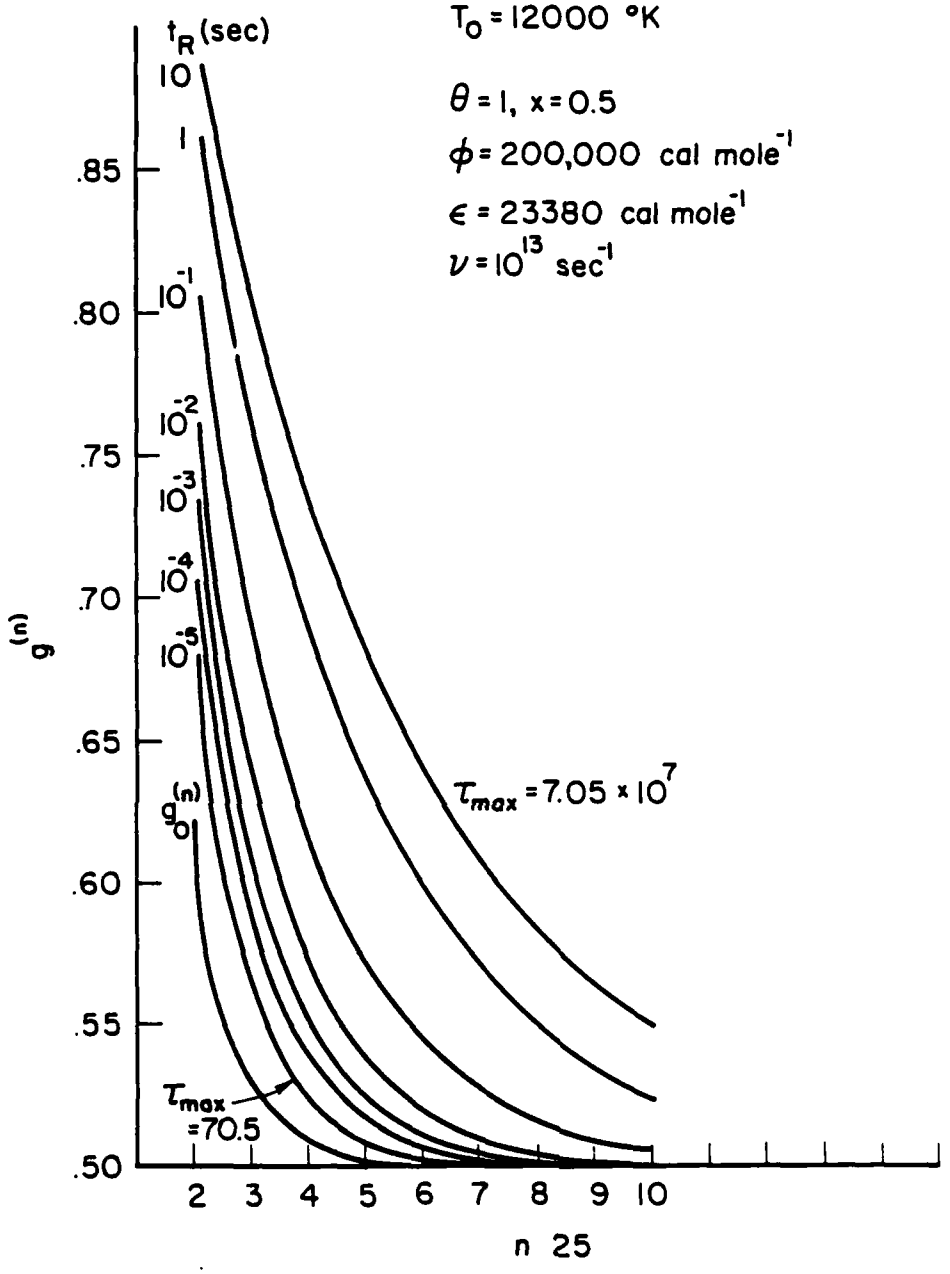
$T_0 = 12000$ °K
$\theta = 1$, $x = 0.5$
$\phi = 200{,}000$ cal mole^{-1}
$\epsilon = 23380$ cal mole^{-1}
$\nu = 10^{13}$ sec^{-1}
t_R (sec)
10
1
10^{-1}
10^{-2}
10^{-3}
10^{-4}
10^{-5}
$g_0^{(n)}$
$\tau_{max} = 7.05 \times 10^7$
$\tau_{max} = 70.5$
$g_0^{(n)}$
.85
.80
.75
.70
.65
.60
.55
.50
2 3 4 5 6 7 8 9 10
n 25

Figure 2

From this equation we see that as $t \to \infty$ τ approaches a maximum value τ_{max},

$$\tau_{max} = \frac{\nu_o e^{-a\psi}}{b\psi} \tag{68}$$

As indicated at the end of section III, τ_{max} represents the average number of steps allowed to an atom during the cooling process. Clearly, if τ_{max} is small the system will get "stuck". From Eq. (68), large values of b and ψ, i.e. of cooling rate and activation energy for jumping, lead to small τ_{max}.

The dependence of λ on time will be

$$\lambda = e^{-a\varepsilon} e^{-b\varepsilon t} \tag{69}$$

Solving for t in Eq. (67) and inserting the result in Eq. (69) gives

$$\begin{aligned} \lambda &= e^{-a\varepsilon} \left\{ 1 - \left[\frac{b\psi e^{a\psi}}{\nu_o} \right] \tau \right\}^{\varepsilon/\psi} \\ &= e^{-a\varepsilon} \left[1 - \frac{\tau}{\tau_{max}} \right]^{\varepsilon/\psi} \end{aligned} \tag{70}$$

so that λ may be expressed as a function of τ for the purpose of use in Eq. (39).

Again the lowest curve in the Figure is for $g_0^{(n)}$. We see that even for $t_R = 10^{-5}$ sec corresponding to an average cooling rate of 1.2×10^9 deg K sec^{-1} some correlation develops. In general the curve of Fig. 2 exhibits more correlation than those of Fig. 1 even though the range of τ_{max} is the same. This demonstrates the increase in mobility made possible by the greater free volume, i.e. the larger number of vacancies, and a comparison which we promised earlier.

Incidentally, as $n\to\infty$ and correlation vanishes $g^{(n)}\to x$ as it does in every curve of Figures 1 and 2.

To see the effect of an increase in ψ in reducing the mobility we pass to a system in which x remains at 0.5, but in which ψ is increased from 200,000 to 300,000 cal $mole^{-1}$. Figure 3 illustrates curves for this sytem. The principal feature of these curves is a dramatic reduction in τ_{max}. In fact, the curve for $t_R=10^{-5}$ sec is virtually indistinguishable from $g_0^{(n)}$ and corresponds to $\tau_{max} = 0.714$, i.e. less than <u>one</u> step per atom is allowed. Clearly the effect of increasing the activation energy for jumping is much larger than that due to removal of free volume. The situation could of course be reversed in the extreme limit that <u>all</u> of the free volume is "squeezed out".

<u>Acknowledgement</u>

The author is indebted to Dr. Brice Carnahan of the University of Michigan for performing the numerical computations in this paper. This research was supported by the Defense Advanced Research Projects Agency of the Department of Defense under Contract No. MDA903-80C-0505 with The University of Michigan.

To express a and b in more physical terms we denote the initial (high) temperature by T_0 and room temperature (say 300°K) by T_R while denoting the time required to reach room temperature by t_R. Then it follows immediately that

$$a = \frac{1}{kT_o} \tag{64}$$

and

$$b = \frac{1}{kt_R} \left(\frac{1}{T_R} - \frac{1}{T_o} \right) \tag{65}$$

Thus if t_R is small (cooling rate, high) b is large. Sometimes it will be convenient to replace k by the gas constant (calories per mole per degree) in which case the size and units of a and b will change accordingly.

In terms of Eq. (62) the time dependence of ν is

$$\nu = \nu_o e^{-a\psi} e^{-b\psi t} \tag{66}$$

and from Eq. (40)

$$\tau = \frac{\nu_o e^{-a\psi}}{b\psi} \left(1 - e^{-b\psi t} \right) \tag{67}$$

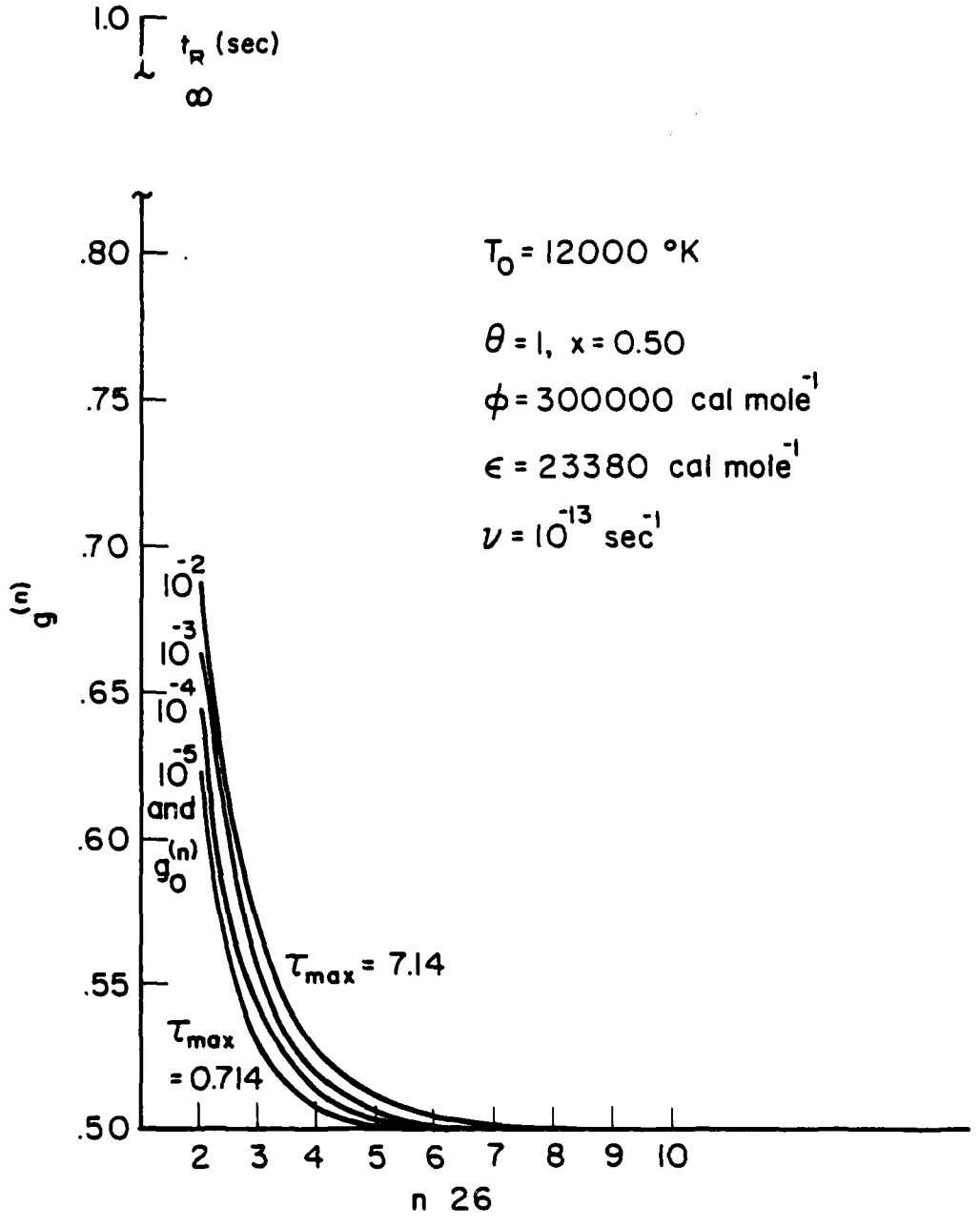
1.0
t_R (sec)
∞
.80
.75
.70
.65
.60
.55
.50
$g_0^{(n)}$
T_0 = 12000 °K
θ = 1, x = 0.50
ϕ = 300000 cal mole^{-1}
ϵ = 23380 cal mole^{-1}
$\nu = 10^{-13}$ sec^{-1}
10^{-2}
10^{-3}
10^{-4}
10^{-5}
and
τ_{max} = 7.14
τ_{max} = 0.714
2 3 4 5 6 7 8 9 10
n 26

Figure 3

VARIATIONAL METHODS FOR CALCULATING J & M INTEGRALS AND ACOUSTIC SCATTERING FROM CRACKS

G. S. Kino

ABSTRACT

It is difficult to calculate acoustic scattering coefficients, stress intensity factor and energy integrals of cracks of arbitrary shape and with non-uniform applied stress fields. We derive here a variational technique for this purpose, which uses a trial function for the crack opening displacement ΔU. We show that the method is easily adaptable to the use of Fourier transform techniques and hence can make use of the FTT (Fast Fourier Transform)

i.e. at 12000°K. This value of g_{10} was obtained from Eq. (43) with $\lambda=\lambda(o)$. The solution to Eq. (43) is

$$g_{10} = \frac{-\lambda(1+\theta)}{2\theta(1-\lambda)} + \left\{\frac{\lambda^2(1+\theta)^2}{4\theta^2(1-\lambda)^2} + \frac{\lambda}{(1-\lambda)\theta}\right\}^{\frac{1}{2}} \tag{77}$$

Since $\lambda=0$ when T=0, i.e. at absolute zero (achieved at τ_{max})

$$g_{10}(T=0) = 0, \tag{78}$$

i.e., in the thermodynamic limit, no atoms are adjacent to vacancies and all atoms are adjacent to other atoms. Thus with an infinitely slow quench ($t_R=\infty$) we expect to achieve a structure with $g_{10}= 0$. Eq. (61) then requires

$$g^{(n)} = 1, \text{ all } n \tag{79}$$

This represents the limiting degree of correlation in the quench, and can only be achieved with infinitely slow cooling. We will denote the equilibrium values of $g^{(n)}$ at $T=T_o$ and T=0 by $g_0^{(n)}$ and $g_\infty^{(n)}$ respectively.

Our primary interest will be the actual nonequilibrium values of $g^{(n)}$ produced at $\tau=\tau_{max}$, i.e. the quenched-in structures. These are obtained by substituting the solution of Eq. (39) at $\tau=\tau_{max}$ into Eq. (61).

VARIATIONAL METHODS FOR CALCULATING J & M INTEGRALS AND ACOUSTIC SCATTERING FROM CRACKS

G. S. Kino

INTRODUCTION

It is normally difficult to calculate the stress intensity factor of flat crack of arbitrary shape. Similarly, the J & M integrals or the closely related scattering coefficient of an acoustic wave reflected from a crack can only be calculated easily for certain simple crack shapes (ellipses or strips). A further difficult problem is to determine these quantities when the applied stress is non-uniform over the area of the crack.

At the 1975 MRC Conference, the author derived an acoustic wave scattering theory[1,2,3] which could be stated in variational form. In essence the use of such variational theories could make it possible to employ a trial function ΔU for the crack opening displacement. A more accurate guess is then obtained for the energy related quantity of interest such as the M integral or acoustic wave scattering coefficient. The variational method has the advantage of making it possible to use physical intuition in the choice of the trial function and Rayleigh-Ritz techniques to improve the trial function. Furthermore, it lends itself, as we shall see, to the use of FFT (Fast Fourier Transform) techniques and makes it possible to employ many of the powerful methods that have been used earlier in electromagnetic scattering theories.

Figure 1 shows some results for $g^{(n)}(\tau_{max})$ out to n=10, i.e. out to the ninth nearest neighbor. The curves in this Figure correspond to a system for which x=0.75 and for which ψ = 200,000 cal mole^{-1}. The starting distribution $g_o^{(m)}$ is shown as the lowest curve in the Figure. It may be seen that correlation virtually disappears (for the starting state at 12000°K) at site 5, i.e. the fourth nearest neighbor. The curves lying above $g_o^{(n)}$ correspond to $g^{(n)}(\tau_{max})$ for increasingly slow quenches. As expected more correlation develops (the curves are higher) as the quench is slowed. The times, t_R, to reach room temperature (300°K) from 12000°K are indicated at the left end of each curve. The horizontal line at 1.0 on the ordinate is $g_\infty^{(n)}$.

The values of τ_{max} are shown on each curve. Thus for t_R=10 sec. an atom is allowed to take 7.05×10^7 steps in the quench period. It is not surprising that considerable correlation develops. For $t_R=10^{-2}$ sec the system cools 12000°K in 10^{-2} sec for an average rate of 1.2×10^6 deg K sec^{-1}. Still some correlation develops.

Although the effect of squeezing out "free volume" is not fully handled by our model since x and therefore the number of vacancies, 1-x, is constant throughout the quench, we can get some idea of the effect by comparing the curves of Fig. 1 with those for another system where the only difference is a reduced value of x and hence an increased number of vacancies. For this purpose we choose x=0.5. Results for this system are shown in Fig. 2.

Such techniques do not involve the use of singular integral equations nor the Wiener Hopf methods. So, mathematically they are relatively simple and suitable for numerical computation, and are not restricted only to elastostatic solutions. The theory may therefore be useful, ultimately, in applications to acoustic wave scattering theory at arbitrary frequencies.

In this paper we have re-derived the variational theory by a simpler, hopefully, more easily understood method.

We show that it may be generalized to determine not only the scattering coefficient of acoustic waves, but also the interaction energy of a crack and its M integral.

We then go on to demonstrate the use of Fourier transform techniques on a simple problem, that of a plane crack in static Mode I plane strain. We show that the use of a relatively crude triangular trial function for the crack opening displacement $\Delta U = a-|x|$, instead of the true function $\Delta U = (a^2-x^2)^{\frac{1}{2}}$ where 2a is the crack length and x the distance along its surface, gives an interaction energy and stress intensity factor, 15% and 8% lower than the true values respectively.

SCATTERING COEFFICIENT AND ENERGY INTEGRALS

We employ the Rayleigh-Betti reciprocity theorem to determine the energy change due to the presence of a flaw. We consider the material to be stressed in a testing machine. Suppose that without a flaw present the displacement, stress and strain at any point in the material are U_i^A, σ_{ij}^A, and ε_{ij}^A, respectively, With the flaw present the displacement and stress at U_i, σ_{ij}, ε_{ij}, respectively.

$T_0 = 12000\ °K$

$\theta = 3,\ x = 0.75$

$\phi = 200000\ \text{cal mole}^{-1}$

$\epsilon = 23880\ \text{cal mole}^{-1}$

$\nu = 10^{13}\ \text{sec}^{-1}$

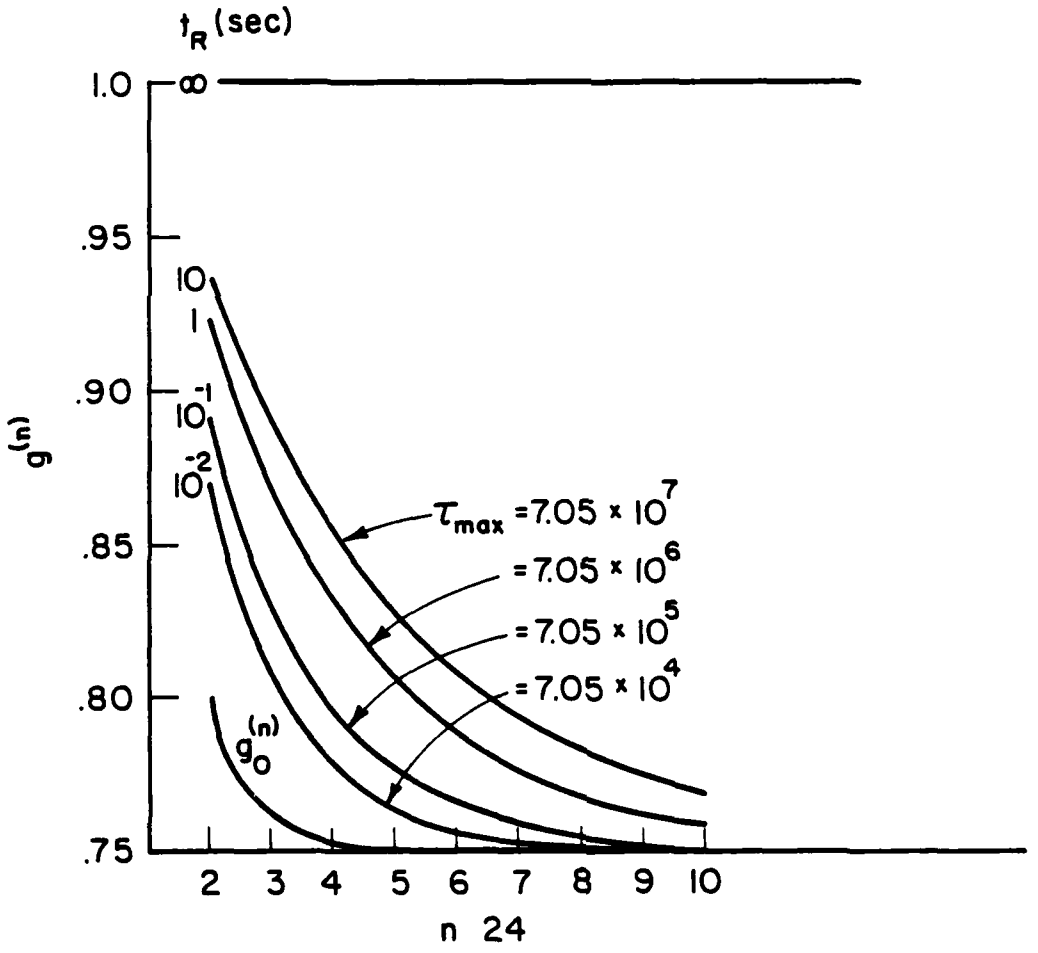

Figure 1

By the use of the Rayleigh-Betti reciprocity theorem in the material region outside the flaw, it follows that:

$$\int_S (\sigma^A_{ij} U_j - \sigma_{ij} U^A_j) n_i ds = -\int_{S_F} (\sigma^A_{ij} U_j - \sigma_{ij} U^A_j) n_i ds \qquad (1)$$

Where S is the outer surface of material, S_F the surface of the flaw, and n_i the outward normal from these surfaces.

We note that the only contribution to the integral S comes from the two ends of the material where, we assume it is supported in rigid clamps. ($\sigma_{ij} n_i = 0$ at a free surface). Then at the clamps $U_j = U^A_j$. So it will be seen that the interaction energy with a flaw is W where:

$$W = \frac{1}{2} \int_S U^A_j (\sigma^A_{ij} - \sigma_{ij}) n_i ds = -\frac{1}{2} \int_{S_F} (\sigma^A_{ij} U_j - \sigma_{ij} U^A_j) n_i ds \qquad (2)$$

When the flaw is a crack $\sigma_{ij} n_i = 0$ on the crack surface. So it follows that the crack energy is

$$W = -\frac{1}{2} \int_{S_F} (\sigma^A_{ij} \Delta U_j) n_i ds \qquad (3)$$

Where ΔU_j is the crack opening displacement, n_i is the outward normal on one side of the crack. The energy of a more general flaw is

$$W = \frac{1}{2} \int_{S_F} (\sigma_{ij} U^A_j - \sigma^A_{ij} U_j) n_i ds \qquad (4)$$

These results agree with those of Eshelby.[4]

It follows from Budiansky and O'Connell[5] that the interaction energy of a crack is

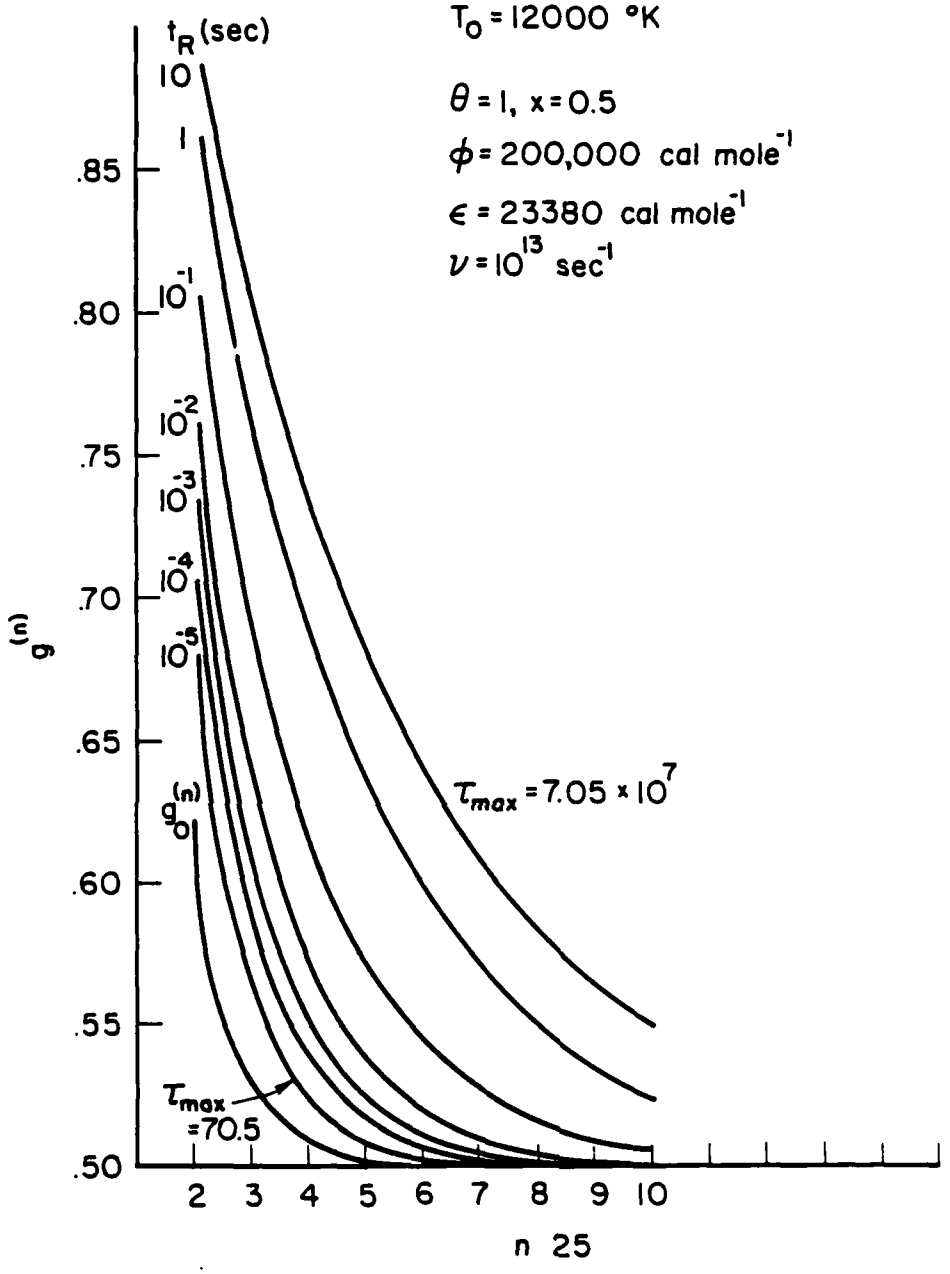
$T_0 = 12000$ °K
$\theta = 1$, $x = 0.5$
$\phi = 200{,}000$ cal mole^{-1}
$\epsilon = 23380$ cal mole^{-1}
$\nu = 10^{13}$ sec^{-1}
t_R (sec)
10
1
10^{-1}
10^{-2}
10^{-3}
10^{-4}
10^{-5}
$g_0^{(n)}$
$\tau_{max} = 7.05 \times 10^7$
$\tau_{max} = 70.5$
$g_0^{(n)}$
.85
.80
.75
.70
.65
.60
.55
.50
2 3 4 5 6 7 8 9 10
n 25

Figure 2

$$W = \frac{1-\nu^2}{3E} \oint_c \rho \left[K_I^2 + K_{II}^2 + K_{III}^2/(1-\nu) \right] d\ell \qquad (5)$$

where ρ and ℓ are based on the crack based coordinates shown in Fig. 1. E is Young's modulus, ν is Poisson's ratio and K_I, K_{II}, and K_{III} are the stress intensity factors for plane strain and anti-plane shear.[5] In turn, Rice's J integral[6] of fracture mechanics is defined as

$$J = \frac{1-\nu^2}{E} \left[K_I^2 + K_{II}^2 + K_{III}^2/(1-\nu) \right] \qquad (6)$$

while the M integral of Knowles and Sternberg is defined by the relation

$$M = \int J d\ell \qquad (7)$$

It therefore follows that

$$W = M/3 \qquad (8)$$

We conclude that if we can evaluate W we can, in turn evaluate M. Furthermore, it was shown by Kino that when an acoustic wave is scattered from a crack, the back scatter reflection coefficient of the wave of frequency ω is[2,3]

$$S_{11} = \frac{1}{4} j\omega \int_{S_F} (\Delta U_j \sigma_{ij}^A) n_i ds \qquad (9)$$

where, now, U_j, σ_{ij}^A are the values of U_j, σ_{ij}^A at the crack when there is unit power emitted by a transducer. So S_{11} is just $j\omega$ W/4, with an applied stress equivalent to that of unit power in the incident acoustic wave.

Again the lowest curve in the Figure is for $g_0^{(n)}$. We see that even for $t_R = 10^{-5}$ sec corresponding to an average cooling rate of 1.2×10^9 deg K sec^{-1} some correlation develops. In general the curve of Fig. 2 exhibits more correlation than those of Fig. 1 even though the range of τ_{max} is the same. This demonstrates the increase in mobility made possible by the greater free volume, i.e. the larger number of vacancies, and a comparison which we promised earlier.

Incidentally, as $n\to\infty$ and correlation vanishes $g^{(n)}\to x$ as it does in every curve of Figures 1 and 2.

To see the effect of an increase in ψ in reducing the mobility we pass to a system in which x remains at 0.5, but in which ψ is increased from 200,000 to 300,000 cal $mole^{-1}$. Figure 3 illustrates curves for this sytem. The principal feature of these curves is a dramatic reduction in τ_{max}. In fact, the curve for $t_R=10^{-5}$ sec is virtually indistinguishable from $g_0^{(n)}$ and corresponds to $\tau_{max} = 0.714$, i.e. less than <u>one</u> step per atom is allowed. Clearly the effect of increasing the activation energy for jumping is much larger than that due to removal of free volume. The situation could of course be reversed in the extreme limit that <u>all</u> of the free volume is "squeezed out".

<u>Acknowledgement</u>

The author is indebted to Dr. Brice Carnahan of the University of Michigan for performing the numerical computations in this paper. This research was supported by the Defense Advanced Research Projects Agency of the Department of Defense under Contract No. MDA903-80C-0505 with The University of Michigan.

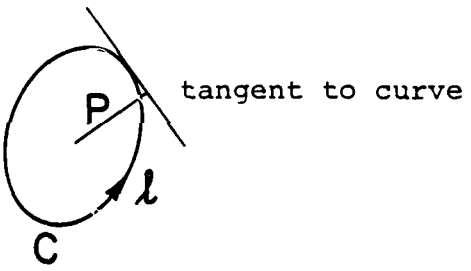

Figure 1. An illustration of crack based coordinates.

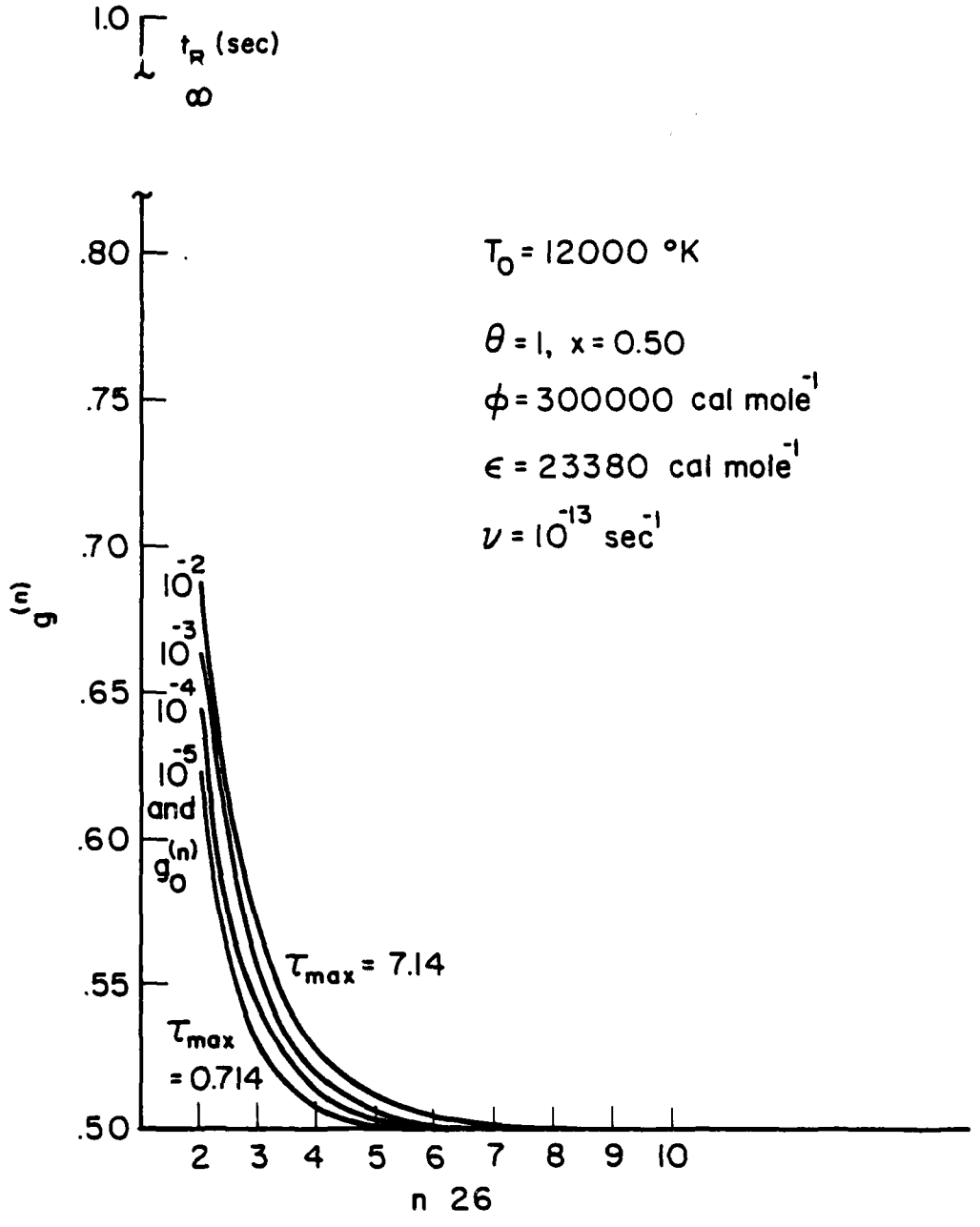
1.0
t_R (sec)
∞
.80
.75
.70
.65
.60
.55
.50
$g_0^{(n)}$
T_0 = 12000 °K
θ = 1, x = 0.50
ϕ = 300000 cal mole^{-1}
ϵ = 23380 cal mole^{-1}
$\nu = 10^{-13}$ sec^{-1}
10^{-2}
10^{-3}
10^{-4}
10^{-5}
and
τ_{max} = 7.14
τ_{max} = 0.714
2 3 4 5 6 7 8 9 10
n 26

Figure 3

Therefore, if we can evaluate W correctly, we can determine M and S_{oo}, parameters of importance in fracture mechanics or in the determination of acoustic wave scattering from a crack. For an exact calculation we need to know the applied field σ^A_{ij} and the crack opening displacement ΔU_j in the pressure of the applied field. Thus it is necessary to solve for ΔU_j when

$$\Delta U_j = 0 \qquad \text{outside the crack}$$

$$\sigma_{ij} n_i = 0 \qquad \text{at the crack surface}$$

and σ^A_{ij} is known.

VARIATIONAL THEORY

We have found that the energy stored in a crack is

$$W = \int_S (\sigma^A_{ij} U_j - \sigma_{ij} U^A_j) n_i ds \tag{10}$$

Suppose we use a trial function for the fields within the interior in which U_i, σ_{ij}, etc., differ to 1st order error from the correct quantities U^o_i, σ^o_{ij}. Then if we consider the quantity, called the reaction, by Rumsey[8]

$$\Delta W = \int_S (\sigma_{ij} U^o_j - \sigma^o_{ij} U_j) n_i ds \tag{11}$$

taken around the outer periphery, we see that when $\sigma_{ij} = \sigma^o_{ij}$, $U_j = U^o_j$, $\Delta W = 0$.

Suppose now we require ΔW to differ from zero only to 2nd order in error. Then if U_j is the applied displacement at the grips $U_j = U^o_j = U^A_j$.

VARIATIONAL METHODS FOR CALCULATING J & M INTEGRALS AND ACOUSTIC SCATTERING FROM CRACKS

G. S. Kino

ABSTRACT

It is difficult to calculate acoustic scattering coefficients, stress intensity factor and energy integrals of cracks of arbitrary shape and with non-uniform applied stress fields. We derive here a variational technique for this purpose, which uses a trial function for the crack opening displacement ΔU. We show that the method is easily adaptable to the use of Fourier transform techniques and hence can make use of the FTT (Fast Fourier Transform) numerical methods commonly employed in other fields. We give a very simple analytic example of a plane crack in Mode I plane strain. Using a crude triangular trial function for the crack opening displacement we obtain interaction energy (M integral) 15% lower than the true value, with a corresponding stress intensity factor 8% lower than the true value. We suggest the use of Rayleigh-Ritz techniques to obtain more accurate results.

We write

$$\Delta W = \int_S (\sigma_{ij}-\sigma^o_{ij})U^A_j n_i ds = \int_S (\sigma_{ij}-\sigma^A_{ij})U^A_j n_i ds - \int_S (\sigma^A_{ij}-\sigma^o_{ij})U^A_j n_i ds \quad (12)$$

So it follows from Eq. (2) that

$$\Delta W = \int (\sigma_{ij}-\sigma^A_{ij})U^A_j n_i ds - W \quad (13)$$

It therefore follows that if $\Delta W = 0$ to 1st order in error,

$$\Delta W = -\int_{S_F} (\sigma_{ij}U^o_j-\sigma^o_{ij}U_j)n_i ds = 0 \quad (14)$$

at the flaw.

If the flaw is a crack $\sigma^o_{ij}n_i = 0$ at the crack surface and so ΔW becomes

$$\Delta W = -\int_{S_F} (\Delta U^o_j \sigma_{ij})n_i ds = 0 \quad (15)$$

is the requriement for zero 1st order error in W, where n_i is the outward normal from one surface of the crack. But $\sigma_{ij}n_i$ is only non-zero at the crack to 1st order in error. Hence we can replace ΔU^o_j by ΔU_j and only contribute terms in error to 2nd order in ΔW. So

$$\Delta W = -\int_{S_F} (\Delta U_j \sigma_{ij})n_i ds = 0 \quad (16)$$

is an equally valid assumption.

It follows that Eq. (16) is the requirement for our variational principle. It requires continuity of

$$\int (\sigma_{ij}\Delta U_j)n_i ds$$

VARIATIONAL METHODS FOR CALCULATING J & M INTEGRALS AND ACOUSTIC SCATTERING FROM CRACKS

G. S. Kino

INTRODUCTION

It is normally difficult to calculate the stress intensity factor of flat crack of arbitrary shape. Similarly, the J & M integrals or the closely related scattering coefficient of an acoustic wave reflected from a crack can only be calculated easily for certain simple crack shapes (ellipses or strips). A further difficult problem is to determine these quantities when the applied stress is non-uniform over the area of the crack.

At the 1975 MRC Conference, the author derived an acoustic wave scattering theory[1,2,3] which could be stated in variational form. In essence the use of such variational theories could make it possible to employ a trial function ΔU for the crack opening displacement. A more accurate guess is then obtained for the energy related quantity of interest such as the M integral or acoustic wave scattering coefficient. The variational method has the advantage of making it possible to use physical intuition in the choice of the trial function and Rayleigh-Ritz techniques to improve the trial function. Furthermore, it lends itself, as we shall see, to the use of FFT (Fast Fourier Transform) techniques and makes it possible to employ many of the powerful methods that have been used earlier in electromagnetic scattering theories.

through the crack instead of the far more stringent boundary condition: $\sigma_{ij}n_i = 0$.

Now consider W. When we use a trial function ΔU_i, it follows that

$$W = \frac{1}{2}\int\left[(\sigma_{ij}-\sigma^s_{ij})\Delta U_j\right]n_i ds \tag{17}$$

Where the total field is

$$\sigma_{ij} = \sigma^A_{ij}+\sigma^s_{ij} \tag{18}$$

So σ^s_{ij} is the stress field due to the displacement ΔU_i. Because

$$\int(\sigma_{ij}\Delta U_j)n_i ds = 0$$

we see that

$$W = \frac{1}{2}\int(-\sigma^s_{ij}\Delta U_j)n_i ds \tag{19}$$

But as we do not know the amplitude ΔU_j and σ^s_{ij} is proportional to ΔU_j, we could equally well replace ΔU_j by $A\Delta U_j$, where A is a proprotionality factor. In this case it follows that

$$W = -\frac{A^2}{2}\int(\sigma^s_{ij}\Delta U_j)n_i ds \tag{20}$$

However we could equally well have written

$$\sigma^A_{ij} = \sigma^o_{ij}-\sigma^{so}_{ij} \tag{21}$$

In this case

$$W = -\frac{A}{2}\int(\sigma^{so}_{ij}\Delta U_j)n_i ds \tag{22}$$

It follows that as Eqs. (20) and (22) must be identical to 2nd order hence

Such techniques do not involve the use of singular integral equations nor the Wiener Hopf methods. So, mathematically they are relatively simple and suitable for numerical computation, and are not restricted only to elastostatic solutions. The theory may therefore be useful, ultimately, in applications to acoustic wave scattering theory at arbitrary frequencies.

In this paper we have re-derived the variational theory by a simpler, hopefully, more easily understood method.

We show that it may be generalized to determine not only the scattering coefficient of acoustic waves, but also the interaction energy of a crack and its M integral.

We then go on to demonstrate the use of Fourier transform techniques on a simple problem, that of a plane crack in static Mode I plane strain. We show that the use of a relatively crude triangular trial function for the crack opening displacement $\Delta U = a-|x|$, instead of the true function $\Delta U = (a^2-x^2)^{\frac{1}{2}}$ where 2a is the crack length and x the distance along its surface, gives an interaction energy and stress intensity factor, 15% and 8% lower than the true values respectively.

SCATTERING COEFFICIENT AND ENERGY INTEGRALS

We employ the Rayleigh-Betti reciprocity theorem to determine the energy change due to the presence of a flaw. We consider the material to be stressed in a testing machine. Suppose that without a flaw present the displacement, stress and strain at any point in the material are U_i^A, σ_{ij}^A, and ε_{ij}^A, respectively, With the flaw present the displacement and stress at U_i, σ_{ij}, ε_{ij}, respectively.

By the use of the Rayleigh-Betti reciprocity theorem in the material region outside the flaw, it follows that:

$$\int_S (\sigma^A_{ij} U_j - \sigma_{ij} U^A_j) n_i ds = -\int_{S_F} (\sigma^A_{ij} U_j - \sigma_{ij} U^A_j) n_i ds \qquad (1)$$

Where S is the outer surface of material, S_F the surface of the flaw,

scattering from a crack by a signal incident from transducer 1 and received on transducer 2 is

$$S_{21} = \frac{-\frac{j\omega}{4}\int(\sigma_{ij}^{A}{}^{(1)}\Delta U^{(2)})n_i ds \int(\sigma_{ij}^{A}{}^{(2)}\Delta U_j^{(1)})n_i ds}{\int(\sigma_{ij}^{s}{}^{(2)}\Delta U_j^{(1)})n_i ds} \tag{28}$$

where the superscripts (1) and (2) refer to the fields associated

If for instance, $\sigma^s_{zz}(x,y,0)$ has the Fourier transform $\sigma_{zz}(\alpha,\beta)$, it follows from Rayleigh's theorem that

$$\int \sigma^s_{zz}\Delta U_z dxdy = \int \sigma_{zz}(\alpha,\beta)\Delta U^*(\alpha,\beta)d\alpha d\beta \tag{31}$$

Thus it is easy to evaluate the terms we need in the variational theory by relatively simple integrations, and to treat flat cracks of arbitrary shape.

We shall use as an illustration of the variational technique derived here an example calculated for scattering in unpublished work by Kino and Tien, using the earlier 1975 formulation of the variational theory. We take the crack to be located in the z = 0 plane, to be of length 2a in the direction and infinitely long in the y direction, as illustrated in Fig. 2.

We shall treat only the static case of a flame crack with mode I excitation. It will be clear from the treatment how to deal with more complicated situations with time varying excitations and more complicated shapes. We shall compare our results, using simple trial functions, with the exact solution.

We write the displacement in the form

$$\underset{\sim}{U} = \nabla\phi + \nabla\cdot\underset{\sim}{\psi} \tag{32}$$

where

$$\nabla^2\phi + k_\ell^2\phi = 0 \tag{33}$$

$$\nabla^2\underset{\sim}{\psi} + k^2\underset{\sim}{\psi} = 0 \tag{34}$$

with

Therefore, if we can evaluate W correctly, we can determine M and S_{oo}, parameters of importance in fracture mechanics or in the determination of acoustic wave scattering from a crack. For an exact calculation we need to know the applied field σ^A_{ij} and the crack opening displacement ΔU_j in the pressure of the applied field. Thus it is necessary to solve for ΔU_j when

$$\Delta U_j = 0 \qquad \text{outside the crack}$$

$$\sigma_{ij} n_i = 0 \qquad \text{at the crack surface}$$

and σ^A_{ij} is known.

VARIATIONAL THEORY

We have found that the energy stored in a crack is

$$W = \int_S (\sigma^A_{ij} U_j - \sigma_{ij} U^A_j) n_i ds \tag{10}$$

Suppose we use a trial function for the fields within the interior in which U_i, σ_{ij}, etc., differ to 1st order error from the correct quantities U^o_i, σ^o_{ij}. Then if we consider the quantity, called the reaction, by Rumsey[8]

$$\Delta W = \int_S (\sigma_{ij} U^o_j - \sigma^o_{ij} U_j) n_i ds \tag{11}$$

taken around the outer periphery, we see that when $\sigma_{ij} = \sigma^o_{ij}$, $U_j = U^o_j$, $\Delta W = 0$.

Suppose now we require ΔW to differ from zero only to 2nd order in error. Then if U_j is the applied displacement at the grips $U_j = U^o_j = U^A_j$.

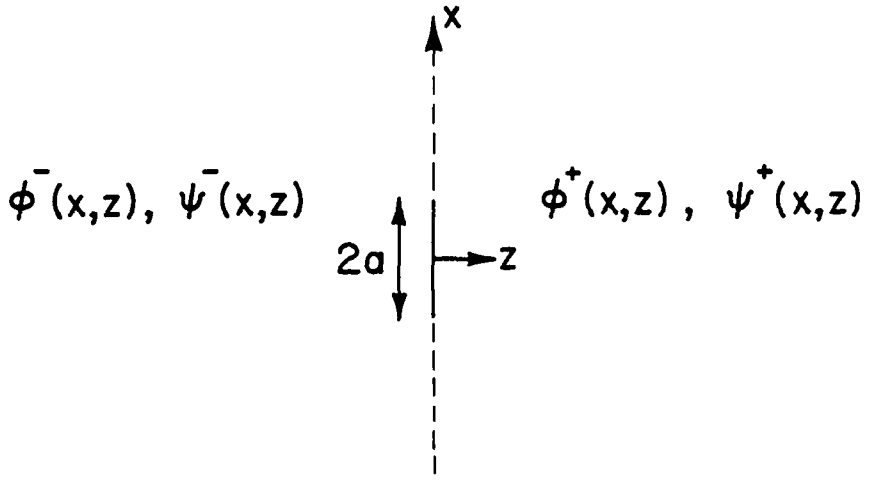

Figure 2. An illustration of the plane crack used in the theory.

We write

$$\Delta W = \int_S (\sigma_{ij}-\sigma^o_{ij})U^A_j n_i ds = \int_S (\sigma_{ij}-\sigma^A_{ij})U^A_j n_i ds - \int_S (\sigma^A_{ij}-\sigma^o_{ij})U^A_j n_i ds \quad (12)$$

So it follows from Eq. (2) that

$$\Delta W = \int (\sigma_{ij}-\sigma^A_{ij})U^A_j n_i ds - W \quad (13)$$

It therefore follows that if $\Delta W = 0$ to 1st order in error,

$$\Delta W = -\int_{S_F} (\sigma_{ij}U^o_j-\sigma^o_{ij}U_j)n_i ds = 0 \quad (14)$$

at the flaw.

If the flaw is a crack $\sigma^o_{ij}n_i = 0$ at the crack surface and so ΔW becomes

$$\Delta W = -\int_{S_F} (\Delta U^o_j \sigma_{ij})n_i ds = 0 \quad (15)$$

is the requriement for zero 1st order error in W, where n_i is the outward normal from one surface of the crack. But $\sigma_{ij}n_i$ is only non-zero at the crack to 1st order in error. Hence we can replace ΔU^o_j by ΔU_j and only contribute terms in error to 2nd order in ΔW. So

$$\Delta W = -\int_{S_F} (\Delta U_j \sigma_{ij})n_i ds = 0 \quad (16)$$

is an equally valid assumption.

It follows that Eq. (16) is the requirement for our variational principle. It requires continuity of

$$\int (\sigma_{ij}\Delta U_j)n_i ds$$

$$k_\ell^2 = \omega^2 \rho_{mo}/(\lambda+2\mu) \tag{35}$$

$$k_s^2 = \omega^2 \rho_{mo}/\mu \tag{36}$$

for waves whose components vary as exp jωt. The mass density of the material is ρ_{mo} and the Lamé constants λ and μ.

The potentials on each side of the crack are taken to be $\phi^+(x,z)$; $\psi^+(x,y)$; and $\phi^-(x,z)$; $\psi^-(x,z)$, respectively.

We can carry out Fourier transforms in the x direction of these quantities and write

$$\phi^+(x,z) = \int A(\alpha) e^{-j\alpha x} e^{-j\beta_\ell z} d\alpha \tag{35}$$

$$\psi^+(x,z) = \int B(\alpha) e^{-j\alpha x} e^{-j\beta_s z} d\alpha \tag{36}$$

$$\phi^-(x,z) = \int C(\alpha) e^{-j\alpha x} e^{j\beta_\ell z} d\alpha \tag{37}$$

$$\psi^-(x,z) = \int D(\alpha) e^{-j\alpha x} e^{j\beta_s z} d\alpha \tag{38}$$

where

$$\alpha^2+\beta_\ell^2 = k_\ell^2 \tag{39}$$

$$\alpha^2+\beta_s^2 = k_s^2 \tag{40}$$

It will be seen that

$$A(\alpha) = \frac{1}{2\pi} \int \phi^+(x,0) e^{j\alpha x} dx \tag{41}$$

$$B(\alpha) = \frac{1}{2\pi} \int \psi^+(x,0) e^{j\alpha x} dx \tag{42}$$

$$C(\alpha) = \frac{1}{2\pi} \int \phi^-(x,0) e^{j\alpha x} dx \tag{43}$$

$$D(\alpha) = \frac{1}{2\pi} \int \psi^-(x,0) e^{j\alpha z} dx \tag{44}$$

through the crack instead of the far more stringent boundary condition: $\sigma_{ij}n_i = 0$.

Now consider W. When we use a trial function ΔU_i, it follows that

$$W = \frac{1}{2}\int\left[(\sigma_{ij}-\sigma^s_{ij})\Delta U_j\right]n_i ds \tag{17}$$

Where the total field is

$$\sigma_{ij} = \sigma^A_{ij}+\sigma^s_{ij} \tag{18}$$

So σ^s_{ij} is the stress field due to the displacement ΔU_i. Because

$$\int(\sigma_{ij}\Delta U_j)n_i ds = 0$$

we see that

$$W = \frac{1}{2}\int(-\sigma^s_{ij}\Delta U_j)n_i ds \tag{19}$$

But as we do not know the amplitude ΔU_j and σ^s_{ij} is proportional to ΔU_j, we could equally well replace ΔU_j by $A\Delta U_j$, where A is a proprotionality factor. In this case it follows that

$$W = -\frac{A^2}{2}\int(\sigma^s_{ij}\Delta U_j)n_i ds \tag{20}$$

However we could equally well have written

$$\sigma^A_{ij} = \sigma^o_{ij}-\sigma^{so}_{ij} \tag{21}$$

In this case

$$W = -\frac{A}{2}\int(\sigma^{so}_{ij}\Delta U_j)n_i ds \tag{22}$$

It follows that as Eqs. (20) and (22) must be identical to 2nd order hence

In order to find σ_{ij}^{s}, we take the boundary conditions at the crack to be

$$\Delta U_z = U_z^+(x,0) - U_z^-(x,0) \tag{45}$$

$$\Delta U_x = U_x^+(x,0) - U_x^-(x,0) = 0 \tag{46}$$

$$\sigma_{zz}^+(x,0) = \sigma_{zz}^-(x,0) = \sigma_{zz}^s \tag{47}$$

$$\sigma_{xz}^+(x,0) = \sigma_{xz}^-(s,0) \tag{48}$$

The use of Eq. (45) with Eqs. (41), (42), and (32) yields the result

$$\beta_L(A+C) + \alpha(B-D) = \frac{j}{2\pi}\int \Delta U_z e^{j\alpha x} dx \tag{49}$$

Similarly from Eq. (46) it follows that

$$\alpha(A-C) - \beta_s(B+D) = 0 \tag{50}$$

It may similarly be shown from Eq. (48) that

$$2\alpha\beta_\ell(A+C) + (\alpha^2-\beta_s^2)(B-D) = 0 \tag{51}$$

Where we have used the relation

$$\frac{\lambda+2\mu}{\mu} = \frac{k_s^2}{k_\ell^2} = \frac{\alpha^2+\beta_s^2}{\alpha^2+\beta_\ell^2} \tag{52}$$

Continuity of σ_{zz} [Eq. (47)] yields the result

$$(\beta_s^2-\alpha^2)(A-C) + 2\alpha\beta_s(B+D) = 0 \tag{53}$$

It follows from Eqs. (50) and (53) that

$$A = \frac{\int (\sigma_{ij}^{o} \Delta U_j) n_i ds}{\int (\sigma_{ij}^{so} \Delta U_j) n_i ds} \tag{23}$$

and

$$W = \frac{-\left[\int (\sigma_{ij}^{so} \Delta U_j) n_i ds\right]^2}{2 \int (\sigma_{ij}^{s} \Delta U_j) n_i ds} \tag{24}$$

or

$$W = -\frac{\left[\int (\sigma_{ij}^{A} \Delta U_j) n_i ds\right]^2}{2 \int (\sigma_{ij}^{s} \Delta U_j) n_i ds} \tag{25}$$

This is the variational formula required.

We can prove that this formula is variational by writing

$$\sigma_{ij}^{s}(\underset{\sim}{x}) n_i = \int G_{ij}(\underset{\sim}{x}, \underset{\sim}{x}') \Delta U_j(\underset{\sim}{x}') n_i ds' \tag{26}$$

where $\underset{\sim}{x}$, $\underset{\sim}{x}'$ are coordinates on the crack surface, and the Green's function $G_{ij}(\underset{\sim}{x}, \underset{\sim}{x}')$ is normally symmetric and the $\underset{\sim}{x}$ and $\underset{\sim}{x}'$ coordinates. It follows from Eqs. (25) and (26) that

$$2\delta W\left[\int (\sigma_{ij}^{so} \Delta U_j) n_i ds\right] = 2\left[\int (\sigma_{ij}^{A} \Delta U_j^{o}) n_i ds\right]\left[\int (\sigma_{ij}^{A} \delta(\Delta U_j)\right] n_i ds$$
$$-4W^{o} \int \delta(\Delta U_i) G_{ij}(\underset{\sim}{x}, \underset{\sim}{x}') \Delta U_j^{o}(\underset{\sim}{x}') n_i ds ds' \tag{27}$$

Substitution from Eqs. (21) and (26) in Eq. (27) leads to the result $\delta W = 0$. So the formula of Eq. (25) is variation.

The theory can be generalized fairly easily using the methods of reference 1 to show that the variational formula for

$$A = C \tag{54}$$

$$D = -B \tag{55}$$

So from Eqs. (51), (54) and (55) we see that

$$B = -\frac{2\alpha\beta_\ell}{\alpha^2-\beta_s^2} A \tag{56}$$

It therefore follows, after substitution of Eqs. (54), (55) and (56) in Eq. (49) that

$$A = \frac{j}{4\pi} \frac{\left[\beta_s^2-\alpha^2\right]}{\beta_\ell(\beta^2+\alpha^2)} \int \Delta U_z e^{j\alpha x} dx \tag{57}$$

with

$$\Delta U_z = -2j \int \beta_\ell \frac{\beta^2-\alpha^2 \; A e^{-j\alpha x} d\alpha}{\beta_s^2-\alpha^2} \tag{58}$$

and

$$\sigma_{zz}^s = -\mu \int A\left[\frac{(\beta_s^2-\alpha^2) + 4\alpha^2\beta_s\beta_\ell}{\beta_s^2 - \alpha^2}\right] e^{-j\alpha x} d\alpha \tag{59}$$

It follows that

$$\int \sigma_{zz}^s \Delta U_z dx = +2j\mu \int_{-\infty}^{\infty} |A| \beta_\ell^2 \frac{(\beta_s^2+\alpha^2)\left[(\beta_s^2-\alpha^2)^2+4\alpha^2\beta_s\beta_\ell\right]}{(\beta_s^2 - \alpha^2)^2} d\alpha$$

We note that β_s and β_ℓ must always be positive, i.e., we take their magnitude. So it is convenient to write

$$\int \sigma_{zz}^s \Delta U_z dx = 4j\mu \int_0^{\infty} |A|^2 \frac{\beta_s \cdots \left[(\beta_s^2-\alpha^2)+4\alpha^2\beta_s\beta_\ell\right]}{(\beta_s^2 - \alpha^2)^2} d\alpha \tag{61}$$

scattering from a crack by a signal incident from transducer 1 and received on transducer 2 is

$$S_{21} = \frac{-\frac{j\omega}{4}\int(\sigma_{ij}^{A}{}^{(1)}\Delta U^{(2)})n_i ds \int(\sigma_{ij}^{A}{}^{(2)}\Delta U_j^{(1)})n_i ds}{\int(\sigma_{ij}^{s}{}^{(2)}\Delta U_j^{(1)})n_i ds} \tag{28}$$

where the superscripts (1) and (2) refer to the fields associated with incident waves from transducers 1 and 2, respectively.

FOURIER ANALYSIS AND VARIATIONAL TECHNIQUES FOR A CRACK

The variational methods lend themselves well to the use of Fourier analysis techniques, and in particular the application of the Fast Fourier Transform numerical computer routines which are now widely available.

Our basic approach will be to use a trial function for ΔU_z on the crack surface z = 0. Then on the plane z = 0 we can write

$$\Delta U_z(x,y,0) = \int_{-\infty}^{\infty}\int_{-\infty}^{\infty} \Delta U(\alpha,\beta) e^{-j(\alpha x+\beta y)} d\alpha d\beta \tag{29}$$

with

$$\Delta U_z(\alpha,\beta) = \frac{1}{4\pi^2}\int \Delta U_z \; e^{-j(\alpha x+\beta y)} dx dy \tag{30}$$

It is relatively easy to write down the Fourier transform of other quantities U_x, U_y, U_z, $\sigma_{zz}, \sigma_{xx}, \sigma_{xy}$. Then at any point in space we can use the plane wave angular spectrum analysis to find the connections between these various quantities.

If $A(\alpha)$ is known, this integral can be evaluated numerically. We put

$$A(\alpha) = R(\alpha) \frac{\beta_s^2 - \alpha^2}{\beta_\ell(\beta^2 + \alpha^2)} \tag{62}$$

where

$$R = \frac{j}{4\pi} \int \Delta U_z \, e^{j\alpha x} dx \tag{63}$$

So it follows that

$$\int \sigma_{zz}^s \Delta U_z \, dx = 8j\mu\pi \int_0^\infty |R|^2 \frac{[(\beta_s^2-\alpha^2) + 4\alpha^2\beta_s\beta_\ell]}{\beta_\ell(\beta_s^2 + \alpha^2)} \, d\alpha \tag{64}$$

We shall now evaluate the static case for which $k_s \to 0$, $k_\ell \to 0$. In this case the integral reduces to the form

$$\int \sigma_{zz} \Delta U_z dx = -16\mu\pi \int_0^\infty |R|^2 \alpha \left(1 - \frac{k_\ell^2}{k^2}\right) d\alpha \tag{65}$$

or

$$\int \sigma_{zz}^s \Delta U_z dx = -\frac{4E\pi}{(1-\nu^2)} \int_0^\infty |R^2| \alpha \, d\alpha \tag{66}$$

where E is Young's modulus, ν is Poisson's ratio.

Thus it follows that

$$W = \frac{\left[\int \sigma_{zz}^A \Delta U_z ds\right]^2}{\frac{8E\pi}{1-\nu^2} \int |R|^2 \alpha \, d\alpha}$$

where R is given by Eq. (63).

We now use the variational formula of Eq. (67) to evaluate W. We assume σ_{zz}^A = constant, initially.

Example I: Exact Solution

$$\Delta U_z = K(a^2-x^2)^{\frac{1}{2}} \qquad x < a$$
$$\Delta U_z = 0 \qquad x > a \tag{68}$$

In this case it can be shown that

$$R = jK(a/4\alpha)\ J_1(\alpha a) \tag{69}$$

Where $J_1(x)$ is a 1st order Bessel function of the 1st kind.

So it follows that

$$W = \frac{8(\sigma^A_{zz})^2(1-\nu^2)}{\pi E} \frac{\left[\int_0^a (a-x)^{\frac{1}{2}} dx\right]^2}{\int_0^\infty \frac{a^2}{\alpha} J_1^2(\alpha a) d\alpha} \tag{70}$$

This expression yields the correct result:

$$W = \pi a^2(\sigma^A_{zz})^2(1-\nu^2)/E \tag{71}$$

We note, however, that the result obtained is independent of the proportionately factor K.

Now suppose we try the approximate trial function

$$\Delta U_z = K(a-|x|) \qquad |x| < a$$
$$\Delta U_z = 0 \qquad |x| > a \tag{72}$$

In this case Eq. (67) yields the result

$$W = 2{\cdot}67a^2(\sigma^A_{zz})^2(1-\nu^2)/E$$

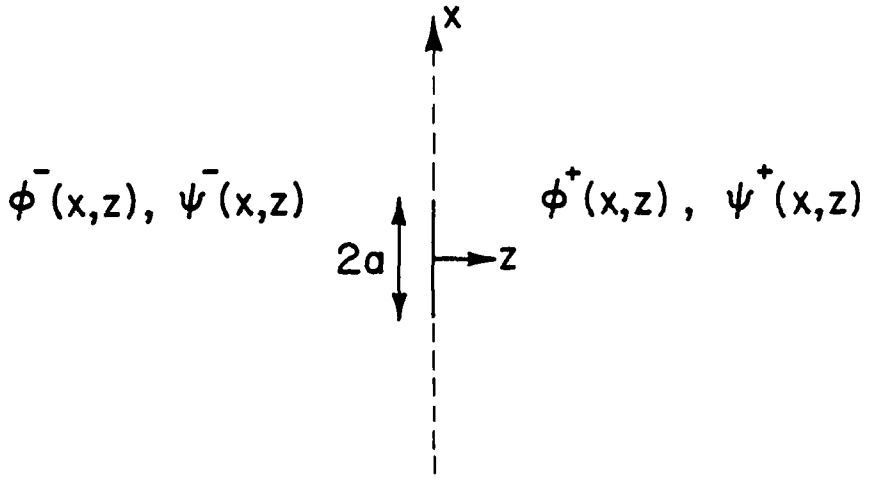

Figure 2. An illustration of the plane crack used in the theory.

or $$W_{trial}/W_{correct} = 0.85$$

This is a fairly crude result, however, the trial function is also a fairly crude one relative to the correct choice. But this choice, ΔU has dropped to half its maximum value at $x = 0.5$, while the true function has dropped to half its maximum value at $x = 0.87$. So the stored energy should be higher for the true value of ΔU.

CONCLUSION

We have derived a variational principle to determine the value of the stored energy or acoustic scattering coefficient of a plane crack. We use the crack opening displacement as a trial function. A simple example for a plane crack using a triangular trial function for ΔU_z gave a result with an error of 15%. This would lead to an error of 8% in estimating K_I. The use of Rayleigh-Ritz techniques or a better choice of trial function could improve this result.

The technique is very easy to modify to take account of non-uniform applied stresses. As an example, if we take a bending stress of the form $\sigma^A_{zz} = \sigma^B|x/a|$, $\Delta U = (a^2-x^2)^{\frac{1}{2}}$, we find that

$$W = 0.18\pi a^2(\sigma^B)^2(1-\nu^2)/E$$

This would imply that the stress intensity factor is reduced by 0.42 from the value with a uniform applied stress σ^B. The result for the exact solution is a reduction 0.5, so the error is 16%.[9]

Again the use of Rayleigh-Ritz methods would be helpful in obtaining more exact results.

$$k_\ell^2 = \omega^2 \rho_{mo}/(\lambda+2\mu) \tag{35}$$

$$k_s^2 = \omega^2 \rho_{mo}/\mu \tag{36}$$

for waves whose components vary as exp jωt. The mass density of the material is ρ_{mo} and the Lamé constants λ and μ.

The potentials on each side of the crack are taken to be $\phi^+(x,z)$; $\psi^+(x,y)$; and $\phi^-(x,z)$; $\psi^-(x,z)$, respectively.

We can carry out Fourier transforms in the x direction of these quantities and write

$$\phi^+(x,z) = \int A(\alpha) e^{-j\alpha x} e^{-j\beta_\ell z} d\alpha \tag{35}$$

$$\psi^+(x,z) = \int B(\alpha) e^{-j\alpha x} e^{-j\beta_s z} d\alpha \tag{36}$$

$$\phi^-(x,z) = \int C(\alpha) e^{-j\alpha x} e^{j\beta_\ell z} d\alpha \tag{37}$$

$$\psi^-(x,z) = \int D(\alpha) e^{-j\alpha x} e^{j\beta_s z} d\alpha \tag{38}$$

where

$$\alpha^2+\beta_\ell^2 = k_\ell^2 \tag{39}$$

$$\alpha^2+\beta_s^2 = k_s^2 \tag{40}$$

It will be seen that

$$A(\alpha) = \frac{1}{2\pi} \int \phi^+(x,0) e^{j\alpha x} dx \tag{41}$$

$$B(\alpha) = \frac{1}{2\pi} \int \psi^+(x,0) e^{j\alpha x} dx \tag{42}$$

$$C(\alpha) = \frac{1}{2\pi} \int \phi^-(x,0) e^{j\alpha x} dx \tag{43}$$

$$D(\alpha) = \frac{1}{2\pi} \int \psi^-(x,0) e^{j\alpha z} dx \tag{44}$$

ACKNOWLEDGEMENT

This research was supported by the Defense Advanced Research Projects Agency of the Department of Defense under Contract No. MDA903-80C-0505 with The University of Michigan.

In order to find σ_{ij}^{s}, we take the boundary conditions at the crack to be

$$\Delta U_z = U_z^+(x,0) - U_z^-(x,0) \tag{45}$$

$$\Delta U_x = U_x^+(x,0) - U_x^-(x,0) = 0 \tag{46}$$

$$\sigma_{zz}^+(x,0) = \sigma_{zz}^-(x,0) = \sigma_{zz}^s \tag{47}$$

$$\sigma_{xz}^+(x,0) = \sigma_{xz}^-(s,0) \tag{48}$$

The use of Eq. (45) with Eqs. (41), (42), and (32) yields the result

$$\beta_L(A+C) + \alpha(B-D) = \frac{j}{2\pi}\int \Delta U_z e^{j\alpha x} dx \tag{49}$$

Similarly from Eq. (46) it follows that

$$\alpha(A-C) - \beta_s(B+D) = 0 \tag{50}$$

It may similarly be shown from Eq. (48) that

$$2\alpha\beta_\ell(A+C) + (\alpha^2-\beta_s^2)(B-D) = 0 \tag{51}$$

Where we have used the relation

$$\frac{\lambda+2\mu}{\mu} = \frac{k_s^2}{k_\ell^2} = \frac{\alpha^2+\beta_s^2}{\alpha^2+\beta_\ell^2} \tag{52}$$

Continuity of σ_{zz} [Eq. (47)] yields the result

$$(\beta_s^2-\alpha^2)(A-C) + 2\alpha\beta_s(B+D) = 0 \tag{53}$$

It follows from Eqs. (50) and (53) that

REFERENCES

1. G. S. Kino, Variational Formulae for Scattering of Acoustic Waves by Flaws, and for Acoustic Wave Propagation, Materials Research Council 1975 Report, also GLG Report #2634, Ginzton Laboratory, Stanford University, November 1976.

2. G. S. Kino, Perturbation Theory for Scattering of Acoustic Waves by Flaws, Materials Research Council 1975 Report.

3. G. S. Kino, J. Appl. Phys. 49, 6 (1978).

4. J. D. Eshelby, The Determination of the Elastic Field of an Ellipsoidal Inclusion, and Related Problems, Proc. Roy. Soc. (London) A24 1, 376 (1957).

5. B. Budiansky and R. J. O'Connell, Elastic Moduli of a Cracked Solid, Int. J. Solid Structures 12, 81-97 (1976).

6. J. R. Rice, A Path Independent Integral and the Approximate Analysis of Strain Concentration by Notches and Cracks, J. Appl. Mech. (June 1967).

7. J. K. Knowles and E. Sternberg, On a Class of Conservation Laws in Linearized and Finite Elastostatics, Archiv. Rat. Mech. Anal. 44, 3 (1972).

8. J. H. Rumsey, The Reaction Concept in Electromagnetic Theory, Phys. Rev., Ser. 2, 94, 6, 1483-1491 (1954).

9. A. H. Lackenbrush, Depth and Spacing of Tension Cracks, J. Geophys. Res. 66, 12, 4273-4292 (1961).

$$A = C \tag{54}$$

$$D = -B \tag{55}$$

So from Eqs. (51), (54) and (55) we see that

$$B = -\frac{2\alpha\beta_\ell}{\alpha^2-\beta_s^2} A \tag{56}$$

It therefore follows, after substitution of Eqs. (54), (55) and (56) in Eq. (49) that

$$A = \frac{j}{4\pi} \frac{\left[\beta_s^2-\alpha^2\right]}{\beta_\ell(\beta^2+\alpha^2)} \int \Delta U_z e^{j\alpha x} dx \tag{57}$$

with

$$\Delta U_z = -2j \int \beta_\ell \frac{\beta^2-\alpha^2 \; A e^{-j\alpha x} d\alpha}{\beta_s^2-\alpha^2} \tag{58}$$

and

$$\sigma_{zz}^s = -\mu \int A\left[\frac{(\beta_s^2-\alpha^2) + 4\alpha^2\beta_s\beta_\ell}{\beta_s^2 - \alpha^2}\right] e^{-j\alpha x} d\alpha \tag{59}$$

It follows that

$$\int \sigma_{zz}^s \Delta U_z dx = +2j\mu \int_{-\infty}^{\infty} |A| \beta_\ell^2 \frac{(\beta_s^2+\alpha^2)\left[(\beta_s^2-\alpha^2)^2+4\alpha^2\beta_s\beta_\ell\right]}{(\beta_s^2 - \alpha^2)^2} d\alpha$$

We note that β_s and β_ℓ must always be positive, i.e., we take their magnitude. So it is convenient to write

$$\int \sigma_{zz}^s \Delta U_z dx = 4j\mu \int_0^{\infty} |A|^2 \frac{\beta_s \cdots \left[(\beta_s^2-\alpha^2)+4\alpha^2\beta_s\beta_\ell\right]}{(\beta_s^2 - \alpha^2)^2} d\alpha \tag{61}$$

ON THE MECHANICS OF INJURY TO TISSUE

F. A. McClintock

ABSTRACT

Elementary mechanics solutions are presented as an aid to interpreting experiments on injury to biological tissues, and to comparing the response of different organs in different animals. Modifications of the Stapp criterion are expressed in terms of history of stress or strain. The stress and strain are found for idealized cases involving blood vessels, bag-like organs, and the brain. Damage may be due to membrane stress, deformation, or penetration. Critical experiments are suggested.

ON THE MECHANICS OF INJURY TO TISSUE

F. A. McClintock

INTRODUCTION

Damage to biological tissues may be described as arising from three different sources: pressure differences across membranes, cavitation in organs due to negative pressure, and distortion of organs. It is the job of mechanics to relate the sources of trauma to these local characteristics, and to suggest ways of running experiments to test the damage criteria. In spite of the copious literature on injury (e.g., Stapp Car Crash Conferences and the Journal of Biomechanics), it appears possible to improve the understanding and predictibility of injury by attention to micromechanics. This understanding will be facilitated by more widespread availability of finite element studies (e.g., Nahum, et al., 1979) giving much more precise estimates of local stress and strain histories.

Both experiments and finite element studies will benefit from normalizing (scaling) the results as suggested by the simple analyses described here.

The Time-Dependent Strength of Tissues

The time to fracture of rate-dependent inorganic materials is often found to be a power function of time. For time-varying stress this suggests a damage criterion similar to the Stapp criterion. With numerical constants σ_c and t_c introduced for

Example I: Exact Solution

$$\Delta U_z = K(a^2-x^2)^{\frac{1}{2}} \qquad x < a$$
$$\Delta U_z = 0 \qquad x > a \tag{68}$$

In this case it can be shown that

$$R = jK(a/4\alpha)\ J_1(\alpha a) \tag{69}$$

Where $J_1(x)$ is a 1st order Bessel function of the 1st kind.

So it follows that

$$W = \frac{8(\sigma^A_{zz})^2(1-\nu^2)}{\pi E} \frac{\left[\int_0^a (a-x)^{\frac{1}{2}} dx\right]^2}{\int_0^\infty \frac{a^2}{\alpha} J_1^2(\alpha a) d\alpha} \tag{70}$$

This expression yields the correct result:

$$W = \pi a^2(\sigma^A_{zz})^2(1-\nu^2)/E \tag{71}$$

We note, however, that the result obtained is independent of the proportionately factor K.

Now suppose we try the approximate trial function

$$\Delta U_z = K(a-|x|) \qquad |x| < a$$
$$\Delta U_z = 0 \qquad |x| > a \tag{72}$$

In this case Eq. (67) yields the result

$$W = 2{\cdot}67a^2(\sigma^A_{zz})^2(1-\nu^2)/E$$

dimensional consistency,

$$\eta = \int_{t_1}^{t_2} (\sigma/\sigma_c)^n d(t/t_e) \qquad (1)$$

When the stress σ is proportional to the deceleration g, a Stapp criterion results. The constant of proportionality will be found from mechanics for several different cases in the following sections. In other situations the impact velocity sets the stress level.

Vessels

Rupture of blood vessels seems to be one of the main sources of trauma. The vessels may be relatively unsupported, as in the chest cavity, they may be surrounded by tissues of different density, or they may be stretched by distortion of the surrounding tissue. In this section, consider the effect of density differences.

For simplicity consider a column of height h, of a fluid whose density is greater than that of the surroundings by $\Delta\rho$. In an acceleration field of strength g, the pressure difference will become

$$\Delta p = \Delta\rho\, g\, h \qquad (2)$$

For a thin-walled tube of radius R and wall thickness w, the circumferential (tangential) stress σ_t is then

$$\sigma_t = \frac{pR}{w} = \frac{\Delta\rho g h R}{w} \qquad (3)$$

For an unconstrained convoluted tube the axial stress σ_z is the same as for a closed end tube:

or $$W_{trial}/W_{correct} = 0.85$$

This is a fairly crude result, however, the trial function is also a fairly crude one relative to the correct choice. But this choice, ΔU has dropped to half its maximum value at $x = 0.5$, while the true function has dropped to half its maximum value at $x = 0.87$. So the stored energy should be higher for the true value of ΔU.

CONCLUSION

We have derived a variational principle to determine the value of the stored energy or acoustic scattering coefficient of a plane crack. We use the crack opening displacement as a trial function. A simple example for a plane crack using a triangular trial function for ΔU_z gave a result with an error of 15%. This would lead to an error of 8% in estimating K_I. The use of Rayleigh-Ritz techniques or a better choice of trial function could improve this result.

The technique is very easy to modify to take account of non-uniform applied stresses. As an example, if we take a bending stress of the form $\sigma^A_{zz} = \sigma^B|x/a|$, $\Delta U = (a^2-x^2)^{\frac{1}{2}}$, we find that

$$W = 0.18\pi a^2(\sigma^B)^2(1-\nu^2)/E$$

This would imply that the stress intensity factor is reduced by 0.42 from the value with a uniform applied stress σ^B. The result for the exact solution is a reduction 0.5, so the error is 16%.[9]

Again the use of Rayleigh-Ritz methods would be helpful in obtaining more exact results.

$$\sigma_z = \sigma_t/2 \tag{4}$$

Introducing Eq. (3) into Eq. (1) gives

$$\eta = \int_{t_1}^{t_2} \left(\frac{\Delta\rho g h R}{w\sigma_c} \right)^n \frac{dt}{t_c} \tag{5}$$

Since vessels begin to rupture at a few times the normal blood pressure, p_n, the corresponding strength may be used to compare the results from one species to another. Define

$$\sigma_c = p_n R/w \tag{6}$$

Then

$$\eta = \int_{t_1}^{t_2} \left(\frac{\Delta\rho g h}{p_n} \right)^n \frac{dt}{t_c} \tag{7}$$

Eq. (7) gives a more physical basis for the Stapp equation. Typically, one would expect the exponent n to be larger than the value 2.5 commonly used. Evidence for this is that the Head Injury Criterion with an exponent of 2.5 overestimates the damage due to long time loading (Hodgson and Thomas, 1972). Otherwise, Eq. (7) is consistent with the Stapp equation but goes beyond it to include effects of interspecies variation (particularly in dimension h), and in the effect of density differences $\Delta\rho$. Clearly the most damage for a given application will occur in the thorax, where the density difference is between that of blood and air. In vessels of the brain, where far smaller density differences exist, far higher g-loadings are possible.

Experiments on the rate-dependent rupture of blood vessels should be carried out (if they have not been already made) to determine the exponent n and the time constant t_c of Eq. (7). They could be done by transient pressurization of a closed-ended segment of vessel, possible with the simultaneous superposition of axial loads to separate the effects of σ_t and σ_z. (This separation may be of secondary importance because nature has probably optimized the design for the usual condition with $\sigma_z = \sigma_t/2$.)

Flexible Organs

Different problems arise depending on whether organs are flexibly encased, such as the heart, or rather rigidly encased, such as the brain in the skull, which will be discussed in the next section. Flexibly encased organs may suffer injury due to tearing of the case, due to excessive distortion which ruptures blood vessels by axial strain, or due to penetration.

1. The tearing strength of the heart may be estimated by regarding it as a blood vessel and applying Eq. (5). On the other hand, stretching of the heart may allow very significant flattening, reducing h. Since the mechanical behavior of the heart wall is likely to be very non-linear (e.g., Fung 1967), this estimate may well require more than one elastic constant and nonlinear stress-strain relations, even with an idealized geometry.

2. Distortion of the heart wall, even before gross tearing, may elongate some blood vessels enough to rupture them. Such deformation may well be important in other organs. Perhaps the resulting strain-dependent damage can be correlated by a strain-based form of the Stapp equation. For a stretch ratio $\lambda = L/L_o$,

REFERENCES

1. G. S. Kino, Variational Formulae for Scattering of Acoustic Waves by Flaws, and for Acoustic Wave Propagation, Materials Research Council 1975 Report, also GLG Report #2634, Ginzton Laboratory, Stanford University, November 1976.

2. G. S. Kino, Perturbation Theory for Scattering of Acoustic Waves by Flaws, Materials Research Council 1975 Report.

3. G. S. Kino, J. Appl. Phys. 49, 6 (1978).

4. J. D. Eshelby, The Determination of the Elastic Field of an Ellipsoidal Inclusion, and Related Problems, Proc. Roy. Soc. (London) A24 1, 376 (1957).

5. B. Budiansky and R. J. O'Connell, Elastic Moduli of a Cracked Solid, Int. J. Solid Structures 12, 81-97 (1976).

6. J. R. Rice, A Path Independent Integral and the Approximate Analysis of Strain Concentration by Notches and Cracks, J. Appl. Mech. (June 1967).

7. J. K. Knowles and E. Sternberg, On a Class of Conservation Laws in Linearized and Finite Elastostatics, Archiv. Rat. Mech. Anal. 44, 3 (1972).

8. J. H. Rumsey, The Reaction Concept in Electromagnetic Theory, Phys. Rev., Ser. 2, 94, 6, 1483-1491 (1954).

9. A. H. Lackenbrush, Depth and Spacing of Tension Cracks, J. Geophys. Res. 66, 12, 4273-4292 (1961).

$$\eta_\lambda = \int_{t_1}^{t_2} (\lambda-1)^m \, dt/t_c \qquad (8)$$

The validity of such a criterion could be determined by experiments on blood vessels of the type determined above, where axial strain histories are imposed on blood vessels, under both the constant volume and the drained conditions.

3. Penetration by a projectile or other foreign object will cause local tearing due to stretching. For a relatively long object, plane strain conditions will approximately hold. For incompressibility, the new radius r of a point originally at r_o is found from the increase in the enclosed area A_p:

$$\pi r^2 = \pi r_o^2 + A_p = \pi r_o^2 + \pi r_p^2 \qquad (9)$$

The largest principal stretch ratio is then

$$\lambda = \frac{r}{r_o} = \sqrt{1 + \left(\frac{r_p}{r_o}\right)^2} \qquad (10)$$

For example, if a stretch ratio of 1.2 causes injury, the injured region, after closure, will extend to

$$\frac{r_o}{r_p} = 1/\sqrt{\lambda^2 - 1} = 1.51 \qquad (11)$$

With high velocity impact the outward radial velocity will cause injury much farther out. This has no doubt been analyzed for the linear range and calculated for shock conditions, but the solutions are not known to the author. A plane strain solution involves Bessel functions, but the spherical solution is more

ON THE MECHANICS OF INJURY TO TISSUE

F. A. McClintock

ABSTRACT

Elementary mechanics solutions are presented as an aid to interpreting experiments on injury to biological tissues, and to comparing the response of different organs in different animals. Modifications of the Stapp criterion are expressed in terms of history of stress or strain. The stress and strain are found for idealized cases involving blood vessels, bag-like organs, and the brain. Damage may be due to membrane stress, deformation, or penetration. Critical experiments are suggested.

tractable, and the superposition of a series of spherical solutions emanating from points along the path of the projectile would give valuable insight for the linear problem.

The Brain

Trauma to the brain, aside from lethal effects due to laceration of the brain in skull fracture, is associated with either translation or rotation.

1. Translation may cause trauma either by distortions of the brain associated with density differences (Eq. (7)), or by cavitation under the negative pressures caused by stress waves. As a first approximation to stress wave effects, consider a plane wave introduced into a body by an acoustically thinner plate impacting on it. Assume a triangular wave form of the type shown in Fig. 1. Reflection of the wave at the free surface gives a tensile stress of which can be expressed in terms of the bulk modulus B, the dilatational (uniaxial strain) wave speed c_d, and the velocity of impact V:

$$-p = B\ V/c_d \tag{12}$$

For instance for water, with B = 2000 MN/m^2, c_d = 1500 m/s, and an impact velocity of only 1 m/s, -p = 1.3 MN/m^2 = 13 atm! The time of impact is very short however, of the order of the wave travel time through the impacting object. For a 1 mm thick steel plate, with g = 5000 m/s, this is only

$$\Delta t = 2t/c_d = 4\ 10^{-3}m/5000(m/s) = 0.8\ \mu s. \tag{13}$$

The effects of such sharp, short stresses should be studied.

ON THE MECHANICS OF INJURY TO TISSUE

F. A. McClintock

INTRODUCTION

Damage to biological tissues may be described as arising from three different sources: pressure differences across membranes, cavitation in organs due to negative pressure, and distortion of organs. It is the job of mechanics to relate the sources of trauma to these local characteristics, and to suggest ways of running experiments to test the damage criteria. In spite of the copious literature on injury (e.g., Stapp Car Crash Conferences and the Journal of Biomechanics), it appears possible to improve the understanding and predictibility of injury by attention to micromechanics. This understanding will be facilitated by more widespread availability of finite element studies (e.g., Nahum, et al., 1979) giving much more precise estimates of local stress and strain histories.

Both experiments and finite element studies will benefit from normalizing (scaling) the results as suggested by the simple analyses described here.

The Time-Dependent Strength of Tissues

The time to fracture of rate-dependent inorganic materials is often found to be a power function of time. For time-varying stress this suggests a damage criterion similar to the Stapp criterion. With numerical constants σ_c and t_c introduced for

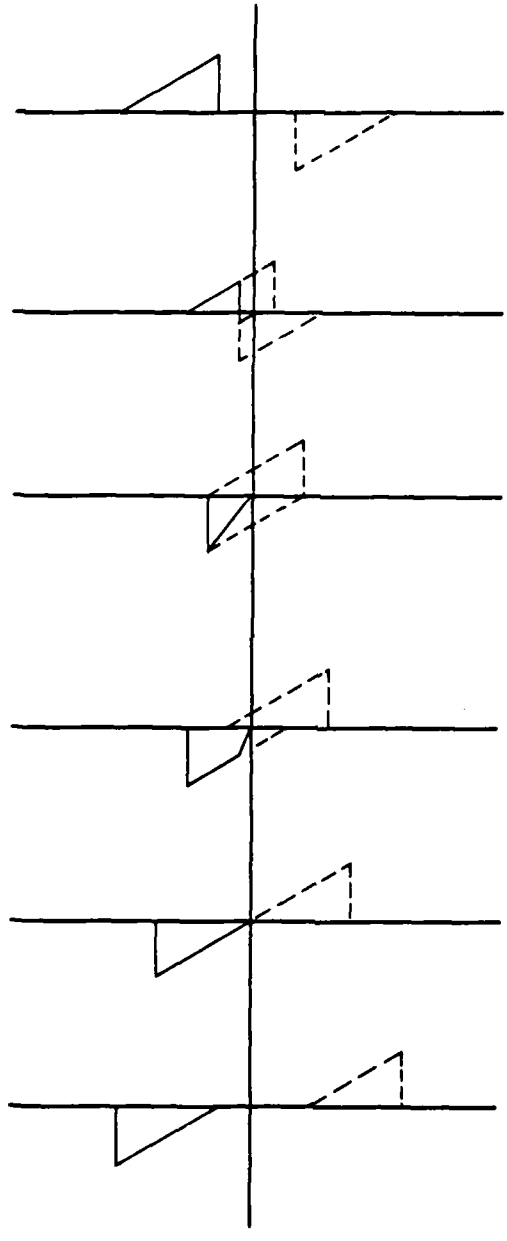

Figure 1. Reflection of a wave from a free surface regarded as a superposition of a negative wave, producing tension.

dimensional consistency,

$$\eta = \int_{t_1}^{t_2} (\sigma/\sigma_c)^n d(t/t_e) \qquad (1)$$

When the stress σ is proportional to the deceleration g, a Stapp criterion results. The constant of proportionality will be found from mechanics for several different cases in the following sections. In other situations the impact velocity sets the stress level.

Vessels

Rupture of blood vessels seems to be one of the main sources of trauma. The vessels may be relatively unsupported, as in the chest cavity, they may be surrounded by tissues of different density, or they may be stretched by distortion of the surrounding tissue. In this section, consider the effect of density differences.

For simplicity consider a column of height h, of a fluid whose density is greater than that of the surroundings by $\Delta\rho$. In an acceleration field of strength g, the pressure difference will become

$$\Delta p = \Delta\rho\, g\, h \qquad (2)$$

For a thin-walled tube of radius R and wall thickness w, the circumferential (tangential) stress σ_t is then

$$\sigma_t = \frac{pR}{w} = \frac{\Delta\rho g h R}{w} \qquad (3)$$

For an unconstrained convoluted tube the axial stress σ_z is the same as for a closed end tube:

When the shape and compliance of the skull are taken into account, the process is much more complicated. Experiments show that wave propagation speeds and peak pressures are much reduced but occur over times corresponding to many wave travel times across the skull (Nahum, et al., 1979). They have shown that finite element calculations, even assuming a rigid skull, can duplicate the experiments if Poisson's ratio and the skull openings are chosen appropriately.

2. Rotation of the brain is a source of trauma because it is only slightly restricted by the shape of the skull. An impulse of tangential velocity, V_t, will introduce a wave with shear strain γ traveling with the shear wave velocity c_s

$$\gamma = V_t/c_s \tag{14}$$

The shear wave velocity is given in terms of the shear modulus μ and density ρ:

$$c_s = \sqrt{\mu/\rho} \tag{15}$$

For instance for V_t of only 1 m/s, μ = 14000 N/m^2 (2 psi) from Ward (1980). Then

$$c_s = 14000/1000 = 4 \text{ m/s}, \tag{16}$$

$$\gamma = 1/4 \tag{17}$$

For more gradual rotation, with times long compared to the shear wave travel time across the skull,

$$t >> d/c_s \tag{18}$$

$$\sigma_z = \sigma_t/2 \tag{4}$$

Introducing Eq. (3) into Eq. (1) gives

$$\eta = \int_{t_1}^{t_2} \left(\frac{\Delta\rho g h R}{w\sigma_c} \right)^n \frac{dt}{t_c} \tag{5}$$

Since vessels begin to rupture at a few times the normal blood pressure, p_n, the corresponding strength may be used to compare the results from one species to another. Define

$$\sigma_c = p_n R/w \tag{6}$$

Then

$$\eta = \int_{t_1}^{t_2} \left(\frac{\Delta\rho g h}{p_n} \right)^n \frac{dt}{t_c} \tag{7}$$

Eq. (7) gives a more physical basis for the Stapp equation. Typically, one would expect the exponent n to be larger than the value 2.5 commonly used. Evidence for this is that the Head Injury Criterion with an exponent of 2.5 overestimates the damage due to long time loading (Hodgson and Thomas, 1972). Otherwise, Eq. (7) is consistent with the Stapp equation but goes beyond it to include effects of interspecies variation (particularly in dimension h), and in the effect of density differences $\Delta\rho$. Clearly the most damage for a given application will occur in the thorax, where the density difference is between that of blood and air. In vessels of the brain, where far smaller density differences exist, far higher g-loadings are possible.

a steady state stress distribution may hold. The shear stress τ on a circular cylinder of diameter D, required to give an angular acceleration α, is found from

$$\tau(\pi DL)(D/2) = \rho(\pi(D/2)^4 L/2)\alpha;$$

$$\tau = \rho D^2 \alpha/16 \tag{19}$$

Assuming that allowable stresses are related to normal blood pressure p_n suggests that angular acceleration data in experiments should be normalized into the form

$$\alpha^* = \frac{\alpha \rho D^2}{16 p_n} \tag{20}$$

For scaling animal brains to human brains, the diameter ratio should be based on the minimum diameter about the axis of rotation, which is relatively smaller in animals due to the elongated shape of their brains. For instance, a 50 mm diameter monkey brain should withstand 4 times the angular acceleration of a 100 mm diameter human brain.

For the monkey experiments of Hodgson and Thomas (1979), assuming an effective diameter of D = 50 mm, $\alpha = 20\times10^3/s^2$, and $\rho = 1000$ kg/m^3, Eq. (17) gives

$$\tau = \frac{1000(.050)^2\ 20\times10^3}{16} = 3000\ N/m^2 \tag{21}$$

giving

$$\gamma = \tau/\mu = 3000/14000 = 0.2 \tag{22}$$

which is about that observed. There may be inconsistencies, however, for the oscillations show a fastest period of 2 ms, which from Eq. (16) would require a wave speed of

Experiments on the rate-dependent rupture of blood vessels should be carried out (if they have not been already made) to determine the exponent n and the time constant t_c of Eq. (7). They could be done by transient pressurization of a closed-ended segment of vessel, possible with the simultaneous superposition of axial loads to separate the effects of σ_t and σ_z. (This separation may be of secondary importance because nature has probably optimized the design for the usual condition with $\sigma_z = \sigma_t/2$.)

Flexible Organs

Different problems arise depending on whether organs are flexibly encased, such as the heart, or rather rigidly encased, such as the brain in the skull, which will be discussed in the next section. Flexibly encased organs may suffer injury due to tearing of the case, due to excessive distortion which ruptures blood vessels by axial strain, or due to penetration.

1. The tearing strength of the heart may be estimated by regarding it as a blood vessel and applying Eq. (5). On the other hand, stretching of the heart may allow very significant flattening, reducing h. Since the mechanical behavior of the heart wall is likely to be very non-linear (e.g., Fung 1967), this estimate may well require more than one elastic constant and nonlinear stress-strain relations, even with an idealized geometry.

2. Distortion of the heart wall, even before gross tearing, may elongate some blood vessels enough to rupture them. Such deformation may well be important in other organs. Perhaps the resulting strain-dependent damage can be correlated by a strain-based form of the Stapp equation. For a stretch ratio $\lambda = L/L_o$,

$$c_s = \frac{2D}{t} = \frac{0.100\ m}{0.002\ s} = 50\ m/s$$

Perhaps these oscillations are due to dilational wave interactions, with the 40 ms fundamental period corresponding to a shear wave velocity of 2.5 m/s, compared to the 4 m/s of Eq. (14). In any event, the shear moduli are likely to be highly time-dependent, so more work is required.

CONCLUSIONS

Elementary mechanics solutions help to give order-of-magnitude estimates of trauma-related processes during impact. They should therefore be useful in normalizing and scaling the results of both experiments and more exact analytical and finite element studies. In particular,

1. Damage η is related to density differences, $\Delta\rho$, between the organ and its surroundings, to the acceleration, g, to the extent h of the organ in the field, to the normal blood pressure p_n, and to a time constant t_c by

$$\eta = \int_{t_1}^{t_2} \left(\frac{\Delta\rho g h}{p_n} \right)^n \frac{dt}{t_c} \tag{7}$$

2. For deformation of an organ, trauma due to tearing of the blood vessels may be correlated by a version of the Stapp equation in terms of the history of stretch ratio $\lambda = L/L_o$:

$$\eta_\lambda = \int_{t_1}^{t_2} (\lambda - 1)^m \, dt/t_c \tag{8}$$

Dynamic tests on segments of vessels could put Eqs. (7) and (8) on

$$\eta_\lambda = \int_{t_1}^{t_2} (\lambda-1)^m \, dt/t_c \qquad (8)$$

The validity of such a criterion could be determined by experiments on blood vessels of the type determined above, where axial strain histories are imposed on blood vessels, under both the constant volume and the drained conditions.

3. Penetration by a projectile or other foreign object will cause local tearing due to stretching. For a relatively long object, plane strain conditions will approximately hold. For incompressibility, the new radius r of a point originally at r_o is found from the increase in the enclosed area A_p:

$$\pi r^2 = \pi r_o^2 + A_p = \pi r_o^2 + \pi r_p^2 \qquad (9)$$

The largest principal stretch ratio is then

$$\lambda = \frac{r}{r_o} = \sqrt{1 + \left(\frac{r_p}{r_o}\right)^2} \qquad (10)$$

For example, if a stretch ratio of 1.2 causes injury, the injured region, after closure, will extend to

$$\frac{r_o}{r_p} = 1/\sqrt{\lambda^2 - 1} = 1.51 \qquad (11)$$

With high velocity impact the outward radial velocity will cause injury much farther out. This has no doubt been analyzed for the linear range and calculated for shock conditions, but the solutions are not known to the author. A plane strain solution involves Bessel functions, but the spherical solution is more

a firmer footing, and allow correlations of trauma with much less extensive testing.

3. For essentially static penetration, to a radius r_p, the maximum principal strain ratio at a point initially at r_o is

$$\lambda = r/r_o = \sqrt{1 + (r_p/r_o)^2} \tag{10}$$

4. Dynamic penetration at high velocities relative to the dilatational wave speed of about 1500 m/s can be approximated by a series of spherical waves. The results are no doubt in the literature, but not immediately at hand.

5. The strain and pressure due to dilatational (uniaxial strain) waves due to an impact of velocity V on a material with density ρ and bulk modulus B are

$$\varepsilon = v/c_d, \text{ where } c_d = B/\rho \quad , \tag{12}$$

and

$$p = B\varepsilon.$$

Similar equations hold for shear. Reflection of dilatational waves can give rise to negative pressures which cause trauma through cavitation, but the effects are too intimately related to the shape and compliance of the skull, its openings, and the point of impact for any simple correlations. Detailed strain histories obtained experimentally should be correlated with detailed finite element calculations.

6. Rotation of the brain requires shear stress, suggesting a correlation of angular acceleration α on the basis of density ρ, minimum diameter D through the axis of rotation, and normal blood

tractable, and the superposition of a series of spherical solutions emanating from points along the path of the projectile would give valuable insight for the linear problem.

The Brain

Trauma to the brain, aside from lethal effects due to laceration of the brain in skull fracture, is associated with either translation or rotation.

1. Translation may cause trauma either by distortions of the brain associated with density differences (Eq. (7)), or by cavitation under the negative pressures caused by stress waves. As a first approximation to stress wave effects, consider a plane wave introduced into a body by an acoustically thinner plate impacting on it. Assume a triangular wave form of the type shown in Fig. 1. Reflection of the wave at the free surface gives a tensile stress of which can be expressed in terms of the bulk modulus B, the dilatational (uniaxial strain) wave speed c_d, and the velocity of impact V:

$$-p = B\ V/c_d \tag{12}$$

For instance for water, with B = 2000 MN/m^2, c_d = 1500 m/s, and an impact velocity of only 1 m/s, -p = 1.3 MN/m^2 = 13 atm! The time of impact is very short however, of the order of the wave travel time through the impacting object. For a 1 mm thick steel plate, with g = 5000 m/s, this is only

$$\Delta t = 2t/c_d = 4\ 10^{-3}m/5000(m/s) = 0.8\ \mu s. \tag{13}$$

The effects of such sharp, short stresses should be studied.

pressure p_n

$$\alpha^* = \frac{\alpha \rho D^2}{16 p_n} \tag{20}$$

7. Nonlinear and rate-dependent behavior of brain tissue should be measured.

ACKNOWLEDGEMENT

This research was supported by the Defense Advanced Research Projects Agency of the Department of Defense under Contract No. MDA903-80C-0505 with The University of Michigan.

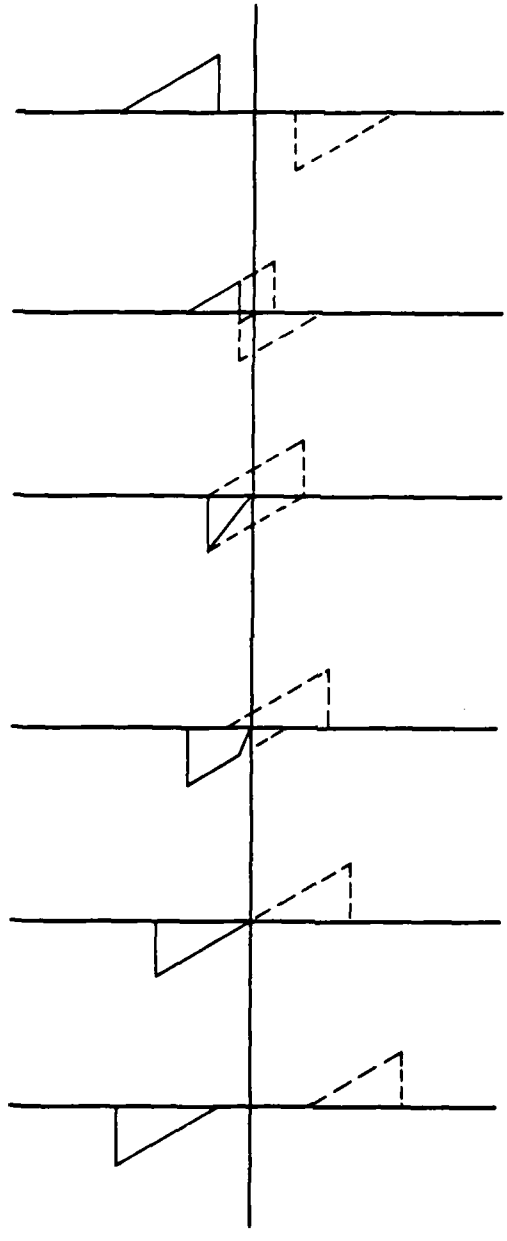

Figure 1. Reflection of a wave from a free surface regarded as a superposition of a negative wave, producing tension.

References

1. Nahum, A.M., Smith, R., Raasch, F., and Ward, C., (1979) "Intracranial Pressure Relationship in the Protected and Unprotected Head", Proc. 23rd Stapp Car Crash Conference, Soc. Auto. Eng. pp. 616-636.

2. Hodgson, V. R., and Thomas, L. M., (1972), "Effect of Long-Duration Impact on Head" Proc. 16th Stapp Car Crash Conference, Soc. Auto. Eng., pp. 292-295.

3. Fung, Y. C. B. (1967) "Elasticity of Soft Tissues in Simple Elongation", Am. J. Physical 213, 1532-1544.

4. Ward, C. (1980) Personal communication.

5. Hodgson, V. R., and Thomas, L. M., (1979) "Acceleration Induced Shear Strains on a Monkey Brain Hemisection", Prec. 23rd Stapp Car Crash Conference, Soc. Auto. Eng., pp 587-611.

When the shape and compliance of the skull are taken into account, the process is much more complicated. Experiments show that wave propagation speeds and peak pressures are much reduced but occur over times corresponding to many wave travel times across the skull (Nahum, et al., 1979). They have shown that finite element calculations, even assuming a rigid skull, can duplicate the experiments if Poisson's ratio and the skull openings are chosen appropriately.

2. Rotation of the brain is a source of trauma because it is only slightly restricted by the shape of the skull. An impulse of tangential velocity, V_t, will introduce a wave with shear strain γ traveling with the shear wave velocity c_s

$$\gamma = V_t/c_s \tag{14}$$

The shear wave velocity is given in terms of the shear modulus μ and density ρ:

$$c_s = \sqrt{\mu/\rho} \tag{15}$$

For instance for V_t of only 1 m/s, μ = 14000 N/m^2 (2 psi) from Ward (1980). Then

$$c_s = 14000/1000 = 4 \text{ m/s}, \tag{16}$$

$$\gamma = 1/4 \tag{17}$$

For more gradual rotation, with times long compared to the shear wave travel time across the skull,

$$t >> d/c_s \tag{18}$$

BROADBAND ACOUSTIC EMISSION TRANSDUCERS

G. S. Kino

ABSTRACT

A study has been made of acoustic emission transducers for operation in the frequency range from 100 KHz to 2 MHz. We consider the basic design required for receiving both Rayleigh waves and longitudinal waves incident on the transducer over a wide angular range. Various types of piezoelectric transducers, the capacitor transducer, the fiber optic transducer, and acousto-electric transducers and array transducers are considered. We conclude that a conventional PZT 5H contacting transducer of approximately 1 mm diameter is the best choice for an acoustic emission detector operating from 100 KHz to 2 MHz.

a steady state stress distribution may hold. The shear stress τ on a circular cylinder of diameter D, required to give an angular acceleration α, is found from

$$\tau(\pi DL)(D/2) = \rho(\pi(D/2)^4 L/2)\alpha;$$

$$\tau = \rho D^2 \alpha/16 \tag{19}$$

Assuming that allowable stresses are related to normal blood pressure p_n suggests that angular acceleration data in experiments should be normalized into the form

$$\alpha^* = \frac{\alpha \rho D^2}{16 p_n} \tag{20}$$

For scaling animal brains to human brains, the diameter ratio should be based on the minimum diameter about the axis of rotation, which is relatively smaller in animals due to the elongated shape of their brains. For instance, a 50 mm diameter monkey brain should withstand 4 times the angular acceleration of a 100 mm diameter human brain.

For the monkey experiments of Hodgson and Thomas (1979), assuming an effective diameter of D = 50 mm, $\alpha = 20\times10^3/s^2$, and $\rho = 1000$ kg/m^3, Eq. (17) gives

$$\tau = \frac{1000(.050)^2\ 20\times10^3}{16} = 3000\ N/m^2 \tag{21}$$

giving

$$\gamma = \tau/\mu = 3000/14000 = 0.2 \tag{22}$$

which is about that observed. There may be inconsistencies, however, for the oscillations show a fastest period of 2 ms, which from Eq. (16) would require a wave speed of

BROADBAND ACOUSTIC EMISSION TRANSDUCERS

G. S. Kino

INTRODUCTION

The design of acoustic transducers for use in acoustic emission testing has mainly followed the methods used for NDE transducers. The minor changes in design usually made for this purpose mainly concentrate on the facts that the frequency of operation is typically below 400 KHz, and that an omni-directional sensor is required. In addition, because of the often difficult working environment, a great deal of attention has to be paid to the need to differentiate against interfering signals.

We shall consider here the design problem for AE (acoustic emission) transducers to operate over a broad band in the range from 100 KHz-2MHz. We shall be concerned with transducers that can respond to Rayleigh waves, longitudinal waves and shear waves. We shall consider the use of standard piezoelectric transducer ceramic materials and also non-standard materials such as ZnO thin films, PVF_2 plastic and composites. New concepts such as the use of fiber optic and acoustoelectric transducers are also of interest and will be considered.

BASIC NEEDS FOR ACOUSTIC EMISSION TRANSDUCERS

Pao[1] has discussed simple types of AE sources. In his terms, a small crack opening up or grain boundary cracking could

be regarded as a double force source, a single couple or a double couple without movement. In each case, if the force has a frequency spectrum f_ω, it can be shown that there are radiated displacement amplitude components from a buried source of the form $\omega f_\omega (\exp - jkR)/R$ where $k=\omega/v$ is associated with a propagating shear or longitudinal wave, and ω is the radian frequency. As a typical source corresponds to a step function release in stress, f_ω varies as $1/\omega$. Thus the displacement amplitude spectrum from a small source of this type should be uniform over the frequency range of interest.

The situation becomes more complicated for finite crack sizes because of crack resonances and Rayleigh wave propagation along the crack surface and Doppler shifts associated with moving crack fronts. Furthermore, when the wave guiding properties of the structure itself are taken into account, the situation changes. For instance, a surface crack will emit a surface wave signal that falls off as $\exp - jk_R R/\sqrt{R}$ where k_R is the Rayleigh wave propagation constant. Therefore the surface wave excitation tends to become dominant at some distance from the exciting source and its frequency dependence different from that of a bulk wave. It is apparent that the frequency distortion will be even more severe when multiple Lamb modes are excited. At all events, at short distances from the flaw, a detector on the surface of a structure will tend to observe all possible modes that are excited by AE sources. At longer distances from the source, if the source is within a Rayleigh wavelength from the surface, acoustic

a firmer footing, and allow correlations of trauma with much less extensive testing.

3. For essentially static penetration, to a radius r_p, the maximum principal strain ratio at a point initially at r_o is

$$\lambda = r/r_o = \sqrt{1 + (r_p/r_o)^2} \tag{10}$$

4. Dynamic penetration at high velocities relative to the dilatational wave speed of about 1500 m/s can be approximated by a series of spherical waves. The results are no doubt in the literature, but not immediately at hand.

5. The strain and pressure due to dilatational (uniaxial strain) waves due to an impact of velocity V on a material with density ρ and bulk modulus B are

$$\varepsilon = v/c_d, \text{ where } c_d = B/\rho \quad , \tag{12}$$

and

$$p = B\varepsilon.$$

Similar equations hold for shear. Reflection of dilatational waves can give rise to negative pressures which cause trauma through cavitation, but the effects are too intimately related to the shape and compliance of the skull, its openings, and the point of impact for any simple correlations. Detailed strain histories obtained experimentally should be correlated with detailed finite element calculations.

6. Rotation of the brain requires shear stress, suggesting a correlation of angular acceleration α on the basis of density ρ, minimum diameter D through the axis of rotation, and normal blood

surface wave signals may well be dominant at the detector. On the other hand with a buried AE source, only bulk waves will tend to be present, unless there is some conversion from bulk waves to surface waves at sharp corners.

Thus the basic transducer must be able to detect normal displacements of the surface of the structure. In principle, this will make it possible to detect longitudinal waves and surface waves, both of which have such displacements present. A shear wave arriving at an angle to the surface normal will also excite such a transducer. But a shear wave source directly underneath the transducer would only give rise to a displacement parallel to the surface, which would have to be detected by a shear wave transducer. This is a relatively rare case, so we will, in the main, concentrate on transducers capable of detecting displacements normal to the surface.

Since we do not normally know the position of the emission source beforehand, it is appropriate to design an omni-directional transducer capable of detecting bulk waves or surface waves. In a few cases where the position of the possible source is known, such as a crack in a particular bolt hole, it may be appropriate to design to receive surface wave or bulk wave signals from a particular position. This makes the task easier. Therefore we will address ourselves only to the problem of design of an omni-directional broadband 100 KHz-2 MHz transducer. If this can be solved well, the design of other narrower band, narrower acceptance angle transducers should not be a major problem.

pressure p_n

$$\alpha^* = \frac{\alpha \rho D^2}{16 p_n} \tag{20}$$

7. Nonlinear and rate-dependent behavior of brain tissue should be measured.

ACKNOWLEDGEMENT

This research was supported by the Defense Advanced Research Projects Agency of the Department of Defense under Contract No. MDA903-80C-0505 with The University of Michigan.

THE DIAMETER OF A BROADBAND TRANSDUCER

Suppose we wish to design a transducer to detect a surface wave of propagation constant k_R propagating at an arbitrary angle ϕ to the x axis as shown in Fig. 1. The transducer is supposed to detect the normal displacement u_z of the surface, and we can write

$$u_z = u\, e^{-jk_R(x\cos\phi + y\sin\phi)} \tag{1}$$

A piezoelectric, fiber optic, or capacitive transducer placed in contact with the surface basically responds to the average value of u_z over the area of the transducer. Hence, in order to make the response independent of ϕ, the transducer must be cylindrical in shape of radius a. In this case, its response will be of the form

$$V = \frac{1}{\pi a^2} \int e^{-jk_R(x\cos\phi + y\sin\phi)}\, dxdy \tag{2}$$

writing $x = r\cos\phi'$, $y = r\sin\phi'$

$$V = \frac{1}{\pi a^2} \int_0^a \int_0^{2\pi} re^{-jk_R r\cos(\phi'-\phi)}\, d\phi' dr \tag{3}$$

This integral can be shown to give the result

$$V = \frac{2J_1(k_R a)}{k_R a} \tag{4}$$

where $J_1(x)$ is a Bessel function of the first kind and first order with its first zero at $k_R a = 3.83$. The 3 dB points of this function are where

$$\left(\frac{a}{\lambda_R}\right)_{3dB} = 0.24 \tag{5}$$

References

1. Nahum, A.M., Smith, R., Raasch, F., and Ward, C., (1979) "Intracranial Pressure Relationship in the Protected and Unprotected Head", Proc. 23rd Stapp Car Crash Conference, Soc. Auto. Eng. pp. 616-636.

2. Hodgson, V. R., and Thomas, L. M., (1972), "Effect of Long-Duration Impact on Head" Proc. 16th Stapp Car Crash Conference, Soc. Auto. Eng., pp. 292-295.

3. Fung, Y. C. B. (1967) "Elasticity of Soft Tissues in Simple Elongation", Am. J. Physical 213, 1532-1544.

4. Ward, C. (1980) Personal communication.

5. Hodgson, V. R., and Thomas, L. M., (1979) "Acceleration Induced Shear Strains on a Monkey Brain Hemisection", Prec. 23rd Stapp Car Crash Conference, Soc. Auto. Eng., pp 587-611.

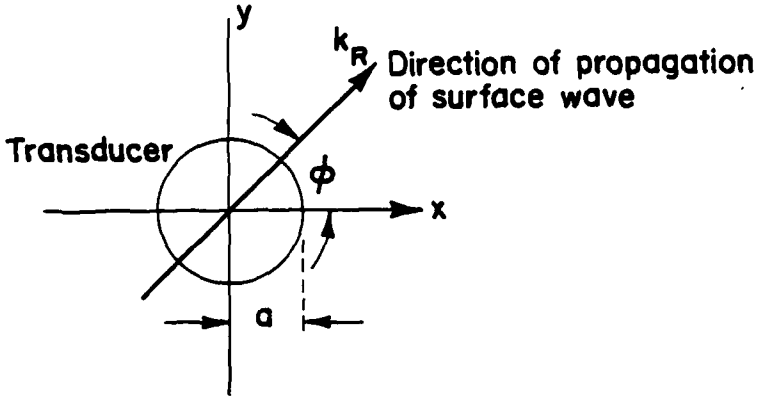

Figure 1. Illustration of a surface wave propagating at an angle ϕ to the x-axis.

BROADBAND ACOUSTIC EMISSION TRANSDUCERS

G. S. Kino

ABSTRACT

A study has been made of acoustic emission transducers for operation in the frequency range from 100 KHz to 2 MHz. We consider the basic design required for receiving both Rayleigh waves and longitudinal waves incident on the transducer over a wide angular range. Various types of piezoelectric transducers, the capacitor transducer, the fiber optic transducer, and acousto-electric transducers and array transducers are considered. We conclude that a conventional PZT 5H contacting transducer of approximately 1 mm diameter is the best choice for an acoustic emission detector operating from 100 KHz to 2 MHz.

On the other hand it can be shown from the work of Ref. 2 that if we consider a longitudinal wave of wavelength λ_L amplitude u_0 incident on the transducer at an angle θ to the normal, it has an amplitude $u_z = u_0 \cos\theta \exp -jk_L x \sin\theta$ normal to the surface, as illustrated in Fig. 2. Thus at the surface, the effective response varies as

$$\Phi = 2 \cos\theta \frac{J_1(k_\ell a \sin\theta)}{k_\ell a \sin\theta} \tag{6}$$

It follows that because of the cos θ term, under no circumstances can the transducer respond to longitudinal waves arriving at an angle nearly 90° to the normal.

If we use the requirement of Eq. (5) and take $k_\ell \simeq 0.5\ k_R$ as is typical for most material, we observe that the 3 dB points for Rayleigh waves gives $k_\ell a \simeq 0.12$. Hence the transducer will have its 3 dB longitudinal wave angular response points close to ±45°.

It will be observed that this requirement is a severe one, which it is tempting to relax. For a transducer operating up to a frequency of 2 MHz with typical metals ($V_R \sim 3\times10^5$cm/sec), Eq. (5) implies that the diameter must be less than 0.75 mm. Even for a transducer operating only up to a frequency of 400 KHz, the requirement is for a diameter of the order of 4 mm.

As we shall see, piezoelectric transducers respond to the rf velocity rather than displacement, i.e., ωu. Hence for this reason the response to emission tends to increase with frequency. Therefore it may be appropriate to work with a larger transducer than is indicated by this result. Nevertheless, if we still require a good angular response function, it follows from Eq. (6) that

BROADBAND ACOUSTIC EMISSION TRANSDUCERS

G. S. Kino

INTRODUCTION

The design of acoustic transducers for use in acoustic emission testing has mainly followed the methods used for NDE transducers. The minor changes in design usually made for this purpose mainly concentrate on the facts that the frequency of operation is typically below 400 KHz, and that an omni-directional sensor is required. In addition, because of the often difficult working environment, a great deal of attention has to be paid to the need to differentiate against interfering signals.

We shall consider here the design problem for AE (acoustic emission) transducers to operate over a broad band in the range from 100 KHz-2MHz. We shall be concerned with transducers that can respond to Rayleigh waves, longitudinal waves and shear waves. We shall consider the use of standard piezoelectric transducer ceramic materials and also non-standard materials such as ZnO thin films, PVF_2 plastic and composites. New concepts such as the use of fiber optic and acoustoelectric transducers are also of interest and will be considered.

BASIC NEEDS FOR ACOUSTIC EMISSION TRANSDUCERS

Pao[1] has discussed simple types of AE sources. In his terms, a small crack opening up or grain boundary cracking could

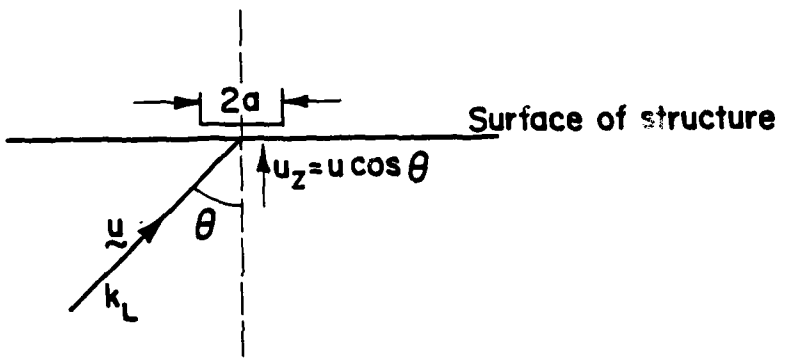

Figure 2. Illustration of a longitudinal wave incident on the surface at an angle θ.

be regarded as a double force source, a single couple or a double couple without movement. In each case, if the force has a frequency spectrum f_ω, it can be shown that there are radiated displacement amplitude components from a buried source of the form $\omega f_\omega (\exp - jkR)/R$ where $k=\omega/v$ is associated with a propagating shear or longitudinal wave, and ω is the radian frequency. As a typical source corresponds to a step function release in stress, f_ω varies as $1/\omega$. Thus the displacement amplitude spectrum from a small source of this type should be uniform over the frequency range of interest.

The situation becomes more complicated for finite crack sizes because of crack resonances and Rayleigh wave propagation along the crack surface and Doppler shifts associated with moving crack fronts. Furthermore, when the wave guiding properties of the structure itself are taken into account, the situation changes. For instance, a surface crack will emit a surface wave signal that falls off as $\exp - jk_R R/\sqrt{R}$ where k_R is the Rayleigh wave propagation constant. Therefore the surface wave excitation tends to become dominant at some distance from the exciting source and its frequency dependence different from that of a bulk wave. It is apparent that the frequency distortion will be even more severe when multiple Lamb modes are excited. At all events, at short distances from the flaw, a detector on the surface of a structure will tend to observe all possible modes that are excited by AE sources. At longer distances from the source, if the source is within a Rayleigh wavelength from the surface, acoustic

it is necessary to keep the diameter small, and the slight relaxation of our requirements for Rayleigh waves can only result in increasing the diameter to perhaps 1 mm. We shall consider in our design a transducer of this diameter. We shall also consider other types of larger diameter transducers for operation at lower frequencies.

IMPEDANCE MISMATCH FOR VARIOUS TYPES OF TRANSDUCERS

We shall consider first a transducer operating into an extremely high impedance load, i.e., an open circuited transducer. Later we shall consider the effect of a capacitive load.

We shall consider the transducer to be in contact with the surface. We shall be concerned with excitation of a longitudinal wave approaching the transducer at normal incidence to the transducer. Thus the stress reflection coefficient of the incident wave is

$$\Gamma = \frac{Z_L - Z_1}{Z_L + Z_1} \tag{7}$$

where Z_1 is the impedance of the substrate and Z_L the impedance presented by the transducer.

The velocity transmission coefficient is

$$T = \frac{v_1}{v^+} = 1 - \Gamma = \frac{2Z_1}{Z_L + Z_1} \tag{8}$$

where v_1 is the input velocity at the transducer surface and v^+ the velocity amplitude of the wave traveling toward the surface as illustrated in Fig. 3.

surface wave signals may well be dominant at the detector. On the other hand with a buried AE source, only bulk waves will tend to be present, unless there is some conversion from bulk waves to surface waves at sharp corners.

Thus the basic transducer must be able to detect normal displacements of the surface of the structure. In principle, this will make it possible to detect longitudinal waves and surface waves, both of which have such displacements present. A shear wave arriving at an angle to the surface normal will also excite such a transducer. But a shear wave source directly underneath the transducer would only give rise to a displacement parallel to the surface, which would have to be detected by a shear wave transducer. This is a relatively rare case, so we will, in the main, concentrate on transducers capable of detecting displacements normal to the surface.

Since we do not normally know the position of the emission source beforehand, it is appropriate to design an omni-directional transducer capable of detecting bulk waves or surface waves. In a few cases where the position of the possible source is known, such as a crack in a particular bolt hole, it may be appropriate to design to receive surface wave or bulk wave signals from a particular position. This makes the task easier. Therefore we will address ourselves only to the problem of design of an omni-directional broadband 100 KHz-2 MHz transducer. If this can be solved well, the design of other narrower band, narrower acceptance angle transducers should not be a major problem.

It is not as simple to calculate the reflection coefficient of a Rayleigh wave. However, we can make a reasonable estimate of the excitation by making use of the results for excitation of waves in a solid by a piston transducer. It has been shown that when a piston transducer, excited with a longitudinal wave, is placed in contact with a solid, the transducer excites longitudinal, shear and Rayleigh waves in the solid.[2,3] The effective impedance presented to the transducer is Z_1'. The theory has been calculated in detail for an infinitely long rectangular transducer and a piston transducer placed in contact with a solid.[2,3] The result of the calculation showed that $Z_1' \simeq Z_1$ the longitudinal wave impedance if the width of the transducer is greater than $\lambda_L/2$ in the solid substrate. Otherwise Z_1' has a reactive component with $\mathrm{Re}Z_1' < Z_1$.

We shall suppose that the total velocity normal to the transducer surface is

$$v_1 = v_R^+ + v^- \tag{9}$$

where v^- is the wave excited in the substrate and v_R^+ the rf velocity of the Rayleigh wave.

We are essentially assuming a sliding contact so that the longitudinal stress at the transducer is

$$T = -v_1 Z_L \tag{10}$$

But this stress excites waves in the substrate, with

$$T = v^- Z_1' \tag{11}$$

THE DIAMETER OF A BROADBAND TRANSDUCER

Suppose we wish to design a transducer to detect a surface wave of propagation constant k_R propagating at an arbitrary angle ϕ to the x axis as shown in Fig. 1. The transducer is supposed to detect the normal displacement u_z of the surface, and we can write

$$u_z = u\, e^{-jk_R(x\cos\phi + y\sin\phi)} \tag{1}$$

A piezoelectric, fiber optic, or capacitive transducer placed in contact with the surface basically responds to the average value of u_z over the area of the transducer. Hence, in order to make the response independent of ϕ, the transducer must be cylindrical in shape of radius a. In this case, its response will be of the form

$$V = \frac{1}{\pi a^2} \int e^{-jk_R(x\cos\phi + y\sin\phi)}\, dxdy \tag{2}$$

writing $x = r\cos\phi'$, $y = r\sin\phi'$

$$V = \frac{1}{\pi a^2} \int_0^a \int_0^{2\pi} re^{-jk_R r\cos(\phi'-\phi)}\, d\phi' dr \tag{3}$$

This integral can be shown to give the result

$$V = \frac{2J_1(k_R a)}{k_R a} \tag{4}$$

where $J_1(x)$ is a Bessel function of the first kind and first order with its first zero at $k_R a = 3.83$. The 3 dB points of this function are where

$$\left(\frac{a}{\lambda_R}\right)_{3dB} = 0.24 \tag{5}$$

It follows that

$$v_1\left(1 + \frac{Z_L}{Z_1'}\right) = v_R^+ \tag{12}$$

or

$$v_1 = \frac{Z_1'}{Z_L + Z_1'} v_R^+ \tag{13}$$

with

$$v^- = - \frac{Z_L}{Z_L + Z_1'} v_R^+ \tag{14}$$

It will be seen that the dependence of v_1 on v_R^+ is of just the same form as that of Eq. (8). For our purposes, in order to make estimates of efficiency we shall assume that $Z_1' \simeq Z_1$.

THE THEORETICAL RESPONSE CHARACTERISTICS OF VARIOUS TYPES OF TRANSDUCERS

We shall initially consider the individual transducers of interest to be terminated by an infinite electrical impedance, where appropriate. Later we shall concern ourselves with this assumption and show that for many types of transducers of the small size required for our purposes, the capacity of the transducer is so small that this assumption cannot be justified in practice.

For simplicity, we will consider only the response of a transducer to a normally incident longitudinal wave. However, by taking account of the angular response characteristic using Eq. (6) and by taking account of the Rayleigh wave response characteristic using Eqs. (4) and (13), it is possible to change the estimates made in this theory by factors of 2 or so to take account of these effects.

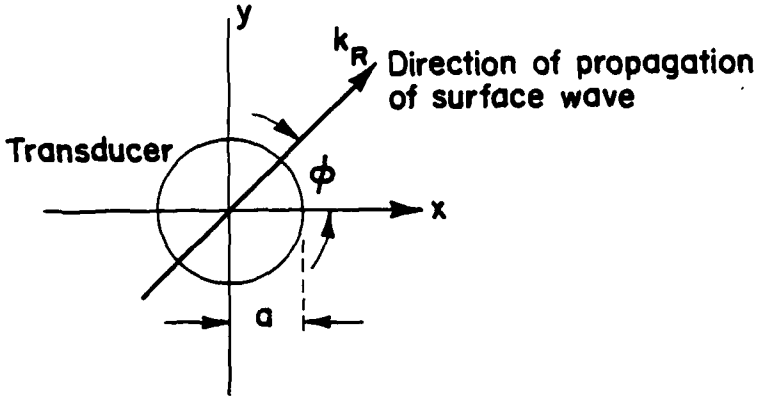

Figure 1. Illustration of a surface wave propagating at an angle ϕ to the x-axis.

The Capacitor Transducer

We suppose that the transducer consists of a metal electrode spaced by a distance ℓ from the surface of the structure. The space is normally taken to be a thin airgap. Thus the acoustic impedance of the transducer is essentially zero, providing the support structure does not interfere with the incident wave.

An alternative structure uses a high dielectric constant unpoled ceramic material of the type employed for the capacitive transducer. This would present a finite acoustic impedance to the incident wave which could be estimated in the same manner as we shall do for piezoelectric transducers. In this case, the transducer would have to have a rigid backing or matched impedance backing, so the front surface of the transducer can move relative to the back surface. The advantage could be easier and more mechanically stable alignment, higher capacity, and much higher breakdown fields. The disadvantage would be the far higher dc potentials required, a more complicated response characteristic and still a very weak response relative to the piezoelectric transducer.

Suppose now a dc field E_0 is applied to an airgap transducer. The applied voltage is $V_0 = E_0\ell$. The voltage change generated by a displacement u is

$$V = E_0 u \tag{15}$$

so the output of the transducer is proportional to the displacement of the acoustic wave.

On the other hand it can be shown from the work of Ref. 2 that if we consider a longitudinal wave of wavelength λ_L amplitude u_0 incident on the transducer at an angle θ to the normal, it has an amplitude $u_z = u_0 \cos\theta \exp -jk_L x \sin\theta$ normal to the surface, as illustrated in Fig. 2. Thus at the surface, the effective response varies as

$$\Phi = 2 \cos\theta \frac{J_1(k_\ell a \sin\theta)}{k_\ell a \sin\theta} \tag{6}$$

It follows that because of the cos θ term, under no circumstances can the transducer respond to longitudinal waves arriving at an angle nearly 90° to the normal.

If we use the requirement of Eq. (5) and take $k_\ell \simeq 0.5\ k_R$ as is typical for most material, we observe that the 3 dB points for Rayleigh waves gives $k_\ell a \simeq 0.12$. Hence the transducer will have its 3 dB longitudinal wave angular response points close to ±45°.

It will be observed that this requirement is a severe one, which it is tempting to relax. For a transducer operating up to a frequency of 2 MHz with typical metals ($V_R \sim 3\times10^5$cm/sec), Eq. (5) implies that the diameter must be less than 0.75 mm. Even for a transducer operating only up to a frequency of 400 KHz, the requirement is for a diameter of the order of 4 mm.

As we shall see, piezoelectric transducers respond to the rf velocity rather than displacement, i.e., ωu. Hence for this reason the response to emission tends to increase with frequency. Therefore it may be appropriate to work with a larger transducer than is indicated by this result. Nevertheless, if we still require a good angular response function, it follows from Eq. (6) that

The Piezoelectric Transducer

The terminated transducer: We make use of the Mason model of the transducer illustrated in Fig. 3[4] to show that its voltage output is

$$V_3 = \frac{h}{j\omega} (v_1 + v_2) \tag{16}$$

where v_2 is the input velocity on the right hand side of the transducer, $h = e/\varepsilon^S$, e is the piezoelectric stress constant, and ε^S the constant strain dielectric constant.

When the transducer is terminated in a matched impedance Z_0 it follows that

$$v_2 = -v_1 \, e^{-j\beta\ell} \tag{17}$$

where ℓ is the transducer length, $\beta = \omega/V_0$ the propagation constant of the wave inside the transducer, and V_0 the wave velocity in the transducer material.

It therefore follows from Eqs. (8) and (17) that

$$V_3 = \frac{h}{j\omega} (1-e^{-j\beta\ell}) \, \frac{2Z_1}{Z_1+Z_0} \, v^+ \tag{18}$$

At resonance $\beta\ell = \pi$ and $\omega=\omega_0$, so it follows that

$$V_3 = \frac{2h}{\pi V_0} \, \frac{2Z_1}{Z_0+Z_1} \, v^+ \tag{19}$$

At low frequencies $\beta\ell \to 0$, so it will be seen that

$$V_3 \to \frac{jh\ell}{V_0} \, \frac{2Z_1}{Z_0+Z_1} \, v^+ \tag{20}$$

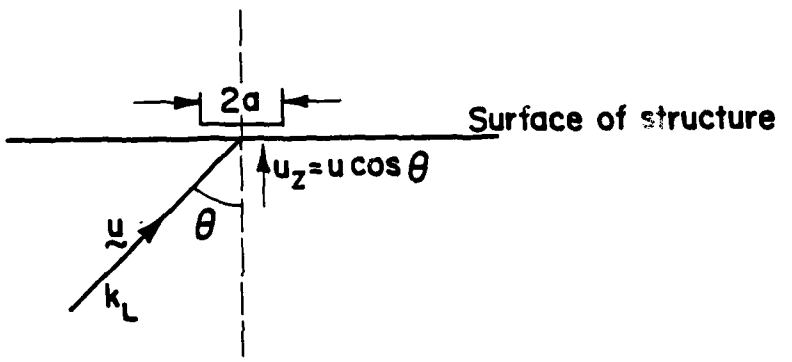

Figure 2. Illustration of a longitudinal wave incident on the surface at an angle θ.

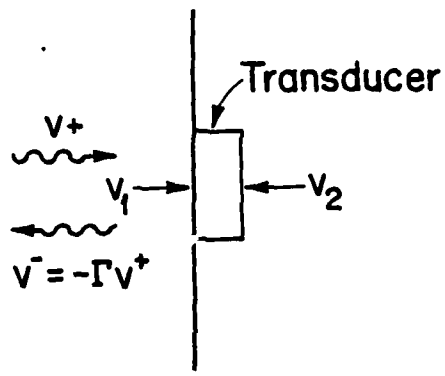

Figure 3. Schematic of a transducer with velocities v_1, v_2 on its two sides, excited by a wave of velocity amplitude v^+ incident on the surface of the substrate.

it is necessary to keep the diameter small, and the slight relaxation of our requirements for Rayleigh waves can only result in increasing the diameter to perhaps 1 mm. We shall consider in our design a transducer of this diameter. We shall also consider other types of larger diameter transducers for operation at lower frequencies.

IMPEDANCE MISMATCH FOR VARIOUS TYPES OF TRANSDUCERS

We shall consider first a transducer operating into an extremely high impedance load, i.e., an open circuited transducer. Later we shall consider the effect of a capacitive load.

We shall consider the transducer to be in contact with the surface. We shall be concerned with excitation of a longitudinal wave approaching the transducer at normal incidence to the transducer. Thus the stress reflection coefficient of the incident wave is

$$\Gamma = \frac{Z_L - Z_1}{Z_L + Z_1} \tag{7}$$

where Z_1 is the impedance of the substrate and Z_L the impedance presented by the transducer.

The velocity transmission coefficient is

$$T = \frac{v_1}{v^+} = 1 - \Gamma = \frac{2Z_1}{Z_L + Z_1} \tag{8}$$

where v_1 is the input velocity at the transducer surface and v^+ the velocity amplitude of the wave traveling toward the surface as illustrated in Fig. 3.

It follows that the piezoelectric transducer responds to the incident rf velocity of the wave rather than its displacement. Its voltage response at zero frequency to velocity is increased by a factor $\pi/2$ from that at resonance. However its power output is decreased (note the change in phase). The response to acoustic displacement u^+ is another matter. As $v^+ = j\omega u^+$, the response of the transducer to displacement varies linearly with frequency.

Rigid backing: This situation may be of interest for transducer materials like PVF_2 which have a relatively low impedance and can be used with a rigid backing of brass or other relatively high impedance material.

In this case $v_2 = 0$ and

$$\frac{T_1}{v_1} = j \cot\beta\ell \tag{21}$$

so it follows that

$$V_3 = \frac{h}{j\omega} \frac{2Z_1}{Z_1 - jZ_0 \cot\beta\ell} \tag{22}$$

At resonance $\beta_a \ell = \pi/2$, and

$$V_3 = \frac{4h\ell}{j\pi V_0} v^+ \tag{23}$$

As $\omega \to 0$

$$V_3 \to \frac{2h\ell}{V_0} v^+ \tag{24}$$

We note that if $Z_1 = Z_0$ the matched transducers and rigid backed transducers have essentially the same responses at the two

It is not as simple to calculate the reflection coefficient of a Rayleigh wave. However, we can make a reasonable estimate of the excitation by making use of the results for excitation of waves in a solid by a piston transducer. It has been shown that when a piston transducer, excited with a longitudinal wave, is placed in contact with a solid, the transducer excites longitudinal, shear and Rayleigh waves in the solid.[2,3] The effective impedance presented to the transducer is Z_1'. The theory has been calculated in detail for an infinitely long rectangular transducer and a piston transducer placed in contact with a solid.[2,3] The result of the calculation showed that $Z_1' \simeq Z_1$ the longitudinal wave impedance if the width of the transducer is greater than $\lambda_L/2$ in the solid substrate. Otherwise Z_1' has a reactive component with $\mathrm{Re}Z_1' < Z_1$.

We shall suppose that the total velocity normal to the transducer surface is

$$v_1 = v_R^+ + v^- \tag{9}$$

where v^- is the wave excited in the substrate and v_R^+ the rf velocity of the Rayleigh wave.

We are essentially assuming a sliding contact so that the longitudinal stress at the transducer is

$$T = -v_1 Z_L \tag{10}$$

But this stress excites waves in the substrate, with

$$T = v^- Z_1' \tag{11}$$

major frequency ranges of interest. For the same resonant frequency, the rigidly backed transducer is half the length of the matched backed transducer.

Air backed structure: In this case the stress at the back of the transducer is zero, and we can write

$$v_1 = -v_2 \cos\beta\ell \tag{25}$$

This implies that

$$V_3 = -\frac{h}{j\omega} \frac{2Z_1}{(Z_1+jZ_0 \tan\beta\ell)\cos\beta\ell} v^+ \tag{26}$$

At resonance ($\beta\ell = \pi$)

$$V_3 = \frac{4v^+h\ell}{j\pi V_0} \tag{27}$$

As $\omega \to 0$ it follows that

$$V_3 \to \frac{jv^+h\omega\ell^2}{V_0^2} \tag{28}$$

Thus the response falls off at low frequencies. This is because the back of the transducer is free to move with the front surface, and so at low frequencies there tends to be no net applied strain. We therefore conclude that, as we might have expected, air backing is poor for use in broadband transducers.

THE FIBER OPTIC TRANSDUCER

A new type of transducer which has generated considerable interest employs fiber optics. The basic idea behind this transducer is that when external pressure is applied to a fiber optic

It follows that

$$v_1\left(1 + \frac{Z_L}{Z_1'}\right) = v_R^+ \tag{12}$$

or

$$v_1 = \frac{Z_1'}{Z_L + Z_1'} v_R^+ \tag{13}$$

with

$$v^- = - \frac{Z_L}{Z_L + Z_1'} v_R^+ \tag{14}$$

It will be seen that the dependence of v_1 on v_R^+ is of just the same form as that of Eq. (8). For our purposes, in order to make estimates of efficiency we shall assume that $Z_1' \simeq Z_1$.

THE THEORETICAL RESPONSE CHARACTERISTICS OF VARIOUS TYPES OF TRANSDUCERS

We shall initially consider the individual transducers of interest to be terminated by an infinite electrical impedance, where appropriate. Later we shall concern ourselves with this assumption and show that for many types of transducers of the small size required for our purposes, the capacity of the transducer is so small that this assumption cannot be justified in practice.

For simplicity, we will consider only the response of a transducer to a normally incident longitudinal wave. However, by taking account of the angular response characteristic using Eq. (6) and by taking account of the Rayleigh wave response characteristic using Eqs. (4) and (13), it is possible to change the estimates made in this theory by factors of 2 or so to take account of these effects.

The Capacitor Transducer

We suppose that the transducer consists of a metal electrode spaced by a distance ℓ from the surface of the structure. The space is normally taken to be a thin airgap. Thus the acoustic impedance of the transducer is essentially zero, providing the support structure does not interfere with the incident wave.

An alternative structure uses a high dielectric constant unpoled ceramic material of the type employed for the capacitive transducer. This would present a finite acoustic impedance to the incident wave which could be estimated in the same manner as we shall do for piezoelectric transducers. In this case, the transducer would have to have a rigid backing or matched impedance backing, so the front surface of the transducer can move relative to the back surface. The advantage could be easier and more mechanically stable alignment, higher capacity, and much higher breakdown fields. The disadvantage would be the far higher dc potentials required, a more complicated response characteristic and still a very weak response relative to the piezoelectric transducer.

Suppose now a dc field E_0 is applied to an airgap transducer. The applied voltage is $V_0 = E_0\ell$. The voltage change generated by a displacement u is

$$V = E_0 u \tag{15}$$

so the output of the transducer is proportional to the displacement of the acoustic wave.

where k is the propagation constant of the optical wave and A is a constant. This relation is similar in form to that of Eq. (18) for the piezoelectric transducer. Thus the magnitude of the phase response will vary as

$$|\phi| = Ak\ell \left| \frac{\sin\beta\ell/2}{\beta\ell/2} \right| \tag{30}$$

Therefore the 3 dB response of this transducer will be at a frequency f_0 where $\beta\ell = .9\pi/2$, i.e., where

$$f_0 = \frac{.45\ell}{V_0} \tag{31}$$

It follows that the area of the fiber pancakes limits the frequency and angular response in acoustic emission applications, and the total thickness of the pancake layers limits the frequency of the response because of the phase shift from layer to layer.

We can estimate the sensitivity of the fiber optic sensor by using the results of Budiansky, et al. for application of hydrostatic pressure.[6] They show that the relative change in phase $\Delta\phi/\phi$ for quartz fiber is

$$\frac{\Delta\phi}{\phi} = 2.2\times10^{-12}\ p \tag{32}$$

Yariv[7] has shown that if the fiber is placed in a bridge circuit with the two fiber arms injected into a mixer, the signal to noise ratio of the system is

$$\frac{S}{N} = \frac{P\eta(\Delta\phi)^2}{4h\nu\Delta\nu} \tag{33}$$

where ν is the optical frequency, $\Delta\nu$ the required bandwidth, P

The Piezoelectric Transducer

The terminated transducer: We make use of the Mason model of the transducer illustrated in Fig. 3[4] to show that its voltage output is

$$V_3 = \frac{h}{j\omega} (v_1 + v_2) \tag{16}$$

where v_2 is the input velocity on the right hand side of the transducer, $h = e/\varepsilon^S$, e is the piezoelectric stress constant, and ε^S the constant strain dielectric constant.

When the transducer is terminated in a matched impedance Z_0 it follows that

$$v_2 = -v_1 \, e^{-j\beta\ell} \tag{17}$$

where ℓ is the transducer length, $\beta = \omega/V_0$ the propagation constant of the wave inside the transducer, and V_0 the wave velocity in the transducer material.

It therefore follows from Eqs. (8) and (17) that

$$V_3 = \frac{h}{j\omega} (1-e^{-j\beta\ell}) \, \frac{2Z_1}{Z_1+Z_0} \, v^+ \tag{18}$$

At resonance $\beta\ell = \pi$ and $\omega=\omega_0$, so it follows that

$$V_3 = \frac{2h}{\pi V_0} \, \frac{2Z_1}{Z_0+Z_1} \, v^+ \tag{19}$$

At low frequencies $\beta\ell \to 0$, so it will be seen that

$$V_3 \to \frac{jh\ell}{V_0} \, \frac{2Z_1}{Z_0+Z_1} \, v^+ \tag{20}$$

the optical power of the laser, η the quantum efficiency of the detector and h Planck's constant. It follows that

$$\frac{S}{N} = 1.21\times10^{-24}\ \frac{P\eta p^2\phi^2}{4h\nu\Delta\nu} \tag{34}$$

However if the impedance of the material of the transducer is Z_0 it follows that

$$\frac{S}{N} = 1.21\times10^{-24}\ \frac{P\eta Z_0^2\phi^2}{h\nu\Delta\nu}\left(\frac{Z_1}{Z_0+Z_1}\right)^2 v^{+2} \tag{35}$$

THE ACOUSTOELECTRIC TRANSDUCER

The acoustoelectric transducer makes use of the fact that when a piezoelectric semiconductor is excited by an acoustic wave, an acoustoelectric potential is set up along its length which is proportional to the square of the input signal. For this reason the device adds the square of the magnitudes of all entering signals and gives an output proportional to its length adding all signals entering its surface. Thus the device is phase insensitive and has a directivity which varies as $\cos\theta$, assuming electrodes are placed on its back and front surfaces.

Initially, therefore, it looks like a very attractive candidate for an acoustic emission sensor. But as it is a second order detector, its response is weak. Consequently, on the basis of very crude estimates, we reject it as a sensor for this purpose.

PHASE ARRAY DETECTORS

One way out of the difficulty of the insensitivity of the acoustoelectric detector is to use an array of small transducers

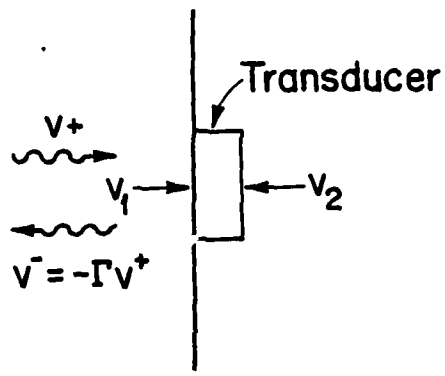

Figure 3. Schematic of a transducer with velocities v_1, v_2 on its two sides, excited by a wave of velocity amplitude v^+ incident on the surface of the substrate.

each connected to an individual high impedance amplifier. The outputs of these amplifiers are fed into individual square law detectors and summed. Now the resultant device could be made of large area, and as sensitive as an individual piezoelectric transducer, without being phase sensitive.

A second possibility is to record the signal from each amplifier separately and process it appropriately. Suppose that the transducers were spaced a distance d and the signal arrived at an angle θ to normal to the array. Then if the emission signal is F(t), a surface wave signal arriving along the substrate at the n^{th} transducer, at an angle θ to the normal of the plane of the array, is of the form

$$F(t - T - x_n \sin\theta / V_R)$$

at the n^{th} element, whose coordinates are $x_n, 0$, as illustrated in Fig. 4. By taking the time correlation of these signals with the signal from one element, say $x_n = 0$

$$G(t) = \int F(\tau - T) F(t + \tau - T - x_n \sin\theta / V_R) d\tau \qquad (36)$$

we should observe a correlation peak at a time

$$t = x_n \sin\theta / V_R \qquad (37)$$

Hence we can find the angular position from which the signal arrived. In principle we need only two transducers for this purpose, but more would eliminate aliasing effects.

It follows that the piezoelectric transducer responds to the incident rf velocity of the wave rather than its displacement. Its voltage response at zero frequency to velocity is increased by a factor $\pi/2$ from that at resonance. However its power output is decreased (note the change in phase). The response to acoustic displacement u^+ is another matter. As $v^+ = j\omega u^+$, the response of the transducer to displacement varies linearly with frequency.

Rigid backing: This situation may be of interest for transducer materials like PVF_2 which have a relatively low impedance and can be used with a rigid backing of brass or other relatively high impedance material.

In this case $v_2 = 0$ and

$$\frac{T_1}{v_1} = j \cot\beta\ell \tag{21}$$

so it follows that

$$V_3 = \frac{h}{j\omega} \frac{2Z_1}{Z_1 - jZ_0 \cot\beta\ell} \tag{22}$$

At resonance $\beta_a \ell = \pi/2$, and

$$V_3 = \frac{4h\ell}{j\pi V_0} v^+ \tag{23}$$

As $\omega \to 0$

$$V_3 \to \frac{2h\ell}{V_0} v^+ \tag{24}$$

We note that if $Z_1 = Z_0$ the matched transducers and rigid backed transducers have essentially the same responses at the two

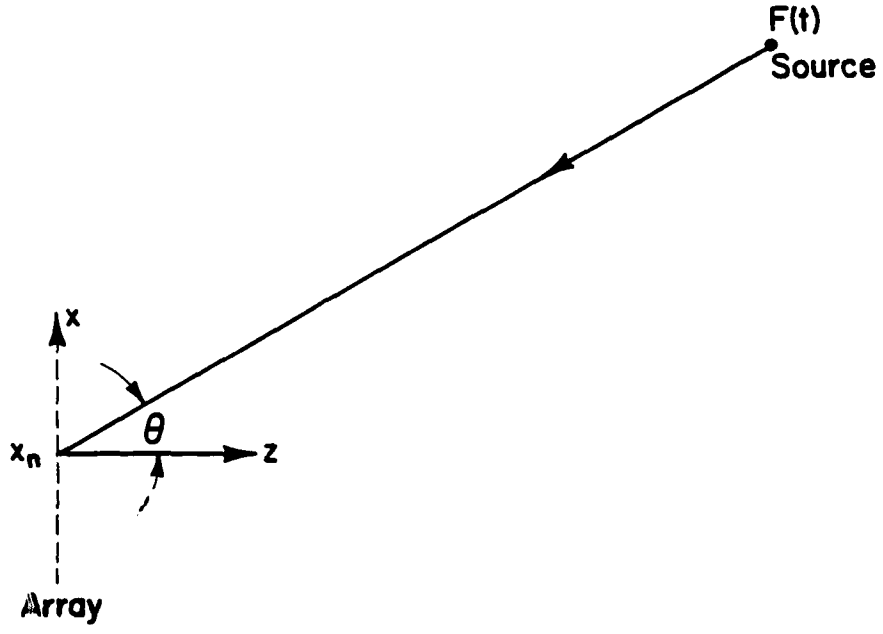

Figure 4. Illustration of an array receiving a signal from a distant source.

AD-A099 917 MICHIGAN UNIV ANN ARBOR COLL OF ENGINEERING F/G 5/2
PRELIMINARY REPORTS, MEMORANDA AND TECHNICAL NOTES OF THE MATER--ETC(U)
JUL 80 M J SINNOTT MDA903-80-C-0505
UNCLASSIFIED 018324 NL

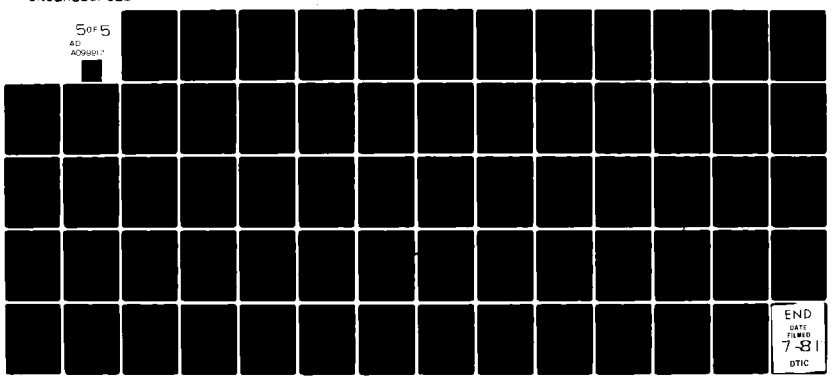

waveguide, there is a phase shift of the optical wave passing through the guide; this phase shift is proportional to the applied pressure. If the applied pressure is due to an incident acoustic

The low capacity of the transducer militates against the use of a PVF_2 plastic piezoelectric material. Although the transmitting constant h is comparable to PZT, $\varepsilon^S/\varepsilon_0 \sim 4$, so a small transducer will be severely loaded by the external circuit.

where k is the propagation constant of the optical wave and A is a constant. This relation is similar in form to that of Eq. (18) for the piezoelectric transducer. Thus the magnitude of the phase response will vary as

$$|\phi| = Ak\ell \left| \frac{\sin\beta\ell/2}{\beta\ell/2} \right| \tag{30}$$

Therefore the 3 dB response of this transducer will be at a frequency f_0 where $\beta\ell = .9\pi/2$, i.e., where

$$f_0 = \frac{.45\ell}{V_0} \tag{31}$$

It follows that the area of the fiber pancakes limits the frequency and angular response in acoustic emission applications, and the total thickness of the pancake layers limits the frequency of the response because of the phase shift from layer to layer.

We can estimate the sensitivity of the fiber optic sensor by using the results of Budiansky, et al. for application of hydrostatic pressure.[6] They show that the relative change in phase $\Delta\phi/\phi$ for quartz fiber is

$$\frac{\Delta\phi}{\phi} = 2.2\times10^{-12}\ p \tag{32}$$

Yariv[7] has shown that if the fiber is placed in a bridge circuit with the two fiber arms injected into a mixer, the signal to noise ratio of the system is

$$\frac{S}{N} = \frac{P\eta(\Delta\phi)^2}{4h\nu\Delta\nu} \tag{33}$$

where ν is the optical frequency, $\Delta\nu$ the required bandwidth, P

CONCLUSIONS

A study has been made of the merits of different types of broadband acoustic transducers for observing acoustic emission in the frequency range from 100 KHz-2 MHz. The criteria for good frequency response to Rayleigh waves and good frequency and angular response to longitudinal waves have been derived. We conclude that a transducer of the order of 1mm diameter is required.

The sensitivies for capacitor transducers, piezoelectric transducers, and fiber optic transducers have been derived. It has been shown that piezoelectric transducers which are velocity sensitive are several orders of magnitude more sensitive than capacitor transducers in the frequency range of interest. Capacitor sensors are, at best, only suitable for calibration purposes. PZT ceramic transducers terminated in a matched backing are the best choice because of the high dielectric constant of the material, which implies a transducer with a reasonable impedance at the frequencies of interest. ZnO thin film integrated circuit transducers are not a good choice because the FET used has too high a gate capacity, the ZnO layer is likely to be too thin for good sensitivity, and it is difficult but not impossible to provide a matched backing layer. PVF_2 transducers are not suitable because they have too low a capacity, so they tend to be too heavily loaded by the input amplifier at the frequencies of interest.

The fiber optic transducer has been analyzed. It is shown that for sensitivity comparable to a PZT transducer, approximately 1 meter length must be employed. The fiber must be coiled in the

the optical power of the laser, η the quantum efficiency of the detector and h Planck's constant. It follows that

$$\frac{S}{N} = 1.21\times10^{-24}\ \frac{P\eta p^2\phi^2}{4h\nu\Delta\nu} \tag{34}$$

However if the impedance of the material of the transducer is Z_0 it follows that

$$\frac{S}{N} = 1.21\times10^{-24}\ \frac{P\eta Z_0^2\phi^2}{h\nu\Delta\nu}\left(\frac{Z_1}{Z_0+Z_1}\right)^2 v^{+2} \tag{35}$$

THE ACOUSTOELECTRIC TRANSDUCER

The acoustoelectric transducer makes use of the fact that when a piezoelectric semiconductor is excited by an acoustic wave, an acoustoelectric potential is set up along its length which is proportional to the square of the input signal. For this reason the device adds the square of the magnitudes of all entering signals and gives an output proportional to its length adding all signals entering its surface. Thus the device is phase insensitive and has a directivity which varies as $\cos\theta$, assuming electrodes are placed on its back and front surfaces.

Initially, therefore, it looks like a very attractive candidate for an acoustic emission sensor. But as it is a second order detector, its response is weak. Consequently, on the basis of very crude estimates, we reject it as a sensor for this purpose.

PHASE ARRAY DETECTORS

One way out of the difficulty of the insensitivity of the acoustoelectric detector is to use an array of small transducers

form of several pancake spiral layers embedded in a tungsten epoxy matrix. But the minimum diameter can only be of the order of 1cm thus making the angular response unsuitable for this application. The frequency response is limited also by the thickness of the multiple layer system because of the phase change of the acoustic waves passing through these layers. Thus with a 1 cm diameter the frequency response would drop off at approximately 200 KHz. By coiling the fiber to a diameter of 2-3 mm the working frequency could be raised to 1 MHz, but at the risk of a very short life.[8] The development of smaller diameter single mode fibers could change this conclusion and make it possible to use fibers at higher frequencies. At all events the fiber optic sensor is an attractive candidate for lower frequency operation because it should not suffer from electromagnetic interference.

ACKNOWLEDGEMENT

The main part of this work was supported by the Advanced Research Projects Agency of the Department of Defense under Contract No. MDA903-80C-0505 with the University of Michigan. It was completed at Stanford with support by the Air Force Office of Scientific Research under Contract No. F49620-79C-0217.

each connected to an individual high impedance amplifier. The outputs of these amplifiers are fed into individual square law detectors and summed. Now the resultant device could be made of large area, and as sensitive as an individual piezoelectric transducer, without being phase sensitive.

A second possibility is to record the signal from each amplifier separately and process it appropriately. Suppose that the transducers were spaced a distance d and the signal arrived at an angle θ to normal to the array. Then if the emission signal is F(t), a surface wave signal arriving along the substrate at the n^{th} transducer, at an angle θ to the normal of the plane of the array, is of the form

$$F(t - T - x_n \sin\theta / V_R)$$

at the n^{th} element, whose coordinates are $x_n, 0$, as illustrated in Fig. 4. By taking the time correlation of these signals with the signal from one element, say $x_n = 0$

$$G(t) = \int F(\tau - T) F(t + \tau - T - x_n \sin\theta / V_R) d\tau \qquad (36)$$

we should observe a correlation peak at a time

$$t = x_n \sin\theta / V_R \qquad (37)$$

Hence we can find the angular position from which the signal arrived. In principle we need only two transducers for this purpose, but more would eliminate aliasing effects.

References

1. Y. Pao, "Theory of Acoustic Emission," Elastic Wave and Non-Destructive Testing of Materials, AMD 29, edited by Y. H. Pao, ASME, 1978.

2. G. S. Kino and C. S. DeSilets, "The Design of Slotted Transducer Arrays with Matched Backing," Ultrasonic Imaging 1, 189-209 (1979).

3. G. F. Miller and H. Pursey, "The Field and Radiation Impedance of Mechanical Radiations on the Free Surface of a Semi-Infinite Isotropic Solid," Proc. Roy. Soc. London 223, 521-541 (1954).

4. B. A. Auld, Acoustic Fields and Waves in Solids, Vol. 1, Wiley, 1973.

5. G. S. Kino and R. M. Thomson, "Detection and Evaluation of Small Flaws in Optical Fibers," MRC Report, DARPA Materials Research Council, July 1980.

6. B. Budiansky, D. Drucker, G. S. Kino and J. Rice, "The Pressure Sensitivity of a Clad Optical Fiber," Appl. Optics 18, 4085, Dec. 15, 1979.

7. A. Yariv and H. V. Winsor, Proposal for Detection of Magnetic Fields Through Magnetostructive Perturbation of Optical Fibers, Optics Letters 5, 87, March 1980.

8. T. Yamanishi, K. Yoshimura, S. Seuuki, S. Seikai, and N. Ochida, "Modified Silicone as a New Type of Primary Coat for Optical Fibre," Electronics Letters 16, 3, pp. 100-101 (1980).

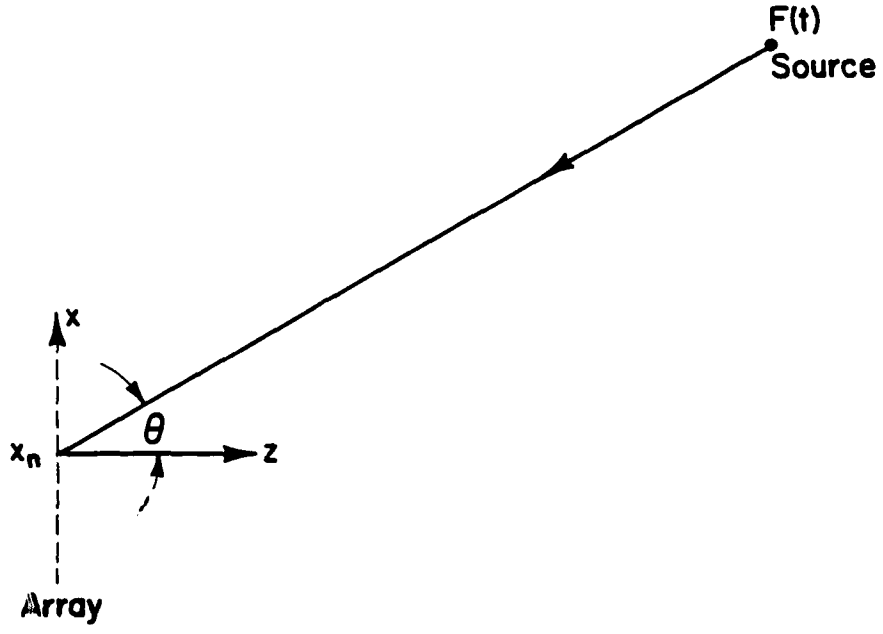

Figure 4. Illustration of an array receiving a signal from a distant source.

A MECHANICAL MODEL FOR SOME MARTENSITIC PHASE TRANSFORMATIONS

B. Budiansky

ABSTRACT

Phase-transformation toughening of growing cracks has been observed in ceramics containing zirconia (ZrO_2) particles. The toughening is attributed to a stress-induced permanent transformation of the particle from a tetragonal to a monoclinic structure in the vicinity of the crack tip. The mechanical model for zirconia phase changes developed herein is motivated by the need for a rational analysis of this toughening process.

The model is chosen to be consistent with the known data concerning zirconia:

(i) The tetragonal phase is unstable at room temperature and zero pressure, preferring a monoclinic phase, having a 4% dilatation e_1 and ≈16% shear strain γ_1 with respect to the tetragonal phase.

(ii) The tetragonal phase can be stabilized by pressure, and under decreasing pressure transforms at $\bar{p} \approx 3.8$ GPa, at room temperature.

(iii) Restabilizing of the tetragonal phase under increasing pressure has not been observed. Hysteresis is presumed.

(iv) Sufficiently small zirconia particles embedded in a matrix of conformable stiffness are stable (at room temperature) in the tetragonal phase.

(v) Embedded particles are initially stress-free (they are not stabilized by external pressures).

(vi) At a sufficiently high matrix stress, the embedded particle transforms to the monoclinic phase. The transformation does not reverse upon removal of the applied stress.

The mechanical model is based on a polynomial representation of internal energy as a function of transformation shear strain. In turn, the transformation dilatation is presumed to be a function of this shear strain, and equilibrium states are determined by minimization of the Gibbs free energy (at zero temperature). Several key parameters are identified, such as

$$\lambda = \frac{\bar{p}e_1}{|\Delta\phi|} \tag{1}$$

and

$$\rho = \frac{G_1\gamma_1^2}{|\Delta\phi|} \tag{2}$$

where $|\Delta\phi|$ is the energy density release ($\simeq$230 MPa) during room temperature transformation (at zero pressure), and G_1 is the shear modulus associated with λ_1 in the monoclinic phase.

Models consistent with the observed behavior of zirconia, and the estimate $\lambda \simeq 2/3$, have been developed. The experimental evaluation of additional crystal properties (such as G_1, and the cross-stiffness $dp/d\gamma$ in the monoclinic phase) is required to assess the internal consistency of the model or the need for its improvement.

Alternatively we could take the Fourier transform of the signal and look at any particular frequency component ω. Then standard time delay or phase delay imaging techniques used on each frequency component would make it possible to locate the angular position of this component.

If the transducers are well spaced then the method of Eq. (36) tends to reduce to a triangulation technique and makes it possible to find the position of the source unequivocally.

NUMERICAL CALCULATIONS

As an example for a PZT 5H transducer with a matched backing and a resonant frequency of 2 MHz, ℓ = 1.1 mm, $h = e/\varepsilon^S = 3.76\times10^9$ V/m, so $V_3 = 962v^+$. Now a 2N5558 low noise JFET has a response of $200\times10^{-9}V/\sqrt{Hz}$, so the noise over a 2 MHz bandwidth is 2.83×10^{-4} volts. Therefore, if we assume that for noise like emission sources we need a signal to noise ratio of 10 dB in order to observe emission unequivocally, we find that the minimum detectable velocity is $v = 9.1\times10^{-7}$ m/sec and the minimum detectable displacement is therefore $u = 1.4\times10^{-13}$ f, where f is the operating frequency in MHz. If we take the diameter of the transducer to be 1 mm so the response falls off slightly more than 3 dB at 2 MHz in accordance with Eq. (5), we find that for PZT 5H, ($\varepsilon^S_{33}/\varepsilon_0 = 830$, $\varepsilon^T_{33}/\varepsilon_0 = 1700$) the capacity is between 6 and 12 pf. As the JFET has a capacity of the order of 2 pf, it will not load the transducer too severely.

METAL HYDRIDE ALKYLS, HYDROXIDES AND ALKOXY DERIVATIVES AS PROPELLANT ADDITIVES

J. L. Margrave, J. W. Kauffman, M. M. Konarski
and R. H. Hauge

ABSTRACT

New high-energy solids can be made by reacting metal atoms with alkanes, alcohols or ethers at low temperatures. These species -- HMR, MMOR and RMOR should be useful additives to propellants to provide higher temperatures and increased impulse.

The low capacity of the transducer militates against the use of a PVF_2 plastic piezoelectric material. Although the transmitting constant h is comparable to PZT, $\varepsilon^S/\varepsilon_0 \sim 4$, so a small transducer will be severely loaded by the external circuit.

A ZnO thin film transducer would suffer from the same difficulties, so the only realistic small diameter transducer that can be used is one made of PZT ceramic.

A similar calculation can be made for capacitor transducers. If we suppose that we use a transducer with 2 μm spacing, with very large applied field E_0 of 10^7 v/m corresponding to an applied voltage of 20V, it follows from Eq. (15) that the 2N558 JFET would give a 10 dB signal to noise ratio with a displacement $v = 9\times10^{-11}$ m. It will be seen that a PZT transducer would have the same sensitivity at a frequency of 1.5 KHz. At higher frequencies the sensitivity of the PZT transducer increases linearly with frequency and so normally far exceeds that of the capacitive transducer.

For a fiber optic transducer with P = 1 mw, $\nu = 3\times10^8$ MHz, $\Delta\nu = 2$ MHz, and $\eta = 0.5$, we find that $\Delta\phi = 1.8\times10^{-4}$ for a 10 dB signal to noise ratio. Taking the impedance of the glass to be 15×10^6 kg/m^2-sec, we find that for a sensitivity equal to that of PZT $v = 9.1\times10^{-7}$ m/sec, $p = Z_0 v = 13.7$ kg/m^2. Hence with $\Delta\phi/\phi = 2.2\times10^{-12}$ p, $\Delta\phi/\phi = 2.7\times10^{-11}$ and $\phi = 6.6\times10^6$ radians, i.e., about 10^6 wavelengths. This corresponds to a fiber length of approximately 1 meter. Such a fiber could be coiled up into approximately 30 turns of 1 cm diameter in the form of several pancake layers, as already described.

METAL HYDRIDE ALKYLS, HYDROXIDES AND ALKOXY DERIVATIVES AS PROPELLANT ADDITIVES

J. L. Margrave, J. W. Kauffman, M. M. Konarski
and R. H. Hauge

It has become common practice in developing optimum propellant compositions to add small amounts (1-15%) of a reactive metal (Al, Li, Be, Mg, etc.) to increase the heat of combustion and provide other improved properties--higher densities, higher specific impulses, etc. Such additions can be in the form of powdered or flaked pure metals or in the form of their binary hydrides--AlH_3, LiH, BeH_2, MgH_2[m] etc.[1] Actually, the hydrides are often difficult to synthesize and hydrolytically sensitive, so that the metal powders are usually preferred. Slurries of Al in hydrazine/hydrazine nitrate, Be in liquid oxygen to be mixed with liquid hydrogen, Li/$LiBH_4$ gelled with liquid hydrogen and burned with liquid fluorine, or Al or Mg - powders in diesel fuel have all been tested.[1,2] Performances are erratic, but sometimes sensational. Settling out, clogging nozzles and other mechanical problems have limited these systems.

In this note some new syntheses are reported in which gaseous metal atoms are reacted at low temperatures with HOH, ROH, ROR, and RH to form high-energy products.[3] These compounds should be useful propellant additives and are especially attractive since they

CONCLUSIONS

A study has been made of the merits of different types of broadband acoustic transducers for observing acoustic emission in the frequency range from 100 KHz-2 MHz. The criteria for good frequency response to Rayleigh waves and good frequency and angular response to longitudinal waves have been derived. We conclude that a transducer of the order of 1mm diameter is required.

The sensitivies for capacitor transducers, piezoelectric transducers, and fiber optic transducers have been derived. It has been shown that piezoelectric transducers which are velocity sensitive are several orders of magnitude more sensitive than capacitor transducers in the frequency range of interest. Capacitor sensors are, at best, only suitable for calibration purposes. PZT ceramic transducers terminated in a matched backing are the best choice because of the high dielectric constant of the material, which implies a transducer with a reasonable impedance at the frequencies of interest. ZnO thin film integrated circuit transducers are not a good choice because the FET used has too high a gate capacity, the ZnO layer is likely to be too thin for good sensitivity, and it is difficult but not impossible to provide a matched backing layer. PVF_2 transducers are not suitable because they have too low a capacity, so they tend to be too heavily loaded by the input amplifier at the frequencies of interest.

The fiber optic transducer has been analyzed. It is shown that for sensitivity comparable to a PZT transducer, approximately 1 meter length must be employed. The fiber must be coiled in the

show limited solubilities in both polar and organic solvents.

Thus, in general, one can write

(a) $M + H_2O \longrightarrow M : \ddot{O}H_2$

$\downarrow h\nu$

HMOH

$\downarrow$ xs metal, $h\nu$

HMOMH or HM_2OH

(b) $M + ROH \longrightarrow M : \ddot{O}(R)(H)$

$\downarrow h\nu$

HMOR (usually preferred over RMOH)

$\downarrow$ xs metal, $h\nu$

HMOMR or HM_2OR

(c) $M + ROR \longrightarrow M : \ddot{O}(R)(R)$

$\downarrow h\nu$

RMOR

$\downarrow$ xs metal, $h\nu$

RMOMR or RM_2OR

form of several pancake spiral layers embedded in a tungsten epoxy matrix. But the minimum diameter can only be of the order of 1cm thus making the angular response unsuitable for this application. The frequency response is limited also by the thickness of the multiple layer system because of the phase change of the acoustic waves passing through these layers. Thus with a 1 cm diameter the frequency response would drop off at approximately 200 KHz. By coiling the fiber to a diameter of 2-3 mm the working frequency could be raised to 1 MHz, but at the risk of a very short life.[8] The development of smaller diameter single mode fibers could change this conclusion and make it possible to use fibers at higher frequencies. At all events the fiber optic sensor is an attractive candidate for lower frequency operation because it should not suffer from electromagnetic interference.

ACKNOWLEDGEMENT

The main part of this work was supported by the Advanced Research Projects Agency of the Department of Defense under Contract No. MDA903-80C-0505 with the University of Michigan. It was completed at Stanford with support by the Air Force Office of Scientific Research under Contract No. F49620-79C-0217.

Examples of all of these reactions are currently known. In a few cases (Sc, Al, Ti) the neutral adduct does not persist even at liquid He temperatures and direct reactions to form HMOH or $M(OH)_x$ + H_2 or MO + H_2 occur. In other cases (Ni-atoms) no reaction seems to occur. In general, more active metals form adducts and those with absorptions in the visible or UV regions of the spectrum undergo the oxidative insertion to form hydrido-hydroxides, hydrido-alkoxy or alkyl-alkoxy products.

With methane, there is no adduct, but UV-photolysis of Mn + CH_4, Fe + CH_4, Co + CH_4, Cu + CH_4, Zn + CH_4, Ag + CH_4 and Au + CH_4 produces the species

$$HMCH_3$$

where M = Mn, Fe, Co, Cu, Zn, Ag or Au. Thus far, no such reactions are observed for Group II elements (Mg or Ca) or for the lighter transition metals--Sc, Ti, V, or Cr. Al and Group III elements are yet to be tried.

The process has been tested with Fe to show that insertion in C_2H_6 to form

$$H - Fe - C_2H_5$$

does occur. Higher alkane reactions are being tried. Among the sorts of interesting ideas for insertion products are

(a) $Fe + C_6H_{14} \longrightarrow H - Fe - C_6H_{13}$

(b) $Fe + C_6H_{12} \longrightarrow$ 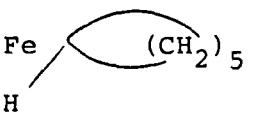

References

1. Y. Pao, "Theory of Acoustic Emission," Elastic Wave and Non-Destructive Testing of Materials, AMD 29, edited by Y. H. Pao, ASME, 1978.

2. G. S. Kino and C. S. DeSilets, "The Design of Slotted Transducer Arrays with Matched Backing," Ultrasonic Imaging 1, 189-209 (1979).

3. G. F. Miller and H. Pursey, "The Field and Radiation Impedance of Mechanical Radiations on the Free Surface of a Semi-Infinite Isotropic Solid," Proc. Roy. Soc. London 223, 521-541 (1954).

4. B. A. Auld, Acoustic Fields and Waves in Solids, Vol. 1, Wiley, 1973.

5. G. S. Kino and R. M. Thomson, "Detection and Evaluation of Small Flaws in Optical Fibers," MRC Report, DARPA Materials Research Council, July 1980.

6. B. Budiansky, D. Drucker, G. S. Kino and J. Rice, "The Pressure Sensitivity of a Clad Optical Fiber," Appl. Optics 18, 4085, Dec. 15, 1979.

7. A. Yariv and H. V. Winsor, Proposal for Detection of Magnetic Fields Through Magnetostructive Perturbation of Optical Fibers, Optics Letters 5, 87, March 1980.

8. T. Yamanishi, K. Yoshimura, S. Seuuki, S. Seikai, and N. Ochida, "Modified Silicone as a New Type of Primary Coat for Optical Fibre," Electronics Letters 16, 3, pp. 100-101 (1980).

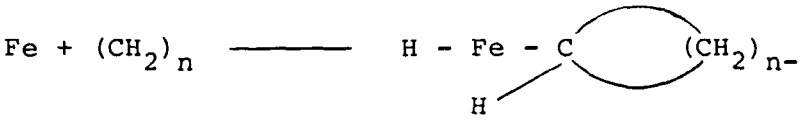

(c)

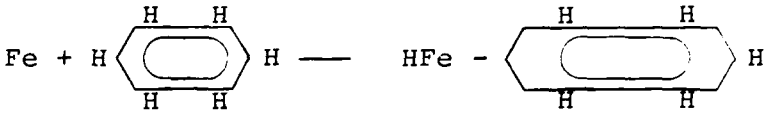

(d) etc., with other metals and other organic species

The organometallic species described here will have high heats of combustion in air or oxygen. Many are already known to be pyrophoric. This family of compounds, with long chain or cyclic hydrocarbon tails on the divalent metal hydride moiety, should provide new ways to achieve higher temperatures and greater specific impulse from propellant systems.

References

1. "Ignition," John D. Clark, Rutgers University Press, New Brunswick, New Jersey (1972).
2. "High Explosives and Propellants," S. Fordham, Second Edition, Pergamon Press (1980).
3. J. W. Kauffman, M. M. Konarski, R. H. Hauge and J. L. Margrave, to be published (1980).

PHASE TRANSITION VERSUS DISORDERED PHASE: A CRITERION DERIVED FROM THE MONTROLL THEORY OF THE TWO DIMENSIONAL FERROMAGNET

H. Reiss and E. W. Montroll

ABSTRACT

Montroll has extended the formalism for the so-called Glauber model of the one dimensional ferromagnet to the two dimensional case involving a simple square lattice of spins. The Glauber model, in one dimension, allows one to follow the spin configuration analytically, kinetically, until equilibrium is established. Reiss was able to extend the Glauber model, in the one dimensional case, to the situation in which the system was being cooled and to obtain analytical solutions for the kinetic behavior even though temperature was changing with time. In this way, the "spin glass" which developed was able to provide some information on quenched-in structures, and these structures were assumed to have some features in common with real glasses. In particular these were features which were independent of the program of cooling. Models with features, independent of cooling program have been used to characterize amorphous systems obtained by very rapid solidification processes. The exact results for the "spin glass" therefore confirmed the usefulness of such models.

(v) Embedded particles are initially stress-free (they are not stabilized by external pressures).

(vi) At a sufficiently high matrix stress, the embedded particle transforms to the monoclinic phase. The transformation does not reverse upon removal of the applied stress.

The mechanical model is based on a polynomial representation of internal energy as a function of transformation shear strain. In turn, the transformation dilatation is presumed to be a function of this shear strain, and equilibrium states are determined by minimization of the Gibbs free energy (at zero temperature). Several key parameters are identified, such as

$$\lambda = \frac{\bar{p}e_1}{|\Delta\phi|} \tag{1}$$

and

$$\rho = \frac{G_1\gamma_1^2}{|\Delta\phi|} \tag{2}$$

where $|\Delta\phi|$ is the energy density release ($\simeq$230 MPa) during room temperature transformation (at zero pressure), and G_1 is the shear modulus associated with λ_1 in the monoclinic phase.

Models consistent with the observed behavior of zirconia, and the estimate $\lambda \simeq 2/3$, have been developed. The experimental evaluation of additional crystal properties (such as G_1, and the cross-stiffness $dp/d\gamma$ in the monoclinic phase) is required to assess the internal consistency of the model or the need for its improvement.

In the two dimensional case the possibility of a phase transition to an ordered state exists and therefore Montroll's formulation contains the seeds of a criterion for determining what kind of cooling program will avoid the phase transition and favor the disordered phase. We have examined this possibility with success.

Montroll's formulation involves a hierachy of sets, of differential-difference equations, each set referring to the spin correlation functions of a given order. Each equation of a set contains a part which is clearly applicable to high temperature processes (and therefore cannot involve the phase transition) and another part involving coupling between correlations of different orders which is ultimately responsible for the transition. The latter part can be bounded by a definite function of reduced time.

The equations containing the bounding function can be solved to give a solution for the spin correlations which contain the part not involving the transition and an upper bound to the part leading to the transition. Thus one can arrive at an upper bound for the amount of ordered phase developable during a given quench.

The results show that if the quench is rapid enough the system is effectively confined to the high temperature phase (even at low temperature). These results should be of use in connection with RSR studies.

METAL HYDRIDE ALKYLS, HYDROXIDES AND ALKOXY DERIVATIVES AS PROPELLANT ADDITIVES

J. L. Margrave, J. W. Kauffman, M. M. Konarski
and R. H. Hauge

ABSTRACT

New high-energy solids can be made by reacting metal atoms with alkanes, alcohols or ethers at low temperatures. These species -- HMR, MMOR and RMOR should be useful additives to propellants to provide higher temperatures and increased impulse.

PHASE TRANSITION VERSUS DISORDERED PHASE: A CRITERION DERIVED FROM THE MONTROLL THEORY OF THE TWO DIMENSIONAL FERROMAGNET

H. Reiss and E. W. Montroll

INTRODUCTION

Montroll[1] has recently established the mathematical framework for the two-dimensional analog of Glauber's treatment[2] of the kinetics of the one-dimensional ferromagnet. This formalism, from which much can be learned without ever solving the equations[1], manifests itself as a hierarchy of differential-difference equations involving the spin correlations. The lowest order set of these equations is for the average values of single spins (the singlet "correlation" function) and contains terms involving the correlation of three spins (triplet correlation functions). The next set of equations in the hierarchy is for the pair correlation function and involves a connection to the quartet correlations. Each set in the hierarchy connects correlation functions of order m and m+2.

The following is a typical equation from the first set

$$\frac{d\langle\sigma_k\rangle}{dt} = -\alpha\langle\sigma_k\rangle + \frac{\alpha\gamma}{4}\{\langle\sigma_{k+i}\rangle+\langle\sigma_{k-i}\rangle+\langle\sigma_{k+j}\rangle+\langle\sigma_{k-j}\rangle\} + \frac{\alpha\delta}{4}\langle\sigma_{k+i}\sigma_{k-i}\sigma_{k+j}\sigma_{k-j}(\sigma_{k+i}+\sigma_{k-i}+\sigma_{k+j}+\sigma_{k-j})\rangle \tag{1}$$

METAL HYDRIDE ALKYLS, HYDROXIDES AND ALKOXY DERIVATIVES AS PROPELLANT ADDITIVES

J. L. Margrave, J. W. Kauffman, M. M. Konarski
and R. H. Hauge

It has become common practice in developing optimum propellant compositions to add small amounts (1-15%) of a reactive metal (Al, Li, Be, Mg, etc.) to increase the heat of combustion and provide other improved properties--higher densities, higher specific impulses, etc. Such additions can be in the form of powdered or flaked pure metals or in the form of their binary hydrides--AlH_3, LiH, BeH_2, MgH_2[m] etc.[1] Actually, the hydrides are often difficult to synthesize and hydrolytically sensitive, so that the metal powders are usually preferred. Slurries of Al in hydrazine/hydrazine nitrate, Be in liquid oxygen to be mixed with liquid hydrogen, Li/$LiBH_4$ gelled with liquid hydrogen and burned with liquid fluorine, or Al or Mg - powders in diesel fuel have all been tested.[1,2] Performances are erratic, but sometimes sensational. Settling out, clogging nozzles and other mechanical problems have limited these systems.

In this note some new syntheses are reported in which gaseous metal atoms are reacted at low temperatures with HOH, ROH, ROR, and RH to form high-energy products.[3] These compounds should be useful propellant additives and are especially attractive since they

In this equation the angular brackets denote ensemble averages and σ is the spin value, +1 or -1. σ_k is the spin at the kth lattice site. The lattice is a two dimensional square lattice with a coordination of 4. Interaction occurs between nearest neighbors only, and the four singlet correlations in the second term on the right are for the four sites, nearest neighbors to the kth. The k+i site is the nearest neighbor in the positive x-direction while k-i lies in the negative x-direction. Sites k+j and k-j lie in the y-direction.

The last term on the right in Eq. (1) contains the connection to the triplet correlations. That these <u>are</u> triplet correlations becomes clear when the term in angular brackets is expanded. Thus consider the first term obtained by such multiplication. It is

$$(\sigma_{k+i})^2 \ \sigma_{k-i}\sigma_{k+j}\sigma_{k-j} \tag{2}$$

clearly $(\sigma_{k+i})^2$ must always be unity, and the term reduced to

$$\sigma_{k-i}\sigma_{k+j}\sigma_{k-j} \tag{3}$$

i.e., to a triplet.

The functions α, γ and δ are of special and central interest. They represent the functions

$$\alpha = \nu_o e^{-\varepsilon/k_B T} \tag{4}$$

$$\gamma = \tfrac{1}{2}\{\tanh \frac{4J}{k_B T} + 2 \tanh \frac{2J}{k_B T}\} \tag{5}$$

$$\delta = \tfrac{1}{2}\{\tanh \frac{4J}{k_B T} - 2 \tanh \frac{2J}{k_B T}\} \tag{6}$$

show limited solubilities in both polar and organic solvents.

Thus, in general, one can write

(a) $M + H_2O \longrightarrow M : \ddot{O}H_2$

$\downarrow h\nu$

HMOH

$\downarrow$ xs metal, $h\nu$

HMOMH or HM_2OH

(b) $M + ROH \longrightarrow M : \ddot{O}(R)(H)$

$\downarrow h\nu$

HMOR (usually preferred over RMOH)

$\downarrow$ xs metal, $h\nu$

HMOMR or HM_2OR

(c) $M + ROR \longrightarrow M : \ddot{O}(R)(R)$

$\downarrow h\nu$

RMOR

$\downarrow$ xs metal, $h\nu$

RMOMR or RM_2OR

In these equations T is temperature, k_B, the Boltzmann constant, and J the exchange integral which couples the spins. The quantity ε is an activation energy for the flipping of spins and ν_0 is a constant (temperature independent) frequency. In Glauber's original model[2] the Arrhenius-like structure for α was not introduced and α simply appeared as a constant. However, Reiss[3] recently extended Glauber's treatment to the case where temperature was changing with time. Some dependence of both the rate and coupling parameters on time then had to be assumed. The basic assumption finally made was that these parameters sensed the temperature of the "heat bath" immediately, and retained their isothermal forms. Their dependences on time were then established through the dependence of temperature on time. For α it was therefore necessary to introduce some form for the isothermal dependence on temperature and the Arrhenius type form was chosen.

For very fast rates of cooling, the dependences on time can (for a real system) only be approximations at best. Nevertheless, any improvement can only be achieved through a disproportionate increase in complexity.

SOME OBVIOUS FEATURES OF THE HIERARCHY

Each set of equations of a given order in the hierarchy has the same basic form. Only the orders of the correlation functions are different. Thus we may confine our remarks to Eq. (1). First, it should be noted that at high temperature δ approaches

Examples of all of these reactions are currently known. In a few cases (Sc, Al, Ti) the neutral adduct does not persist even at liquid He temperatures and direct reactions to form HMOH or $M(OH)_x$ + H_2 or MO + H_2 occur. In other cases (Ni-atoms) no reaction seems to occur. In general, more active metals form adducts and those with absorptions in the visible or UV regions of the spectrum undergo the oxidative insertion to form hydrido-hydroxides, hydrido-alkoxy or alkyl-alkoxy products.

With methane, there is no adduct, but UV-photolysis of Mn + CH_4, Fe + CH_4, Co + CH_4, Cu + CH_4, Zn + CH_4, Ag + CH_4 and Au + CH_4 produces the species

$$HMCH_3$$

where M = Mn, Fe, Co, Cu, Zn, Ag or Au. Thus far, no such reactions are observed for Group II elements (Mg or Ca) or for the lighter transition metals--Sc, Ti, V, or Cr. Al and Group III elements are yet to be tried.

The process has been tested with Fe to show that insertion in C_2H_6 to form

$$H - Fe - C_2H_5$$

does occur. Higher alkane reactions are being tried. Among the sorts of interesting ideas for insertion products are

(a) $Fe + C_6H_{14} \longrightarrow H - Fe - C_6H_{13}$

(b) $Fe + C_6H_{12} \longrightarrow$ 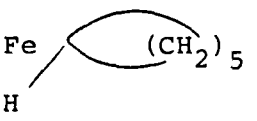

$$\delta \simeq \tfrac{1}{2}\{\tfrac{4J}{kT} - 2(\tfrac{2J}{kT})\} = 0 \qquad (7)$$

and hence vanishes while

$$\gamma \simeq \tfrac{1}{2}\{\tfrac{4J}{kT} + 2(\tfrac{2J}{kT})\} = \tfrac{4J}{kT} \qquad (8)$$

Thus, at high enough temperatures the last term in Eq. (1) may be ignored and the equation fully determines the singlet correlations, the higher order correlations playing no role. The same is true for other sets in the hierarchy. Each set will fully determine the correlation function to which it corresponds; the connections between the various order correlations will have been broken. Since it is these connections which finally lead to phase transitions, there can obviously be no transitions in this limit.

At the other limit - at low temperature - the tanh functions approach unity. Thus

$$\delta \simeq \tfrac{1}{2}\{1-2(1)\} = -\tfrac{1}{2} \qquad (9)$$

and remains bounded. Similarly,

$$\gamma \simeq \tfrac{1}{2}\{1+2(1)\} = \tfrac{3}{2} \qquad (10)$$

Now consider the case where temperature changes with time and the system is quenched, i.e., the case of rapid cooling. If it is possible to conduct the quench rapidly enough, it may happen that the major contribution of δ, as it depends on time, to the overall process will come in a region of temperature where δ is

still very small. In that case the last term of Eq. (1) may be ignored throughout the entire quench (since the terms in the angular brackets are at most of order unity) and the time dependence of the quench may be described using the high temperature formalism alone. This formalism admits of an exact analytical solution, however, again no phase transition is possible. Thus the cooling rate is such that only the disordered phase may be formed and we have a criterion for identifying cooling rates which prevent the establishment of long range order. Actually, as we shall see, this statement must be softened to "a criterion for identifying cooling rates which allow only a certain fraction of the system to undergo the phase transition." However if that fraction is sufficiently small, the transition will have been avoided for all practical purposes.

Thus far our criterion has been only qualitative and perhaps only conceptual. We can however make it more quantitative, and we begin this task in the next section.

FORMAL SOLUTION OF THE SET OF FIRST ORDER EQUATIONS AND A MORE QUANTITATIVE CRITERION

We return to the set of equations generated from Eq. (1) by allowing k to assume values for all lattice sites. Furthermore, we now regard α, γ and δ as appropriate functions of time. We first transform the equations by writing

$$\langle \sigma_k \rangle = U_k e^{-\int_0^t \alpha(t')dt'} \tag{11}$$

PHASE TRANSITION VERSUS DISORDERED PHASE: A CRITERION DERIVED FROM THE MONTROLL THEORY OF THE TWO DIMENSIONAL FERROMAGNET

H. Reiss and E. W. Montroll

ABSTRACT

Montroll has extended the formalism for the so-called Glauber model of the one dimensional ferromagnet to the two dimensional case involving a simple square lattice of spins. The Glauber model, in one dimension, allows one to follow the spin configuration analytically, kinetically, until equilibrium is established. Reiss was able to extend the Glauber model, in the one dimensional case, to the situation in which the system was being cooled and to obtain analytical solutions for the kinetic behavior even though temperature was changing with time. In this way, the "spin glass" which developed was able to provide some information on quenched-in structures, and these structures were assumed to have some features in common with real glasses. In particular these were features which were independent of the program of cooling. Models with features, independent of cooling program have been used to characterize amorphous systems obtained by very rapid solidification processes. The exact results for the "spin glass" therefore confirmed the usefulness of such models.

Then Eq. (1) becomes

$$\frac{dU_k}{dt} = \frac{\alpha\gamma}{4}\left\{U_{k+i}+U_{k-i}+U_{k+j}+U_{k-j}\right\} + \frac{\alpha\delta}{4}\, e^{\int_0^t \alpha dt'} \quad \langle \text{triplet terms} \rangle \qquad (12)$$

The sum of triplet terms can be, at most, of absolute magnitude 4, and so the maximum contribution of the last term in Eq. (12) is bounded by 4 times the coefficient of the angular brackets. Therefore since we are interested in this "maximum" contribution we simplify Eq. (12) to

$$\frac{dU_k}{dt} = \frac{\alpha\gamma}{4}\left\{U_{k+i}+U_{k-i}+U_{k+j}+U_{k-j}\right\} + \alpha\delta e^{\int_0^t \alpha dt'} \qquad (13)$$

Next we define a reduced time,

$$\tau = \tfrac{1}{4}\int_0^t \alpha(t')\gamma(t')dt' \qquad (14)$$

Rewriting Eq. (13) in terms of the reduced time yields

$$\frac{dU_k}{d\tau} = \left\{U_{k+i}+U_{k-i}+U_{k+j}+U_{k-j}\right\} + H(\tau) \qquad (15)$$

where

$$h(\tau) = \frac{4\delta}{\gamma}\, e^{\int_0^t \alpha(t')dt'} \qquad (16)$$

This can be made more explicitly a function of time by noting, from Eq. (14) that

$$\alpha dt = \frac{4d\tau}{\gamma} \qquad (17)$$

In the two dimensional case the possibility of a phase transition to an ordered state exists and therefore Montroll's formulation contains the seeds of a criterion for determining what kind of cooling program will avoid the phase transition and favor the disordered phase. We have examined this possibility with success.

Montroll's formulation involves a hierachy of sets, of differential-difference equations, each set referring to the spin correlation functions of a given order. Each equation of a set contains a part which is clearly applicable to high temperature processes (and therefore cannot involve the phase transition) and another part involving coupling between correlations of different orders which is ultimately responsible for the transition. The latter part can be bounded by a definite function of reduced time.

The equations containing the bounding function can be solved to give a solution for the spin correlations which contain the part not involving the transition and an upper bound to the part leading to the transition. Thus one can arrive at an upper bound for the amount of ordered phase developable during a given quench.

The results show that if the quench is rapid enough the system is effectively confined to the high temperature phase (even at low temperature). These results should be of use in connection with RSR studies.

Then

$$H(\tau) = \frac{4\delta(\tau)}{\gamma(\tau)} e^{4\int_0^\tau \frac{d\tau'}{\gamma(\tau')}} \tag{18}$$

Now the set of equations represented by Eq. (15) may be written in vector form as

$$\frac{d\vec{U}}{d\tau} = \vec{w} + \underset{\sim}{M}\cdot\vec{U} + \vec{1}H(\tau) \tag{19}$$

In this equation $\vec{U}$ is the column symbol consisting of all the U's and $\underset{\sim}{M}$ is a matrix of ones and zeros derived from the coefficients in the second term on the left in Eq. (15). The vector $\vec{w}$ accounts for the possibility that some of the U's may be assigned definite values (boundary conditions). Finally $\vec{1}$ is the unit vector.

The formal solution of Eq. (19) can be given immediately. It is

$$\vec{U} = e^{\tau\underset{\sim}{M}}\cdot U(0) + e^{\tau\underset{\sim}{M}}\cdot\int_0^\tau e^{-\tau'\underset{\sim}{M}}\vec{w}d\tau' + e^{\tau\underset{\sim}{M}}\cdot\int_0^\tau e^{-\tau'\underset{\sim}{M}}\cdot\vec{1}H(\tau')d\tau' \tag{20}$$

It is the last term of this equation which contains the correlations, and it is this term whose magnitude is of primary interest.

This last term may also be expressed as

$$\int_0^\tau e^{(\tau-\tau')\underset{\sim}{M}}\cdot\vec{1}H(\tau')d\tau' \tag{21}$$

However, to truly estimate the influence of the triplet terms on the overall process it is best to generate a specific (non-formal) solution for $\vec{U}$. We accomplish this in the next section.

PHASE TRANSITION VERSUS DISORDERED PHASE: A CRITERION DERIVED FROM THE MONTROLL THEORY OF THE TWO DIMENSIONAL FERROMAGNET

H. Reiss and E. W. Montroll

INTRODUCTION

Montroll[1] has recently established the mathematical framework for the two-dimensional analog of Glauber's treatment[2] of the kinetics of the one-dimensional ferromagnet. This formalism, from which much can be learned without ever solving the equations[1], manifests itself as a hierarchy of differential-difference equations involving the spin correlations. The lowest order set of these equations is for the average values of single spins (the singlet "correlation" function) and contains terms involving the correlation of three spins (triplet correlation functions). The next set of equations in the hierarchy is for the pair correlation function and involves a connection to the quartet correlations. Each set in the hierarchy connects correlation functions of order m and m+2.

The following is a typical equation from the first set

$$\frac{d\langle\sigma_k\rangle}{dt} = -\alpha\langle\sigma_k\rangle + \frac{\alpha\gamma}{4}\{\langle\sigma_{k+i}\rangle+\langle\sigma_{k-i}\rangle+\langle\sigma_{k+j}\rangle+\langle\sigma_{k-j}\rangle\} + \frac{\alpha\delta}{4}\langle\sigma_{k+i}\sigma_{k-i}\sigma_{k+j}\sigma_{k-j}(\sigma_{k+i}+\sigma_{k-i}+\sigma_{k+j}+\sigma_{k-j})\rangle \tag{1}$$

SOLUTION FOR ONE SPIN INITIALLY FIXED

It is easy to generate the solution when one spin is initially fixed so that, for it, $\langle\sigma\rangle = 1$ at t=0. However, we do not hold this spin fixed as time evolves, but rather allow $\langle\sigma\rangle$ to eventually decay to zero.

Holding the spin fixed for all time would involve the use of a non-zero $\vec{w}$ and a somewhat more complicated matrix $\underset{\sim}{M}$.

To obtain the most symmetric matrix $\underset{\sim}{M}$ it is best to order the spins according to the following scheme[4]

$$\begin{array}{l} U_{11}\ U_{12} \text{ ---------- } U_{1N} \\ U_{21}\ U_{22} \text{ ---------- } U_{2N} \\ \quad | \\ \quad | \\ U_{N1}\ U_{N2} \text{ ---------- } U_{NN} \end{array} \qquad (22)$$

where U_{11} is the first component of the vector, U_{1N} the Nth component, U_{21}, the N+1 component, etc., and U_{NN} the N^2 component where the total number of spins is of course N^2. For the case where no spins are held fixed, other than initially, the matrix $\underset{\sim}{M}$ then takes the form

$$\begin{aligned} M_{ij,k\ell} &= 1 \quad , \quad i \neq k \\ &\qquad\qquad\ \ j = \ell \\ &= 1 \quad , \quad i = k \\ &\qquad\qquad\ \ j = \ell \pm 1 \\ &= 0 \quad , \quad \text{otherwise} \end{aligned} \qquad (23)$$

where the index $ij,k\ell$ refers to pairs of subscripts in Eq. (22).

In this equation the angular brackets denote ensemble averages and σ is the spin value, +1 or -1. σ_k is the spin at the kth lattice site. The lattice is a two dimensional square lattice with a coordination of 4. Interaction occurs between nearest neighbors only, and the four singlet correlations in the second term on the right are for the four sites, nearest neighbors to the kth. The k+i site is the nearest neighbor in the positive x-direction while k-i lies in the negative x-direction. Sites k+j and k-j lie in the y-direction.

The last term on the right in Eq. (1) contains the connection to the triplet correlations. That these <u>are</u> triplet correlations becomes clear when the term in angular brackets is expanded. Thus consider the first term obtained by such multiplication. It is

$$(\sigma_{k+i})^2 \ \sigma_{k-i}\sigma_{k+j}\sigma_{k-j} \tag{2}$$

clearly $(\sigma_{k+i})^2$ must always be unity, and the term reduced to

$$\sigma_{k-i}\sigma_{k+j}\sigma_{k-j} \tag{3}$$

i.e., to a triplet.

The functions α, γ and δ are of special and central interest. They represent the functions

$$\alpha = \nu_o e^{-\varepsilon/k_B T} \tag{4}$$

$$\gamma = \tfrac{1}{2}\{\tanh \frac{4J}{k_B T} + 2 \tanh \frac{2J}{k_B T}\} \tag{5}$$

$$\delta = \tfrac{1}{2}\{\tanh \frac{4J}{k_B T} - 2 \tanh \frac{2J}{k_B T}\} \tag{6}$$

The eigenvectors and eigenvalues of this hermitian matrix are well known and form a complete basis. The normalized eigenvectors have components

$$a_{\vec{k}}(\vec{\ell}) = \frac{1}{N} e^{\frac{2\pi i \, \vec{k}\cdot\vec{\ell}}{N}} \tag{24}$$

where $\vec{k}$ is the vector with integer components k_1 and k_2 lying between 0 and N-1 and $\vec{\ell}$ is the vector whose components, ℓ_1, ℓ_2, are one of the subscripts in Eq. (22), also integers, lying between 1 and N. The eigenvectors have, of course, N^2 components. The eigenvalue going with the $\vec{k}$th eigenvector is

$$\lambda_{\vec{k}} = \cos \frac{2\pi k_1}{N} + \cos \frac{2\pi k_2}{N} \tag{25}$$

The appropriate time dependent eigenvectors which satisfy the homogeneous part of Eq. (19) are

$$\lambda_{\vec{k}} = \vec{a}_{\vec{k}} \, e^{\lambda_{\vec{k}}\tau} \tag{26}$$

Setting $\vec{w} = 0$ in Eq. (19), we assume a solution in the form

$$\vec{U} = \sum_{\vec{k}} C_{\vec{k}}(\tau)\vec{\alpha}_{\vec{k}}(\tau) \tag{27}$$

where the sum is a double summation over the components k_1 and k_2 of $\vec{k}$. Substitution of Eq. (20) into Eq. (19) (with $\vec{w}=0$), noting that $\vec{\alpha}_{\vec{k}}$ satisfies the homogeneous equation, taking the scalar product of the result with $\vec{\alpha}_{\vec{s}}^{\,*}$ (where the * indicates complex conjugate), and making use of the ortho-normality condition

$$\vec{\alpha}^{*}_{\vec{s}} \cdot \vec{\alpha}_{\vec{k}} = \delta_{\vec{s},\vec{k}} e^{2\lambda \vec{s} \tau} \tag{28}$$

leads to the differential equation

$$e^{2\lambda_{\vec{s}}\tau} \frac{dC_{\vec{s}}}{d\tau} = \vec{\alpha}^{*}_{\vec{s}} \cdot \vec{I} H(\tau) = H(\tau) e^{\lambda_{\vec{s}}\tau} \sum_{\vec{\ell}} a^{*}_{\vec{s}}(\vec{\ell})$$

or

$$\frac{dC_{\vec{s}}}{d\tau} = \{\sum_{\vec{\ell}} a^{*}_{\vec{s}}(\vec{\ell})\} H(\tau) e^{-\lambda_{\vec{s}}\tau} \tag{29}$$

where the sum is the double sum over ℓ_1 and ℓ_2. Eq. (29) can be integrated immediately to give

$$C_{\vec{s}}(\tau) = C_{\vec{s}}(0) + \{\sum_{\vec{\ell}} a^{*}_{\vec{s}}(\vec{\ell})\} \int_0^{\tau} H(\tau') e^{-\lambda_{\vec{s}}\tau'} d\tau' \tag{30}$$

For the sum we have

$$\sum_{\vec{\ell}} a^{*}_{\vec{s}}(\vec{\ell}) = \frac{1}{N} \sum_{\ell_1=1}^{N} \sum_{\ell_2=1}^{N} e^{-\frac{2\pi i s_1 \ell_1}{N}} e^{-\frac{2\pi i s_2 \ell_2}{N}} = N\delta_{\vec{s},\vec{o}} \tag{31}$$

where δ is the Kronecke delta. Substitution of this result into Eq. (30) gives

$$C_{\vec{s}}(\tau) = C_{\vec{s}}(0) + N\delta_{\vec{s},\vec{o}} \int_0^{\tau} H(\tau') e^{-\lambda_{\vec{s}}\tau'} d\tau' \tag{32}$$

Finally, substitution into Eq. (27) gives

$$\vec{U} = \sum_{\vec{k}} C_{\vec{k}}(0) \vec{\alpha}_{\vec{k}}(\tau) + N \sum_{\vec{k}} \vec{\alpha}_{\vec{k}}(\tau) \delta_{\vec{k},\vec{o}} \int_0^{\tau} H(\tau') e^{-\lambda_{\vec{k}}\tau'} d\tau'$$

$$= \sum_{\vec{k}} C_{\vec{k}}(0) \vec{a}_{\vec{k}} e^{\lambda_{\vec{k}}\tau} + N\vec{a}_{\vec{o}} \int_0^{\tau} e^{\lambda_{\vec{o}}(\tau-\tau')} H(\tau') d\tau'$$

In these equations T is temperature, k_B, the Boltzmann constant, and J the exchange integral which couples the spins. The quantity ε is an activation energy for the flipping of spins and ν_0 is a constant (temperature independent) frequency. In Glauber's original model[2] the Arrhenius-like structure for α was not introduced and α simply appeared as a constant. However, Reiss[3] recently extended Glauber's treatment to the case where temperature was changing with time. Some dependence of both the rate and coupling parameters on time then had to be assumed. The basic assumption finally made was that these parameters sensed the temperature of the "heat bath" immediately, and retained their isothermal forms. Their dependences on time were then established through the dependence of temperature on time. For α it was therefore necessary to introduce some form for the isothermal dependence on temperature and the Arrhenius type form was chosen.

For very fast rates of cooling, the dependences on time can (for a real system) only be approximations at best. Nevertheless, any improvement can only be achieved through a disproportionate increase in complexity.

SOME OBVIOUS FEATURES OF THE HIERARCHY

Each set of equations of a given order in the hierarchy has the same basic form. Only the orders of the correlation functions are different. Thus we may confine our remarks to Eq. (1). First, it should be noted that at high temperature δ approaches

$$= \sum_{\vec{k}} C_{\vec{k}}(0)\vec{a}_{\vec{k}} e^{\lambda_{\vec{k}}\tau} + \vec{I}\int_0^\tau e^{2(\tau-\tau')}H(\tau')d\tau' \tag{33}$$

where we have used the facts that $\lambda_{\vec{0}} = 2$ and that $\vec{a}_{\vec{0}} = \vec{I}/N$.

Now we choose as our initial condition

$$\vec{U}(\vec{\ell}) = \delta_{\ell_1,1}\,\delta_{\ell_2,1} \tag{34}$$

and from Eq. (33) we find

$$\vec{U}(0) = \sum_{\vec{k}} C_{\vec{k}}(0)\vec{\alpha}_{\vec{k}}(0) = \sum_{\vec{k}} C_{\vec{k}}(0)\vec{a}_{\vec{k}} \tag{35}$$

Taking the scalar product with $\vec{a}_{\vec{s}}^{\,*}$ we find

$$\vec{a}_{\vec{s}}^{\,*} \cdot \vec{U}(0) = \vec{a}_{\vec{s}}^{\,*}(1,1) = C_{\vec{s}}(0) \tag{36}$$

where we have used Eq. (34) and the orthonormality condition. Substitution of this result into Eq. (33) then gives

$$\vec{U} = \sum_{\vec{k}} \vec{a}_{\vec{k}}^{\,*}(1,1)\vec{a}_{\vec{k}} e^{\lambda_{\vec{k}}\tau} + \vec{I}\int_0^\tau e^{2(\tau-\tau')}H(\tau')d\tau' \tag{37}$$

Comparing the last terms of Eq. (37) with Eq. (21) shows that the exact solution is obtainable from the formal solution by replacing $\underset{\sim}{M}$ with its largest eigenvalue. Using Eqs. (30) and (31), the first term on the right becomes, for the $\vec{\ell}$th component,

$$\frac{1}{N^2}\left\{\sum_{\vec{k}_1} e^{\frac{2\pi i k_1(\ell_1-1)}{N}} e^{\tau\cos\frac{2\pi k_1}{N}}\right\} \cdot \left\{\sum_{\vec{k}_2} e^{\frac{2\,ik_1(\ell_2-1)}{N}} e^{\tau\cos\frac{2\pi k_2}{N}}\right\} \tag{38}$$

$$\delta \simeq \tfrac{1}{2}\{\tfrac{4J}{kT} - 2(\tfrac{2J}{kT})\} = 0 \qquad (7)$$

and hence vanishes while

$$\gamma \simeq \tfrac{1}{2}\{\tfrac{4J}{kT} + 2(\tfrac{2J}{kT})\} = \tfrac{4J}{kT} \qquad (8)$$

Thus, at high enough temperatures the last term in Eq. (1) may be ignored and the equation fully determines the singlet correlations, the higher order correlations playing no role. The same is true for other sets in the hierarchy. Each set will fully determine the correlation function to which it corresponds; the connections between the various order correlations will have been broken. Since it is these connections which finally lead to phase transitions, there can obviously be no transitions in this limit.

At the other limit - at low temperature - the tanh functions approach unity. Thus

$$\delta \simeq \tfrac{1}{2}\{1-2(1)\} = -\tfrac{1}{2} \qquad (9)$$

and remains bounded. Similarly,

$$\gamma \simeq \tfrac{1}{2}\{1+2(1)\} = \tfrac{3}{2} \qquad (10)$$

Now consider the case where temperature changes with time and the system is quenched, i.e., the case of rapid cooling. If it is possible to conduct the quench rapidly enough, it may happen that the major contribution of δ, as it depends on time, to the overall process will come in a region of temperature where δ is

Making the transformation

$$\theta = \frac{2\pi k_1}{N} \tag{39}$$

and allowing $N \to \infty$, the first bracketed term is easily transformed to the form

$$\frac{N}{\pi} \int_0^{\pi} \{\cos(\ell_1 - 1)\theta\} e^{\tau \cos\theta} d\theta = N I_{\ell_1 - 1}(\tau) \tag{40}$$

with a similar relation for the second bracketed term. $I_{\ell_1 - 1}(\tau)$ is the ℓ_1-1 order Bessel Function of completely imaginary argument. Thus our final solution for the component of Eq. (37) is

$$U(\vec{\ell}) = I_{\ell_1 - 1}(\tau) I_{\ell_2 - 1}(\tau) + \int_0^{\tau} e^{2(\tau - \tau')} H(\tau') d\tau' \tag{41}$$

Introducing this result into Eq. (11) gives

$$\begin{aligned} \langle \sigma_{\vec{\ell}} \rangle = {} & I_{\ell_1 - 1}(\tau) I_{\ell_2 - 1}(\tau) e^{-\int_0^{\tau} \frac{4}{\gamma(\tau')} d\tau'} \\ & + 4 \int_0^{\tau} e^{2(\tau - \tau')} \frac{\delta(\tau')}{\gamma(\tau')} e^{-\int_{\tau_1}^{\tau} \frac{4}{\gamma(\tau'')}} d\tau' \end{aligned} \tag{42}$$

The first term is the high temperature solution, and the second bounds the contributions of the triplet correlations. Depending on the rate of cooling τ will have an upper limit, $\tau = \tau_{max}$. The ratio of the second term on the right, in Eq. (42), to the first term with $\tau = \tau_{max}$ provides a measure of the fraction of phase transition which occurs during the cooling process. For $\vec{\ell} = (1,1)$

still very small. In that case the last term of Eq. (1) may be ignored throughout the entire quench (since the terms in the angular brackets are at most of order unity) and the time dependence of the quench may be described using the high temperature formalism alone. This formalism admits of an exact analytical solution, however, again no phase transition is possible. Thus the cooling rate is such that only the disordered phase may be formed and we have a criterion for identifying cooling rates which prevent the establishment of long range order. Actually, as we shall see, this statement must be softened to "a criterion for identifying cooling rates which allow only a certain fraction of the system to undergo the phase transition." However if that fraction is sufficiently small, the transition will have been avoided for all practical purposes.

Thus far our criterion has been only qualitative and perhaps only conceptual. We can however make it more quantitative, and we begin this task in the next section.

FORMAL SOLUTION OF THE SET OF FIRST ORDER EQUATIONS AND A MORE QUANTITATIVE CRITERION

We return to the set of equations generated from Eq. (1) by allowing k to assume values for all lattice sites. Furthermore, we now regard α, γ and δ as appropriate functions of time. We first transform the equations by writing

$$\langle \sigma_k \rangle = U_k e^{-\int_0^t \alpha(t')dt'} \tag{11}$$

for which $\langle\sigma\rangle$ is initially unity. The measure of the integrated degree of relaxation is $1-\langle\sigma\rangle$. If the fraction of phase transition, relative to the fraction of relaxation, is small then it is fair to say that the relaxation has occurred essentially within the high temperature phase. It would be more appropriate to deal with the problem in which $\langle\sigma\rangle$ for site 1,1 is maintained at unity during the cooling process. As indicated earlier, this is a more complicated problem. Nevertheless, upon cooling, $\langle\sigma_{\vec{\ell}}\rangle$ for each site except $\vec{\ell} = (1,1)$ would indicate a degree of ordering and the ratio of the second to the first term in this case would measure the influence of the phase transition in the ordering process.

THE COOLING PROGRAM

A realistic cooling program[3] is one described by

$$\frac{1}{T} = a + bt \tag{43}$$

where a and b are constants. If a quench is conducted, beginning at a temperature, T_o, then

$$a = \frac{1}{T_o} \tag{44}$$

The quantity b is a measure of the cooling rate. In fact if T_R is room temperature (say 300°K), then

$$b = \frac{1}{t_R}\left\{\frac{1}{T_R} - \frac{1}{T_o}\right\} \tag{45}$$

where t_R is the time required to quench from T_o to T_R. The smaller the value of t_R, the larger is b.

Then Eq. (1) becomes

$$\frac{dU_k}{dt} = \frac{\alpha\gamma}{4}\left\{U_{k+i}+U_{k-i}+U_{k+j}+U_{k-j}\right\} + \frac{\alpha\delta}{4}\, e^{\int_0^t \alpha dt'} \quad \langle \text{triplet terms} \rangle \qquad (12)$$

The sum of triplet terms can be, at most, of absolute magnitude 4, and so the maximum contribution of the last term in Eq. (12) is bounded by 4 times the coefficient of the angular brackets. Therefore since we are interested in this "maximum" contribution we simplify Eq. (12) to

$$\frac{dU_k}{dt} = \frac{\alpha\gamma}{4}\left\{U_{k+i}+U_{k-i}+U_{k+j}+U_{k-j}\right\} + \alpha\delta e^{\int_0^t \alpha dt'} \qquad (13)$$

Next we define a reduced time,

$$\tau = \tfrac{1}{4}\int_0^t \alpha(t')\gamma(t')dt' \qquad (14)$$

Rewriting Eq. (13) in terms of the reduced time yields

$$\frac{dU_k}{d\tau} = \left\{U_{k+i}+U_{k-i}+U_{k+j}+U_{k-j}\right\} + H(\tau) \qquad (15)$$

where

$$h(\tau) = \frac{4\delta}{\gamma}\, e^{\int_0^t \alpha(t')dt'} \qquad (16)$$

This can be made more explicitly a function of time by noting, from Eq. (14) that

$$\alpha dt = \frac{4d\tau}{\gamma} \qquad (17)$$

If we substitute $z = bt$ into Eq. (14) we obtain

$$\tau = \frac{1}{4b} \int_0^{bt} \alpha(z')\gamma(z')dz' \tag{46}$$

Since $\alpha \to 0$ and $\gamma \to 3/2$ as $z' \to \infty$, the integral in Eq. (39) is bounded as $t \to \infty$. Thus τ approaches a maximum value τ_{max} given by

$$\tau_{max} = \frac{1}{4b} \int_0^{\infty} \alpha(z')\gamma(z')dz' \tag{47}$$

and τ_{max} varies inversely with b.

In order to obtain $\langle\sigma\rangle$ at τ_{max} it is convenient to transform Eq. (42) from τ back to t. Then we may write

$$\langle\tau_{\vec{\ell}}\rangle_{max} = I_{\ell_1-1}(\tau_{max}) I_{\ell_2-1}(\tau_{max}) \exp\left[-\int_0^{\infty} \alpha(t')dt'\right]$$

$$+ \int_0^{\infty} \alpha(t')\delta(t') \exp\left\{-\int_0^{\infty} \alpha(t'')[1-\tfrac{1}{2}\gamma(t'')]dt''\right\} dt' \tag{48}$$

with Eq. (43) we have

$$\alpha(t) = \gamma_0 e^{-\frac{\epsilon}{k_B}(a+bt)} \tag{49}$$

$$\gamma(t) = \tfrac{1}{2}\left\{\tanh \frac{4J}{k_B}(a+bt) + 2\tanh \frac{2J}{k_B}(a+bt)\right\} \tag{50}$$

$$\delta(t) = \tfrac{1}{2}\left\{\tanh \frac{4J}{k_B}(a+bt) - 2\tanh \frac{2J}{k_B}(a+bt)\right\} \tag{51}$$

We have examined the following case (identical with that studied in the one dimensional analysis of Ref. 3):

Then

$$H(\tau) = \frac{4\delta(\tau)}{\gamma(\tau)} e^{4\int_0^\tau \frac{d\tau'}{\gamma(\tau')}} \tag{18}$$

Now the set of equations represented by Eq. (15) may be written in vector form as

$$\frac{d\vec{U}}{d\tau} = \vec{w} + \underset{\sim}{M}\cdot\vec{U} + \vec{1}H(\tau) \tag{19}$$

In this equation $\vec{U}$ is the column symbol consisting of all the U's and $\underset{\sim}{M}$ is a matrix of ones and zeros derived from the coefficients in the second term on the left in Eq. (15). The vector $\vec{w}$ accounts for the possibility that some of the U's may be assigned definite values (boundary conditions). Finally $\vec{1}$ is the unit vector.

The formal solution of Eq. (19) can be given immediately. It is

$$\vec{U} = e^{\tau\underset{\sim}{M}}\cdot U(0) + e^{\tau\underset{\sim}{M}}\cdot\int_0^\tau e^{-\tau'\underset{\sim}{M}}\vec{w}d\tau' + e^{\tau\underset{\sim}{M}}\cdot\int_0^\tau e^{-\tau'\underset{\sim}{M}}\cdot\vec{1}H(\tau')d\tau' \tag{20}$$

It is the last term of this equation which contains the correlations, and it is this term whose magnitude is of primary interest.

This last term may also be expressed as

$$\int_0^\tau e^{(\tau-\tau')\underset{\sim}{M}}\cdot\vec{1}H(\tau')d\tau' \tag{21}$$

However, to truly estimate the influence of the triplet terms on the overall process it is best to generate a specific (non-formal) solution for $\vec{U}$. We accomplish this in the next section.

$$T_o = 7500 \text{ deg K or } a = 1.33\times10^{-4} \text{ deg}^{-1} \text{ K}^{-1} \quad (52)$$

$$b = 1.0\times10^{-1},\ 1.0,\ 5.26\times10^{1},\ 1.0\times10^{2},\ 1.0\times10^{3}$$
$$1.0\times10^{4} \text{ deg}^{-1} \text{ K}^{-1} \text{ sec}^{-1} \quad (53)$$

$$\varepsilon = 1.32\times10^{-11} \text{ erg} \quad (54)$$

$$J = 2.08\times10^{-14} \text{ erg} \quad (55)$$

$$\nu_o = 10^{13} \text{ sec}^{-1} \quad (56)$$

The results are summarized in Table 1.

The first column of the Table lists the various b values and the second column indicates the range of cooling rates associated with the quench. The hyperbolic cooling rate specified by Eq. (43) is not constant, but is greater in the high temperature range of the quench. The values of τ_{max} (corresponding to $t = \infty$) are specified in the third column. The quantity $\langle\sigma\rangle_{max^1}$, in the fourth column, stands for the value, at τ_{max}, of the first term in Eq. (48) for the case where $\bar{\ell} = (1,1)$, i.e., for the spin whose value was originally set to unity. This first term is the value of $\langle\sigma\rangle_{max}$ which would be realized if the higher order correlations (leading to the phase transitions) played no role. On the other hand, $|\langle\sigma\rangle_{max^2}|$ stands for the absolute value of the second term in Eq. (48), i.e., for the upper bound to contributions of the higher order correlations. The last column shows the ratio, $|\langle\sigma\rangle_{max^2}|/\langle\sigma\rangle_{max^1}$. This quantity measures the upper bound to the relative contribution of the processes leading to the phase

SOLUTION FOR ONE SPIN INITIALLY FIXED

It is easy to generate the solution when one spin is initially fixed so that, for it, $\langle\sigma\rangle = 1$ at t=0. However, we do not hold this spin fixed as time evolves, but rather allow $\langle\sigma\rangle$ to eventually decay to zero.

Holding the spin fixed for all time would involve the use of a non-zero $\vec{w}$ and a somewhat more complicated matrix $\underset{\sim}{M}$.

To obtain the most symmetric matrix $\underset{\sim}{M}$ it is best to order the spins according to the following scheme[4]

$$\begin{array}{l} U_{11}\ U_{12} \text{ ---------- } U_{1N} \\ U_{21}\ U_{22} \text{ ---------- } U_{2N} \\ \quad | \\ \quad | \\ U_{N1}\ U_{N2} \text{ ---------- } U_{NN} \end{array} \qquad (22)$$

where U_{11} is the first component of the vector, U_{1N} the Nth component, U_{21}, the N+1 component, etc., and U_{NN} the N^2 component where the total number of spins is of course N^2. For the case where no spins are held fixed, other than initially, the matrix $\underset{\sim}{M}$ then takes the form

$$\begin{aligned} M_{ij,k\ell} &= 1 \quad , \quad i \neq k \\ &\qquad\qquad\ \ j = \ell \\ &= 1 \quad , \quad i = k \\ &\qquad\qquad\ \ j = \ell \pm 1 \\ &= 0 \quad , \quad \text{otherwise} \end{aligned} \qquad (23)$$

where the index $ij,k\ell$ refers to pairs of subscripts in Eq. (22).

TABLE 1

b ($deg^{-1}sec^{-1}$)	Range of Cooling Rates (deg sec^{-1})	τ_{max}	$\langle\sigma\rangle_{max_1}$	$\lvert\langle\sigma\rangle_{max_2}\rvert$	$\frac{\lvert\langle\sigma\rangle_{max_2}\rvert}{\langle\sigma\rangle_{max_1}}$
1.0×10^{-1}	10^{6} -10^{3}	6.73×10^{1}	0	3.24×10^{-4}	∞
1.0	10^{7} -10^{4}	6.73	0	2.29×10^{-4}	∞
5.26×10^{1}	10^{8} -10^{5}	1.28×10^{-1}	2.67×10^{-3}	1.13×10^{-4}	4.24×10^{-2}
1.0×10^{2}	10^{9} -10^{6}	6.73×10^{-3}	4.43×10^{-2}	9.65×10^{-5}	2.18×10^{-3}
1.0×10^{3}	10^{10}-10^{7}	6.73×10^{-3}	7.32×10^{-1}	2.25×10^{-5}	3.07×10^{-5}
1.0×10^{4}	10^{11}-10^{8}	6.73×10^{-4}	9.97×10^{-1}	2.52×10^{-6}	2.53×10^{-6}

The eigenvectors and eigenvalues of this hermitian matrix are well known and form a complete basis. The normalized eigenvectors have components

$$a_{\vec{k}}(\vec{\ell}) = \frac{1}{N} e^{\frac{2\pi i \, \vec{k}\cdot\vec{\ell}}{N}} \tag{24}$$

where $\vec{k}$ is the vector with integer components k_1 and k_2 lying between 0 and N-1 and $\vec{\ell}$ is the vector whose components, ℓ_1, ℓ_2, are one of the subscripts in Eq. (22), also integers, lying between 1 and N. The eigenvectors have, of course, N^2 components. The eigenvalue going with the $\vec{k}$th eigenvector is

$$\lambda_{\vec{k}} = \cos \frac{2\pi k_1}{N} + \cos \frac{2\pi k_2}{N} \tag{25}$$

The appropriate time dependent eigenvectors which satisfy the homogeneous part of Eq. (19) are

$$\lambda_{\vec{k}} = \vec{a}_{\vec{k}} \, e^{\lambda_{\vec{k}}\tau} \tag{26}$$

Setting $\vec{w} = 0$ in Eq. (19), we assume a solution in the form

$$\vec{U} = \sum_{\vec{k}} C_{\vec{k}}(\tau)\vec{\alpha}_{\vec{k}}(\tau) \tag{27}$$

where the sum is a double summation over the components k_1 and k_2 of $\vec{k}$. Substitution of Eq. (20) into Eq. (19) (with $\vec{w}=0$), noting that $\vec{\alpha}_{\vec{k}}$ satisfies the homogeneous equation, taking the scalar product of the result with $\vec{\alpha}_{\vec{s}}^{\,*}$ (where the * indicates complex conjugate), and making use of the ortho-normality condition

transition. When the quantity is small it may be assumed that the relaxation of $\langle\sigma\rangle$ takes place almost entirely within the "high temperature disordered phase" in spite of the fact that the quench continues to T = 0.

The quantity $\langle\sigma\rangle_{max_2}$ was of course obtained through the numerical integration of the second term in Eq. (48).

As an example of what can be learned from Table 1, consider the row corresponding to $b = 1.0\times10^{3}$ involving a cooling rate of about 10^{10} deg K sec^{-1}. We note that $\langle\sigma\rangle_{max_1}$ is 0.732 and that $|\langle\sigma\rangle_{max_2}|$, at 2.25×10^{-5}, is so much smaller that $\langle\sigma\rangle_{max_1}$ represents essentially the whole of $\langle\sigma\rangle_{max}$ which must therefore have relaxed considerably from 1.0 to 0.732. However, in spite of this considerable relaxation the ratio in the last column is only 3.07×10^{-5} so that the contributions of processes leading toward the phase transition are negligible. Thus at such a high cooling rate the relaxation occurs essentially within the high temperature phase.

It is instructive to plot the ratio of the last column which, for convenience, may be denoted by ρ, i.e.,

$$\rho = \frac{|\langle\sigma\rangle_{max_2}|}{\langle\sigma\rangle_{max_1}} \tag{57}$$

against b. Actually, in view of the great range of the numbers, it is more convenient to plot the logarithms of these quantities. Such a plot appears in Fig. 1.

The curve rises rapidly with decreasing b and passes off towards infinity at b = 41.6 or log b = 1.6 deg^{-1} sec^{-1} as

$$\vec{\alpha}^{*}_{\vec{s}} \cdot \vec{\alpha}_{\vec{k}} = \delta_{\vec{s},\vec{k}} e^{2\lambda \vec{s} \tau} \tag{28}$$

leads to the differential equation

$$e^{2\lambda_{\vec{s}}\tau} \frac{dC_{\vec{s}}}{d\tau} = \vec{\alpha}^{*}_{\vec{s}} \cdot \vec{I} H(\tau) = H(\tau) e^{\lambda_{\vec{s}}\tau} \sum_{\vec{\ell}} a^{*}_{\vec{s}}(\vec{\ell})$$

or

$$\frac{dC_{\vec{s}}}{d\tau} = \{\sum_{\vec{\ell}} a^{*}_{\vec{s}}(\vec{\ell})\} H(\tau) e^{-\lambda_{\vec{s}}\tau} \tag{29}$$

where the sum is the double sum over ℓ_1 and ℓ_2. Eq. (29) can be integrated immediately to give

$$C_{\vec{s}}(\tau) = C_{\vec{s}}(0) + \{\sum_{\vec{\ell}} a^{*}_{\vec{s}}(\vec{\ell})\} \int_0^{\tau} H(\tau') e^{-\lambda_{\vec{s}}\tau'} d\tau' \tag{30}$$

For the sum we have

$$\sum_{\vec{\ell}} a^{*}_{\vec{s}}(\vec{\ell}) = \frac{1}{N} \sum_{\ell_1=1}^{N} \sum_{\ell_2=1}^{N} e^{-\frac{2\pi i s_1 \ell_1}{N}} e^{-\frac{2\pi i s_2 \ell_2}{N}} = N\delta_{\vec{s},\vec{o}} \tag{31}$$

where δ is the Kronecke delta. Substitution of this result into Eq. (30) gives

$$C_{\vec{s}}(\tau) = C_{\vec{s}}(0) + N\delta_{\vec{s},\vec{o}} \int_0^{\tau} H(\tau') e^{-\lambda_{\vec{s}}\tau'} d\tau' \tag{32}$$

Finally, substitution into Eq. (27) gives

$$\vec{U} = \sum_{\vec{k}} C_{\vec{k}}(0) \vec{\alpha}_{\vec{k}}(\tau) + N \sum_{\vec{k}} \vec{\alpha}_{\vec{k}}(\tau) \delta_{\vec{k},\vec{o}} \int_0^{\tau} H(\tau') e^{-\lambda_{\vec{k}}\tau'} d\tau'$$

$$= \sum_{\vec{k}} C_{\vec{k}}(0) \vec{a}_{\vec{k}} e^{\lambda_{\vec{k}}\tau} + N\vec{a}_{\vec{o}} \int_0^{\tau} e^{\lambda_{\vec{o}}(\tau-\tau')} H(\tau') d\tau'$$

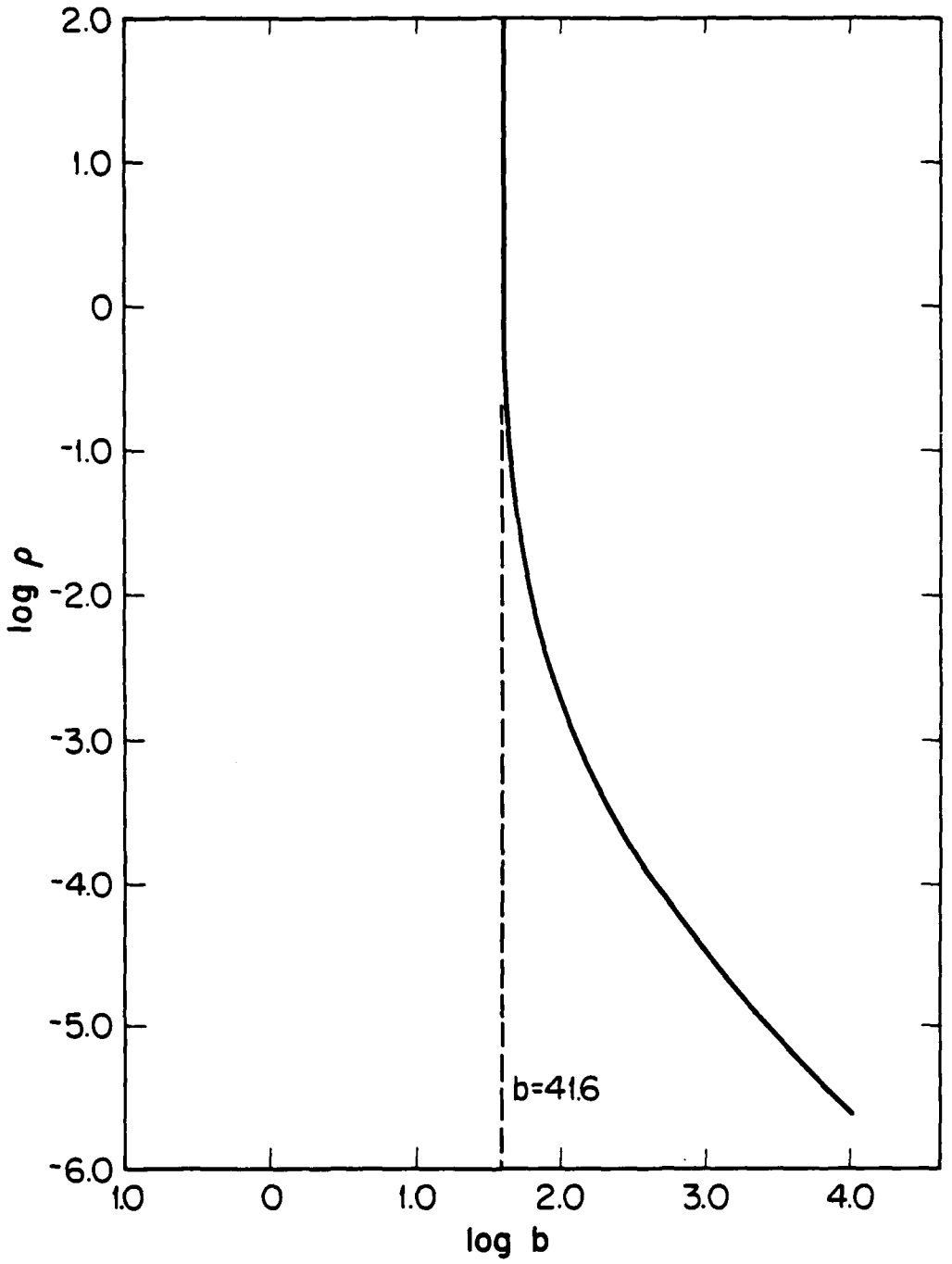

Figure 1. Plot log ρ versus log b showing critical rise of ρ at b = 41.6.

$$= \sum_{\vec{k}} C_{\vec{k}}(0)\vec{a}_{\vec{k}} e^{\lambda_{\vec{k}}\tau} + \vec{I}\int_0^\tau e^{2(\tau-\tau')}H(\tau')d\tau' \tag{33}$$

where we have used the facts that $\lambda_{\vec{0}} = 2$ and that $\vec{a}_{\vec{0}} = \vec{I}/N$.

Now we choose as our initial condition

$$\vec{U}(\vec{\ell}) = \delta_{\ell_1,1}\,\delta_{\ell_2,1} \tag{34}$$

and from Eq. (33) we find

$$\vec{U}(0) = \sum_{\vec{k}} C_{\vec{k}}(0)\vec{\alpha}_{\vec{k}}(0) = \sum_{\vec{k}} C_{\vec{k}}(0)\vec{a}_{\vec{k}} \tag{35}$$

Taking the scalar product with $\vec{a}_{\vec{s}}^{\,*}$ we find

$$\vec{a}_{\vec{s}}^{\,*} \cdot \vec{U}(0) = \vec{a}_{\vec{s}}^{\,*}(1,1) = C_{\vec{s}}(0) \tag{36}$$

where we have used Eq. (34) and the orthonormality condition. Substitution of this result into Eq. (33) then gives

$$\vec{U} = \sum_{\vec{k}} \vec{a}_{\vec{k}}^{\,*}(1,1)\vec{a}_{\vec{k}} e^{\lambda_{\vec{k}}\tau} + \vec{I}\int_0^\tau e^{2(\tau-\tau')}H(\tau')d\tau' \tag{37}$$

Comparing the last terms of Eq. (37) with Eq. (21) shows that the exact solution is obtainable from the formal solution by replacing $\underset{\sim}{M}$ with its largest eigenvalue. Using Eqs. (30) and (31), the first term on the right becomes, for the $\vec{\ell}$th component,

$$\frac{1}{N^2}\left\{\sum_{\vec{k}_1} e^{\frac{2\pi i k_1(\ell_1-1)}{N}} e^{\tau\cos\frac{2\pi k_1}{N}}\right\} \cdot \left\{\sum_{\vec{k}_2} e^{\frac{2\,ik_1(\ell_2-1)}{N}} e^{\tau\cos\frac{2\pi k_2}{N}}\right\} \tag{38}$$

indicated by the broken vertical line. In fact ρ passes through unity ($\log \rho = 0$), from very small to very large values within a very small range of cooling rates. Thus at $b = 100$ deg^{-1} sec^{-1}, $\rho \simeq 0.002$ whereas at $b = 42$ deg^{-1} sec^{-1}, $\rho \simeq 10$. Thus halving the cooling rate increases ρ by a factor of 5000. We may take $\rho = 1$ to mark the point at which the contributions of processes leading to the phase transition make their appearance. This means, effectively, that at the associated cooling rate, the phase transition is, in essence, nucleated. Thus, in the case under discussion the critical (low) cooling rate for nucleation is about 42 deg^{-1} sec^{-1}. At slightly higher rates the system is quenched into the high temperature phase while at slightly lower rates it is quenched to the low temperature phase.

All of this is consistent with the usual tradition surrounding processes of nucleation. We are forced to deal with a kinetic phenomenon whose rate varies over a very large range, as an external variable is changed. The value of the variable when the rate passes through the "laboratory" time frame is usually defined as the "critical" value. However, in the more conventional system we consider the rate of transformation at different fixed values of the variable (e.g., fixed temperatures). Here we try to change the <u>variable</u> at rates both smaller and larger than the nucleation rate in order to bound that rate and thus determine it.

It should be borne in mind that the curve in Fig. 1 is only an upper <u>bound</u>. Nevertheless, granting this, the current treatment probably represents the first fully rigorous treatment

Making the transformation

$$\theta = \frac{2\pi k_1}{N} \tag{39}$$

and allowing $N \to \infty$, the first bracketed term is easily transformed to the form

$$\frac{N}{\pi} \int_0^{\pi} \{\cos(\ell_1 - 1)\theta\} e^{\tau \cos\theta} d\theta = N I_{\ell_1 - 1}(\tau) \tag{40}$$

with a similar relation for the second bracketed term. $I_{\ell_1 - 1}(\tau)$ is the ℓ_1-1 order Bessel Function of completely imaginary argument. Thus our final solution for the component of Eq. (37) is

$$U(\vec{\ell}) = I_{\ell_1 - 1}(\tau) I_{\ell_2 - 1}(\tau) + \int_0^{\tau} e^{2(\tau - \tau')} H(\tau') d\tau' \tag{41}$$

Introducing this result into Eq. (11) gives

$$\begin{aligned} \langle \sigma_{\vec{\ell}} \rangle = {} & I_{\ell_1 - 1}(\tau) I_{\ell_2 - 1}(\tau) e^{-\int_0^{\tau} \frac{4}{\gamma(\tau')} d\tau'} \\ & + 4 \int_0^{\tau} e^{2(\tau - \tau')} \frac{\delta(\tau')}{\gamma(\tau')} e^{-\int_{\tau_1}^{\tau} \frac{4}{\gamma(\tau'')}} d\tau' \end{aligned} \tag{42}$$

The first term is the high temperature solution, and the second bounds the contributions of the triplet correlations. Depending on the rate of cooling τ will have an upper limit, $\tau = \tau_{max}$. The ratio of the second term on the right, in Eq. (42), to the first term with $\tau = \tau_{max}$ provides a measure of the fraction of phase transition which occurs during the cooling process. For $\vec{\ell} = (1,1)$

of a nucleation process, albeit in a specialized model. It should also be noted that if the phase transition occurs the equilibrium value of $\langle\sigma\rangle$ at $T = 0$ need not be zero.

ACKNOWLEDGEMENT

This research was supported by the Defense Advanced Research Projects Agency of the Department of Defense under Contract No. MDA903-80C-0505 with The University of Michigan.

References

1. E. W. Montroll, these Proceedings.
2. R. J. Glauber, J. Math. Phys. 4, 294(1963).
3. H. Reiss, Chemical Physics 47, 15(1980).
4. Advice of E. W. Montroll.

for which $\langle\sigma\rangle$ is initially unity. The measure of the integrated degree of relaxation is $1-\langle\sigma\rangle$. If the fraction of phase transition, relative to the fraction of relaxation, is small then it is fair to say that the relaxation has occurred essentially within the high temperature phase. It would be more appropriate to deal with the problem in which $\langle\sigma\rangle$ for site 1,1 is maintained at unity during the cooling process. As indicated earlier, this is a more complicated problem. Nevertheless, upon cooling, $\langle\sigma_{\vec{\ell}}\rangle$ for each site except $\vec{\ell} = (1,1)$ would indicate a degree of ordering and the ratio of the second to the first term in this case would measure the influence of the phase transition in the ordering process.

THE COOLING PROGRAM

A realistic cooling program[3] is one described by

$$\frac{1}{T} = a + bt \tag{43}$$

where a and b are constants. If a quench is conducted, beginning at a temperature, T_o, then

$$a = \frac{1}{T_o} \tag{44}$$

The quantity b is a measure of the cooling rate. In fact if T_R is room temperature (say 300°K), then

$$b = \frac{1}{t_R}\left\{\frac{1}{T_R} - \frac{1}{T_o}\right\} \tag{45}$$

where t_R is the time required to quench from T_o to T_R. The smaller the value of t_R, the larger is b.

ELASTIC WAVE EMISSION FROM DAMAGE PROCESSES

J. R. Rice

ABSTRACT

The theory of elastic wave emission (i.e., acoustic emission, AE) from damage processes such as slip and microcracking is discussed. Analogous developments in the literature on earthquake seismology and dynamic dislocation theory are noted and utilized. A general representation of the displacement field of an AE event is given in terms of the double couple response to a distribution of "moment density tensor" in the source region. Results are specialized to a point source model and to a general far-field analysis of outgoing elastic waves, and conditions for validity of such representations and their low-frequency specializations are noted. Emitted wave fields are compared for tensile opening and slip events, and procedures which might enable the approximate determination of the size or area increase of tensile microcracks are discussed.

If we substitute $z = bt$ into Eq. (14) we obtain

$$\tau = \frac{1}{4b} \int_0^{bt} \alpha(z')\gamma(z')dz' \tag{46}$$

Since $\alpha \to 0$ and $\gamma \to 3/2$ as $z' \to \infty$, the integral in Eq. (39) is bounded as $t \to \infty$. Thus τ approaches a maximum value τ_{max} given by

$$\tau_{max} = \frac{1}{4b} \int_0^{\infty} \alpha(z')\gamma(z')dz' \tag{47}$$

and τ_{max} varies inversely with b.

In order to obtain $\langle\sigma\rangle$ at τ_{max} it is convenient to transform Eq. (42) from τ back to t. Then we may write

$$\langle\tau_{\vec{\ell}}\rangle_{max} = I_{\ell_1-1}(\tau_{max}) I_{\ell_2-1}(\tau_{max}) \exp\left[-\int_0^{\infty} \alpha(t')dt'\right]$$

$$+ \int_0^{\infty} \alpha(t')\delta(t') \exp\left\{-\int_0^{\infty} \alpha(t'')[1-\tfrac{1}{2}\gamma(t'')]dt''\right\} dt' \tag{48}$$

with Eq. (43) we have

$$\alpha(t) = \gamma_0 e^{-\frac{\epsilon}{k_B}(a+bt)} \tag{49}$$

$$\gamma(t) = \tfrac{1}{2}\left\{\tanh \frac{4J}{k_B}(a+bt) + 2\tanh \frac{2J}{k_B}(a+bt)\right\} \tag{50}$$

$$\delta(t) = \tfrac{1}{2}\left\{\tanh \frac{4J}{k_B}(a+bt) - 2\tanh \frac{2J}{k_B}(a+bt)\right\} \tag{51}$$

We have examined the following case (identical with that studied in the one dimensional analysis of Ref. 3):

ELASTIC WAVE EMISSION FROM DAMAGE PROCESSES

J. R. Rice

INTRODUCTION

Acoustic emission (AE) is concerned with the detection of elastic waves generated by what might generically be termed "damage" processes in stressed solids. These processes may consist of various types of inelastic deformations (slip, twinning, phase transformations) and microcracking. In order to advance the opportunities for quantitative study of damage processes by AE, it is important to have available the relation of processes in the source region (e.g., the location, spatial extent, orientation and time-dependence of a slip or cracking event) to the resulting elastic wave field. The presentation of such relations, especially for microcracking and slip processes, is the concern of this paper.

The relation of source processes to elastic wave fields is, of course, a major concern of earthquake seismology. Accordingly, major references for the present study are provided by analyses of wave generation by seismic sources; this literature has been summarized recently in portions of a book on quantitative seismology by Aki and Richards (1980) and in a review on the mechanics of earthquake rupture by Rice (1980). While no attempt is made here to comprehensively review the relevant

$$T_o = 7500 \text{ deg K or } a = 1.33\times10^{-4} \text{ deg}^{-1} \text{ K}^{-1} \quad (52)$$

$$b = 1.0\times10^{-1},\ 1.0,\ 5.26\times10^{1},\ 1.0\times10^{2},\ 1.0\times10^{3}$$
$$1.0\times10^{4} \text{ deg}^{-1} \text{ K}^{-1} \text{ sec}^{-1} \quad (53)$$

$$\varepsilon = 1.32\times10^{-11} \text{ erg} \quad (54)$$

$$J = 2.08\times10^{-14} \text{ erg} \quad (55)$$

$$\nu_o = 10^{13} \text{ sec}^{-1} \quad (56)$$

The results are summarized in Table 1.

The first column of the Table lists the various b values and the second column indicates the range of cooling rates associated with the quench. The hyperbolic cooling rate specified by Eq. (43) is not constant, but is greater in the high temperature range of the quench. The values of τ_{max} (corresponding to $t = \infty$) are specified in the third column. The quantity $\langle\sigma\rangle_{max^1}$, in the fourth column, stands for the value, at τ_{max}, of the first term in Eq. (48) for the case where $\bar{\ell} = (1,1)$, i.e., for the spin whose value was originally set to unity. This first term is the value of $\langle\sigma\rangle_{max}$ which would be realized if the higher order correlations (leading to the phase transitions) played no role. On the other hand, $|\langle\sigma\rangle_{max^2}|$ stands for the absolute value of the second term in Eq. (48), i.e., for the upper bound to contributions of the higher order correlations. The last column shows the ratio, $|\langle\sigma\rangle_{max^2}|/\langle\sigma\rangle_{max^1}$. This quantity measures the upper bound to the relative contribution of the processes leading to the phase

literature, a brief summary of key papers should perhaps begin with the adaption to shear faults by Vvedenskaya (1956) of Nabarro's (1951) solution for a dynamically introduced dislocation, with DeHoop's (1958) development of an elastodynamic representation theorem for radiation from surfaces of displacement discontinuity, and with the refinement of the theory of double-couple representations of seismic sources by Burridge and Knopoff (1964). Other notable contributions are the development of the seismic moment parameter by Maruyama (1963) and Aki (1966) for characterizing far-fields of sources, its generalization by Kostrov (1973, 1974) who noted that a second-rank moment tensor characterized the far-field for general sources (see also Backus and Mulcahy, 1976), and the application of the general formulations to analyze radiation from spreading dislocations by Haskell (1964, 1966) and from spreading cracks by Richards (1973, 1976) and Madariaga (1976, 1977). Brune, et al. (1979) have recently summarized work on inference of source size from high frequency properties of far-field spectra.

These or analogous elastodynamic developments from crystal dislocation theory (e.g., the work of Mura, 1968) have been used in developing the theory of AE. A noteworthy paper is that of Malén and Bolin (1974), and subsequent work has been reported by Simmons and Clough (1976, 1980), Hsu, et al. (1977), Pao (1978), and Wadley, et al. (1980). These works are focused on a point-source model and hence eliminate information on propagation through the source region (such information may be of limited relevance for

TABLE 1

b ($deg^{-1}sec^{-1}$)	Range of Cooling Rates (deg sec^{-1})	τ_{max}	$\langle\sigma\rangle_{max_1}$	$\lvert\langle\sigma\rangle_{max_2}\rvert$	$\frac{\lvert\langle\sigma\rangle_{max_2}\rvert}{\langle\sigma\rangle_{max_1}}$
1.0×10^{-1}	10^{6} -10^{3}	6.73×10^{1}	0	3.24×10^{-4}	∞
1.0	10^{7} -10^{4}	6.73	0	2.29×10^{-4}	∞
5.26×10^{1}	10^{8} -10^{5}	1.28×10^{-1}	2.67×10^{-3}	1.13×10^{-4}	4.24×10^{-2}
1.0×10^{2}	10^{9} -10^{6}	6.73×10^{-3}	4.43×10^{-2}	9.65×10^{-5}	2.18×10^{-3}
1.0×10^{3}	10^{10}-10^{7}	6.73×10^{-3}	7.32×10^{-1}	2.25×10^{-5}	3.07×10^{-5}
1.0×10^{4}	10^{11}-10^{8}	6.73×10^{-4}	9.97×10^{-1}	2.52×10^{-6}	2.53×10^{-6}

typical materials, however, because of problems with high frequency signal propagation through microscale heterogeneities such as grains). Also, the relation of source parameters such as microcrack size and orientation to properties of the emitted wave fields have not yet been very fully documented. The utility of results of this type is of course dependent on existing practical limitations on the detectability of AE signals, but it seems advisable to have available the principal features of results on how AE fields are related to processes of damage. For slip processes key results can be read off with little alteration from the seismic source literature, whereas for cracking processes some new results are derived here.

Source Representation

This section follows closely the presentation by Rice (1980). The equations governing displacements $\underline{u}$ of a continuum of mass density ρ are

$$\partial\sigma_{\alpha\beta}/\partial x_\alpha + f_\beta = \rho\ \partial^2 u_\beta/\partial t^2 \quad , \tag{1}$$

and for linear elastic response stress $\underline{\sigma}$ is related to strain $\underline{\varepsilon}$ by a modulus tensor $\underline{C}$ such that

$$\sigma_{\alpha\beta} = C_{\alpha\beta\gamma\delta}\ \varepsilon_{\gamma\delta} \quad \text{where } 2\varepsilon_{\gamma\delta} = \partial u_\gamma/\partial x_\delta + \partial u_\delta/\partial x_\delta \quad . \tag{2}$$

The tensor $\underline{C}$ is taken to be that for a homogeneous body or at least one with smoothly varying properties on the macroscale; microscale heterogeneities such as individual grains are ignored, which implies a limitation of results to wavelengths that are

transition. When the quantity is small it may be assumed that the relaxation of $\langle\sigma\rangle$ takes place almost entirely within the "high temperature disordered phase" in spite of the fact that the quench continues to T = 0.

The quantity $\langle\sigma\rangle_{max_2}$ was of course obtained through the numerical integration of the second term in Eq. (48).

As an example of what can be learned from Table 1, consider the row corresponding to $b = 1.0\times10^{3}$ involving a cooling rate of about 10^{10} deg K sec^{-1}. We note that $\langle\sigma\rangle_{max_1}$ is 0.732 and that $|\langle\sigma\rangle_{max_2}|$, at 2.25×10^{-5}, is so much smaller that $\langle\sigma\rangle_{max_1}$ represents essentially the whole of $\langle\sigma\rangle_{max}$ which must therefore have relaxed considerably from 1.0 to 0.732. However, in spite of this considerable relaxation the ratio in the last column is only 3.07×10^{-5} so that the contributions of processes leading toward the phase transition are negligible. Thus at such a high cooling rate the relaxation occurs essentially within the high temperature phase.

It is instructive to plot the ratio of the last column which, for convenience, may be denoted by ρ, i.e.,

$$\rho = \frac{|\langle\sigma\rangle_{max_2}|}{\langle\sigma\rangle_{max_1}} \tag{57}$$

against b. Actually, in view of the great range of the numbers, it is more convenient to plot the logarithms of these quantities. Such a plot appears in Fig. 1.

The curve rises rapidly with decreasing b and passes off towards infinity at b = 41.6 or log b = 1.6 deg^{-1} sec^{-1} as

large compared to grain size. The displacement field generated by an arbitrary distribution of body force $\underline{f}$ throughout some volume V is written as

$$u_\nu(\underline{x},t) = \int_{-\infty}^{t} \int_V G_{\nu\beta}(\underline{x},\underline{x}',t-t') f_\beta(\underline{x}',t') d^3\underline{x}' dt' \quad , \tag{3}$$

which defines the Green's function $G_{\nu\beta}(\underline{x},\underline{x}',t)$ for the medium.

Disturbances associated with the alteration of matter (which in degeneate cases may include slip and/or crack opening, and are collectively called damage here) can be regarded as being generated by a "transformation" strain $\underline{\varepsilon}^T$. This is <u>defined</u> so that $\underline{\sigma}$ and $\underline{\varepsilon}$ satisfy

$$\sigma_{\alpha\beta} = C_{\alpha\beta\gamma\delta}(\varepsilon_{\gamma\delta} - \varepsilon^T_{\gamma\delta}) \tag{4}$$

throughout the source region where C is the same modulus tensor as existed before the damage process. In the special cases of concern here for which the source process involve the generation of a displacement discontinuity on a discrete surface S (a surface of slip or cracking), but elastic behavior elsehwere, $\underline{\varepsilon}^T$ is Dirac singular on S. In particular, if the sides of S are labelled + and -, and if $\underline{n}$ is the normal to S directed from - to + and Δu is defined on S as $\underline{u}^+ - \underline{u}^-$, then for any small volume δV intersected by δS of surface,

$$\int_{\delta V} \varepsilon^T_{\alpha\beta} \, d^3\underline{x} = \tfrac{1}{2}(n_\alpha \, \Delta u_\beta + n_\beta \, \Delta u_\alpha)\delta S \quad . \tag{5}$$

Hence, for surface discontinuities one writes

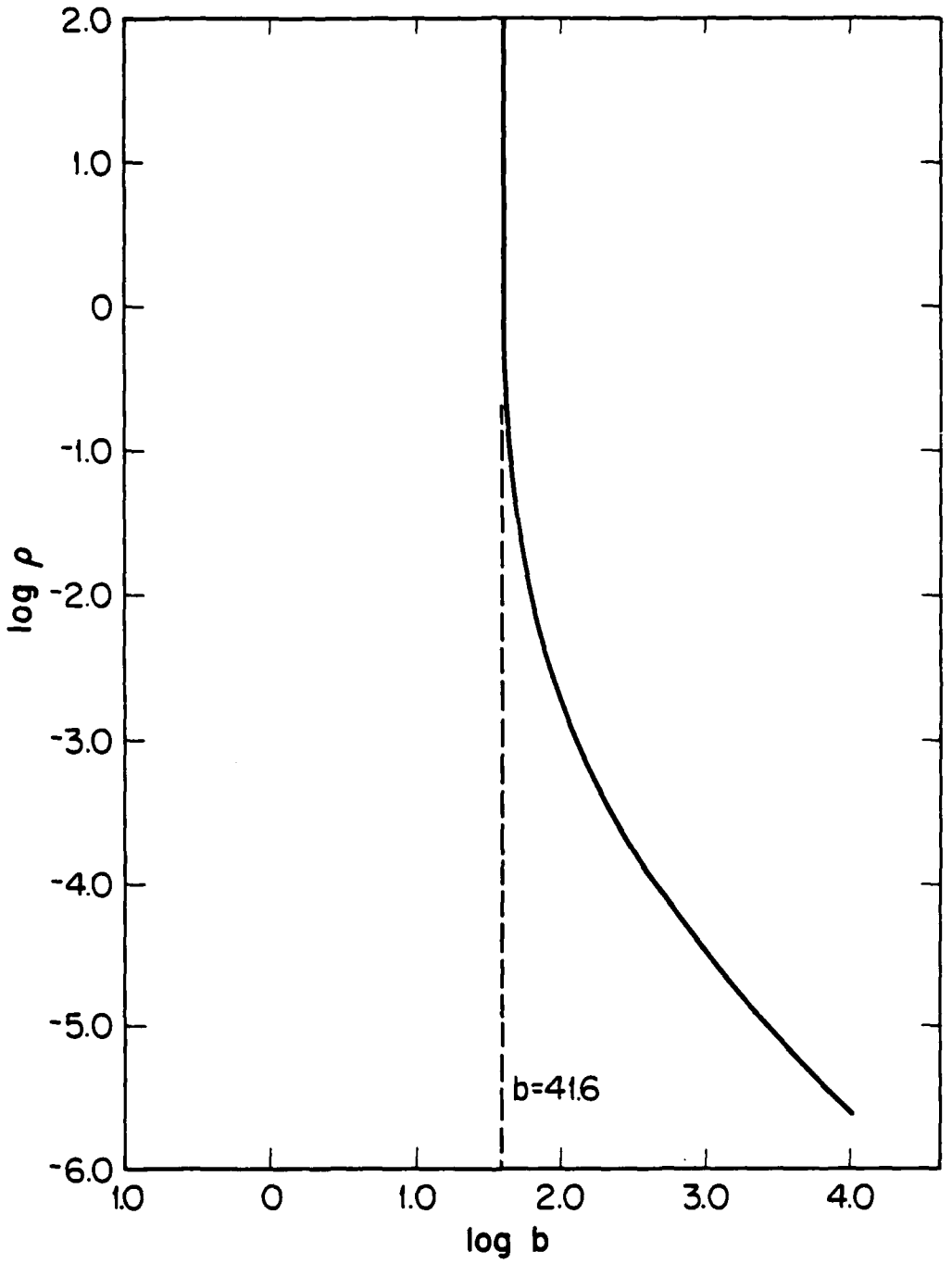

Figure 1. Plot log ρ versus log b showing critical rise of ρ at b = 41.6.

$$\varepsilon^{T}_{\alpha\beta} = \tfrac{1}{2}(n_\alpha \, \Delta u_\beta + n_\beta \, \Delta u_\alpha)\delta_D(S) \qquad (6)$$

where $\delta_D(S)$ is a surface Dirac function, converting any volume integral over a region intersected by some part of S to a surface integral over that part of S.

By using Eq. (4) in (1) and identifying an effective

indicated by the broken vertical line. In fact ρ passes through unity ($\log \rho = 0$), from very small to very large values within a very small range of cooling rates. Thus at $b = 100$ deg^{-1} sec^{-1}, $\rho \simeq 0.002$ whereas at $b = 42$ deg^{-1} sec^{-1}, $\rho \simeq 10$. Thus halving the cooling rate increases ρ by a factor of 5000. We may take $\rho = 1$ to mark the point at which the contributions of processes leading to the phase transition make their appearance. This means, effectively, that at the associated cooling rate, the phase transition is, in essence, nucleated. Thus, in the case under discussion the critical (low) cooling rate for nucleation is about 42 deg^{-1} sec^{-1}. At slightly higher rates the system is quenched into the high temperature phase while at slightly lower rates it is quenched to the low temperature phase.

All of this is consistent with the usual tradition surrounding processes of nucleation. We are forced to deal with a kinetic phenomenon whose rate varies over a very large range, as an external variable is changed. The value of the variable when the rate passes through the "laboratory" time frame is usually defined as the "critical" value. However, in the more conventional system we consider the rate of transformation at different fixed values of the variable (e.g., fixed temperatures). Here we try to change the <u>variable</u> at rates both smaller and larger than the nucleation rate in order to bound that rate and thus determine it.

It should be borne in mind that the curve in Fig. 1 is only an upper <u>bound</u>. Nevertheless, granting this, the current treatment probably represents the first fully rigorous treatment

$$\tilde{f}(\underline{x},\omega) = \int_{-\infty}^{+\infty} f(\underline{x},t)e^{-i\omega t}\,dt \quad , \tag{10}$$

and recalling that time-convolutions of functions transform to products, one has the frequency version of Eq. (7) as

$$\tilde{u}_\nu(\underline{x},\omega) = \int_V \tilde{H}_{\nu\alpha\beta}(\underline{x},\underline{x}',\omega)\tilde{m}_{\alpha\beta}(x',\omega)d^3\underline{x}' \quad . \tag{11}$$

It is convenient in using this representation to observe that

$$\tilde{\dot{m}}_{\alpha\beta}(\underline{x},\omega) = i\omega\,\tilde{m}_{\alpha\beta}(\underline{x},\omega) \quad , \tag{12}$$

where $\dot{m}_{\alpha\beta}(\underline{x},t)$ is the time rate of $m_{\alpha\beta}(\underline{x},t)$, so that the expression can be written as

$$\tilde{u}_\nu(\underline{x},\omega) = \int_V [(1/i\omega)H_{\nu\alpha\beta}(\underline{x},\underline{x}',\omega)]\,\tilde{\dot{m}}_{\alpha\beta}(\underline{x}',\omega)d^3\underline{x}' \quad . \tag{13}$$

Here the quantity in brackets is the transform of

$$\int_{o-}^{t} H_{\nu\alpha\beta}(\underline{x},\underline{x}',\tau)d\tau$$

which is the response to double couples without moments formed from forces which are suddenly applied and held constant for subsequent time, rather than from impulses. The representation of Eq. (13) is more convenient than Eq. (11), since the limit of the bracketed term in Eq. (13) defines a non-zero function of position in the limit $\omega\to o$.

of a nucleation process, albeit in a specialized model. It should also be noted that if the phase transition occurs the equilibrium value of $\langle\sigma\rangle$ at $T = 0$ need not be zero.

ACKNOWLEDGEMENT

This research was supported by the Defense Advanced Research Projects Agency of the Department of Defense under Contract No. MDA903-80C-0505 with The University of Michigan.

References

1. E. W. Montroll, these Proceedings.
2. R. J. Glauber, J. Math. Phys. 4, 294(1963).
3. H. Reiss, Chemical Physics 47, 15(1980).
4. Advice of E. W. Montroll.

Point-Source Model

Let the origin of coordinates be chosen somewhere in or very near to the source region. If the spatial extent of the source is small compared to the distance r_o ($=|\underline{x}|$) to the receiver position, Eq. (13) is suggestive of a "point-source" model in which the resulting field is written as

$$\tilde{u}_\nu(\underline{x},\omega) \simeq [(1/i\omega)H_{\nu\alpha\beta}(\underline{x},\underline{o},\omega)]\ \tilde{\dot{M}}_{\alpha\beta}(\omega) \tag{14}$$

where

$$M_{\alpha\beta}(t) = \int_V m_{\alpha\beta}(\underline{x},t)d^3\underline{x} = \int_V C_{\alpha\beta\gamma\delta}\ \varepsilon^T_{\gamma\delta}(\underline{x},t)d^3\underline{x} \tag{15}$$

for general sources or, in the case of planar discontinuities,

$$M_{\alpha\beta}(t) = \int_S C_{\alpha\beta\gamma\delta}\ n_\gamma(\underline{x})\ \Delta u_\delta(\underline{x},t)d^2\underline{x} \tag{16}$$

This quantity $M_{\alpha\beta}$ is referred to as the (seismic) moment tensor of the source.

It is important to have a clear understanding of the approximation involved in Eq. (14). Obviously, it is assumed that $r_o/a >> 1$, where a is some typical radius of the source region. There is, however, also a frequency restriction involved in using Eq. (14) in that wavelengths involved must be large compared to a. This seems not always to be well understood but will be clearer when specific forms of Eq. (7) or (13) for an unbounded isotropic solid are considered next. Essentially, the high frequency portions of the radiated signal are sensitive to the spatial distribution of origins in the source zone from which

ELASTIC WAVE EMISSION FROM DAMAGE PROCESSES

J. R. Rice

ABSTRACT

The theory of elastic wave emission (i.e., acoustic emission, AE) from damage processes such as slip and microcracking is discussed. Analogous developments in the literature on earthquake seismology and dynamic dislocation theory are noted and utilized. A general representation of the displacement field of an AE event is given in terms of the double couple response to a distribution of "moment density tensor" in the source region. Results are specialized to a point source model and to a general far-field analysis of outgoing elastic waves, and conditions for validity of such representations and their low-frequency specializations are noted. Emitted wave fields are compared for tensile opening and slip events, and procedures which might enable the approximate determination of the size or area increase of tensile microcracks are discussed.

ELASTIC WAVE EMISSION FROM DAMAGE PROCESSES

J. R. Rice

INTRODUCTION

Acoustic emission (AE) is concerned with the detection of elastic waves generated by what might generically be termed "damage" processes in stressed solids. These processes may consist of various types of inelastic deformations (slip, twinning, phase transformations) and microcracking. In order to advance the opportunities for quantitative study of damage processes by AE, it is important to have available the relation of processes in the source region (e.g., the location, spatial extent, orientation and time-dependence of a slip or cracking event) to the resulting elastic wave field. The presentation of such relations, especially for microcracking and slip processes, is the concern of this paper.

The relation of source processes to elastic wave fields is, of course, a major concern of earthquake seismology. Accord-

literature, a brief summary of key papers should perhaps begin with the adaption to shear faults by Vvedenskaya (1956) of Nabarro's (1951) solution for a dynamically introduced dislocation, with DeHoop's (1958) development of an elastodynamic representation theorem for radiation from surfaces of displacement discontinuity, and with the refinement of the theory of double-couple representations of seismic sources by Burridge and Knopoff (1964). Other notable contributions are the development of the seismic moment parameter by Maruyama (1963) and Aki (1966) for character-

Then the solution for a step-function point source $M_{\alpha\beta}$ (this corresponds to using $M_{\alpha\beta}(t_r)$ and ignoring information in oscillation frequencies higher than those for which $e^{i\omega t_r} \simeq 1$) applied at t=o is

$$\underline{u}(\underline{x},t) = \sum_k M_{\alpha\beta}\varepsilon^{(k)}_{\alpha\beta}\ \underline{u}^{(k)}(\underline{x})\{1-\cos\ \omega^{(k)}t\}/\{\omega^{(k)}\}^2 \qquad (22)$$

where $\varepsilon^{(k)}_{\alpha\beta}$ is the strain in the k^{th} mode at the place of the point source. For linear damping without coupling between modes the time dependent terms become (approximately, for light damping)

$$1 - \exp(-\omega^{(k)}t/2Q^{(k)})\ \cos\ \omega^{(k)}t$$

where $Q^{(k)}$ is the quality factor for damping in the k^{th} mode. This form shows also how the long-time static field evolves.

Far-field Results for Isotropic Homogeneous Bodies

Here results are given for the displacement field at points distant from the source in an otherwise isotropic and homogeneous material. The results presented are for outgoing waves from the source region, calculated as if the source resided in an unbounded body. They apply until wave reflections from boundaries intervene, but do not include the reflection and waveguide effects associated with finite regions.

In this case $\underline{u}$ can be written as a sum of dilational ($\underline{u}^d$) and shear (u^s) contributions,

$$\underline{u}(\underline{x},t) = \underline{u}^d(\underline{x},t) + \underline{u}^s(\underline{x},t) \quad . \qquad (23)$$

These are given by (e.g., Rice, 1980, or equivalent expressions

typical materials, however, because of problems with high frequency signal propagation through microscale heterogeneities such as grains). Also, the relation of source parameters such as microcrack size and orientation to properties of the emitted wave fields have not yet been very fully documented. The utility of results of this type is of course dependent on existing practical limitations on the detectability of AE signals, but it seems advisable to have available the principal features of results on how AE fields are related to processes of damage. For slip processes key results can be read off with little alteration from the seismic source literature, whereas for cracking processes some new results are derived here.

Source Representation

This section follows closely the presentation by Rice (1980). The equations governing displacements $\underline{u}$ of a continuum of mass density ρ are

$$\partial\sigma_{\alpha\beta}/\partial x_\alpha + f_\beta = \rho\ \partial^2 u_\beta/\partial t^2 \quad , \tag{1}$$

and for linear elastic response stress $\underline{\sigma}$ is related to strain $\underline{\varepsilon}$ by a modulus tensor $\underline{C}$ such that

$$\sigma_{\alpha\beta} = C_{\alpha\beta\gamma\delta}\ \varepsilon_{\gamma\delta} \quad \text{where } 2\varepsilon_{\gamma\delta} = \partial u_\gamma/\partial x_\delta + \partial u_\delta/\partial x_\delta \quad . \tag{2}$$

The tensor $\underline{C}$ is taken to be that for a homogeneous body or at least one with smoothly varying properties on the macroscale; microscale heterogeneities such as individual grains are ignored, which implies a limitation of results to wavelengths that are

in Aki and Richards, 1980)

$$u_\nu^d(\underline{x},t) = \partial^3\mu_{\alpha\beta}(\underline{x},t;c_d)/\partial x_\nu\partial x_\alpha\partial x_\beta$$

$$u_\nu^s(\underline{x},t) = \nabla^2[\partial\mu_{\nu\beta}(\underline{x},t;c_s)/\partial x_\beta] - \partial^3\mu_{\alpha\beta}(\underline{x},t;c_s)/\partial x_\nu\partial x_\alpha\partial x_\beta \tag{24}$$

where $\mu_{\alpha\beta}(\underline{x},t;c)$ is defined by

$$\mu_{\alpha\beta}(\underline{x},t;c) = \int_V \int_{-\infty}^{t} \frac{\{|\underline{x}-\underline{x}'|-c(t-t')\}U\{c(t-t')-|\underline{x}-\underline{x}'|\}}{4\pi\rho c|\underline{x}-\underline{x}'|} m_{\alpha\beta}(x',t')dt'd^3\underline{x}' \tag{25}$$

and where $U\{...\}$ is the unit step function; here c_d is the dilational (or longitudinal) wave speed and c_s is the shear (or transverse) wave speed.

Corresponding results may also be given in the frequency domain by writing $\tilde{\underline{u}}$ in place of $\underline{u}$ and $\tilde{\underline{\mu}}$ in place of $\underline{\mu}$ in Eq. (24). The expression for $\tilde{\underline{\mu}}(\underline{x},\omega;c)$ is

$$\tilde{\mu}_{\alpha\beta}(\underline{x},\omega;c) = \int_V \frac{\exp\{-i\omega|\underline{x}-\underline{x}'|/c\}}{4\pi\rho\omega^2|\underline{x}-\underline{x}'|} \tilde{m}_{\alpha\beta}(\underline{x}',\omega)d^3\underline{x}' \tag{26}$$

To obtain the "far-field" displacement distribution, it is now assumed that the receiver point at $\underline{x} = r_o\underline{\gamma}$ is far enough removed that

$$r_o >> a \quad \text{and} \quad r_o >> c/\omega \quad . \tag{27}$$

The far-field approximation should not be confused with the point-source approximation, which assumes that

large compared to grain size. The displacement field generated by an arbitrary distribution of body force $\underline{f}$ throughout some volume V is written as

$$u_\nu(\underline{x},t) = \int_{-\infty}^{t} \int_V G_{\nu\beta}(\underline{x},\underline{x}',t-t') f_\beta(\underline{x}',t') d^3\underline{x}' dt' \quad , \tag{3}$$

which defines the Green's function $G_{\nu\beta}(\underline{x},\underline{x}',t)$ for the medium.

Disturbances associated with the alteration of matter (which in degeneate cases may include slip and/or crack opening, and are collectively called damage here) can be regarded as being generated by a "transformation" strain $\underline{\varepsilon}^T$. This is <u>defined</u> so that $\underline{\sigma}$ and $\underline{\varepsilon}$ satisfy

$$\sigma_{\alpha\beta} = C_{\alpha\beta\gamma\delta}(\varepsilon_{\gamma\delta} - \varepsilon^T_{\gamma\delta}) \tag{4}$$

throughout the source region where C is the same modulus tensor as existed before the damage process. In the special cases of concern here for which the source process involve the generation of a displacement discontinuity on a discrete surface S (a surface of slip or cracking), but elastic behavior elsehwere, $\underline{\varepsilon}^T$ is Dirac singular on S. In particular, if the sides of S are labelled + and -, and if $\underline{n}$ is the normal to S directed from - to + and Δu is defined on S as $\underline{u}^+ - \underline{u}^-$, then for any small volume δV intersected by δS of surface,

$$\int_{\delta V} \varepsilon^T_{\alpha\beta} \, d^3\underline{x} = \tfrac{1}{2}(n_\alpha \, \Delta u_\beta + n_\beta \, \Delta u_\alpha)\delta S \quad . \tag{5}$$

Hence, for surface discontinuities one writes

$$r_o >> a \quad \text{and} \quad c/\omega >> a \tag{28}$$

although it is obvious from these inequalities that for sufficiently small a/r_o there will be a range of (low) frequencies where both sets of inequalities are satisfied simultaneously. The calculation of the far-field is simplest in the frequency domain and begins with the recognition that

$$|\underline{x}-\underline{x}'| = (r_o - \underline{\gamma}\cdot\underline{x}')[1 + O(\underline{\gamma}\cdot\underline{x}'/r_o)] \tag{29}$$

and that (see Eqs. 24 and 26)

$$\partial^3[\exp\{-i\omega|\underline{x}-\underline{x}'|/c\}/|\underline{x}-\underline{x}'|]/\partial x_\nu \partial x_\alpha \partial x_\beta$$
$$= (i\omega^3/r_o c^3)\gamma_\nu\gamma_\alpha\gamma_\beta \exp\{-i\omega r_o/c + i\omega\underline{\gamma}\cdot\underline{x}'/c\}[1 + O(\underline{\gamma}\cdot\underline{x}'/r_o, c/\omega r_o)] \tag{30}$$

The far-field approximation is such that the bracketed terms in Eqs. (29,30) reduce to unity and, after a little calculation, one has results in the frequency domain in the form

$$\tilde{u}^d_\nu(\underline{\gamma}r_o,\omega) = \frac{e^{-i\omega r_o/c_d}}{4\pi\rho c_d^3\, r_o}\gamma_\nu\gamma_\alpha\gamma_\beta \int_V \tilde{\dot{m}}_{\alpha\beta}(\underline{x}',\omega)\, e^{i\omega\underline{\gamma}\cdot\underline{x}'/c_d}\, d^3\underline{x}'$$

$$\tilde{u}^s_\nu(\underline{\gamma}r_o,\omega) = \frac{e^{-i\omega r_o/c_s}}{4\pi\rho c_s^3\, r_o}\{\tfrac{1}{2}(\delta_{\nu\alpha}\gamma_\beta + \delta_{\nu\beta}\gamma_\alpha) - \gamma_\nu\gamma_\alpha\gamma_\beta\} \tag{31}$$
$$\times \int_V \tilde{\dot{m}}_{\alpha\beta}(\underline{x}',\omega)\, e^{i\omega\underline{\gamma}\cdot\underline{x}'/c_s}\, d^3\underline{x}'$$

Corresponding results in the time domain can be written at once by observing that

$$\varepsilon^T_{\alpha\beta} = \tfrac{1}{2}(n_\alpha \, \Delta u_\beta + n_\beta \, \Delta u_\alpha)\delta_D(S) \tag{6}$$

where $\delta_D(S)$ is a surface Dirac function, converting any volume integral over a region intersected by some part of S to a surface integral over that part of S.

By using Eq. (4) in (1) and identifying an effective body force, the displacement field generated by an arbitrary distribution of $\underline{\varepsilon}^T$ within some region V can be written as

$$u_\nu(\underline{x},t) = \tfrac{1}{2}\int_V \int_{-\infty}^{t} H_{\nu\alpha\beta}(\underline{x},\underline{x}',t-t')m_{\alpha\beta}(\underline{x}',t')dt' \, d^3\underline{x}' \tag{7}$$

Here $\underline{m}$ is the (seismic) moment density tensor, namely the symmetric second rank tensor defined by

$$m_{\alpha\beta} = C_{\alpha\beta\gamma\delta} \, \varepsilon^T_{\gamma\delta} \equiv C_{\alpha\beta\gamma\delta} \, \varepsilon_{\gamma\delta} - \sigma_{\alpha\beta} \tag{8}$$

and

$$H_{\nu\alpha\beta}(\underline{x},\underline{x}',t) = \partial G_{\nu\beta}(\underline{x},\underline{x}',t)/\partial x'_\alpha + \partial G_{\nu\alpha}(\underline{x},\underline{x}',t)/\partial x'_\beta \tag{9}$$

is the response $u_\nu(\underline{x},t)$ to a "double couple without moment" exerted at $\underline{x}'$ at time t = 0. Such a double couple is generated by a pair of impulsive force dipoles; e.g., $\partial G_{\nu\beta}/\partial x'_\alpha$ is the response u_ν generated, in the limit $h \to o$, by a pair of oppositely directed point impulses of magnitude 1/h, one acting in the negative β direction at $\underline{x}'$ and the other in the positive β direction at a point removed by distance h in the α direction from $\underline{x}'$.

Defining the Fourier transform on time of a function $f(\underline{x},t)$ by

$$e^{-i\omega r_o/c} \int_V \tilde{\dot{m}}_{\alpha\beta}(\underline{x}',\omega)\, e^{i\omega \underline{\gamma}\cdot\underline{x}'/c}\, d^3\underline{x}' \tag{32}$$

is the transform of

$$\int_V \dot{m}_{\alpha\beta}(\underline{x}', t - r_o/c + \underline{\gamma}\cdot\underline{x}'/c)\, d^3\underline{x}' \quad ; \tag{33}$$

this latter form has an obvious interpretation in terms of a retardation of time between the source process and its reception.

The expressions in Eqs. (31), transformed to the time domain as in Eqs. (32,33), make evident the origin of conditions (17) and (18) as requirements for validity of a point-source model.

For isotropic materials

$$\begin{aligned} m_{\alpha\beta} &= C_{\alpha\beta\gamma\gamma}\, \varepsilon^T_{\gamma\delta} = \Lambda\delta_{\alpha\beta}\, \varepsilon^T_{\gamma\delta} + 2G\, \varepsilon^T_{\alpha\beta} \\ &= \rho(c_d^2 - 2c_s^2)\delta_{\alpha\beta}\, \varepsilon^T_{\gamma\gamma} + 2\rho c_s^2\, \varepsilon^T_{\alpha\beta} \end{aligned} \tag{34}$$

where Λ,G are the Lamé elastic constants. Hence for the particular case of a surface S with normal $\underline{n}$ across which velocity discontinuities $\Delta\underline{\dot{u}}$ occur,

$$\begin{aligned} \int_V \tilde{\dot{m}}_{\alpha\beta}(\underline{x},\omega)\, e^{i\omega\underline{\gamma}\cdot\underline{x}/c} d^3\underline{x} = \int_S \{ &\rho(c_d^2 - 2c_s^2)\delta_{\alpha\beta} n_\gamma(\underline{x})\, \Delta\tilde{\dot{u}}_\gamma(\underline{x},\omega) \\ &+ \rho c_s^2 [n_\alpha(\underline{x})\, \Delta\tilde{\dot{u}}_\beta(\underline{x},\omega) + n_\beta(\underline{x})\, \Delta\tilde{\dot{u}}_\alpha(\underline{x},\omega)]\}\, e^{i\omega\underline{\gamma}\cdot\underline{x}/c}\, d^2\underline{x} \end{aligned} \tag{35}$$

Results for Planar Surfaces of Tensile Opening and Slip

A general displacement discontinuity can be resolved into an opening displacement and into two tangential slip displacements.

$$\tilde{f}(\underline{x},\omega) = \int_{-\infty}^{+\infty} f(\underline{x},t)e^{-i\omega t}\,dt \quad , \tag{10}$$

and recalling that time-convolutions of functions transform to products, one has the frequency version of Eq. (7) as

$$\tilde{u}_\nu(\underline{x},\omega) = \int_V \tilde{H}_{\nu\alpha\beta}(\underline{x},\underline{x}',\omega)\tilde{m}_{\alpha\beta}(x',\omega)d^3\underline{x}' \quad . \tag{11}$$

It is convenient in using this representation to observe that

$$\tilde{\dot{m}}_{\alpha\beta}(\underline{x},\omega) = i\omega\,\tilde{m}_{\alpha\beta}(\underline{x},\omega) \quad , \tag{12}$$

where $\dot{m}_{\alpha\beta}(\underline{x},t)$ is the time rate of $m_{\alpha\beta}(\underline{x},t)$, so that the expression can be written as

$$\tilde{u}_\nu(\underline{x},\omega) = \int_V [(1/i\omega)H_{\nu\alpha\beta}(\underline{x},\underline{x}',\omega)]\,\tilde{\dot{m}}_{\alpha\beta}(\underline{x}',\omega)d^3\underline{x}' \quad . \tag{13}$$

Here the quantity in brackets is the transform of

$$\int_{o-}^{t} H_{\nu\alpha\beta}(\underline{x},\underline{x}',\tau)d\tau$$

which is the response to double couples without moments formed from forces which are suddenly applied and held constant for subsequent time, rather than from impulses. The representation of Eq. (13) is more convenient than Eq. (11), since the limit of the bracketed term in Eq. (13) defines a non-zero function of position in the limit $\omega\to o$.

These cases are considered separately here for the special case in which S is a flat surface ($\underline{n}$ constant).

Observing that for a displacement discontinuity $\Delta\underline{u}$ in the direction of any fixed unit vector $\underline{v}$, one may write

$$\Delta\underline{u}(\underline{x},t) = \underline{v}\,\Delta u(\underline{x},t) \tag{36}$$

where Δu is the magnitude of the discontinuity, Eqs. (31-33) and (35) lead to

$$\begin{aligned}
\underline{u}^d(\underline{\gamma} r_o,t) &= \frac{\underline{\gamma}\,\Omega(t;c_d)}{4\pi r_o\, c_d}\,\{\underline{n}\cdot\underline{v} + 2(c_s^2/c_d^2)(\underline{n}\cdot\underline{\gamma}\;\underline{\gamma}\cdot\underline{v} - \underline{n}\cdot\underline{v})\} \\
\underline{u}^s(\underline{\gamma} r_o,t) &= \frac{\Omega(t;c_s)}{4\pi r_o\, c_s}\,\{(\underline{\gamma}\cdot\underline{v})\underline{n} + (\underline{\gamma}\cdot\underline{n})\underline{v} - 2(\underline{n}\cdot\underline{\gamma}\;\underline{\gamma}\cdot\underline{v})\underline{\gamma}\}
\end{aligned} \tag{37}$$

where

$$\Omega(t;c) = \int_S \Delta\dot{u}(\underline{x},t-r_o/c + \underline{\gamma}\cdot\underline{x}/c)\; d^2\underline{x} \quad . \tag{38}$$

Corresponding results in the frequency domain are obtained by observing that the transform of $\Omega(t;c)$ is

$$\tilde{\Omega}(\omega;c) = e^{-i\omega r_o/c} \int_S \Delta\tilde{\dot{u}}(\underline{x},\omega) e^{i\underline{\gamma}\cdot\underline{x}\omega/c}\; d^2\underline{x} \tag{39}$$

One may observe that $\underline{u}^d$ has the direction of $\underline{\gamma}$ and that $\underline{u}^s$ is perpendicular to $\underline{\gamma}$.

To examine specific cases suppose with reference to Fig. 1 that the axes are chosen so that x_2 has the direction of $\underline{n}$, i.e., perpendicular to S, and that x_1, x_3 lie in the plane of S. Then for angles ϕ,θ as shown

Point-Source Model

Let the origin of coordinates be chosen somewhere in or very near to the source region. If the spatial extent of the source is small compared to the distance r_o ($=|\underline{x}|$) to the receiver position, Eq. (13) is suggestive of a "point-source" model in which the resulting field is written as

$$\tilde{u}_\nu(\underline{x},\omega) \simeq [(1/i\omega)H_{\nu\alpha\beta}(\underline{x},\underline{o},\omega)]\ \tilde{\dot{M}}_{\alpha\beta}(\omega) \tag{14}$$

where

$$M_{\alpha\beta}(t) = \int_V m_{\alpha\beta}(\underline{x},t)d^3\underline{x} = \int_V C_{\alpha\beta\gamma\delta}\ \varepsilon^T_{\gamma\delta}(\underline{x},t)d^3\underline{x} \tag{15}$$

for general sources or, in the case of planar discontinuities,

$$M_{\alpha\beta}(t) = \int_S C_{\alpha\beta\gamma\delta}\ n_\gamma(\underline{x})\ \Delta u_\delta(\underline{x},t)d^2\underline{x} \tag{16}$$

This quantity $M_{\alpha\beta}$ is referred to as the (seismic) moment tensor of the source.

It is important to have a clear understanding of the approximation involved in Eq. (14). Obviously, it is assumed that $r_o/a >> 1$, where a is some typical radius of the source region. There is, however, also a frequency restriction involved in using Eq. (14) in that wavelengths involved must be large compared to a. This seems not always to be well understood but will be clearer when specific forms of Eq. (7) or (13) for an unbounded isotropic solid are considered next. Essentially, the high frequency portions of the radiated signal are sensitive to the spatial distribution of origins in the source zone from which

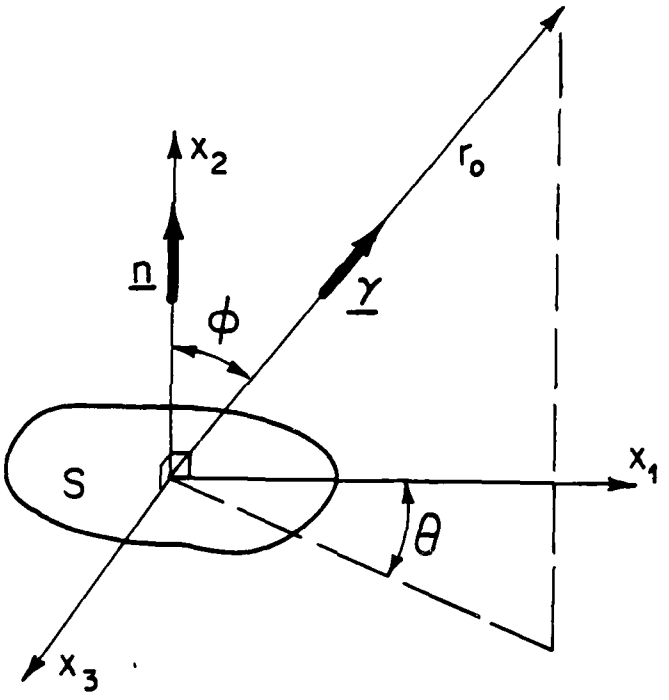

FIGURE 1

disturbances emanate. These origins have a different set of propagation times to a receiver at, say, reception point $r_o\underline{\gamma}'$ than at another reception point, $r_o\underline{\gamma}''$. Hence, high frequency information, involving periods comparable to differences in these propagation times, is different for the receiver at $r_o\underline{\gamma}'$ than at $r_o\underline{\gamma}''$. Looking ahead to the isotropic results, the essential requirement for independence of the receiver orientation, and hence validity of Eq. (14), is that for disturbances spreading at speed c, the frequency ω be low enough that

$$\int_V \tilde{\dot{m}}_{\alpha\beta}(\underline{x}',\omega)\, e^{i\underline{\gamma}\cdot\underline{x}'\omega/c}\, d^3\underline{x}' \simeq \int_V \tilde{\dot{m}}_{\alpha\beta}(\underline{x}',\omega)\, d^3\underline{x}' \equiv \tilde{\dot{M}}_{\alpha\beta}(\omega). \qquad (17)$$

This condition will be met for all $\underline{\gamma}$ if $e^{i\omega a/c} \simeq 1$ or $\omega a/c << 1$. The corresponding approximation in the time domain is that

$$\int_V \dot{m}_{\alpha\beta}(\underline{x}',t+\underline{\gamma}\cdot\underline{x}'/c)\, d^3\underline{x}' \simeq \int_V \dot{m}_{\alpha\beta}(\underline{x}',t)\, d^3\underline{x}' \equiv \dot{M}_{\alpha\beta}(t) \quad , \qquad (18)$$

which means that time differences should not be resolved finer than periods of order a/c.

Suppose that transformations $\underline{\varepsilon}^T$, or displacement discontinuities Δu, in the source region have effectively reached their long-time (static) values at a time t_r. Then for sufficiently low ω, such that $e^{i\omega t_r} \simeq 1$ (i.e., $\omega << 1/t_r$),

$$\tilde{\dot{M}}_{\alpha\beta}(\omega) \equiv \int_0^\infty \dot{M}_{\alpha\beta}(t)\, e^{-i\omega t}\, dt \simeq \int_0^{t_r} \dot{M}_{\alpha\beta}(t)\, dt = M_{\alpha\beta}(t_r). \qquad (19)$$

Hence for frequencies at which $e^{i\omega t_r} \simeq 1$, the point source model reduces to

$$\gamma_1 = \sin\phi\cos\theta \quad , \quad \gamma_2 = \cos\phi \quad , \quad \gamma_3 = \sin\phi\sin\theta \quad . \tag{40}$$

Tensile opening: For this case $\underline{v} = \underline{n}$, i.e., $\underline{v}$ has the direction of x_2. Hence

$$\begin{aligned} \underline{u}^d(r_o\underline{\gamma},t) &= \frac{\underline{\gamma}\,\Omega(t;c_d)}{4\pi r_o\, c_d}\{1-(2c_s^2/c_d^2)\sin\phi\} \\ \underline{u}^s(r_o\underline{\gamma},t) &= \frac{\underline{\lambda}\,\Omega(t;c_s)}{4\pi r_o\, c_s}\sin 2\phi \end{aligned} \tag{41}$$

where

$$\underline{\lambda} = (\underline{n} - \underline{\gamma}\cos\phi)/\sin\phi \tag{42}$$

is a unit vector which is tangent to great circles in the plane of $\underline{n}$ and $\underline{\gamma}$, and which always has a positive projection onto the direction of $\underline{n}$ (i.e., $\underline{\lambda}$ *is a unit vector in the direction of decreasing* ϕ). Since $2c_s^2/c_d^2 = 2G/(\Lambda+2G)$, the orientation term in the expression for $\underline{u}^d$ is always positive.

Note that not all of the orientation dependence is displayed explicitly in the above formulae; Ω as defined in Eqs. (38, 39) also depends on $\underline{\gamma}$, although this orientation dependence can be neglected in the low frequency limit as discussed in connection with Eqs. (17) and (18).

The radiation patterns of Eqs. (41) are shown in Fig. 2. Zeros (0) on the s wave pattern denote nodes; there are no nodes on the d pattern. Both patterns shown are rotationally symmetric about the x_2 axis.

Slip: Now let $\underline{v}$ be in the x_1 direction. Eqs. (37) lead in this case to

$$\tilde{u}_\nu(\underline{x},\omega) = [(1/i\omega)H_{\nu\alpha\beta}(\underline{x},\underline{o},\omega)]M_{\alpha\beta}(t_r) \qquad (20)$$

This shows that it is the moment $M_{\alpha\beta}(t_r)$ at the completion of the source process which governs the low frequency range of elastic wave emission.

From the results presented it is clear that at low frequencies (in the sense $e^{i\omega a/c} \simeq 1$) the basic observable quantities for a small AE source are the six functions $M_{\alpha\beta}(t)$ of Eqs. (15,16), low-pass filtered in the sense of Eqs. (17,18). Further, at what are generally yet lower frequencies (i.e., $e^{i\omega t_r} \simeq 1$), the observable quantities reduce to the six constants $M_{\alpha\beta}(t_r)$ corresponding to the static state in the source region at completion of the damage event.

Aki and Richards (1980) use the representation of Eq. (14) and solve for the Raleigh (and Love) wave radiation from an arbitrary point source in a half space (Chp. 7). This solution may have relevance to particular experimental situations for detection of AE signals.

Another approach for which the point source model is useful is for an examination of the excitation of normal modes of the body in which the AE event takes place. The solution can be read-off from Aki and Richards (1980)(Chp. 8). Let $\underline{u}^{(k)}(\underline{x})$, $k = 1,2...$, denote the normal modes and suppose these are normalized so that

$$\int_{\text{body}} \rho(\underline{x})\, u_\alpha^{(j)}(\underline{x})\, u_\alpha^{(k)}(\underline{x})\, d^3\underline{x} = \delta_{jk} \qquad (21)$$

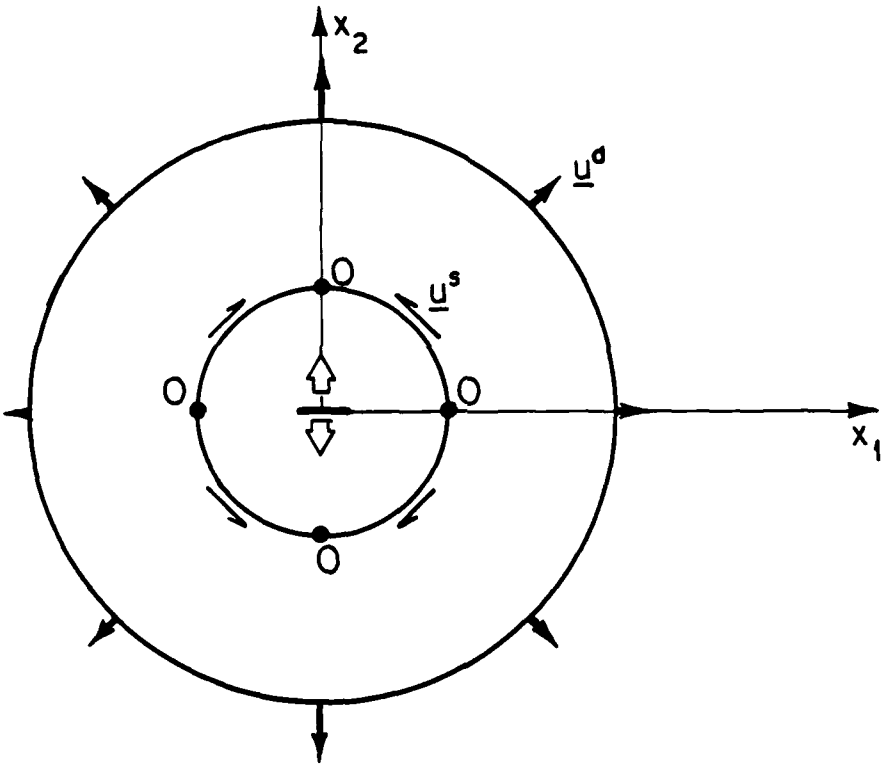

TENSILE OPENING
(symmetric about x_2 axis)

FIGURE 2

Then the solution for a step-function point source $M_{\alpha\beta}$ (this corresponds to using $M_{\alpha\beta}(t_r)$ and ignoring information in oscillation frequencies higher than those for which $e^{i\omega t_r} \simeq 1$) applied at t=o is

$$\underline{u}(\underline{x},t) = \sum_k M_{\alpha\beta}\varepsilon^{(k)}_{\alpha\beta}\ \underline{u}^{(k)}(\underline{x})\{1-\cos\ \omega^{(k)}t\}/\{\omega^{(k)}\}^2 \qquad (22)$$

where $\varepsilon^{(k)}_{\alpha\beta}$ is the strain in the k^{th} mode at the place of the point source. For linear damping without coupling between modes the time dependent terms become (approximately, for light damping)

$$1 - \exp(-\omega^{(k)}t/2Q^{(k)})\ \cos\ \omega^{(k)}t$$

where $Q^{(k)}$ is the quality factor for damping in the k^{th} mode. This form shows also how the long-time static field evolves.

Far-field Results for Isotropic Homogeneous Bodies

Here results are given for the displacement field at points distant from the source in an otherwise isotropic and homogeneous material. The results presented are for outgoing waves from the source region, calculated as if the source resided in an unbounded body. They apply until wave reflections from boundaries intervene, but do not include the reflection and waveguide effects associated with finite regions.

In this case $\underline{u}$ can be written as a sum of dilational ($\underline{u}^d$) and shear (u^s) contributions,

$$\underline{u}(\underline{x},t) = \underline{u}^d(\underline{x},t) + \underline{u}^s(\underline{x},t) \quad . \qquad (23)$$

These are given by (e.g., Rice, 1980, or equivalent expressions

$$\underline{u}^d(\underline{\gamma} r_o, t) = \frac{\underline{\gamma}\, c_s^2\, \Omega(t; c_d)}{4\pi r_o\, c_d^3} \sin 2\phi \cos\theta$$

$$\underline{u}^s(\underline{\gamma} r_o, t) = \frac{\Omega(t; c_s)}{4\pi r_o\, c_s} (-\cos 2\phi \cos\theta\, \underline{\lambda} + \cos\phi \sin\theta\, \underline{\mu}) \qquad (43)$$

where $\underline{\lambda}$ is defined above and $\underline{\mu}$ is a unit vector in the direction of decreasing θ.

The resulting radiation patterns are shown in Fig. 3; both contain nodes. As is well known for this case, the slip plane orientation cannot be determined uniquely from the far-field radiation patterns, but can only be reduced to two candidate directions at 90° with one another.

Moments: For the tensile opening

$$M_{22}(t) = (\Lambda+2G) M_{33}(t)/\Lambda = (\Lambda+2G) M_{11}(t)/\Lambda = (\Lambda+2G) \int_S \Delta u(\underline{x}, t)\, d^2\underline{x} \qquad (44)$$

are the only non-vanishing component of moment and, in circumstances for which the orientation-dependent parts of Ω, Eq. (38), can be neglected (low frequency limit)

$$\Omega(t; c) = \dot{M}_{22}(t - r_o/c)/(\Lambda+2G) \quad . \qquad (45)$$

Similarly, for the slip case

$$M_{12}(t) = M_{21}(t) = G \int_S \Delta u(\underline{x}, t)\, d^2\underline{x} \qquad (46)$$

are the non-vanishing components of moment and, in the same circumstances as above

in Aki and Richards, 1980)

$$u_\nu^d(\underline{x},t) = \partial^3\mu_{\alpha\beta}(\underline{x},t;c_d)/\partial x_\nu\partial x_\alpha\partial x_\beta$$

$$u_\nu^s(\underline{x},t) = \nabla^2[\partial\mu_{\nu\beta}(\underline{x},t;c_s)/\partial x_\beta] - \partial^3\mu_{\alpha\beta}(\underline{x},t;c_s)/\partial x_\nu\partial x_\alpha\partial x_\beta \tag{24}$$

where $\mu_{\alpha\beta}(\underline{x},t;c)$ is defined by

$$\mu_{\alpha\beta}(\underline{x},t;c) = \int_V \int_{-\infty}^{t} \frac{\{|\underline{x}-\underline{x}'|-c(t-t')\}U\{c(t-t')-|\underline{x}-\underline{x}'|\}}{4\pi\rho c|\underline{x}-\underline{x}'|} m_{\alpha\beta}(x',t')dt'd^3\underline{x}' \tag{25}$$

and where $U\{...\}$ is the unit step function; here c_d is the dilational (or longitudinal) wave speed and c_s is the shear (or transverse) wave speed.

Corresponding results may also be given in the frequency domain by writing $\tilde{\underline{u}}$ in place of $\underline{u}$ and $\tilde{\underline{\mu}}$ in place of $\underline{\mu}$ in Eq. (24). The expression for $\tilde{\underline{\mu}}(\underline{x},\omega;c)$ is

$$\tilde{\mu}_{\alpha\beta}(\underline{x},\omega;c) = \int_V \frac{\exp\{-i\omega|\underline{x}-\underline{x}'|/c\}}{4\pi\rho\omega^2|\underline{x}-\underline{x}'|} \tilde{m}_{\alpha\beta}(\underline{x}',\omega)d^3\underline{x}' \tag{26}$$

To obtain the "far-field" displacement distribution, it is now assumed that the receiver point at $\underline{x} = r_o\underline{\gamma}$ is far enough removed that

$$r_o >> a \quad \text{and} \quad r_o >> c/\omega \quad . \tag{27}$$

The far-field approximation should not be confused with the point-source approximation, which assumes that

$$\Omega(t;c) = \dot{M}_{12}(t-r_o/c)/G \quad . \tag{47}$$

Comparison of tensile opening versus slip: The main comparison of these two damage modes follows from a comparison of Figs. 2 and 3. The tensile opening radiation patterns are axi-symmetric (at least to the neglect of "propagation" or "directivity" effects which occur at sufficiently high frequencies for the $\underline{\gamma}$ dependence of Ω, Eqs. (38,39), to be non-negligible) and thereby enable a unique determination of the orientation of the surface S on which the opening occurs. However, no information is retained on the shape of S, at least in the low frequency range. For slip events the radiation patterns are not axi-symmetric and divide the unit sphere into four sectors formed by great circles connecting diametrically opposite nodes in Fig. 3. These sectors are differently located on the unit sphere for d versus s radiation. As commented, the patterns do not uniquely determine the slip plane normal, but only two directions of which either one may be the normal and the other the slip direction.

The ratios of the maximum amplitudes of d and s waves are different for tensile opening versus slip. In the opening case this ratio is (Eq. 41)

$$|\underline{u}^d|_{max}/|\underline{u}^s|_{max} = c_s/c_d \simeq 0.58 \tag{48}$$

whereas for slip (Eq. 43)

$$|\underline{u}^d|_{max}/|\underline{u}^s|_{max} = (c_s/c_d)^3 \simeq 0.19 \tag{49}$$

The numbers are for the case $\Lambda = G$, for which the Poisson ratio $\nu = \frac{1}{4}$.

$$r_o >> a \quad \text{and} \quad c/\omega >> a \tag{28}$$

although it is obvious from these inequalities that for sufficiently small a/r_o there will be a range of (low) frequencies where both sets of inequalities are satisfied simultaneously. The calculation of the far-field is simplest in the frequency domain and begins with the recognition that

$$|\underline{x}-\underline{x}'| = (r_o - \underline{\gamma}\cdot\underline{x}')[1 + O(\underline{\gamma}\cdot\underline{x}'/r_o)] \tag{29}$$

and that (see Eqs. 24 and 26)

$$\partial^3[\exp\{-i\omega|\underline{x}-\underline{x}'|/c\}/|\underline{x}-\underline{x}'|]/\partial x_\nu \partial x_\alpha \partial x_\beta$$
$$= (i\omega^3/r_o c^3)\gamma_\nu\gamma_\alpha\gamma_\beta \exp\{-i\omega r_o/c + i\omega\underline{\gamma}\cdot\underline{x}'/c\}[1 + O(\underline{\gamma}\cdot\underline{x}'/r_o, c/\omega r_o)] \tag{30}$$

The far-field approximation is such that the bracketed terms in Eqs. (29,30) reduce to unity and, after a little calculation, one has results in the frequency domain in the form

$$\tilde{u}^d_\nu(\underline{\gamma}r_o,\omega) = \frac{e^{-i\omega r_o/c_d}}{4\pi\rho c_d^3\, r_o}\gamma_\nu\gamma_\alpha\gamma_\beta \int_V \tilde{\dot{m}}_{\alpha\beta}(\underline{x}',\omega)\, e^{i\omega\underline{\gamma}\cdot\underline{x}'/c_d}\, d^3\underline{x}'$$

$$\tilde{u}^s_\nu(\underline{\gamma}r_o,\omega) = \frac{e^{-i\omega r_o/c_s}}{4\pi\rho c_s^3\, r_o}\{\tfrac{1}{2}(\delta_{\nu\alpha}\gamma_\beta + \delta_{\nu\beta}\gamma_\alpha) - \gamma_\nu\gamma_\alpha\gamma_\beta\} \tag{31}$$
$$\times \int_V \tilde{\dot{m}}_{\alpha\beta}(\underline{x}',\omega)\, e^{i\omega\underline{\gamma}\cdot\underline{x}'/c_s}\, d^3\underline{x}'$$

Corresponding results in the time domain can be written at once by observing that

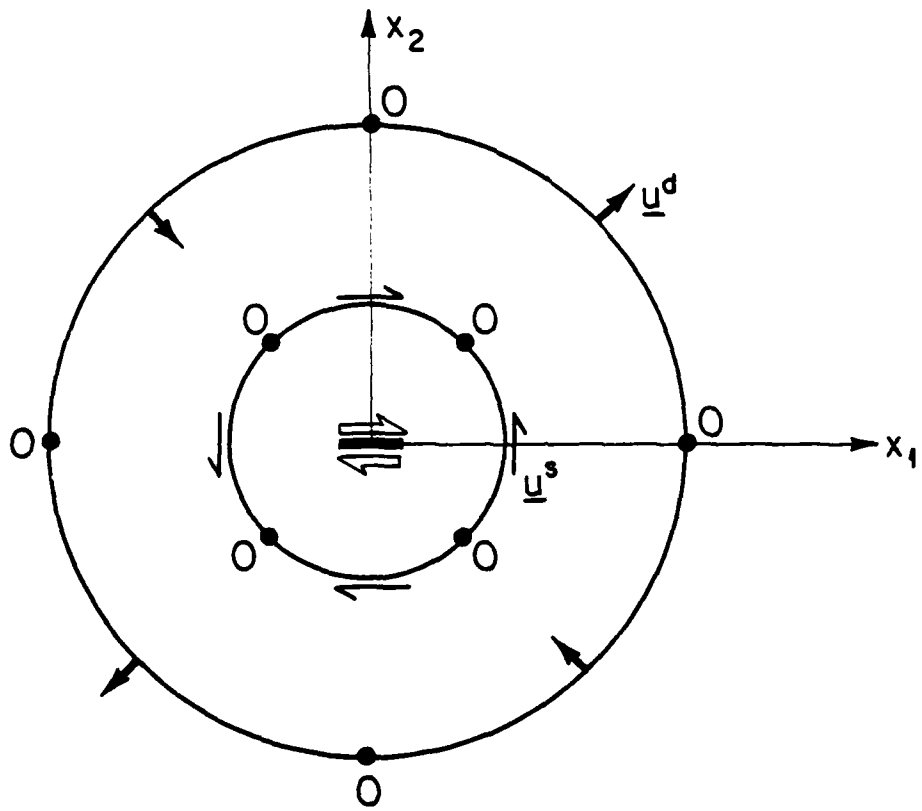

SLIP (results on plane $\theta=0$)

FIGURE 3

$$e^{-i\omega r_o/c} \int_V \tilde{\dot{m}}_{\alpha\beta}(\underline{x}',\omega)\, e^{i\omega \underline{\gamma}\cdot\underline{x}'/c}\, d^3\underline{x}' \tag{32}$$

is the transform of

$$\int_V \dot{m}_{\alpha\beta}(\underline{x}', t - r_o/c + \underline{\gamma}\cdot\underline{x}'/c)\, d^3\underline{x}' \quad ; \tag{33}$$

this latter form has an obvious interpretation in terms of a retardation of time between the source process and its reception.

The expressions in Eqs. (31), transformed to the time domain as in Eqs. (32,33), make evident the origin of conditions (17) and (18) as requirements for validity of a point-source model.

For isotropic materials

$$\begin{aligned} m_{\alpha\beta} &= C_{\alpha\beta\gamma\gamma}\, \varepsilon^T_{\gamma\delta} = \Lambda\delta_{\alpha\beta}\, \varepsilon^T_{\gamma\delta} + 2G\, \varepsilon^T_{\alpha\beta} \\ &= \rho(c_d^2 - 2c_s^2)\delta_{\alpha\beta}\, \varepsilon^T_{\gamma\gamma} + 2\rho c_s^2\, \varepsilon^T_{\alpha\beta} \end{aligned} \tag{34}$$

where Λ,G are the Lamé elastic constants. Hence for the particular case of a surface S with normal $\underline{n}$ across which velocity discontinuities $\Delta\underline{\dot{u}}$ occur,

$$\begin{aligned} \int_V \tilde{\dot{m}}_{\alpha\beta}(\underline{x},\omega)\, e^{i\omega\underline{\gamma}\cdot\underline{x}/c} d^3\underline{x} = \int_S \{ &\rho(c_d^2 - 2c_s^2)\delta_{\alpha\beta} n_\gamma(\underline{x})\, \Delta\tilde{\dot{u}}_\gamma(\underline{x},\omega) \\ &+ \rho c_s^2 [n_\alpha(\underline{x})\, \Delta\tilde{\dot{u}}_\beta(\underline{x},\omega) + n_\beta(\underline{x})\, \Delta\tilde{\dot{u}}_\alpha(\underline{x},\omega)]\}\, e^{i\omega\underline{\gamma}\cdot\underline{x}/c}\, d^2\underline{x} \end{aligned} \tag{35}$$

Results for Planar Surfaces of Tensile Opening and Slip

A general displacement discontinuity can be resolved into an opening displacement and into two tangential slip displacements.

Propagation in source region: In principle, the high frequency portions of the radiated field contain details of the space-time distribution of the damage event throughout the source region. The frequency range for which such effects are observable is that for which $\omega a/c$ is of order unity or larger. There may in some materials be a reasonable range of frequencies between $\omega a/c = 1$ and $\omega d/c = 1$, where d is grain size and the latter equation refers to a cut-off frequency at which heterogeneities at the grain size make signal interpretation impossible. Obviously, for use of this range in quantitative AE, it is necessary that $a >> d$. This condition will frequently not be met for microcracking processes.

The high-frequency spectrum of slip events and its relation to propagation processes in the source region is discussed by Aki and Richards (1980) (chps. 14, 15) as well as by Das and Aki (1977), Madariaga (1976, 1977), Rice (1980), and Richards (1973, 1976). Such results are not pursued here except to note that from Eqs. (37,41,43), when transformed to the frequency domain, the frequency content of the far-field radiation is determined by $\tilde{\Omega}(\omega;c)$ of Eq. (39). This expression can be re-written as

$$\tilde{\Omega}(\omega;c) = e^{-i\omega r_o/c} \int_{-\infty}^{+\infty} \int_S \dot{\Delta u}(\underline{x},t) e^{-i\omega t - i\underline{k}\cdot\underline{x}} \, d^2\underline{x} \, dt \qquad (50)$$

where $\underline{k} = -\underline{\gamma}\omega/c$. The integrals define the full space-time Fourier transform of the velocit[illegible]inuity, and observation of the far-field at orientation $\underline{\gamma}$ corresponds to sampling this space-time transform along the ray $\underline{k} = -\underline{\gamma}\omega/c$ in $\underline{k}$-ω space. (Since $|\underline{\gamma}| = 1$, this sampling even if carried out for all orientations cannot even

These cases are considered separately here for the special case in which S is a flat surface ($\underline{n}$ constant).

Observing that for a displacement discontinuity $\Delta\underline{u}$ in the direction of any fixed unit vector $\underline{v}$, one may write

$$\Delta\underline{u}(\underline{x},t) = \underline{v}\,\Delta u(\underline{x},t) \tag{36}$$

where Δu is the magnitude of the discontinuity, Eqs. (31-33) and (35) lead to

$$\begin{aligned}
\underline{u}^d(\underline{\gamma} r_o,t) &= \frac{\underline{\gamma}\,\Omega(t;c_d)}{4\pi r_o\, c_d}\,\{\underline{n}\cdot\underline{v} + 2(c_s^2/c_d^2)(\underline{n}\cdot\underline{\gamma}\;\underline{\gamma}\cdot\underline{v} - \underline{n}\cdot\underline{v})\} \\
\underline{u}^s(\underline{\gamma} r_o,t) &= \frac{\Omega(t;c_s)}{4\pi r_o\, c_s}\,\{(\underline{\gamma}\cdot\underline{v})\underline{n} + (\underline{\gamma}\cdot\underline{n})\underline{v} - 2(\underline{n}\cdot\underline{\gamma}\;\underline{\gamma}\cdot\underline{v})\underline{\gamma}\}
\end{aligned} \tag{37}$$

where

$$\Omega(t;c) = \int_S \Delta\dot{u}(\underline{x},t-r_o/c + \underline{\gamma}\cdot\underline{x}/c)\; d^2\underline{x} \quad . \tag{38}$$

Corresponding results in the frequency domain are obtained by observing that the transform of $\Omega(t;c)$ is

$$\tilde{\Omega}(\omega;c) = e^{-i\omega r_o/c} \int_S \Delta\tilde{\dot{u}}(\underline{x},\omega) e^{i\underline{\gamma}\cdot\underline{x}\omega/c}\; d^2\underline{x} \tag{39}$$

One may observe that $\underline{u}^d$ has the direction of $\underline{\gamma}$ and that $\underline{u}^s$ is perpendicular to $\underline{\gamma}$.

To examine specific cases suppose with reference to Fig. 1 that the axes are chosen so that x_2 has the direction of $\underline{n}$, i.e., perpendicular to S, and that x_1, x_3 lie in the plane of S. Then for angles ϕ,θ as shown

in principle enable one to fully reconstruct the function $\Delta\dot{u}(\underline{x},t)$. The spatial structure along S of a given frequency component of $\Delta\dot{u}$ is resolvable only over a range of wave numbers k_1, k_3 that are smaller in magnitude than ω/c; information involving shorter wavelengths is evidently not transmitted to the far-field.)

Cracks

Suppose that a crack exists along a planar surface A_o and, in a damage event, spreads to area A ($=A_o + \Delta A$) in the same plane. As a special case, A_o may vanish. For simplicity, it is assumed that the crack plane is perpendicular to the tensile direction so that Δu consists only of tensile opening; more complicated cases of tensile opening in combination with shear are deferred to later treatment.

From earlier discussions it is clear that at sufficiently low frequencies that $e^{i\omega t_r} \simeq 1$, the approximation of Eq. (19) applies and (Eqs. 44,39,45)

$$\tilde{\dot{M}}_{22}(\omega) \simeq M_{22}(t_r) \simeq (\Lambda + 2G)\, e^{i\omega r_o/c}\, \tilde{\Omega}(\omega;c) \simeq (\Lambda + 2G)\Delta V \qquad (51)$$

where ΔV is the change in volume displaced by the crack surfaces in going from one statical configuration to the other:

$$\Delta V = \int_A (\Delta u)_A^{\text{static}}\, dA - \int_{A_o} (\Delta u)_{A_o}^{\text{static}}\, dA_o \qquad (52)$$

Hence it is the change in crack volume which is the basic observable quantity in the low-frequency limit, as noted by Wadley, et al. (1980), at least in the present case when the crack opens parallel

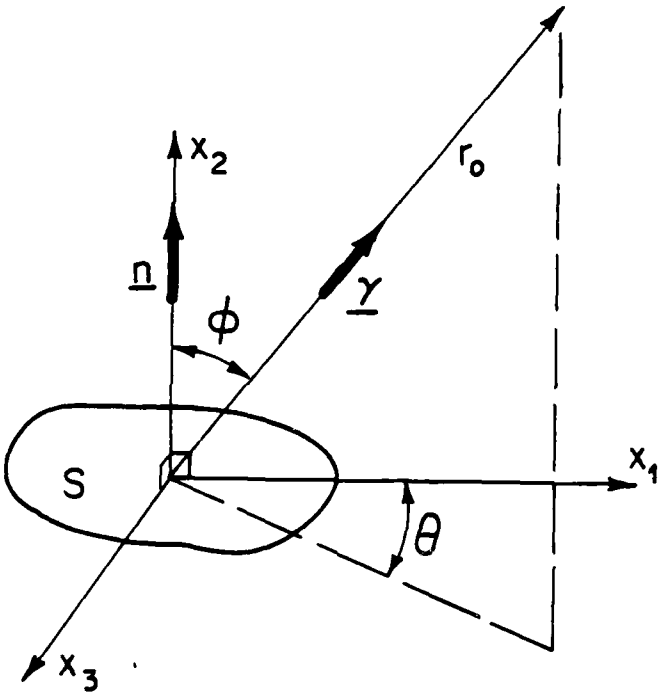

FIGURE 1

to the tensile direction. In particular, the low-frequency amplitude spectra of the outgoing d and s waves are (Eq. 41, transformed)

$$|\tilde{\underline{u}}^d(\underline{\gamma} r_o,\omega)| = (\Delta V/4\pi r_o c_d)\{1-2(c_s^2/c_d^2)\sin^2\phi\}$$
$$|\tilde{\underline{u}}^s(\underline{\gamma} r_o,\omega)| = (\Delta V/4\pi r_o c_s)|\sin 2\phi| \tag{53}$$

and the general point-source result for this case, Eq. (20), reduces to

$$\tilde{u}_\nu(\underline{x},\omega) = \Delta V\{(1/i\omega)[(\Lambda+2G)H_{\nu 22}(\underline{x},\underline{o},\omega) + \Lambda H_{\nu 11}(\underline{x},\underline{o},\omega) + \Lambda H_{\nu 33}(\underline{x},\underline{o},\omega)]\} \tag{54}$$

In view of the potential observability of ΔV, it is useful to have estimates which enable its quantitative relation to crack size or crack growth. The volume opening V of a disc-shaped crack of radius a subjected to tensile stress σ can be calculated from the expression for the static crack surface opening (e.g., Green and Zerna, 1954),

$$\Delta u = \{4\sigma(1-\nu)/\pi G\}(a^2-r^2)^{\frac{1}{2}} \tag{55}$$

where r is distance from the crack center, and hence

$$V = 2\pi \int_o^a \Delta u\, r dr = 8(1-\nu)\sigma a^3/3G \quad . \tag{56}$$

For new crack formation ($A_o = 0$ in Eq. 52), $\Delta V = V$ and hence an equivalent disc-shaped crack radius a can be associated with AE event. (The corresponding procedure for a slip event is less successful, since it cannot then be assumed that the drop σ in

$$\gamma_1 = \sin\phi\cos\theta \quad , \quad \gamma_2 = \cos\phi \quad , \quad \gamma_3 = \sin\phi\sin\theta \quad . \tag{40}$$

Tensile opening: For this case $\underline{v} = \underline{n}$, i.e., $\underline{v}$ has the direction of x_2. Hence

$$\begin{aligned} \underline{u}^d(r_o\underline{\gamma},t) &= \frac{\underline{\gamma}\,\Omega(t;c_d)}{4\pi r_o\, c_d}\{1-(2c_s^2/c_d^2)\sin\phi\} \\ \underline{u}^s(r_o\underline{\gamma},t) &= \frac{\underline{\lambda}\,\Omega(t;c_s)}{4\pi r_o\, c_s}\sin 2\phi \end{aligned} \tag{41}$$

where

$$\underline{\lambda} = (\underline{n} - \underline{\gamma}\cos\phi)/\sin\phi \tag{42}$$

is a unit vector which is tangent to great circles in the plane of $\underline{n}$ and $\underline{\gamma}$, and which always has a positive projection onto the direction of $\underline{n}$ (i.e., $\underline{\lambda}$ *is a unit vector in the direction of decreasing* ϕ). Since $2c_s^2/c_d^2 = 2G/(\Lambda+2G)$, the orientation term in the expression for $\underline{u}^d$ is always positive.

Note that not all of the orientation dependence is displayed explicitly in the above formulae; Ω as defined in Eqs. (38, 39) also depends on $\underline{\gamma}$, although this orientation dependence can be neglected in the low frequency limit as discussed in connection with Eqs. (17) and (18).

The radiation patterns of Eqs. (41) are shown in Fig. 2. Zeros (0) on the s wave pattern denote nodes; there are no nodes on the d pattern. Both patterns shown are rotationally symmetric about the x_2 axis.

Slip: Now let $\underline{v}$ be in the x_1 direction. Eqs. (37) lead in this case to

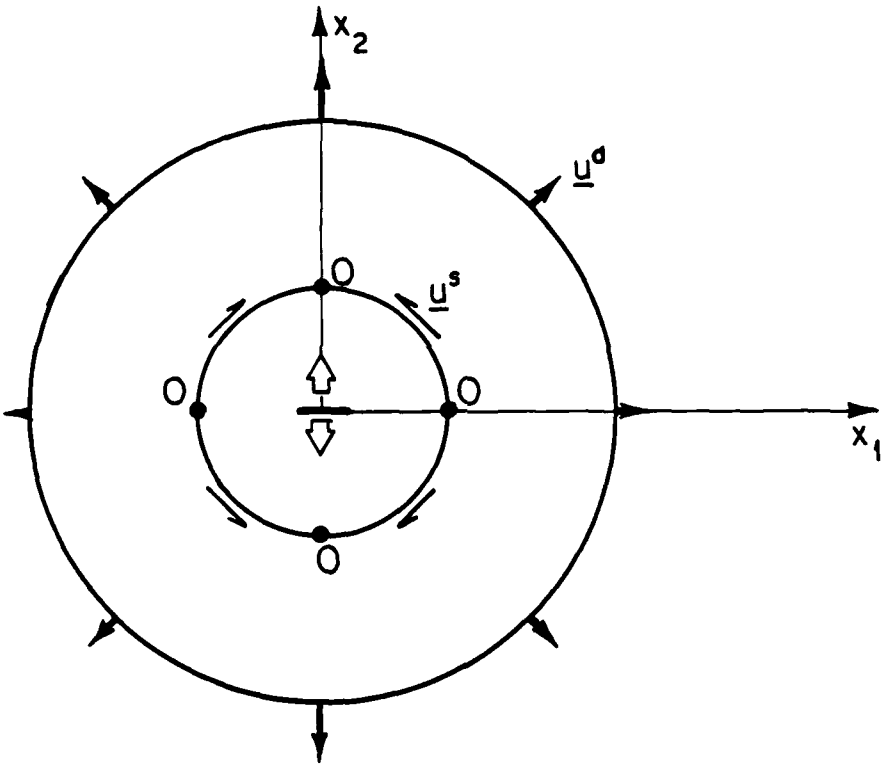

TENSILE OPENING
(symmetric about x_2 axis)

FIGURE 2

$$\underline{u}^d(\underline{\gamma} r_o, t) = \frac{\underline{\gamma}\, c_s^2\, \Omega(t; c_d)}{4\pi r_o\, c_d^3} \sin 2\phi \cos\theta$$

$$\underline{u}^s(\underline{\gamma} r_o, t) = \frac{\Omega(t; c_s)}{4\pi r_o\, c_s} (-\cos 2\phi \cos\theta\, \underline{\lambda} + \cos\phi \sin\theta\, \underline{\mu}) \qquad (43)$$

where $\underline{\lambda}$ is defined above and $\underline{\mu}$ is a unit vector in the direction of decreasing θ.

The resulting radiation patterns are shown in Fig. 3; both contain nodes. As is well known for this case, the slip plane orientation cannot be determined uniquely from the far-field radiation patterns, but can only be reduced to two candidate directions at 90° with one another.

Moments: For the tensile opening

$$M_{22}(t) = (\Lambda+2G) M_{33}(t)/\Lambda = (\Lambda+2G) M_{11}(t)/\Lambda = (\Lambda+2G) \int_S \Delta u(\underline{x}, t)\, d^2\underline{x} \qquad (44)$$

are the only non-vanishing component of moment and, in circumstances for which the orientation-dependent parts of Ω, Eq. (38), can be neglected (low frequency limit)

$$\Omega(t; c) = \dot{M}_{22}(t - r_o/c)/(\Lambda+2G) \quad . \qquad (45)$$

Similarly, for the slip case

$$M_{12}(t) = M_{21}(t) = G \int_S \Delta u(\underline{x}, t)\, d^2\underline{x} \qquad (46)$$

are the non-vanishing components of moment and, in the same circumstances as above

References

Aki, K., (1966), Bull. Earthquake Res. Inst. 44, 73.

Aki, K., and Richards, P. G., (1980), Quantitative Seismology, 2 volumes, W. H. Freeman, San Francisco.

Backus, G. and Mulcahy, M., (1976), Geophys. J. 46, 341 and 47, 301.

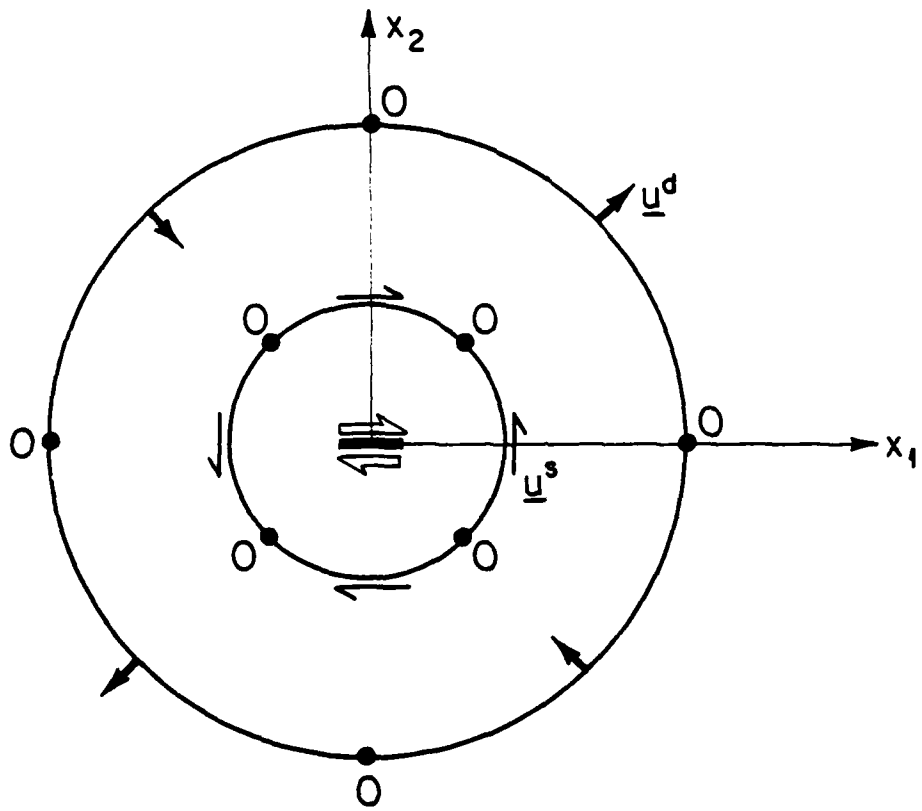

SLIP (results on plane $\theta=0$)

FIGURE 3

Propagation in source region: In principle, the high frequency portions of the radiated field contain details of the space-time distribution of the damage event throughout the source region. The frequency range for which such effects are observable is that for which $\omega a/c$ is of order unity or larger. There may in some materials be a reasonable range of frequencies between $\omega a/c = 1$ and $\omega d/c = 1$, where d is grain size and the latter equation refers to a cut-off frequency at which heterogeneities at the grain size make signal interpretation impossible. Obviously, for use of this range in quantitative AE, it is necessary that $a >> d$. This condition will frequently not be met for microcracking processes.

The high-frequency spectrum of slip events and its relation to propagation processes in the source region is discussed by Aki and Richards (1980) (chps. 14, 15) as well as by Das and Aki (1977), Madariaga (1976, 1977), Rice (1980), and Richards (1973, 1976). Such results are not pursued here except to note that from Eqs. (37,41,43), when transformed to the frequency domain, the frequency content of the far-field radiation is determined by $\tilde{\Omega}(\omega;c)$ of Eq. (39). This expression can be re-written as

$$\tilde{\Omega}(\omega;c) = e^{-i\omega r_o/c} \int_{-\infty}^{+\infty} \int_S \dot{\Delta u}(\underline{x},t) e^{-i\omega t - i\underline{k}\cdot\underline{x}} \, d^2\underline{x} \, dt \qquad (50)$$

where $\underline{k} = -\underline{\gamma}\omega/c$. The integrals define the full space-time Fourier transform of the velocit[illegible]inuity, and observation of the far-field at orientation $\underline{\gamma}$ corresponds to sampling this space-time transform along the ray $\underline{k} = -\underline{\gamma}\omega/c$ in $\underline{k}$-ω space. (Since $|\underline{\gamma}| = 1$, this sampling even if carried out for all orientations cannot even

in principle enable one to fully reconstruct the function $\Delta\dot{u}(\underline{x},t)$. The spatial structure along S of a given frequency component of $\Delta\dot{u}$ is resolvable only over a range of wave numbers k_1, k_3 that are smaller in magnitude than ω/c; information involving shorter wavelengths is evidently not transmitted to the far-field.)

Cracks

Suppose that a crack exists along a planar surface A_o and, in a damage event, spreads to area A ($=A_o + \Delta A$) in the same plane. As a special case, A_o may vanish. For simplicity, it is assumed that the crack plane is perpendicular to the tensile direction so that Δu consists only of tensile opening; more complicated cases of tensile opening in combination with shear are deferred to later treatment.

From earlier discussions it is clear that at sufficiently low frequencies that $e^{i\omega t_r} \simeq 1$, the approximation of Eq. (19) applies and (Eqs. 44,39,45)

$$\tilde{\dot{M}}_{22}(\omega) \simeq M_{22}(t_r) \simeq (\Lambda + 2G)\, e^{i\omega r_o/c}\, \tilde{\Omega}(\omega;c) \simeq (\Lambda + 2G)\Delta V \qquad (51)$$

where ΔV is the change in volume displaced by the crack surfaces in going from one statical configuration to the other:

$$\Delta V = \int_A (\Delta u)_A^{\text{static}}\, dA - \int_{A_o} (\Delta u)_{A_o}^{\text{static}}\, dA_o \qquad (52)$$

Hence it is the change in crack volume which is the basic observable quantity in the low-frequency limit, as noted by Wadley, et al. (1980), at least in the present case when the crack opens parallel

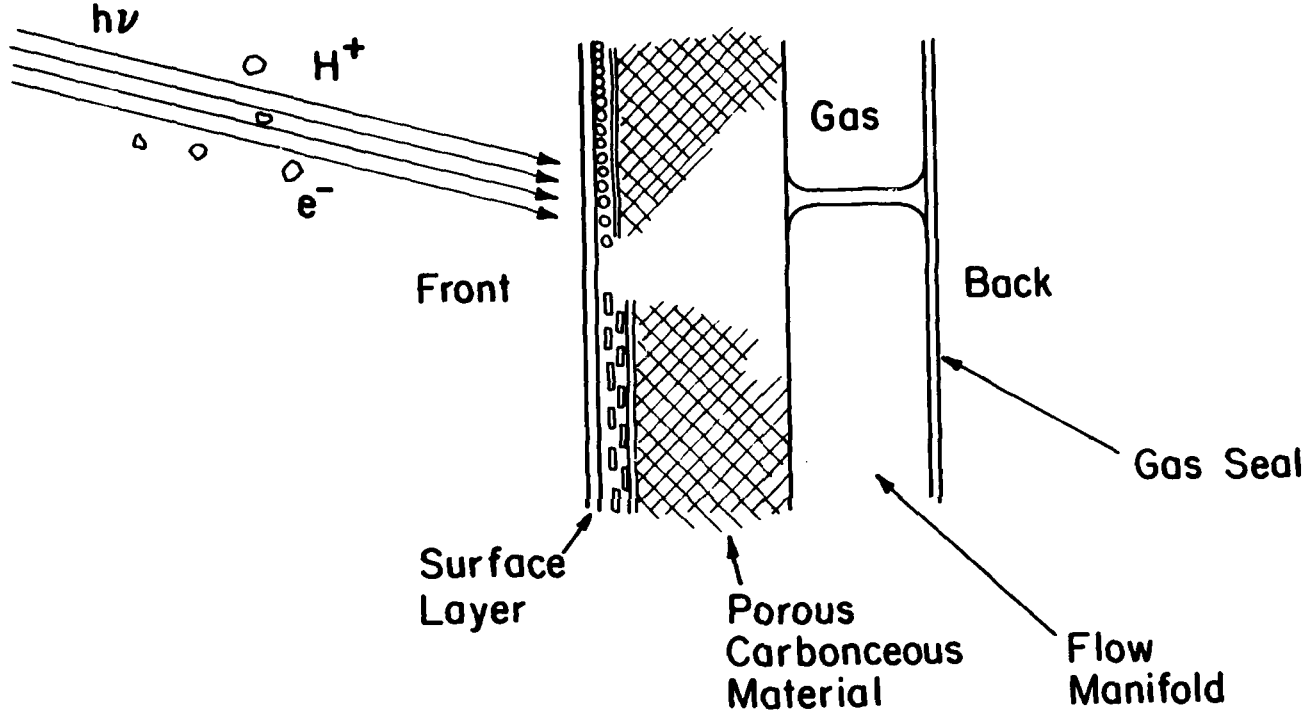

Figure 1. Model of Ablating Surface.

to the tensile direction. In particular, the low-frequency amplitude spectra of the outgoing d and s waves are (Eq. 41, transformed)

$$|\tilde{\underline{u}}^d(\underline{\gamma} r_o,\omega)| = (\Delta V/4\pi r_o c_d)\{1-2(c_s^2/c_d^2)\sin^2\phi\}$$
$$|\tilde{\underline{u}}^s(\underline{\gamma} r_o,\omega)| = (\Delta V/4\pi r_o c_s)|\sin 2\phi| \tag{53}$$

and the general point-source result for this case, Eq. (20), reduces to

$$\tilde{u}_\nu(\underline{x},\omega) = \Delta V\{(1/i\omega)[(\Lambda+2G)H_{\nu 22}(\underline{x},\underline{o},\omega) + \Lambda H_{\nu 11}(\underline{x},\underline{o},\omega) + \Lambda H_{\nu 33}(\underline{x},\underline{o},\omega)]\} \tag{54}$$

In view of the potential observability of ΔV, it is useful to have estimates which enable its quantitative relation to crack size or crack growth. The volume opening V of a disc-shaped crack of radius a subjected to tensile stress σ can be calculated from the expression for the static crack surface opening (e.g., Green and Zerna, 1954),

$$\Delta u = \{4\sigma(1-\nu)/\pi G\}(a^2-r^2)^{\frac{1}{2}} \tag{55}$$

where r is distance from the crack center, and hence

$$V = 2\pi \int_o^a \Delta u\, r dr = 8(1-\nu)\sigma a^3/3G \quad . \tag{56}$$

For new crack formation ($A_o = 0$ in Eq. 52), $\Delta V = V$ and hence an equivalent disc-shaped crack radius a can be associated with AE event. (The corresponding procedure for a slip event is less successful, since it cannot then be assumed that the drop σ in

A number of practical materials are available, including organic resins, which can be pyrolyzed to yield foamed (low-density) carbonaceous residues[1]; natural cork, which can be ground and reconstituted in sheets; grafoil-layered sheets; graphite felts; silica felts;[2] porous glass structures;[3] or metal-graphite structures like TBR or TAC.[4] As such surface/pyrolyzing layers are heated one absorbs energy with production of hot CO, CO_2, H_2O and other gases and creation of a plasma. In all cases, the ultimate material for vacuum (non-oxidizing) environments is graphite which does not melt and has a very high heat of sublimation; in oxidizing atmospheres, metal-doped resins which yield SiC or ZrC or some other metal-carbon species which forms a protective oxide layer are preferred.

In both situations, if one anticipates multiple exposures to a laser threat, it would be desirable to have a "repair" process to rebuild ablated structures and extend the protective life. Most promising in this area is some type of chemical vapor deposition (CVD). Thus, after surviving an initial heat threat and before complete cooling, one could deposit

(1) A layer of carbon by pyrolyzing methane.

(2) A layer of boron by pyrolyzing diborane.

(3) Metallic layers from carbonyls $\left[W(CO)_6, Ni(CO)_4\right]$ etc.

(4) Refractory hard layers $(TiCl_4+CH_4) \rightarrow TiC$

$(TiCl_4+B_2H_6) \rightarrow TiB_2$

shear stress transmitted across the slip surface is equal to the applied shear stress.)

Another perspective on the problem is provided by recognition that $\sigma\ \Delta V/2$, with ΔV defined by Eq. (52), is the static energy reduction due to introducing a crack in a loaded elastic body (this energy loss goes partly to wave emission and partly to the work of fracture). However, the energy loss can also be calculated by growing the crack from the initial configuration (A_o) to the final configuration (A). A given infinitesimal step of this growth involves crack advance by amounts $\delta a(s)$ along the crack front, Γ, parameterized by arc length s along it. Hence

$$\tfrac{1}{2}\sigma\,\delta V = \int_{\Gamma} g\,\delta a(s)\,ds \tag{57}$$

where g is Irwin's elastic energy release rate, related to the stress intensity factor K by

$$g = (1-\nu)K^2/2G \quad . \tag{58}$$

One may therefore write

$$\Delta V = 2\bar{g}\ \Delta A/\sigma \tag{59}$$

where $\bar{g}$ is the average g that would be encountered in <u>statically</u> enlarging the crack area by ΔA.

In some cases it would seem appropriate to assume that $\bar{g}$ is less than or equal to the macroscopic crack toughness g_{Ic} for the material (e.g., the microcracking takes place in the weaker regions of a material with statistically variable properties).

Various design parameters and special effects including the "sun-cup" phenomenon were also discussed. Chemical smokes and plasmas created by pyrolysis/vaporization, etc., offer the possibilities of absorbing incident radiation, ejecting electrons, re-radiating electromagnetically and scattering particles as energy dissipative processes.

Future investigations which should lead to better materials for ablator designs include

(a) Studies of emissivities, reflectivities and other optical properties over wide ranges of temperature and wavelengths for pure metals, alloys and refractory carbides, borides, etc.

(b) Studies of vacuum pyrolysis of different cellulosic or other carbon-based materials.

(c) Synthesis and investigation of high-temperature properties of organometallic/polymer combinations like those which produce TBR or TAC.

(d) Studies of smokes as absorptive or scattering systems for protection from laser radiation.

(e) Studies of CO/CO_2 or $CO/CO_2/H_2O$ or $C/CO/CO_2$ plasmas as systems for absorbing reflecting or scattering laser radiation.

(f) Studies of CVD processes for interim "repair" of ablative coatings.

ACKNOWLEDGEMENT

This research was supported by the Defense Advanced Research Projects Agency of the Department of Defense under Contract No. MDA903-80C-0505 with The University of Michigan.

In such case the ΔV inferred from the AE event provides a lower bound to the change in crack area, in the form

$$\Delta A \geq \sigma \, \Delta V / 2 g_{Ic} \tag{60}$$

ACKNOWLEDGEMENT

This research was supported by the Defense Advanced Research Projects Agency of the Department of Defense under Contract No. MDA903-80C-0505 with The University of Michigan. The author is grateful to M. Buckley, G. Kino, J. Simmons and H. Wadley for helpful discussion.

REFERENCES

(1) E. Fitzer, K. Mueller and W. Schaefer, Chem. & Phys. of Carbon 7, pp.237-383, (1971).

2. M. Waldrop, Chem. Eng. News, May 12, 1980, pp.27-29.

3. V. Apollonov, P. Bystrov, V. Goncharov, A. Prokhorov and V. Kmoich, Sov. J. Quantum Electronics 9(12), 1499 (1979).

4. R. C. Shaffer, Hitco, Gardena, California, private communication.

References

Aki, K., (1966), Bull. Earthquake Res. Inst. 44, 73.

Aki, K., and Richards, P. G., (1980), Quantitative Seismology, 2 volumes, W. H. Freeman, San Francisco.

Backus, G. and Mulcahy, M., (1976), Geophys. J. 46, 341 and 47, 301.

Brune, J. N., Archuleta, R. J. and Hartzell, S., (1979), J. Geophys. Res. 84, 2262.

Burridge, R. and Knopoff, L., (1964), Bull. Seism. Soc. Amer. 54, 1875.

Das, S. and Aki, K., (1977), J. Geophys. Res. 82, 5658.

DeHoop, A. T., (1958), Doctoral Thesis, Delft Univ. of Technology.

Green, A.E. and Zerna, W., (1954), Theoretical Elasticity, Oxford (Clarendon) Press, Oxford.

Haskell, N., (1964), Bull. Seism. Soc. Amer. 54, 1811.

Haskell, N., (1966), Bull. Seism. Soc. Amer. 56, 25.

Hsu, N. N., Simmons, J. A. and Hardy, S. C., (1977), Materials Evaluation, 100.

Kostrov. B. V., (1973), Publ. Inst. Geophys. Polish Acad. Sci. 62, 25.

Kostrov. B. V., (1974), Izv. AN SSR Phys. Sol. Earth 23.

Madariaga, R., (1976), Bull. Seism. Soc. Amer. 66, 639.

Madariaga, R., (1977), Geophys. J. 51, 625.

Malén, K. and Bolin, L., (1974), Phys. Stat. Sol. B61, 637.

Maruyama, T., (1963), Bull Earthquake Res. Inst. 41, 467.

Mura, T., (1968), in Advances in Materials Research, Vol. 3, Edited by H. Herman, p. 1.

Nabarro, F. R. N., (1951), Phil. Mag. 42, 313.

Pao, Y-H, (1978), in Elastic Waves and Non-destructive Testing of Materials, edited by Y-H Pao, ASME Appl. Mech. Div., Vol. 29, p. 107.

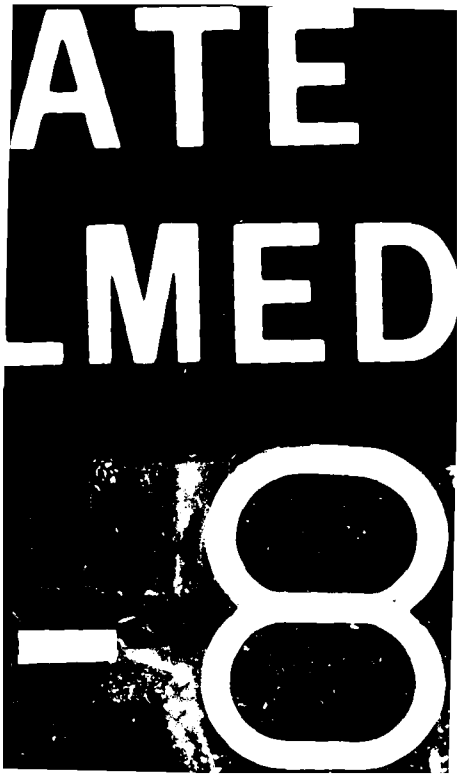
ATE
LMED
-8

Rice, J. R., (1980), in Proc. of the School on Physics of the Earth's Interior (Course LXXVIII, 1979, Int. School of Physics "Enrico Fermi", Italian Physical Soc.), edited by E. Boschi, North Holland.

Richards, P. G., (1973), Int. J. Solids Structures 9, 843.

Richards, P. G., (1976), Bull. Seism. Soc. Amer. 66, 1.

Simmons, J. A. and Clough, R., (1976), in Proc. 8th World Conf. on Non-destructive Testing. (Cannes, France).

Simmons, J. A. and Clough, R., (1980), manuscript in unpublished draft form.

Vvedenskaya, A. V., (1956), Izv. AN SSR Ser. Geophys. 3, 277.

Wadley, H. N. G., Scruby, C. B., and Shrimpton, G., (1980), Acta Met., in press.

THE ULTIMATE ABLATOR

J. L. Margrave

A discussion of basic physical, chemical and mechanical concepts of ablation processes was led by Major Harry Winsor. Participants were E. Hucke, F. McClintock, A. Francis, D. Drucker, M. Sinnott and J. L. Margrave. The ultimate ablator is constructed from a combination of materials with suitable reflective, refractory and heat dissipative properties so that the ablative coating can survive several exposures to high intensities of laser irradiation and still provide adequate protection for a heat and/or radiation sensitive payload.

Major Winsor discussed the search for an ultimate ablator in terms of the model shown in Fig. 1. To evaluate a given structure of given materials one needs to consider chemical properties, structural functions of components, radiation properties of materials, atmospheric functions, surface properties, etc. Ideally, one wants a refractory surface structure of high reflectivity, with an underlying layer of low thermal conductivity and a porous material which can absorb considerable heat while undergoing pyrolysis, e.g., a cellulosic or carbonaceous layer which leaves a low-density graphitic residue. If this is not sufficient ablative protection, one can design cooling manifolds with circulating liquids, like hydrogen, for counter flow heat exchange.

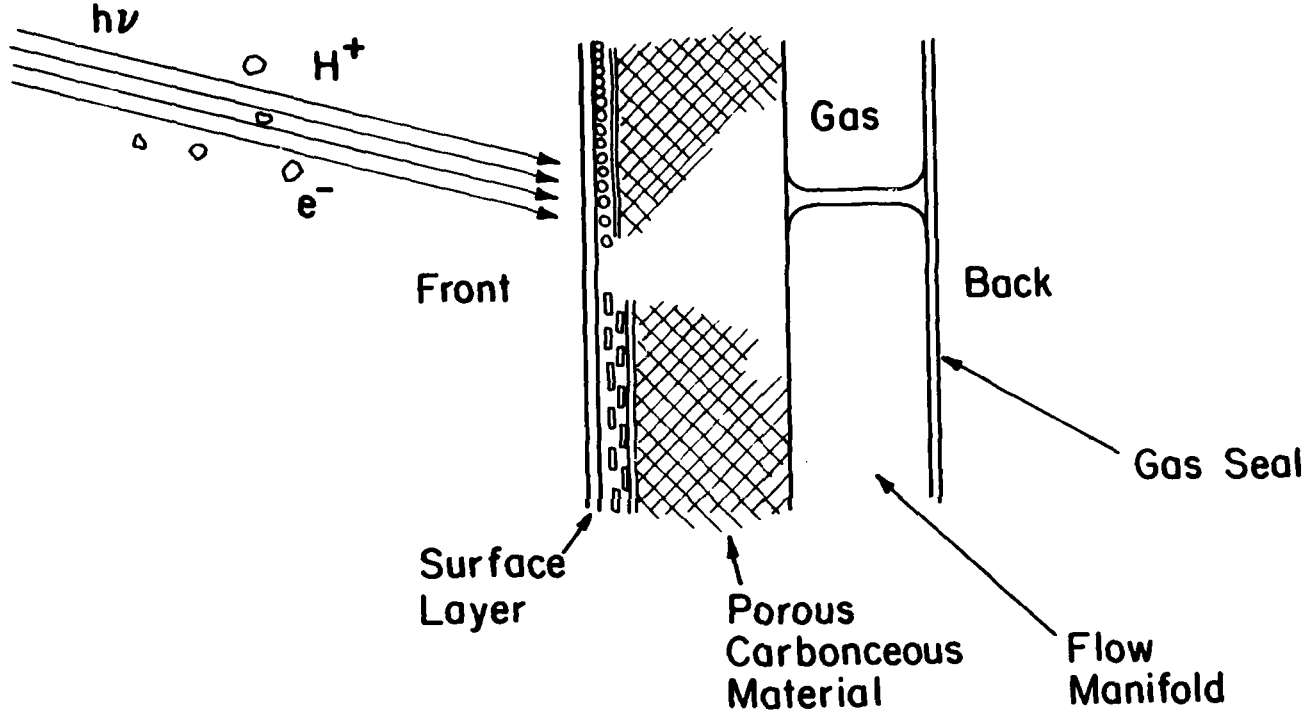

Figure 1. Model of Ablating Surface.

A number of practical materials are available, including organic resins, which can be pyrolyzed to yield foamed (low-density) carbonaceous residues[1]; natural cork, which can be ground and reconstituted in sheets; grafoil-layered sheets; graphite felts; silica felts;[2] porous glass structures;[3] or metal-graphite structures like TBR or TAC.[4] As such surface/pyrolyzing layers are heated one absorbs energy with production of hot CO, CO_2, H_2O and other gases and creation of a plasma. In all cases, the ultimate material for vacuum (non-oxidizing) environments is graphite which does not melt and has a very high heat of sublimation; in oxidizing atmospheres, metal-doped resins which yield SiC or ZrC or some other metal-carbon species which forms a protective oxide layer are preferred.

In both situations, if one anticipates multiple exposures to a laser threat, it would be desirable to have a "repair" process to rebuild ablated structures and extend the protective life. Most promising in this area is some type of chemical vapor deposition (CVD). Thus, after surviving an initial heat threat and before complete cooling, one could deposit

(1) A layer of carbon by pyrolyzing methane.

(2) A layer of boron by pyrolyzing diborane.

(3) Metallic layers from carbonyls $\left[W(CO)_6, Ni(CO)_4\right]$ etc.

(4) Refractory hard layers $(TiCl_4+CH_4) \rightarrow TiC$

$(TiCl_4+B_2H_6) \rightarrow TiB_2$

Various design parameters and special effects including the "sun-cup" phenomenon were also discussed. Chemical smokes and plasmas created by pyrolysis/vaporization, etc., offer the possibilities of absorbing incident radiation, ejecting electrons, re-radiating electromagnetically and scattering particles as energy dissipative processes.

Future investigations which should lead to better materials for ablator designs include

(a) Studies of emissivities, reflectivities and other optical properties over wide ranges of temperature and wavelengths for pure metals, alloys and refractory carbides, borides, etc.

(b) Studies of vacuum pyrolysis of different cellulosic or other carbon-based materials.

(c) Synthesis and investigation of high-temperature properties of organometallic/polymer combinations like those which produce TBR or TAC.

(d) Studies of smokes as absorptive or scattering systems for protection from laser radiation.

(e) Studies of CO/CO_2 or $CO/CO_2/H_2O$ or $C/CO/CO_2$ plasmas as systems for absorbing reflecting or scattering laser radiation.

(f) Studies of CVD processes for interim "repair" of ablative coatings.

ACKNOWLEDGEMENT

This research was supported by the Defense Advanced Research Projects Agency of the Department of Defense under Contract No. MDA903-80C-0505 with The University of Michigan.

REFERENCES

(1) E. Fitzer, K. Mueller and W. Schaefer, Chem. & Phys. of Carbon 7, pp.237-383, (1971).

2. M. Waldrop, Chem. Eng. News, May 12, 1980, pp.27-29.

3. V. Apollonov, P. Bystrov, V. Goncharov, A. Prokhorov and V. Kmoich, Sov. J. Quantum Electronics 9(12), 1499 (1979).

4. R. C. Shaffer, Hitco, Gardena, California, private communication.

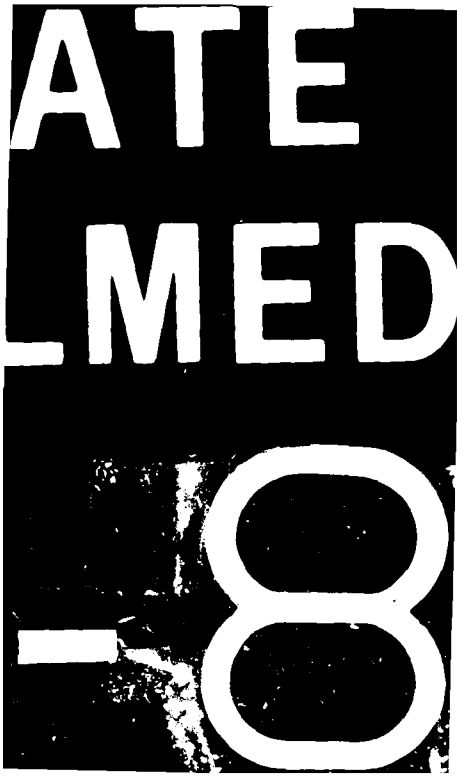
ATE
LMED
-8